PFC/RR-82-19 DOE UC-20 C, D, E

POTENTIAL CONSEQUENCES OF TOKAMAK FUSION REACTOR ACCIDENTS: THE MATERIALS IMPACT

S. J. Piet*
M. S. Kazimi
L. M. Lidsky

June 1982

Plasma Fusion Center
and the
Department of Nuclear Engineering
Massachusetts Institute of Technology
Cambridge, Massachusetts 02139

Prepared for
E.G. & G. Idaho, Inc.
and
The U.S. Department of Energy
Idaho Operations Office
under
DOE Contract #DE-AP07-79ID0019

*For part of the study, author was supported by a Magnetic Fusion Energy Technology Fellowship.

SUMMARY

Seven potential safety concerns for D-T fusion reactors were examined and the influence of blanket material choice determined. This influence was quantified in terms of Relative Consequence Indices (RCI) according to prescribed consequence criteria. The safety concerns included:

1) continued plasma heating after a loss-of-coolant,
2) afterheat after loss-of-coolant,
3) plasma disruption effects,
4) transients due to rapid chemical combustion or leakage of pressurized fluids,
5) rapid structural oxidation and volatilization,
6) corrosion, and
7) public health consequences of unit volume amounts of released radioactivity.

Selected combinations of structural material (316 SS, HT-9, V-alloy, or TZM), primary coolant (pressurized water, helium, lithium, or flibe), and tritium breeder ($LiAlO_2$, lithium, or $Li_{17}Pb_{83}$) were examined. The analyses and indices were structured to focus on the specific material properties that influence the results, which allows for comparison of materials not included in the present study.

Major advances in this work include estimation of the rapid oxidation rates of vanadium and molybdenum, modeling of corrosion product formation and behavior for the coolant/structure combinations, and development of a fusion accident consequence code entitled

FUSECRAC and its data base to calculate public health effects from fusion-specific radioisotope releases.

The safety concerns that were found to be relatively insensitive (differing by less than an order of magnitude) to material choice are: the rate of temperature increase from continued plasma heating following a loss of coolant and electromagnetic effects of plasma disruptions. The range of the RCI's was about an order of magnitude for problems concerning afterheat removal, corrosion, and the thermal effects of disruptions. The severity of the following problems were found to range over several orders of magnitude according to material choice: potential public health effects from radioactivity release, rapid structural oxidation, blanket chemical combustion and coolant pressurization.

When combustion, rapid structural oxidation, and the thermal effects of plasma disruptions are assumed solvable by identified design approaches, the Relative Consequence Indices relating to the most important safety problems illustrate the advantages of vanadium, liquid metals, and flibe.

In summary, it is possible to quantify the relative merits of various materials from a safety perspective. However, due to conflicting preferences from individual safety problems, the overal material choice is tempered by the ability of the design to render certain accidents improbable.

PUBLICATIONS UNDER CONTRACT #K-1702 ON FUSION SAFETY

1. M. S. Kazimi et al., "Aspects of Environmental Safety Analysis of Fusion Reactors," MITNE-212, Dept. of Nuclear Engineering, M.I.T., October 1977.

2. R. W. Sawdye, J. A. Sefcik, M. S. Kazimi, "Reliability Requirements for Admissible Radiological Hazards from Fusion Reactors," Trans. Am. Nucl. Soc. 27, 65-66, November 1977.

3. D. A. Dube, M. S. Kazimi and L. M. Lidsky, "Thermal Response of Fusion Reactor Containment to Lithium Fire," 3rd Top. Meeting in Fusion Reactor Technology, May 1978.

4. R. W. Sawdye and M. S. Kazimi, "Application of Probabilistic Consequence Analysis to the Assessment of Potential Radiological Hazards of Potential Hazards of Fusion Reactors," MITNE-220, Dept. of Nuclear Engineering, M.I.T., July 1978.

5. D. A. Dube and M. S. Kazimi, "Analysis of Design Strategies for Mitigating the Consequences of Lithium Fire within Containment of Controlled Thermonuclear Reactors," MITNE-219, Dept. of Nuclear Engineering, M.I.T., July 1978.

6. R. W. Sawdye and M. S. Kazimi, "Fusion Reactor Reliability Requirements Determined by Consideration of Radiological Hazards," Trans. Am. Nucl. Soc. 32, 66, June 1979.

7. R. W. Green and M. S. Kazimi, "Safety Considerations in the Design of Tokamak Toroidal Magnet Systems," Trans. ANS 32, 69, June 1979.

8. R. W. Green and M. S. Kazimi, "Aspects of Tokamak Toroidal Magnet Protection," PFC/TR-79-6, Plasma Fusion Center, M.I.T., July 1979.

9. S. J. Piet and M. S. Kazimi, "Uncertainties in Modeling of Consequences of Tritium Release from Fusion Reactors," PFC/TR-79-5, Plasma Fusion Center, M.I.T., July 1979.

10. M. J. Young and S. J. Piet, "Revisions to AIRDOS-II," PFC/TR-79-8, Contract #K-1702, Plasma Fusion Center, M.I.T., August 1979.

11. S. J. Piet and M. S. Kazimi, "Implications of Uncertainties in Modeling of Tritium Releases from Fusion Reactors," Proc. Tritium Technology in Fission, Fusion and Isotopic Applications, April 1980.

12. M. S. Tillack and M. S. Kazimi, "Development and Verification of the LITFIRE Code for Predicting the Effects of Lithium Spills in Fusion Reactor Containments," PFC/RR-80-11, Plasma Fusion Center, M.I.T., July 1980.

Publications Under Contract #K-1702 (continued)

13. M. S. Kazimi and R. W. Sawdye, "Radiological Aspects of Fusion Reactor Safety: Risk Constraints in Severe Accidents," J. of Fusion Energy, Vol. 1, No. 1, pp. 87-101, January 1981.

14. P. J. Krane and M. S. Kazimi, "An Evaluation of Accidental Water-Reactions with Lithium Compounds in Fusion Reactor Blankets," PFC/RR-81-26, Plasma Fusion Center, M.I.T., July 1981.

15. D. R. Hanchar and M. S. Kazimi, "Tritium Permeation Modelling of a Conceptual Fusion Reactor Design," PFC/RR-81-27, Plasma Fusion Center, M.I.T., July 1981.

16. M. S. Kazimi, "IAEA Workshop on Fusion Safety March 23-27, 1981, Vienna, Austria," J. of Fusion Energy, Vol. 1, No. 3, pp. 241-243, 1981.

17. M. S. Tillack and M. S. Kazimi, "Modelling of Lithium Fires," Nuclear Technology/Fusion, Vol. 2, No. 2, pp. 233-245, April 1982.

18. S. J. Piet, M. S. Kazimi and L. M. Lidsky, "Potential Consequences of Tokamak Fusion Reactor Accidents: The Materials Impact," PFC/RR-82-19, MIT Plasma Fusion Center, June 1982.

19. S. J. Piet, V. J. Gilberti, "FUSECRAC: Modifications of CRAC for Fusion Application," Nuclear Eng. Dept. and Plasma Fusion Center, M.I.T., PFC/RR-82-19, June 1982.

ACKNOWLEDGEMENTS

This work could not have been done without the financial and personal support of J. Crocker and his staff at E.G. & G. Idaho, Inc. The financial sting of graduate school for the first author was alleviated by the Magnetic Fusion Energy Technology fellowship administered for the Department of Energy by the Oak Ridge Associated Universities. Typing the manuscript was most ably accomplished by Gail Jacobson and Wynter Snow.

Several people assisted in various technical phases of this effort. Most notable were J. Jung of ANL for his values of first wall radioactivity, D. Kocher of ORNL for the external dose factors, W. Hagel and P. Grobner of the Climax Co. of Michigan for the steel oxidation data, A. Fraas for his very valuable discussions on fusion technology development, and Professor G. Yurek of MIT for his help on the rapid oxidation of refractory metals.

TABLE OF CONTENTS

Table of Contents (continued)

Table of Contents (continued -3-)

Table of Contents (continued -4-)

LIST OF FIGURES

List of Figures (continued)

List of Figures (continued -3-)

List of Figures (continued -4-)

List of Figures (continued -5-)

LIST OF TABLES

List of Tables (continued)

List of Tables (continued -3-)

List of Tables (continued -4-)

List of Tables (continued -5-)

List of Tables (continued -6-)

List of Tables (continued -7-)

List of Tables (continued -8-)

List of Tables (continued -9-)

List of Tables (continued -10-)

LIST OF SYMBOLS

a	plasma minor radius, m
A	area, m^2
A_i	wetted-wall coolant tube area in of the blanket, m^2
A_o	wetted-wall coolant tube area out of the blanket, m^2
ACT	radioactivity, Ci/cc of first wall
b	plasma heigh, m
B	magnetic field, T
B_P	poloidal magnetic field, T
B_T	toroidal magnetic field, T
Ba	Blanket attention factor, m^{-1}
c	MHD factor (Chapter 3)
C	concentration
c_p	constant pressure specific heat, J/kg°C
c_v	constant volume specific heat, J/kg°C
d	distance, thickness, m
d_{bw}	back wall thickness, m
d_m	depth of melting
d_{mm}	maximum depth of malting
d_{mv}	maximum depth of vaporization
d_{fw}	first wall thickness, m
d_v	depth of vaporization
$\dot{d}$	wall corrosion rate, μm/yr
$\dot{d}^r$	wall material release rate, μm/yr
D	diameter, m
D_e	equivalent hydraulic diameter, m
DS	dose, rem
DSC	dose committment, man-rem
DE(t)	decay heat time function (Chapter 3)
DF	dose factor
DF_{cs}	cloudshine dose factor, rem-m^3/yr-Ci

List of Symbols (continued)

DF_{gs}	groundshine dose factor, rem-m^2/yr-Ci
DF_{ig}	ingestion dose factor, rem/Ci-ingested
DF_{in}	inhalation dose factor, rem/Ci-inhaled
E	energy, J
E_e	plasma electromagnetic energy, J
ΔE	change in energy, J
E_y	Young's modules, GPa
f	function, varies
F	force, N
Fo	Fourier number
FF	friction factor
FP	fractional power (Chapter 3)
g	accelleration due to gravity, 9.8 m/sec^2
G	free energy, J/kg
ΔG	change of free energy, J/kg
h	film heat transfer coefficient, W/m^2-°C
H	entropy, J/kg
H_f	heat of melting, J/kg
H_{fg}	H_g-H_f, J/kg
H_g	heat of vaporization, J/kg
Ha	Hartmann number
ΔH	heat of reaction
I	current, Amp
I_p	plasma current, Amp
INV	radioactivity inventory, Ci or g ^3H
INV_c	coolant inventory, Ci or g-^3H
INV_d	diffusive-held inventory, Ci or g-^3H
INV_o	initial inventory, Ci or g-^3H
INV_{od}	initial diffusive-held inventory, Ci or g-^3H

List of Symbols (continued -3-)

INV_{os}	initial solubility inventory, Ci or g-^3H
INV_r	releasable inventory, Ci or g-^3H
INV_s	solubility-controlled inventory, Ci or g-^3H
INV_w	inventory on wall, Ci/m^2
J	current density, Amp/m^2
k	thermal conductivity, W/m-°C
k	reaction rate constant
k_p	linear reaction rate constant
k_s	parabolic reaction rate constant
K	Sievert's constant
L	inductance, H
m	mass, kg
$\dot{m}$	rate of change of mass, kg/sec
M	molecular mass (Chapter 6)
M	blanket energy multiplication (Chapter 2, Appendices B,C)
M_s	magnetostriction constant (Appendix D), μm/m
N	concentration
P	pressure, Pa
P_{O_2}	oxygen partial pressure, Pa
P_T	tritium partial pressure, Pa
ΔP_{loop}	pressure drop around coolant loop, Pa
PE	plasma elongation (=b/a)
q"	heat flux, W/m^2
q''_n	neutron heat flux, W/m^2
q''_T	total heat flux, W/m^2
q''_w	particle wall heat flux, W/m^2
q"'	volumetric heat generation rate, W/m^3
q'''_a	afterheat volumetric heat generation rate, W/m^3
q'''_n	nuclear (plasma neutron) volumetric heat generation rate W/m^3

List of Symbols (continued -4-)

Q	mass flow rate, m^3/sec
QD	decay heat fraction (Chapter 3)
QP	plasma heat coefficient (Chapter 3), m^{-1}
r	radius, m
r_{fw}	first wall tube radius, m
r_M	major radius of torus, m
r_w	wall radius of torus, m
R	gas constant
R_w	electrical wall resistance, ohm
RCI^i_j	relative consequence indices, see Table 9.4
s	stress, Pa
s_c	compressive stress, Pa
s_m	magnetic stress, Pa
s_p	pressure stress, Pa
s_t	tensile stress, Pa
s_T	thermal stress, Pa
s_y	yield stress, Pa
s_{uts}	ultimate tensile stress, Pa
S	entropy, J/kg °C
ΔS	change in entropy, J/kg°C
SM	safety margin
S_{mt}	stress limit, Pa
t_d	time to cause damage, sec
t_e	time for coolant to empty, sec
t_m	time to cause melting, sec
t_{pd}	time duration of plasma disruption, sec
t_v	time to cause vaporization, sec
t_w	electrical wall time constant, sec
T	temperature, °C

List of Symbols (continued -5-)

T_b	breeder temperature, °C
T_m	melting temperature, °C
T_o	operating temperature, °C
T_v	vaporization temperature, °C
ΔT_b	temperature drop across the blanket, °C
ΔT_{fw}	temperature drop across the first wall, °C
ΔT_{loop}	temperature drop around the coolant loop, °C
ΔT_{om}	$T_m - T_o$, °C
ΔT_{ov}	$T_v - T_o$, °C
ΔT_{rise}	temperature rise during a transients, °C
U	internal energy, J/kg
v	velocity, m/sec
V	volume, m^3
V_b	breeder zone volume, m^3
V_c	coolant volume, m^3
VF	view factor
x,y,z	spatial orientations
W	wall deposit thickness, kg/m^2
Z	blanket depth, m
α	thermal diffusivity, m^2/s
β	coefficient of linear expansion, $°C^{-1}$
γ	c_p/c_v
ε	emissivity
λ	decay constant, sec^{-1}
ρ	density, kg/m^3
$\Delta\phi$	potential drop, volt
ν	Poisson's ratio
μ	viscosity
μ_m	magnetic permeability

List of Symbols (continued -6-)

τ	shear stress
σ	electrical conductivity
σ_s	Stefan-Boltzman constant

CHAPTER 1. INTRODUCTION

Accident safety considerations should be included in fusion reactor research, development, and design decisions. The primary goal of this work is to discuss and quantify the relative influence of blanket material (structural material, coolant and tritium breeder) on fusion reactor accident consequences. This requires development of new safety assessment methodology and also allows some discussion of design recommendations to minimize accident consequence and frequency. The choice of the materials and specific safety issues is fairly broad; the analysis is intended to define a consistent framework to view the trade-offs among materials as well as quantify the comparison.

1.1 Purpose

1.1.1 Problem

Considerable effort has been spent on identification of proper blanket materials for fusion reactors. Each reactor design study has had to select some combination of materials for use in the blanket surrounding the plasma. Past studies have focused on the relative engineering and economic merits of various blanket materials and design concepts (see for example [1.1], [1.2]).

Other work has examined some aspects of safety and/or environmental considerations [1.3 - 1.6], although serious issues were either not addressed or not quantified. Furthermore, a consistent overview of how material selection influences reactor safety has been lacking.

Many factors have and will be included in material selection decisions. These include engineering feasibility, economics, environment

(normal operation), and safety (accidents). Current paper design studies influence the experimental program by helping to raise important issues, focusing attention on critical problems, and providing a framework to view the state-of-knowledge. Current experiments determine the future data base required in future design studies and experiments. If certain materials are improperly excluded from current research and development in favor of less appropriate ones, it will become progressively more difficult in the future to find errors and correct the development path. Obviously, research time, manpower, and money are limited; thus, the problem is to focus on the most appropriate materials.

It would be inappropriate for safety considerations to be the sole determining factor in materials choice. In the extreme, a fusion reactor could be made perfectly safe by making it so expensive that none are built. On the other hand, if safety is examined at the proper time and to the proper degree, solutions to problems can be found beforehand and woven into the fusion technology and alloy development. This offers the possibility that the future product will be substantially improved and that fusion's potential safety advantages over other energy sources will become reality.

The worst thing that could happen is if incomplete safety considerations lead to material selections that not only worsen economic and engineering feasibility, but actually decrease the overall safety of the product. This is why a consistent framework is needed to examine a variety of safety issues. Further discussion of safety (risk assessment) issues is given in Section 1.3 and Chapter 9. The three most obvious accident/safety issues have been the stored chemical energy in elemental lithium, the induced structural radioactivity, and the amount

and behavior of tritium. The attention given to lithium fires has directed development away from liquid lithium breeders. Because of the coupling between material choice (compatibility is a function of structural materials, coolants, and tritium breeders) and safety issues, this development direction may make other problems worse, indeed worsening the overall safety picture. These issues were the motivation for the present study.

1.1.2 Hypothesis

Explicitly stated, the hypothesis is that blanket material selection can significantly influence fusion safety; furthermore, that it is possible at this time to analyze the various problems and quantify the differences among materials.

In fission, the fundamental hazard source is the radioactivity caused by the fissioning process. The material selection and design does very significantly influence the possible accident scenarios and overall risk. However, the radioactive fission products and actinides are sources of hazards largely independent of the structure or coolant.

In fusion, it appears that material choice is more important. The fundamental hazard sources are the presence of a radioactive fuel (e.g., tritium, a fuel cycle and breeder question) and induced structural radioactivity (function of material choice and fuel cycle).

1.1.3 Goal

The goal is to analyze and compare a variety of important safety areas as a function of material. This must begin with the selection of the safety areas themselves and the materials of interest. In most

safety areas, improved analytical tools are needed to determine the severity of the problem. Development of new tools and use of old ones then allows comparison of potential hazard for the selected materials. If done in a consistent manner, this provides a basis for an overall examination of how material choice influences accident safety. Finally, the process should identify some specific design ideas to help minimize safety problems.

1.1.4 Scope of Work

The risk associated with a fusion reactor can be quantified as

$$\text{risk} = \sum_{\text{events}} \text{accident consequence} \times \text{accident frequency} \qquad (1.1)$$

The data base is inadequate and the design stage insufficient to perform a probablistic risk assessment of a fusion reactor. However, some of the contribution to accident probability is independent of the specific blanket design and material choice—external events (seismic, wind, flood, etc.) and some internal events (magnet malfunctions, plasma disruption). The study is basically limited to the relative consequences. For example, although the frequency of plasma disruptions is not studied, the relative consequences to various structural materials are. Although not a complete picture of fusion accident risk, it is intended that this study provide adequate insight into the relative impact of selecting different materials.

Only blanket materials are examined. Of these, analysis is primarily focused on the structural material, primary circuit coolant, and

tritium breeder. Other blanket materials such as neutron multiplier (if needed), first wall coatings (if needed), divertor/limiter structure, and reflectors are not generally considered. The combination of structure, coolant, and breeder is likely to strongly influence both design and safety, with other materials being secondary influences.

Although the safety areas considered here are generally present (qualitatively if not quantitatively) in fusion reactors of different fuel cycles and physics confinement schemes, the analysis will be based (where relevant) on one fuel cycle (D-T) and one physics scheme (steady state tokamak). The selection of a D-T tokamak and some differing aspects of alternatives are discussed in Chapter 2.

A total of seven safety problems were selected for study (see Section 1.3). This does not include all safety problems; however, those aspects which appeared most important are addressed. Eleven combinations of four structural materials, four coolants, and three tritium breeders were selected. While other materials have been mentioned, those selected are generally representative of the possibilities discussed in the fusion community. Furthermore, where possible, the precise scaling of the consequence with specific material properties is identified. Thus, it is hoped that other materials can be examined and compared, as desired, in the future. The range of materials (and their properties) selected assisted in identifying the severity of problems and the material property dependence.

1.2 Reference Material Selection

The problem of selecting materials for fusion reactors is quite complex. Besides the narrow problem here of blanket materials (primary

coolant, tritium breeder, and structure), proper materials are needed for vacuum seals, magnet shield, reflector region, limiter/divertor, and magnetic coils. Furthermore, a first wall coating and neutron multiplier may be needed. These problems are not specifically addressed in this study.

1.2.1 Selection Criteria

For this study, the criteria that were used to select specific materials and their combinations for analysis are as follows:

1) Representative of materials proposed within the fusion community.
2) Represent a fairly broad range of alternatives. For example, selection of multiple versions of austenitic steel would not have contributed much to the understanding of the material impact.
3) Not have obvious major engineering or safety problems. For example, water and elemental lithium were not used in the same combination due to the very serious potential for chemical combustion.
4) Have an adequate data base.

1.2.2 Coolant Selection

Proposed primary loop coolants fall into four categories: water, gas, liquid metals, and molten salts. Among water options (pressurized water, boiling water, and steam), pressurized water is selected due to the greater experience and fewer tritium problems. As discussed in

Chapter 8, tritium leakage through the coolant pathway is a serious problem. A one loop design such as boiling water appears to cause significantly higher problems in this regard than a two loop (primary, steam cycle) pressurized water design.

Helium is the preferred gas coolant, although others like CO_2 are possible. As helium seems the preferred gas in fission technology, there is no reason to suspect that another would be preferred for fusion.

Liquid metal coolants include Li, Na, K, and Li-Pb. Lithium and Li-Pb have the significant advantage of possible use as both coolant and tritium breeder, simplifying blanket design. The selected case, lithium, has been given far more attention in the fusion community and an extensive data base exists. Li-Pb is retained as a breeder option.

A large number of molten salts have been examined [1.7] for use as fusion reactor coolants, although few design studies have included them. None have as extensive a data base as the other coolants selected. However, molten salts appear to offer significant advantages and disadvantages compared to the alternatives; hence, they are an interesting case. The $LiF\text{-}BeF_2$ compound, flibe, was selected due to its good heat transfer properties and larger data base. In addition, flibe has some tritium breeding potential.

1.2.3 Breeder Selection

Since the D-T fuel cycle was selected, some form of lithium is required to breed tritium. The possible forms include pure liquid lithium, high temperature ceramic, liquid alloy, and solid alloy. The problems and required technology with liquid lithium are generally well known. The potential advantages of and significant attention to lithium require

its inclusion in the study.

The ceramic compounds (Li_2O, $LiAlO_2$, Li_2SiO_3, etc.) are generally alike in physical properties and behavior. The STARFIRE study [1.8] selected $LiAlO_2$ due to such advantages (perceived at the time of this study) as lower tritium inventory and chemical activity. Although $LiAlO_2$ requires a neutron multiplier for adequate tritium breeding, it was selected for this study.

Proposed alloys include Li-Pb and Li-Al compounds, although the Li-Pb series is better known and has received more attention. The lead rich alloys would be used in the liquid form. $Li_{17}Pb_{83}$ melts at 235°C. They exhibit lower chemical reactivity (see Chapter 5). The lithium rich alloys would be used in a solid form, e.g. Li_7Pb_2, but have some of the same chemical reactivity problems of liquid lithium (see Chapter 5) without the advantages of being liquid and being used as a coolant. $Li_{17}Pb_{83}$ was selected for this study.

Tritium can be recovered from the breeder and used as fuel by either in-situ or batch processing. Continuous in-situ recovery has numerous advantages over batch processing (periodic removal of tritiated breeder). As virtually all design studies have used in-situ recovery, it is adopted here. This is straightforward for the liquid breeders by simply diverting a small fraction to a tritium recovery unit. Solid breeders necessitate a purge stream (typically helium) flowing through the blanket breeding zone to carry tritium out of the blanket after it diffuses out of the solid.

1.2.4 Structural Material Selection

The selection of structural materials proved to be more difficult

than the coolant or breeder because 1) they do not tend to fall into different categories so that one could be selected from each, 2) a broader variety of materials have been proposed, and 3) all options have some serious drawbacks in either performance or data base. Some of these options are listed in Table 1.1.

The low possible operating temperatures of aluminum alloys severely limit their usefulness in a commercial reactor. High temperature super-alloys based on cobalt and nickel generally have better high temperature performance than do steels and have been proposed for blanket use, generally with helium coolant. However, the activation and radiation damage seems more severe than for steels. To limit the size of the study, these were eliminated in favor of the steels. The major difference between austenitic and ferritic steels is nickel content. The analysis in this study indicated that nickel is an unfavorable component. Hence nickel-based super alloys would tend to be less favorable than austenitic steels due to higher nickel content. Cobalt-based alloys would have excessive ^{60}Co activity.

Steels are generally compatible with a variety of coolants, have extensive data bases, and have been included in numerous design studies. The two steels selected are 316 SS and HT-9. The properties and compositions are described in Appendix B. 316 SS is an austenitic steel with a FCC crystal structure due to the presence of nickel. HT-9 is a ferritic steel with a tempered martensitic structure (forming some ferrite). Because it is a BCC, the ductile-brittle transition temperature (DBTT) is fairly distinct, unlike FCC metals. Unfortunately, there is evidence that the DBTT would rise above room temperature for HT-9 due to radia-

TABLE 1.1

Possible Structural Materials

Material	Key Relative Advantage	Key Relative Disadvantage
Aluminum alloys	Low long-term activation	Low operating temperatures
Cobalt alloys	Commercial alloys available Very good thermo-physical properties	Very high radioactivity
Nickel alloys	Commercial alloys available Very good thermo-physical properties	High radioactivity Radiation damage
Austenitic steels	Large data base and experience	Poor thermo-physical properties
Ferritic steels	Commercial alloys available Good thermo-physical properties	High ductile-brittle transition temperature
Copper alloys	Good thermal conductivity	Poor ductility and corrosion resistance
Titanium alloys	Commercial alloys available Lower radioactivity	High tritium solubility
Vanadium alloys	Very good thermo-physical properties Low radioactivity	High oxidation potential and tritium permeability
Niobium alloys	Very good thermo-physical properties	High long-term radioactivity and tritium permeability Need for superconductors
Molybdenum	Excellent thermo-physical properties and high temperature performance	High oxidation potential and long-term radioactivity High ductile-brittle transition temperature
Ceramics (C, SiC)	Low radioactivity	Least developed design concepts

tion [1.8, 1.9]. Thus proper design would have to solve the problem of HT-9 becoming brittle after shutdown as the temperature falls below its DBTT.

Titanium has a variety of good qualities, but the tritium solubility is very high. Hence a titanium first wall and blanket would likely have very high tritium inventories [1.10] which would be both an economic (fuel wasted in structure) and safety problem. Also, low thermal conductivity, poor high temperature creep resistance, and poor ductility appear to make it unattractive [1.11]. Copper alloys have also been mentioned but do not appear to have superior performance relative to other options which are more typical of fusion designs [1.11], hence there is little incentive to include them.

Vanadium and niobium alloys have very good high temperature thermophysical properties but high tritium permeability (Chapter 8). These two group VB elements are fairly similar except that niobium has slightly better thermo-physical properties and oxidation resistance, and vanadium has superior (low) radioactivity and afterheat. Because of their similarities, it was decided to select only one for this study. Since vanadium offers the potential for a relatively low activation blanket, it appeared more interesting for this study. The reference vanadium alloy is V-15Cr-5Ti.

Of the group VIB metals, attention has focused on molybdenum. The high temperature thermophysical properties are excellent. Unfortunately, the DBTT of molybdenum and TZM may rise as high as 1000°C [1.11, 1.14]. Further data may be required to clarify or reduce this problem. If the DBTT is not reduced, the design problems

are formidable and high temperature operation (to stay above the DBTT) is forced. To include a very high temperature option with superb thermo-physical properties (e.g., the TZM alloy has five times the thermal conductivity of 316 SS), the molybdenum alloy TZM was selected.

Recent attention has been given to ceramic structures such as graphite and SiC. These offer some significant advantages for the long term due to very low radioactivity and afterheat. However, there is fairly little understanding of how these brittle materials would be realistically used in a blanket concept, especially at the time this study started. The blanket concepts with the previously mentioned metals are somewhat interchangeable; it would have been extremely difficult to directly include ceramic structure in the comparative analysis—particularly since the design and construction of such a large brittle structure is so undetermined.

A recent comparative study of structural metals with respect to design properties [1.11] determined that HT-9 and vanadium-alloy were the most promising. TZM would have been so determined except for the DBTT problem which might be solvable. All three have been included in this study along with 316 SS which has been selected in many designs largely due to its extensive data base. Although only 316 SS is presently understood sufficiently to build a large fusion machine today, e.g., a Fusion Energy Device, other materials should be considered for development of future commercial reactors.

1.2.5 Other Materials

Although the prime materials of interest have been discussed, other materials had to be used in the analysis. The breeder $LiAlO_2$ requires

a neutron multiplier to provide adequate tritium breeding. The STARFIRE study [1.8] focused on beryllium and Zr_5Pb_3, and selected Zr_5Pb_3 largely due to resource considerations. In matters where the multiplier enters the current analysis, beryllium is superior due to far lower radioactivity and afterheat. It was decided not to bias results against $LiAlO_2$ by selecting Zr_5Pb_3. Although beryllium is included where necessary in this study, the reader should note that selection of $LiAlO_2$ as a breeder does necessitate a multiplier which may add to associated safety problems.

Where a reflector at the back of the blanket was needed in thermal analysis, a simple block of graphite was specified. See Chapter 2 and Appendix C for specific designs.

The analysis in this study assumes a bare metal wall facing the plasma; to specify otherwise would have either added another dimension to the study (choice of first wall coating) or biased the results to a single first wall coating. A variety of possible materials could be used to help isolate the structural wall from the plasma [1.1, 1.8]. In Chapter 6, beryllium and graphite are discussed in this regard to see if they suffer from rapid gas-solid reaction and would offer protection of the underlying structure in such an accident. In Chapter 9, some aspects of how first wall coating choice would impact safety are briefly summarized.

1.2.6 Compatibility

If all combinations of the selected materials were included, there would be 48 cases. Compatibility and practicality considerations reduce this number to 11.

First, the compatibility between coolant and breeder can be examined

(Table 1.2). The lithium/water case is unacceptable due to chemical combustion. If lithium is used as a coolant, then there is no incentive to use anything else for a breeder. The converse is not true: selection of lithium as a breeder does not force its use as a coolant. The two possible reasons are the MHD pumping power requirements necessary to force lithium across magnetic field lines as a coolant and the higher vulnerability of a lithium coolant system to accident than a breeder-only system.

Although $Li_{17}Pb_{83}$ could be used with helium and flibe coolants, there is relatively little to be learned by examining both lithium and $Li_{17}Pb_{83}$ with these coolants. The main difference between lithium and $Li_{17}Pb_{83}$ in this analysis occurs where the coolant and structure are not included—combustion (Chapter 5) and tritium (Chapter 8). Hence the analysis was simplified by not explicitly including the helium/$Li_{17}Pb_{83}$ and flibe/$Li_{17}Pb_{83}$ cases. The operating temperatures of flibe and $LiAlO_2$ do not match well. $LiAlO_2$ is used between 500 and 850°C [1.8], while flibe (melts at 459°C) may be used at higher temperatures (especially with TZM structure). Little additional would be learned if a flibe/$LiAlO_2$ case were included with the other cases. Furthermore, there may not be a metal which is compatible with both flibe and $LiAlO_2$.

Thus the twelve possible coolant/breeder combinations can be reduced to six cases with little loss of information. These six cases must then be compared with the four possible metals (Table 1.3). With the exception of the flibe/lithium case, two metals were included with each of the coolant breeder cases, leaving eleven overall combinations. The refractory metal alloys, V-15Cr-5Ti and TZM are generally not considered

TABLE 1.2

Coolant and Breeder Compatibility*

Breeder: / Coolant	Lithium	$Li_{17}Pb_{83}$	$LiAlO_2$
Water	Unacceptable	Fair**	Good**
Helium	Good**	Good	Good**
Lithium	Good**	No Reason	No Reason
Flibe	Good**	Good	Temperature Problems

*Water and lithium have an unacceptably high combustion potential. If lithium is already selected as the coolant with associated disadvantages, there is no reason to use any other breeder.

**Included in this study.

TABLE 1.3

Metal Compatibility with Coolants and Breeders

	316 SS	HT-9	V-alloy	TZM
Water/$LiAlO_2$	Good*	Good*	Poor	Poor
Water/$Li_{17}Pb_{83}$	Fair*	Fair*	Poor	Poor
Helium/Lithium	Fair*	Fair*	Poor	Poor
Helium/$LiAlO_2$	Good*	Good*	Poor	Poor
Lithium/Lithium	Fair*	Fair	Good*	Good
Flibe/Lithium	Poor	Poor	Unknown	Good*

*Included in this study.

compatible with water and helium (see Chapter 7). The steels may not be very compatible with the liquid metals, but design studies have included these cases.

Among the lithium/lithium options, 316 SS and V-alloy were selected for their differences. Finally, TZM is most resistant to flibe. Since flibe must operate well above its melting point (459°C), and the steels do not seem usable above 500°C, those cases were eliminated. The compatibility of flibe with vanadium is unknown; furthermore, there may not be an acceptable operating temperature window and little additional would be learned by including the flibe/lithium/V-alloy case.

1.2.7 Reference Combinations

The eleven reference material combinations are listed in Table 1.4. Most of the present analysis was structured to separate the effects of coolant, breeder, and structure from each other. This allows direct comparison of the options for each. Many of the safety comparisons proved to be only dependent on one of the components. The major exception was the area of corrosion where the fluid and structure are inherently coupled.

1.3 Selection of Reference Safety Comparison Bases

Having selected the materials to be studied, the bases of comparison must be established. Some examination of the relevant subsystems and their interactions is included in Appendix A. Here the reasons for the selection of the seven specific safety problems are discussed.

TABLE 1.4

Reference Material Combinations

Coolant	Breeder	Structure
Water	$LiAlO_2$	316 SS
Water	$LiAlO_2$	HT-9
Water	$Li_{17}Pb_{83}$	316 SS
Water	$Li_{17}Pb_{83}$	HT-9
Helium	$LiAlO_2$	316 SS
Helium	$LiAlO_2$	HT-9
Helium	Lithium	316 SS
Helium	Lithium	HT-9
Lithium	Lithium	316 SS
Lithium	Lithium	V-alloy
Flibe	Lithium	TZM

1.3.1 The Ideal Future Comparison

Since probabilistic risk assessment (PRA) techniques were first applied to fission reactor assessments in the Reactor Safety Study [1.12], they have become a major factor in safety analysis and regulatory actions in the fission industry. Today the study of risk has become very complex, including the so-called level 2 definition of risk [1.13] which incorporates the degree of certainty of the estimate (see Figures 1.1, 1.2). The level 1 definition of risk is more simply the estimated accident frequency and consequence.

Eventually, a detailed, optimized, design will exist for a specific fusion reactor design. With adequate data, money, time, and manpower, a PRA could be done on each material combination in this study. This technique automatically sums over "all" accident scenarios. Then, the "safest" combination could be chosen. (See Chapter 9.)

Such an effort is well beyond our needs as well as our abilities in the fusion community. The early stage of fusion development and the limited data, money, time, and manpower eliminate the option of performing one full PRA analysis, let alone eleven. Thus, a far more modest approach is sought—hopefully one that results in as much information as required.

1.3.2 Consistent Consequence Framework

Throughout the analysis, a series of Relative Consequence Indices are defined as functions of material safety comparison base (e.g., plasma disruption) and consequence criterion (e.g., time to material melting):

$$RCI_{Y}^{X} = f \text{ (material properties)} \qquad (1.2)$$

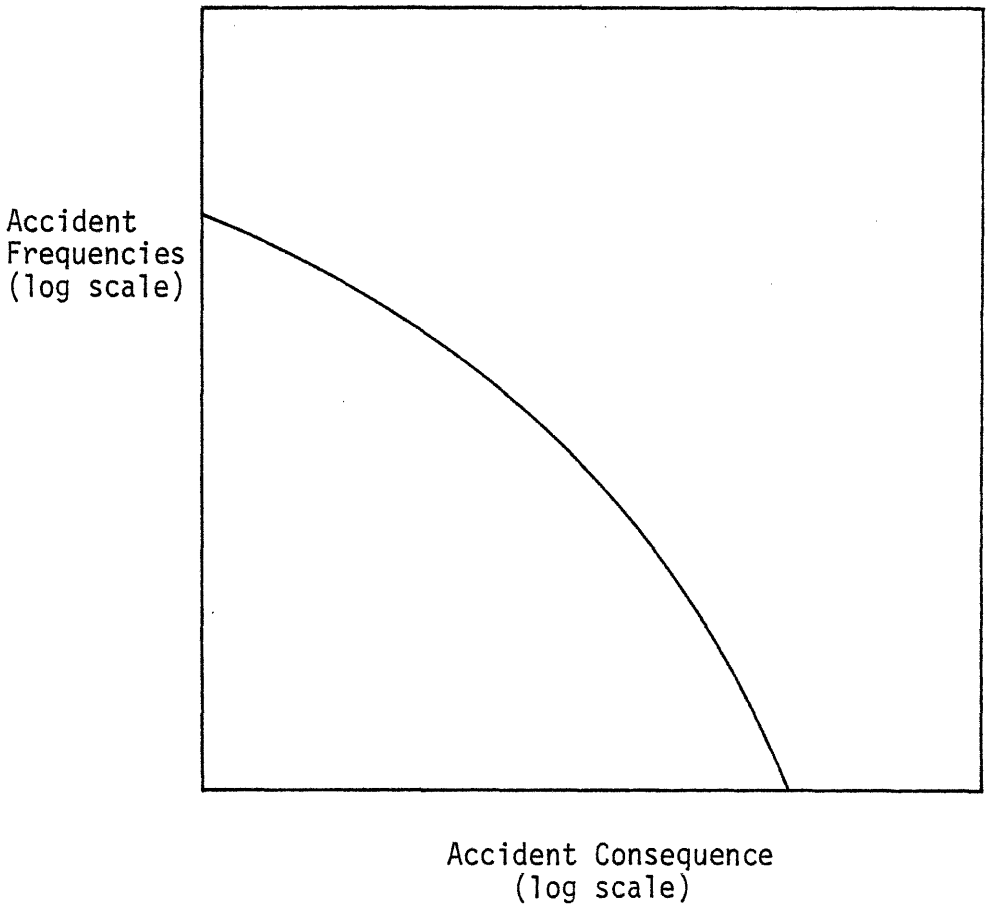

Fig. 1.1: Risk curve as a function of accident frequency and consequence—Level 1 definition of risk (see Ref. 1.13).

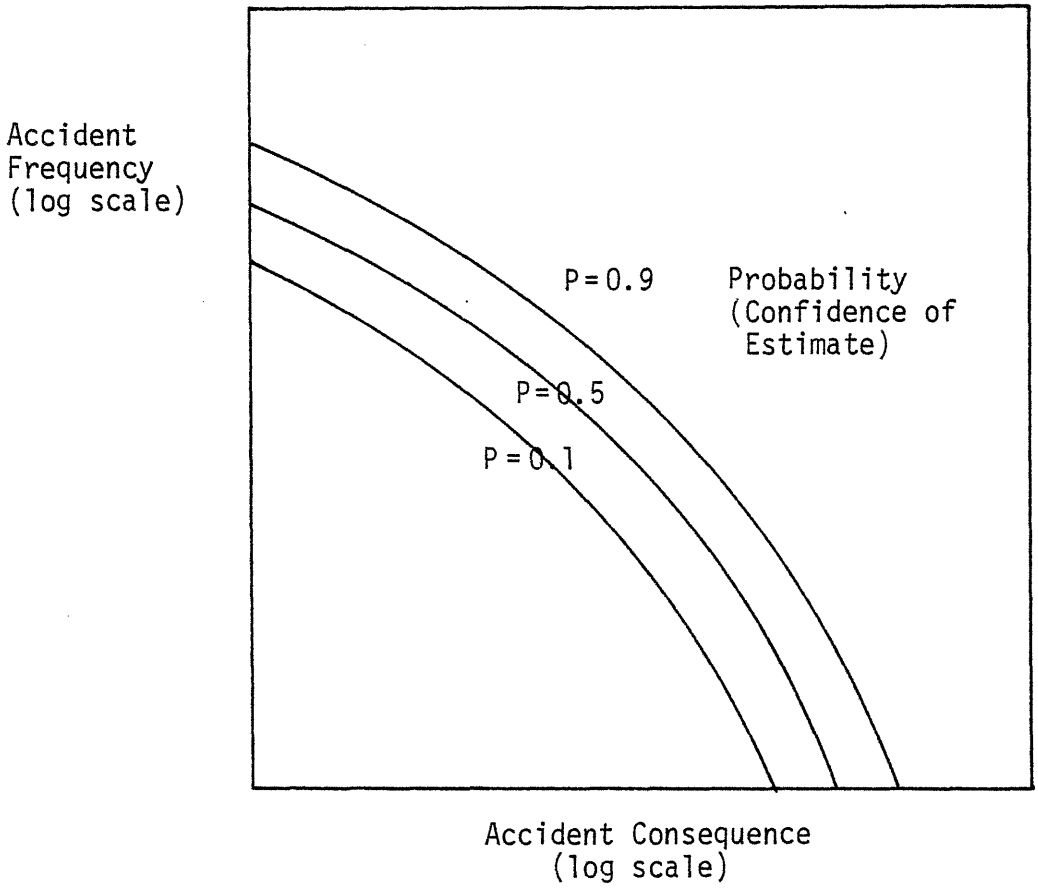

Fig. 1.2: Risk curves as functions of the probability of accident frequency and consequence - Level 2 definition of risk (see ref. 1.13).

X = consequence criterion

Y = safety comparison base

f = some implicit or explicit function of materials

These RCI's are consistently defined such that low values are preferred. Note that the same criterion may be used for different safety comparisons. For example, the inverse of the time to reach melting criterion is used for the bases of plasma disruption, loss-of-coolant with continued plasma heating, and loss-of-coolant with only afterheat. Since this is a comparative study, and the absolute magnitude of the problem is sometimes unknown or unimportant, the indices defined are relative (or normalized). Generally, the RCI's are normalized such that the individual best case is given the value 1.0. In some cases, the best value for the criterion is either zero or very uncertain. In those cases, a somewhat arbitrary normalization value is selected with the aim that an RCI of 1.0 represents an "acceptable" level of a problem or the most realistic best estimate. Therefore an RCI less then one is possible. An example is the oxidation rate of structural materials. The best case is zero; however, for the accident transient problem of mobilizing radioactive structural material, a normalization value of 1 mm of metal per day was deemed an appropriate normalization value.

Although this methodology does not contain as much information as a PRA, especially probabilities, it does represent a first order attempt to quantify the various safety differences among materials.

1.3.3 Hazard Identification

The fundamental hazard to the public is the release of radioactivity to the plant surroundings in quantities above negligible fractions of

natural radioactivity. As indicated in Table 1.5, both normal continuous release and accident releases are of concern. The radioactive fuel tritium is a major concern. The neutrons from the D-T reaction activate the blanket materials and even the building atmosphere. As the structure corrodes, activated corrosion products become mobile. The activation of the building atmosphere is insignificant in accidents, although sufficiently important under normal operation that the STARFIRE study used a CO_2 atmosphere to avoid nitrogen activation to ^{14}C.

The foci of this study are the contributions to accidental releases of tritium, corrosion products, and activated structure. Continuous releases, maintenance problems, and waste disposal/material recycling issues are not addressed. One exception is that some examination of tritium normal releases through the coolant pathway is included in Chapter 8.

Chemical toxicity is another fundamental hazard (for example, see Ref. [1.6]). These problems are not explicitly addressed in this study, although all the measures of merit concerning release of radioactive material are equally relevant to release of toxic material. The missing aspect is a thorough comparison of chemical and radiological toxicity of all the materials present. Unfortunately, the understanding of chemical toxicity is inadequate to quantify the hazard, especially compared to radioactivity. With some possible exceptions, as beryllium, the radioactive hazards appear to dominate over chemical toxicity from fusion accidents.

Other hazards to the public from fusion accidents do not appear important. For example, in principle, a fire could start somewhere at

TABLE 1.5

Radioactivity and Fusion

Radioactive Species	Continuous Release	Accidental Release
Tritium	Major concern	Easier to release, lower consequence
Activated Corrosion Products	Minor concern (major maintenance concern)	Easy to release, modest consequence
Activated Structure	Unknown level of concern (solid wastes)	Difficult to release, higher consequence
Activated Building Atmosphere	Significant concern	Easiest to release, lowest consequences

a reactor site which could be directly hazardous to the public. Except insofar as such a fire releases toxic agents, the exclusion zone around a reactor would tend to eliminate fire spreading to the public. In any case, such external fires would seem independent of blanket materials enclosed in the containment building (any blanket fire would be more important in terms of radioactivity release).

1.3.4 Energy Sources/Mechanisms

As other studies have indicated, there are large amounts of stored energy present in a reactor. The relevant question is whether there is a possible mechanism to actually couple this stored energy to the reactor components in such a way as to mobilize and release radioactivity. There is the auxiliary question of whether there is a mechanism that causes reactor component damage which could in turn lead to later radioactivity release and/or severe economic consequences (not directly considered in this safety study). Table 1.6 shows the possible release modes with further discussion in Appendix A.

The important issues are thus 1) the mechanisms that may produce high stresses or temperatures, 2) the oxidation and volatization rate of structure materials, and 3) the consequence of the radioactivity if it were released.

The possible mechanisms that may produce high stresses or temperatures are listed in Table 1.7. Those mechanisms external to the blanket were not considered. In a sense, the relative influence to accident safety of materials from these external events is covered by the oxidation rate and radioactivity consequence measures.

TABLE 1.6

Possible Accidental Release Modes

Release Species	Release Mode	Possible Causes
Tritium	Breeder or coolant system integrity breached	—high stresses or temperatures —component failure
Activated Corrosion Products	Coolant line integrity breached	—high stresses or temperatures —component failure
Activated Structural Radioactivity	1) Melting	—very high temperatures
	2) Rapid Metal Oxidation and volatilization	—high temperatures and oxidant available

TABLE 1.7

Possible Mechanisms that Couple Stored Energy to Systems Resulting in Accidental Releases

High temperatures due to plasma operation with loss-of-cooling

High temperatures due to radioactive afterheat with loss-of-cooling

High temperatures and/or stresses due to a plasma disruption

High temperatures or pressures due to chemical combustion

High temperatures or stresses due to a magnet quench/failure or auxiliary plasma system (not considered in this study)

External events (seismic, wind, flood, etc.) (not considered in this study)

The remaining four mechanisms were adopted as safety comparison bases. The first three are thermo-mechanical considerations. Since the relative scaling of materials differs between plasma heating and afterheat with loss-of-cooling, these mechanisms are separated as discussed in Chapter 3.

The area of chemical reactions involved more than combustion (Table 1.8). For present purposes, combustion is defined to include fluid-fluid rapid chemical reactions and fluid-$LiAlO_2$ chemical reactions. The combustion chapter (5) also includes pressurization problems from pressurized water and helium. Fluids include the liquid coolants and breeders, air and CO_2 (possible building atmospheres), helium and steam (from coolants), and $LiAlO_2$ (which fits best into this category).

Structural oxidation refers to rapid gas-metal reactions which can oxidize (damage) and volatilize structural radioactivity if temperatures are sufficiently high (from whatever mechanism) and oxidants (air, CO_2, steam) are present. The Zircaloy-steam reaction is a fission example. Corrosion products are slowly evolved due to fluid-metal reactions (neutron sputtering is also included) and thus represent mobilized radioactivity. Solid-solid reactions are possible in principle, like the Zircaloy-UO_2 interaction in fission reactors; however, these were not examined. In general, solid-solid reactions do not appear to offer significant (relative to the alternative mechanisms) potential for severe accident safety problems.

1.3.5 Reference Safety Comparison Bases

The four accident mechanisms internal to the blanket (Table 1.7) are

TABLE 1.8

Possible Classes of Chemical Reactions*

	Gas	Liquid (and $LiAlO_2$)	Structural Metal
Gas	Combusion (5)	Combustion (5)	Structural Oxidation (6)
Liquid	—	Combustion (5)	Corrosion Products (7)
Solid	—	—	Not included in this study
Included Materials	Air (O_2, N_2) Steam Helium (CO_2)	Water Lithium $Li_{17}Pb_{83}$ Flibe $LiAlO_2$	3.6 SS HT-9 V-alloy TZM (Be, C)**

*Chapter numbers are indicated in parentheses.

**Possible first wall coatings of beryllium and graphite were discussed to indicate the widespread nature of the structural oxidation problem.

four of the safety issues. Rapid structural oxidation is a prime mechanism for actual radioactivity mobilization given elevated temperatures and an oxidant. Another mobilization mechanism is corrosion so that at any given time a certain (small) fraction of the reactor radioactivity is in the form of corrosion products which may be fairly mobile. These two mobilization pathways are additional safety issues. The final safety concern is the actual public consequence from released radioactivity, both short- (acute) and long-term (latent cancers). The seven safety issues are listed in Table 1.9.

It is important to note that non-accident issues were excluded. Hence selection criteria for materials on the bases of such issues as material resource, waste generation and disposal, material recycling, and reactor decommissioning were not addressed.

1.3.6 Task Organization

The organization of the various tasks in this study is shown in Figure 1.3. The selection of safety issues and material combinations was discussed in this chapter with some additional examination in Appendix A. The values of material properties used are indicated in Appendix B. The selection of reference design parameters and blanket concepts required for the specific individual analyses is discussed in Chapter 2 with some details in Appendix C. Chapters 3 through 8 contain analyses in the various safety areas and are generally independent of each other. The two LOCA-related issues are grouped into Chapter 3; the other five chapters are devoted to the other five safety issues. The results of the analyses are briefly summarized in Chapter 9 along with a detailed discussion of the results and implications for material selection.

TABLE 1.9

Reference Safety Comparison Bases

LP — LOCA-Plasma Heating: Thermal transients from continued plasma heating after loss-of-coolant

LA — LOCA-Afterheat: Thermal transients from afterheat after loss-of-coolant

PD — Plasma Disruption: Effects from plasma disruption

TP — Temperature and Pressure: Transients due to rapid chemical combustion and leakage of pressurized fluids

SO — Structural Oxidation: Rate of structural oxidation and mobilization from rapid gas-structural-metal reaction

CP — Corrosion Products: Amount and associated problems of corrosion products

RC — Radioactivity Consequences: Public health consequences of unit amounts of released radioactivity

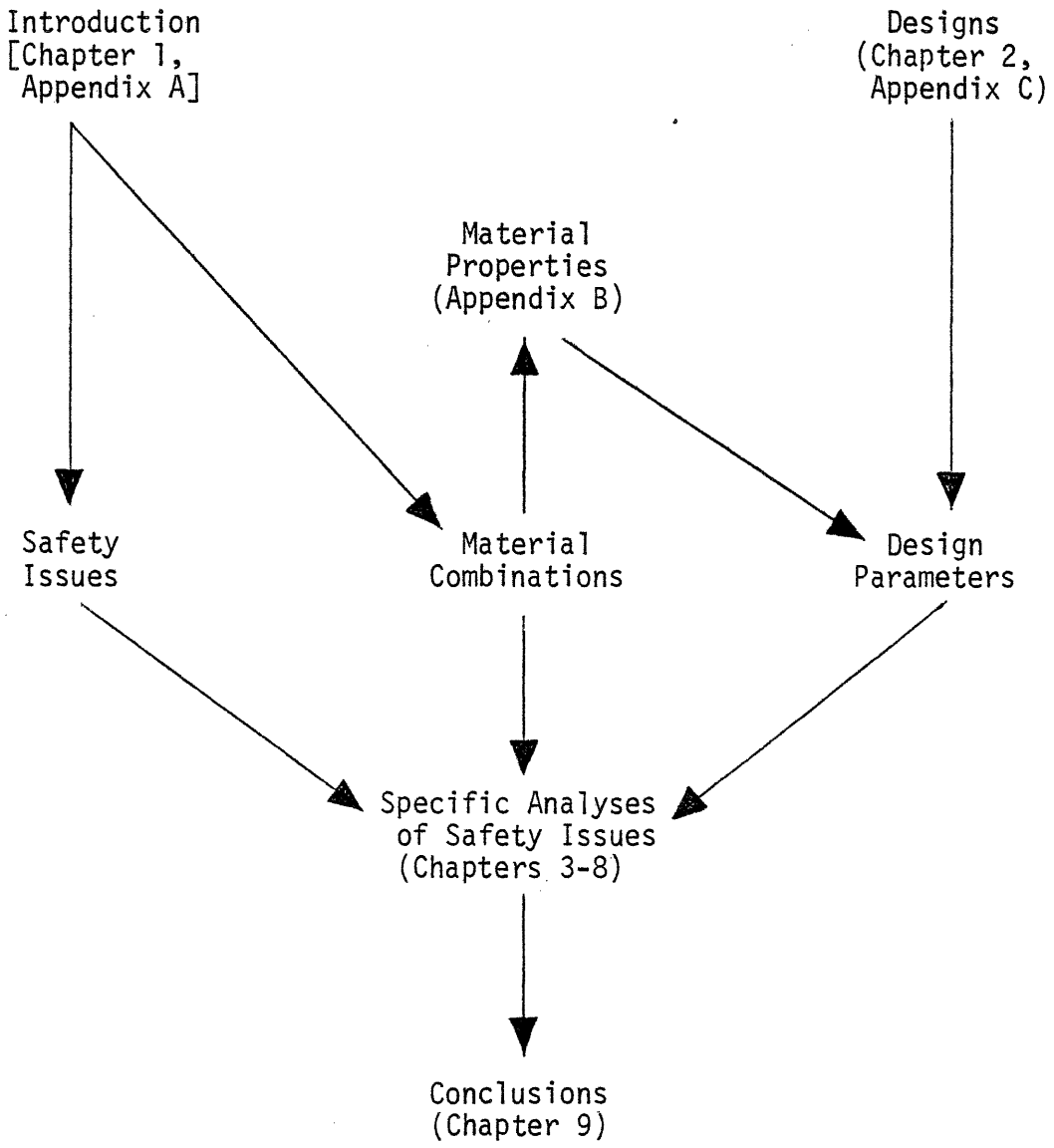

Fig. 1.3: Task organization flow chart.

REFERENCES

1.1 D. C. Smith, et al., "Fusion Reactor Blanket/Shield Design Study," ANL/FPP-79-1, 7/1979.

1.2 "Fusion Reactor First Wall/Blanket Systems Analysis' Tokamak Concepts," EPRI-ER-582, 11/1977.

1.3 J. R. Young, "An Environmental Analysis of Fusion Power to Determine Related R & D Needs," BNWL-2010, 11/1976, see also the series, BNWL-2010-2028.

1.4 D. Steiner and A. P. Fraas, "Preliminary Observations on the Radiological Implications of Fusion Power," Nuclear Safety, 13 (5), 353 (1972).

1.5 W. E. Kastenberg, et al., "Some Safety Considerations for Conceptual Tokamka Fusion Power Reactors," EPRI-ER-546, 7/1978.

1.6 W. Hafele, et al., Fusion and Fast Breeder Reactors, International Institute for Applied Systems Analysis, Laxenburg, Austria, Report A-2361, 11/1976.

1.7 W. R. Grimes and S. Cantor, "Molten Salts as Blanket Fluids in Controlled Fusion Reactors," Chemistry of Fusion Technology, 1972.

1.8 C. C. Baker, et al., "STARFIRE—A Commercial Tokamak Fusion Power Plant Study," ANL/FPP-80-1, 9/1980.

1.9 R. W. Conn, et al., "SATYR Studies of a D-D Fueled Axisymmetric Tandem Mirror Reactor," PPG-576(UCLA), 9/1981.

1.10 "STARFIRE—An Interim Report," ANL/FPP/TM-125, 12/1979.

1.11 G. P. Yu, "Relationship of Material Properties to the Design of a Fusion Reactor First Wall," Sc.D. thesis, Department of Nuclear Engineering, Massachusetts Institute of Technology, 1981.

1.12 "Reactor Safety Study," WASH-1400, 10/1975.

1.13 S. Kaplan and B. J. Garrick, "On the Quantitative Definitions of Risk," Risk Analysis, 1(1), 1981.

1.14 B. L. Cox and F. W. Wiffen, "The Ductility in Bending of Molybdenum Alloys Irradiated Between 425 and 1000°C," Journal of Nuclear Materials, 85 and 86 (1979), p. 901.

CHAPTER 2. REFERENCE REACTOR DESIGNS

A consistent reactor design basis is required to compare the material effects on accident safety. Yet, the choice of coolant, breeder, and structural material forces significant design differences. Ideally, one would compare materials on the basis of a fully optimized design for each combination. The state-of-knowledge in fusion reactor design does not permit this; furthermore, the meaning of "optimized" for a fusion design is not itself determined. A secondary goal of this work is to provide some design guidelines and suggestions to aid in factoring safety into future designs.

The approach taken here is to fix some plant parameters for all material combinations, these include overall size, confinement scheme, wall loading, and (within the variation of blanket energy multiplication) the reactor power output. This is discussed in section 2.1

For each material combination case, some blanket parameters are needed. These parameters are established by appropriate scaling and modification of representative blanket design concepts already available in the literature. The safety analysis does not generally focus on very detailed aspects of design; rather, the emphasis is on producing a general result. Although the parameters and blanket concepts are not fully optimized, the values used are intended to be typical and representative of current design concepts.

2.1 Reference Size Reactor

Initial analyses of the safety problems indicated that a variety

of design parameters were required to complete the calculations. Unfortunately, some of these parameters are not directly calculated in previous design studies. The most detailed design studies currently available are based on tokamaks. The most detailed tokamak design study is STARFIRE [2.1].

2.1.1 Plasma Confinement Scheme

At the current stage of fusion research, the plasma confinement scheme and fuel cycle are uncertain. However, it is generally agreed that the first generation pure fusion reactor will utilize a D-T fuel cycle, which is adopted here. Selection of a more advanced fuel cycle would significantly alter some safety conclusions. The amount of tritium, lithium compound, wall loadings, and induced radioactivity can all change. Similarly, a fission/fusion hybrid would have some significantly different safety problems. Depending on the amount of fissioning allowed, the afterheat and radioactivity of the fission zone could be more important than that of the other materials. Although the current study is limited to a D-T cycle, some problems associated with materials are generic, e.g., highly pressurized water, rapid gas-metal reactions, and some corrosion aspects.

Recently some studies [2.14 - 2.16] have examined the difference between various fusion fuel cycles, primarily D-D versus D-T. The result appears that D-D is not necessarily better than D-T even though the D-D cycle has half the amount of energy leaving the plasma as neutrons, lower energy neutrons (2.45 MeV versus 14.1 MeV), and does not have to breed tritium. The fundamental problems include a lower power density which greatly increases the volume of material required (which can then become

activated) and a higher number of neutrons (although at lower energy). Although the absolute severity of the various safety problems may differ from D-T to D-D, many of the relative comparisons appear not to, including corrosion, rapid structural oxidation, LOCA-plasma heating, and plasma disruptions. Chemical combustion would be altered due to the elimination of lithium compounds. Since the specific isotope mix for the different isotopes may change, the relative comparison among materials in the areas of radioactivity and afterheat may be altered. However, the biological hazard potential in air (BHP_{air}) did not change very significantly from D-T to D-D for the materials 316 SS, V-15Cr-5Ti, and Ti4381 [2.15], suggesting that the relative rank ordering in radioactivity and afterheat may not be affected.

A wealth of plasma confinement schemes is being considered by the fusion community. These range from light ion particle beam (inertial confinement) to tokamaks (magnetic confinement). The various physics schemes result in some differences in the blanket zone which would affect safety. These include 1) the presence, strength, orientation, and off-normal behavior of the magnetic fields; 2) the geometry of the blanket; 3) first wall design and constraints; and 4) over power/transient plasma problems (e.g., plasma disruptions in tokamaks). The most detailed and understood blanket engineering and designs have been done for the tokamak confinement concept. Furthermore, there are some safety-related aspects of tokamak blankets that are not as severe in other physics concepts, e.g., plasma disruptions. The present analysis is based on a steady state tokamak design concept.

2.1.2 Selection of STARFIRE Design

The analysis was limited to one generic reactor design, STARFIRE [2.1]. Some of the variables fixed (and their values) by this selection are listed in Table 2.1. The most significant of these for the current study are the neutron wall loading (q''_n), surface heat flux (q''_w), major radius (r_M), and average minor wall radius (r_w). The current trend in tokamak designs is toward neutron wall loadings in the 3-4 Mw/m^2 range with corresponding heat flux. There has also been some convergence of reactor size. In these respects, the STARFIRE design parameters are representative.

Although current physics seems to indicate better plasma performance for elongated plasmas (PE = b/a $\sim$ 1.6), the analysis will be primarily based on a simplified circular cross section torus. Thus, the poloidal variation in wall radius and neutron and heat wall loadings will be ignored in favor of analysis based on average values.

Steady state operation is common for the alternative physics confinement schemes of torsatron/stellerators, EBT's, and mirrors. The STARFIRE design is the first steady state tokamak design. For the present purpose, the primary impact of steady state operation will be to relax first wall design constraints and allow longer module lifetimes.

2.2 Blanket Parameter Selection Approach

A variety of blanket parameters are used in some safety analysis. A list of the major parameters is shown in Table 2.2. The coolant and breeder volumes refer to the entire volume in the circuit, in or out of the blanket. Some values were not calculated in past design studies, for example the wetted coolant tube wall areas, and had to be calculated

TABLE 2.1

Reference Machine Parameters
(from STARFIRE [2.1])

Neutron Wall Loading	3.6 MW/m^2
Surface Heat Flux	0.9 MW/m^2
Major Radius	7.0 m
Plasma Half-width	1.94 m
Average Wall Radius*	2.8 m
Plasma Elongation	1.6
Plasma Current	10.1 MAmp
Average Toroidal Beta	6.7%
Toroidal Field on Axis	5.8 T
Maximum Toroidal Field	11.1 T
Number of Toroidal Field Coils	12
Base Thermal Power Output	4000 MW
First Wall Area	780 m^2
Reactor Building Volume	2.5×10^5 m^3
Stored Energy in Toroidal Coils	4.17×10^9 J/coil

*wall radius giving same total first wall area as STARFIRE for a circular cross section.

Table 2.2

Some Required Blanket Design Parameters

First Wall Thickness, d_{fw}

Temperature Drop Across the First Wall, ΔT_{fw}

First Wall Tube Radius, r_{fw}

Structural Operating Temperature, T_o

Blanket Depth, Z

Coolant Pressure, P

Coolant Mass Flow Rate, Q

Coolant Volume, V_c

Wetted Surface Area, In-blanket, A_i

Wetted Surface Area, Out-blanket, A_o

Coolant Temperatures

Breeder Volume, V_b

Breeder Zone Temperature, T_b

here. Some specifics of the calculations are discussed in Appendix C.

2.2.1 Selection Criteria

The parameters and blanket concepts choices were guided by three criteria. First, the conceptual design and parameters should be representative of current thinking. Second, designs with the same coolant should be as similar as practical to make comparisons easier. Third, the designs should have a minimum of serious flaws. No attempt was made to fully optimize each base case, although the reference design parameters should represent a fair example of a representative design for each material combination.

An alternative approach would have been to use one blanket concept for all material combinations, as has been done by some past blanket trade-off studies. The selection of materials for a fusion blanket is inherently three-dimensional - structure, coolant, breeder. Selection of first wall coatings and neutron multipliers, if needed, would further complicate the issue. Blankets utilizing different materials may look significantly different; for example, the selection of the coolant naturally guides the designer to different blanket concepts.

Whereas specific designs for various combinations may differ from the parameters used here, it is hoped that the representative nature of the values leads to a general result. Furthermore, the influence of design parameters is indicated throughout the analysis. Finally, in many cases, the relative comparison among materials is independent of design specifics.

For each material combination, the first step is the adoption of a conceptual blanket design. This is strongly driven by the coolant characteristics, especially the operating pressure. Specific design paramaters are then determined, partially influenced by structural material design limits.

2.2.2 Coolant Pressure Influence

The operating pressures of fusion reactor coolants range from 15 MPa (helium) to under 1 MPa (flibe), with helium (5 MPa) and lithium (1 MPa) intermediate. A primary design question, relevant to accident analysis, is whether the entire module is designed to withstand full coolant pressure or only coolant tubes contain the pressure. The latter case may lead to high pressure coolant entering the low pressure breeding zone and causing structural damage as the module fails (see Chapter 5). Since the general maintenance approach is to remove and replace failed blanket modules, an accident that could sufficiently deform a module to prevent removal would be extremely economically serious.

Flibe operates at such low pressures that accidental pressurization of a breeder zone is not a serious concern. The same holds true for lithium, especially when used as both coolant and breeder. Helium and water would be used at high pressures.

There are two general approaches to helium design. First, the entire module may be designed to withstand full 5 MPa pressurization. This reduces the accidental breeder zone pressurization problem. Second, only discrete coolant tubes are designed to the helium coolant

pressure. Since the breeder zone structure is not built to withstand coolant pressure, a leakage of helium to the breeder zone results in module failure. The first approach is used for helium in this study. The higher operating pressure for water (about 15MPa) appears to force the second (coolant tube) design approach for pressurized water.

2.2.3 Determination of First Wall Thickness

The appropriate structural design of a fusion first wall/blanket is an immensely complicated problem. As usual, the worse difficulties arise at the first wall. The fundamental approach here will be to examine appropriate stress constraints and select first wall thickness.

The required data on material properties irradiated in a fusion environment does not exist for any material. More is thought to be known about stainless steel, largely through extrapolation from fission data. Data on vanadium and molybdenum alloys are poor; there are even severe gaps in the unirradiated data base. Thus, the present study will use unirradiated metal properties as indicated in Appendix B.

Irradiation tends to alter material properties such as strength, ductility, and swelling. The values of these properties for materials in a fusion environment is not known. Neither is the precise alloy composition which also influences these properties. Early recognition of this problem led to structuring the analysis to focus on those properties which are relatively independent of irradiation and alloying effects: thermal conductivity, heat capacity, density, and electrical conductivity. Thus the uncertainty due to irradiation and alloy development is minimized in this study. The major uncertainty in this study from alloy composition is radioactivity/afterheat: relatively small changes in alloy composition

could significantly change radioactivity and afterheat values.

Design limits were established to be about 10^5 hrs (11 years) and 10^3 cycles (1 cycle/week for a steady state machine). The lifetime design value is more conservative than that expected in design studies, for example 6 yr. for STARFIRE [2.1] modules and 2 yr for Westinghouse/ORNL modules [2.2], which partially offsets the use of unirradiated properties. The low number of cycles essentially removes the fatigue constraint, as one would expect for steady state operation.

The relevant stress criteria for fusion have been studied elsewhere [2.2 - 2.6], sometimes based on the relevant section of the ASME code [2.7]. The ASME code requires that the primary stress be less than the time dependent stress intensity value, S_{mt}. For a cylinder we obtain the pressure stress, s_p, as

$$s_p = P \frac{r_{fw}}{d_{fw}} \tag{2.1}$$

where r_{fw} = cylinder radius (first wall coolant tube radius)

d_{fw} = cylinder wall thickness

Therefore the minimum first wall thickness is given by

$$d_{fw}\Big|_{min} = Pr_{fw}/S_{mt}(10^5 \text{ hrs}) \tag{2.2}$$

The values for S_{mt} were obtained from Yu [2.4], see Appendix B.

The maximum thickness is largely determined by thermal stress, s_T, considerations. The thermal stress of a cylinder unconstrained in

the axial direction is given by

$$s_T = \frac{E_y \beta q''_w}{2k(1-\nu)} \tag{2.3}$$

The problem can become quite complex as indicated in previous stress analyses [2.2 - 2.6]. However, assumption of steady state simplifies the analysis. These constraints are considered here. First, the effective combined stress should be less than the yield stress. Second, the corresponding temperature drop across the first wall is limited for each conceptual design by temperature constraints (maximize coolant temperature, minimize the maximum structural temperatures). Third, the fatigue limit is addressed.

The total stress from pressure and thermal affects should be less than yield for purely elastic behavior:

$$s_p + s_T < s_y \tag{2.4}$$

Substituting expressions for s_p and s_T, we have

$$Pr_{fw}/d_{fw} + \frac{E_y \beta q''_w}{2k(1-\nu)} d_{fw} < s_y \tag{2.5}$$

where q''_w = wall heat flux = 0.9 MW/m^2.

The minimum total stress is then given by

$$d_{fw}(\text{minimum stress}) \sim \left[\frac{2Pr_{fw}k(1-\nu)}{E\beta q''_w}\right] 1/2 \tag{2.6}$$

The maximum practical temperature drop across the first wall leads to an upper limit on wall thickness

$$d_{fw}\Big|_{max} = \frac{k}{q''_w} \Delta T_{fw}\Big|_{max} \tag{2.7}$$

The fatigue limit on cyclic thermal stresses is given by [2.4,2.5],

$$d_{fw}\Big|^{fatigue}_{max} = \frac{2k(1-\nu)}{\beta q''_w} \varepsilon_T \ (10^3 \text{ cycles}) \tag{2.8}$$

where ε_T (10^3 cycles) = maximum strain for 10^3 cycles (values from reference 2.4).

It should be noted that other design limits are possible (see for example reference 2.6), however these first order guidelines will be seen to lead to values similar to those resulting from detailed design studies.

2.2.4 Neutronics Constraints

Neutronics plays a major role in fusion reactor blanket design. The tritium breeding ratio must be greater than one to close the fuel cycle. The blanket thickness must be sufficient to obtain a good breeding ratio and limit the neutron flux to the magnet shield and magnet. The amount of energy multiplication in the blanket also determines the total thermal output. This output is given for the reference size machine approximately by

$$\text{Power } (MW_e) \sim 700 + 2800 \times M \qquad (2.9)$$

where M = Blanket multiplication energy factor

700 = Heat incident on first wall

2800 = Neutron energy deposited in blanket.

Additional energy is deposited in the limiter.

The exact values for the blanket depth and energy multiplication can be determined by detailed neutronics calculation. It was deemed beyond the scope of this study to perform such calculations for each material combination. To first approximation, the choice of breeder determines these parameters. Thus, approximate values were used for this study (Table 2.3) based on previous design study values (see Appendices B, C).

2.3 Water-Cooled Designs

The major features of a pressurized water design are the accomodation of high pressures (15.2 MPa) but lower coolant temperatures ($\sim$ 300°C). The high pressures make it impractical to design the module interior to withstand full coolant pressure [2.5]. The result is a tube design, keeping the water within discrete tubes and allowing the breeder material to operate near atmospheric pressure.

The reference design study for water-cooled designs is STARFIRE [2.1]. All of the necessary information is thus available for the $LiAlO_2$ / 316 SS case. The problem is then to rescale the design for the other three water cases. Two adjustments must be made - change of breeder material and structural material.

Table 2.3

Approximate Neutronics Values Used for Reference Designs*

Breeder	Blanket Depth, Z (m).	Energy Multiplication, M
$LiAlO_2$	0.45 (with 0.05 multiplier)	1.15
Lithium	0.60	1.20
$Li_{17}Pb_{83}$	0.50	1.25

*see Appendices B, C

2.3.1 Breeder Change

Use of $Li_{17}Pb_{83}$ breeder rather than $LiAlO_2$ causes a variety of changes. The higher energy multiplication causes slightly higher coolant flow rates. The neutron multiplier is removed, as well as the second wall in the STARFIRE design which cools it. Finally, since the thermal conductivity of $Li_{17}Pb_{83}$ is more than 10-fold that of $LiAlO_2$, there would be need for fewer coolant tubes in the breeder zone (fewer tubes with more coolant). The average wall heat flux through the coolant tubes in the $LiAlO_2$ breeder is 0.38 MW/m^2. The higher conductivity of $Li_{17}Pb_{83}$ could result in use of a 50% higher coolant wall heat flux with a corresponding 50% decrease in tube wall area.

2.3.2 Metal Change

The change in structural material requires examination of the stresses involved. The maximum structural temperature in STARFIRE is 450°C for 316 SS. Examination of S_{mt} values in reference 2.4 lead to adoption of the same temperature for HT-9. Using Eqs. (2.1) and (2.3), the pressure and thermal stresses for 316 SS are seen to be 100 MPa and 194 MPa respectively. These meet the stress limitations as follows

$$s_p = 100 \text{ MPa} < 108 = S_{mt}(10^5 \text{ hr}) \tag{2.10}$$

$$s_p + s_p = 294 \text{ MPa} < 520 = s_y \tag{2.11}$$

The more detailed analysis in the STARFIRE study showed a total stress of

about 207 MPa for much of the first wall panel, but 560 MPa for the worst constrained junction.

For HT-9, the stresses are given by

$$s_p \text{ (MPa)} = \frac{150}{d_{fw}} \text{ (mm)} \tag{2.12}$$

$$s_T \text{ (MPa)} = 54 \times d_{fw} \text{(mm)} \tag{2.13}$$

The minimum wall thickness given by Eq. (2.2) is then 0.94 mm. The maximum stress from the yield criterion (Eq. (2.4)) is 6 mm. To keep the first wall temperature drop below 100°C implies a maximum thickness of 3 mm. The minimum total stress (Eq. (2.6)) occurs at about 1.6 mm. For the present study a value of 1.5 mm. is adopted, the same as for 316 SS. A summary of parameters occurs in Table 2.4; calculation details are in Appendix C. The blanket concepts are shown in Figs. 2.1, 2.2.

2.4 Helium-Cooled Designs

In contrast to water, there have been many more helium designs, with large differences in design philosophy (e.g., pressurized cannister, breeder block, see reference 2.5). The pressure problem has already been mentioned. The other major problem is first wall design.

2.4.1 Reference Design Concept

A variety of attempts have been made to design an acceptable helium-cooled blanket module. Providing adequate cooling of the structure, especially the first wall, is quite difficult. One of the most

Table 2.4

Blanket Parameters for Water-Cooled Designs

Structure	316 SS	HT-9	316 SS	HT-9
Breeder	$LiAlO_2$	$LiAlO_2$	$Li_{17}Pb_{83}$	$Li_{17}Pb_{83}$
Neutron Multiplier	Be	Be	———	———
First Wall Thickness (mm)	1.5	1.5	1.5	1.5
Breeder Depth (m)	0.45	0.45	0.5	0.5
Multiplier Depth (m)	0.05	0.05	———	———
In-Blanket Wetted Area (m^2)	11,600	11,600	9,300	9,300
Out-Blanket Wetted Area(m^2)	48,000	48,000	48,000	48,000
Breeder Volume (m^3)*	340	340	∿500	500
Coolant Volume (m^3)*	550	550	550	550
Mass Flow Rate (m^3/s)	24	24	25.5	25.5
Coolant Pressure (MPa)	15.2	15.2	15.2	15.2
First Wall Temperature	450	450	450	450
Coolant Inlet Temperature	280	280	280	280
Coolant Outlet Temperature	320	320	320	320
Breeder Temperature	650	650	500	500
First Wall Temperature drop	68	48	68	48
Number of modules	240	240	240	240

*Includes out of blanket volumes

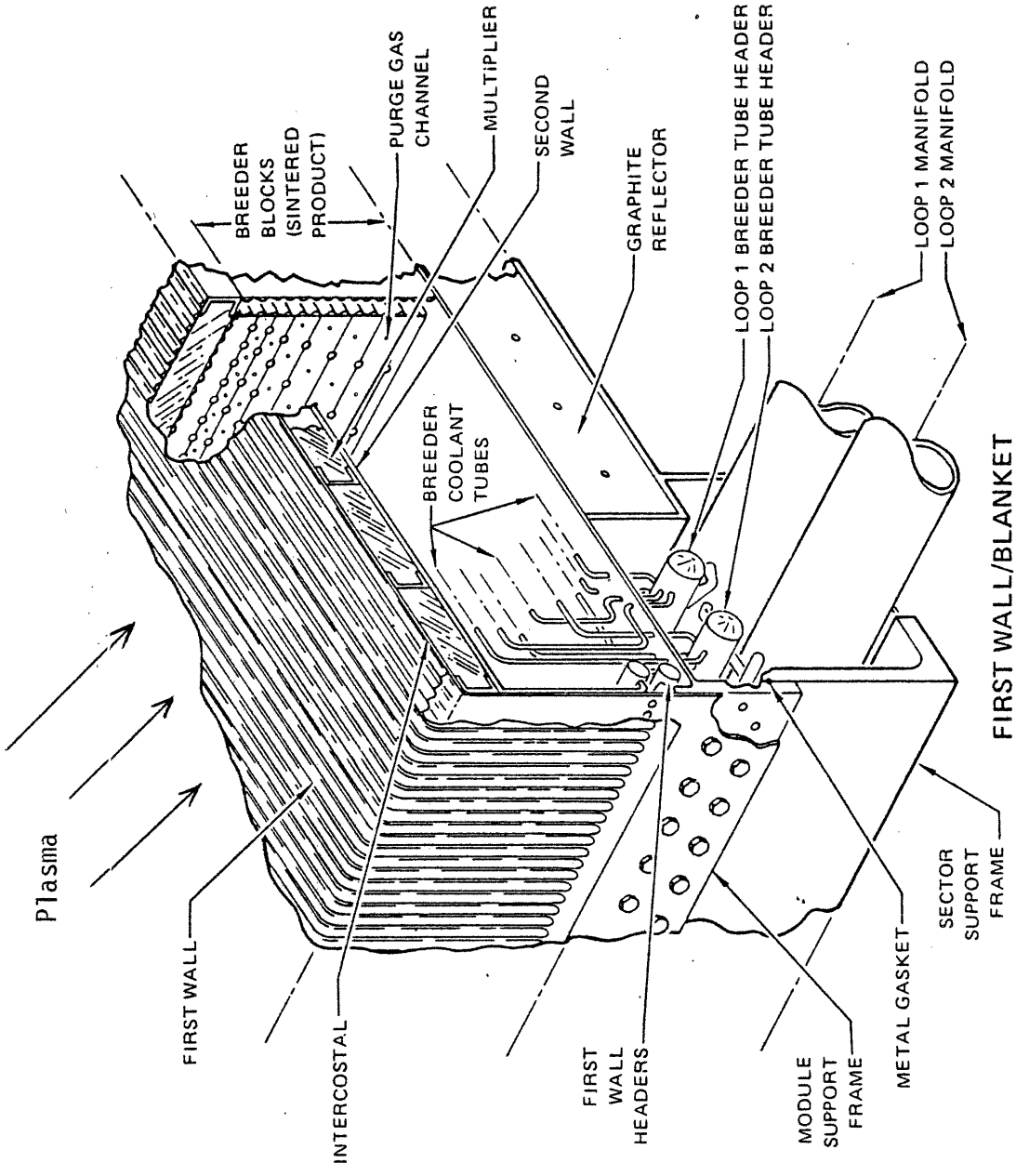

Fig. 2.1: Reference Water/$LiAlO_2$ Blanket Concept—STARFIRE [2.1]

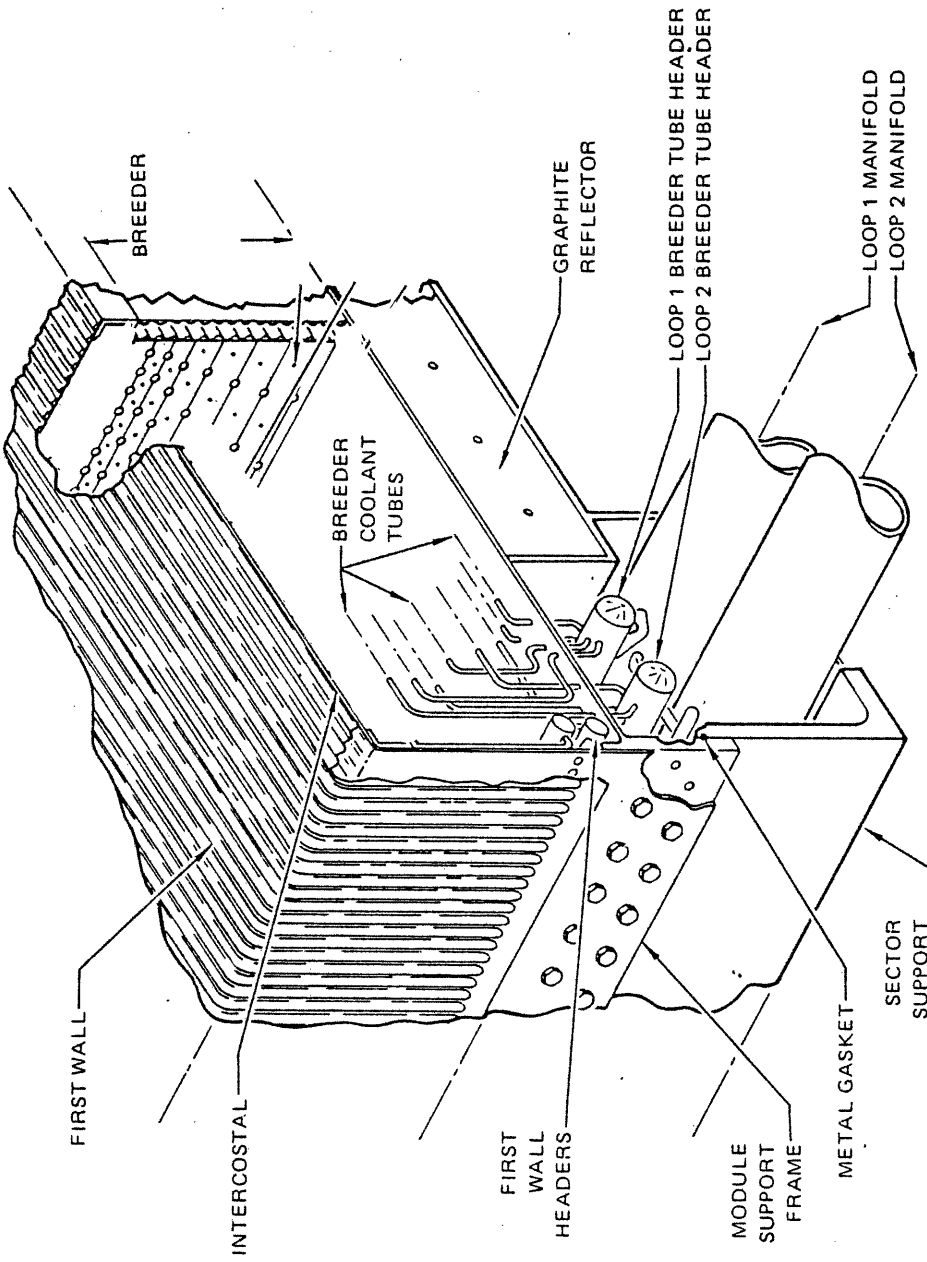

Fig. 2.2: Reference Water/$Li_{17}Pb_{83}$ Blanket Concept—
Altered Version of STARFIRE [2.1]

recent and detailed design studies was conducted by Westinghouse/ORNL [2.2, 2.3]. This is the reference concept adopted for the present work, shown in Figs. 2.3 and 2.4 for the breeders of interest. The pressurized cannister approach is more forgiving since a small leak from coolant to breeder zone does not result in module rupture (see Chapter 5).

The ANL blanket comparison design study [2.5] also suggested a pressurized cylinder approach, but with a floating (unconstrained) tube bank as the first wall, shown in Fig. 2.5. This approach seperates the first wall design from the pressurized cannister portion, hopefully improving both. If this approach had been adopted, however, helium designs would have looked worse from the accident safety standpoint, due to more metal next to the plasma and lower thermal contact between first wall and blanket. The former would worsen problems of sputtering into the helium (Chapter 7), induced structural radioactivity (Chapter 8), and afterheat removal (Chapter 3). The latter would worsen accidental heat removal from the first wall (Chapter 3).

Another alternative would be the breeder block/discrete tube approach, such as that analyzed by Bickford [2.8], for coolant sputtering problems. This concept (Fig. 2.6) has less metal near the first wall but more coolant surfaces normal to the neutron flux. As shown in Chapter 7, the two effects tend to cancel in terms of contamination of the helium coolant loop by sputtered radioactive species. On the other hand, accidental pressurization of the breeder zone would be a problem.

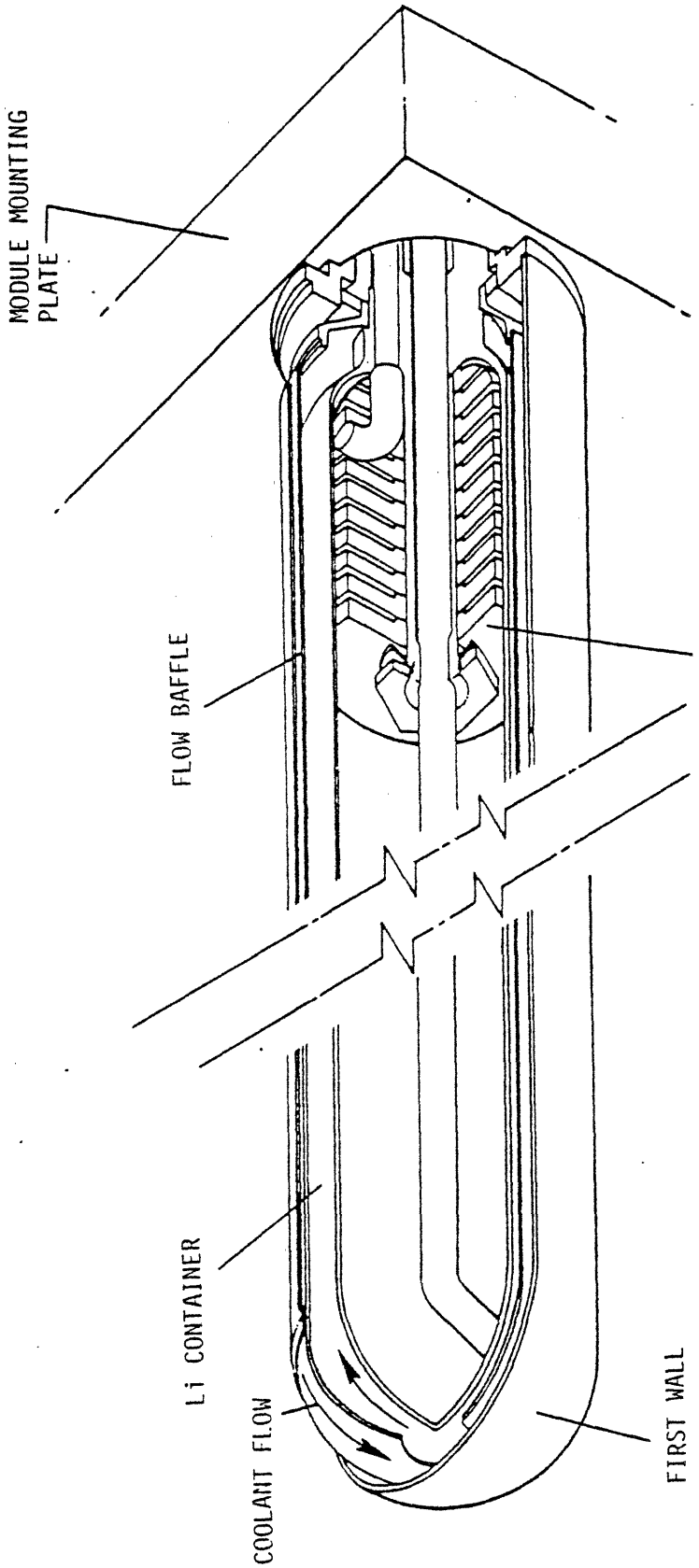

Fig. 2.3: Reference Helium/Lithium Blanket Concept—Westinghouse/ORNL [2.2, 2.3]

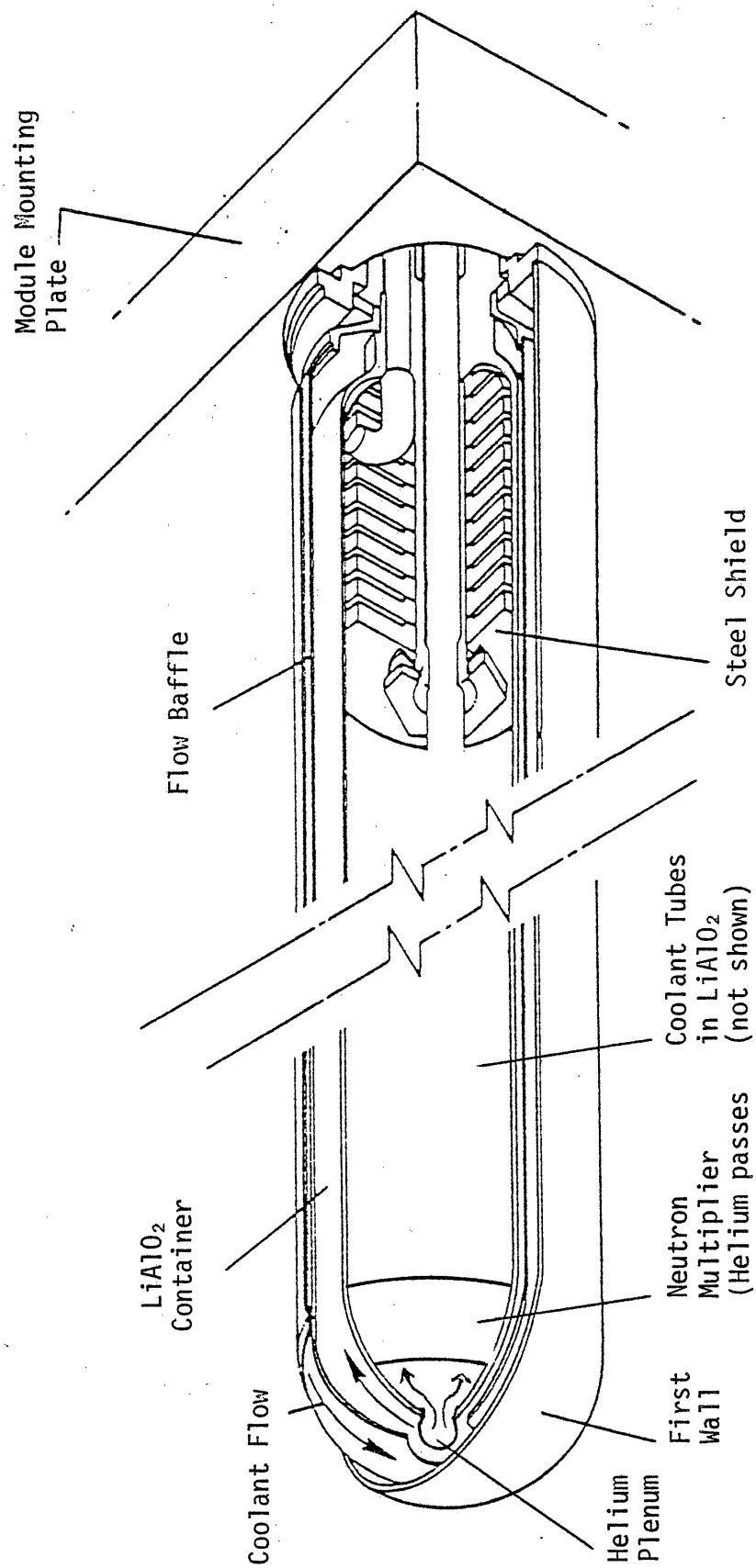

Fig. 2.4: Reference Helium/$LiAlO_2$ Blanket Concept—Altered Version of Westinghouse/ORNL [2.2, 2.3]

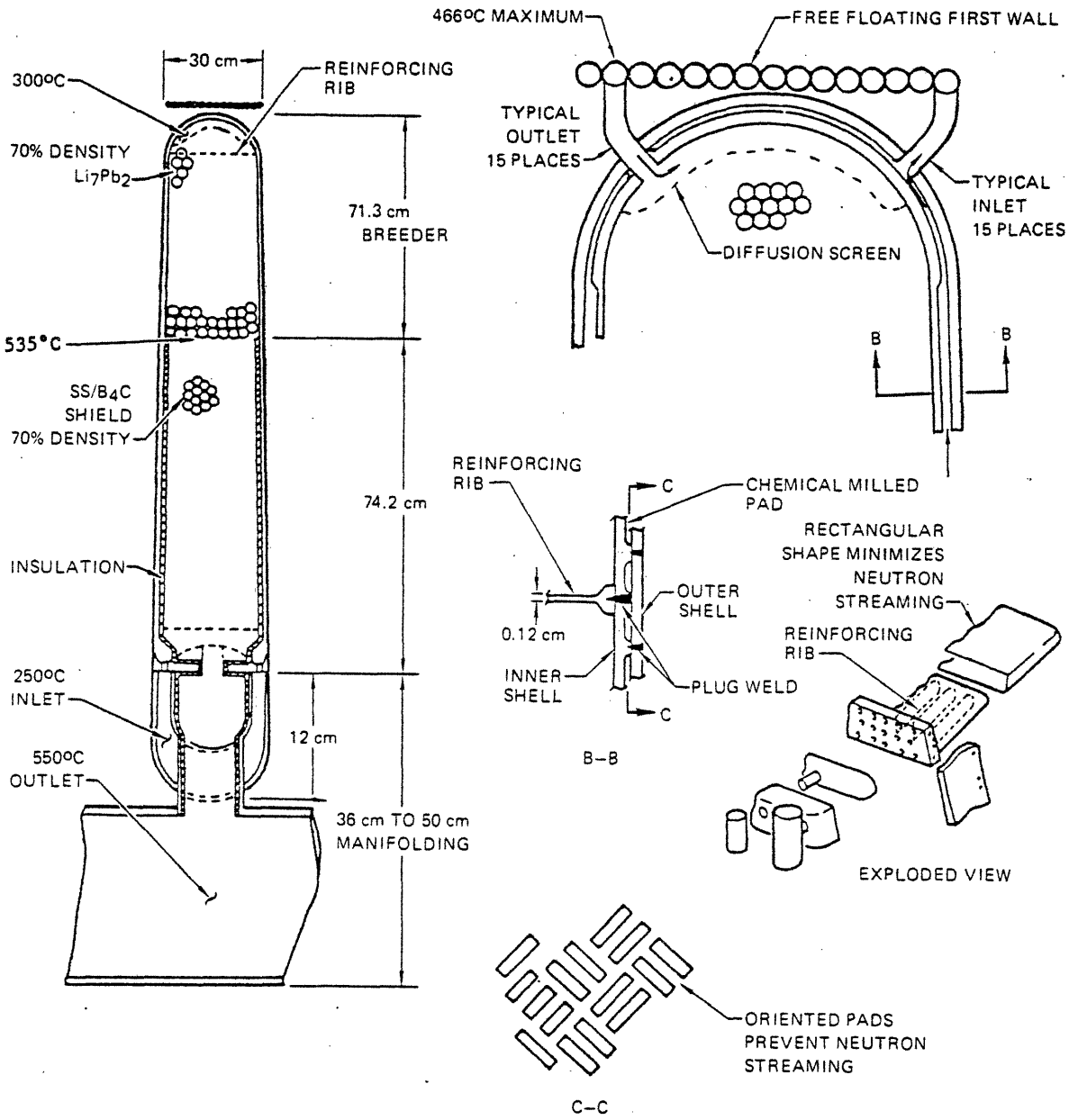

Fig. 2.5: Alternative Helium Blanket Concept [2.5]

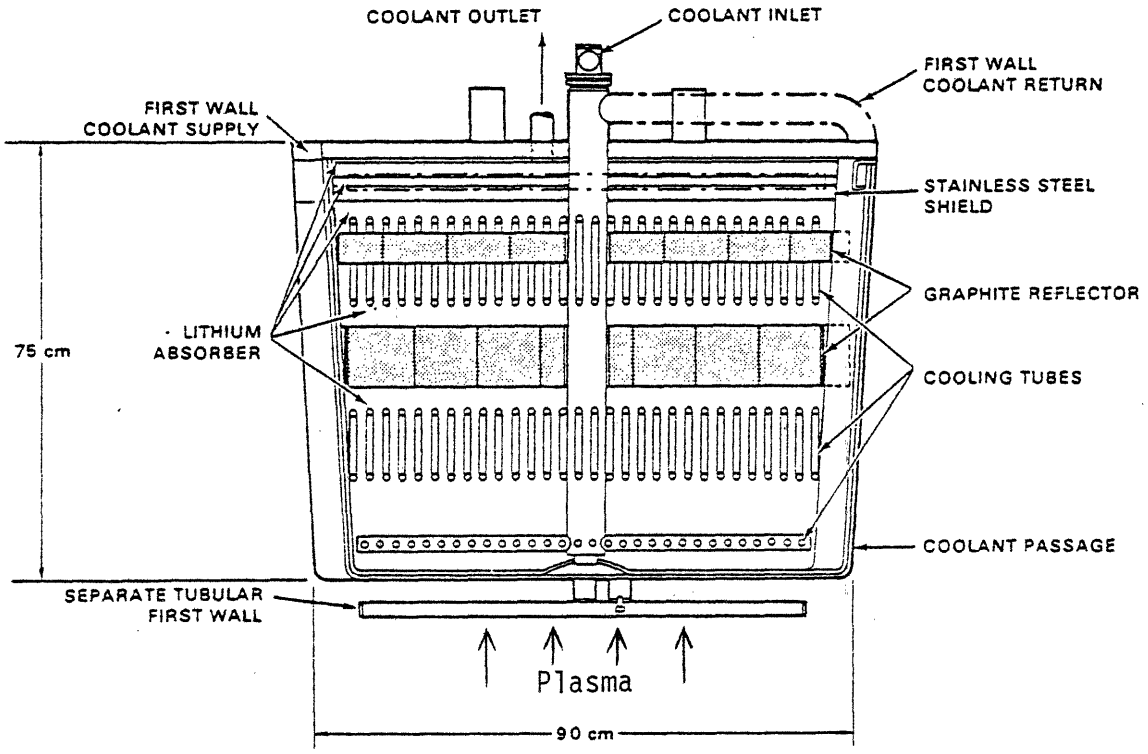

Fig. 2.6: Alternative Helium Blanket Concept, Breeder Zone Cannot Withstand Coolant Pressure [2.8]

Although there is a considerable range of helium-cooled designs, the adopted reference design concept is as representative as any and most alternatives have obvious safety disadvantages. It is beyond the scope of this study to judge the engineering feasiblity and expected lifetimes of all the alternatives.

2.4.2 Metal Change

The effect of different metals again centers on the first wall thickness. Here, the first wall is a hemisphere, so the pressure stress is given by

$$s_p = Pr_{fw}/2d_{fw} \tag{2.14}$$

rather than equation 2.1. In the manner of section 2.2.3, the relevant criteria can be used to calculate limits on first wall thickness. The results are shown in Table 2.5. As is the case for water designs, the better thermal conductivity of HT-9 gives more flexibility in selecting a design thickness. Note that for 316 SS, the total of pressure and thermal stress is minimized at a thickness which violates the pressure stress. The 316 SS thickness used in the Westinghouse/ORNL design [2.2] was 1.6 mm. The same value, which minimizes first wall stresses, is adopted for HT-9.

The thermal/hydraulics analysis for the Westinghouse/ORNL design shows a maximum first wall temperature drop of 90°C. If this is scaled from 1.0 MW/m^2 heat loading to the present case of 0.9 MW/m^2, the value would be 81°C, in good agreement with the simple calculation

Table 2.5

Limits on First Wall Thickness in Helium Designs (mm)

	316 SS	HT-9
Minimum Thickness Due to Pressure Stress (Equation 2.14)	1.3	0.9
Maximum Thickness Due to Yielding (Equation 2.5)	3.7	6.0
Maximum Thickness to Keep First Wall Temperature Drop Below 100°C (Equation 2.7)	2.1	3.0
Maximum Thickness Due to Fatigue (Equation 2.8)	8.9	23.0
Thickness to Produce Minimum Total Stress (Equation 2.6)	1.1	1.6

used here (Eq. (2.7) gives a value of 72°C). Note that the coolant outlet temperature is 435°C compared to the maximum structural temperature of 450°C at the first wall. This is only possible by having the low temperature inlet helium flow directly to the first wall, then continue back to cool the module interior. In the water case, the temperature drop around the loop was only 40°C, compared to 235°C here, and at lower temperatures, so there is less need for water to be directed immediately to the first wall without absorbing any heat in transit. This aspect of helium designs tends to "waste" coolant wall area. In the reference design, 75% of the coolant area is not an interface between the module interior and coolant. Thus most of the heat transfer from module to coolant occurs through 25% of the wall area.

The use of HT-9 does allow (Table 2.5) reduction in first wall thickness compared to 316 SS. However, as in the water-cooled case, the total stress can be minimized by keeping the same design thickness.

2.4.3 Breeder Change

The use of $LiAlO_2$, rather than the lithium breeder used in the Westinghouse/ORNL design [2.3, 2.4], causes three changes - 1) addition of a neutron multiplier to the front of the module, 2) shortening of the cannister, and 3) use of coolant tubes in the module interior.

The addition of the multiplier would entail a very difficult engineering problem due to cooling requirements. Furthermore, the low thermal conductivity of $LiAlO_2$ necessitates additional cooling within the breeding zone. A rough solution to this problem would be to direct some of the return helium flow through the multiplier and $LiAlO_2$ at

about a 20 mm spacing. The STARFIRE study [2.1] found this spacing required to keep $LiAlO_2$ cool for their water design. In fact the Westinghouse/ORNL design study [2.3] suggested a return tube through the center of the lithium breeding zone if a larger radius cylinder were used. The exact design details are very difficult, requiring extensive thermal/hydraulic analysis which is beyond the scope of this study. There would also need to be seperate helium purge streams through the breeder for tritium removal.

The details of calculations are discussed in Appendix C. The reference design parameters for helium are shown in Table 2.6.

2.5 Lithium-Cooled Designs

2.5.1 Reference Design Concept

The pressure in water and helium systems is determined by the need to maintain the liquid state and obtain adequate heat transfer. The lithium system pressure is determined by the pressure drop through the loop such that flow is maintained. Thus the maximum pressure is given by

$$P(\text{MPa}) \sim 0.1 + \Delta P_{loop} \tag{2.15}$$

The lowest pressure in the loop would be atmospheric (0.1 MPa). One would like to minimize the blanket pressure drop to lower operating pressures and lower pumping power. Unfortunately, use of lithium entails MHD pressure losses as the conducting fluid crosses the magnetic field.

The reference conceptual design for the lithium case is that

Table 2.6

Helium Design Reference Parameters

Structure	316 SS	HT-9	316 SS	HT-9
Breeder	$LiAlO_2$	$LiAlO_2$	Li	Li
Neutron Multiplier	Be	Be	———	———
First Wall Thickness (mm)	1.6	1.6	1.6	1.6
First Wall Cap Radius, Cylinder Radius (mm)	50	50	50	50
Breeder Depth (m)	0.45	0.45	0.6	0.6
Multiplier Depth (m)	0.05	0.05	———	———
In-Blanket Wetted Area (m^2)	48,000	48,000	54,000	54,000
Out-Blanket Wetted Area (m^2)	——— undetermined ———			
Breeder Volume (m^3)*	300	300	600	600
Coolant Volume (m^3)*	600	600	600	600
Mass Flow Rate (m^3/s)	696	696	721	721
Coolant Pressure (MPa)	5.5	5.5	5.5	5.5
First Wall Temperature	450	450	450	450
Coolant Inlet Temperature	200	200	200	200
Coolant Outlet Temperature	435	435	435	435
Breeder Temperature	650	650	500	500
First Wall Temperature Drop	72	52	72	52

*Includes out-of-blanket volume

recommended in the ANL blanket design study [2.5], which is similar to that in UWMAK I [2.9] and UWMAK-III [2.10]. The concept is illustrated in Fig. 2.7. This concept has also been used in a blanket decommissioning study [2.11]. A relatively high pressure for lithium of 2.8 MPa is used to allow for MHD pressure drops. The primary design questions are the module width and first wall thickness.

An alternative concept for a liquid metal blanket is that of a cauldron [2.8] or large sector-sized tank, shown in Fig. 2.8. The concept has some potential advantages. Some of these concepts are discussed in Chapters 3 and 9. They include lower wetted surface wall area and lower complexity. However, detailed thermal-hydraulics-magnetic calculations have not been performed to examine the feasibility of the concept as a pure lithium blanket.

2.5.2 Metal Change

The decomissioning study [2.11] used a module width of 0.6 m which indicates a first wall radius of 0.15 m (see Fig. 2.7) for a V-alloy design. Decreasing the module width, hence first wall radius, increases the wetted surface area and structural percentage of the blanket but reduces the stress. Module widths of 0.6, 0.4, 0.3 m were considered for 316 SS and V-alloy. It is not possible to design an acceptable 316 SS module with a width of 0.6 m and the 0.4 case was marginal (see Appendix C). Thus the reference 316 SS module width was selected to be 0.3 m compared to 0.6 for V-alloy. Reduction of lithium pressure would allow larger steel modules. The reference lithium design parameters are listed in Table 2.7.

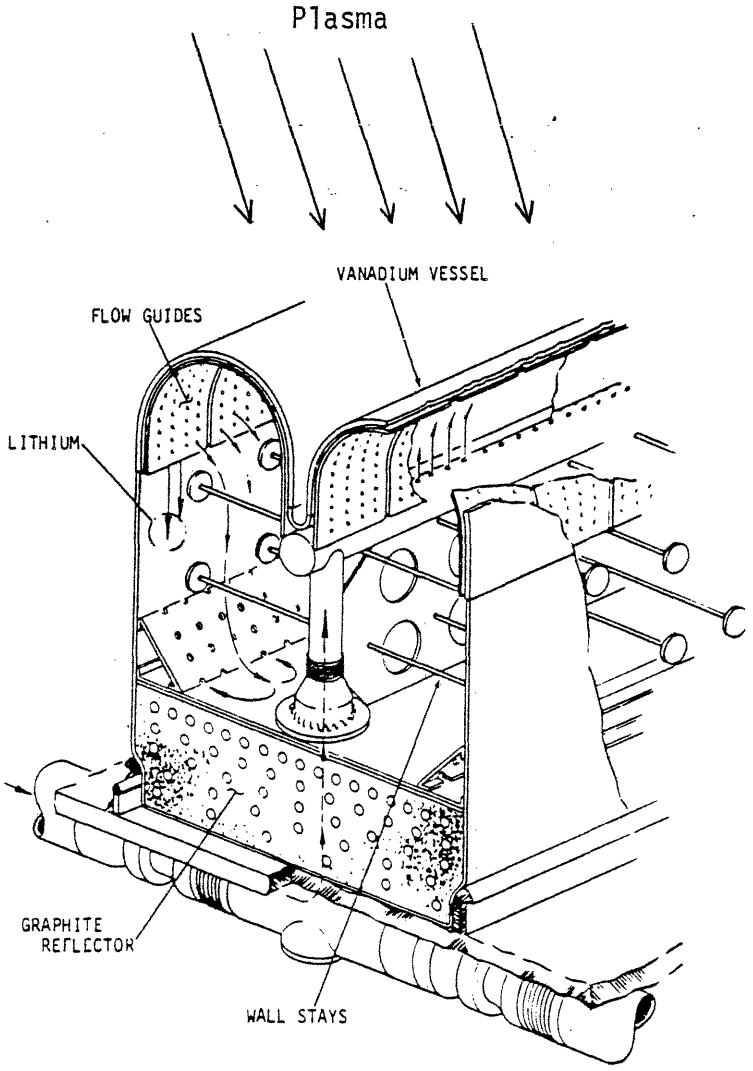

Fig. 2.7: Reference Lithium/Lithium Blanket Concept—ANL [2.5]

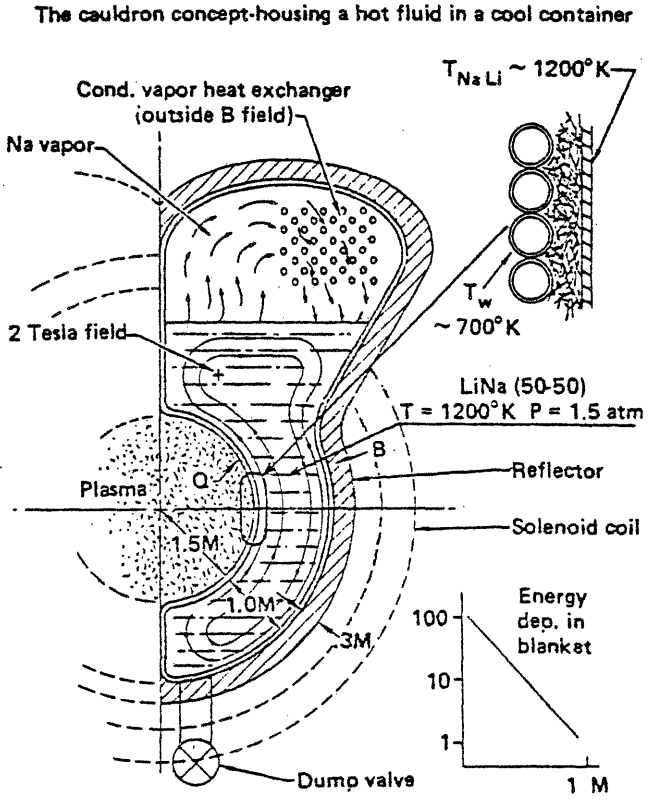

Fig. 2.8: Alternative Liquid Metal Tank Blanket Concept [2.12]

Table 2.7

Reference Blanket Design Parameters for Lithium-Cooled Designs

Structure	316 SS	V-alloy
Breeder	Li	Li
First Wall Thickness (mm)	2.0	3.8
First Wall Radius (mm)	75	150
Breeder Depth (m)	0.6	0.6
In-blanket Area (m^2)	11,800	9,000
Out-blanket Area (m^2)	20,000	20,000
Breeder/Coolant Loop Volume (m^3)*	800	800
Mass Flow Rate (m^3/s)	8.4	7.6
Coolant Pressure (MPa)	2.8	2.8
First Wall Temperature	450	600
Coolant Inlet Temperature	230	300
Coolant Outlet Temperature	450	550
Breeder Temperature	500	600
First Wall Temperature Drop	90	110
Number of Modules	1440	720

* Includes out of module volume

2.6 Flibe-Cooled Design

Molten salt blankets have not been extensively studied for fusion designs. Flibe's coolant properties are somewhat similar to water except for its high melting point (459°C) and far lower pressure. Like lithium, the operating pressure is determined by pressure drop alone. Unlike lithium, the MHD pressure losses are quite modest. Of the material combinations studies, the TZM/Li/flibe case proved to allow the most design flexibility. If a lower melting temperature salt were found which was sufficiently compatable with structural materials, it could be very promising. The high melting point of flibe and its compatability problems (see Chapter 7) seem to limit its use to a molybdenum-based alloy.

The reference concept is shown in Fig. 2.9 which is similar to previous flibe concepts [2.13] except the first wall design is based on STARFIRE. The design approach is that developed by McManamy [2.13] with details shown in Appendix C. The resulting reference design parameters are listed in Table 2.8. As seen in the table, the result is a design with low stresses and low wall temperature drops due to the low operating pressure of the flibe ($\sim$ atmospheric) and the high thermal conductivity of TZM (over 100 W/m°C). When the design parameters were established, a thin first wall was selected, minimizing metal near the plasma which reduces afterheat and activation. Analysis in the course of this study indicated that perhaps a thicker wall would be better from various safety viewpoints, notably plasma disruption effects and rapid structural oxidation. If desired,

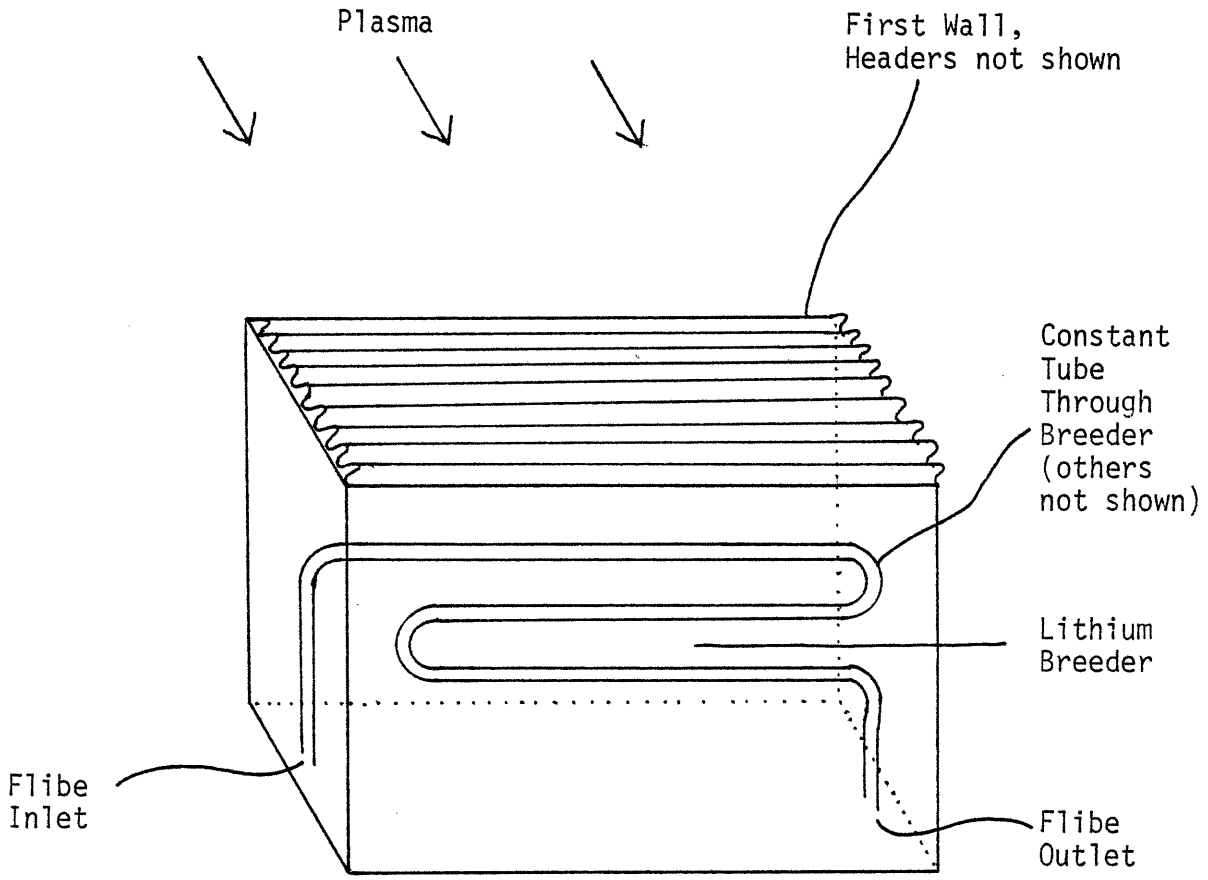

Fig. 2.9: Reference Flibe/Lithium Blanket Concept

Table 2.8

Reference Blanket Design Parameters for Flibe-Cooled Design

Structure	TZM
Breeder	Li
First Wall Thickness (mm)	1
First Wall Radius (mm)	5
Breeder Depth (m)	0.6
In-blanket Area (m^2)	8,500
Out-Blanket Area	20,000
Breeder Volume (m^3)*	600
Coolant Volume (m^3)*	200
Mass Flow Rate (m^3/s)	9.1
Coolant Pressure (MPa)	0.2
First Wall Temperature	900
Coolant Inlet Temperature	700
Coolant Outlet Temperature	800
Breeder Temperature	900
First Wall Temperature Drop	10
Number of Modules	240

*Includes out-of-blanket volumes

a TZM/flibe first wall could be significantly thicker (up to 10 mm), with corresponding penalties in afterheat and radioactivity.

2.7 Summary

Based on calculations whose details appear in Appendix C, reference design parameters were established for the eleven material combinations. These parameters are listed in Tables 2.4, 2.6. 2.7, and 2.8. Whereas these are not fully optimized, the parameters and blanket concepts are somewhat representative of those in the literature. Some general comments are relevant:

1) The high pressure required for water prohibits designing a module to withstand full coolant pressure
2) Helium system pressures may allow a module to be designed to withstand accidental pressurization
3) The higher thermal conductivity of the liquid breeders allows use of fewer coolant tubes with resulting savings in complexity and wetted wall area
4) High thermal stresses for 316 SS first wall narrows design options and lead to highly stressed modules
5) Although the thermal conductivity is higher for HT-9, one tends to use similar wall thicknesses as for 316 SS. However, the design flexibility is higher.
6) A TZM/Li/flibe combination appears to tend to have highest design flexibility.

REFERENCES

2.1 C. C. Baker, et al., "STARFIRE—A Commercial Tokamak Fusion Power Plant Study," ANL/FPP-80-1, 9/1980.

2.2 J. S. Karbowski, et al., "Tokamak Blanket Design Study: FY 78 Summary Report," ORNL/TM-6847, 6/1979.

2.3 J. S. Karbowski, et al., "Tokamak Blanket Design Study, Final Report," ORNL/TM-7049, 1980.

2.4 G. P. Yu, "Relationship of Material Properties to the Design of a Fusion Reactor First Wall," Sc.D. thesis, Department of Nuclear Engineering, Massachusetts Institute of Technology, 1981.

2.5 D. L. Smith, et al., "Fusion Reactor Blanket/Shield Design Study," ANL/FPP-79-1, 7/1979.

2.6 O. A. Adegbulugbe, "Structural Design Limits for Fusion First Walls," Sc.D. thesis, Department of Nuclear Engineering, Massachusetts Institute of Technology, 1981.

2.7 "Class I Components in Elevated Temperature Service," Case of ASME Boiler and Pressure Vessel Code, Case 1592-7, 1975.

2.8 W. E. Bickford, "Transport and Deposition of Activation Products in a Helium Cooled Fusion Power Plant," PNL-3487, 9/1980.

2.9 B. Badger, et al., "UWMAK-I, Wisconsin Toroidal Fusion Reactor Design," UWFDM-68, 1973.

2.10 B. Badger, et al., "UWMAK-III, A Noncircular Tokamak Power Reactor Design," EPRI-ER-368, 6/1976.

2.11 J. H. Opelka, et al., "Decommissioning Study of a Commercial Tokamak Reactor," ANL/ES-93, 1/1981.

2.12 T. R. Galloway, "Some Process Aspects of Hydrogen Production Using the Tandem Mirror Reactor," UCRL-84285, 10/1980.

2.13 T. J. McManamy, "Fusion Reactor Blanket Heat Removal Using Helium and Flibe" Ph.D. thesis, Department of Nuclear Engineering, Massachusetts Institute of Technology, 1979.

2.14 R. W. Conn, et al., "SATYR Studies of a D-D Fueled Axisymmetric Tandem Mirror Reactor," PPG-576, 9/1981.

2.15 C. C. Baker, et al., "The Impact of Alternate Fusion Fuels on Fusion Reactor Technology—An Initial Assessment Study," ANL/FPP/TM-128, 11/1979.

2.16 K. E. Evans, et al., "D-D Tokamak Reactor Studies," ANL/FPP/TM-138, 11/1980.

CHAPTER 3. LOSS-OF-COOLANT-INDUCED THERMAL TRANSIENTS

If cooling is perturbed, the blanket faces the potential for damage and loss of structural integrity. The question arises as to how serious this threat is and how the choice of material/coolant/breeder may influence it. The heat source of concern may be either the plasma (plasma remains on) or decay afterheat (plasma off).

3.1 Problem Identification

Cooling disruption accidents may include loss-of-coolant (LOCA) due to a leak or rupture, loss-of-flow (LOFA) due to tube plugging or pump loss, or loss-of-heat removal (LOHR) at the primary loop heat exchanger. The spatial scale may range from individual tube plugging to loss of the entire coolant inventory. The time scale may range from sub-second temperature rise from continued plasma heating to days/weeks heating from decay heat after the plasma terminates. Finally, if the breeder is a liquid, it too may drain, altering heat transport and thermal response.

3.1.1 Accident Type

All of the above accidents are potential concerns. Additional heat-related accidents include over-power transients (TOP) and disruptions which exhibit extremely short time scales and are discussed in Chapter 4. Most of the few studies in this area have focussed on LOFA's. Chan [3.1] has discussed some of the problems associated with LOCA, LOFA, LOHR, and TOP accidents (plasma heating only). His analysis focuses on how fast coolant heat transfer is lost. His results are discussed in Section 3.3. As Chan notes, the LOCA is generally the most severe, greater and faster

loss of heat transfer. A typical assumption of previous works is that the coolant loss time rate may be scaled directly from fission. Unfortunately, some types of geometries for fusion reactors allow coolant losses at the blanket level with a greater break area/coolant volume ratio (section 3.2.3), implying faster coolant losses. Hence, faster LOCA's are possible than Chan analyzed. The present study will be limited to the more severe LOCA's as these largely determine design criteria- e.g., is an auxiliary cooling system needed? The base scenarios and maximum coolant loss rates are discussed in section 3.2.

3.1.2 Spatial Scale

A great variety of heat-removal accidents may be examined. The least serious, but perhaps the most probable, is individual tube plugging. This causes a local temperature rise. An example of this analysis is found in the STARFIRE study [3.2]. Adjacent tubes assist heat removal and limit temperature problems. The basic cause, corrosion and mass transfer, is discussed in Chapter 7. A key problem will be instrumentation and detection.

The next spatial scale would be loss of cooling for an entire module. Then, other modules would still operate, providing cooling. If the leak/rupture were at a module side, the release of coolant to the plasma chamber automatically terminates the plasma, resulting in a pure afterheat problem.

The worst case would be a loss-of-coolant to all modules. The STARFIRE design aims to minimize this by specifying two independent coolant loops, so that only half the cooling may be lost. This case is the easiest to treat since all modules experience the same transient. It is also the

least design-dependent since the thermal connection (highly specific to individual designs) between modules is ignored. As the primary purpose of the present study is to focus on material effects, the design dependence should not dominate.

The total cooling loss case limits the worst result. As will be seen in section 3.4, the afterheat problem is sufficiently minor (for most material combinations) that less complete cooling losses (one module or an individual tube) do not represent important afterheat concerns. Thus, the worst case analysis can best examine relevant material effects.

3.1.3 Time Scale

From the onset of the accident there are two heat sources of concern. First, the plasma will continue to heat the blanket by neutron and surface heating until it is terminated by either 1) the cause of the accident itself, e.g., magnet quench, 2) the entry of blanket coolant or breeder into the plasma chamber, 3) an active shutdown mechanism, or 4) a passive shutdown, e.g., Be first wall coating vaporization in STARFIRE. After plasma termination, the heat source is the decay afterheat due to the induced structural radioactivity. In all cases the first wall is the key point due to high surface heating (20% of all heat directly to the first wall) and, later, to afterheat (highest specific radioactivity is induced in the first wall). Thus the critical question is how fast the first wall gets into trouble.

As will be seen, the plasma heat time scale is of the order of seconds. One way or another the plasma will terminate quickly (a TZM structure may be a special case). If nothing else works, eventually the first wall

would melt, leading to material entering the plasma zone and stopping the plasma.

The afterheat time scale stretches from hours to years. Ideally, one would like a structure that literally allowed one to walk away without a serious meltdown or structural damage occuring. As will be seen, this appears possible.

Actually, of course, the two problems merge. The longer the plasma stays on, the higher the temperatures are (and closer to overall melting). Merrill's [3.3] LOFA analysis handles this most graphically by allowing first wall temperatures (following LOFA) to reach melting before assuming plasma termination.

3.1.4 Present Problem

The chief goal is the identification of the impact of material choice on the potential relative temperature rise problems. Absolute answers and design effects are secondary concerns. This implies establishing the problem so as to be able to directly focus on the key effect of the individual blanket materials. For reasons outlined above, the present study will be limited to analysis of a LOCA, where all modules lose coolant. Furthermore, the analysis will be divided into two separate pieces — plasma and afterheat. The afterheat problem will generally be started at $t = 0$, i.e., no heat-up from continued plasma heating. This allows separation of the problem and direct identification of material behavior. This case corresponds to accidents where the plasma is immediately terminated by some aspect of the accident itself. It also removes a variable from the problem, namely how long the plasma continues. Nevertheless, some analysis is discussed in section 3.4.2

which indicates how the two pieces relate.

3.2 Input, Assumptions, and Criteria

Having identified the problem to be solved, the method of solution must be outlined.

3.2.1 Model and Assumptions

3.2.1.1 Boundary Conditions

The basic geometry for the analysis is shown in Figure 3.1. Because all modules are assumed to experience the same transient, the front and side faces have adiabatic boundaries (except for the incoming plasma surface heat flux). In reality, the back of the module has a variety of thermal connections including structural support, inlet/outlet for coolant, and inlet/outlet for breeder or breeder purge stream. These connections (and radiation heat transport) allow heat to flow to other parts of the reactor and ultimately to the building. These parts of the building generally serve as massive heat sinks. Unfortunately, these aspects are highly design dependent and fairly independent of blanket material choice. Thus, the back wall is taken to be insulated from the rest of the reactor. Whereas this has no effect on plasma heat rates, it has a definite effect on long-term afterheat results. This is discussed in section 3.4. However, isolation of the back wall (hence, the entire module) produces a conservative result. At long times, the loss of heat from the blanket would serve to reduce blanket temperatures.

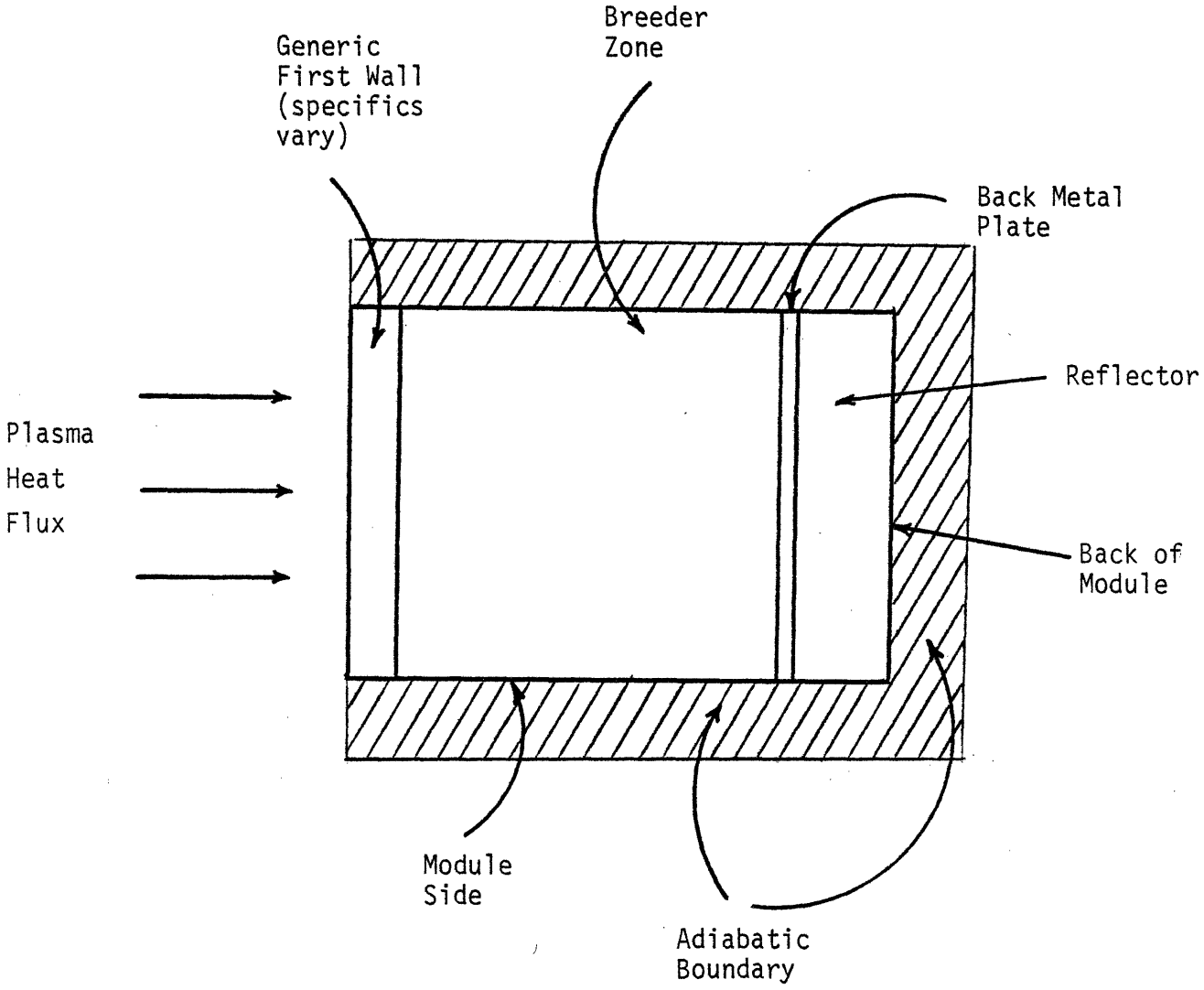

Fig. 3.1: Basic Geometry for LOCA Analysis with Boundary Conditions Indicated

3.2.1.2 Heat Transfer Mechanisms

There are three heat transfer mechanisms. First, conduction is allowed between any materials in contact. Second, where the coolant is still present, forced convection heat coefficients are relevant. Third, for cases with voids (coolant or liquid breeder gone), radiation heat transfer plays a vital role in transferring heat from the first wall to the reflector and back wall. Free convection is ignored. For coolants, a LOCA indicates that only forced convection is important, unlike a LOFA where a non-flowing coolant may experience free convection. For liquid breeders (Li, $Li_{17}Pb_{83}$), Gierszewski [3.4, 3.5] has examined free convection versus conduction under normal conditions. The strong MHD force is found to severely limit free convection such that it is insignificant for Li, and reduced for $Li_{17}Pb_{83}$. For the latter case of $Li_{17}Pb_{83}$, the temperature drop across the breeding zone is so low (section 3.4) anyway from afterheat, that ignoring free convection has a small effect.

3.2.1.3 Computer Code

The finite difference heat transfer code HEATING3 [3.6] was modified for the analysis. The code handles 1, 2, or 3 dimensions in either cartesian or cylindrical geometry. Temperature dependent conductivity, density, and heat capacity are allowed. Time dependent boundary temperatures, and heat generation (also spatially dependent) can be user specified. Radiation heat transfer between opposing surfaces is allowed.

The major drawback to the code is the limited capacity to model coolant behavior. Convection heat coefficients must be user supplied

rather than determined by code-calculated conditions. The code was modified for this study to allow time and spatially varying coefficients. Similarly, the boundary temperatures (including convection boundary) must be user specified. These matters are further discussed in section 3.3.3.

A minor limit was specification of heat flux boundary conditions. The code was modified to allow time dependent specified heat flux, necessary for plasma shut-off and disruption modeling.

Another problem was a geometrical limit on radiation heat transfer. The code allows radiation heat transfer only between opposing nodes on two specified surfaces as in Figure 3.2a. In reality the picture would look more like Figure 3.2b. As discussed in section 3.4, most of the analysis could be done in one-dimension, eliminating the node problem. For 2-D cases, this code limitation limits the geometries than can be studied.

3.2.2 Input

A large amount of input was necessary for the analysis. Unfortunately, the data base often had significant uncertainties.

3.2.2.1 Material Properties

The material properties (thermal conductivity, density, and specific heat capacity) had to be specified for all the structural metals (316 SS, HT-9, V-alloy, and TZM), reflector (assumed to be graphite) solid breeder ($LiAlO_2$, 60% dense), liquid breeders (Li, $Li_{17}Pb_{83}$), coolants (He, water, Li, flibe), and neutron multiplier (Be,70% dense). The values used and their sources are found in Appendix B.

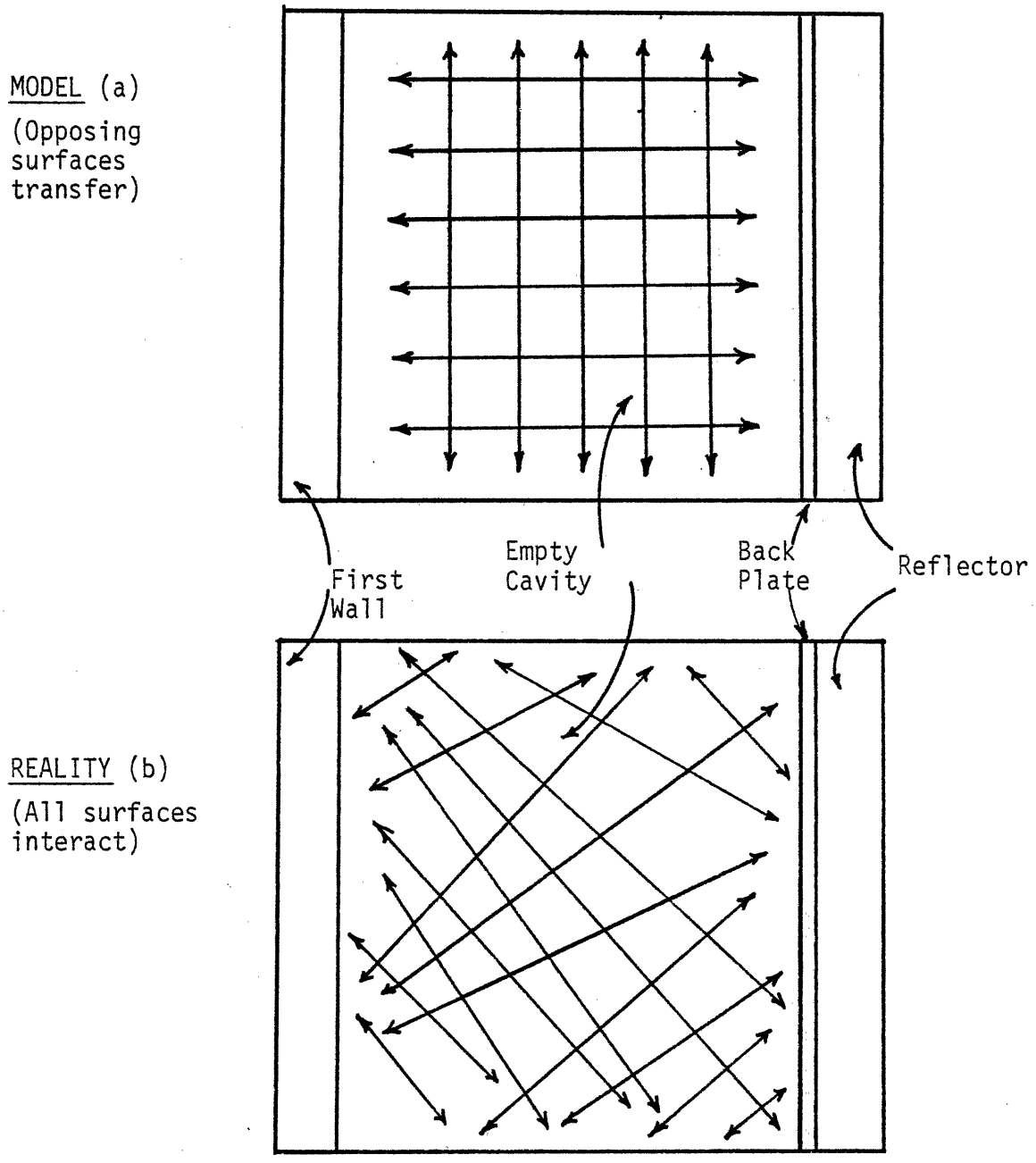

Fig. 3.2: Comparison of Modeled Heat Transfer to Actual

To limit the analysis, only one reflector material was used. For the present purpose, the reflector serves only as a pure heat sink and graphite is a representative substance for a reflector.

Only beryllium was considered as a neutron multiplier (needed for $LiAlO_2$). Others are possible (e.g., Zr_5Pb_3 in STARFIRE) but most are themselves a source of afterheat. In the case of Zr-Pb, half the decay heat in the STARFIRE design for short times (< day) came from the multiplier. For the present purpose of comparing structural/coolant/breeder hazards, it was deemed inappropriate to bias the $LiAlO_2$ case by adding Zr-Pb afterheat, since a better (from afterheat considerations at least) multiplier is available, namely Be. In this sense, the Be/$LiAlO_2$ combination is the best case for comparing $LiAlO_2$ to Li and $Li_{17}Pb_{83}$. As is seen, even the best $LiAlO_2$ case is worse than either of the liquid breeders. Using Zr-Pb would only worsen the comparison.

3.2.2.2 Boundary Conditions

The only external conditions are 1) adiabatic-isolated boundary, and 2) plasma surface heat flux. The base case for all the analysis is $q''_w = 9 \times 10^5$ W/m^2 corresponding to a neutron wall loading of $q''_n = 3.6 \times 10^6$ W/m^2 — same values used in STARFIRE. One should note that other non D-T Tokamak devices may have a differing ratio between surface and neutron heat loads. For plasma heating, the surface heat flux strongly dominates. For D-D devices, this component (relative to same power output) would be worse. On the other hand, any device with a lower surface heat load would experience a lower plasma heat-up rate (see Section 3.3 for scaling) from a LOCA.

3.2.2.3 Heat Generation Rates

The volumetric heat generation rate must be specified for both plasma neutron flux and afterheat. Chao [3.7] modeled the neutron heating as

$$q_n'''(r) = q_n'' \times QP \times \exp(-Ba \times \Delta r) \tag{3.1}$$

where Δr = radial depth into blanket (m)

Ba = attraction of neutrons into blanket (m^{-1})

QP = plasma heating coefficient.

The plasma heating coefficient is defined as

$$QP = \frac{q_n'''(\Delta r = 0)}{q_n''} \tag{3.2}$$

such that the volumetric heating scales with the wall loading. Chao found that this model was an adequate representation for thermal-mechanics purposes of the nuclear heating rate.

In this present study, this is extended for afterheat as

$$q_a'''(r,t) = q_n'' \times QP \times \exp(-Ba \times \Delta r) \times QD \times DE(t) \tag{3.3}$$

where $DE(t)$ = decay heat time function ($DE(t=0) = 1.0$)

QD = initial decay heat fraction

Parameters, QP, QD, Ba, and DE(t) are all functions of materials selected. A full detailed neutronics calculation for each case was beyond the scope of this study. Equations (3.1) and (3.3) allow an approximation of the heat rates based on previous neutronic calculations.

Implicit in Equation (3.3) is the separation of space and time. The neutron energy spectrum changes as a function of position and this leads to a differing mix of induced isotopes, hence a varying of afterheat rates. Analysis of the data for cases with 316 SS [3.3] shows that the de-coupling of space and time is good within about 10% ($t \leq 1$ day). The agreement is best near the first wall for short times - where it is most important. Due to the lack of detailed space and time afterheat results for all the material combinations of interest, the Equations (3.1) and (3.3) are taken to adequately represent volumetric heat generation.

The model has the advantage that material relevant behavior is separated into easily identifiable parts. This allows comparison of heating results from previous works.

The parameter Ba is primarily a function of blanket coolant and breeder. Table 3.1 lists the values used. These are based on fitting Eq. (3.1) to heating rates found in the literature (Appendix B). The agreement among studies for same material was generally good.

The definition for QD has some subtle aspects. Typically one quotes the afterheat rate as some percentage of the reactor operating power. The initial fractional total afterheat is given by

$$\text{total FP} = \frac{\text{initial total afterheat}}{\text{total operating power}} \tag{3.4}$$

TABLE 3.1

Values of Blanket Attenuation Factor*

Coolant	Breeder	Ba (m^{-1})
water	$LiAlO_2$	9.0
water	Li-Pb	8.0
He	Li	8.0
He	Li	3.7
Li	Li	4.0
flibe	Li	4.5

*See Appendix B

Since the operating power is being placed in structure, coolant, and breeder and afterheat is primarily generated in structure alone, the volumetric fractional afterheat is different. This is given by

$$\text{volumetric FP} = QD \times \exp(-Ba \times \Delta r) \quad (3.5)$$

thus the initial total fractional afterheat is given by

$$\text{total FP} = \frac{\int QD_i \times \exp(-Ba \times \Delta r)\, dr \times QP_i}{\int \exp(-Ba \times \Delta r)\, dr \times QP_i} \quad (3.6)$$

where the integral is over the entire blanket volume and QD_i varies as a function of material (metal, coolant, breeder). Thus, although the total afterheat at shutdown for fusion systems is about 1% of operating power, this heat source is concentrated in the structural metal. The first wall afterheat generation rate is about 4% of the first wall operating power ($QD \sim 4\%$). The volumetric heat source, rather than the total, controls heat transfer and thermal response. The values for QD and QP are listed in Table 3.2. The product QD x QP determines the initial afterheat scaling (see Eq. (3.3)). Determination of the values is discussed in Appendix B.

The decrease in afterheat as a function of time, DE(t), was obtained by examining the time behavior of materials in various previous studies (see Appendix B). There is some variance among studies, sometimes due to differing alloy compositions. The values used roughly correspond to two years of operation. For longer times, the variance increases. Figure 3.3 shows the functions used. The definition of DE(t) in Eq. (313) implies that DE(t=0) = 1.0 so that the function is strictly

TABLE 3.2

Values of Neutron and Afterheat Parameters*

Material	QD	QP(m^{-1})	QD x QP(m^{-1})
316 SS	0.04	10	0.40
HT-9	0.04	9.5	0.38
V-alloy	0.05	6.0	0.30
TZM	0.06	6.5	0.39
Li	0.006	4	0.024
flibe	0.062	8	0.50
$LiAlO_2$	0.019	9	0.17
$Li_{17}Pb_{83}$	?	10	low
He	~0	~0	~0
water	~0	18	~0
Be	0.005	9	0.045

*See Appendix B

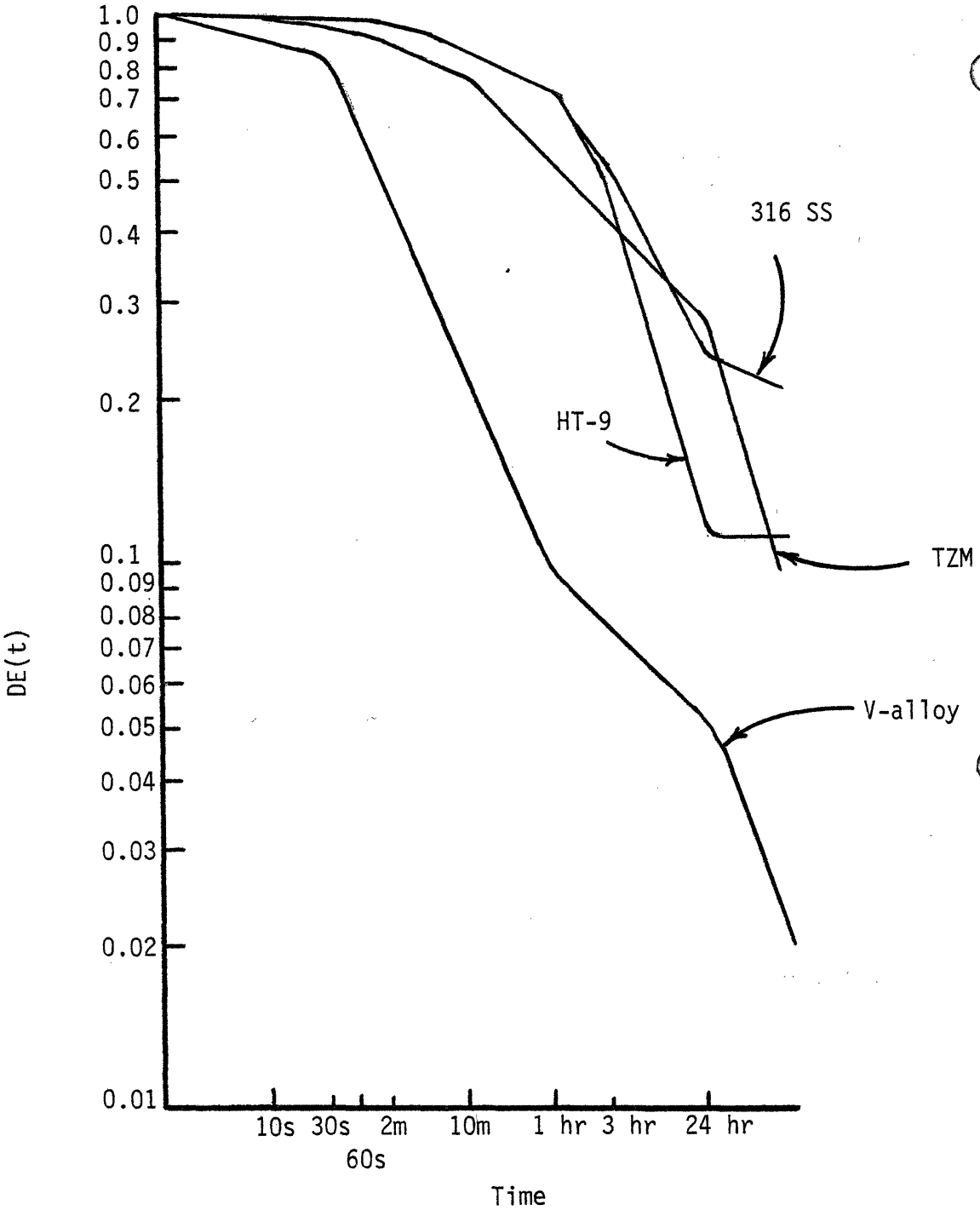

Fig. 3.3: Input Values of Afterheat Decay Function, DE(t)

related to time behavior.

3.2.2.4 Surface Emissivity and View Factors

The radiation heat flux from surface 1 to 2 is given by

$$q'' = \sigma_R \, VF_{12} \, (\varepsilon_1 \, T_1^4 - \varepsilon_2 \, T_2^4) \qquad (3.7)$$

where temperatures are in absolute degrees (°K). Both the view factor (VF) and emissivity (ε) range from zero to one and represent deviations from maximum heat radiation due to 1) the fact that surface two may be only a part of the area enclosing surface one and 2) the surface conditions may decrease emission.

The model of Eq. (3.7) incorporates the assumption that surfaces acting as gray, diffuse emitters and reflectors. This means that emission and reflection are angle (diffuse) and wavelength (gray) independent; otherwise the factors would have to be summed over angle and wavelength. The gray, diffuse approximation is a common one for engineering application and is forced here due to the lack of more specific data.

For surfaces i (i = 2, ...) enclosing surface one, we have

$$\Sigma_i \, VF_{1i} = 1 \qquad (3.8)$$

For present purpose, heat is being transferred only between opposing surfaces, and $VF_{12} = 1.0$ (no heat to other surfaces). Furthermore heat is only transferred between surfaces of similar material. Since (as discussed below) the emissivity is not highly temperature dependent, Eq. (3.7) becomes

$$q'' = \sigma\varepsilon(T_1^4 - T_2^4) \qquad (3.8)$$

The emissivity in general is temperature, material, and surface-condition dependent. In the present analysis, the relevant surfaces are all internal within the module and are exposed to either a coolant or breeder fluid. As discussed in Chapter 7, all these surfaces will be oxidized to some degree. This results in a very high emissivity (see Appendix B, Table 3.3) that is fairly constant with temperature. Exterior surfaces, those repeatedly heated and cooled (un-oxidized), would show significantly lower emissivity. Even worse would be new, clean, polished surfaces where emissivities of these metals would fall near 0.1.

3.2.2.5 Initial Temperature

The initial temperatures of components materials were established, based on Chapter 2 and Appendix C. The values used are listed in Table 3.4

3.2.3 Coolant Loss Rates

A critical question is how fast a blanket fluid, coolant or breeder, may empty.

3.2.3.1 Basic Geometry

The various scale lengths of various accidents were discussed in Section 3.1. The basic geometry of blanket modules influences emptying rates. Two of the basic approaches to blanket design are shown in Fig. 3.4. The most common design of a Tokamak blanket is divided into toroidal sectors so that individual units may be moved between toroidal field coils for replacement. One approach (more common) is to subdivide

TABLE 3.3

Surface Emissivities*

Condition	Metal	Emissivity
Oxidized	Steel	0.88
Oxidized	V-alloy	0.85 (estimated)
Oxidized	TZM	0.82

*See Appendix B for discussion of values

TABLE 3.4

Initial Temperatures for LOCA Analysis

Material	Temperature (°C)	Use
316 SS	450	structure
HT-9	450	structure
V-alloy	600	structure
TZM	900	structure
$LiAlO_2$	650	Breeder
Be	500	Multiplier
$Li_{17}Pb_{83}$	500	Breeder
Li	500	Breeder with SS structure
Li	600	Breeder with V structure
Li	900	Breeder with Mo structure
Li	450	Coolant with SS structure
Li	550	Coolant with V structure
He	435	Coolant
Water	320	Coolant
Flibe	800	Coolant

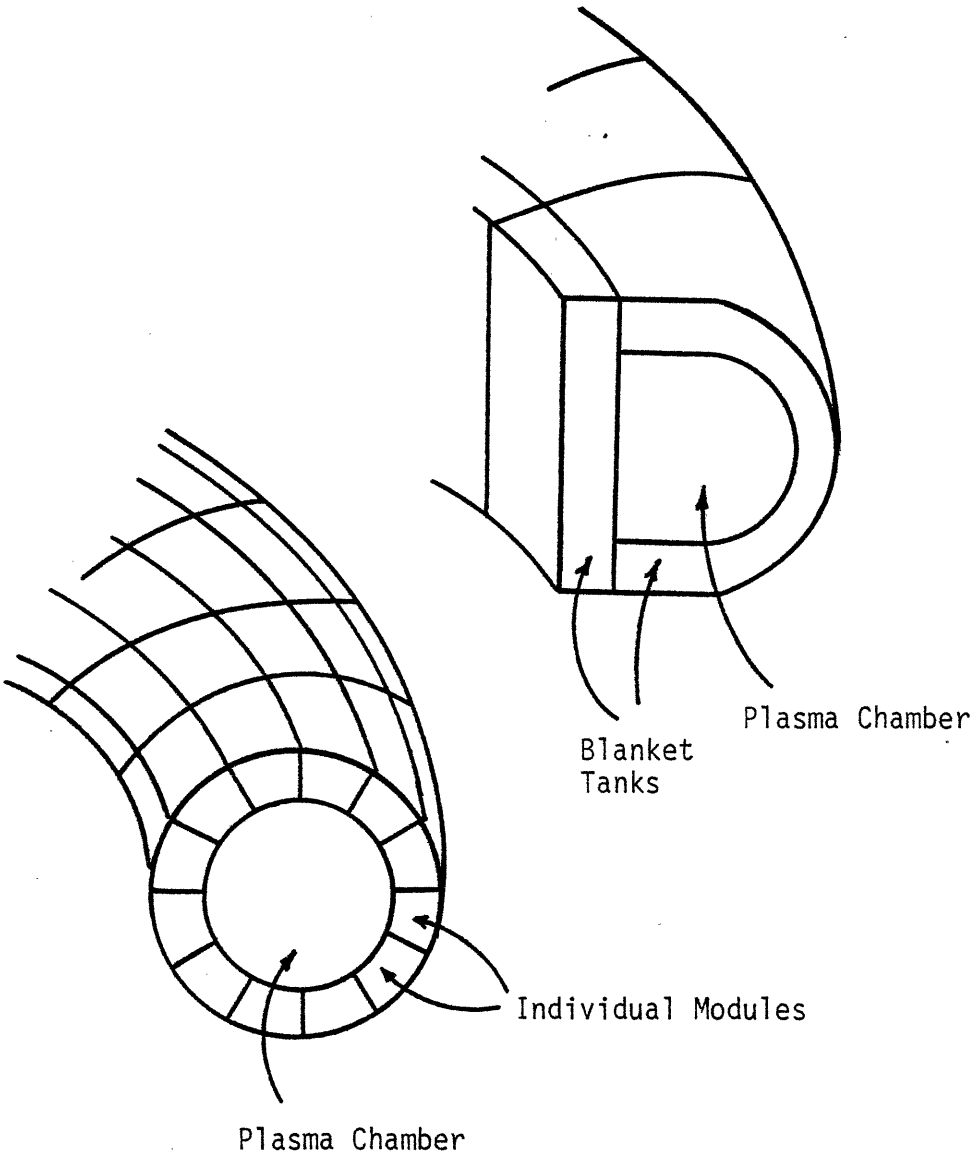

Fig. 3.4: Comparison of Blanket Sector with Modules Divided Poloidally Versus Sector-Sized Tanks

these sectors into modules (Figure 3.4a). This approach is followed, for instance, by the STARFIRE [3.2] and Westinghouse/ORNL [3.11] designs. The high number of individual units (240 for STARFIRE, 66,000 for Westinghouse/ORNL) combined with the placement of much of the manifolding coolant volume external to the module unit decreases the ratio of coolant volume/potential break area (V/A_b) relative to sector-size tanks or fission geometries.

The time to empty will be seen to scale as V/A_b so that the more common small module could experience rapid depressurization. Classic LOCA analysis assumes the worst case to be a single large pipe break. For such a case the relevant volume is the entire coolant inventory which must empty through the single break.

With small modules, the inlet and outlet pipes (indeed all connections) are within about two meters or less of each other. The close proximity reduces the independence of failure between them. A variety of common cause failures (seismic events, magnetic forces, etc.) can be envisioned that can break both inlet and outlet pipes. For this case the relevant coolant volume is only that which is contained within an individual module. For example, the entire coolant volume in STARFIRE is about 550 m^3, but the total volume in the modules alone is only 20 m^3. Thus, if small modules are employed and a double break occurs, the coolant loss rate would be significantly higher than for a single break system.

Furthermore, if such a geometry were used, the vulnerability of the design (common cause failure) increases the difficulty of designing a credible emergency auxiliary cooling system. How does one cool a module if it is possible for all connections (placed close together)

are severed? There are two possible solutions. First, make it impossible for module/support severing to occur. The analysis for this is beyond the scope of this study. Second, design the module and select materials so that auxiliary cooling is not required.

There is an additional problem. If sectors are subdivided into modules around the minor radius (Figure 3.5), there will be a variance in the orientations of each module. For coolants whose loss rates are gravity dominated (liquid metal or salt) rather than those forced out by pressure (helium, water), this differing orientation causes differing transients. The best case is a module positioned above the plasma since the pipe breaks will not allow the liquid to drain and any remaining liquid will be in contact with the first wall. The worst case is a module below the plasma. Then a pipe break allows complete draining and any drainage will tend to result in a void between cooling liquid and first wall. Again, sectioning of sectors into small units imposes a LOCA-safety penalty. The overall trade-offs on this question are discussed in Chapter 9.

The exact coolant loss rates are difficult to determine and design dependent, but it is possible to determine estimates of the time scales involved.

3.2.3.2 Water-Cooled Loss Rates

Of the coolants under study, water would operate at the highest pressure ($\sim$15.2 MPa). There is also a large body of analysis of LOCA events in a PWR. There are two fundamental differences between fission and fusion water-LOCA's. The first, already explained, is the relatively lower volume of water to empty in fusion designs, resulting in less time

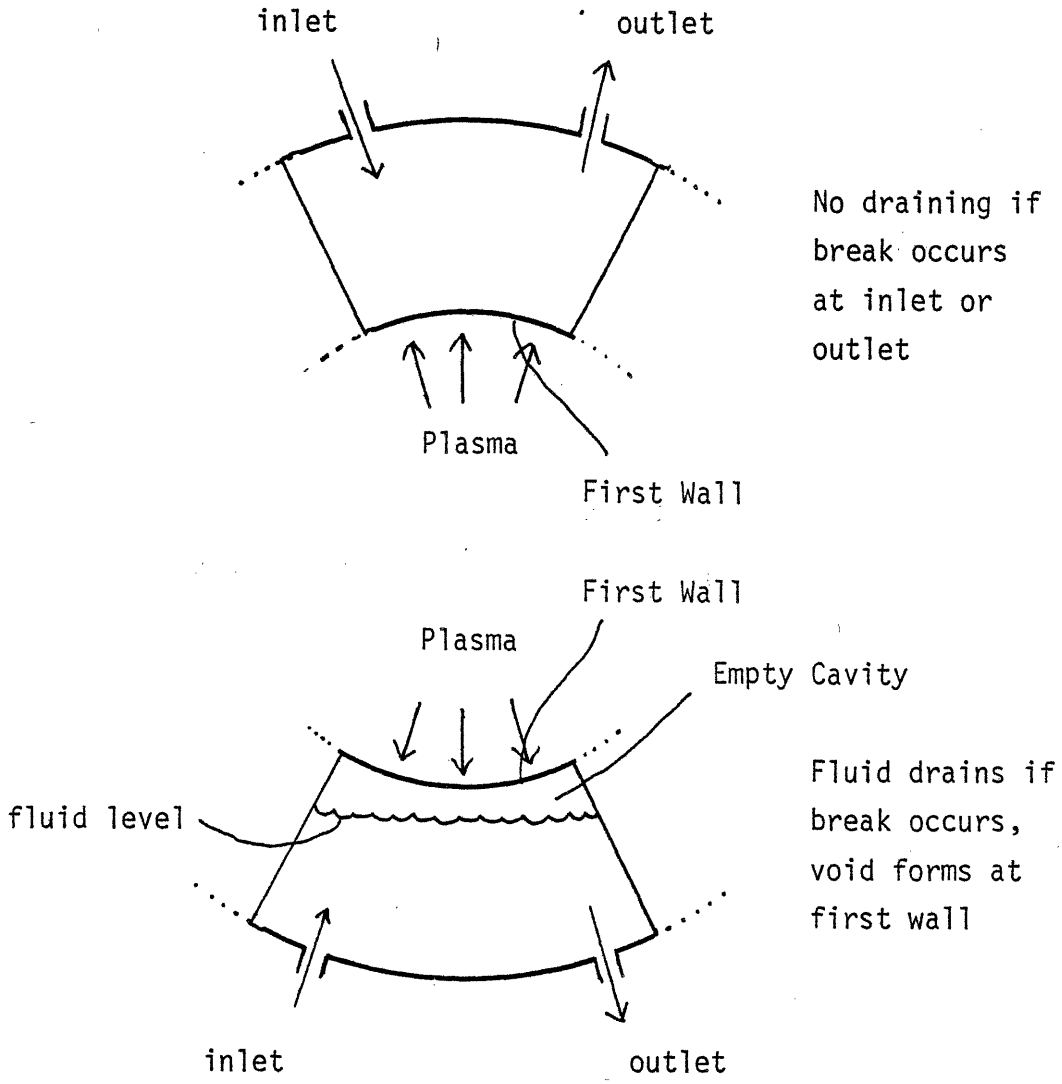

Fig. 3.5: Comparison of Blanket Module Above the Plasma with One Located Below the Plasma

needed to empty for the case of small units. Second, the power density (and accident heat-up rates) are lower in fusion, reducing the relevance of what happens in the initial time period. Thus, overall, a fusion blanket takes less time to empty and less heat-up may occur per unit time. Both effects combine to reduce the contribution of cooling during the depressurization for a fusion design.

PWR-LOCA analysis is very complex, but one can note the basic time scale. A sensitivity analysis by Green and Lawther [3.12] showed that dryout heat transfer regime was reached between 0.01 - 0.08 seconds with film boiling $\lesssim$0.5 sec. Figs. 3.6, 3.7 show a smoothed out time history of the transient pressure and heat transfer coefficient. Whereas these time scales are very relevant to fission analysis, we shall see that only about a 50 °C temperature rise is possible (first wall, plasma heating, adiabatic case) in this time frame. Thus, the most the depressurizing water could do for a fusion design is to delay a 50 °C temperature rise by a half second.

With such a high module pressure, the flow out the break will be a choked flow virtually instantaneously. A common expression for the flow rate is

$$\dot{m}/A = 0.61\sqrt{2(P_o - P_b)\rho} \qquad (3.10)$$

where $\dot{m}/A$ = flow rate (kg/m^2-sec) through break

ρ = fluid density

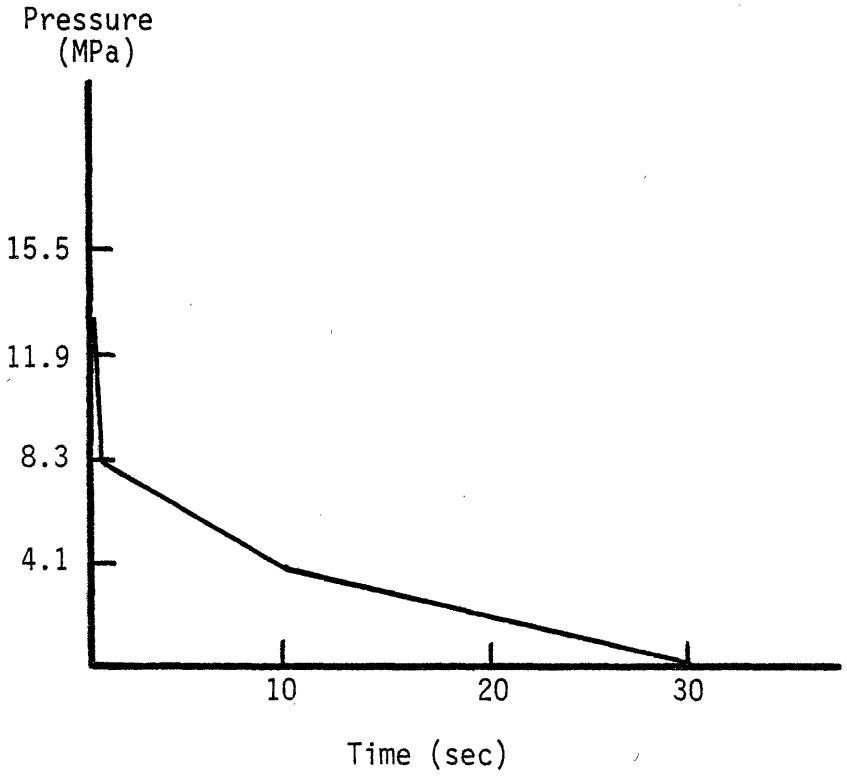

Fig. 3.6: Time History of Water Pressure Following LOCA

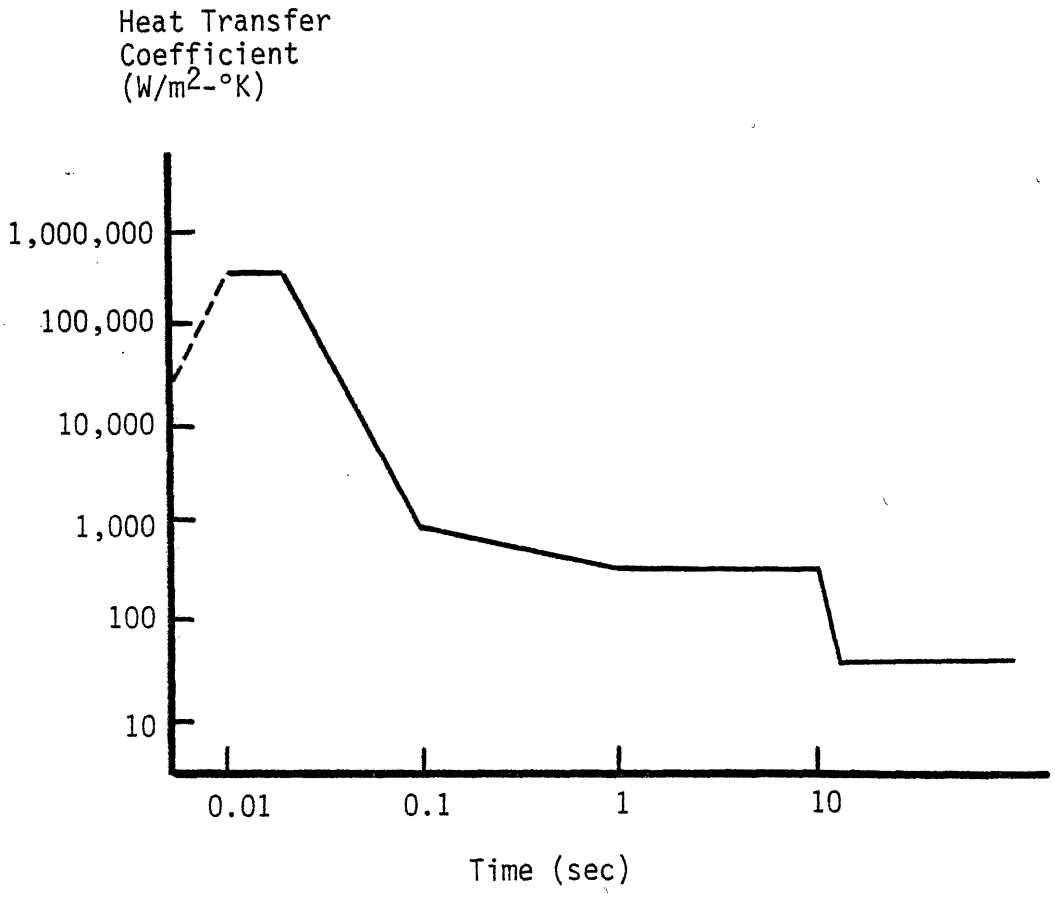

Fig. 3.7: Time History of Water Heat Transfer Coefficient Following LOCA

P_o = internal fluid pressure

P_b = containment (external) pressure

for conditions of interest a conservative estimate of external pressure is $0.1 \times P_o$. Thus,

$$\dot{m} = 0.82\, A_b \sqrt{P\rho} \quad \text{kg/sec} \tag{3.11}$$

Conservation of mass in the blanket volume gives the equation

$$V \frac{d\rho}{dt} = -\, 0.82\, A \sqrt{P} \sqrt{\rho} \tag{3.12}$$

$$\dot{\rho} = \left(\frac{0.82A}{V} P^{\frac{1}{2}} \right) \rho^{\frac{1}{2}} \tag{3.13}$$

This is not easily solvable since P is a function of ρ. However one can estimate the time to empty by making the following assumptions. Fix $P \sim \frac{1}{2} P_o \sim 8$ MPa and set A_b/V for a water design as $\gtrsim 0.25\ m^{-1}$ (see Appendix C). Then

$$\dot{\rho} = 580\, \rho^{\frac{1}{2}} \tag{3.14}$$

and the time to empty is given by

$$t_e(\text{water}) \sim \frac{\sqrt{\rho_o}}{(0.5)(580)} < 0.1 \text{ sec} \tag{3.15}$$

An alternative approach is to assume choked flow within the tubing. Then

$$t_e(\text{water}) \sim L/v \tag{3.16}$$

where L = length of tube pass through module

v = choked flow velocity,

Since $$v \sim \frac{\dot{m}}{A_\rho} = 0.82 \sqrt{\frac{P}{\rho}} \text{ m/sec} \sim 100 \text{ m/sec} \tag{3.17}$$

then one obtains

$$t_e(\text{water}) \sim 0.01 \text{ sec} \tag{3.18}$$

In either case, the time scale to empty is at least as short as for a PWR. As an estimate of the cooling provided, the heat transfer coefficient in Figure 3.7 was used based on results in Reference 3.12.

3.2.3.3 Helium-Cooling Loss Rates

The analysis for helium is simpler and less uncertain due to the one-phase behavior. There is also a different behavior at long times. Since a helium loop is designed for high-speed gas-phase, then the blower/pump may continue operating as depressurization occurs if unaffected by the accident itself. Depending on the ultimate pressure of the building, and the placement of the break relative to the pump, the loop will still provide some cooling. A water pump would cavitate.

Depending on design and size, a fission gas-cooled reactor has depressurization time constants between 30 sec [3.13] and 60 sec [3.14] with an exponential decay. The mass flow of an ideal gas through a break is given by (see reference 3.15 for example)

$$m = \frac{AP_o}{RT_o} \sqrt{2c_pT_o\left(\frac{P}{P_o}\right)^{2/\gamma} - \left(\frac{P}{P_o}\right)^{\frac{\gamma+1}{\gamma}}} \tag{3.19}$$

where P_o = initial internal pressure

P = exit pressure

T_o = internal absolute temperature

R = 2079 J/kg °K for helium

γ = 1.667 for helium

Choked flow results in P/P_o reaching a maximum of

$$P/P_o = \left(\frac{2}{\gamma+1}\right)^{\gamma/\gamma-1} \tag{3.20}$$

For helium, this leads to

$$\dot{m}_{maximum} = \frac{A_bP_o}{\sqrt{T_o}} \times 0.0159 \ \frac{\sec\ (°K)^{\frac{1}{2}}}{m} \tag{3.21}$$

Using the ideal gas law and conservation of mass, one obtains

$$-\frac{dP}{dt} = \left(\frac{A_b}{V} R \sqrt{T_o} \times 0.0159\right) \times P \tag{3.22}$$

Again the factor A_b/V appears. For the reference design (Appendix C), a typical value is $0.25m^{-1}$. Equation 3.22 is solvable for the isothermal case. Then

$$P = P_o\, e^{-\omega t} \tag{3.23}$$

relates to the absorption of heat due to melting. The maximum depth of melting as t_{pd} is varied is given by

$$d_{mm} = \frac{1}{\pi}\left(\frac{E/A}{\rho c_p(T_m - T_o)}\right) \tag{4.8}$$

at a plasma disruption time given by

$$(t_{pd})_{\substack{max \\ melting}} = \frac{1}{\alpha\pi}\left(\frac{E/A}{\rho c_p(T_m - T_o)}\right)^2 \tag{4.9}$$

The neglect of the heat of melting can be eliminated by using finite difference methods. Furthermore, vaporization can be included. Fraas and Thompson [4.7] performed such calculations, assuming the vaporized material does not move, using dimensionless variables. Again, the geometry was a semi-infinite flat plate subjected to a step heat flux. Calculations were performed for INTOR [4.3] for 316 SS and aluminum which included transport of the vapor phase.

In their analysis, Fraas and Thompson defined several dimensionless variables to produce more general results. Dimensionless heat of melting and vaporization were defined as the ratio of the heat of phase change to the margin of sensible heat before melting:

$$\eta_m = H_f/c_p(T_m - T_o) \tag{4.10}$$

$$\eta_v = H_g/c_p(T_m - T_o) \tag{4.11}$$

For a variety of metals, these values are fairly constant with $\eta_m \sim 0.42$

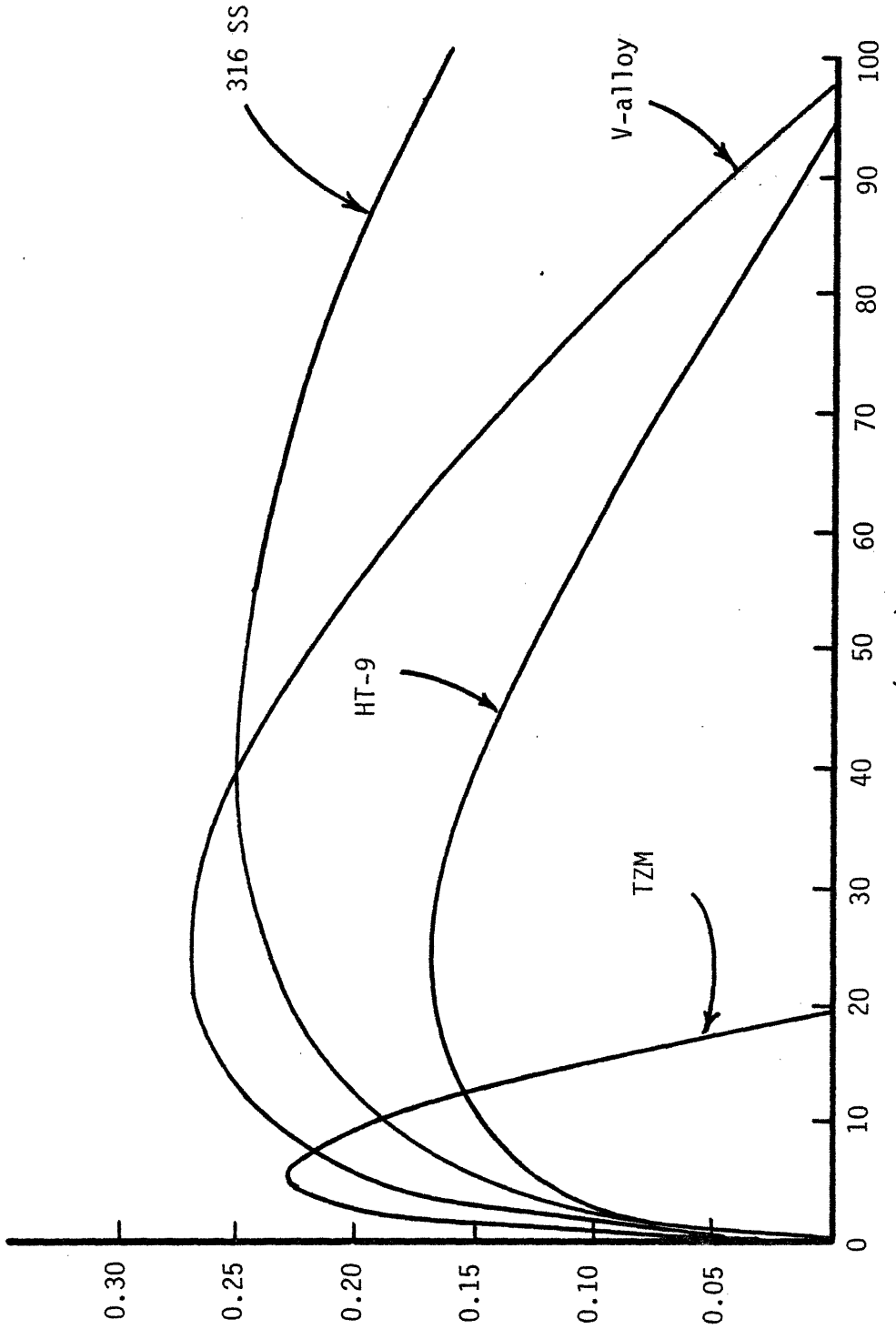

Fig. 4.3: Calculated Depth of Melting Caused by Disruptions of Varying Time Scale, Simple Analytic Model [4.7], Latent Heat of Melting Ignored

TABLE 4.7

Minimum Disruption Time (msec) to Avoid Melting and Vaporization*

	Minimum to Avoid Melting	Minimum to Avoid Vaporization
316 SS	160	28
HT-9	92	16
V	97	19
TZM	19	3.7

*Low values preferred, Eqs. (4.5), (4.6) used

$$t_v = \frac{4}{\pi}\left(\frac{E}{A\Delta T_{ov}}\right)^2 \frac{1}{\rho c_p k} \qquad (4.6)$$

where $\Delta T_{om} = T_m - T_o$

$\Delta T_{ov} = T_v - T_o$

Ideally, these should include the variance of material properties due to temperature and latent heat of melting and vaporization. In fact, there is considerable uncertainty in the heat of melting and vaporization, especially for V-alloy and TZM. To first approximation, the minimum disruption times to produce melting and vaporization can be calculated using Eqs. (4.5) and (4.6) and material properties at 800°C (see Appendix B). The results are presented in Table 4.7.

A simple analytical expression for the depth of melting is possible if the latent heat of melting is ignored. Fraas and Thompson [4.7] examined the depth of melting for a uniform semi-infinite plate with a step heat flux profile. For the case where material properties are independent of temperature (average values used) and the latent heat of melting is ignored, they obtain the depth of melting, d_m, as a function of disruption time and material properties:

$$d_m(t_{pd}) = \frac{2}{\sqrt{\pi}}(\alpha t_{pd})^{1/2} - \frac{\rho c_p (T_m - T_o)}{E/A}(\alpha t_{pd}) \qquad (4.7)$$

This is plotted for the reference materials in Fig. 4.3 (material properties evaluated at 800°C). The first term, which controls at very short times, relates to the penetration of the temperature wave. The second

TABLE 4.6

STARFIRE Maximum Temperatures**
From Plasma Disruptions

Location	t_{pd} = 25 msec	t_{pd} = 100 msec
Beryllium Coating	1325*	1020
316 SS First Wall	795	790

*Beryllium would have melted, ignored in analysis

**From reference 4.4

TABLE 4.5

Safety Margin Against Melting

	Relative Value**	Absolute Values			
		t_{pd} = 25 msec		t_{pd} = 100 msec	
		Eq. (4.3)	Code	Eq. (4.3)	Code
316 SS	2.86	2.53	2.69	1.27	1.40
HT-9	2.17	1.92	2.02	0.96	1.05
V-alloy	2.23	1.97	2.16	0.98	1.18
TZM	1.00	0.88	0.88	0.44	0.42

*$SM_m = \Delta T_{rise}/(T_m - T_o)$, low values preferred

**Relative to TZM

so that SM = 1 implies the onset of melting; low values are preferred. This factors in an additional material property: $T_{melt} - T_{operation}$ ($= T_{om}$). The relative values are shown in Table 4.5. The absolute values at t_{pd} = 25 msec, 100 msec from computer run results are also listed.

It is instructive to note the results of the STARFIRE analysis for their 316 SS structure (1.5 mm) with a 1.0 mm Be coating (Table 4.6). The coating takes the main impact of the disruption. The coating has several effects: 1) keeps ΔT_{rise} for structure $\lesssim$ 350°C, 2) de-couples material suffering the worst temperature rise (coating) from material providing structural support (316 SS), 3) decreases time dependence, and 4) allows for the possibility of easier repair if needed since the coating may be repaired in-situ. The ability of the two materials to stay in contact was not addressed in reference 4.4 and could be a problem.

4.2.1.3 Short Time Scale

As seen above, if the disruption time is short enough, surface melting will occur. At even shorter times, surface vaporization may occur. Equation (4.3) can be re-written and solved for the disruption time that results in the onset of melting or vaporization (latent heats ignored),

$$t_m = \frac{4}{\pi} \left(\frac{E}{A \Delta T_{om}} \right)^2 \frac{1}{\rho c_p k} \qquad (4.5)$$

TABLE 4.4

Relative First Wall Temperature Rise*

	Basic Scaling (Eq. 4.3)	Normalized Temperature Rise from Code Calculations t_{pd} = 25 msec	t_{pd} = 100 msec
316 SS	1.64	1.75	1.89
HT-9	1.23	1.30	1.40
V-alloy	1.69	1.86	2.11
TZM	1.00	1.00	1.00

*Relative to TZM, low values preferred

the maximum temperatures. This is expected since the ramp-down model has an initially higher heat flux, resulting in faster heat-up. The ramp-down model results in maximum temperatures being reached before the end of the disruption. The TZM case shows less variation, possibly because the variation from Eq. (4.3) (high Fourier number) is cancelling the effect of surface heat flux modeling.

In any case, the impact of the exact time profile for the heat flux is relatively small as compared to uncertainties in E/A and t_{pd}. Onega, et. al. [4.1] used two different heat flux profile models (at one time, t_{pd} - 24 msec; one material, 316 SS) and similarly found less than a 10% temperature variation.

The code runs also verified the non-influence of first wall thickness. The six references cases of Chapter 3 (d_{fw} from 1 mm to 3.8 mm) were used and the first wall thickness had less than a ∿1% impact on maximum temperatures. The thermal wave did not penetrate through the first wall in this time. Of course, varying wall thickness and coolant performance would alter the rate of first wall cool-down.

The relative first wall temperature rise for the four materials is listed in Table 4.4. This is simply the relative value of $(\rho C_p k)^{-1/2}$ (properties evaluated at 800°C, see Appendix B) - the material property dependence, from Eq. (4.3). The relative temperature rise from code runs is also presented. V-alloy and 316 SS are seen about the same with TZM significantly better.

The safety margin against melting was defined as

$$SM = \Delta T_{rise}/(T_m - T_o) \qquad (4.4)$$

TABLE 4.3

Disruption Maximum Temperature Rises,*
Comparison Between Unit Step and Ramp-down Models

Structure	316-SS	HT-9	V	TZM
t_{pd} = 25 msec				
Unit Step, Eq. (4.3)	2480	1860	2560	1514
Ramp-down, Code	2640	1960	2811	1508
% difference	-6%	-6%	-10%	+1%
t_{pd} = 100 msec				
Unit Step, Eq. (4.3)	1240	930	1280	757
Ramp-down, Code	1370	1020	1530	723
% difference	-10%	-10%	-20%	+5%

*Surface melting is ignored

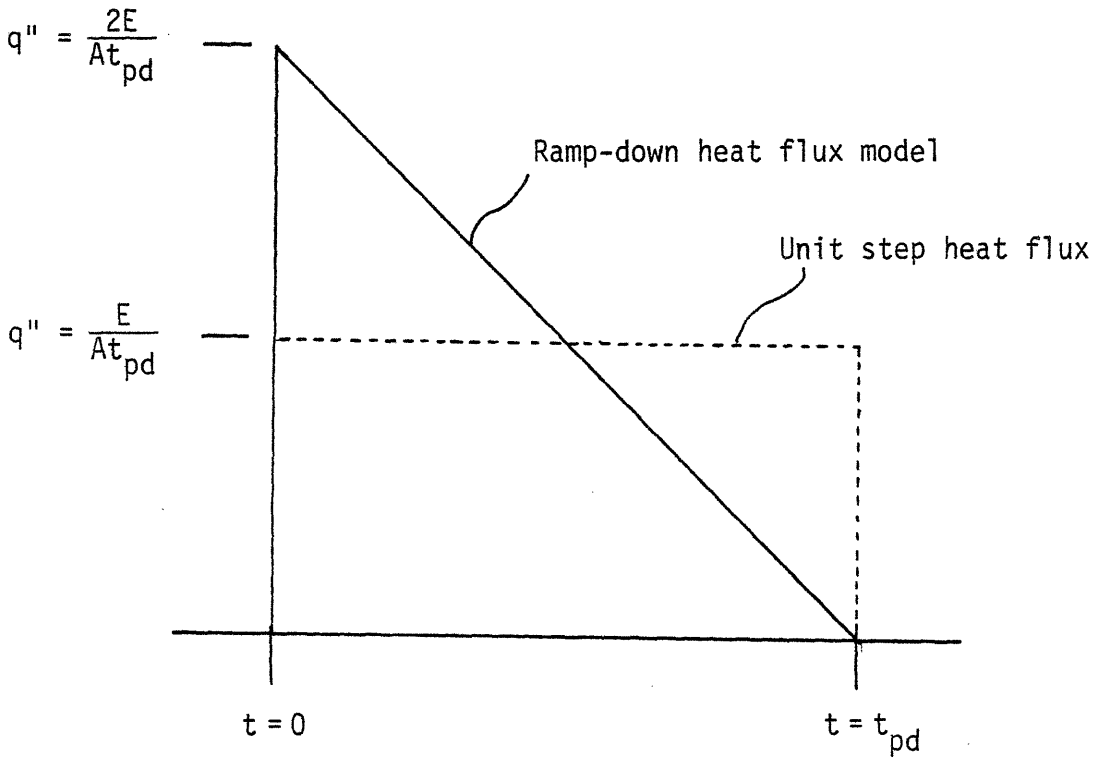

Fig 4.2: Comparison of Unit Step and Ramp-down Heat Flux Models

case where the heat flux rises instantaneously to a fixed value for the duration of the disruption, the temperature rise can be solved analytically. Jakob [4.8] gives the temperature at the surface of a semi-infinite thick plate as

$$T(t) = T_o + 2 \frac{q''_w}{k} \sqrt{\frac{\alpha t}{\pi}} \tag{4.2}$$

Given that $q''_w t_{pd} = E/A$

E = total thermal energy of the plasma

A = incident area

the final temperature at the end of the disruption (maximum temperature) is given by

$$\Delta T_{rise} = E/A \, (\rho c_p k)^{-1/2} \left(\frac{4}{\pi t_{pd}} \right)^{1/2} \tag{4.3}$$

As indicated in section 4.14, E/A is set as 3.8 MJ/m^2.

The analytical expressions for temperature rise, Eqs. (4.2), (4.3), are based on a step heat flux to the surface, see Fig. 4.2. Calculations were performed with the code HEATING3, also used in Chapter 3 (details of geometry in Appendix C) to compare the step shape results with a ramp-down profile (Fig. 4.2), assumed in the STARFIRE study. Disruption times of 25 msec and 100 msec were used, as in STARFIRE. The integrated energy deposition, E/A, is the same for both cases. As seen in Table 4.3, the calculated maximum temperatures are similar between the two time profile models. For 316 SS, HT-9, and V-alloy, the step model underpredicts

TABLE 4.2

Disruption Times Controlling
Temperature Rise Scaling with d_{fw} = 2 mm

Temperature Rise Scaling	Long Times (Eq. 4.1)	Intermediate, Short Times (Eq. 4.2)
Fourier Number Criteria	$F_o \gg 1$	$F_o < 0.3$
Disruption Time which qualifies (msec)		
316 SS	>> 700	240
HT-9	>> 900	310
V-alloy	>> 400	130
TZM	>> 100	34

thermal conduction in the first wall to bring the gradient to equilibrium. In the limit of long times (really possible only for an over-power transient) the new temperature drop across the first wall can be expressed in terms of the previous conditions and the percentage increase in heat flux. Chan [4.5] writes

$$\Delta T'_{fw} = \Delta T_{fw}\left(1 + \frac{X}{100}\right) \tag{4.1}$$

where ΔT_{fw} = initial temperature drop across first wall

$\Delta T'_{fw}$ = new gradient due to increased power level

X = percent increase in power level.

The dimensionless time relevant in these problems is given by the Fourier number, F_o, with

$$F_o \equiv \frac{\alpha t_{pd}}{d_{fw}^2}$$

where t_{pd} = disruption time

α = thermal diffusivity = $k/\rho c_p$

d_{fw} = first wall thickness.

The power increase equation, 4.1, appears valid for $F_o \gg 1$. For conditions of interest, this implies $t_{pd} > 1$ sec, which is quite long - more than would be implied by disruption time scaling.

4.2.1.2 Intermediate Time Scale

For $F_o \lesssim 0.3$, the thermal diffusion becomes important [4.6]. For conditions of interest, this is satisfied (see Table 4.2). For the

vaporization, d_{mv}, are relevant.

The scaling of thermal stresses with material properties indicates how material choice influences resulting stresses. Although the appropriate failure criterion to judge stresses among materials is unknown, a representative value is the generated stress relative to the yield stress.

The temperature rise due to induced currents is calculated and shown to be minor compared to the surface heat flux. The magnetic stresses relative to material choice are important. Again, a representative criterion to judge the impact of stresses is comparison to the yield stress.

4.2 Surface Heat Flux Effects

The effects of the particle flux on the first wall are analyzed, ignoring the magnetic field.

4.2.1 First Wall Temperature Rise

Of all the effects generated by a disruption, the resulting first wall temperature rise and possible melting and vaporization have been the most studied. There are good reasons for this. The phenomena (heat flux, thermal conduction, etc.) are understood enough for reasonably accurate results to be obtained. The analysis itself is relatively straight-forward. Finally, the blanket design is fairly unimportant. These aspects are not true for the other disruption effects.

4.2.1.1 Long Time Scale - Over Power Transients

If the disruption scale is long enough, there is adequate time for

TABLE 4.1

Quantitative Measures
Concerning Plasma Disruption Effects

Thermal Effects - Temperature Rise

1. First Wall Temperature Rise, $\Delta T_{rise} = T(t, \text{surface}) - T_o$
2. Safety Margin Against Melting, $SM_m = \Delta T_{rise}/(T_m - T_o)$
3. Minimum Disruption Time to Avoid Melting, t_m
4. Maximum Depth of Melting, d_{mm}
5. Minimum Disruption Time to Avoid Vaporization, t_v
6. Maximum Depth of Vaporization, d_{mv}

Thermal Effects - Thermal Stresses

1. Relative Thermal Stress, s_T
2. Safety Margin Against Yielding, $SM_y = s_T/s_y$

Magentic Effect - Eddy Current Resistance Heating

1. Temperature Rise, ΔT_{rise}

Magnetic Effect - Magnetic Stresses

1. First Wall Magnetic Stress, s_{wm}
2. Blanket (Breeder Zone) Magnetic Stress, s_{bm}
3. Safety Margin Against Wall Yielding, $SM_y = s_{wm}/s_y$

the STARFIRE case would have lead to a reference energy deposition of 5.36 MJ/m^2 rather than 3.8 MJ/m^2. Present numerical results are based on a single deposition value of 3.8 MJ/m^2 (with possible range of 0.0 to 5.39 MJ/m^2), although comparison among materials is independent of the value used.

4.1.5 Failure Criteria

The variety of effects generated by disruptions leads to a large number of criteria to judge material selection. The uncertainty in time scale causes uncertainly in the thermal and magnetic effects and the scaling with material properties. The uncertainty in expected frequency causes uncertainty in failure criteria and the relative ability of materials to withstand calculated stresses. Nonetheless, some quantitative measures are possible and appropriate.

These measures are listed in Table 4.1. Both the absolute temperature rise and temperature rise compared to melting are important scaling measures. Melting of the surface, even for a short time, is to be avoided. The melted material may be lost, causing severe wall erosion [4.3]. Even if the material were to remain in place, the microstructure resulting from the melting and re-freezing would likely be different than that of the previous alloy, with potentially unfortunate consequences in wall behavior. Thus the minimum disruption time, t_m, that causes melting and the maximum depth of melting, d_{mm}, are relevant. Vaporization of material is worse than melting - material is lost from the wall and radioactivity mobilized. Thus the minimum disruption time that causes surface vaporization, t_v, and maximum depth of

combination is beyond the scope of the study. As discussed in Chapter 2, only the basic parameters are established to allow general examination of safety problems for typical design concepts. Precise details such as the placement of structure supports are not provided. This is appropriate since the intended comparison in this study is not among specific designs but rather among generic safety problems imposed by the selection of certain material combinations. The relative impact of selecting one material over another should not be tied to a specific detailed design. This limits the analysis of precise thermal and magnetic effects, but allows determination of the general scaling of those effects among materials. Since the first wall thickness for a given structural material varies among the reference cases as a function of coolant, a constant first wall thickness of 2 mm was assumed in this analysis to decouple design specifics from relative structural material behavior. Unfortunately, appropriate failure criteria are uncertain.

For the present study, values of plasma energy, E, and incident area, A, were taken from the STARFIRE study (reference size plasma). Thus E = 920 MJ and A = 30% of total (800 m^2) = 240 m^2. Thus the energy deposition is 3.8 MJ/m^2.

For the smaller INTOR [4.3], the assumption was that 70% of the total energy (200 MJ) would be deposited in 30% of the area, leading to a deposition of 1.45 MJ/m^2. However, the reference INTOR case was to allow a localizing peaking faction of 2.0, with energy deposition of 2.89 MJ/m^2. Applying the INTOR assumption and peaking factor to

effect of fusion radiation environment on materials is poorly known, particularly for materials like vanadium and molybdenum.

The ideal solution would be use of plasma physics predictions and detailed reactor design to calculate stresses and temperatures. These would be compared to appropriate failure criteria, depending on the expected frequency of the disruptions.

4.1.4 Scope of Present Study

Unfortunately, disruptions and the somewhat similar problems of other confinement schemes are poorly understood. The precise behavior over time and the time scale itself are unknown. The expected frequency in a commercial reactor is uncertain. The materials properties in an irradiated state are poorly estimated. The ideal solution is not yet possible.

The purpose of the current analysis is to explore disruption effects sufficiently to identify the important material properties which influence the severity of the effect. As noted above, these properties and their relative impact are a function of time scale. The scaling of the effects with properties allows determination of the impact of material selection.

As discussed in chapters 1 and 2, current knowledge of irradiated material properties, principally material strength (yield, fracture toughness, ductility), for the reference materials does not allow use of irradiated property values. This work incorporates only unirradiated property values.

Furthermore, establishing a full detailed design for each material

design would allow precise examination of localized effects and the complex flow of currents induced in the structure. The total result would be calculation of stresses and temperatures in a design.

Identification of the expected frequency of disruptions is needed to know the appropriate failure criteria. A variety are outlined here to demonstrate the uncertainty involved.

If disruptions in commercial reactors are very rare, unexpected in a typical blanket lifetime, the survival goal would be to avoid gross structural failure. Thus material properties like the fracture toughness and ultimate tensile stress, s_{UTS}, are relevant.

If disruptions might be likely a few times over the lifetime, the survival goal would need to include the ability to replace damaged parts. Since the general maintenance scheme appears to be removal and replacement of individual failed modules, it is vital that structural deformation be minimal to allow modules to be free to be pulled out. The relevant material properties would be elongation and the yield stress, s_y.

If designers are faced with the likelihood of frequent disruptions, an even more stringent criteria would be needed. Multiple bursts of heat flux make material resistance to fatigue relevant.

Since the frequency of disruptions in a commercial reactor is unknown, then, the relevant material properties which control failure is unknown. The scaling among materials is thus somewhat dependent on what constitutes failure. Additionally, short term heating might alter finely-tuned microstructure within an alloy. Finally, the

reactor size tokamak is unknown. Consequently, the appropriate effects were determined for differing time scales. As presented later, the temperature rise and thermal stresses show differing material property behavior scaling at different time scales. Thus the relative comparison among materials differs with the disruption time scale. The question of whether an effect is even relevant for a given material depends on the disruption time. The relative consequence comparison is meaningless if the effect itself is too small to be significant.

Current size devices have submillisecond disruption times [4.1-4.3], $t_{pd} < 1$ msec. Although uncertain, the disruption time is expected to scale upwards as devices increase in size, density, etc., to commercial reactor size. Directly applying the scaling of reference 4.1 to the STARFIRE plasma (reference case for this study) results in $t_{pd} \sim 55$ msec (see Appendix C). The STARFIRE design team [4.4] examined disruption effects for that design for two cases: $t_{pd} = 100$ msec (reference case) and $t_{pd} = 25$ msec (alternate). Differences in current and density profiles increase the scaling uncertainties. The expected INTOR time scale is 20 msec [4.3]. For all cases, a longer disruption time scale (other parameters held constant) reduces all effects.

4.1.3 Ideal Solution

Ideally, the plasma physics of disruptions would be sufficiently known to allow prediction of the time scale, t_{pd}; energy, E; target surface area, A; and the temporal and spatial profile of the flux as well as induced currents and forces. Perhaps a range of values, with some probability density, would be expected. Furthermore, a detailed

The stresses (thermal and magnetic) act on the first wall and surrounding structure at the same time that structural temperatures may have risen due to the heat flux and resistence heating. The elevated temperatures can severely reduce structural yield stress. Thus the coupling of effects is worse than either alone.

Of all parts of the current study of material impact, this is the portion most tied to the tokamak plasma confinement scheme. Tokamaks have disruptions and the relative structural influence on their effects must be determined.

Other magnetic confinement schemes (e.g., torsatron, stellerators, EBT's, and mirrors) and the inertial confinement approaches (driven by light ion particle beams or lasers) are basically disruption free. However, at least some of these may suffer some disruption-type effects. Any rapid destruction of magnetic confinement could, in principle, lead to first wall heat flux due to particles and magnetic forces generated by transient currents and magnetic fields. Abnormal auxiliary heating behavior, such as a neutral beam mis-aim, is another potential source of increased surface heat flux. A mis-aim of an inertial confinement driver may cause a short-term lead load on a first wall structure. Thus, although the present analysis is limited to tokamak disruption modeling, various pieces of the work (and resulting implications and conclusions) may be relevant to other confinement devices.

4.1.2 Time Scale

The disruption time, t_{pd}, is critically important in determining the effects. Unfortunately, the time scale for disruptions in a commercial

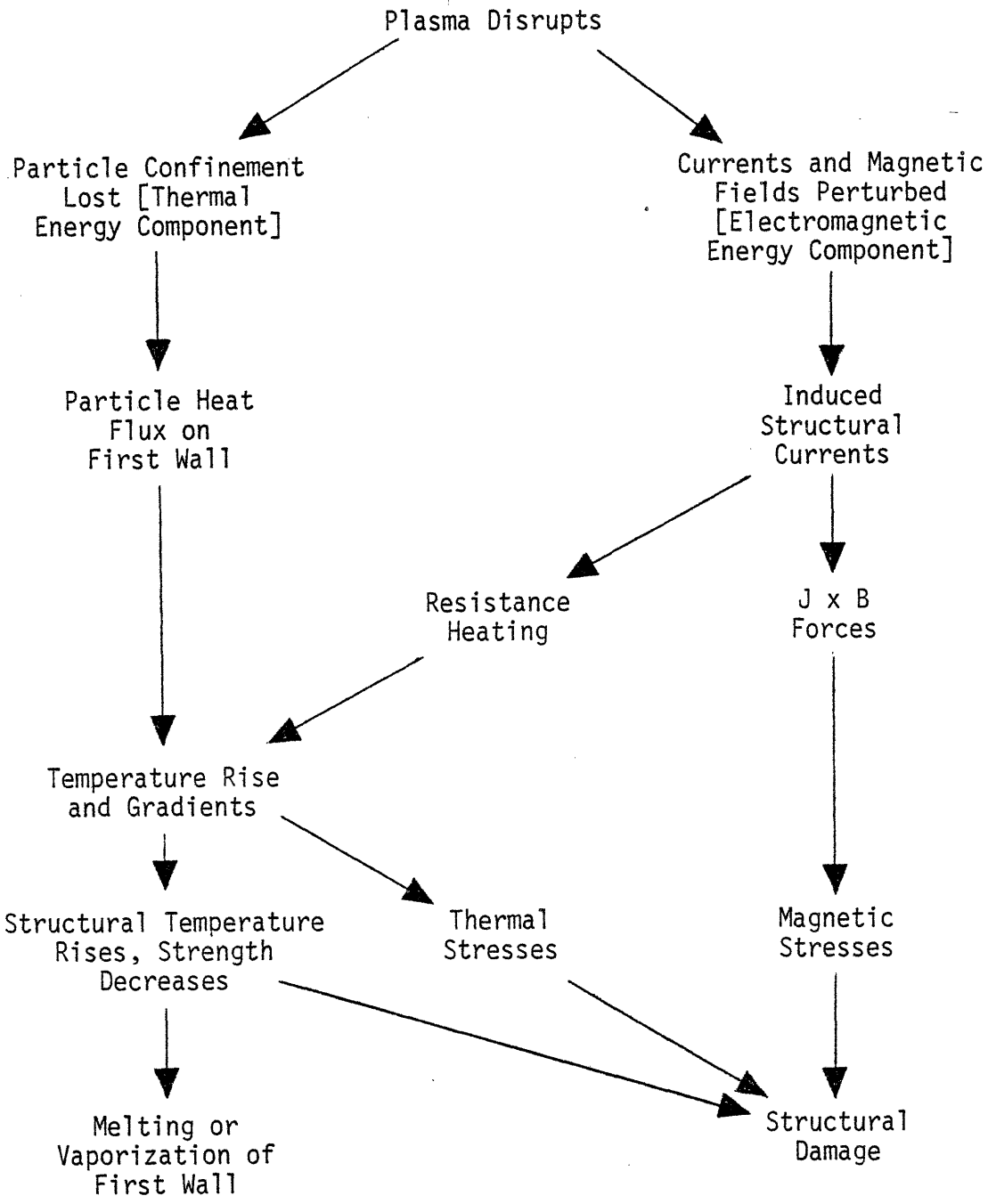

Fig. 4.1: Illustration of Possible Interactions of Plasma Disruption Effects on the First Wall

CHAPTER 4. PLASMA DISRUPTION EFFECTS

Misbehavior of the fusion plasma may cause problems within the blanket, offering the potential for reactor damage and public-health consequences.

4.1 Problem Description

This chapter contains the analysis of consequences of plasma misbehavior. The primary effects to surrounding blanket structure can be divided into thermal and magnetic. Although the specific misbehavior discussed is plasma disruption, the resulting analysis and some safety criteria have a more general application.

4.1.1 General Problem

Present day experimental tokamak devices have experienced a very rapid (sometimes very violent) loss of plasma confinement due to collective behavior of the particles. The process results in the plasma particles striking some fraction of the first wall (generally the inboard side of the torus), the plasma currents being displaced into surrounding structure, and the magnetic fields being perturbed.

The particle flux causes a burst of heat load on the first wall as do the induced structural currents. These constitute the thermal effect - temperature rise and thermal stresses due to non-uniform temperature rise. The currents and magenetic fields combine to produce magnetic forces on structural members. This constitutes the magnetic field effect.

A general diagram, illustrating both effects, is given in Fig. 4.1.

3.16 C.P.C. Wong, et al., "Thermal-Hydraulics Design Comparisons for the Tandem Mirror Hybrid Reactor Blanket," loc. cit. [3.3], p. 757, also GA-A16069 (1981).

3.17 G.A. Carlson, "Magnetohydrodynamic Pressure Drop of Lithium Flowing in Conducting Wall Pipe in a Transverse Magnetic Field—Theory and Experiment," Proceedings of the First Topical Meeting on the Technology on Controlled Nuclear Fusion, CONF-740402-P1, (1974), p. 642.

3.18 "Some Safety Considerations for Conceptual Tokamak Fusion Power Reactors," EPRI-ER-546 (7/1978).

3.19 D.K. Sze, "Emergency Cooling and Afterheat Effects of a CTR Blanket," loc. cit. [3.17], p. 599.

3.20 B. Badger, et al., "UWMAK-I Wisconsin Toroidal Fusion Reactor Design," UWFDM-68 (1973).

3.21 E.T. Cheng, et al., "Safety and Personnel Access Aspects of Low Activation Fusion Blankets," loc. cit. [3.3], p. 1248, also GA-A16081 (1981).

3.22 C.P.C. Wong, et al., "Moving Ring Field-Reversed Mirror Blanket Design Considerations," loc. cit. [3.3], p. 765, also GA-A16097 (1981).

REFERENCES

3.1 C.K. Chan, "Safety Study of Primary Coolants in Fusion Power Reactor First Wall Design," Nuclear Engineering and Design, 51 (1979), pp. 253-262.

3.2 C.C. Baker, et al, "STARFIRE," ANL/FPP-80-1, 9/1980.

3.3 B.J. Merrill, "First Wall and Blanket Module Safety Enhancement by Material Selection and Design," Proceedings of Fourth Topical Meeting on the Technology of Controlled Nuclear Fusion, CONF-801011, (1981), p. 1296.

3.4 P.J. Gierszewski, et al, "Natural Circulation in Fusion Reactor Blankets," M.I.T. Nuclear Engineering Department, unpublished report, 12/1979.

3.5 P.J. Gierszewski, et al, "Natural Circulation of Electrically Conducting Liquids in Fusion Reactor Blankets," submitted to Nuclear Engineering and Design.

3.6 W.D. Turner, and M. Siman-Tov, HEATING 3 Manual, ORNL-TM-3208, 2/1971.

3.7 J. Chao, et al, "A Parameter Study of a Lithium-Cooled Tokamak Blanket," Nuclear Technology, 42, (1/1979), pp. 22-33.

3.8 E.M. Sparrow and R.D. Cess, Radiation Heat Transfer, 1978, p. 45.

3.9 W.H. McAdams, Heat Transmission, 1954, p. 472.

3.10 M.N. Ozisik, Radiative Transfer, 1973, p. 103.

3.11 "Tokamak Blanket Design Study: Final Report," ORNL/TM-7049 (1980).

3.12 W.J. Green and K.R. Lawther, "A Study of the Sensitivity of LOCA Heat Transfer Analysis for a Water-Cooled Reactor System," Nuclear Engineering and Design, 47, (1978), pp. 87-99.

3.13 D. Wilhelm, "Transient Analysis of a 1000-MW Gas-Cooled Fast Reactor," Nuclear Technology, 39, (6/1978), pp. 30-40.

3.14 D.R. Buttemer and J.A. Larrimore, "Response of Gas-Cooled Fast Breeder Reactors to Depressurization Accidents," Nuclear Engineering and Design, 26, (1974), pp. 195-200.

3.15 M.M. El-Wakil, Nuclear Heat Transport, 1978.

TABLE 3.32

Time Required for Worse Cases to Suffer Damage or Melting

	Damage	Melting
Plasma Heating	2.5 sec	10 sec
Afterheat	1 hr	10 hr

consequence relative to a material selection. For both cases there are two criteria: 1) the reciprocal of the time required for damage, and 2) the reciprocal of the time required for melting. Thus, a low RCI is preferred. The values for RCI_{LP} are relative to the most realistic TZM case. The selection of breeder has only a minor effect.
The values for RCI_{LA} for the metals are relative to the V-alloy case with coolant and breeder held fixed. The values for RCI_{LA} for breeders are relative to $Li_{17}Pb_{83}$ for the 316 SS metal (used with all breeders). The coolant choice has only a minor direct effect.

Finally, the overall time scales are listed in Table 3.32 for the worst case scenarios.

TABLE 3.31

Relative Consequence Index for
LOCA-Afterheat (Breeders)*

Criterion: (Time to Damage)$^{-1}$ relative to $Li_{17}Pb_{83}$
(316 SS metal) (RCI^{d}_{LA})

	fluid breeders drain	fluid breeders do not drain
$LiAlO_2$/Be	2.7	300
Li	1	5
$Li_{17}Pb_{83}$	1	1

Criterion: (Time to Melting)$^{-1}$ relative to $Li_{17}Pb_{83}$
(316 SS metal) (RCI^{m}_{LA})

	fluid breeders drain	fluid breeders do not drain
$LiAlO_2$/Be	1-5	150
Li	1	5
$Li_{17}Pb_{83}$	1	1

Rank Ordering: Best to Worst

$$Li_{17}Pb_{83} > Li > LiAlO_2/Be$$

*Based on reference design parameters, results from Tables 3.23, 3.24.
low values preferred.

TABLE 3.30

Relative Consequence Indices for LOCA-Afterheat (Metals)*

Criterion: $(\text{Time to Damage})^{-1}$ relative to V-alloy (coolant, breeder held fixed) (RCI^{d}_{LA})

316 SS	6-11
HT-9	3-8
V-alloy	1
TZM	5-9

Criterion: $(\text{Time to Melting})^{-1}$ relative to V-alloy (coolant, breeder held fixed) (RCI^{m}_{LA})

316 SS	7-12
HT-9	3-8
V-alloy	1
TZM	3-8

Rank Ordering: best to worst

$$V >> HT\text{-}9 \gtrsim TZM \gtrsim 316\ SS$$

*based on reference design parameters, and results from Tables 3.23-3.27 low values preferred

TABLE 3.29

Relative Consequence Indices for LOCA-Plasma Heating*

Criterion: (Time to Damage)$^{-1}$ relative to most realistic TZM/Flibe case (RCI^{d}_{Lp})

	Coolant		
	Water, Helium	Lithium	Flibe
316 SS	2.0 - (2.3)	0.7 - (2.0)	—
HT-9	1.5 - (1.6)	—	—
V-alloy	—	0.6 - (1.4)	—
TZM	—	—	1.0 - (4.0)

Criterion: (Time to Melting)$^{-1}$ relative to most realistic TZM/Flibe case (RCI^{m}_{Lp})

	Coolant		
	Water, Helium	Lithium	Flibe
316 SS	10.2 - (13.5)	1.9 - (12.6)	—
HT-9	5.8 - (9.0)	—	—
V-alloy	—	1.3 - (6.2)	—
TZM	—	—	(0.4) - 1.0

*Based on reference design parameters, results from Tables 3.14, 3.15
Low Values preferred; Breeder dependence is low
Numbers outside parentheses are for maximum loss rate case
(for lithium this may not be conservative since lithium is assumed not to drain in this time period)
Numbers inside parentheses are for case where coolant is assumed to disappear instantaneously at t = 0.

Rank Ordering: TZM(best) > HT-9 $\gtrsim$ V-alloy $\gtrsim$ 316 SS

3.5.3 Consequence Index

The most critical overall design parameter is the first wall thickness, but the two aspects of the problem (plasma, afterheat) result in conflicting directions. Plasma heat rates go as $\sim 1/d_{fw}$ so a thick first wall is best. Opposite scaling is true for afterheat. Therefore, any afterheat generating mass near the first wall (highest specific afterheat area) should be used as effectively as possible. From the plasma heat perspective this means a thicker first wall, rather than flow gap connectors, second walls, etc.

Among structural materials, there is less than a factor of two difference in behavior with two exceptions. A TZM first wall is an order of magnitude better from the plasma heat perspective. A V-alloy structure is an order of magnitude better from the afterheat perspective.

Among breeders, there is very little impact on the plasma heating case. For afterheat $Li_{17}Pb_{83}$ is slightly better than Li, although both may drain. $LiAlO_2$, even with the best case neutron multiplier, is significantly worse.

Among coolants, the pressurized coolants (water, helium) may experience very rapid rates of coolant loss (<0.1 sec). For these the only important impacts are those indirect through design (first wall thickness, restriction of breeder and structure choice). The other coolants only drain by gravity, and thus may assist the plasma heat case. In all cases the primary coolant may disappear before significant afterheat assistance.

Relative Consequence Indices (RCI) are defined for the cases of LOCA-plasma heating only (RCI_{LP}) and LOCA-afterheat (RCI_{LA}) (see Tables 3.29-3.31). This allows a (imperfect) quantification of the potential

where the spatial integrals are over the blanket radially.

Since the first wall ($\Delta r = 0$) has the highest specific activity/afterheat, a thin first wall is preferred. Flow gap connectors and module edges contribute more mass (heat source) and do little in assisting heat transfer from the first wall. Since any additional mass near the first wall contributes to afterheat, it should be as effective as possible in reducing plasma heat trouble. Thus flow gap connectors and extra module edge thickness (if made of the same structural material) are bad ideas (little help for plasma heating, significant harm for afterheat). The most effective design variable is first wall thickness. Thick first walls reduce temperature rise due to plasma heating while worsening afterheat. A first wall coating with low afterheat provides a good means of reducing plasma heat troubles (more heat sink) without worsening afterheat concerns.

The simple scaling Eq. (3.51) fails for the $LiAlO_2$ case since the low thermal conductivity thermally isolates the first wall and causes a large temperature drop across the blanket. A Be neutron multiplier does assist, (while Zr-Pb would hinder) but the Be/$LiAlO_2$ case is still significantly worse than other cases. The liquid breeders (Li, $Li_{17}Pb_{83}$) greatly reduce temperature rises, if they have not drained. Even if they have, radiation heat transfer across the empty breeder zone is still preferable to $LiAlO_2$.

A V-alloy structure offers a potentially significant improvement over the other structural materials; possibly an ofder of magnitude better.

Coolants can only directly influence afterheat for the maximum LOCA case. There is an indirect influence through the design.

The worst case for afterheat is 316 SS/$LiAlO_2$, whereas the best is V/Li or V/$Li_{17}Pb_{83}$.

reference cases are shown in Tables 3.23 - 3.27.

To first order the above expressions, give a conservative estimate of required shutdown times and safety margin for structural material comparisons. The generally strongest influenece of coolants and breeders is through the impact on design, e.g., first wall thickness. Non-pressurized coolants, because they require more time to leave, have a greater potential to hold down temperatures (increase safety margins).

The safety margin is directly proportional to d_{fw}, so that a thicker first wall is preferred. Flow gap connectors and module edges provide some benefit, but do not appear very effective — especially since they make afterheat worse.

3.5.2 Afterheat

For the cases studied, the decay afterheat will not cause structural damage before an hour, even in the worst case of 316 SS/$LiAlO_2$. At least 10 hours is required for melting. Since the present model thermally isolates the blanket module from the surrounding reactor structure (potential heat sink), actual times would be expected to be longer, providing more of a safety margin. This latter impact is likely to be design dependent (supports, arrangement, etc.). The potential clearly exists for a design that would not melt. It may also be possible to design (and choose materials) that could not experience damage due to afterheat; thus one could "walk away" from an accident.

To first order the expected temperature rise for time t can be simply calculated from

$$\Delta T_{rise} = \left(\frac{1}{\rho c_p}\right)\left(QD \times QP \int_o^t DE(t)\, dt\right)\left(q''_n \frac{\int dx\, e^{-Ba \times \Delta x}}{\int dx}\right) \quad (3.51)$$

effectively thermally isolated from the rest of the blanket, a safety margin against damage was defined ($SM_d \leq 1$ implies damage likely) as:

$$SM_d = \frac{\rho c_p \, d_{fw}}{q''_w \, t_{sd}} (300\ °C) = \frac{\rho c_p \, k(\Delta T_{fw})}{(q''_w)^2 \, t_{sd}} (300\ °C) \quad (3.59)$$

The safety margin against melting was defined ($SM_m \leq 1$ implies melting likely) as:

$$SM_m = \frac{\rho c_p \, d_{fw}}{q''_w \, t_{sd}} (\Delta T_{om}) = \frac{\rho c_p \, k \, \Delta T_{fw} \, \Delta T_{om}}{(q''_w)^2 \, t_{sd}} \quad (3.60)$$

This can also be expressed in terms of the required shutdown time for damage or melting

$$t_d = \frac{\rho c_p \, d_{fw}}{q''_w} (300\ °C) = \frac{\rho c_p \, k \, \Delta T_{fw}}{(q''_w)^2} (300\ °C) \quad (3.48, 3.50)$$

$$t_m = \frac{\rho c_p \, d_{fw}}{q''_w} (\Delta T_{om}) = \frac{\rho c_p \, k \, \Delta T_{fw}}{(q''_w)^2} (\Delta T_{om}) \quad (3.48, 3.50)$$

For maximum coolant loss rates (worse case LOCA's), the reference case values do not greatly vary from the above (for damage evaluate material properties at operation temperature; for melting evaluate material properties at $\sim 1/2\ (T_{melt} + T_{operation})$.
The exception is TZM, where the time scale increases by over an order of magnitude (for the case of melting). The best estimates for

variation (heat capacity shows an increase with temperature, especially for HT-9, which decreases the temperature rise), the 316 SS and HT-9 results are in good agreement. The V-alloy cases are not in good agreement. The afterheat rates used in the General Atomic analysis was significantly different from other V-cases discussed in Appendix B. Since the disagreement was largest at about t = 1 hour, the adiabatic case results differed significantly. The difference in afterheat rates may be due to a variance in alloy composition. The variance in afterheat rates would be expected to have a lesser impact for the more important non-adiabatic cases since the overall afterheat rates (over a longer range in time) do not vary as much as they do at one hour.

Sze [3.19] examined non-adiabatic afterheat effects for the UWMAK-I design. As mentioned in section 3.1, his model allows for radiation heat transfer from the back of the module to an isothermal magnet shield (whereas the module was considered isolated in the present study). In this case the maximum temperature ($\sim$ 570 °C) was reached 2-3 hours after shutdown, temperatures falling thereafter.

3.5 Conclusions and Summary

The effects of a loss-of-coolant accident have been examined, focusing on the influence of material selection. This divides into the cases of plasma heating and afterheat.

3.5.1 Plasma Heating

If the plasma is not otherwise terminated, first wall damage will typically occur in about 2.5 s and melting will begin at about 10 s for the cases studied. Tables 3.14 and 3.15 give the specific results for various material combinations. For the simple case of a first wall

TABLE 3.28

Comparison of Adiabatic Time to Melt (hours)

Material	Adiabatic Melt Down Time*	Time to Melt (Adiabatic)** Present Study	Time to Melt (Reference Case)*** Present Study
C	∞	—	—
SiC	∞	—	—
V-Alloy	1.7	15.0	>130
HT-9	1.1	1.9	>10
316 SS	0.8	1.2	>10
Ti-Alloy	0.8	—	—
Inconel	0.3	—	—
Al-alloy	0.2	—	—

*scaled from references 3.21, 3.22
**Adiabatic case - no heat flow from first wall
***Reference case geometries, Fig. 3.11

of the presence of the breeder tends to be greater than the indirect design influence.

The 316 SS tables have more entries due to more 316 SS reference designs.

The worse case is still that of a $LiAlO_2$ breeder. However, the addition of the Be neutron multiplier (heat sink, little heat generation) causes a significant improvement. For damage, the proximity of the Be increases the time to damage by a factor of about 3. For melting, the Be adds a factor of $\sim$2.5. When the breeder is present, the influence of reflector (grapite) thickness is small.

3.4.5 Comparison to Previous Works

The earliest examination of afterheat was simply an assessment of the level of decay heat due to the induced radioactivity. The first examination of the effects was to calculate the initial temperature rise for the adiabatic case. For example, the UWMAK-I 316 SS first wall was calculated to have an initial temperature rise of 0.1 °C/s (at $q_n'' = 1.25$ MW/m^2) [3.20] which scales linearly to 0.29 °C/s at q_n''=3.6 MW/m^2 (the value of the current study). This is in good agreement with the value of 0.32 °C/s found in the present study.

The next most sophisticated study continued the adiabatic analysis further in time by simple time integration of the afterheat rate. A series of General Atomic reports [3.21, 3.22] examined the time to melt for a variety of materials. Those results (scaled to the current study value of 3.6 MW/m^2) are repeated in Table 3.28. Considering that the GA study kept material properties constant while the present study allowed

TABLE 3.27

Time to Damage and Melting for V-Alloy Designs from Afterheat (days)

	Geometry	Coolant	Breeder	With Breeder	Empty Breeder 20 mm Reflector	Empty Breeder 100 mm Reflector
Damage						
	Base	—	Li	18	—	4.2
	Reference	Li	Li	15	0.92	3.5
Melting						
	Base	—	Li	80	—	20
	Reference	Li	Li	87	5.5	16.5

Times greater than 24 hours estimated from temperature rise rate at the end of the first day.

TABLE 3.26

Time to Melting for HT-9 and TZM Designs from Afterheat (hours)

Metal	Geometry	Coolant	Breeder	With Breeder	Empty* Breeder 20 mm Reflector	Empty Breeder 100 mm Reflector
HT-9	Base	——	$LiAlO_2$	3.93	——	——
HT-9	Reference	Water	$LiAlO_2$/Be	11.6	(38)	——
HT-9	Reference	Helium	$LiAlO_2$/Be	10.0	(66)	——
HT-9	Base	——	Li	550	——	——
HT-9	Reference	Helium	Li	550	18	——
HT-9	Base	——	$Li_{17}Pb_{83}$	2400	——	——
HT-9	Reference	Water	$Li_{17}Pb_{83}$	2900	15.7	——
TZM	Base	——	Li	272	——	82
TZM	Reference	Flibe	Li	410	29	125

*Unphysical for a $LiAlO_2$ breeder zone to be empty, some cases included for completeness.

Times greater than 24 hours estimated from temperature rise rate at the end of the first day.

TABLE 3.25

Time to Damage for HT-9 and TZM Designs from Afterheat (hours)

Metal	Geometry	Coolant	Breeder	With Breeder	Empty* Breeder Zone 20 mm Reflector	Empty Breeder 100 mm Reflector
HT-9	Base	—	$LiAlO_2$	0.3	—	—
HT-9	Reference	Water	$LiAlO_2$/Be	1.2	(3.25)	—
HT-9	Reference	Helium	$LiAlO_2$/Be	1.1	(5.5)	—
HT-9	Base	—	Li	99	—	—
HT-9	Reference	Helium	Li	104	2.75	—
HT-9	Base	—	$Li_{17}Pb_{83}$	560	—	—
HT-9	Reference	Water	$Li_{17}Pb_{83}$	650	2.5	—
TZM	Base	—	Li	44	—	11.0
TZM	Reference	Flibe	Li	63	3.4	15.0

*Unphysical for a $LiAlO_2$ breeder zone to be empty, some cases included for completeness.

Times greater than 24 hours estimated from temperature rise rate at the end of the first day.

TABLE 3.24

Time to Melt for 316 SS Designs from Afterheat (hours)

Geometry	Coolant	Breeder	With Breeder	Empty* Breeder (20 mm) Reflector	Empty* Breeder (100 mm) Reflector
Base	—	$LiAlO_2$	3.75	—	(48)
Reference	Water	$LiAlO_2$	10	(20)	(45)
Reference	Helium	$LiAlO_2$	9.4	(33)	(69)
Base	—	Li	216	—	48
Reference	Helium	Li	240	11	54
Reference	Lithium	Li	264	12.3	—
Base	—	$Li_{17}Pb_{83}$	1779	—	48
Reference	Water	$Li_{17}Pb_{83}$	1395	9.8	45

*Unphysical for a $LiAlO_2$ breeder cavity to be empty included for completeness.

Times greater than 24 hours estimated from temperature rise rate at the end of the first day.

TABLE 3.23

Time to Damage for 316 SS Designs from Afterheat

(hours)

Geometry	Coolant	Breeder	With Breeder	Empty* Breeder (20 mm) Reflector	Empty* Breeder (100 mm) Reflector
Base	——	$LiAlO_2$	0.3	——	(6.5)
Reference	Water	$LiAlO_2$	1.0	(3.0)	(5.8)
Reference	Helium	$LiAlO_2$	1.0	(4.5)	(9.0)
Base	——	Li	42	——	6.5
Reference	Helium	Li	46	2.0	7.5
Reference	Lithium	Li	55	2.3	——
Base	——	$Li_{17}Pb_{83}$	391	——	6.5
Reference	Water	$Li_{17}Pb_{83}$	300	1.76	6.1

*Unphysical for a $LiAlO_2$ breeder cavity to be empty, included for completeness.

Times greater than 24 hours estimated from temperature rise rate at the end of the first day.

$LiAlO_2$ - 1

Li - 9.3

$Li_{17}Pb_{83}$ - 14.7

and indeed the time to damage and melt show at least this much variance among breeders. For comparison, the relative value of $\rho c_p k$ for graphite (the heat sink/reflector) is 18.4. However, there is less of it than there is any of the breeder.

A rough comparison of the time required for melting among the various breeders can be given as

$$t_{Li_{17}Pb_{83}} \sim (4-6)\ t_{Li} \sim (50-200)\ t_{LiAlO_2} \qquad (3.58)$$

for the cases studied.

3.4.5 Coolant Effect-Reference Cases

As discussed in section 3.2.3, the loss rates of coolants under severe LOCA's are sufficiently high that there will be no direct effect on cooling of the blanket for afterheat time scales. There is, however, the indirect effect caused by design parameters forced by coolant selection. The six reference geometries were used to examine the overall effect of representative designs for the six coolant/breeder combinations.

The results are shown in Tables 3.23-3.27. The effect of coolant in design is seen as less than that of the breeder (if present). If the breeder zone is empty, the design impact of coolants is about that of the breeders. That is, both coolant and breeder choice influence afterheat results to a similar degree. However, the direct influence

V structure are so slow that the $LiAlO_2$ handicap extends further in time for the V/$LiAlO_2$ case. The present model for $LiAlO_2$ (pure $LiAlO_2$, 60% uniform density) may not adequately represent heat transfer across the zone. Other mechanisms (radiation at the grain scale?) may improve it, so that these estimates may be too low. On the other hand, the gap conductance was ignored, assuming good contact between metal and $LiAlO_2$. This assumption tends to balance the above over-conservatism.

Another limitation is time. As discussed in section 3.1, computer runs were stopped at t = 1 day. The results in the table are linear extrapolations from the temperature rise rate found at t = 1 day. Since additional decay occurs after that time, the results greater than 1 day are too conservative; actual time to melt or damage would be longer. In all cases it must be remembered that the blanket was considered isolated from the rest of the reactor structure. Thus actual times would be significantly longer, and damage or melting less likely. The current results demonstrate the basic behavior.

Only V exhibits a highly significant difference (over a factor of 2) behavior among metals, almost an order of magnitude improvement.

Both Li and $Li_{17}Pb_{83}$ show good thermal sink performance. The effectiveness of a breeder in this respect seems to vary as

$$(\rho c_p k)^x \qquad (x \geq 1) \tag{3.57}$$

since both the heat capacity and conductivity are necessary. The relative values of $\rho c_p k$ for the 3 breeders are

TABLE 3.22

Effect of Breeder Choice on Time to Damage and Melting From Afterheat

Damage (hrs)

Breeder	316	HT	V	TZM
Adiabatic First Wall	0.25	0.36	1.25	0.18
Empty Breeder	6.5	8.1	100.0	11.0
$LiAlO_2$	0.3	0.3	(1.0)	(2.2)
Li	42	99	436	44
$Li_{17}Pb_{83}$	391	560	1722	262

Melt (Days)

Adiabatic First Wall	0.05	0.08	0.63	0.03
Empty Breeder	2.0	4	20	3.4
$LiAlO_2$	0.2	0.2	(0.4)	(0.9)
Li	9	23	80	11†
$Li_{17}Pb_{83}$	72	99	317	42††

( ) $LiAlO_2$ not temperature compatible with V, TZM but cases were for completeness.

† suspect extrapolation to long times since computer CPU time limitations resulted in extrapolation from 16 hr rate rather than 24.

†† No multiplier with $LiAlO_2$. These results compare generic problems with a ceramic breeder. Section 4.4.4 includes the beneficial Be multiplier.

to the opposing edge (mirror image) as shown in Figure 3.2a. In actuality, all surfaces in an empty breeder cavity would interact (Fig. 3.2b), and both second wall and wdge would radiate to the sink (back wall) -- unlike the current modeling. If the edge walls are fairly thin (∿ no thicker than the first/second wall zones), one would expect the basic scaling (Eq. (3.51)) to be maintained, and blanket temperature gradients minimized.

3.4.4 Breeder Effect

The base case one dimensional geometry was used to examine the breeder effect. The geometry was held constant. The results are shown in Table 3.22 along with the adiabatic first wall case. A variety of conclusions are seen from these results.

$LiAlO_2$ acts as a very good thermal insulator. The basic scaling Eq. (3.51) is completely irrelevant and the temperature drops (ΔT_b) across the $LiAlO_2$ zone increase with time rather than decrease. All other cases (except TZM/$Li_{17}Pb_{83}$) show maximum ΔT_b by one hour. For the TZM/$Li_{17}Pb_{83}$ case, the maximum ΔT_b occurs later due to the high conductivity by TZM and low (relative to Li and TZM) conductivity of $Li_{17}Pb_{83}$. A $LiAlO_2$ breeder effectively thermally isolates the first wall from the heat sink. The low density and conductivity of $LiAlO_2$ combine to reduce the effectiveness of $LiAlO_2$ as a heat sink. Furthermore, $LiAlO_2$ has an initial temperature of ∿650°C, higher than the initial temperature of 316 SS, HT-9, and V. Thus, heat flows initially from the breeder to the first wall for those cases. Hence the $LiAlO_2$ case is worse than adiabatic from the damage standpoint. Although a 650°C breeder with a 900°C TZM structure is non-physical (allowing $LiAlO_2$ to assist TZM for shorter times), the case was run for completeness. The temperature rises in a

TABLE 3.21

Effect of Flow Gap Connectors on Temperature Rises due to Afterheat*

Material	at 30 minutes			at 60 minutes		
	Without Connectors	With Connectors	Fractional Worsening	Without Connectors	With Connectors	Fractional Worsening
316	111.7	150.8	1.35	119.8	193.6	1.62
HT-9	96.0	135.8	1.41	110.2	168.7	1.53
V-alloy	14.8	26.6	1.80			
TZM	42.2	76.5	1.81			

*Based on geometry in Fig. 3.10b

Thus, for example, if shutdown were to occur just before damage (ΔT_{rise} (fw) $\lesssim$ 300 °C), then the equivalent blanket temperature rise would be < 50 °C. Thus, if shutdown occurs before damage, the blanket temperature rises are approximated well by the pure afterheat case.

3.4.3 Two Dimensional Effects

The effects of module edges and connectors across the first wall flow gap were addressed. Basically, while both assist in heat transfer, the additional heat sources due to more mass dominate and increase the temperature rises. Since the temperature gradients were low in the one dimension case, especially at times of interest, the potential benefit is low. A connector or edge made of the same structural material experiences heat generation itself, adding significantly to the heat load.

Table 3.21 shows the increase in blanket temperatures caused by the reference set of flow gap connectors. The additional mass (heat source) and increased temperatures tend to reduce the time to damage scale to short enough times that blanket temperature gradients are significant -- hence the simple ΔT_{rise} scaling Eq. (3.51) is no longer valid.

Edges are similarly poor. This suggests that for the scenarios addressed in this study initial failure would occur at the first wall edges (directly opposite from the plasma heat case). The modeling of edges was poor, however, and numerical results inaccurate. The code only allows radiation heat transfer to nodes direct opposite on an opposing surface. Thus, second wall to back region transfer is fairly represented. However, radiation from the edge is only allowed

TABLE 3.20

Effect of Varying the Plasma Shutdown Time (t_{sd}) on Time to Damage and Melting (d_{fw} = 10 mm)*

Time to Damage (seconds)	316 SS	HT-9	V	TZM
$t_{sd} = \infty$ (pure plasma)	6.4	10.1	6.2	7.3
t_{sd} = 15 sec	6.4	10.1	6.2	7.3
t_{sd} = 5 sec	590	1140	1740	290
t_{sd} = 0 (pure afterheat)	900	1260	4500	660
Time to Melting (minutes)				
$t_{sd} = \infty$ (pure plasma)	0.55	0.83	0.62	0.75
t_{sd} = 15 sec	40	67	490	61
t_{sd} = 5 sec	60	104	760	89
t_{sd} = 0 (pure afterheat)	72	114	900	108

*Adiabatic first wall

wall temperatures fall after plasma termination until an afterheat temperature distribution is reached. Then a fairly uniform (over the blanket) temperature rise follows.

In the present study, a limited number of combined cases were run for the adiabatic first wall ($d_{fw} = 10$ mm) case. During the plasma heat phase, a large temperature gradient (into the first wall) arises; i.e., most of the heat goes into rising the temperature at the first wall surface. By the time the first wall surface begins to melt, the average first wall temperature has not risen much. After plasma termination, the gradient relaxes, lowering the first wall surface temperature. Once relaxation occurs, the entire wall continues to rise at the afterheat rate. Thus the combined case can be viewed as causing the afterheat case to start at a higher operating temperature.

A number of runs examining this coupling were done. The results are shown in Table 2.30. The range is from a pure plasma heat case (plasma stays on long enough to produce damage/melting) to a pure afterheat case (plasma terminates at $t = 0$).

If the plasma shutdown is before damage occurs, the first wall temperature drops until the heat added by the plasma between $t = 0$ and $t = t_{sd}$ is distributed throughout the blanket. The equivalent blanket temperature rise corresponding to the first wall temperature rise caused by plasma heating is approximated by

$$\Delta T_{rise}\,(\text{blanket}) \sim \Delta T_{rise}(\text{fw}) \times \frac{d_{fw}}{\int_{\text{blanket}} dx} \tag{3.56}$$

$$\Delta T_{rise} \sim \frac{d_{fw} + e^{-Ba \times \Delta x} d_{bw}}{d_{fw} + d_{bw}} \tag{3.53}$$

where $e^{-Ba \times \Delta x}$ represents the lower specific heating at the back of the blanket. Thus, unlike the plasma heating case, a thinner first wall is desired since for

$$d_{bw} > d_{fw} \tag{3.54}$$

and $e^{-b(\Delta x)}$ small

the expression reaches a limit of

$$\Delta T_{rise} \sim d_{fw}/d_{bw} \tag{3.55}$$

3.4.2 Combined Plasma and Decay Heat

Before proceeding with more detailed afterheat analysis, the connection between plasma and decay heating is discussed.

In reality the plasma and afterheat cases are not separate. Under accident conditions, the continued plasma heating dumps additional heat into the structure, reducing the margin for afterheat temperature rise. Thus, the quicker the plasma is terminated, the greater an afterheat temperature rise can be withstood. It should be noted that there are numerous loss-of-coolant accidents which automatically cause plasma termination, resulting in a pure afterheat case.

Merrill [3.3] examined the combined case assuming plasma termination when the first wall melts. Analysis of his results indicates that first

To better identify material dependence Eq. (3.51) can be rearranged as

$$\Delta T_{rise}^{(t)} = \left(\frac{1}{\rho c_p}\right)\left(QD \times QP \int_o^t DE(t)\, dt\right)\left(q_n'' \frac{\int dx\, e^{-Ba \times \Delta x}}{\int dx}\right) \quad (3.52)$$

The first two terms are structural material dependent; the third, design. The first term contains material thermal properties and simply measures the volumetric ability of a material to absorb heat.

The second term is the neutronic heating behavoir of the material. Whereas the values of QD x QP do not vary significantly among materials, the rapid decay for V-alloy reduces the value of the integral for that metal.

The third term is the design component. A higher operating neutron flux leads to higher specific activity. The two spatial integrals represent the distribution and relative strengths of the heat source and heat sink.

It is important to note the time dependence. Unlike the plasma heating case, the basic scaling with time is not linear. Thus, while materials can be easily compared in terms of ΔT_{rise} for any given time (e.g., $\sim 1/\rho c_p$ scaling). There is no simple expression for the time to melt or time to damage (which would be the inversion of this equation). Thus, for an initial time frame of a few hours, an improvement in design for a V-alloy could have a strong (non-linear) improvement in the time criteria because of the fairly rapid decay (decline of DE(t)) over that time frame. A similar improvement would have less effect on other materials due to the lesser change in DE(t).

For the simple geometry involved, the design term can be re-written as

TABLE 3.19

Time to Damage and Melting from Afterheat in the Simple Plate Geometry (hours)

Damage	First wall = 4 mm Back wall = 100 mm	10 mm 100 mm	10 mm 10 mm
316 SS	4.08	2.20	0.58
HT-9	6.95	3.75	0.85
V	34.1	26	4.9
TZM	3.41	2.01	0.44
Melting			
316 SS	22.9	12.1	2.48
HT-9	45	28	4.4
V	122.6	86	32
TZM	26.7	17.7	3.8

TABLE 3.18

Temperature Difference across Blanket at One Hour for Afterheat-LOCA Case*

First Wall (mm)	Back Wall (mm)	316 SS	HT-9	V-alloy	TZM
1	100	12.8	11.7	0.9	2.2
2	100	23.1	21.7	1.7	4.1
4	100	41.7	29.9	3.2	7.5
10	100	86.7	85.7	7.7	16.2

*Simple two parallel geometry used

3.4 Afterheat Results

The temperature rise due to afterheat was examined for the cases previously described. Somewhat surprisingly, the scaling proved to be relatively simple due to the low temperature gradients across the blanket.

3.4.1 Geometry and Metal Scaling

The adiabatic and plate geometry cases were used to examine the basic scaling among metals and geometrical arrangements. The first wall thickness varied from 1 mm to 10 mm while the back wall and reflector thickness was varied from 0 to 500 mm (with d_{fw} = 100 mm). In all cases the temperature drop across the blanket, $\Delta T_b = T_{fw} - T_{bw}$, was under 100 °C for times greater than one hour. In most cases, the temperature gradient was even lower, see Table 3.18. Reducing the back wall/reflector thickness decreased ΔT_b, while increasing it increased ΔT_b, since the effectiveness of the back heat sink in absorbing first wall heat determined ΔT_b. For the cases studied, the low temperature differentials at times of interest (melting and damage) resulted in a simple scaling for the first wall temperature rise:

$$\Delta T_{rise}^{(t)} = \frac{\int q_a'''(\text{volume})dt}{\rho c_p(\text{volume})} = \frac{q_n'' \times QD \times QP \int dx\ e^{-Ba\Delta x} \int_o^t DE(t)dt}{\rho c_p \int dx} \quad (3.51)$$

where the spatial integrals are taken over the radial arrangement of materials. The actual times to damage and melting are shown in Table 3.19.

Sze [3.19] examined the UWMAK-I design for a lithium LOFA with 316 SS structure. He expected damage to occur between 10 and 60 seconds after flow began to stop. The closest case to this in the present study is the static lithium coolant (316 SS) case where damage is predicted at ~7 seconds into the accident. This is good agreement since a LOFA would be expected to allow longer times than an immediate flow stoppage.

Chan [3.1] analyzed a variety of coolant transients. His only cases similar to the present study were lithium and helium coolant loss-of-flow. For a 0.36 MW/m^2 wall loading (maximum studied) the time to melt was 25 and 26 seconds respectively. If this is a surface heat flux value (0.9 MW/m^2 in the present study) his values would extrapolate to 10 and 10.4 seconds, in good agreement with the present study.

His study identified three parameter groups for LOFA's

$\frac{q'''}{\rho c_p}$ first wall heat flux

$\frac{h}{\rho c_p d_{fw}}$ first wall heat transfer

h = first wall coolant heat transfer coefficient.

Kv_o fluid dynamic

K = effective flow resistance

v_o = effective flow velocity

where $K = \Delta P/2L$ = pressure drop through loop/ twice the loop length

Although these LOFA groups differ from the worse case LOCA case studied here, the same linear scaling of ρ, c_p, q, and d_{fw} is evident.

TABLE 3.17

Loss-of-Flow Results

[Ref. 3.3]

Case:	1	2	3	4	5
First Wall Structure	316 SS	316 SS	Ti-6242	316 SS	316 SS
First Wall Coolant	Helium	Water	Helium	Helium	Water
Blanket Structure	316 SS	316 SS	316 SS	316 SS	316 SS
Blanket Breeder	Li	Li	Li	$LiAlO_2$	$LiAlO_2$
Blanket Coolant	He	He	He	He	Water
Time to Structural Yield	2.8	5.5	2.6	2.8	7.0
Time to Structural Melt	8.1	9.0	5.0	8.0	27.2

The reference case for flibe was chosen similar to that of water because the heat transfer properties (normal operation) are similar. This resulted in a thin first wall (less TZM required than 316 SS). However, if one desired a thicker first wall, the TZM/flibe combination offers as good a potential as any, especially considering the high thermal conductivity of TZM (reducing ΔT_{fw} and thermal stress worries). Of course, any such design change affects other safety areas. For example, a thicker first wall results in more induced radioactivity. The values presented for TZM/flibe in the tables should be viewed with this perspective.

3.3.3 Comparison of Previous Work

A variety of studies have touched on the plasma heat problem; those results can be compared to those of the present study.

The UCLA study [3.18] examined a helium LOCA (UWMAK-II design). The first melting of 316 SS occurs at ∿80 sec., not at the first wall. Considering the differences in design geometry the slower helium loss rate, and the lower wall loading, this is not significantly different than the ∿13 sec. calculated in this study for the reference 316 SS cases.

Merrill [3.3] examined 5 blanket material combinations with constant geometry (but varying thicknesses) under LOFA conditions. (Neutron wall loading = 4.0 versus 3.6 MW/m^2 assumed here). Table 3.17 shows his cases and results. These are seen to be very similar to present results (Damage ∿2.5 s; melting ∿13 s for 316 SS). More precise comparisons (e.g., function of first wall thickness) is difficult because his model of first wall was a uniform metal/coolant mixture.

acting as a heat sink, and allowing some convection transfer. At longer times, the role of flibe as a heat sink is less important (small volume compared to that available in the blanket), and the conductivity of flibe ($\sim$ 1/100 x TZM) limits heat transfer across the first wall flow channel -- causing faster temperature rises.

The present model for handling flibe has two off-setting errors. First, the free convection within the channel (assists transfer from first wall to second wall) is not included. Gierszweski's[3.4, 3.5] work implies that the B-field supression of free convection still allows significant heat transfer by convection (unlike the Li case). This modeling neglect acts to overpredict temperatures. Second, although the forced convection transfer has been modeled as a function of time (section 3.2.3), the material properties are only a function of time. Hence the code does not allow the filbe to disappear as was the case for water and helium. However, the effect of this neglect is stronger for flibe. This effect acts to underpredict temperatures at moderate times ($>\sim$2.5 sec) because the flibe is incorrectly still present as a heat sink. It acts to overpredict temperatures at long times (>minute) as the flibe presence prevents radiation heat transfer. In all cases, correction of these modeling inaccuracies would reduce the effect of flibe, moving the values closer to the "empty coolant" case.

There is one additional aspect of the TZM/flibe/Li case. Of all the coolants studied, unpressurized, low-MHD flibe potentially offers the widest range of designs (see Chapter 2). The pressurized coolants result in relatively thin, small radius ($\sim$tubes) first walls. Lithium is the opposite, tending toward thicker first walls, larger modules. The properties of flibe do not tend to so strongly force the design.

Although the modeling of the water and helium was poor, the net effect was to overpredict the impact of having either present. Since this still resulted in a very minor effect, the true effect would be nil. Thus, complete loss of either at t = 0 can be assumed.

For lithium as a coolant, it may not be possible for drainage to occur in a several second time frame (section 3.2.3). Therefore, the maximum LOCA case presented here is simply a constant, static (conduction into lithium only, no convection) lithium coolant. The computer modeling was not as complex as in the previous cases, water and helium. The presence of Li (and its good conductivity) makes even static lithium a good heat sink for the first wall. ($Li_{17}Pb_{83}$ as a coolant could be expected to be at least as good). However, one should note that if rapid drainage were possible, the maximum (worse case) LOCA case would approach the empty coolant limit. On the other hand, lithium-cooled designs tend to have thicker first walls, which significantly improve performance over water and helium designs, even without lithium being present in the first wall flow channel.

The TZM/flibe/Li combination is perhaps the most interesting. A distinguishing factor is that the thermal conductivity of TZM is higher than all other materials in the study (including coolants and breeders). Thus, basically whenever non-TZM substances are added, the situation gets worse and the strong advantage of TZM slightly reduced at long times. At short times this is not necessarily true.

As the tables show, addition of Li to the breeder chamber has no effect at short times (damage) but reduces the TZM advantage at long times (melting). The addition of flibe to the flow gap helps initially,

could not be handled. Neglect of such heat transfer resulted in 10-30% higher temperatures at longer times. Incorporation of radiation heat transfer at all times, however, would underpredict temperature rises. The values in the Tables 3.14, 3.15 correspond to the best estimates given the significant modeling limitations. The values for the coolant case probably overestimate the time allowable before damage or melting) because of the neglect of heat generation in the water and the inaccurate handling of transient water material properties (only temperature dependence allowed, pressure dependence ignored). The conclusion is, therefore, that the presence of water in the extreme LOCA case does not significantly affect the result. The indirect design affect of choosing water as a coolant, thinner first walls, is the dominant coolant-dependent effect.

Helium is more easily modeled. The dependences of heat generation and radiation heat transfer are far less. An insignificant amount of heat is directly generated in the helium under full pressure and density. Further, helium is more transparent under normal conditions; hence radiation heat transfer was allowed in all cases.

Material properties could be more accurately modeled. The only major inaccuracy was the inability to account for the time dependence of material properties due to pressure loss. Therefore the maximum LOCA case overpredicts the beneficial impact of the helium since heat capacity (ρc_p) is included even after depressurization is assumed to have occurred. As with the case of water, even the overpredicted maximum LOCA case indicates that the direct effect of helium (under maximum loss rate conditions) is small. The design impact is again more important, especially at longer times.

TABLE 3.16

Complexities in Modeling of Water-Cooled LOCA's

Variable	Dependence
Density	temperature and pressure (phase)
Heat Capacity	temperature and pressure (phase)
Thermal Conductivity	temperature and pressure (phase)
Volumetric Nuclear Heating	water density, plasma condition
Convection Heat Transfer	water density, conductivity, velocity, temperature, pressure wall surface temp.
Radiation Heat Transfer	water density, temperature, wall surface temp.

TABLE 3.15

Time to Melting (sec) for LOCA
(Plasma Heating On)

Material	Coolant	Breeder	Empty Breeder Empty Coolant	Static Breeder Empty Coolant	Static Breeder Maximum LOCA*
316 SS	water	$LiAlO_2$	12.7	12.7	(12.9)
316 SS	water	$Li_{17}Pb_{83}$	12.5	12.8	(12.9)
316 SS	He	$LiAlO_2$	9.9	9.9	12.0
316 SS	He	Li	9.8	9.9	12.0
316 SS	Li	Li	10.5	10.5	68.3
HT-9	water	$LiAlO_2$	20.5	20.5	(22.1)
HT-9	water	$Li_{17}Pb_{83}$	20.3	21.0	(22.7)
HT-9	He	$LiAlO_2$	14.9	14.9	18.7
HT-9	He	Li	14.6	15.0	18.8
V	Li	Li	21.2	29.6	104.7
TZM	flibe	Li	300.0	143.0	132.0

*See text for discussion of the limitation of the modeling for the presence of water.

TABLE 3.14

Time to Damage (sec) for LOCA
(Plasma Heating On)

Material	Coolant	Breeder	Empty Breeder Empty Coolant	Static Breeder Empty Coolant	Static Breeder Maximum LOCA*
316 SS	water	$LiAlO_2$	2.28	2.28	(2.51)
316 SS	water	$Li_{17}Pb_{83}$	2.28	2.28	(2.51)
316 SS	He	$LiAlO_2$	2.23	2.23	2.42
316 SS	He	Li	2.24	2.23	2.41
316 SS	Li	Li	2.60	2.59	7.07
HT-9	water	$LiAlO_2$	3.26	3.26	(3.47)
HT-9	water	$Li_{17}Pb_{83}$	3.26	3.26	(3.47)
HT-9	He	$LiAlO_2$	3.13	3.13	3.39
HT-9	He	Li	3.13	3.13	3.38
V	Li	Li	3.59	3.56	8.97
TZM	flibe	Li	1.27	1.26	5.11

*See text for discussion of limitation of the modeling for the presence of water.

3.3.2.3 Coolant Impact

The inclusion of the coolant to the combinations completes the analysis. The six reference geometries representing the six combinations of coolant/breeder were used to examine the effect of coolant. Besides the direct effect of providing some cooling during the LOCA transients, there is the indirect effect through design influences (mainly through the determination of first wall thickness). Table 3.14, 3.15 show the time to damage and melting for the reference geometries.

There proved to be a modeling difficulty for the water case. The two phase nature of water during a LOCA results in the need to vary nuclear heating and radiation heat transfer with the change in phase. For an empty water channel, there is no nuclear heating, no material properties (ρ, c_p, k), and unrestricted radiation heat transfer across the flow gap. With water present, there is a high nuclear heating input directly to the water, varying material properties (ρ, c_p, k) and a varying film transfer coefficient. Table 3.16 summarizes the relevant variable dependencies.

The most critical difficulties arose from the variance of volumetric nuclear heating and radiation heat transfer. The time and space dependence of heat generation in the code must be user input. Using a constant volumetric rate as the density drops to the steam phase results in extreme non-physical heating of the steam resulting in incorrectly high steam temperatures. The results presented here neglect heat generated in the water.

The convection film coefficient was estimated (section 3.2.3) which allowed estimation of the cooling assistance due to the water during depressurization. The time dependence of the radiation heat transfer

TABLE 3.13

Effect of Flow Gap Connectors

Material	Time to Damage*(s)			Time to Melt*(s)		
	without connection	with connection	% improvement	without connection	with connection	% improvement
316 SS	2.56	2.67	4%	10.2	14.6	43%
HT-9	3.58	3.86	8%	15.3	21.5	41%
V	1.95	2.18	12%	12.4	20.6	66%
TZM	1.92	3.00	56%	269	∿350	30%

*Plasma remains on

3.3.2.2 Geometry: Edge and Connectors

Module edges have a very slight effect on temperature rises. Using the two-dimensional base case, the edge thickness was varied from 1 mm to 50 mm (d_{fw} = 2 mm). For all cases except TZM, this had <2% effect on temperature rises for the first wall away from the edge. The first wall in front of the edge had a lower rise, but the distance laterally along the first wall and the limited conductivity prevents the presence of the edge from influencing the overall first wall temperature. Failure would thus be expected to occur near the mid-point of the module first wall, not at the edge.

Again, TZM proved to be the exception; however, the effect is still limited. For a 10 mm edge, the temperature 40 mm from the edge is lowered by less than 10%. Damage in a typical size module would still be virtually unaffected. Melting would appear to be affected: the additional thermal mass offers the potential to further lengthen the time required before melting could occur for a TZM blanket.

Connectors across the flow gap allow thermal conductivity to assist radiation transfer in cooling the first wall. For the arrangement and spacing in the base case geometry, there is a significant improvement. Table 3.13 shows the time to damage and melt for the cases with (and without) flow gap connectors. For TZM, connectors do relatively less to help prevent melting since the temperature drop across the flow gap is held low at long times by radiation heat transfer at those high temperatures.

first regime (0 - 300 °C) is dominated by the thermal inertia of the first wall itself, thus there is little variation.

The second regime ($\sim$300 - $\sim$900) is dominated by radiation transfer to the second wall and that wall's thermal inertia. Here the breeder (or lack of it) makes no difference, but there is a difference from the isolated case. The other structural materials do not progress beyond this point due to lower melting poinsts. Further, the transition temperatures for other materials is higher due to lower thermal conductivity.

The third regime ($\gtrsim$900) is controlled by what is behind the second TZM wall. Where the breeder is present (and in direct contact with the second wall), the temperature rises are slower. The high volumetric heat capacity of $Li_{17}Pb_{83}$ keeps temperatures lower than a Li breeder.

The fourth regime (varies) is controlled by the graphite reflector heat sink (higher conductivity than Li or Li-Pb). Eventually, the Li and $Li_{17}Pb_{83}$ insulate the first wall from the heat sink. That is, at these temperatures and distance, radiation heat transfer is better than thermal conduction.

The net result is that the time scale for melting in a TZM structure is minutes rather than $\sim$10 seconds, representing over an order of magnitude improvement. A thicker first wall would slow the adiabatic case temperature rise ($\sim 1/d_{fw}$) but also reduce the heat flux through the walls, damping the change of thermal control mechanisms. These results are conservative since the heat of vaporization in the lithium breeder is not taken into account.

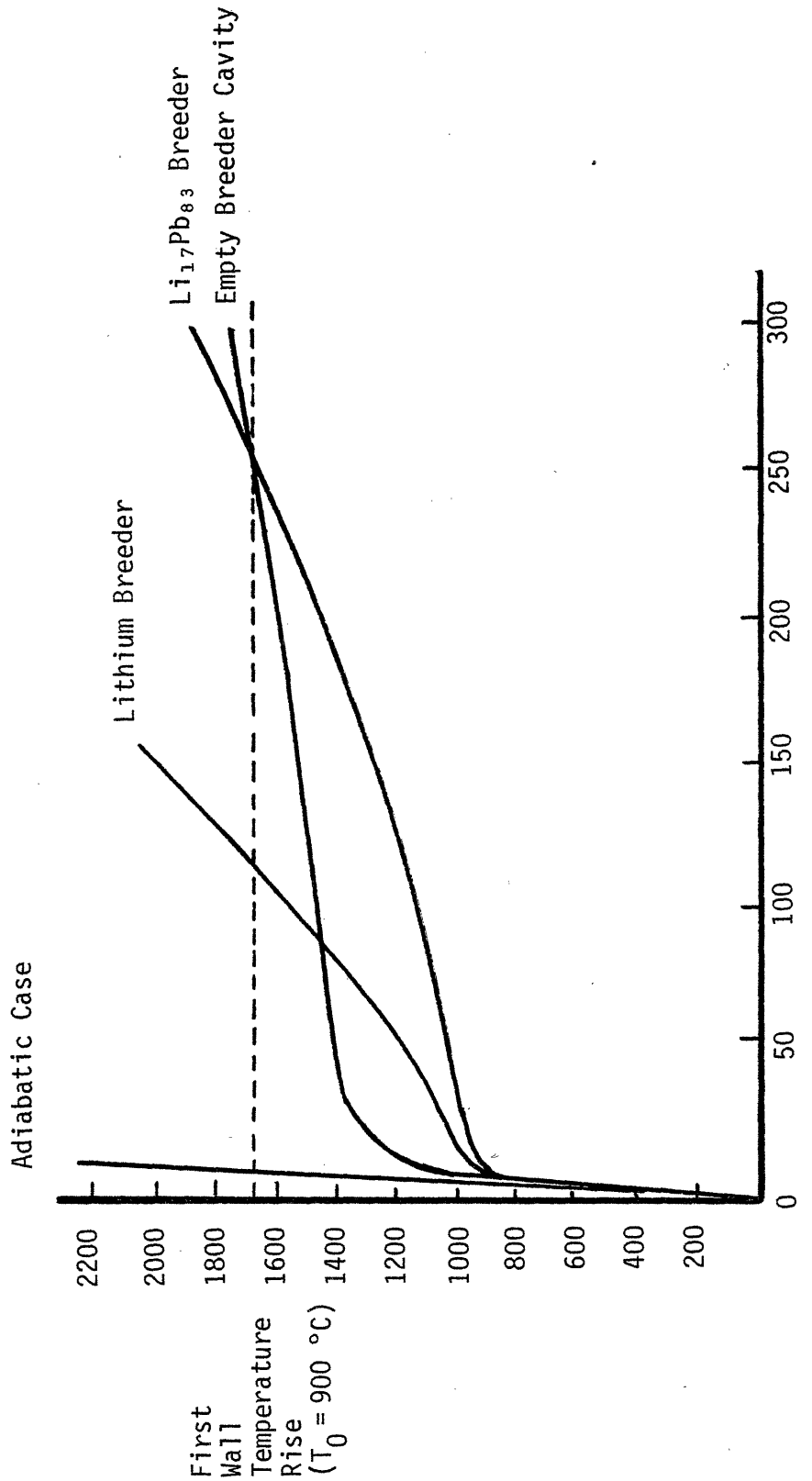

Fig. 3.12: Time Histories of Temperature Rises for Various TZM Blanket Cases

TABLE 3.12

Effect of Radiation Heat Transfer Across Flow Gap*
(d_{fw} = 2 mm)

	Material	Isolated First Wall	Radiate across Flow Gap	Percent Improvement (%)
time to damage (seconds)	316	2.55	2.56	<1
	HT	3.56	3.58	1
	V	1.92	1.95	2
	TZM	1.86	1.92	3
time to melting (seconds)	316	9.44	10.23	8
	HT	13.81	15.32	11
	V	9.04	12.4	37
	TZM	11.1	269.0	2423

*Plasma heating only, parallel plate geometry

3.3.2.1 Breeder and Reflector

Using the plate and base case geometries, the impact of different breeders and reflectors was examined. In all of these cases, the first wall can only lose heat to the rest of the module by radiation heat transfer across the voided flow gap.

Varying the breeder and depth of the reflector had $\lesssim$ 2% effect for all cases except TZM (discussed later). There was, however, a difference between all of these cases and the isolated first wall case. That is, any material which the first wall can radiate to provides some help; however, the details of what is behind the first wall (with an empty flow gap) do not matter. Table 3.12 shows the time to damage and melting for the base case geometry (d_{fw} = 2 mm, empty breeder zone) versus the isolated case. In terms of damage avoidance, there is little effect. However, the longer time to melt (and higher temperatures) allows a significant impact by radiation heat transfer, especially for TZM.

TZM is a special case due to its very high conductivity, (permitting more heat through the first wall), high melting point and operating temperature (radiation heat transfer goes as T^4). The temperature rise is determined by different mechanisms at different temperature regimes.

Figure 3.12 shows the temperature rise for a TZM first wall (d_{fw} = 2 mm, base case geometry) for isolated first wall, empty breeder, and Li, Li-Pb breeder. The behavior shown would exist for the other materials (and does in computer runs) except that the strong deviations occur above the material melting points and are thus irrelevant. The

TABLE 3.11

Safety Margin for LOCA's*
(Plasma Remains On)

Safety Margin against Damage:

$$SM_d = \frac{300\ °C}{\Delta T_{rise}} = \frac{\rho c_p\ d_{fw}}{q''_w\ t_{sd}}\ (300\ °C) = \frac{\rho c_p\ k(\Delta T_{fw})}{(q''_w)^2\ t_{sd}}\ (300\ °C)$$

Safety Margin against Melting:

$$SM_m = \frac{\Delta T_{om}}{\Delta T_{rise}} = \frac{\rho c_p\ d_{fw}\ (T_{melt} - T_{operations})}{q''_w\ t_{sd}} = \frac{\rho c_p k(\Delta T_{fw})(\Delta T_{om})}{(q''_w)^2\ t_{sd}}$$

*Where t_{sd} is the time to plasma shutdown, high values of safety margin are preferred.

TABLE 3.10

Relative Values of Beneficial
Material Properties for Isolated First Wall*

	316 SS	HT-9	V	TZM
Damage				
holding d_{fw} fixed** $\sim \rho c_p$	1	1.30	0.71	0.68
holding ΔT_{fw} fixed $\sim \rho c_p k$	1	1.81	1.10	3.62
Melting				
holding d_{fw} fixed $\sim \rho c_p \Delta T_{om}$	1	1.50	0.93	1.08
holding ΔT_{fw} fixed $\sim \rho c_p k \Delta T_{om}$	1	1.76	1.25	4.71

*relative to 316 SS.

**holding d_{fw} fixed = viewing d_{fw} as a fixed paramater independent of material

holding ΔT_{fw} fixed = viewing ΔT_{fw} as a fixed parameter independent of material

Instead of viewing d_{fw} as a scaling parameter, one can note that

$$d_{fw} = \frac{k\Delta T_{fw}}{q''_w} \tag{3.49}$$

so that the time to melting or damage is given by

$$t_i = \frac{\rho c_p \, k\Delta T_{fw} \, \Delta T_i}{(q''_w)^2} \tag{3.50}$$

where ΔT_{fw} (operating first wall temperature drop) is the fundamental design value and $\rho c_p k$ reveals the material property dependence. For damage, ΔT_i is a constant 300 °C. For melting $\Delta T_2 = \Delta T_{om}$ which is itself a material property. Table 3.10 gives the relative values of these material scaling values. The numbers show that unless one takes advantage of TZM's high conductivity to have a very thick first wall, material choice can not impact necessary response times by more than 80%. The analysis shows that if the maximum first wall thickness is limited by something other than maximum temperature drop, then thermal conductivity is less important in protecting the response of an isolated first wall.

In summary, scaling parameters for the simple isolated first wall have been defined. This allows a direct comparison among structural materials. A safety margin can be defined as the allowable temperature rise divided by the actual caused by a continuation of plasma heating after LOCA for a time, t_{sd}, (see Table 3.11).

$$T(x,t) \sim T_o - \frac{q''_w}{k} x + \frac{q''_w}{2k d_{fw}} x^2 + \frac{q''_w}{\rho c_p d_{fw}} t \qquad (3.45)$$

and

$$\Delta T_{fw} \sim \frac{q''_w}{2k} d_{fw} \text{ (constant)} \qquad (3.46)$$

after an initial transient.

Computer runs indicate that the transient behavior settles into the second mode after a few seconds.

Thus the basic time scale for plasma heat up of an isolated first wall is given by

$$T_{rise}(t) = \frac{q''_w}{\rho c_p d_{fw}} t \qquad (3.47)$$

and the time to reach melting or damage is given by

$$t_i = \frac{\rho c_p d_{fw}}{q''_w} \Delta T_i \qquad (3.48)$$

where $\Delta T_1 = 300$ °C (damage)

$\Delta T_2 = \Delta T_{om}$

This equation slightly underpredicts the time for damage and melting because of the beneficial relaxation of the first wall temperature drop (T_{fw}) from $\frac{q''_w}{k} d_{fw}$ to $\frac{q''_w}{2k} d_{fw}$. For example, for a 2 mm first wall, Eq. (3.48) is accurate within 15% (highest deviation for lowest conductivity material, 316 SS).

3.3 Plasma Heating

The results of computer runs for cases involving only plasma heating (surface and neutronic) will be discussed.

3.3.1 Isolated First Wall

The simplest case is that of a thermally isolated (adiabatic) first wall with only the plasma heat soruces. The volumetric nuclear heating has only a very minor effect with the material temperature response dominated by the surface heat flux. The ratio of volume/surface ratio heating for the first wall is given by

$$\frac{q_n''' \cdot d_{fw}}{q_w''} = \frac{q_n'' \cdot QP \cdot d_{fw}}{q_w''} = QP \times d_{fw} \times \frac{q_n''}{q_w''} \tag{3.42}$$

QP ranges from 6 to 10 (m^{-1}) for alloys studied and d_{fw} ranges from 1 to 4 mm. Thus, at most, volumetric heating is$\sim$16% of the first wall heat input.

Under operating conditions, the steady state temperature distribution through the first wall is approximately

$$T(x) = T_o - \frac{q_w''}{k} x \tag{3.43}$$

and

$$\Delta T_{fw} = \frac{q_w''}{k} d_{fw} . \tag{3.44}$$

Under accident conditions where the back of the first wall is thermally isolated, the temperature is approximated by

lies behind the first wall, it is relevant to know if connections across the gap, forming discrete channels, assists in heat transfer.

The one-dimension case was used to examine (in a constant, representative geometry) void (no breeder due to leakage), $LiAlO_2$, Li, and $Li_{17}Pb_{83}$.

3.2.5.4 Reference Cases

The six reference case geometries (Appendix C) correspond to the six combinations of coolant and breeder. These represent the reference designs for these combinations from Chapter 2. Thus, these cases allow the design influence of material choice to be added to the material properties in examination of the material impact. As such, these are the most accurate and appropriate in terms of determining the actual time scales.

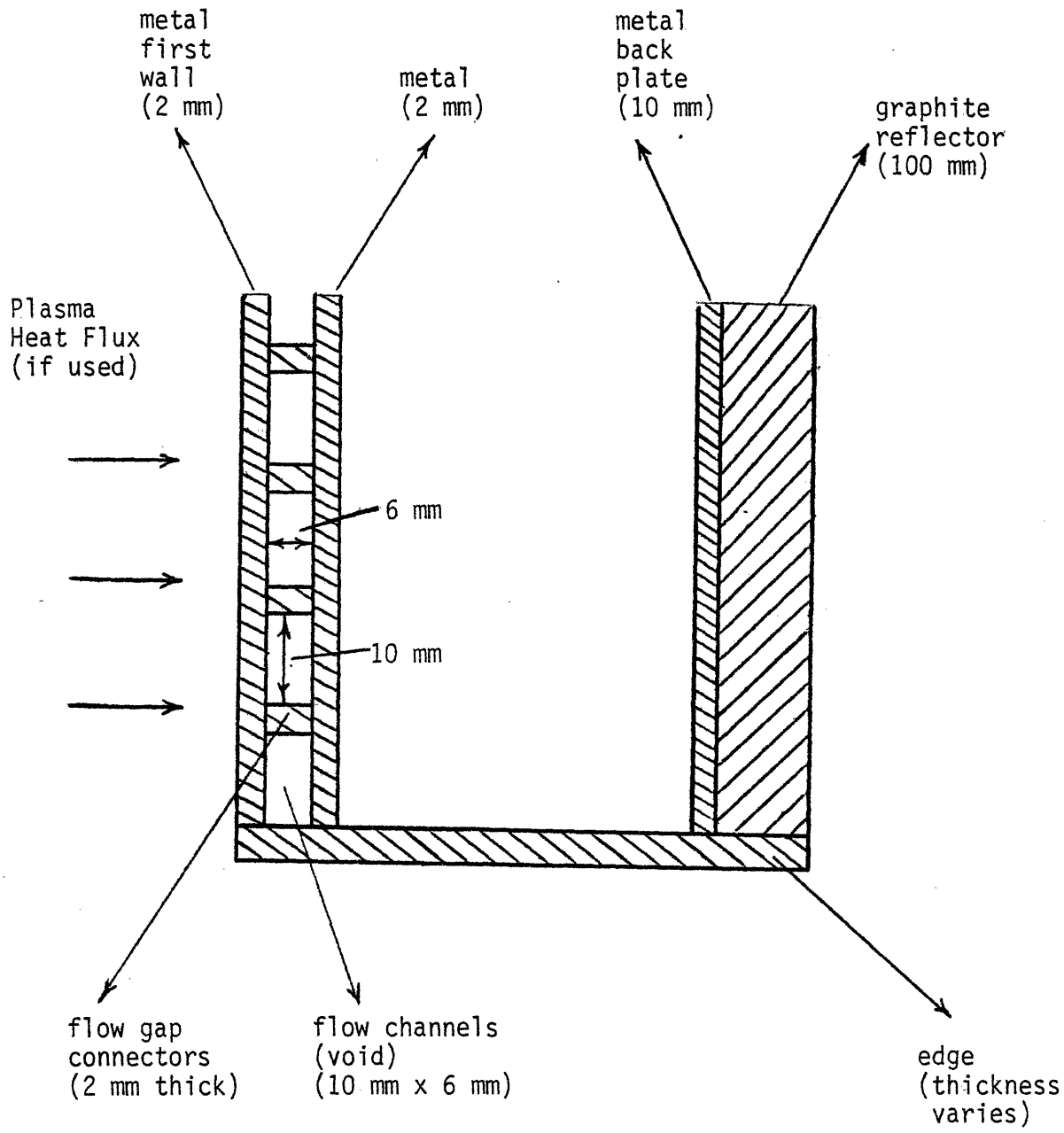

Fig. 3.11: Two Dimensional Base Case Geometry for LOCA Analysis

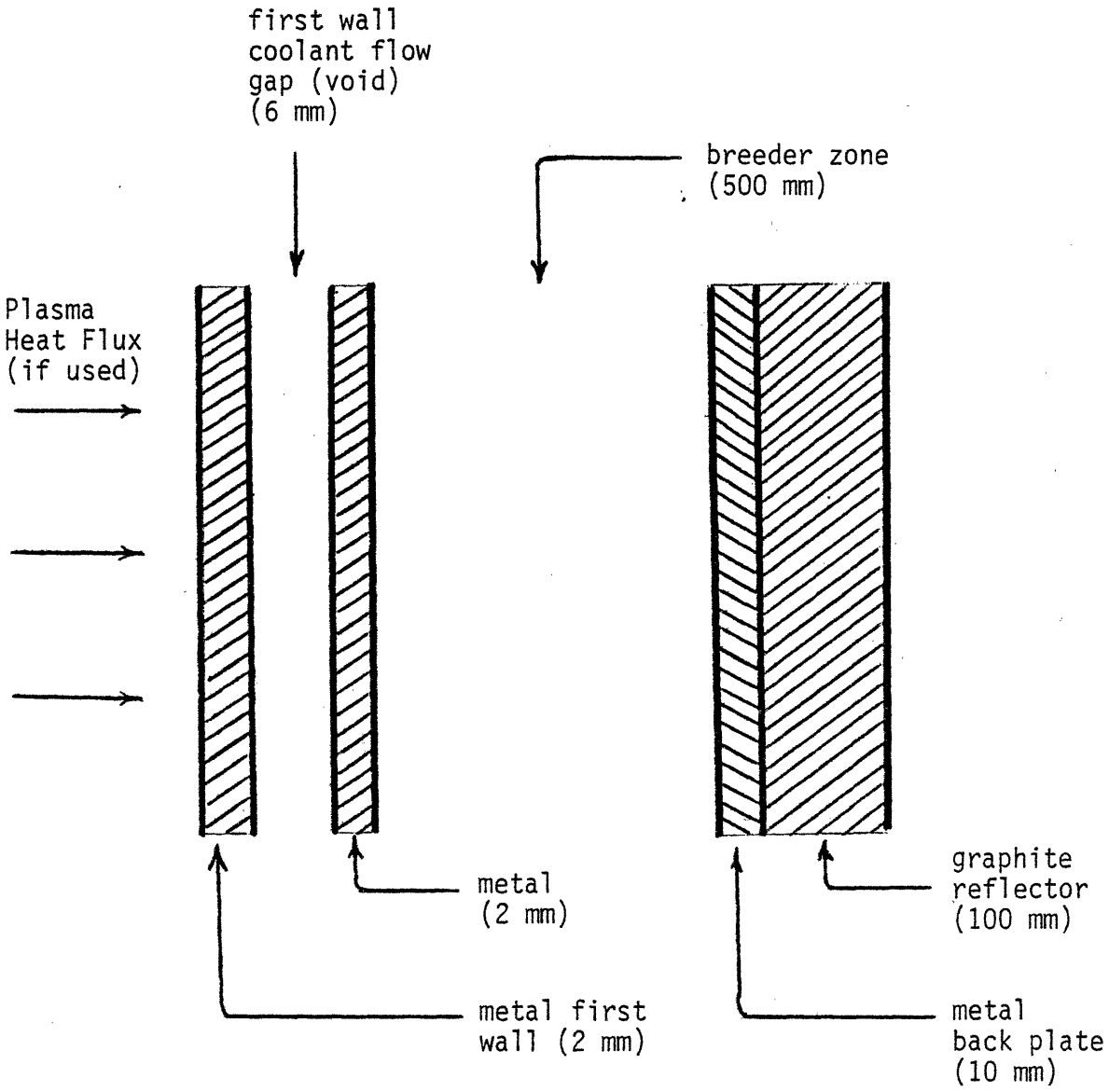

Fig. 3.10: One Dimensional Base Case Geometry for LOCA Analysis

3.2.5.1 Adiabatic Case

Several studies have mentioned initial temperature rise (°C/sec) rates from either afterheat or plasma heat. It was decided to first repeat the adiabatic calculation for the materials in this study to compare with previous works. Furthermore, this simple case allows direct comparison among structural materials.

For afterheat, the size of the volume input to the code is unimportant, (if q''' is uniform over the volume). For plasma heating, as will be seen, the thickness of the first wall is important. Two cases were analyzed d_{fw} = 2 mm, 10 mm.

3.2.5.2 Plates

The next level case analyzed was that of parallel plates, corresponding to a one-dimensional version of an empty module. This consists of a first wall (front plate) and a back wall. Radiation heat transfer is allowed between them. This was used to examine the effect of radiation heat transfer in keeping front and back of the module in thermal contact as well as allow examination of the scaling effects of varying d_{fw} and d_{bw}.

The first wall was varied from 1 mm to 10 mm and the back wall (d_{bw}) (including reflector) was varied from 10 mm to 500 mm. No breeder or coolant materials were used.

3.2.4.3 Base Cases

Figures 3.10 and 3.11 show the one and two dimension base case geometry. The two dimension case allows examination of edge and connector effects. The question arises as to whether the edge of the module assists in transferring heat from front to back of the module. Since a coolant gap

of the module of the module to fall to 300 °C. Furthermore, freezing is less of a safety problem since it implies that temperatures (hence radioactivity mobilization) are low. The entire problem is heavily dependent on the design of the start-up/shutdown procedure and the thermal coupling between modules and surrounding material. To some degree, however, those cases with less damage potential (less heating) may have a higher freezing concern. Although beyond the scope of the present analysis, the problem of undesired freezing is an area of future work.

The blanket modules contribute to neutron attenuation, minimizing neutron flux (hence nuclear heating) to the magnet and magnet shield. A rapid change in the attenuation characteristics in the blanket is of potential concern. The worst would be the loss of a liquid breeder (Li or $Li_{17}Pb_{83}$). The loss of a liquid coolant (water, flibe, Li) represents less blanket volume. Helium has a very small neutronic effect. The loss would have to occur before the plasma terminates for a problem to occur. The time scale of breeder loss indicates that it is not likely to be a problem in this regard. The worst case may be a water coolant, the only case with sub-second loss time scale (other than helium).

3.2.5 Geometries

Several geometries were used to explore structural material, breeder, and coolant effects. These range from a simple adiabatic box to 2-D reference cases for each coolant/breeder combination. The motivation and details are now described. Detailed descriptions of the geometries appear in Appendix C.

TABLE 3.9

Temperature Margins Against Melting (°C)

Metal	T_{melt}	$T_{operation}$	ΔT_{om}
TZM	2620	900	1720
vanadium	1900	600	1300
HT-9	1420	450	970
316 SS	1430	450	980

This value (ΔT_{rise} = 300 °C) is adopted as the criterion for determining the time required for damage. Although imperfect, it is a representative criterion.

Ideally, a detailed temperature-stress transient analysis would determine likely locations of damage. This is beyond the scope of the present study. Furthermore, the element of time needs to be addressed. A short period of temperature rise (if then cooled) may be associated with higher temperatures (for short time) than prolonged exposure to a lower elevated temperature (although the generated thermal stress are even lower in the latter case).

The second criterion is the onset of melting (always occurs first at the first wall for the materials studied). Besides representing a higher temperature rise than for the onset of structural damage, the time to melt introduces an additional material property, ΔT_{om}, where

$$\Delta T_{om} = T_{melting} - T_{operating} \tag{3.41}$$

The refractory metals with their higher melting temperatures have higher ΔT_{om} even though their operating temperatures are also higher (Table 3.9).

Preventing damage from freezing is part of the general question of how to start and shut down a fusion reactor with a liquid metal or salt fluid which is solid at room temperatures. The specific concern here is that the normal shutdown procedure/equipment would not be available after an accident, leading to freezing for long times after an accident. Sze [3.19] found this not to be a problem. His analysis treated the magnet shield as an isothermal sink. Even so, it took 50 hrs. for the back wall

3.2.4 Relative Hazard Criteria

To compare the various structural materials, breeders, and coolants, there must be a consistent set of criteria. The primary concern with LOCA's is the rise in temperatures due to inadequate cooling. This concern consists of two parts, 1) damage due to thermal stresses and weakening material strength of elevated temperatures, and 2) melting. Either results in economic and safety problems, e.g., mobilization of radioactivity, reactor damage. There are two secondary concerns. First, Sze [3.19] mentions the potential for reactor damage due to freezing of liquid metals as the structure eventually cools. Second, the UCLA safety study [3.18] discusses the problem of an increased neutron flux to the magnets if a liquid metal breeder were to empty and create a void. Each of these concerns will be examined.

The most probable problem from a LOCA (or similar accident) is likely to be reactor damage because 1) required temperature rises are less than melting, and the other two concerns (freezing and voiding) look manageable. Because of the desire for good thermal efficiciency, operating structural temperatures will be as high as practical. As temperatures rise in an accident, the metal strength decreases as the same time that additional thermal stresses (non-uniform heating) are generated. Sze [3.19] suggested that a UWMAK-I 316 SS first wall could survive short times at 600 °C ($\Delta T_{rise} \sim 125$ °C) but would likely undergo damage by 800 °C ($\Delta T_{rise} \sim 325$ °C).

Analysis of metal strength curves versus temperature would indicate that all metals have significant reduction of material properties by a 300°C temperature rise from the assumed maximum operation point (see Appendix B.) Also the microstructure of the alloy would be degraded (Appendix B.)

Li coolant to empty is several minutes, but the time scale for a Li-breeder to empty (breeder only, hence a small tube size) is days. For a Li-Pb breeder, the time scale is a few hours. These MHD numbers are too uncertain (with the exception of flibe) and there is too much variance between MHD and non-MHD to base specific LOCA scenario results on them. They do demonstrate that Li or Li-Pb is likely to remain in place and provide heat sink for a significant amount of time. One may bracket this effect by two cases — 1) no fluid, 2) fluid remains through accident but only stagnant. For flibe the reference case is for the coolant to empty in about 2.5 sec.

3.2.3.5 Loss-of-Coolant Rates Conclusion

Given the time scales involved, the effects of fluids can be estimated. The minimum for coolants is no effect. For afterheat time regimes, the coolant in all cases (even Li) can be assumed to have emptied and there is no coolant effect for the present LOCA analysis. For the plasma heating time scale, the maximum can be estimated by approximate heat transfer values as function of time for water, He, and flibe. For lithium, the lithium is assumed to stop flowing but not drain (to find maximum effect).

For fluid breeders, the minimum is unknown. For afterheat, the effect again approaches zero (non-MHD). The maximum effect for afterheat is approximated by retention of stagnant breeder (no contact with first wall). For plasma heating, the time scales appear to suggest that the breeder can not drain significantly before plasma termination (by whichever method). However, as seen in section 3.3, the presence of the breeder has only a slight effect anyway.

TABLE 3.8

Time to Drain for MHD Conditions

Metal	Steel	V	TZM	TZM	Steel
Fluid	Li	Li	Li	flibe	$Li_{17}Pb_{83}$
Case 1					
fluid as coolant (min)	3.1	5.7	—	0.003	—
fluid as breeder (hr)	35	63	116	—	1.7
Case 2					
fluid as coolant (min)	8.3	15.0	—	0.008	—

TABLE 3.7

Maximum Flow Rates under MHD Conditions*

Metal	Fluid	v_{max} (m/s)
Steel	Li	0.0020
V	Li	0.0011
TZM	Li	0.0006
TZM	flibe	2.06**
Steel	$Li_{17}Pb_{83}$	0.0410

*for relevant operating temperatures, $B \sim 5T$, d_w = 1 mm, r = 10 mm
note that v_{max} scales as r

**for flibe the scaling with r is different

$$v_{max} \sim v_o \; r(\text{in cm}) \times \frac{15.7}{1 + 14.7\; r\;(\text{in cm})}$$

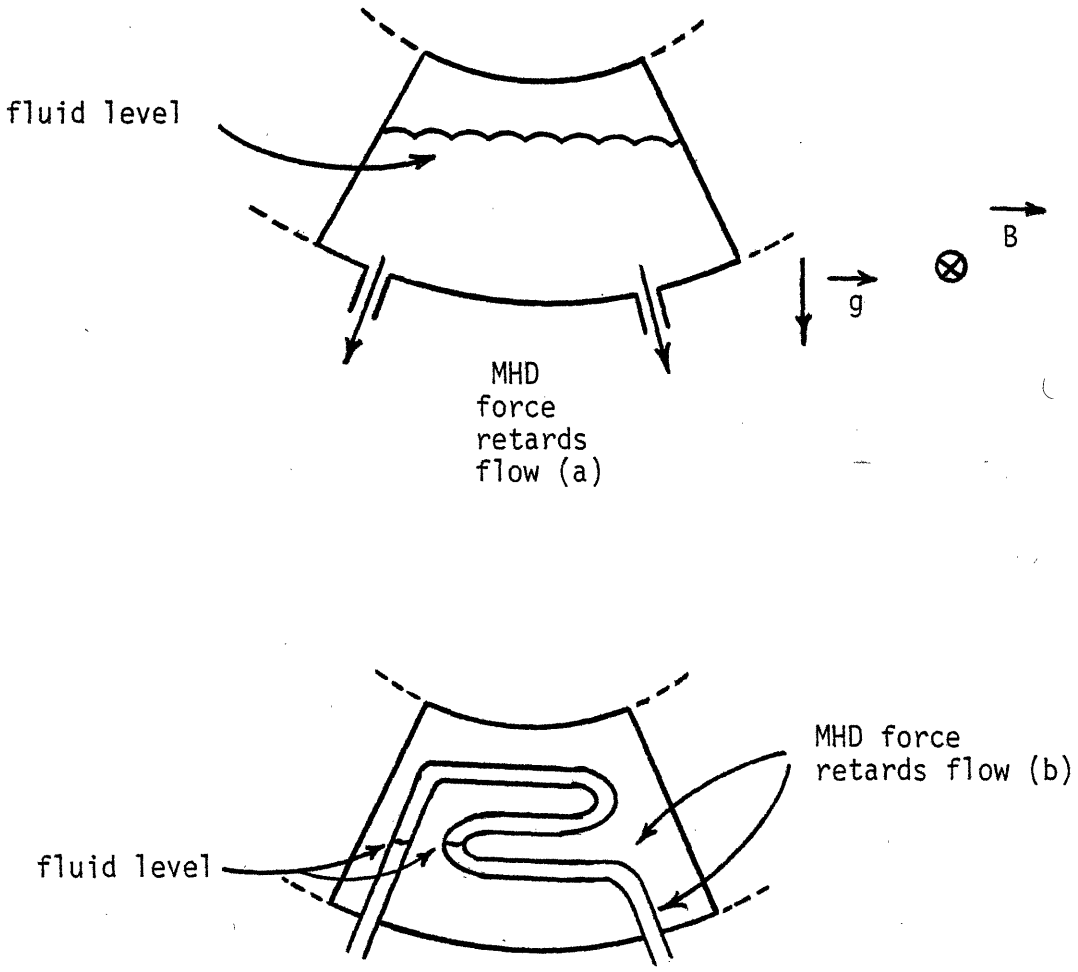

Fig. 3.9: Blanket Geometries for Cases where MHD Force Inhibits Gravity Drain of Fluid Breeder, Worst Case Module Located under the Plasma

d_w = pipe thickness

σ_w = pipe wall conductivity

σ_f = fluid conductivity

Then, the maximum velocity due to gravity perpendicular to the field (see Figure 3.9a,b) is given by [3.18]

$$v_{max}(m/sec) = \frac{pgr^2}{[Ha + Ha^2(\frac{c}{1+c})]} \tag{3.38}$$

Table 3.7 lists the result for conditions (operating temperature, $B \sim 5T, d_w \sim 1$ mm) of interest. With the exception of flibe, these velocities are very low and Li-Pb is less restricted than Li.

This may be a factor in two different ways. For case 1, the restriction is at a break which is perpendicular to the field. Then, the time to empty is given by

$$t_1 = \frac{V}{A_b} \frac{1}{v_{max}} \tag{3.39}$$

For case 2, the restriction is assumed to be at some pipe bend in the blanket, then

$$t_2 \sim \frac{L}{v_{max}} \qquad \text{where } L \sim r \text{ (pipe radius)} \tag{3.40}$$

The results are shown in Table 3.8. Compared to the gravity-only case, one sees that flibe is not MHD limited. The time scale for the

TABLE 3.6

Time to Drain for Liquid-Metals and Molten-Salts (Non-MHD)

Metal	Fluid	As Coolant	As Breeder
Steel	Li	3.9 s	4.9 m
V	Li	3.9 s	4.9 m
TZM	Li	—	4.9 m
TZM	flibe	2.4 s	—
Steel	$Li_{17}Pb_{83}$	—	5.3 m

or

$$t(\text{time to empty}) = \frac{z_o^{1/2}}{0.5} \left[\frac{2g}{(A_1^2/A_2^2-1)}\right]^{-1/2} \tag{3.34}$$

and $$t \sim 0.45 \left(\frac{A_1}{A_2}\right) \sqrt{z_o} \qquad A_1 >> A_2 \tag{3.35}$$

however $V = z_o A_1$, then $A_1/A_2 = (V/A_b) \frac{1}{z_o}$

and

$$t \sim 0.45 \left(\frac{V}{A_b}\right) z_o^{-1/2} \tag{3.36}$$

and once again V/A_b is seen as a primary scale factor. Interestingly, the time is independent of density, only on design parameters. Table 3.6 lists the results for the reference designs. The difference between coolant and breeder use is due to the difference in volume (volume of breeder > volume of coolant), and in tube area ($A_{breeder} < A_{coolant}$ because a slower rate is required).

If MHD forces are present, the rate may be restricted. Carlson [3.17] gives the pressure drop through a pipe perpendicular to a magnetic field as

$$dP/dx = - \frac{\mu v}{r^2} \left[Ha + Ha^2 \left(\frac{c}{1+c}\right)\right] \tag{3.37}$$

where r = pipe radius

Ha = Hartman number = $Br \sqrt{\frac{\sigma}{\mu}}$

$c = \sigma_w d_w / \sigma_f r$

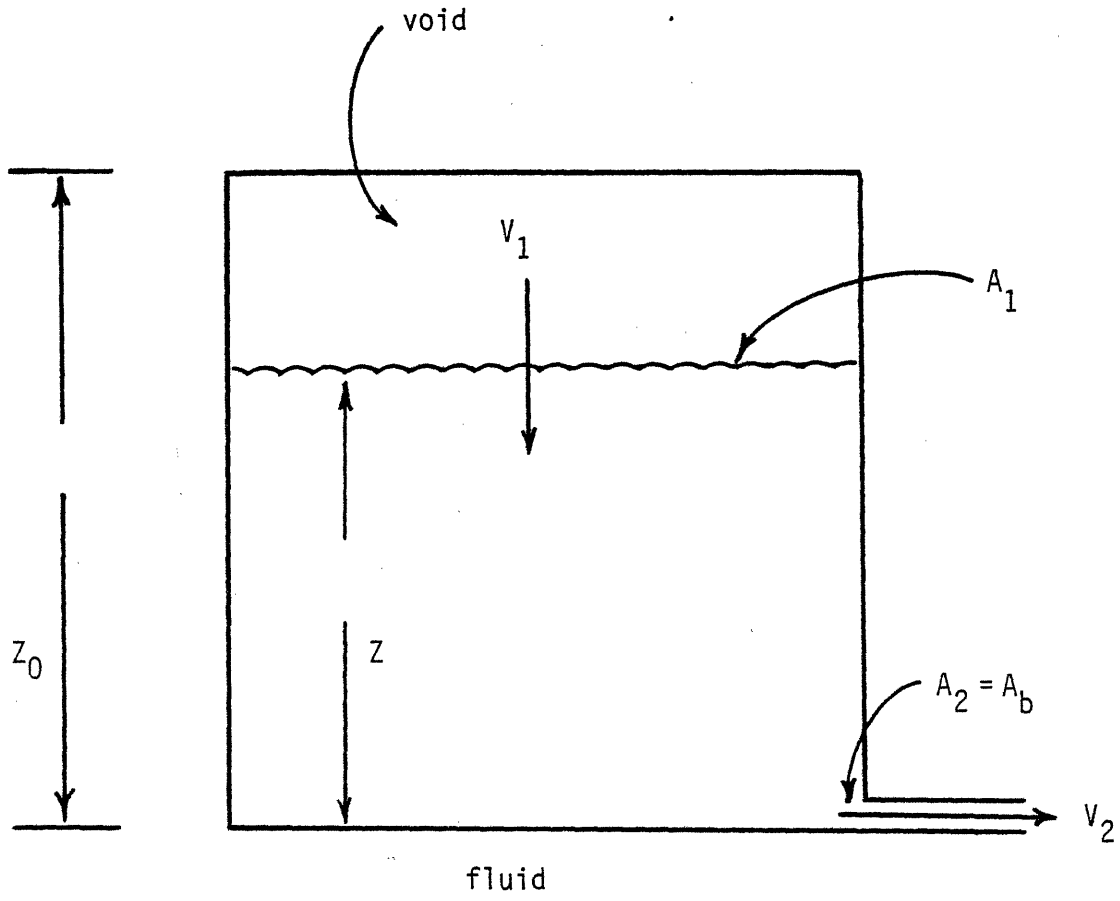

Fig. 3.8: Blanket Geometry for Case where Fluid Breeder Drains Due to Gravity

TABLE 3.5

Liquid-Metal and Molten-Salt Fluids

Fluid	Metal	Fluid Use
Li	steel	coolant
Li	steel	breeder
Li	vanadium	coolant
Li	vanadium	breeder
Li	TZM	breeder
flibe	TZM	coolant
$Li_{17}Pb_{83}$	steel	breeder

be pressure driven, but rather only drained by gravity. Even if MHD pumping requires about MPa pressures for lithium, the low compressibility will result in a rapid pressure drop to that of the building with little drainage. Furthermore, depending on the geometry involved, MHD forces will restrict the rate of drainage. Since the time scale for toroidal fields to decay may be long, the toroidal field MHD forces will likely be present at least through the plasma heating removal stage.

Table 3.5 shows the combinations of materials which must be examined. First, the non-MHD simple gravity drain will be calculated. Second, two MHD calculations are presented.

Without MHD forces and negligible pressure drops, the energy equation is

$$\frac{\rho v_1^2}{2} + pgz = \frac{\rho v_2^2}{2} \qquad \text{(see Figure 3.8)} \qquad (3.32)$$

where

z = depth of fluid

v_1 = internal velocity

v_2 = exit velocity

since $v_1 = -dz/dt$ and $v_1 A_1 = v_2 A_2$ (conservation of mass), one obtains

$$z/dt = \left[\frac{2g}{(A_1^2/A_2^2 - 1)}\right]^{\frac{1}{2}} z^{\frac{1}{2}} \qquad (3.33)$$

or

For conditions of interest the final heat transfer coefficient after ($Re < 3000$) depressurization is about 1000 W/m^2-°K. Thus, a rough estimate of the film coefficient behavior is given by

$$h(t) = 10{,}000 - 90{,}000t \qquad 0 < t < 0.1 \qquad (3.30)$$

$$h(t) = 1{,}000 \qquad t > 0.1 \qquad (3.31)$$

The details (as in the case of water) are not particularly important since (as seen in section 3.3) the depressurizing coolant has a very slight effect.

A helium purge stream in a solid breeder which is at low pressure also may remove some heat from the blanket. Under normal operation the system is not designed for this, but if it continued operation, some transfer might be expected to occur during a thermal transient. For the present analysis, this cooling credit is ignored because 1) the purge stream connections would likely fail if a double coolant break had occurred for small module sizes and 2) the low thermal conductivity of the solid breeders reduces the potential benefit.

3.2.3.4 Liquid-Metal and Molten-Salt Cooled

In the previous cases of the highly pressurized coolants (water and helium), the time scales indicate that the coolants will not have any effect on afterheat removal and have (at best) a slight effect on plasma heating removal for the most severe LOCA's. The high internal pressure drives the coolant out with only choking at the orifice as resistence. The other fluids (Li, flibe, $Li_{17}Pb_{83}$) will not

$$\rho = \rho_o \, e^{-\omega t} \tag{3.24}$$

$$\omega = A/v \cdot R \cdot \sqrt{T_o} \times 0.0159 \, \frac{\text{sec } (°K)^{\frac{1}{2}}}{m} \tag{3.25}$$

For the reference case, $\omega \sim 200$ Hz and the exponential decay time ($1/\omega \lesssim 0.01$ sec) is very short. The time for depressurization is approximately

$$t_e(\text{helium}) \sim \frac{\ln(P_o/P_{final})}{\omega} \tag{3.26}$$

Since $P_o = 5.5$ MPa and $P_{final} \sim 0.1$ MPa, we obtain

$$t_e(\text{helium}) \sim 0.02 \text{ sec} \tag{3.27}$$

The high value of A_b/V results in depressurization in less than 0.1 sec. An estimate of the heat transfer coefficient is given by [3.16]. Due to the uncertainty in coolant time scales, a value of 0.1 sec is adopted for the end of the depressurizing period.

$$h = 0.021 \, Re^{0.8} \, Pr^{0.6} \, \frac{k \times FF}{D_e} \qquad Re > 6000 \tag{3.28}$$

$$h = 8.23 \, k/D_e \qquad Re < 3000 \tag{3.29}$$

where D_e = hydraulic diameter

FF = surface roughness factor heat transfer

and $\eta_v \sim 7.0$ [4.7]. Absolute values for the depth of melting and vaporization can be obtained from their dimensionless results using the definitions of the dimensionless variables:

$$d_m = \delta_m \left[\frac{E/A}{\rho c_p (T_m - T_o)}\right] \tag{4.12}$$

$$d_v = \delta_v \left[\frac{E/A}{\rho c_p (T_m - T_o)}\right] \tag{4.13}$$

$$t_{pd} = \frac{\phi}{\alpha} \left[\frac{E/A}{\rho c_p (T_m - T_o)}\right]^2 \tag{4.14}$$

where δ_m, δ_v = dimensionless depth of melting, vaporization

ϕ = dimensionless time

E/A = 3.83 MJ/m^2 reference value

Use of Fraas and Thompson's model results in Fig. 4.4, with extrapolation (dotted lines) to zero disruption time. In the limit of an instantaneous disruption ($t_{pd} \to 0$), only a thin layer of material will be vaporized so that the temperature versus depth profile is a simple step function. In this limit, the conservation of energy gives

$$E/A = d_v\left(\rho c_p (T_m - T_o) + H_f + \rho c_p (T_v - T_m) + H_g\right) \tag{4.15}$$

Then, to first order we obtain

$$d_v(t_{pd} \to 0) \sim 1/9.4 \left(\frac{E/A}{\rho c_p (T_m - T_o)}\right) \tag{4.16}$$

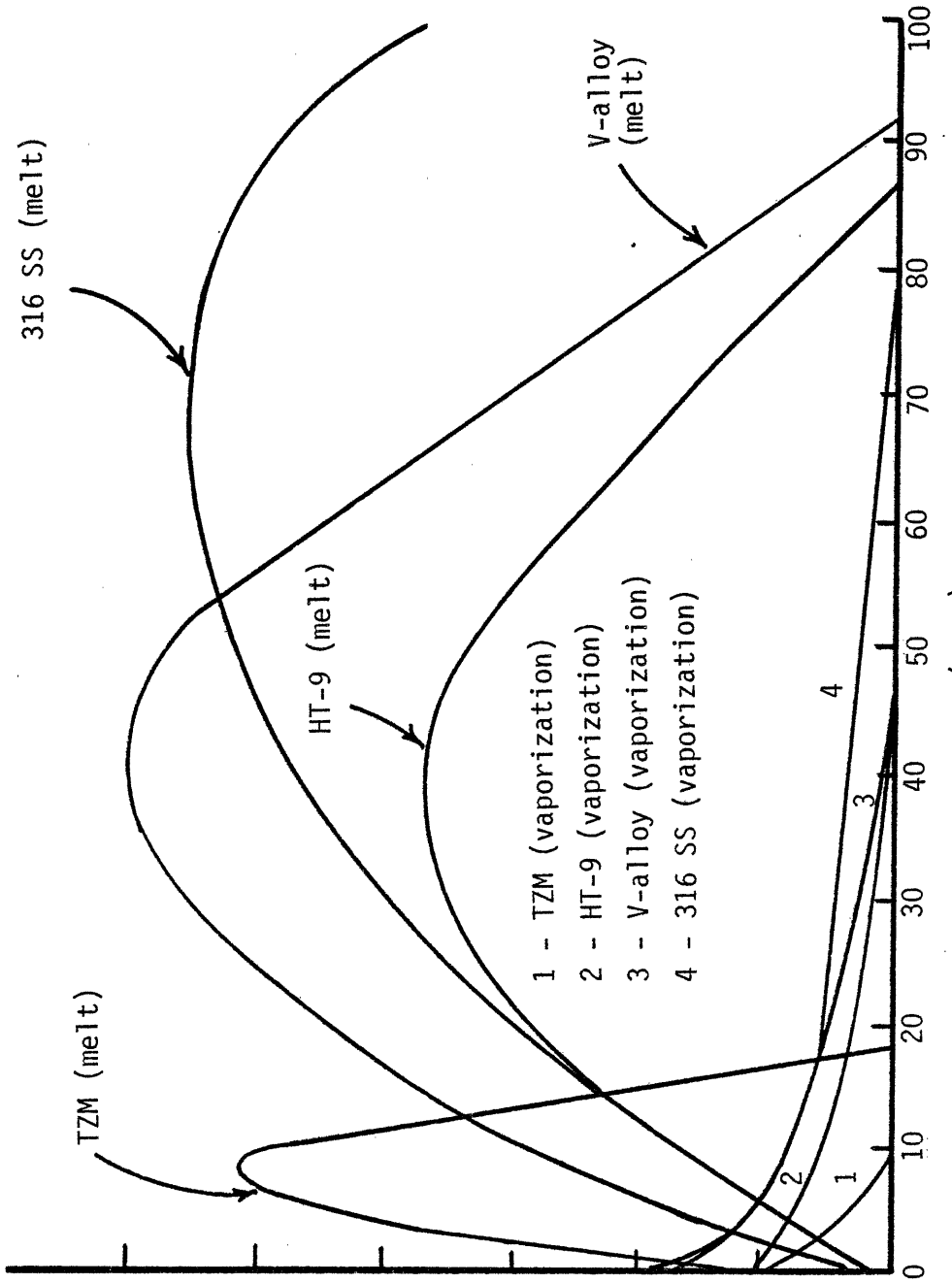

Fig. 4.4: Dept of Melting and Vaporization Caused by Disruptions of Varying Time Scale, Fraas and Thompson Model [4.7]

using the values for the dimensionless parameters η_m and η_v. This allows extrapolation of the depth of vaporization curves to zero disruption times.

The results of the finite difference calculation with latent heats and stationary vapor phase are compared to the simple analytical calculations in Table 4.8. The simple analytical model (Eqs. (4.5) - (4.7)) does not allow estimation of the maximum depth of vaporization which occurs for instantaneous disruptions. The two models produce similar results for the disruption time which starts melting and the maximum depth of melting. When latent heats are included, however, shorter disruption times are required to produce either vaporization and the maximum depth of melting. It is interesting, though, that for those two parameters the ratio between models is fairly constant among materials. Hence, the relative comparison among materials is basically unaffected.

As noted above, the assumption of a static vapor phase can be relaxed, although at a high cost of complexity. The INTOR [4.3] study examined the depth of melting and vaporization for 316 SS at a 20 msec disruption time for different energy deposition values. For the reference value of E/A = 3.8 MJ/m^2, a comparison among all three models is possible, shown in Table 4.9. Incorporation of latent heat of melting reduces the amount melted as expected and discussed above. Incorporation of vapor phase transport reduces the amount vaporized [4.3], but increases the depth of melting.

The maximum amounts of material melted or vaporized do not appear to be significantly different among materials (see Table 4.8). However,

TABLE 4.8

Comparison of Results From
Models With and Without Latent Heats*

	316 SS	HT-9	V-alloy	TZM
Disruption Time to Cause Melting, t_m, msec				
With Latent Heat	156	87	92	19
Without Latent Heat	160	92	97	19
Disruption Time to Cause Vaporization, t_v, msec				
With Latent Heat	80	46	49	9.8
Without Latent Heat	28	16	19	3.7
Maximum Depth of Melting, d_{mm}, mm				
With Latent Heat	0.28	0.19	0.30	0.26
Without Latent Heat	0.25	0.17	0.27	0.23
Time Which Produces Maximum Melting, msec				
With Latent Heat	69	39	41	8.2
Without Latent Heat	40	23	24	4.9
Maximum Depth of Vaporization, d_{mv}, mm				
With Latent Heat	$\sim$0.084	$\sim$0.056	$\sim$0.091	$\sim$0.077

*Calculations with latent heats based on model in reference 4.7

TABLE 4.9

Comparison of Heat Transfer Models For 20 msec Disruption (t_{pd}) and 3.8 MJ/m^2 Energy Deposition (E/A) For 316 SS

	Depth of Melting (mm)	Depth of Vaporization (mm)
Analytical Model No Latent Heats No Vapor Phase	0.23	——
Finite Difference* Latent Heats Included Static Vapor Phase	0.15	0.03
Finite Difference** Latent Heats Included Vapor Phase Transport	∿0.20	∿0.008

*Adapted for 316 SS from reference 4.7

**Adapted for 3.8 MJ/m^2 from reference 4.3

the disruption time that produces maximum melting, or the onset of melting or vaporization, does differ among materials. As seen in Table 4.10 (based on Table 4.8), significantly shorter disruptions may cause such effects as the onset of melting, the maximum depth of melting, and the onset of vaporization. The relative disruption times (defined relative to the best case of TZM) are very similar for the above three effects. Thus, a natural relative consequence index from phase change due to plasma disruption is defined as follows (see Table 4.10)

$$RCI_{PD}^{pc} \sim \frac{t_m}{t_m(TZM)} \sim \frac{t_v}{t_v(TZM)} \sim \frac{(t_{pd})_{max\ melt}}{(t_{pd})_{max\ melt}\ (TZM)} \qquad (4.17)$$

Thus, a plasma disruption will cause similar effects for 316 SS as one 8.2 times shorter for TZM. In other words, a disruption would have to be 8.2 times more severe (shorter time, higher heat flux) for TZM phase changes to be as severe as for 316 SS.

4.2.2 First Wall Thermal Stresses

The increase in temperature is non-uniform through the first wall. This non-uniformity leads to thermal stresses. Fraas and Thompson [4.7] summarize the relationship for the maximum thermal stress in the first wall as

$$s_T = Kn\left(\frac{E_y\beta}{1-a\nu}\right)\Delta T_{fw} \qquad (4.18)$$

where β = linear coefficient of expansion

E_y = Young's modulus

TABLE 4.10

Relative Disruption Times That Produce Undesired Thermal Effects*

	316 SS	HT-9	V-alloy	TZM
Relative Time to Cause Melting ($t_m/t_m(TZM)$)	8.2	4.6	4.8	1.0
Relative Time to Cause Vaporization ($t_v/t_v(TZM)$)	8.2	4.7	5.0	1.0
Relative Time to Cause Maximum Melting	8.4	4.8	5.0	1.0
Relative Consequence Index for Phase Change from Distruptions, RCI_{PD}^{pc}	8.3	4.7	4.9	1.0

*Low values are preferred

a,n = factors dependent on the number of geometrical constraints

K = stress concentration factor

ΔT_{fw} = temperature drop across the first wall

The stress concentration factor is generally greater than one and is higher at notches, corners, and existing cracks. The factor n is in the range $0 \leq n \leq 1$ and depends on the number of dimensions constrained and the surface orientation. For present purposes, the factor Kn is unimportant since the focus is on relative material effects. Present modeling will focus on the general case of a flat plate unconstrained in thickness ($\hat{z}$), but constrained in the plane ($\hat{x}$, $\hat{y}$). For this case $Kn \rightarrow 1$.

The factor a is the number of constrained dimensions minus one. For the present case, the thermal stress is approximately given by

$$s_T = \left(\frac{E_y \beta}{1-\nu}\right) \Delta T_{fw} \tag{4.19}$$

There are four relevant time scales in determining thermal stress.

4.2.2.1 Long-Time Heat Flux

For a heat flux applied for long time scales ($t_{pd} \gtrsim 1$ sec), the temperature rise is given by Eq. (4.1):

$$\Delta T'_{fw} = \Delta T_{fw} \left(1 + \frac{x}{100}\right) \tag{4.1}$$

where ΔT_{fw} = design value

Thus the stress scaling goes as

$$S_T = \left(\frac{E_y \beta}{1-\nu}\right)\left(1 + \frac{x}{100}\right)\Delta T_{fw} = \left(\frac{E_y \beta}{k(1-\nu)}\right)\left(1 + \frac{x}{100}\right) q''_w d_{fw} \qquad (4.20)$$

The relative value among materials is given in Table 4.11. As noted in Section 4.1, a representative scaling is to include the yield stress as a material property. The effect of this property is also shown in Table 4.11. See Appendix B for the values of material properties and yield stresses. 20% cold work is assumed for 316 SS. Since the time scale ($\gtrsim$ 1 sec) is so long compared to the likely disruption time scale, 20 - 100 msec, further analysis is needed.

4.2.2.2 Intermediate Time Scale

Delessandro [4.6] has examined the thermal stress in more detail, using a calculation with a constant heat flux (step function) for a finite thickness (d_{fw}) plate. The minimum compressive and tensile stress are given approximately by [4.6]

$$(s_c)_{max} \sim -\frac{1}{10}\left(\frac{E}{A}\right)\left(\frac{d_{fw}}{t_{pd}}\right)\frac{E_y \beta}{k(1-\nu)} \qquad (4.21)$$

$$(s_t)_{max} \sim \frac{2}{\sqrt{\pi}}\left(\frac{E}{A}\right)\left(\frac{d_{fw}}{t_{pd}}\right)\frac{E_y \beta}{k(1-\nu)} \qquad (4.22)$$

Equation (4.21) is accurate within about 20% for fourier, F_o, numbers between 0.01 to about 0.15. Equation (4.22) is accurate within 20% for

TABLE 4.11

Relative Impact of Thermal Stress for Very Long Time Scales*

Material Property Scaling	$\frac{E_y \beta}{(1-\nu)} \Delta T_{fw}$	$\frac{E_y \beta}{k(1-\nu)}$	$\left(\frac{E_y \beta}{1-\nu}\right) \frac{T_{fw}}{s_y}$
316 SS	2.3	10.0	2.7
HT-9	1.1	4.1	1.9
V - alloy	0.7	2.3	1.2
TZM	1.0	1.0	1.0

*Relative to TZM properties, low values preferred

fourier numbers between about 0.03 to about 0.15. The maximum compressive stress occurs at the surface while tensile stresses are maximum in the wall.

These results (d_{fw} = 2 mm) indicate that the relevant material scaling is $\frac{E_y\beta}{k(1-\nu)}$ for fourier numbers between about 0.02 and 0.10. The relative values are shown in Table 4.12. Any surface melting is ignored. The deviation from this scaling due to differing disruption times and melting are discussed later.

4.2.2.3 Short Time Scale

For short time scales with fourier numbers under 0.001, Delessandro [4.6] has shown that the surface compressive stress is given well by

$$s_c = -\left(\frac{E}{A}\right)\left(\frac{4}{\pi t_{pd}}\right)^{1/2}\left(\frac{E_y\beta}{1-\nu}\right)(\rho c_p k)^{-1/2} \qquad (4.23)$$

which is simply the result of substituting the expression for ΔT_{fw} (Eq. (4.3)) into Eq. (4.19). This is the regime where the semi-infinite plate model is valid. The heat flux burst heats up and expands the surface causing compressive stresses. Unlike the previous case, however, the interior tensile stresses are minimal [4.6], since the heat flux is so rapid. The relative scaling among the reference materials is shown in Table 4.13. The disruption time limit for which this is valid (Fourier number < 0.001) is very short. Expected disruption times are at least an order of magnitude longer.

TABLE 4.12

Relative Thermal Stress Scaling
For Intermediate Time Scales

Material	Disruption Time Range (msec)* F_o = 0.02	F_o = 0.15	Stress Scaling $\frac{E_y \beta}{k(1-\nu)}$	Yield Scaling $\frac{E_y \beta}{k(1-\nu)S_y}$
316 SS	16	120	10.0	11.6
HT-9	21	156	4.0	6.9
V-alloy	8.4	63	2.3	3.9
TZM	2.3	18	1.0	1.0

*Actual disruption time range for which this scaling is most valid, d_{fw} = 2 mm, s_y evaluated at operating temperatures.

TABLE 4.13

Relative Material Thermal Stress Scaling for Short Time Scales*

	Disruption Time for Short Time Scaling ($F_o < 0.001$) msec	Stress Scaling $\frac{E_y \beta}{(1-\nu)}(\rho c_p k)^{-1/2}$	Yield Scaling $\frac{E_y \beta}{1-\nu}(\rho c_p k)^{-1/2}\frac{1}{s_y}$
316 SS	0.8	3.8	4.4
HT-9	1.0	1.3	2.3
V-alloy	0.4	1.2	2.1
TZM	0.1	1.0	1.0

*Relative to TZM, low values preferred, independent of first wall thickness

4.2.2.4 Maximum Surface Stress With Melting

For an instantaneous disruption, the surface material is ablated. The maximum temperature drop in the load carrying solid wall is simply $T_m - T_o$ [4.7]. The maximum surface stress (compressive) is then given by [4.7],

$$s_c = \left(\frac{E_y \beta}{1-\nu}\right)(T_m - T_o) \tag{4.24}$$

The relative stress values for the reference materials and relative stress divided by yield stress is given in Table 4.14.

4.2.2.5 Combined Time Scales

The equations for stress at intermediate and short time scales (melting ignored) can be rewritten in terms of fourier number. The upper limit on the maximum (surface) compressive stress is given by either

$$S_c = \left[\frac{E E_y \beta \alpha}{Ak(1-\nu)d_{fw}}\right] \frac{1}{10} F_o^{-1} \qquad 0.02 \lesssim F_o \lesssim 0.15 \tag{4.25}$$

or by

$$S_c = \left[\frac{E E_y \beta \alpha}{Ak(1-\nu)d_{fw}}\right] \frac{2}{\sqrt{\pi}} F_o^{-1/2} \qquad F_o < 0.001 \tag{4.26}$$

depending on the value of F_o. By converting Delessandro's [4.6] results to this format, Fig. 4.5 is obtained. For expected disruption times of 20 - 100 msec, the corresponding fourier numbers (d_{fw} = 2 mm) range

TABLE 4.14

Relative Material Maximum Surface Thermal Stress for Instantaneous Disruption*

	Stress Scaling $\left(\frac{E_y\beta}{1-\nu}\right)(T_m - T_o)$	Yield Scaling $\left(\frac{E_y\beta}{1-\nu}\right)(T_m - T_o)\frac{1}{s_y}$
316 SS	1.3	1.5
HT-9	0.6	1.1
V-alloy	0.5	0.9
TZM	1.0	1.0

*Relative to TZM, low values preferred

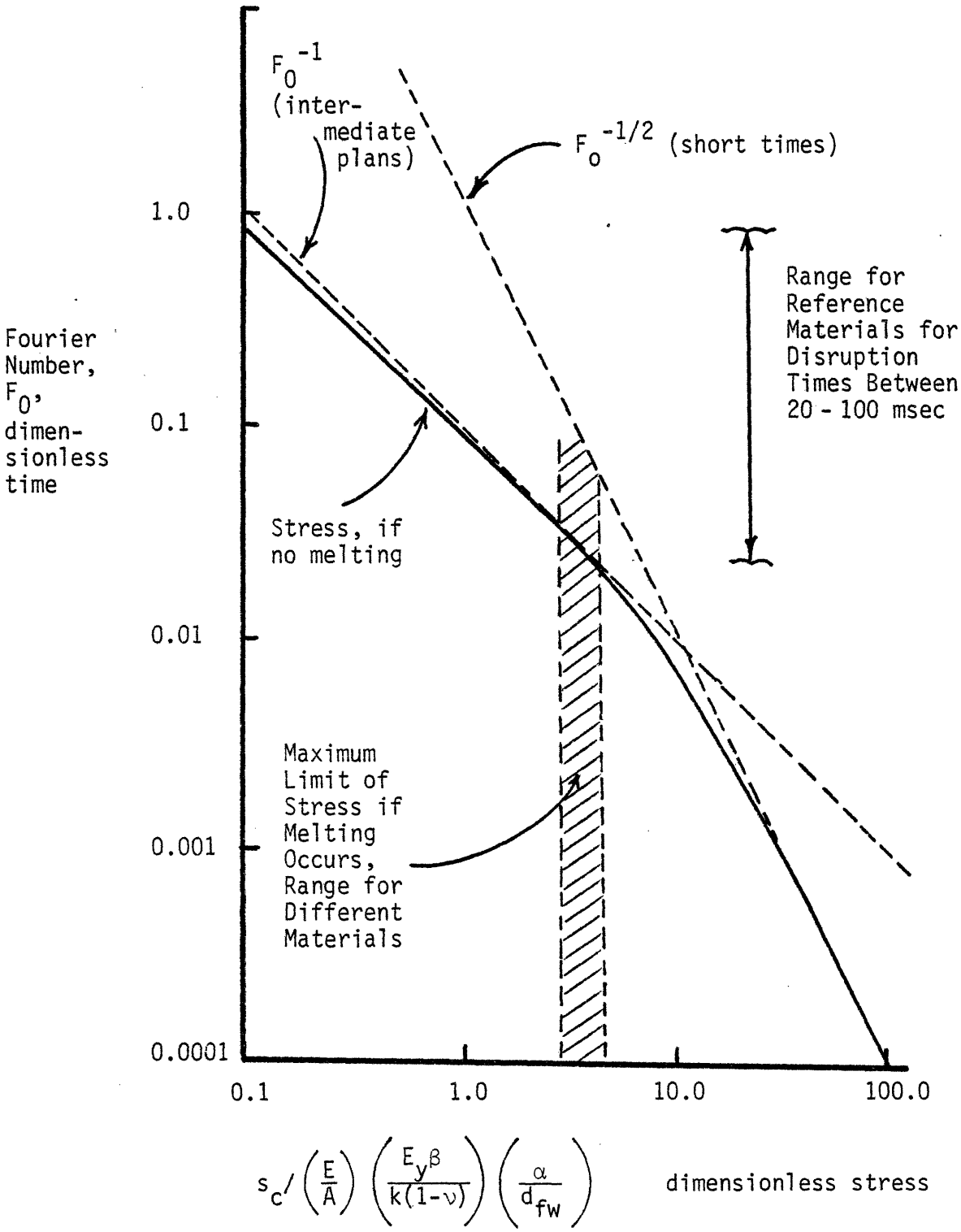

Fig. 4.5: Maximum Compressive Stress as a Function of Disruption Time, Based on Delassandro's Model [4.6]

between 0.02 and about 0.8. The solid line indicates the normalized compressive stress if no surface melting were to occur (from reference 4.6). The figure illustrates that the intermediate time scaling is limiting for disruption times of interest. The short time scaling is not controlling.

In similar fashion, the intermediate time scaling for the maximum tensile stress can be rewritten as

$$s_t \simeq \left[\frac{E E_y \beta\alpha}{Ak(1-\nu)d_{fw}}\right] 0.04\ F_o^{-1} \qquad (4.27)$$

Delessandro's actual results are compared to the simple scaling law in Fig. 4.6. For the disruption times of interest, Eq. (4.27) is a good rough approximation.

Surface melting caused by the disruption complicates stress analysis. In Section 4.2.2.4, the maximum possible compressive stress was obtained. This is graphed in Fig. 4.5. It is seen that melting may limit the maximum possible stresses for disruption times of interest.

The maximum compressive stress is then limited by the minimum of Eqs. (4.21) (intermediate time) and (4.24) (maximum possible if surface melting). This maximum possible stress is indicated for the reference materials in Fig. 4.7. In reality for disruption times that produce melting, the maximum compressive stress would be no higher than that shown in Fig. 4.7 due to the elimination of stress in the melt zone. Furthermore, the progression of the melt zone into

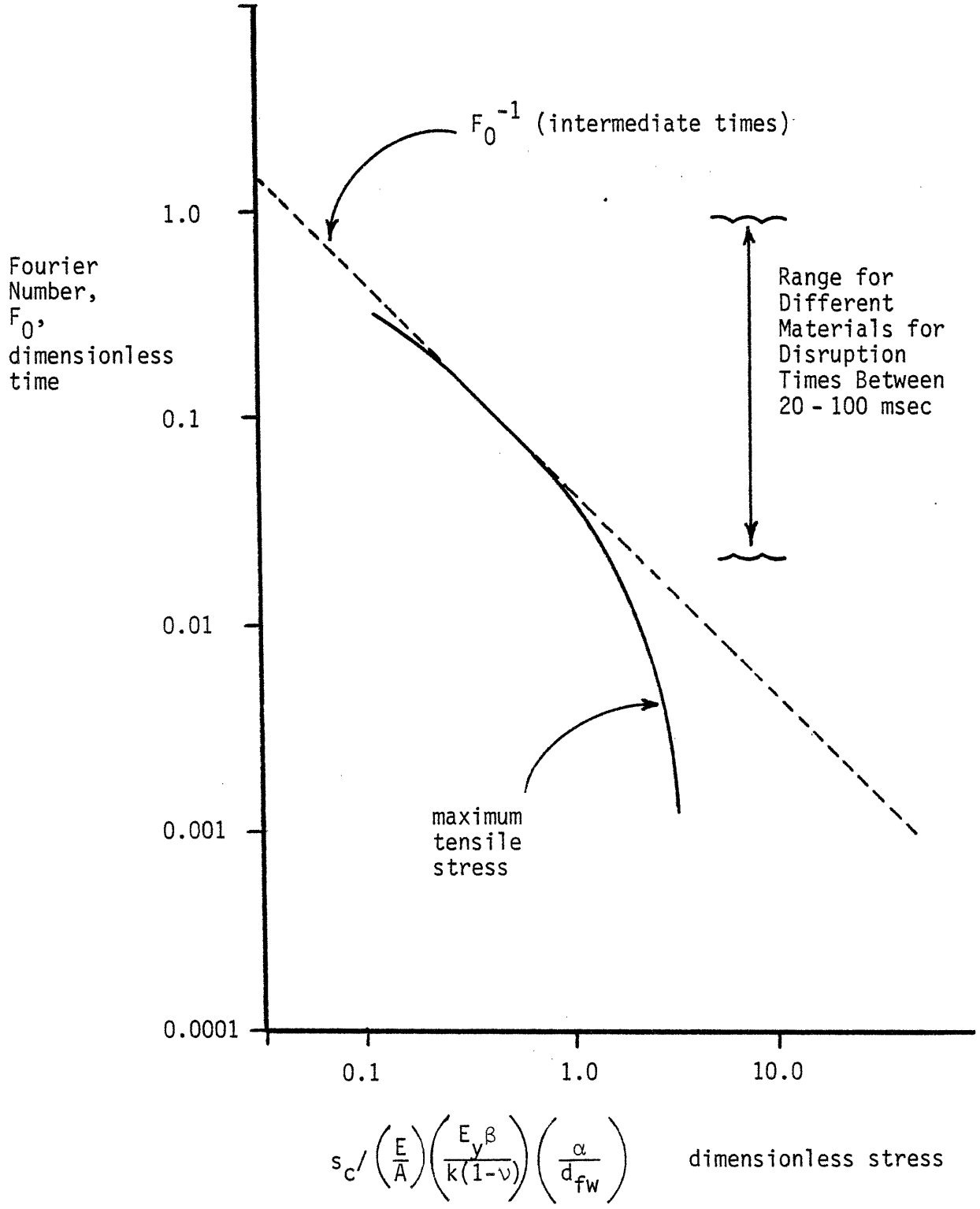

Fig. 4.6: Maximum Tensile Stress as a Function of Disruption Time, Based on Delassandro's Model [4.6]

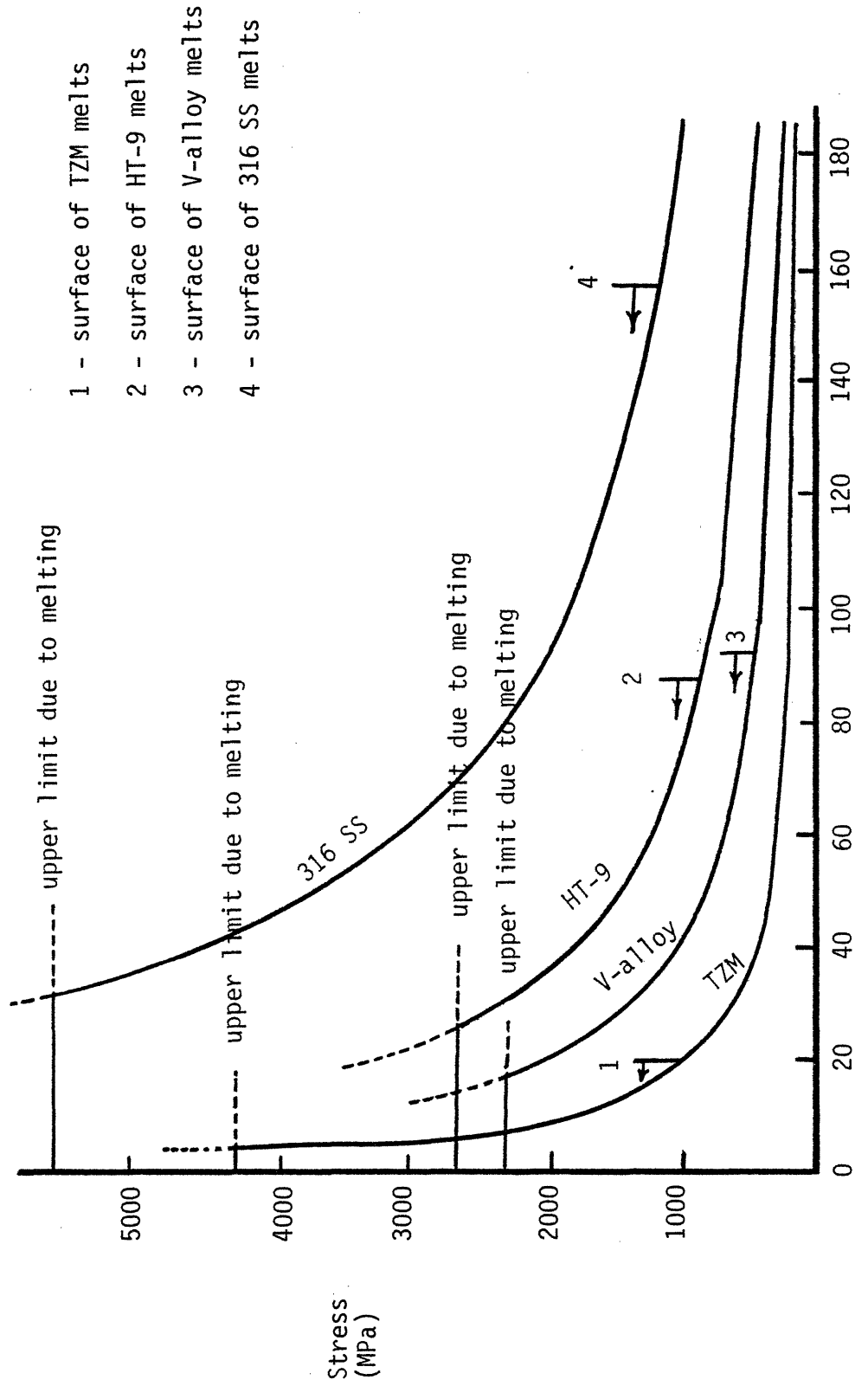

Fig. 4.7: Maximum Compressive Stresses in the First Wall from Disruptions (d_{fw} = 2 mm)

the wall erases some material flaws produced in the solid. For the range of disruption time of most interest the maximum tensile stresses tend to be 2.5 lower than compressive stress and show the same material property scaling, that of intermediate times (Eqs. (4.21), (4.22)).

4.2.2.6 Relative Stress

The thermal stress scaling with material properties has been seen to vary with the disruption time scale. The range of thermal stresses relative to that of TZM is given in Table 4.15 as well as the most appropriate value, that for the intermediate time scale. If one considers the yield stress as an appropriate means to compare thermal stresses among materials, the figure of merit is s_T/s_y. The range for the materials for various time scales is given in Table 4.15 along with the value for the intermediate time scale.

4.5 Electromagnetic Effects

Disruptions may cause a variety of electromagnetic effects. Although considerable effort has been spent in analyzing these effects, the state-of-knowledge is still poor. The most important question is which natural properties influence the result. Although the absolute severity of these problems is not yet known, the following discussion of (primarily) previous work is presented to indicate that the basic material property is electrical conductivity. However, the disruption time and geometrical design parameters appear even more critical and appear to overshadow the material impact. The effects discussed here are eddy current heating and magnetic forces. Other potential problems like

TABLE 4.15

Comparison of Thermal Stresses in Materials Subjected to a Heat Pulse From a Disruption*

	Range of Relative Stresses	Intermediate Time Relative Stresses	Range of Relative Stress/Yield**	Intermediate Time Relative Stress/Yield**
316 SS	1.3 - 10	10	1.5 - 11.6	11.6
HT-9	0.6 - 4.0	4	1.1 - 6.9	6.9
V-alloy	0.5 - 2.3	2	0.9 - 3.9	3.9
TZM	1.0	1.0	1.0	1.0

*Relative to TZM, low values preferred

**Yield stress evaluated at operating temperature

electrical arcing across gaps are very poorly understood and are not discussed. It is not believed that these effects show dependence on variables other than electrical conductivity and design specifics.

4.3.1 Single Component Model

When the disruption takes place, the plasma current is transferred to the surrounding structure. The exact design and potential electrical breakdown paths will determine where the currents will flow. The precise location and time behavior of these currents determines eddy current heating and magnetic forces. Detailed examination of the placement of eddy currents and forces is underway by other researchers [4.9]. The INTOR study used a two component model where the current is assumed to transfer to either the first wall or a seperate blanket circuit, equivalent to 20 mm of 316 SS [4.3].

For present purposes, a single component model is generally adequate. Here, the current is confined to one toroidal circuit. This is conservative since the actual current would be lower due to some current being transferred to other components.

4.3.1.1 Wall Time Constant

A very important parameter is the wall electrical time constant, t_w, which is given by

$$t_w = L/R_w \tag{4.28}$$

where L = Inductance

R_w = Wall Resistance.

For a toroidal shell, the inductance is material independent and given

by [4.4]

$$L = \mu_o \, r_m[\ln(8r_M/r_w)-2] = 9.0\mu H \qquad (4.29)$$

where r_M = major wall radius = 7 m (reference value)

r_w = equivalent minor radius = 2.7 (reference value)

μ_o = magnetic permeability to toroidally flowing currents.

The wall resistance to toroidally flowing currents in a smooth surface is given by [4.4]:

$$R_w = \left(\frac{2\pi r_M}{d_c}\right) \frac{1}{d\sigma_w} \qquad (4.30)$$

where d_c = cross section poloidal perimeter = 18.6 m

σ_w = wall material electrical conductivity

d = cross section thickness

Thus the time constant for the reference size design can be expressed as

$$t_w = (3.81\mu H)d\sigma_w \qquad (4.31)$$

Thus, for a smooth surface, the thickness and electrical conductivity determine the time constant. Values of the time constant for relevant components is given in Table 4.16.

In an actual design, the first wall is generally not expected to be continuous around the torus. Thus jumpers would be needed between

TABLE 4.16

Electrical Time Constants for Single Components

Material	Component	Component Thickness d(mm)	Wall Time Constant t_w (msec)
316 SS	First Wall	2	7.6
HT-9	First Wall	2	8.0
V	First Wall	2	14.1
TZM	First Wall	2	27.7
Be	Multiplier	35	300
Zr_5Pb_3	Multiplier	70	240

modules. The presence of these jumpers will raise the resistance of the breakdown path and lower the wall time constant. For example, the STARFIRE design considered a continuous beryllium multiplier which had a time constant of 300 msec. When jumpers were included the time constant decreased to 40 msec [4.4]. For a single component model, effects are always sharply reduced for lower wall time constants (higher resistance). Thus, for present purposes, the effect of intermodule jumpers is conservatively ignored.

4.3.1.2 Currents

The current in the component as a function of time after the start of the disruption is given by [4.4]

$$I_w(t) = \frac{I_p}{(1-t_{pd}/t_w)}\left(e^{-t/t_w} - e^{-t/t_{pd}}\right) \tag{4.32}$$

where I_p = plasma current.

The reference value of I_p = 10 MAmp is used in these calculations.

4.3.2 Eddy Current Heating

The heat input to the wall due to the resistance is simply

$$E_e = \int_0^\infty dt\ I_w^2(t) R_w \tag{4.33}$$

Performing the integration using the expression (Eq. (4.32)) for the wall current, one obtains

$$E_e = \frac{1}{2} L I_p^2 \left(\frac{t_w}{t_w + t_{pd}} \right) \tag{4.34}$$

The only material dependence occurs in the wall time constraint. For the cases of an instantaneous disruption ($t_{pd} \rightarrow 0$), the input energy reaches a maximum. The current density is approximately uniform through the wall thickness. The wall temperature increase can then be written as

$$\Delta T_{rise} = \frac{E_e}{\rho c_p d_{fw} A} = \left(\frac{L I_p^2}{2A} \right) \left(\frac{t_w / t_w + t_{pd}}{\rho c_p d_{fw}} \right) \tag{4.35}$$

The temperature rise for first walls (d_{fw} = 2 mm) of the four reference materials as a function of plasma disruption time is shown in Fig. 4.8. The temperature rises are very modest compared to that resulting from the particle heat flux and can be ignored. Furthermore, the eddy current heating is fairly uniform through the wall and thus does not contribute to thermal stresses. Thus, although eddy current heating does depend on material choice, the effect is always small compared to the particle heat flux.

Onega, et. al. [4.1] modeled a non-uniform 316 SS wall and discovered that, in like manner, less than 10% of the temperature rise came from eddy current heating. They note that it may cause difficulties for extreme geometries. If the current density in an intermodule jumper were significantly higher than in the wall, the eddy current part of temperature rise might be important.

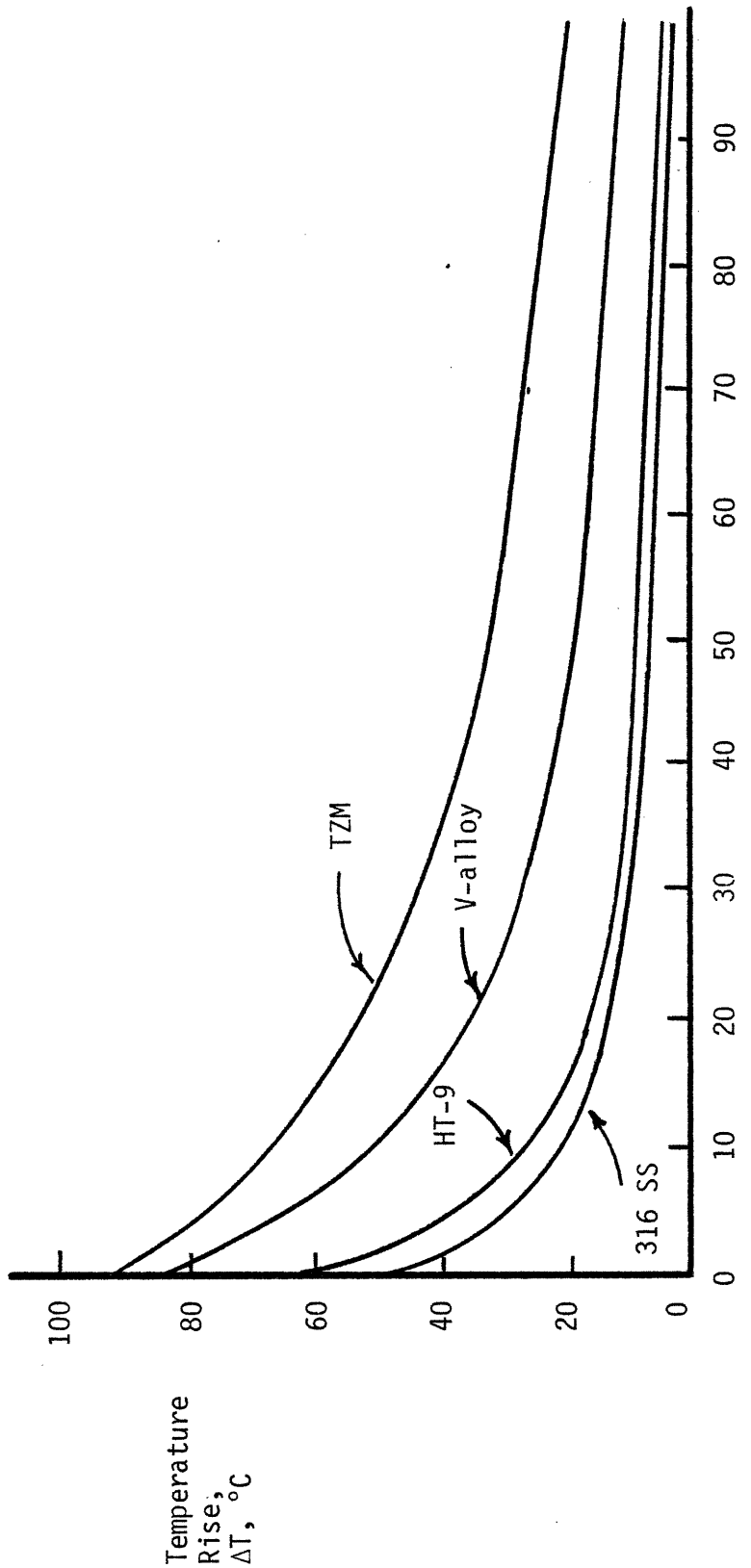

Fig. 4.8: First Wall Temperature Rise (d_{FW} = 2 mm) Caused by Resistance Heating from Induced Currents From a Disruption

4.3.3 First Wall Stresses

The force on the wall is due to the interaction of the wall current with the poloidal field, both varying in time. Using the one component model again, one obtains the pressure (normal to the surface) on the first wall as [4.4]

$$P(t,t_w,t_{pd}) = \left(\frac{B_o^2}{2\mu_o}\right)\left(1-\frac{t_{pd}}{t_w}\right)^{-2} \times \left[\exp\left(-\frac{2t}{t_w}\right) - \left(1-\frac{2t_{pd}}{t_w}\right)\exp\left(-\frac{2t}{t_{pd}}\right) - 2\left(\frac{t_{pd}}{t_w}\right)\exp\left(-t\left(\frac{1}{t_w}+\frac{1}{t_{pd}}\right)\right)\right] \quad (4.36)$$

For the reference plasma, the constant $\frac{B_o^2}{2\mu_o}$ equals 0.4 MPa. The maximum pressure during or after the disruption can not be determined analytically since Eq. (4.36) is too complex.

For the worst case of an instantaneous disruption, Eq. (4.36) becomes

$$P(t,t_w,t_{pd} = 0) = 0.4\ \exp(-2t/t_w)\ \text{MPa} \quad (4.37)$$

The maximum pressure is always 0.4 MPa for an instantaneous disruption of the reference plasma.

The maximum pressure was solved for numerically using Eq. 4.36 for two disruption times, 25 msec and 100 msec. The results are shown in Fig. 4.9 as a function of wall time constant. The maximum magnetic pressures for first walls of the four reference materials can be determined from the figure and are listed in Table 4.17. The scaling among materials is seen to be slower than the electrical conductivity

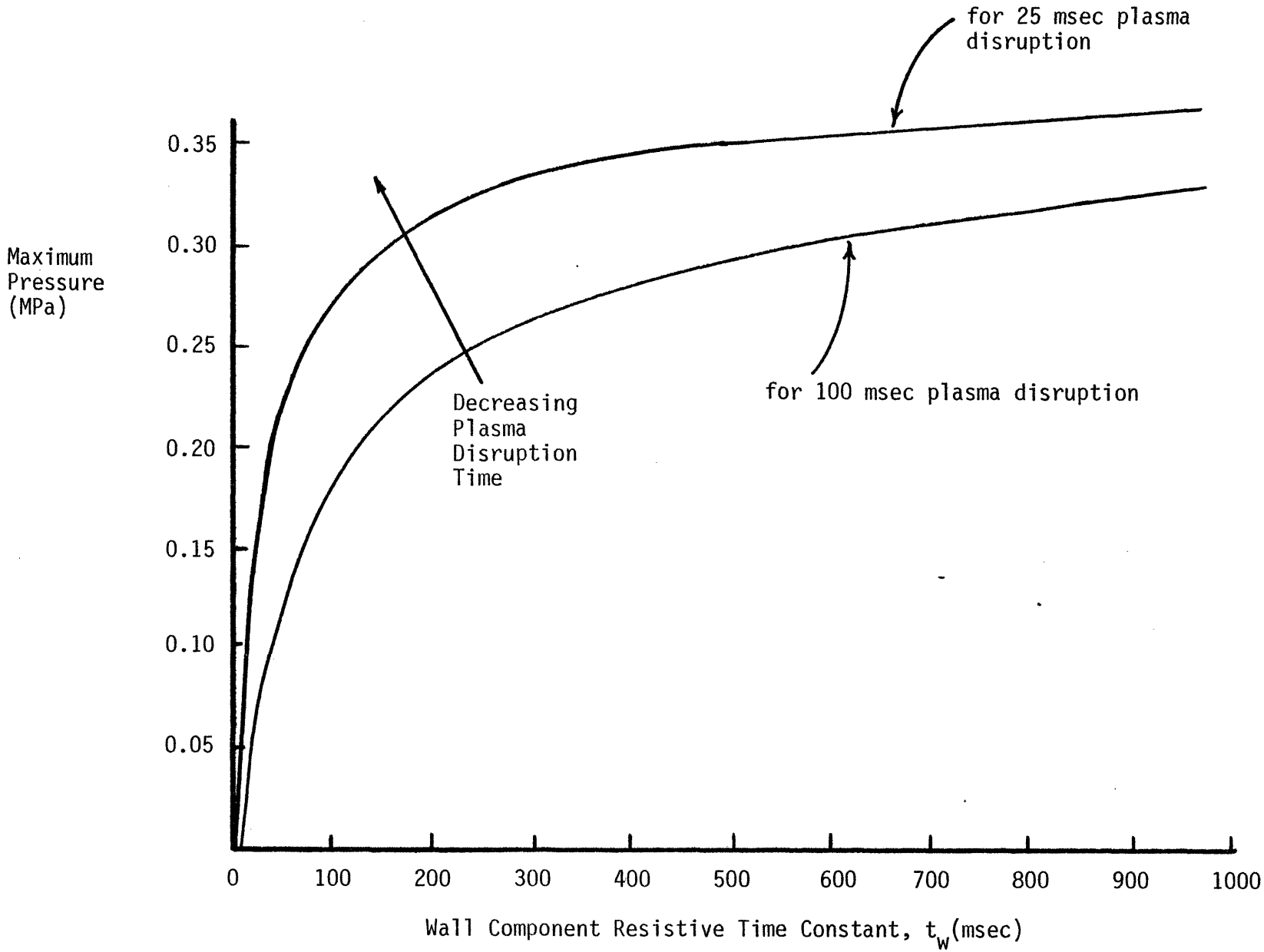

Fig. 4.9: Maximum Pressure on the First Wall Caused by Induced Currents and Magnetic Field from a Disruption

TABLE 4.17

Maximum Magnetic Pressures
Generated in 2 mm First Wall

	25 msec Disruption		100 msec Disruption		Relative* Conductivity
	Actual (MPa)	Relative*	Actual (MPa)	Relative*	
316 SS	0.11	1.0	0.042	1.0	1.00
HT-9	0.11	1.0	0.044	1.0	1.05
V-alloy	0.15	1.4	0.066	1.6	1.85
TZM	0.19	1.8	0.101	2.4	3.64

*Relative to 316 SS, low values preferred

scaling. Again, higher resistance (lower conductivity) is preferred.

The INTOR study [4.3] included a two-component analysis of the maximum magnetic forces. The first wall was either aluminum or 316 SS; the blanket was modeled as a 20 mm thick slab of 316 SS. The wall electrical time constant was assumed the same for both designs, being fixed from plasma physics considerations. Although the conductivity of aluminum is 11-20 times higher, the forces are 5 times higher (less than linear scaling). For an 18 mm O.D. steel tube, the maximum force per unit length was found to be 2.35 kN/m. If this were evenly distributed over the tube, it would compare to a uniform 0.13 MPa outward pressure. This result is similar to the 0.4 MPa uniform pressure for the present reactor size.

It is interesting to note that MHD forces are also generated in a surface melt layer [4.3]. For the INTOR design, a maximum pressure of 275 N/m^2 was found on a uniform melt layer. If surface tension is lower, this provides a mechanism for the melted surface layer to be seperated from the first wall [4.3].

4.3.2 Blanket Magnetic Stresses

A blanket contains more than the first wall and currents (hence forces) may be generated elsewhere. The temperature rise from generated currents has been shown to be insignificant for the case where currents are confined to the first wall. Since the current density is lower if more of the structures is involved, temperature rise from currents can be neglected. Stresses, however, can not be.

4.3.4.1 Solid Breeder

Solid breeder materials have a high resistance, and little current

would be expected to be induced. However, except for Li_2O, the solid breeders require a neutron multiplier. For the present study, two neutron multipliers, Zr_5Pb_3 and Be, were considered with the breeder, $LiAlO_2$. The time constants (see Table 4.16) for such structures are much higher than that of a bare first wall. This is primarily due to the lower resistance cuased by a thicker ($\sim$ 50 mm versus 2 mm first wall) cross section available to carry the current. The uniform outward pressures thus tend to reach the maximum of 0.4 MPa independent of choice of neutron multiplier.

4.3.4.2 Liquid Breeders

The liquid breeders (Li, $Li_{17}Pb_{83}$) and low resistance coolants (Li) will also experience induced currents and forces. The liquid nature, greater radial thicknesses, and non-simple, non-symmetric geometries make analysis very difficult.

If one viewed the fluids as solid conductors with depths similar to a neutron multiplier, the time constant and resulting pressure are not greatly different from the multiplier. Unfortunately, this is not a valid treatment.

Walker and Wells [4.10] have analyzed the forces in a liquid lithium cylindrical module resulting from a changing poloidal field as is the case with a disruption. The system (Fig. 4.10) is a cylinder perpendicular to a constant toroidal field with B_p varying. Two cases were studied, 1) B_p transverse to the cylinder axis and 2) B_y parallel to the axis. The work was part of the Westinghouse/ ORNL demonstration study [4.11].

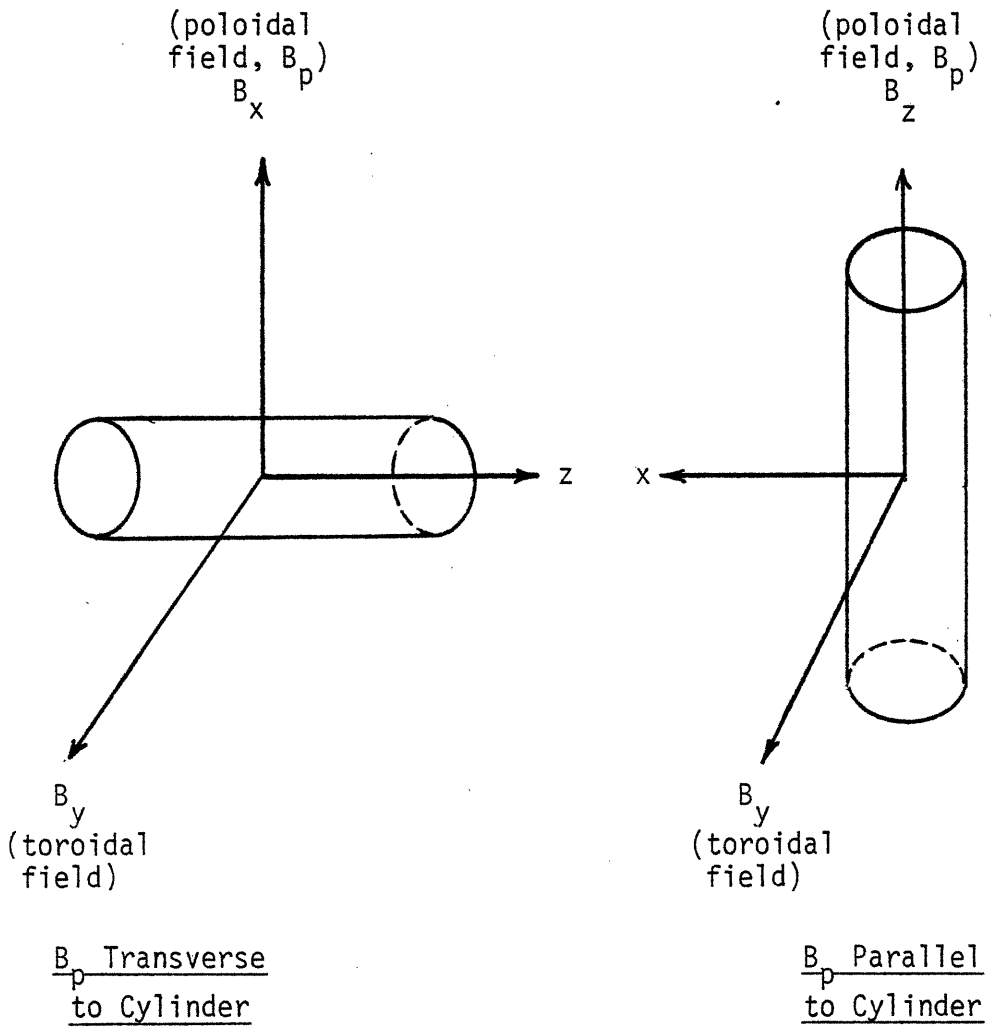

Fig. 4.10: Different Orientations of Cylinder Geometries for Walker and Wells Model [4.10]

The geometry modeled corresponds to the Westinghouse/ORNL blanket design, which is the basis of the He/Li reference design in the current study. However, the geometry of the other present reference designs (water/Li-Pb, Li/Li, flibe/Li) look much different (see Chapter 2) and represent even more difficult cases to analyze due to the lack of even cylindrical symmetry. The validity of the model was expressed in terms of four dimensionless variables as listed in Table 4.18. For the present study, the variables were evaluated at 500°C with a 2 mm wall thickness and 0.5 m fluid characteristic distance, typical of the reference designs. The values obtained are shown in Table 4.19 for disruption times of 25 and 100 msec and fluids lithium and $Li_{17}Pb_{83}$.

As seen in the table, all the criteria are met except that of the magnetic Reynolds number. Indeed, for their study [4.10], the magnetic Reynolds number for their 24 msec disruption case was marginal. The situation is worse here since a larger module is being considered.

The resulting stress laws are listed in Table 4.20. Walker and Wells point out the strong scaling with module size (d_f), which implies that large Li modules may not be possible. However, the increase in d_f makes the small Re_m assumption invalid. This is why it was valid for their study (small radius cylinders, $d_f \sim$ 5-10 cm) but invalid for the current case ($d_f \sim$ 50 cm).

Gierszewski [4.12] notes that the magnetic Reynolds number is a ratio of the effects of the induced magnetic field to the applied field. Thus the effects of induced fields appears important in large size modules.

A full detailed treatment of geometries different from the small

TABLE 4.18

Dimensionless Variables Indicating Validity of Walker and Wells [4.10] Model

Interaction Parameter, desire $N \gg 1$

$$N = B_T^2 \sigma_f t_{pd} / \rho_f$$

Hartman Number, desire $Ha \gg 1$

$$Ha = B_T d_f \left(\frac{\sigma_f}{\mu_f}\right)^{1/2}$$

Magnetic Reynolds Number, desire $Re_m \ll 1$

$$Re_m = \mu_m \sigma_f d_f^2 / t_{pd}$$

MHD Parameter, desire $c \ll 1$, $Ha^{-1} \ll c$

$$c = \sigma_w d_w / \sigma_f d_f$$

where B_T = toroidal field

σ_f, σ_w = electrical conductivity of fluid, wall

μ_f = fluid viscosity

μ_m = magnetic permeability

d_f = characteristic fluid distance

d_w = wall thickness

TABLE 4.19

Tests for Validity of Walker and Wells [4.10] Model

Variable	25 msec Disruption		100 msec Disruption		Desire for Model Validity
	lithium	$Li_{17}Pb_{83}$	Lithium	$Li_{17}Pb_{83}$	
N	5,250	75	21,000	300	$>> 1$
Ha	2.8×10^5	7.3×10^4	2.8×10^5	7.3×10^4	$>> 1$
Re_m	35.6	10	8.9	2.4	$<< 1$
C	1.4×10^{-3}	5.2×10^{-3}	1.4×10^{-3}	5.2×10^{-3}	$<< 1$
					$Ha^{-1} << C$

TABLE 4.20

Magnetic Stresses Due to Liquid Breeders (from reference 4.10) in Cylindrical Geometry

Transverse B_p

$\Delta P_{max} = \pm \frac{1}{8} \sigma_f d_f^2 B_p^2 / t_{pd}$	Maximum Change in Fluid Pressure on Inside Wall
$\tau_{r\theta}/_{length} = d_f \sigma_w B_T B_p / t_{pd}$	Maximum Shear Stress in Wall due to Body Forces in Wall
$\Delta s_\theta = \frac{5}{24} \frac{d_f^3}{d_w} \sigma_f B_p^2 / t_{pd}$	Maximum Change in Hoop Stress
$s_b = (1.023)\sigma_f \frac{d_f^4}{d_w^2} B_p^2 / t_{pd}$	Ring-bending Stress

Parallel B_p

$\Delta P_{max} = \pm \frac{1}{4} d_f d_w \sigma_w B_p^2 / t_{pd}$	Maximum Change in Fluid Pressure
$\Delta s_z/_{length} = \pm \frac{3}{4} d_f \sigma_w B_T B_p / t_{pd}$	Tension Stress
$\Delta s_\theta = - \frac{3}{4} d_f^2 \sigma_w B_p^2 / t_{pd}$	Change in Hoop Stress

cylinder, taking account of the induced fields is well beyond the scope of the present study. However, those results do provide some idea of the scaling involved. The only material properties are the conductivity of fluid and wall. As in previous sections, low conductivity, high resistance is desired.

The resulting forces are listed in Table 4.21 (d_f = 0.50 m, d_w = 2 mm). Walker and Wells found similar high values (e.g., ring-bending sress) for submillisecond disruptions and smaller size modules (in which case $Re_m << 1$ is again violated), and believe these to be very overestimated due to the violation of model assumptions. The induced field in the fluid will tend to reduce the total field, reducing the effect. The most worrisome stresses are the transverse case which are fluid dependent, material independent.

Further analysis would be necessary to determine how severe the stresses actually are. The strong scaling with design parameters dominates over material properties. The worst stresses scale with breeder conductivity, rather than structural wall conductivity, thus structural choice is somewhat unimportant.

4.4 Summary and Conclusions

In spite of the uncertainties involved in understanding disruption effects, there is sufficient evidence to determine the chief material influences.

4.4.1 Thermal Effects

The strong particle heat flux results in rapid first wall temperature rise. There is significant potential for structural damage from thermal

TABLE 4.21

Conservative Estimate of Magnetic Forces
On Cylindrical Liquid Breeders, d_f = 0.5 m, d_w = 2 mm*

	25 msec Disruption				100 msec Disruption			
Transverse B_p	Li		$Li_{17}Pb_{83}$		Li		$Li_{17}Pb_{83}$	
P_{max} (MPa)	3.5		0.96		0.88		0.24	
S (MPa)	1.5×10^3		400		370		100	
S_b (MPa)	1.8×10^6		4.9×10^5		4.5×10^5		1.2×10^5	
Transverse B_p	316 SS	HT-9	V	TZM	316 SS	HT-9	V	TZM
τr_θ/length (MPa/m)	120	126	222	430	30	32	56	108
Parellel B_p	316 SS	HT-9	V	TZM	316 SS	HT-9	V	TZM
ΔP_{max} (MPa)	0.01	0.01	0.02	0.04	—	—	—	—
ΔS_z/length (MPa/m)	90	95	167	320	23	24	42	81
ΔS_θ (MPa)	7.5	7.9	13.9	27.0	1.9	2.0	3.5	6.8

TABLE 4.22

Relative Consequence Indices for
Plasma Disruptions**

	Phase Change RCI_{PD}^{pc}	Thermal Stress RCI_{PD}^{ts}	Magnetic Stress RCI_{PD}^{ms}
316 SS	8.3	10.0	1.0
HT-9	4.7	4.0	1.0 - 1.1
V-alloy	4.9	2.3	1.0 - 1.9
TZM	1.0	1.0	1.0 - 3.6

*Based on model in Ref. [4.10]

**Low values preferred

stresses and/or material surface melting and vaporization. Even without any localized hot spots, the analysis shows that a significant fraction of the first wall ($\sim$ 0.25 mm) may melt, reducing the stress-carrying capability at the worst time. Possible solutions are 1) a first wall coating, 2) no disruptions (non-tokamak?), or 3) long time scale disruptions spread over large fraction of first wall area.

The exact scaling of temperature rises, melting, and thermal stresses among the structural materials depends to some degree on the time scale of the disruption. One relative consequence index for plasma disruptions from phase change was defined largely independent of the time scale:

$$RCI_{PD}^{pc} \sim \frac{t_m}{t_m(TZM)} \sim \frac{t_v}{t_v(TZM)} \sim \frac{(t_{pd})_{max\ melting}}{(t_{pd})_{max\ melting}\ (TZM)} \qquad (4.17)$$

Thus the relative disruption times which produce initial melting, maximum depth of melting, and initial vaporization scale with RCI_{PD}^{pc}. TZM is the best case due to its superior thermal-mechanical properties. In terms of material properties, the RCI_{PD}^{pc} is given by

$$RCI_{PD}^{pc} = \frac{[\rho c_p k (T_m - T_o)^2]_{TZM}}{[\rho c_p k (T_m - T_o)^2]} \qquad (4.38)$$

as indicated in Eqs. (4.5), (4.6), and (4.9) for the quantities t_m, t_v, $(t_{pd})_{max\ melt}$. The RCI_{PD}^{pc} also tends to indicate the relative time scale among materials.

The range of thermal stress scaling among materials varies with disruption time, as indicated in Table 4.15. However, the most relevant

time scale regime is the intermediate case where maximum stresses are given by Eqs. (4.21) and (4.22), which do not account for surface melting and thus conservatively predict maximum stresses. A relative consequence index for thermal stresses from plasma disruptions is defined as

$$RCI_{PD}^{ts} = \frac{(s_T)_{max}}{[(S_T)_{max}]_{TZM}} \qquad \text{for intermediate times} \qquad (4.39)$$

In terms of materials properties this becomes

$$RCI_{PD}^{ts} = \frac{[E_y\beta/k(1-\nu)]}{[E_y\beta/k(1-\nu)]_{TZM}} \qquad (4.40)$$

where again TZM is the best choice. The values for RCI_{PD}^{pc} and RCI_{PD}^{ts} are shown in Table 4.22.

The actual failure criteria from these stresses are unknown, but are needed to compare the severity of stresses among materials. One representative criterion is the material yield stress. The relative yield scaling was compared to the direct stress scaling in Tables 4.12, 4.15, or the intermediate time scale, the basis for RCI_{PD}^{ts}. The use of yield stress in the comparison has the primary effect of increasing the advantage of TZM.

The choice of coolant and breeder have only secondary influence on the plasma disruption thermal effects, principally through influence on design, especially the first wall thickness, d_{fw}. Thicker walls are preferred. To result in the same time scaling, the fourier number must be constant. Thus, the required shorter disruption time to produce the same fourier number for an increase in first wall thickness, d'_{fw}, goes

as

$$t'_{pd} \sim t_{pd} \left(\frac{d'_{fw}}{d_{fw}} \right)^2 \tag{4.41}$$

This influences the thermal stress scaling. The onset of surface melting or vaporization is largely independent of first wall thickness.

4.4.2 Electromagnetic Effects

The absolute severity of the electromagnetic effects of disruptions is quite unknown. However, there is sufficient knowledge to suggest that the fundamental material property which determines the relative impact among materials is electrical conductivity.

Eddy current heating is a minor contributor to the first wall temperature, but not to thermal stress. Although properties other than electrical conductivity determine the eddy current heating, the scaling is unimportant to material choice since the direct thermal flux scaling dominates first wall temperature rise.

Previous work on magnetic forces in both structural walls and liquid metals was examined. The only material property influencing the result was the electrical conductivity. The absolute magnitude of the problem is highly uncertain, especially for forces resulting from liquid metal breeders. The specifics of designs are seen to have a very strong influence on the problem, given the state-of-knowledge. Some magnetic force components show no scaling with conductivity; the maximum scaling was linear with conductivity.

The relative consequence index for magnetic stress for structures materials due to plasma disruptions is therefore defined to be given by

$$1 \leq RCI_{PD}^{ms} \leq \frac{\sigma_w}{\sigma_{316\ SS}} \tag{4.42}$$

The low end, material independent, reflects the fact that some stresses are independent of wall material (section 4.3.4). The high end is the upper bound on increasing magnetic stresses, with 316 SS being the best case (lowest electrical conductivity). The values for RCI_{PD}^{ms} for the reference structural materials is listed in Table 4.22.

The scaling of stresses due to the presence of breeders again seems to range between none and linear. In this regard it appears that $Li_{17}Pb_{83}$ is somewhat better than lithium since its electrical conductivity is 3.7 times lower. $LiAlO_2$ is essentially non-conductive, so no liquid metal breeder effects are possible; however, this means that the currents leaving the plasma that would have been transferred to the liquid breeder are now confined to the metal structure (unless arcing occurs), potentially worsening those effects. The present state of knowledge is insufficient to know how breeder choice influences the overall electromagnetic impact on the blanket.

REFERENCES

4.1 R.J. Onega, W.R. Becraft, C.A. Kukielka, "Thermal Consequences to the First Wall of a D-T Fueled Tokamak Due to a Major Plasma Disruption," Nuclear Science and Engineering, 75, (1980), pp. 243-257.

4.2 International Tokamak Reactor Zero Phase, 1979.

4.3 W.M. Stacey, Jr., et al, "U.S. Contribution to the International Tokamak Reactor Phase I Workshop," INTOR/81-1, 6/1981, Chapter VII.

4.4 C.C. Baker, Jr., et al, "STARFIRE," ANL/FPP-80-1, 9/1980.

4.5 C.K. Chan, "Safety Study of Primary Coolants in Fusion Power Reactor First Wall Design," Nuclear Engineering and Design, 51, (1979), pp. 253-262.

4.6 J.A. Dalessandro, "First Wall Thermal Stress Analysis for Suddenly Applied Heat Fluxes," Proceedings of the Third Topical Meeting on the Technology of Controlled Nuclear Fusion, CONF-780508, pp. 357-364.

4.7 A.P. Fraas and A.S Thompson, "ORNL Demonstration Study: Fluid Flow, Heat Transfer, and Stress Analysis Considerations in the Design of Blankets for Full Scale Fusion Reactors," ORNL/TM-5960, 2/1978.

4.8 M. Jakob, Heat Transfer, 1949, p. 258.

4.9 M. Tillack, personal communication, 1982.

4.10 J.S. Walker, W.M. Wells, "Stresses in Liquid Lithium Modules in a Tokamak Blanket Due to a Changing Poloidal Magnetic Field," ORNL/TM-6907, 9/1979.

4.11 "Tokamak Blanket Design Study: FY 78 Summary Report," ORNL/TM6547, 6/1979, and "Final Report," ORNL/TM-7049, (1980).

4.12 P.J. Gierszewski, et al, "Natural Circulation of Electrically Conducting Liquids in Fusion Reactor Blankets," submitted to Nuclear Engineering and Design.

CHAPTER 5. FLUID CHEMICAL AND PRESSURE HAZARDS

Several potential energy sources exist in the blanket in addition to nuclear heating and external inputs. Specifically, the stored potential energy in the form of chemical or mechanical (pressurized fluids) may result in reactor damage and/or radioactivity mobilization. As other researchers are presently advancing the experimental and analytical understanding of these problems [5.12, 5.16, 5.17], the present discussion is primarily limited to comparing existing results and their implications, rather than developing new analyses.

5.1 Problem Matrix

The first task is an examination of the overall problem. Several chemical reactions are possible. Many of these, however, fall under the category of corrosion—slow reactions between structural materials and either coolants or breeders. These are discussed in Chapter 7. Another group includes rapid structural oxidation—a prime method of radioactivity mobilization due to rapid reaction between structural materials and gases. These are discussed in Chapter 6. The concerns in this chapter are potentially rapid reactions liberating chemical or mechanical energy.

Historically, fusion researchers have been primarily concerned with reactions with lithium. Table 5.1 shows the possible reactive materials. While several combinations are not typically considered in fusion reactor design, they are included here for completeness.

Water and flibe are unlikely to be both present since both are

TABLE 5.1

Possible Combinations of Reactive Fluids*

	Li	$Li_{17}Pb_{83}$	$LiAlO_2$	Flibe
Air	✓	✓	✓	✓
H_2O	✓	✓	✓	—
Concrete	✓	✓	✓	✓
CO_2	✓	✓	✓	✓
Li	—	✓	—	✓

✓ indicates potential combination of fluids in fusion reactor.

*Solid $LiAlO_2$ is included with the liquid lithium compounds for completeness.

coolants. As discussed in Chapter 1, a $Li/LiAlO_2$ combination has no obvious motivation. Air may be present due to an accident that allows containment building atmosphere to enter the blanket or a blanket coolant or breeder spilling into the building. CO_2 has been proposed as an alternative building atmosphere [5.1]. Concrete reactions could be possible if a spill allowed contact between fluid and concrete floor. $LiAlO_2$, although not a fluid, is considered here for completeness since it is an alternative breeder.

Alternative substances, e.g. Li_2O, are also possible, but the problem was limited to the reference lithium compounds of this study, However, some comments on alternative substances are included where appropriate.

Even if there is no chemical reaction to drive an accident (resulting in elevated temperatures and/or pressures), a problem due to pressurized fluids exists. In addition to the reactions in Table 5.1, there is the potential for accidental pressurization of the blanket or building due to ejection of the pressurized coolants, water and helium. Finally, the possible building pressurization needs to be placed in perspective by examination of the possible pressurization due to the release of helium from superconducting coils.

5.2 Chemical Reactions

A variety of chemical reactions may be possible due to the various materials present. Many of these can be eliminated from consideration on the basis of thermodynamic calculations. For the remaining cases, further information is obtained from either previous experimental studies, static calculations, or dynamic calculations. The focus is on what

temperatures and pressures can realistically result from combustion.

5.2.1 Thermodynamics

Thermodynamics serves to eliminate many possible reactions. Endothermic reactions are not an important safety concern. Exothermic ones may be dependent on the dynamics involved. Values of ΔH (heat of reaction) and ΔG (free energy) are taken from References 5.2, 5.3, unless otherwise stated.

5.2.1 Lithium Reactions

Pure liquid lithium reacts exothermically with air (O_2, N_2), H_2O, CO_2, and constituents of concrete. Concrete is discussed separately. The heat of reaction and free energy change are shown in Table 5.2. Some other reaction products are possible, but these are the major ones (see References 5.4, 5.5, 5.6).

The N_2 reaction is unimportant above $\sim$1000°C since free energy considerations lead to dissociation of Li_3N [5.5]. Above $\sim$1100°C, Li_2CO_3 dissociates into $Li_2O + CO_2$. The water reaction is particularly worrisome because of the highly corrosive nature of LiOH and the flammability of H_2.

5.2.1.1 Li-Pb Reactions

The Li-Pb alloys have been proposed as alternatives to pure Li. The central thermodynamic question is how tightly bound the lithium is, i.e., what is the heat of reaction and free energy change for the reaction

TABLE 5.2

Major Lithium Reactions (kcal/g-mole-Li)*

	Free energy change, ΔG			Heat of reaction, ΔH		
	25°C	500°C	1000°C	25°C	500°C	1000°C
$Li + \frac{1}{6} N_2 \rightarrow \frac{1}{3} Li_3N$	-12.2	-6.07	+ 0.3	-15.7	-16.4	-15.1
$Li + \frac{1}{4} O_2 \rightarrow \frac{1}{2} Li_2O$	-66.9	-59.3	-51.1	-71.3	-72.2	-71.4
$Li + H_2O \rightarrow LiOH + \frac{1}{2} H_2$	-48.9	-38.8	-30.8	-48.3	-52.8	-49.0
$Li + \frac{3}{4} CO_2 \rightarrow \frac{1}{2} Li_2CO_3 + \frac{1}{4} C$	-64.7	-47.3	-30.8	-74.9	-76.1	-68.4

*Based on data in Ref. 5.2, 5.3.

$$aLi + bPb \rightarrow Li_aPb_b \tag{5.1}$$

Fortunately the activity of lithium has been measured [5.7] at some temperatures (see Figure 5.1). This allows estimation of partial $\Delta\overline{G}$, $\Delta\overline{H}$ for the reaction

$$Li + Li_mPb_n \rightarrow Li_{m+1}Pb_n \tag{5.2}$$

This is the incremental heat of reaction for lithium addition. The equations are

$$\Delta\overline{G}_{Li} = RT \ln a_{Li} \tag{5.3}$$

$$\Delta\overline{H}_{Li} = -RT \frac{d}{dt} \ln a_{Li} = -RT_1T_2\left(\frac{\ln a_2 - \ln a_1}{T_2 - T_1}\right) \tag{5.4}$$

where a_{Li} = activity of lithium

R = gas constant

The results are shown in Table 5.3. As one would expect, the severity of the reaction decreases to zero as the lithium content of Li_aPb_b increases.

There is one experiment [5.8] that allows a check on these estimated values and the estimated value of heat capacity. Two moles of LiPb (13.88 g Li, 414.4 g Pb) were prepared. Using the atomic percent interpolation (see Appendix B) for heat capacity, one obtains

$$c_p\ (LiPb) \sim 2190\ J/kg°C \tag{5.5}$$

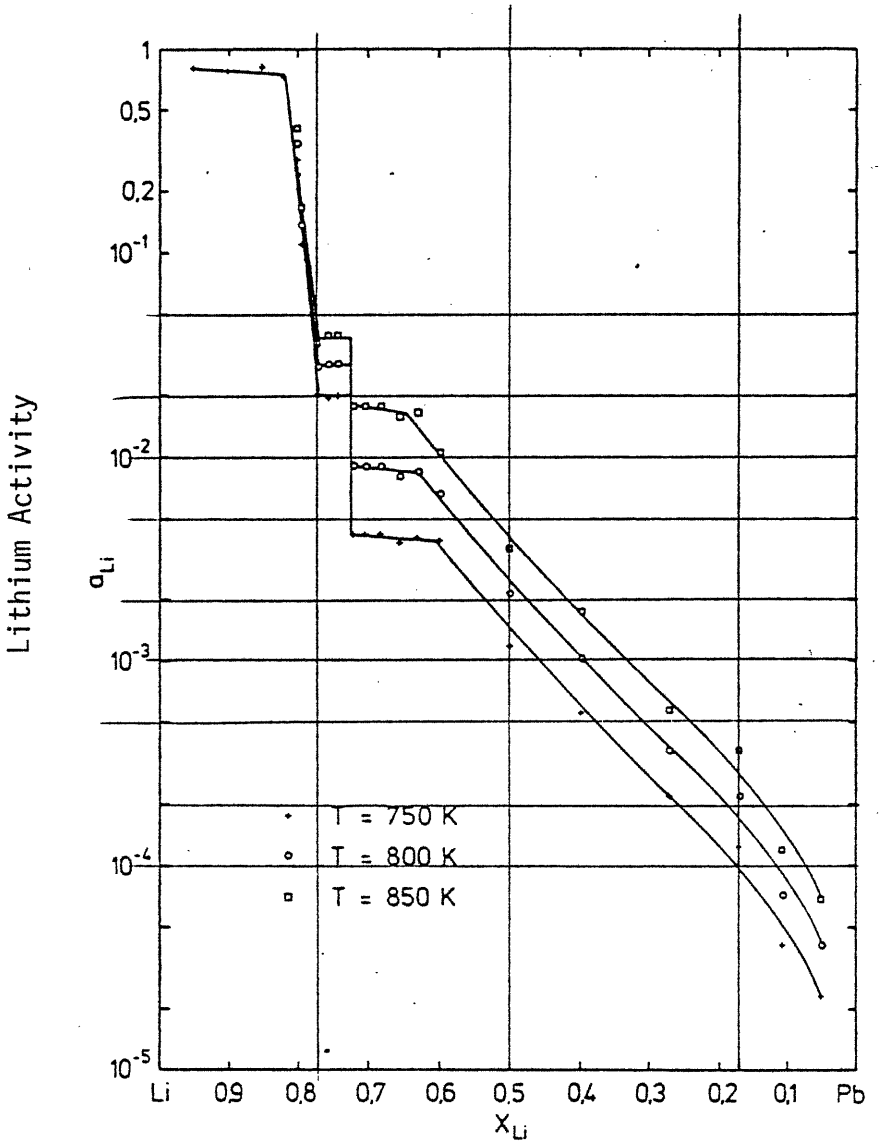

Fig. 5.1: The Activity of Lithium in the Li-Pb System as a Function of Atom Fraction of Lithium Ref. [5.7]

TABLE 5.3

Calculated Values for Heat of Reaction and Free Energy Change for Lithium Addition to Li-Pb alloy (~500°C)(k cal/g-mole-Li)*

Atomic Percent Li of Alloy	Alloy	Free Energy Change, ΔG	Heat of Reaction, ΔH
0.95	$Li_{19}Pb$	- 0.3	~ 0
0.78	Li_7Pb_2	- 5.7	~ 8.4
0.50	LiPb	- 9.5	~-12
0.17	$Li_{17}Pb_{83}$	-13.7	~-13
0.05	$LiPb_{19}$	-16.1	~-13

*From data in Reference 5.7

The partial heat of reaction is not really sufficient since we are concerned with the total reaction from 0% Li to 50% Li. However, an estimate would be to use a value of 13 kcal/g-mole-Li as this appears to be an average over the range of lithium composition. Then the expected temperature rise would be

$$\Delta T = \frac{(13 \text{ k cal/g-atom-Li})(4.1868 \times 10^3 \text{ J/k cal})(2 \text{ moles Li})}{(2190 \text{ J/kg°C})([13.88 + 414.4] \times 10^{-3} \text{ kg})} \quad (5.6)$$

$$= \sim 116°C$$

When the lithium and lead were added and heated above the melting point of Pb (327°C), there was an immediate exothermic reaction with a temperature rise of 193°C [5.8]. Given the uncertainty involved (estimated heat capacity and heat of reaction at one temperature), the agreement is satisfactory.

Thus the thermodynamic matrix can include $Li_{17}Pb_{83}$ as follows

$$\Delta H_{Li_{17}Pb_{83}} \sim \Delta H_{Li} - 13 \text{ k cal/g-mole-Li} \quad (5.7)$$

$$\Delta G_{Li_{17}Pb_{83}} \sim \Delta G_{Li} - 14 \text{ k cal/g-mole-Li} \quad (5.8)$$

Comparing these values with Table 5.2, one sees that based on thermodynamics alone, $Li_{17}Pb_{83}$ (indeed any Li-Pb alloy) would be expected to react exothermically with the substances of interest that Li reacts with. However, the $Li_{17}Pb_{83}$ reaction with N_2 is not favored from the free energy standpoint. As is discussed later, the dynamics of air-$Li_{17}Pb_{83}$ is likely to allow N_2 reaction due to the O_2 reaction. A mixture

of Li with $Li_{17}Pb_{83}$ is a potential problem.

5.2.1.3 $LiAlO_2$ Reactions

One advantage of solid lithium compound breeders is the lower chemical activity. $LiAlO_2$ does not react exothermically with O_2, N_2, H_2O, or CO_2. Concrete is discussed in the next section. It should be noted that the more reactive solid breeder, Li_2O, can react exothermically with H_2O and CO_2 (below $\sim$1100°C):

$$\frac{1}{2} Li_2O + \frac{1}{2} H_2O \rightarrow LiOH \qquad \Delta H_{500°C} = -10.0 \text{ k cal/g-mole-Li} \tag{5.9}$$

$$\frac{1}{2} Li_2O + \frac{1}{2} CO_2 \rightarrow \frac{1}{2} Li_2CO_3 \qquad \Delta H_{500°C} = -27.3 \text{ k cal/g-mole-Li} \tag{5.10}$$

Furthermore, the endothermic reaction

$$LiAlO_2 + \frac{1}{2} CO_2 \rightarrow \frac{1}{2} Al_2O_3 + \frac{1}{2} Li_2CO_3 \tag{5.11}$$

has a favorable ΔG, so that economic damage (degradation of breeder material) upon exposure to CO_2 at elevated temperatures could occur. However, this would not be a safety concern.

5.2.1.4 Flibe reactions

Thermodynamic considerations easily show that the lithium in flibe (Li_2BeF_4) is tightly bound and normal Li-type reactions are impossible. However, flourine-exchange may occur. Flibe is basically a mixture of LiF with BeF_2 which are somewhat loosely bound ($\Delta H < 2$ k cal/mole of F). Some reactions of interest are included in Table 5.4. All of these are

TABLE 5.4

Possible FLIBE Reactions

$$\frac{1}{2}\,O_2 + \frac{1}{2}\,BeF_2 \rightarrow \frac{1}{2}\,OF_2 + \frac{1}{2}\,BeO$$

$$\frac{1}{4}\,O_2 + \frac{1}{2}\,BeF_2 \rightarrow \frac{1}{2}\,F_2 + \frac{1}{2}\,BeO$$

$$\frac{1}{2}\,O_2 + LiF \rightarrow \frac{1}{2}\,OF_2 + \frac{1}{2}\,Li_2O$$

$$\frac{1}{4}\,O_2 + LiF \rightarrow \frac{1}{2}\,F_2 + \frac{1}{2}\,Li_2O$$

$$\frac{1}{2}\,H_2O + \frac{1}{2}\,BeF_2 \rightarrow HF + \frac{1}{2}\,BeO$$

$$\frac{1}{2}\,H_2O + LiF \rightarrow HF + \frac{1}{2}\,Li_2O$$

$$\frac{1}{2}\,CO_2 + \frac{1}{2}\,BeF_2 \rightarrow \frac{1}{2}\,COF_2 + \frac{1}{2}\,BeO$$

$$\frac{1}{4}\,CO_2 + \frac{1}{2}\,BeF_2 \rightarrow \frac{1}{4}\,CF_4 + \frac{1}{2}\,BeO$$

$$\frac{1}{2}\,CO_2 + LiF \rightarrow \frac{1}{2}\,COF_2 + \frac{1}{2}\,Li_2O$$

$$\frac{1}{4}\,CO_2 + LiF \rightarrow \frac{1}{4}\,CF_4 + \frac{1}{2}\,Li_2O$$

endothermic. Hence there is no safety problem with H_2O, O_2, N_2, or CO_2. This is not surprising from the viewpoint of the periodic table. Regions of relative electro-negativity indicate which oxides might react with $LiF\text{-}BeF_2$. A UCLA study [5.9] examined various oxides (concrete constituents). The situation is summarized in Figure 5.2.

There is a potential problem with flibe reactions with liquid metals. Li, Na, and K will all displace Be. Thus mixture of a flibe primary coolant with a Li breeder or Li, Na, or K secondary coolant allows an exothermic reaction.

5.2.1.5 Concrete Reactions

From the thermodynamic viewpoint, concrete is a mixture of various oxides—a mixture, however, that varies considerably. Table 5.5 shows some compositions along with the magnetite concrete used in lithium-concrete tests [5.10]. Thermodynamically, one expects Li to react with most of these, while the stable $LiAlO_2$ appears inert. The UCLA study [5.9] examined reactivity with flibe and found that oxides of Si, Fe, Ti and H were inert with flibe, oxides of Mg, Ca, Al reacted with BeF_2 but not LiF, and the oxides of Na and K reacted exothermically with both. Thus most of concrete (especially the typical magnetite concrete) is unreactive with flibe.

Thus from the thermodynamic viewpoint, one expects $LiAlO_2$ to be inert, flibe a low problem, and Li and $Li_{17}Pb_{83}$ a potentially serious problem with concrete. Based partly on experiment, a value of ΔH of -150 kcal/mole-Li [5.5] for the Li plus concrete reaction is included for completeness.

Possible Reactions with LiF

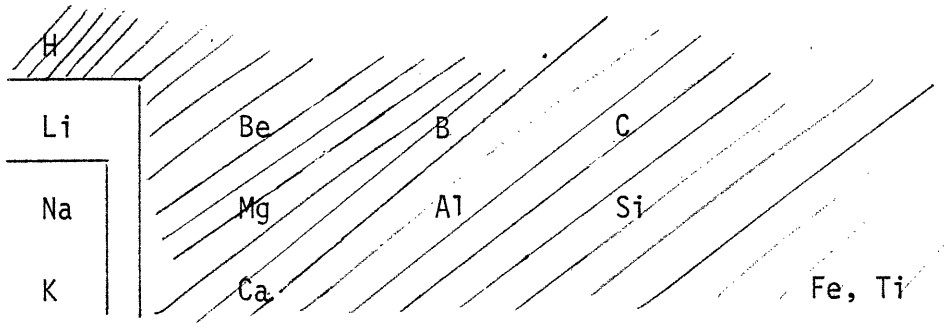

Possible Reactions with BeF_2

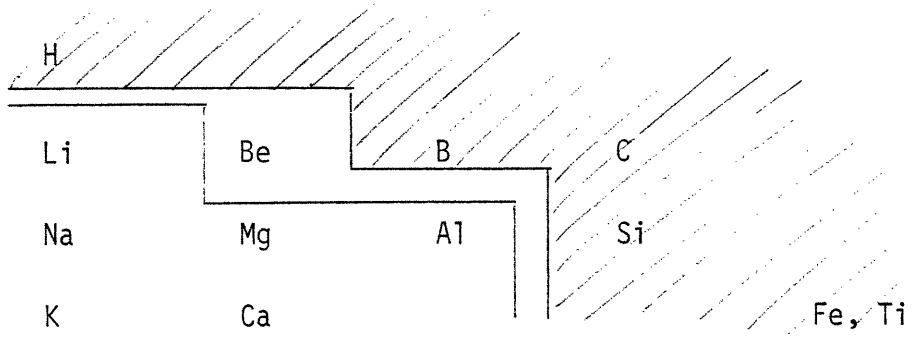

//// - unreactive

Fig. 5.2: Regions of the Periodic Table whose Oxides May React Exothermically with Flibe Constituents, Based on Calculations in this Study and Ref. [5.9]

TABLE 5.5

Concrete Constituents (Weight Percent)* of Some Different Concretes

	Magnetite Concrete	Portland Cement	High Alumina
CaO	8.6	64.1	37.7
Al_2O_3	1.4	5.5	38.5
Fe_2O_3	39.9	3.0	12.7
FeO	23.9	—	3.9
SiO_2	5.9	22	5.3
SO_3/SO_4	0.70	2.1	0.1
S	0.05	—	—
TiO_2	10.1	—	—
Na_2O	0.14	—	—
K_2O	0.07	—	—
CO_2	3.39	—	—
MgO	1.6	1.4	0.1

*Excluding water.

5.2.1.6 Thermodynamic Matrix

Thermodynamic considerations allow screening of possible combustion hazards. The results are shown in Table 5.6.

5.2.2 Experimental Results and Other Literature Review

Having narrowed the potential problem reactions, further examination can be made by examination of the literature.

5.2.2.1 Flibe/Concrete

No experiments with flibe were found. One study [5.9] did analytically examine the concrete-flibe reaction. A very conservative upper limit on temperatures and pressures was obtained by assuming a pathological case where only the exothermic reactions with concrete constituents are allowed while the endothermic reactions of flibe with the majority of concrete constituents were assumed to be kinetically limited. Even then, the maximum temperatures ($\sim$1200°C) and over-pressures (0.1 MPa) [5.11] are fairly modest. The maximum temperature and pressure could not occur simultaneously. Since each maximum value was obtained for a different scenario [5.11], given the very conservative nature of the analysis, the flibe-concrete reaction seems relatively unimportant.

5.2.2.2 Liquid Metal/Concrete

Both concrete oxide constituents and entrained water in the concrete react with lithium. In one test [5.10], a sample of lithium ignited five hours after contact. The lithium initially reacted with water and evolved hydrogen which allowed temperatures to rise to allow reaction with the other concrete constituents. Lithium-concrete reactions appear quite serious.

TABLE 5.6

Thermodynamic Results:
Heat of Reaction at 500°C (k cal/g-mole-Li)*

	Li	$Li_{17}Pb_{83}$	$LiAlO_2$	FLIBE
O_2	- 72.2	- 59	—	—
N_2	- 16.4	- 3	—	—
H_2O	- 52.8	- 40	—	—
CO_2	- 76.1	- 63	—	—
Concrete**	-150	-137	?(∼ 0)	?(low)
Li	- 13	—	—	-25

*Blanks indicate absence of exothermic reaction.

**Uncertain, value dependent on type of concrete.

In a recent test [5.12], small pieces of basalt concrete were added to a $Li_{17}Pb_{83}$ pool already at 500°C. Some of the water in the concrete reacted with the alloy to form a thin crust (LiOH with 9% Li, 66% Pb, 400 ppm Ca) and hydrogen gas (1/2 mole H_2 per H_2O reacted). The absence of significant amounts of other products indicates that the only reaction was [5.12].

$$Li + H_2O \rightarrow LiOH + \frac{1}{2} H_2 \uparrow \qquad (5.12)$$

Unlike the lithium/concrete case, there was only a mild reaction with no significant temperature rise. The main concern would appear to be control of evolved hydrogen gas.

5.2.2.3 Lithium Compounds/Water

In scoping tests [5.13], $LiAlO_2$ was found not to react with water as expected. Li_2O did react. In the same test series, $Li_{17}Pb_{83}$ reacted modestly with water while lithium reacted violently (see Table 5.7). Kinetics apparently limit the $Li_{17}Pb_{83}$/water reaction, although more experiments are needed. The lithium/water reaction is so explosive that it is highly unlikely and unwise that lithium and water would be allowed to come into contact in the reactor. In practice, this means that water should not be present in a reactor design which includes lithium. Further experiments are planned to better define the $Li_{17}Pb_{83}$/water reaction. It should be noted that even if a solid breeder (e.g., $LiAlO_2$) is unreactive with water, it is typically hundreds of degrees hotter than a water coolant. In STARFIRE [5.1], water is at an average temperature of 300°C, while the $LiAlO_2$ ranges between 500 and 850°C.

TABLE 5.7

Water Reactions—Experimental Results

Unreactive:

$LiAlO_2$, Li_2SiO_2, Li_2ZrO_3

Reactive [5.13]:

(initial temperature = 600°C)

Compound	$g_{H_2O} / g_{breeder}$	Peak Temperature	Time to Peak
Li	3.0/20	900	10 s
Li_7Pb_2	2.8/40	770	20 s
$Li_{17}Pb_{83}$	3.0/50	630	60 s
Li_2O	3.0/50	625	50 s
Unreactive	3.0/50	600	—

Descriptions [5.14, 5.13]:

Li, Li_7Pb_2* vigorous, much heat evolved.

Li_2O, $Li_{17}Pb_{83}$ slow, mild.

*ANL test used solid sample of Li_7Pb_2 which was fairly unreactive. HEDL test used a fine powder of Li_7Pb_2 which reacted vigorously. Blanket design studies have utilized solid breeders in a fine powder, small grain size, form.

Thus, a large amount of thermal energy exists to heat up and increase pressure if water enters the breeder zone. Pressure problems are addressed in section 5.3.

5.2.2.4 Lithium/Gases

Lithium-air reactons have been experimentally studied. A variety of lithium loop experiments for corrosion studies have experienced lithium spills resulting in fires. For example, one loop spill had a fire with about 1000°C temperatures [5.15].

A series of lithium tests with air, N_2 and CO_2 have been performed at HEDL [5.10, 5.12, 5.16]. As discussed in section 5.2.4, a computer code has been developed at MIT [5.4-5.6] which appears to reasonably predict the experimental result. Peak temperatures of about 1100°C for the flame and 950°C for the lithium pool have been obtained for lithium-air tests. Judging from the lower temperatures and pressures obtained in Pure N_2, the less exothermic nitrogen reaction (see Table 5.2) tends to surpress the oxygen reaction in air relative to pure oxygen.

Pure CO_2 is more reactive than air with lithium. 540°C lithium was exposed to CO_2 [5.12]. The lithium pool boiled (1347°C) after 2.3 minutes and temperatures surpassed 1400°C (where thermocouples became inaccurate). Most (82%) of the residue was Li_2O with some Li_2C_2 detected and 90% of the aerosol being Li_2CO_3. CO_2 is not an inert gas with respect to lithium.

5.2.2.5 $Li_{17}Pb_{83}$/Gases

There is some data on LiPb reactions with air. At over 500°C in open air,

> "the material melted and smoked vigorously until all of the lithium had escaped as Li_2O and Li_3N and only molten lead was left. Unlike Mg or Li + Mg, however, LiPb would not flame or ignite even when exposed to the flame of a gas-air torch," [5.8].

Since $Li_{17}Pb_{83}$ has less lithium than LiPb, it would be expected to be less reactive. Thus $Li_{17}Pb_{83}$ appears far less reactive with air than does lithium, although experiments are needed to quantify the difference.

5.2.3 Static Calculations

For three of the combinations (flibe-concrete, flibe-Li, $Li_{17}Pb_{83}$-Li) there is thermodynamic evidence of a potential problem, but no experimental data and insufficient understanding for a detailed dynamic calculation. Some simple static calculations can be performed to further examine these cases.

The flibe-concrete case was studied by an UCLA group [5.9] as discussed in section 5.2.2. The actual kinetics would have to be very unfortunate, favoring all the exothermic reactions while hindering the majority of reactions which are endothermic, for a serious problem to exist. Their static calculation found a maximum temperature of ~1200°C if only reactions of Na_2O, CaO, MgO with BeF_2 were allowed. Maximum

over-pressures were always <100kPa [5.11]. This calculation is highly conservative (tending to overpredict temperature rises and pressures) due to the adiabatic, static nature coupled with pathologically worst case kinetics. Further, even this value represents only a ~300°C temperature rise of the flibe from its typical operating temperature in the current reference flibe/TZM blanket. For all these reasons, flibe-concrete reaction is not deemed very serious. However, if interest renews in flibe (or other molten salts), simple scoping tests would be warranted.

The flibe-Li reaction may be more of a problem. The reaction

$$Li + 1/2(Li_2BeF_4) \rightarrow 1/2Be + 2LiF \qquad (5.13)$$

has a substantial heat of reaction, Q = 25 kcal/g-mole-Li reacted. A maximum temperature rise can be estimated very conservatively by assuming the heat of reaction is only absorbed by reaction products. This results in a maximum temperature rise of <800°C. In reality the accident kinetics would likely keep temperature rises far lower. Grimes [5.18] has also concluded that the mixture would be troublesome but not a serious safety concern.

As lithium mixed with LiF - BeF_2 the salt composition would shift to pure LiF. The salt melting temperature would rise gradually from 459°C to 848°C. If the initial temperature were low, freezing of the mixture would be self-limiting. In the present base case, temperature would be sufficiently high that LiF would not freeze (although Be might

precipitate out). However, the mixing of low pressure flibe and lithium would not be very rapid. Further, the high thermal conductivity of lithium and high convection of the salts would serve to effectively dissipate the heat of reaction.

The flibe-lithium reaction may be a minimal safety concern, but appears unlikely to be highly serious.

The lithium-$Li_{17}Pb_{83}$ reaction is another potential concern, although at present no reactor design calls for both to be present in the same blanket. As in the flibe-Li case, the reaction product has an increasing melting temperature. Thus, if the resulting temperatures are too low, the product will freeze when the lithium content becomes high enough - self-limiting the reaction.

The maximum temperature rise due to reaction can be conservatively estimated, as in the flibe-Li case, by assuming that the heat of reaction is restricted to heating the reaction product. Unlike the flibe-Li case, the maximum temperature is a function of how far the reaction proceeds. The reaction can be written

$$(\frac{a}{a+b})Li + (\frac{b}{a+b})Li_{0.17}Pb_{0.83} \rightarrow Li(\frac{a+0.17b}{a+b})Pb(\frac{a+0.83b}{a+b}) \quad (5.14)$$

so that the exact product is a function of the varying amounts of reactants. Furthermore the incremental heat of reaction drops as the lithium content increases (Table 5.3). For products less than 50 % Li, the heat of reaction appears fairly constant. The resulting maximum temperature rise

is given by

$$\Delta T \sim 1860 \frac{(1+b/a)}{(1+0.2\ b/a)(1+25\ b/a)} \quad \text{for } b/a > 1.50 \qquad (5.15)$$

when one takes account of the changing composition. As the amount of lithium to $Li_{17}Pb_{83}$ increases (b/a decreases past 1.50) the heat of reaction begins to decrease to zero and the freezing temperature rises. Even given a maximum temperature rise (no heat leaves reaction product) and an initial $Li_{17}Pb_{83}$ temperature of 500°C, the reaction product would freeze when the composition reached Li_7Pb_2 ($b/a \sim 0.50$). The temperature rise in such a case is below 200°C. A more realistic treatment would not be expected to find the reaction proceeding as far (higher values of b/a, lower temperature rises). For example, if equal volumes react, the product is $Li_{0.64}Pb_{36}$ and the highest possible temperature rise is ~140°C.

Due to the relatively low maximum possible temperatures, the Li-$Li_{17}Pb_{84}$ reaction does not appear a major concern.

5.2.4 Dynamic Calculations

Given the previous discussion, the potential chemical reactions can be rank-ordered (Table 5.8). The most important modeling needs concern Li and $Li_{17}Pb_{83}$. However, even if other reactions (e.g., Li + flibe) are not safety problems, they may have the potential for serious blanket damage (e.g., large amounts of frozen reaction product formed).

TABLE 5.8

Rank-Ordering of Potential Combustion Hazards

	Li	$Li_{17}Pb_{83}$	$LiAlO_2$	flibe
Air	4	3	1	1
H_2O	5	3	1	1
Concrete	4	3	1	2
CO_2	4	3	1	1
Li	1	2	1	2

5 - Known very serious problem, not allowable in design

4 - Known serious problem

3 - Uncertain, significant evidence that a serious problem exists

2 - Uncertain, evidence that only a minimal safety problem exists

1 - No safety problem

The LITFIRE code has been developed at MIT to model lithium compound combustion [5.4-5.6, 5.17] (Table 5.9). The most important and verified option of the code is lithium-air [5.4,5.5]. Lithium pool temperatures appear generally limited to 1200°C [5.4, 5.5], consistent with experiments. If a lithium spill occurred in the building not in the torus, it would be difficult for much heat to be transferred to the blanket. Hence, a spill in the building is mainly a concern in terms of breaching containment (a serious safety concern itself.) Maximum over-pressures for large spills in a STARFIRE size building are of the order of 220kPa [5.4]. If the spilled lithium contacted the concrete floor (presumably protected by a metal liner), the lithium-concrete reaction could be more serious.

On the other hand, if a lithium spill occurred in the torus, the potential exists for raising temperatures of the first wall. While maximum lithium temperatures are insufficient to cause melting, such a fire might provide a mechanism for wall temperatures to rise sufficiently for rapid air-wall metal oxidation to occur (see Chapter 6). However, this requires a second failure, entry of an oxidant into the torus. Preliminary use of a new feature of LITFIRE indicates that maximum temperatures are lower for a torus spill due to insufficient gas transport between the torus chamber and the building (through a $0.5m^2$ area duct with corresponds to a typical RF heating or vacuum pump duct size) [5.17]. It does appear that lithium temperatures are adequate to reach the rapid wall oxidation temperatures of V-alloy and TZM (700°C) but not HT-9 (1300°C). The present version of LITFIRE can not model the heat transfer of a fire in the torus sufficiently to determine if the rapid oxidation

TABLE 5.9

Capabilities of the LITFIRE Code

Allowable Reactions

Lithium - Air (O_2, N_2, inert)

Lithium - Water

Lithium - Concrete

$Li_{17}Pb_{83}$ - Air (O_2, N_2, inert) [Planned]

$Li_{17}Pb_{83}$ - Water

Other Li compounds - Water

temperature of 316SS (1000°C) can be caused by a lithium fire in the torus. Expansion of the air combustion model to $Li_{17}Pb_{83}$ is planned [5.17].

A simple water-lithium compound option exists [5.6]. At present, the fundamental assumption is that the supply of water controls the reaction rate: all water entering the reaction zone is assumed to react immediately. The reaction zone is taken as an expanding sphere in a breeder cavity which is penetrated by water-filled coolant tubes. The current code has a fixed geometry and fixed arrangement of coolant tubes based on the NUWMAK [5.19] design. Pressure considerations are not included, thus explosive reactions like water-lithium may not be adequately modeled. The user must supply the material properties of the lithium compound and the reaction residue (Pb in the case of $Li_{17}Pb_{83}$). This code predicts maximum temperatures of about 1100°C for water/lithium, 900°C for water/$Li_{17}Pb_{83}$, and 750°C for water/Li_2O from an initial temperature of 400°C ($LiAlO_2$ is inert).

5.3 Pressurization

Pressures generated from fluids can cause two different safety problems, 1) overpressure of the containment building with potential for containment failure, and 2) increased pressure stresses in the blanket with potential for blanket damage. As discussed above, these pressures can result from either combustion or escape of pressurized coolants.

5.3.1 Chemical Combustion Results

Unfortunately, experimental data and analytical modeling is insufficient to determine resulting pressurization. The worst cases appear to be lithium/air and liquid metal/concrete. In the former case, overpressures may reach 220kPa for a 22,000 kg spill in a STARFIRE size building [5.4]. The concrete or water cases are pressure concerns due mainly to the production of hydrogen gas.

5.3.2 Pressurized Coolants

If a low pressure fluid like Li, $Li_{17}Pb_{83}$, or flibe were to leak, there is no direct pressure hazard except those already discussed under combustion. Thus, for liquid metals or molten salts, lack of combustion implies lack of pressure problems. Helium and water are more complex cases.

5.3.2.1 Helium

A helium coolant is typically at high pressures (5.52 MPa for the present reference case) to obtain adequate heat transfer. Helium purge streams through solid breeders are typically near atmospheric pressure and thus do not represent overpressure problems.

As discussed in Chapter 2, there are two design approaches to dealing with the helium coolant pressure. First, one can contain the pressurized helium in discrete tubes, and not allow pressurization of the breeder zone. Second, one can design the blanket module to be fully pressurized such that helium leakage into and pressurizing of the breeder zone does not lead to failure (e.g., Westinghouse/ORNL [5.20] design).

These are shown schematically in Figure 5.3.

The former design approach allows more conventional geometries and larger module sizes. The latter design leads to a larger number of small modules (because of the need to withstand full pressure). From the safety viewpoint, the trade-off may be the higher reliability of fewer, more conventional modules versus modules that can withstand pressurization from a helium leak to the breeder zone.

Thus, the pressure hazard in a blanket from helium is strongly dependent on design. In the former case a substantial leak to the breeder zone would likely result in module rupture at some point. Neither the module nor the tritium system connected to it would be capable of surviving pressurization near helium coolant conditions. In the latter case, little or no damage would occur, provided that the attached tritium system lines were protected against the higher pressure or designed to withstand it.

Therefore, unless one pays the design penalty for the module and connected systems to withstand $\sim$5 MPa pressure, a helium coolant leak into the blanket can be expected to cause damage.

A leak into the building is a different matter due to the large volume for expansion. The over pressure has been calculated for the present reference case: STARFIRE size building ($2.5 \times 10^5 m^3$), one-half of total coolant released (see Appendix C). For a rapid depressurization, heat transfer to or from the helium and building atmosphere can be neglected to obtain a conservative estimate of the maximum temperature and pressure. Hence the depressurization is modeled as a constant

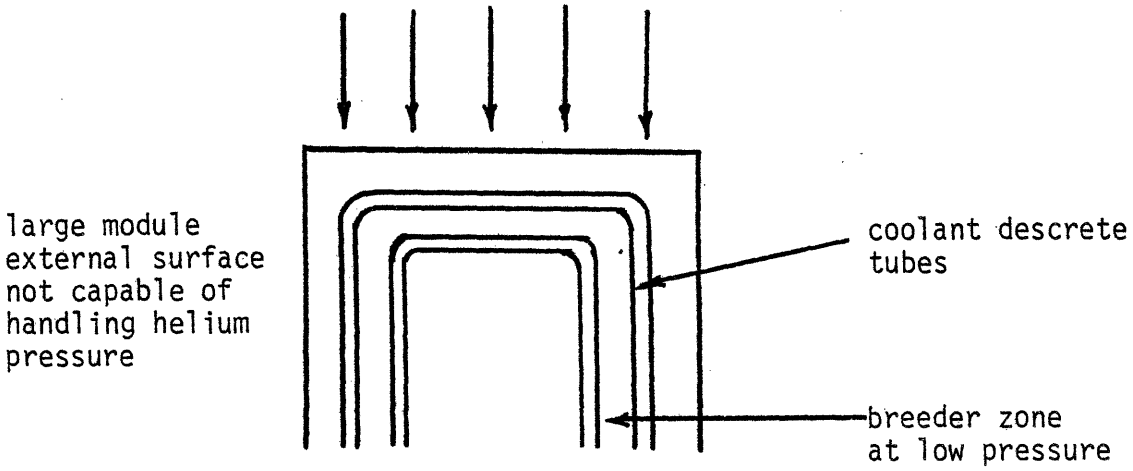

Non-pressurized Module Design Approach (a)

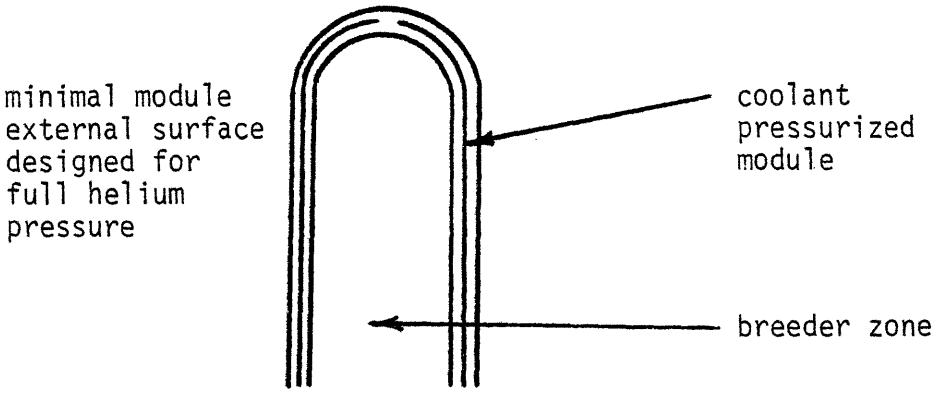

Pressurized Module Design Approach (b)

Fig. 5.3: Comparison of Alternative Blanket Concepts in their Ability to Withstand Pressurization of the Breeder Zone

internal energy process.

Treating air and helium as ideal gases the maximum overpressure following depressurization is ∿5kPa with a temperature of 270°C. Use of CO_2 (or any other near ideal gas) for the building atmosphere does not significatnly affect this result. The approximate scaling of overpressure is linear with the mass of helium released and inversely linear with building volume:

$$\Delta P = 5 \text{ kPa}\left(\frac{m}{m_o}\right)\left(\frac{V_o}{V}\right) \tag{5.16}$$

where $m_o = 1.2 \times 10^3 \text{kg}_{He}$

$V_o = 2.5 \times 10^5 \text{m}^3$

The maximum temperature is only weakly dependent on these variables:

$$T(°K) = 293\left[\frac{(V/V_o) + 0.042(m/m_o)}{(V/V_o) + 0.0174(m/m_o)}\right] \tag{5.17}$$

These pressures and temperatures are less than fission values due to the large volume of the STARFIRE building. For the reference case, the potential temperatures and pressures generated in the building are quite modest.

5.3.2.2 Pressurized Water

A pressurized water coolant runs at pressures 3 times that of helium (15.5 MPa for the reference case). Whereas helium was on the

border between designs that could or could not withstand leak-induced pressurization, a pressurized water loop design appears to lie in the "could not" regime. Attempting to increase pressures in the Westinghouse/ ORNL [5.20] design by 3 would reduce the maximum module radius to impractically small values (<5 cm). Existing fusion design studies do not include attempts at blanket designs where the bulk module could withstand pressurization to near 15 MPa.

For a STARFIRE-type module, any substantial leak of water to the breeder zone ($\sim$0.1 MPa design) would likely result in module and/or tritium purge stream damage and rupture. The higher the breeder zone temperature (500-850° $LiAlO_2$ versus 300° water), the greater the potential for higher generated pressures. Furthermore, the high velocity water/steam jet could represent a significant kinetic energy problem resulting in localized higher stresses.

Building overpressure is also a problem. The precise assumption of the final thermodynamic state has little ($\lesssim$2%) impact on calculated maximum temperatures and pressures [5.21]. For example, assuming liquid phase separation versus a homogeneous mixture has only a <1% effect [5.21]. The maximum building overpressure and temperature have been calculated using a constant internal energy model (that of Ref. [5.22]). This assumes no heat transfer in the initial depressurization to allow estimation of the most severe conditions.

For the reference case (STARFIRE building, one-half of the total coolant inventory) the predicted overpressure is 80 kPa with a temperature

of 85°C. This agrees with the value given in the STARFIRE study of 70-100 kPa [5.1]. Again, these values are lower than typical fission designs due to the large building volume.

Due to the two phase nature of water, the scaling is not so simple as for helium, However, air, behaves as an ideal gas and use of CO_2 or another near-ideal gas would have little affect. The two-phase behavior leads to less than linear scaling since a change in mass or volume can be partially compensated by change in steam quality.

By varying the parameter $(\frac{m}{m})(\frac{V_o}{V})$ over a range of 0.05 to 10.0 the maximum overpressure is found to be given by

$$\Delta P \sim 80\left(\frac{mV_o}{Vm_o}\right)^{+0.85} \text{ kPa} \pm 5\% \tag{5.18}$$

The variance increases toward the ends of the range as Galli and Lord found for their fission reactor case [5.22].

The resulting temperature is approximately given by

$$T(°C) \sim 85°\left(\frac{m}{V}\frac{V_o}{m_o}\right)^{+0.30} \tag{5.19}$$

The agreement is 5% in the range $0.20 < (\frac{m}{V})\left(\frac{V_o}{m_o}\right) \lesssim 4$.

It should be emphasized that these scaling laws are specific to the basic case considered. Galli and Lord found slightly different scaling for a different regime. For their case, they found (there was no discussion of mass scaling).

$$\Delta P \sim \left(\frac{V_o}{V}\right)^{0.68} \tag{5.20}$$

$$T \sim \left(\frac{V_o}{V}\right)^{0.21} \tag{5.21}$$

5.3.3 Superconducting Magnets

The main importance of maximum building pressures lies in the chance of containment being lost and, hence, the survival requirement for building design. If some other design-basis accident can result in higher building pressures, the relevance of a lower result from blanket fluids is minimal. The most likely source of building pressure other than the blanket cases described above is the leakage of helium used to cool the superconducting magnets. To determine the relevance of blanket results, some examination of magnet helium release effects is useful.

An energy balance on the fluids can be written

$$m_{He}\,\Delta u_{He} + m_{air}\,\Delta u_{air} = E \tag{5.22}$$

m_{He}, m_{air} = mass of helium, air

Δu_{He}, ΔH_{air} = change in internal energy

E = added energy from magnet coil stored energy.

Unlike the coolant depressurization, some energy is likely to be added to the fluids. The accident envisioned involves the release of helium from the coil structures due to either 1) a direct leak or

2) rupture due to magnet quench. In either case, a large amount of stored field energy may couple to the heating of magnet helium.

There are two major uncertainties. The number of coils losing helium is unknown, as is the amount of stored energy transfered to the helium/air mixture. For a one coil accident, $m_{He} = 2.4 \times 10^3$ kg, $E_{max} = 4.17 \times 10^9$ J (reference values), one obtains

$$T(°C) = 10°C + E_1 / 2.2 \times 10^8 \quad (5.23)$$

$$\Delta P(kPa) = 2 + E_1 / 6.2 \times 10^8 \quad (5.24)$$

where E_1 = actual amount of energy transfered from one coil. For all twelve coils, $m_{He} = 28.8 \times 10^3$ kg, $E_{max} = 5.0 \times 10^{10}$ J, and one obtains

$$T(°C) = -67 + E_{12} / 3.05 \times 10^8 \quad (5.25)$$

$$\Delta P(kPa) = 19 + E_{12} / 5.2 \times 10^8 \quad (5.26)$$

where E_{12} = actual amount of energy transfered from all twelve coils. As seen in Table 5.10, there is a considerable range in possible results. The UCLA study [5.9] considered $E = 1/3\ E_{max}$ a realistic case. In reality, the mechanics of various helium/magnet accidents is poorly defined in terms of understanding the consequences. The STARFIRE magnet protection scheme is to dump all coil energy into external resistors. If such a scheme effectively minimizes heat input to the containment, the possible consequences to the building are seen to be slight, even if all the helium were vented. However, if a significant amount of

TABLE 5.10

Possible Building Atmosphere Temperatures and Overpressures Resulting from Release of Cryogenic Helium from Superconducting Coils.

	Helium from 1 Coil (m/m_o=1)		Helium from all 12 Coils (m/m_o=12)	
	Overpressure kPa	Temperature °C	Overpressure kPa	Temperature °C
No energy transferred from coil	2	10	19	-67
One-third of stored magnetic energy of affected coils transferred	4.2	16.5	51	-12
Two-thirds of stored magnetic energy of affected coils transferred	6.5	23	83	42
All Stored energy of affected coils transferred	8.7	29	115	97

stored energy were coupled to the helium, the table shows that considerable pressures could result. For all cases, the overpressure scales approximately as

$$\Delta P \sim V^{-1} \tag{5.27}$$

as in the helium coolant case

The table does show that magnet accidents could well dominate the building overpressure design criteria, especially for non-water coolant cases. For water-cooled designs, however, only very severe magnet accidents, involving multiple coils, could exceed the 80 kPa overpressure for a LOCA. Future understanding of magnet helium release consequence is needed.

5.4 Summary

Although significant data and analytical tools exist concerning combustion and pressurization leaks, it is not yet possible to quantify the consequences. Significant programs are on-going at HEDL (experimental) and MIT (analytical) which will greatly clarify the problems.

It is possible to rank the possible cases. One direct concern is maximum temperatures. The relative subjective consequence index for temperatures from combustion ($RSCI^{T}_{TP}$) is listed in Table 5.11. The water/lithium case is so violent as to preclude the use of water and lithium simultaneously in a reactor blanket. The other most worrisome problems are water/$Li_{17}Pb_{83}$ and air and concrete with lithium and $Li_{17}Pb_{83}$. $Li_{17}Pb_{83}$ appears far less reactive than lithium, although the difference

TABLE 5.11

Relative Subjective Consequence Index for Maximum Temperatures from Combustion ($RSCI^{T}_{TP}$)

Coolant	Breeder	Coolant/Breeder Reaction	With Breeder: Air Reaction	With Breeder: Concrete Reaction
Water	Lithium	5	4	4
Helium	Lithium	1		
Lithium	Lithium	1		
Flibe	Lithium	2		
Water	$Li_{17}Pb_{83}$	3	3	3
Helium	$Li_{17}Pb_{83}$	1		
Lithium	$Li_{17}Pb_{83}$	2		
$Li_{17}Pb_{83}$	$Li_{17}Pb_{83}$	1		
Water	$LiAlO_2$	1	1	1
Helium	$LiAlO_2$	1		

1 - No safety problem

2 - Uncertain, evidence that only a minimal safety problem exists

3 - Uncertain, evidence that a serious problem exists

4 - Known serious problem

5 - Known very serious problem, probably not allowable in design.

is not yet quantifiable.

The relative subjective consequence index due to pressurization for either combustion or leakage of pressurized fluids ($RSCI^{P}_{TP}$) is listed in Table 5.12. The results are similar to maximum temperatures, although pressurized water and helium are concerns even without combustion taking place.

Understanding is not yet adequate to determine the influence of structural materials on these hazards. One potential difference among materials is whether the maximum temperatures are adequate to cause rapid gas-structural wall oxidation (other mchanisms do exist to reach these temperatures). The relative impact of this oxidation is discussed in Chapter 6.

TABLE 5.12

Relative Subjective Consequence Index due to Pressurization from Combustion or Leakage of Pressurized Coolants ($RSCI^{P}_{TP}$)

		Coolant/Breeder Reaction	Air Reaction	Concrete Reaction
Water*	Lithium	5	4	4
Helium*	Lithium	1		
Lithium	Lithium	1		
Flibe	Lithium	1		
Water*	$Li_{17}Pb_{83}$	3	3	3
Helium*	$Li_{17}Pb_{83}$	1		
Lithium	$Li_{17}Pb_{83}$	1		
$Li_{17}Pb_{83}$	$Li_{17}Pb_{83}$	1		
Water*	$LiAlO_2$	1	1	1
Helium*	$LiAlO_2$	1		

	Leakage
Water	4
Helium	3
Magnet Helium	4

1 - No safety Problem
2 - Uncertain, evicence that only a mininal safety problem exists
3 - Uncertain, evidence that only serious problem exists
4 - Known serious problem
5 - Known very serious problem probably not allowable in design.

*Not including pressurization due to the pressurization of water and helium.

REFERENCES

5.1 C. C. Baker, Jr., et al., "STARFIRE—a Commercial Tokamak Fusion Power Plant Study," ANL/FPP-80-1, 9/1980.

5.2 O. Kubaschewski and C. B. Alcock, Metallurgical Thermo-Chemistry, 1979.

5.3 JANAF Thermochemical Tables, 1965-68.

5.4 D. A. Dube and M. S. Kazimi, "Analysis of Design Strategies for Mitigating the Consequences of Lithium Fire Within Containment of Controlled Thermonuclear Reactors," MITNE-219, 7/1978.

5.5 M. S. Tillack and M. S. Kazimi, "Development and Verification of the LITFIRE Code for Predicting the Effects of Lithium Spills in Fusion Reactor Containments," PFC/RR-80-11, 7/1980.

5.6 P. J. Krane, "Safety Aspects of Thermonuclear Reactor Designs Employing Use of Lithium-Lead Alloys," M.S. thesis, Department of Nuclear Engineering, Massachusetts Institute of Technology, 1980.

5.7 H. R. Ihle, et al., "The Activity of Lithium, and the Solubility of Deuterium in Lithium-Lead Alloys," Fusion Technology, Proceedings of the Eleventh Symposium on Fusion Technology, Euratom, (EUR-7035-EN), 1980, p. 639.

5.8 W. A. Frigerio and L. L. Lavoy, "The Preparation and Properties of LiPb: A Novel Material for Shields and Collinators," Nuclear Technology, (10), 3/1971, p. 322.

5.9 "Some Safety Considerations for Conceptual Tokamak Fusion Power Reactors," EPRI-ER-546, 7/1978.

5.10 P. W. Jeppson, "Interactions of Liquid Lithium with Various Atmospheres, Concretes, and Insulating Materials; and Filtration of Lithium Aerosols," HEDL-TME-79-7, 6/1979.

5.11 L. A. Casey and A. Z. Ullman, "Comparative Safety Aspects of Candidata Breeding Materials for Fusion Reactors," Second Conference on the Technology of Controlled Nuclear Fusion, CONF-760935, 1976.

5.12 D. W. Jeppson, February Monthly Progress Report to J. G. Crocker (EGG), 2/1982.

5.13 D. W. Jeppson and R. F. Keough, "Fusion Reactor Blanket and Coolant Material Compatibility," Proceedings of the Second Topical Meeting on Fusion Reactor Materials, 1981.

5.14 P. A. Finn, et al., "The Reactions of Li-Pb Alloys with Water," presented at the 1980 Annual Meeting of the American Nuclear Society, June, 1980.

5.15 M. Soenen and J. DeKeyser, "Experimental Facilities at SCK/CEN for Lithium Technology," First Topical Meeting on Fusion Reactor Materials, 1979.

5.16 Personal Communication to M. S. Kazimi (MIT) from D. W. Jeppson (HEDL), 2/1982.

5.17 V. J. Gilberti, M.S. thesis, Nuclear Engineering Department, Massachusetts Institute of Technology, (in progress).

5.18 W. R. Grimes and S. Cantor, "Molten Salts as Blanket Fluids in Controlled Fusion Reactors," Chemistry of Fusion Technology, 1972.

5.19 B. Badger, et al., "NUWMAK—A Tokamak Reactor Design Study," UWFDM-330, 3/1979.

5.20 J. S. Karbowski, et al., "Tokamak Blanket Design Study, Final Report," ORNL/TM-7049, 1980.

5.21 M. Mesarovic and B. Gaberšček, "Pressure-Temperature Transients for Containment Design of Water-Cooled Reactors," Nuclear Engineering and Design, 17 (1971), pp. 428-438.

5.22 R. B. Galli and B. G. Lord, "Calculation of Maximum Equilibrium Pressurized Water Reactor Following Rupture of the Primary Coolant Circuit," Nuclear Engineering and Design, 4 (1966), pp. 331-338.

CHAPTER 6. RAPID STRUCTURAL OXIDATION

As mentioned in Chapter 1, there are three possible methods of mobilizing structural radioactivity: melting, rapid structural oxidation with volatilization, and long term corrosion. Chapters 3, 4, and 5 involve potential temperature rises, which also defines the potential for damage. Chapter 7 concerns corrosion problems. Here, the questions of rapid mobilization of structural radioactivity and reactor damage from oxidation are addressed.

6.1 Problem Identification

Of the seven comparison bases for determining the materials impact on accident consequences, three pertain to chemical hazards. The pure fluid cases (Chapter 5) offer the potential for causing temperature and pressure rises. The structural material response was not included. The long-term corrosion problem (Chapter 7) serves as a mechanism for radioactivity mobilization prior to an accident, as well as being an accident initiator (e.g., coolant tube plugging). This chapter is concerned with the potential for rapid oxidation of structural material (gas-metal reactions).

6.1.1 Potential Hazards

A fusion reactor has an unfortunate design aspect in terms of oxidation. At the center of the device, where the metal temperatures, stresses, and specific radioactivity are highest, a vacuum exists. If an oxidant is allowed to enter the plasma chamber, the potential exists for rapid structural oxidation. In contrast, fission reactors have no vacuum volume; during an accident, the pressure gradient forces

any building atmosphere away from the core (of course the coolant itself may react with the metal). Thus the basic problem is contact of an oxidant with structural metal, presumably the first wall.

There are two safety concerns. First, the oxidation may cause severe reactor damage and loss of structural integrity if sufficient first wall material oxidizes. Second, the oxidation may produce volatile chemical species which would serve as a direct means of mobilizing structural radioactivity. Besides these, there is a worrisome economic concern. Even if structural integrity is maintained, the oxidation may be sufficient to affect the vacuum/plasma impurity properties of the first wall, leading to severe economic losses.

The base accident scenario would be: 1) loss of vacuum boundary integrity due to failure of some penetration (vacuum pump duct, auxiliary heating duct, etc.), 2) building atmosphere streaming into torus, and 3) high metal surface temperature (e.g., afterheat or chemical fire). Thus a model is needed that predicts the reaction rate as a function of wall temperature. This is established for materials of interest in sections 6.2 and 6.3.

6.1.2 Ignition Theory—Source for Uncertainty

If temperatures and oxidant concentrations are high enough, there is the potential for ignition, self-sustaining reaction. Then, even if the initiating event which caused the high temperature were to stop, the gas-metal reaction could continue unabated, consuming the first wall. Unfortunately for the safety analyst, the onset of ignition is highly dependent on the environment, including metal size and thermal loss mechanisms [6.1, 6.2]. Thus, it is virtually impossible to predict whether the first wall would

ignite without conducting experiments representing the geometry involved. The large heat capacity of the blanket behind the first wall would serve to prevent ignition by damping the temperature increase of the first wall.

Laurendeau [6.1] examined the potential for ignition of bulk pieces of metal in oxygen. He defines a variety of relevant temperatures:

- T_{fl} - Final temperature, maximum temperature possible for a given reaction.
- T_{ign} - Ignition temperature
- T_{crit} - Critical temperature, allows spontaneous heating to ignition.
- T_{trans} - Transition temperature, transition between protective oxide scales (parabolic reaction rate) and unprotective scales (linear reaction rate).
- T_{oxid} - Oxidation temperature, temperature above which oxidation is thermodynamically allowed.

Ignition is seen as a balance between chemical energy input ($\dot{q}_{chem}$) versus all heat loss mechanisms ($\dot{q}_{loss}$). The relationships are shown in Fig. 6.1. The specific geometry involved helps to determine the actual heat loss.

The transition and ignition temperatures are most easily measured for a given experiment, whereas the critical temperature is of most concern to the safety analyst. If the temperature exceeds T_{crit}, the metal will simply continue to burn, dependent on the supply of oxygen.

Laurendreau notes that metals divide into those controlled by the critical temperature and those limited by the transition temperature. In the former case, the transition temperature is below the critical temperature for a clean surface. Most metals are critical temperature controlled. In the latter case, the transition temperature is higher

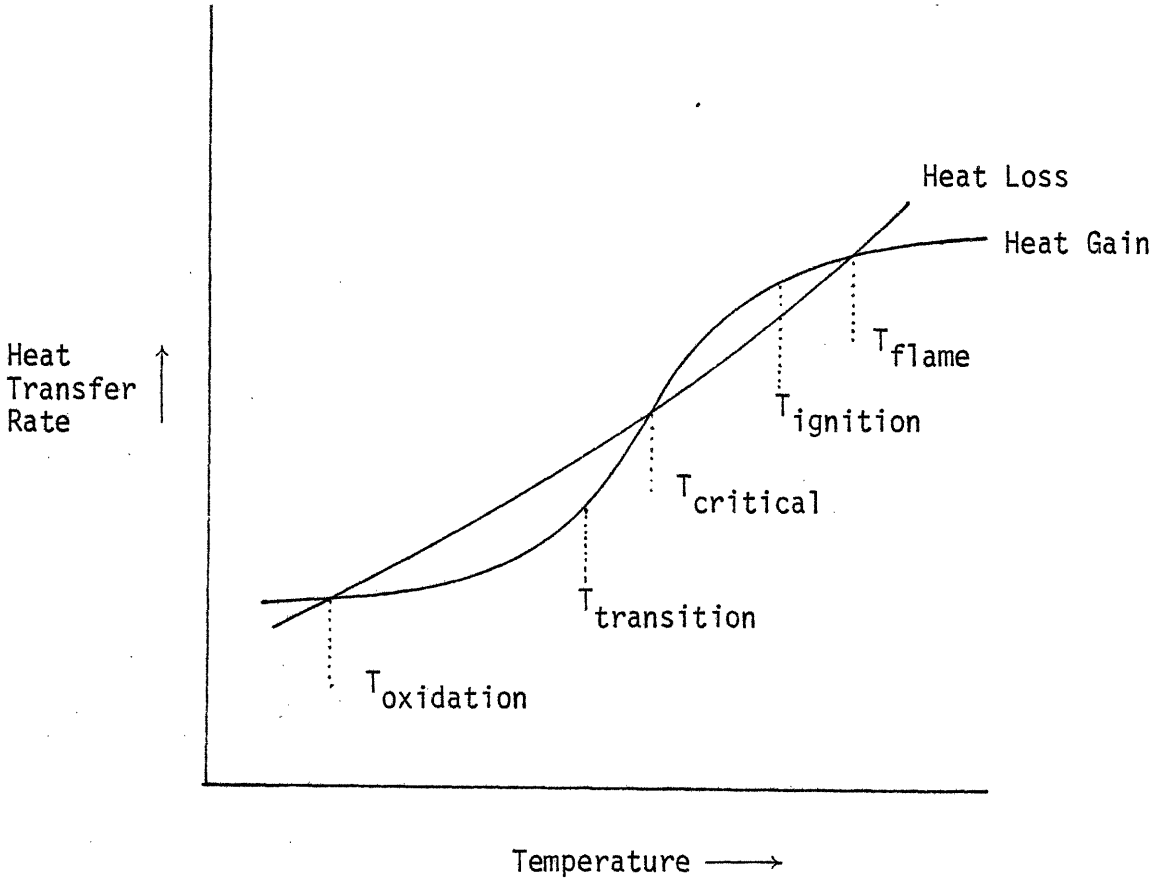

Fig. 6.1: Balance between Heat Loss and Chemical Energy Gain in Determining Metal Ignition Temperatures [6.1]

than the ideal critical temperature for a clean surface. These metals cannot self-heat to ignition unless the protective oxide scale is lost, resulting from temperatures above the transition point. For these cases, the effective critical temperature lies just above the transition temperature.

Furthermore, the critical and ignition temperatures exhibit sample size effects. The transition temperature does not, thus it is the only true reference temperature for assessing ignition danger. Only if temperatures reach the transition point is there the theoretical possibility for ignition. For most cases, even higher temperatures would be required (depending on geometry, etc.).

For surface burning (rather than vapor phase combustion) metals, the ignition temperature is within 100 °C of the metal oxide melting point. These cases include Pb, Fe, and Mo [6.1]. Some temperatures of interest for some metals are shown in Table 6.1.

Ignition may occur in non-oxygen atmospheres. Rhein [6.3, 6.4] studied the ignition of various metal powders in N_2 and CO_2. His results for some metals of interest are listed in Table 6.2. He placed very fine powders in flowing gases. The temperature was increased until the thermocouple output jumped, indicating ignition. Comparing his results with those of Laurendreau indicates the strong sample size dependence. Since the first wall will not be in a fine powder form, Rhein's results are not useful for predictive purposes. They do, however, demonstrate the potential for ignition of various metals in various gases.

TABLE 6.1

Temperatures of Interest for Bulk Metal Ignition for Selected Metals [Ref. 6.1] (°C)

Metal	Metal Oxide	Metal Oxide Melting Point	Transition Temperature	Ignition Temperature
Fe	FeO	1420	>1200	1315
Pb	PbO	897	550	850
Mo	MoO_3	795	700	780
Ti	TiO_2	1855	850	1410
Zr	ZrO_2	2677	$\geq$1300	$\sim$1800

TABLE 6.2

Ignition Temperatures of Metal Powders in Nitrogen, Carbon Dioxide, and Air [Ref. 6.3, 6.4]*

Metal	Particle Size	Ignition Temperatures °C		
		N_2	CO_2	Air
Li	<100μ	388,410	330	353,393
Be	<0.1μ	504,527	25	25
Al	<0.1μ	no ignition below 1080	360,420; 655	466,410; 585
Ti	1-5μ	830	670	602,648
Zr	3μ	490,525	363,366	193,197; 240
Cr	-325 mesh	no ignition below 1170	870	—
Mn	-325 mesh	no ignition below 1316	696	—

*Since these results are for fine powders, they are not predictive of first wall ignition; however, they do demonstrate that metals can ignite in various reactive gases

6.1.3 Materials of Interest

Potential reactive gases in the building which may enter the torus are air (O_2, N_2) and CO_2 (for example, see the STARFIRE design, [6.5]). In addition, if water is the coolant, a LOCA could result in steam being present. If a lithium fire were occurring, various lithium species (e.g., Li_2O) could also be present. Largely due to lack of data for other gases, the base gas studied was air. Where possible, comments on the effect of other gases (CO_2, water, Li-species) are included.

The four reference metals for the overall study, 316 SS, HT-9, V-alloy, and TZM (Mo), are included. To indicate how widespread the problem of structural oxidation is, some comments concerning two potential first wall coatings, beryllium and graphite, are also included.

6.1.4 Approach

Unfortunately, unlike the fluid combustion problem (Chapter 5), a thermodynamic screening of the various gas-metal reactant combinations is not useful. Likewise, simple static calculations are meaningless. For the gases and metals of interest, kinetics, not static thermodynamics, determines the severity of the reaction.

The prime focus will be on the determination of the oxidation rate of each metal as a function of temperature. Where oxide volatility is significant, the rate of loss of volatile oxides is determined. The former is a measure of the potential for reactor damage while the latter is a measure of the potential for radioactivity mobilization. For each there is typically a transition temperature, above which the problem is significant. This is referred to as the lowest trouble temperature, T_{lt}.

The reference structural materials fall into two different categories—refractory metals (Mo, V) and steel (316 SS, HT-9). The underlying mechanisms are somewhat different. The behavior of the first wall coatings, beryllium and graphite, is similar to the refractory metals and is included in Section 6.2.

6.2 Refractory Metals

The refractory metals (groups VB, VIB) react readily with oxygen at high temperatures. As discussed in Chapter 7, the oxidation potentials of water or helium impurities are generally thought sufficient to preclude use of these coolants with refractory metal structures. An accident might allow contact between these metals and reactive gases, principally air. This section examines in detail the theory and experimental data for these metals in order to predict oxidation and volatilization rates (results summarized in Section 6.5).

6.2.1 Mechanism

An overview of the mechanism is given to induce the subject. As discussed in Section 6.3, the oxidation behavior of steels is largely dependent on the behavior and concentration of alloy constituents, especially Cr and Mo. This is not true of the present alloys of refractory metals.

For the conditions of interest, protective solid oxide scales do not form on vanadium and molybdenum. Gulbransen and Jansson [6.6] note that for Mo (P_{O_2} = 0.01 atm), above 700°C, oxidation is limited by a surface chemical process and above 875°C, is limited by gaseous diffusion. For vanadium, the melting of the surface oxide, V_2O_5, at 670°C, indicates that either liquid phase diffusion or surface processes will dominate.

The cause of rapid oxidation in these metals is tied to either the

volatility of oxides present or the presence of a liquid phase [6.6 - 6.9]. The most important cases are the presence of MoO_3 (m.p. 795°C) and V_2O_5 (m.p. 670°C) [6.7] which can lead to disastrous effects on alloys which contain Mo or V. Research on alloying additions has had little effect on raising the melting point. For additions of less than 30% of BeO, MgO, CaO, NiO, MnO, Al_2O_3, Cr_2O_3, and Fe_2O_3 to V_2O_5, the melting point of the base oxide remains below 800°C and generally below 700°C [6.8]. In molybdenum experiments in flowing air at 908°C, reductions of a factor of 100 in the oxidation rate were possible only with additions of 9% Ca, 15% Ni, or 25% Cr [6.8].

The alloys of molybdenum and vanadium presently being considered do not contain enough of these additions for the oxide melting point to be affected. The reference Mo alloy is TZM (99.4% Mo, 0.5 Ti, 0.1 Zr). The reference V alloys are V-15Cr-5Ti and V-20Ti. Since the behavior of the critical oxide of the base metal does not appear affected, it is conservatively assumed that the rapid structural oxidation behavior of the alloys is the same as the base metal. Of course, this does not affect the fact that alloying additions presently considered may have substantial benefit in reducing long-term oxidation (corrosion) at lower temperatures. The possible beneficial effect of other additions on rapid oxidation would be useful to study in the alloy development program. Silicon additions are mentioned by Mrowec and Werber [6.10] as being especially beneficial to high-temperature oxidation.

6.2.1.1 Chemical Species

The first step is the identification of which oxides may be present. Based on references [6.6] and [6.9] and data for vanadium discussed in

Section 6.2.3, the primary condensed surface and volatile oxide species can be identified for conditions of interest (see Table 6.3). Subsurface oxides have not been found to play a significant role for these pressure and temperature regimes, probably due to the dominating mechanisms of surface reactions or gaseous diffusion [6.7, 6.8]. Unfortunately, Mo (group VIB—Cr, Mo, W) and V (group VB—V, Nb, Ta) are the worst cases for oxidation in their respective groups of refractory metals. Chromium is of interest because of its inclusion in steels. Besides a possible structural role, carbon and beryllium may be used as coatings on the first wall.

6.2.1.2 Oxidation below Catastrophic Temperatures

Although not of direct interest to the current task, some mention should be made of V and Mo oxidation behavior at lower temperatures, since the vacuum properties of the first wall could be degraded even if the oxidation rate were too slow to be a safety problem. Protective scales can develop and diffusion takes place by inward oxygen anion diffusion [6.6 - 6.9, 6.11].

Oxidation of Mo and W follows parabolic rate laws (Wagner type diffusion mechanism) until about 475°C for Mo ($P_{O_2} = 0.10$) and 875°C for W ($P_{O_2} = 0.05$) where oxide volatility begins to be important [6.9] and the oxidation becomes paralinear [6.11]. This mixed regime (solid state diffusion and volatility) continues until volatility becomes dominant. This surface reaction limited regime has high oxidation rates [6.9]. Molybdenum oxidation is discussed in Section 6.2.2.

The group VB metals have very poorly understood behavior at lower temperatures. Behavior following rate laws of logarithmic, parabolic, and paralinear has been seen [6.6, 6.11]. Many transitions exist due to break-

TABLE 6.3

Major Oxide Species for Reactions at 500 °C < T < Metal Melting Point and $P_{O_2} > 10^{-4}$ atm

Element		Condensed Oxide		Volatile Oxide
Formula	M.P. °C	Formula	M.P. °C	Formula
C	>3650	CO	-207	CO, CO_2
Cr	1900	Cr_2O_3	2280	Cr, CrO_3
Mo	2617	MoO_3	795	$(MoO_3)_3$
W	3377	WO_3	1472	$(WO_3)_3$
V	1917	V_2O_5	670	VO_2
Nb	2468	Nb_2O_5	1512	NbO_2
Ta	2997	Ta_2O_5	1877	TaO_2
Be	1284	BeO	2580	BeO

away behavior and the non-protective nature of the oxide layer. Surface reactions like oxygen adsorption may be limiting for some cases. Although the data are sparse, this regime appears to extend to the oxide melting point without volatility becoming important in contrast to Mo and W. Vanadium oxidation is discussed in Section 6.2.3. For either V or Mo, oxidation is pressure independent for solid state diffusion regimes, as one would expect for n-type conductors [6.10].

6.2.1.3 Low Pressure Oxidation

Again, although not directly relevant to oxidation at atmospheric level oxygen partial pressures, a few words are needed about oxygen pressures below 10^{-4} atm. Here, different oxide species dominate on the surface (e.g., MoO_2 and VO_2), hence the oxide volatility (for Mo) and oxide melting (VO_2 melts at 1545°C) criteria do not lead to rapid oxidation at as low temperatures. Therefore, lower pressures reduce oxidation by direct reduction in the oxidant and by raising the transition temperatures.

One study examined the oxidation of refractory metals for temperatures from 1100 - 1800°C and pressures 10^{-5} - 10^{-7} atm [6.12]. Oxidation is generally linearly dependent on P_{O_2} in this region, and processes like oxygen adsorption appear important. Due perhaps to the far higher oxygen solubility and diffusion for group VB versus VIB, the group VB metals show higher rates of oxidation upon exposure to air, pure O_2, and water vapor at these pressures, yet there was only about an order of magnitude difference among them. For $T \lesssim 2000$°C and $P_{air} \sim 10^{-6}$, the rates were low, about 6×10^{16} atoms reacted/cm^2-sec. For $T \lesssim 1400$°C, the rates decreased by about a factor of 20 to about 3×10^{15} reactions/cm^2-sec. None of the samples showed any weight loss, confirming the

non-existence of important volatility effects.

6.2.2 Molybdenum Oxidation

There are three transitions of interest for rapid oxidation. At some low pressure, oxide volatility first becomes noticeable. This is also evidenced by an oxygen pressure dependence and a transition to a paralinear rate law. Experiments indicate that this occurs for Cr, Mo, and W [6.6] at about $P_{\text{volatile oxide}} \stackrel{\sim}{=} 10^{-8}(P_{\text{total}})$. Gradually as the temperature rises, volatility becomes more important. Second, when the volatile species pressure becomes $10^{-2}(P_{O_2})$, the oxide volatility becomes the rate controlling step in the oxidation. Here, oxidation is quite rapid. Third, the oxide leaving the surface begins to hamper oxygen reaching the surface. The transition to this gaseous boundary diffusion regime is dependent on partial pressures, gas flow rates, and specimen size [6.6, 6.7, 6.8]. These processes will now be discussed in more detail.

Thermochemistry has very successfully predicted the onset of volatility effects [6.6, 6.9]. At P_{O_2} = 0.10 atm, the volatility of Cr, Mo, and W oxides has been found to become significant at $P_{\text{species}} \sim 10^{-9}$ atm. Figure 6.2 shows log $P_{(MoO_3)_3}$ versus temperature. For $P_{O_2} \gtrsim 10^{-4}$ atm, the equilibrium surface reaction is expected to be [6.9]:

$$MoO_3\ (s,\ell) \rightarrow \tfrac{1}{3}\ (MoO_3)_3\ (g) \qquad (6.1)$$

Unlike the case for chromium, the reaction rate is independent of P_{O_2}. For oxidation in air, volatility should be noticeable at $P_{(MoO_3)_3} \sim 10^{-8}$ atm which comes at T $\sim$ 500 °C. This compares with experimental observations of 475 °C for P_{O_2} = 0.10 atm [6.9] and 525 °C for air [6.13].

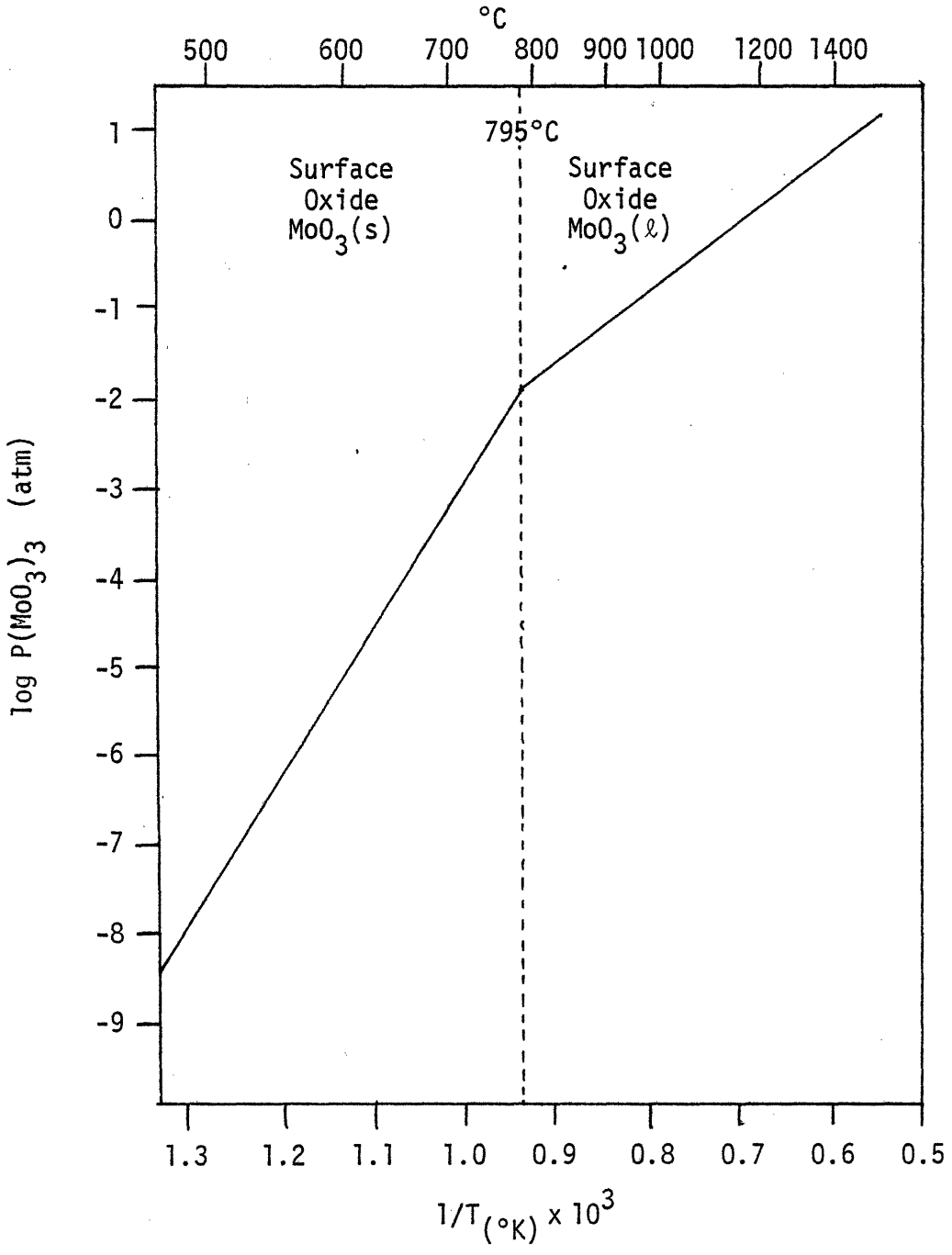

Fig. 6.2: Partial Pressure of $(MoO_3)_3$ in Air over Molybdenum as a Function of Temperature

As this temperature is, in any case, below that of typical TZM operating temperatures (∿900 °C), one can assume that oxide volatility will be of interest in any TZM fusion accident.

This first regime of oxide volatility importance is poorly understood [6.8, 6.13]. The P_{O_2} dependence is erratic, varying from none to linear, indicating a non-protective scale. The regime yields to a completely volatility-dominated region at $P_{(MoO_3)_3} \simeq 10^{-3}$ for $P_{O_2} = P_{total} = 0.10$ atm [6.9]. Unfortunately, the experimental evidence in these regimes is limited. Jones et al. [6.13] have shown that a transition occurs at 659 °C by comparing volatization of Mo with that of pure MoO_3. A decrease in the observed activation energy from ∿88 kcal/mole to ∿52 kcal/mole was noted. They postulated that this is due to a change in MoO_3 crystal structure. Gulbransen reports that volatility becomes completely dominant at 700 - 725°C [6.9] and net weight losses occur. Since the transition temperature must be below the MoO_3 melting point of 795°C and typical operating temperatures are higher, the first mechanism is unimportant to the present case. Thus the precise transition temperature is unimportant.

Therefore, the high operating temperature means that only the latter two mechanisms are of interest, some surface chemical reaction dominating volatility and gaseous diffusion. The surface mechanism is now discussed.

Ideally, experiments would be done in Ar-O_2 mixtures, varying P_{O_2} and P_{total}, keeping one constant at a time as in the case for Cr [6.16]. Unfortunately these experiments appear not to have been done. Experiments with Mo for temperatures above the 700 °C transition point have only been carried out with air or pure oxygen atmospheres (generally $P_{O_2} = 0.10$ atm). The results of three of these are shown in Fig. 6.3.

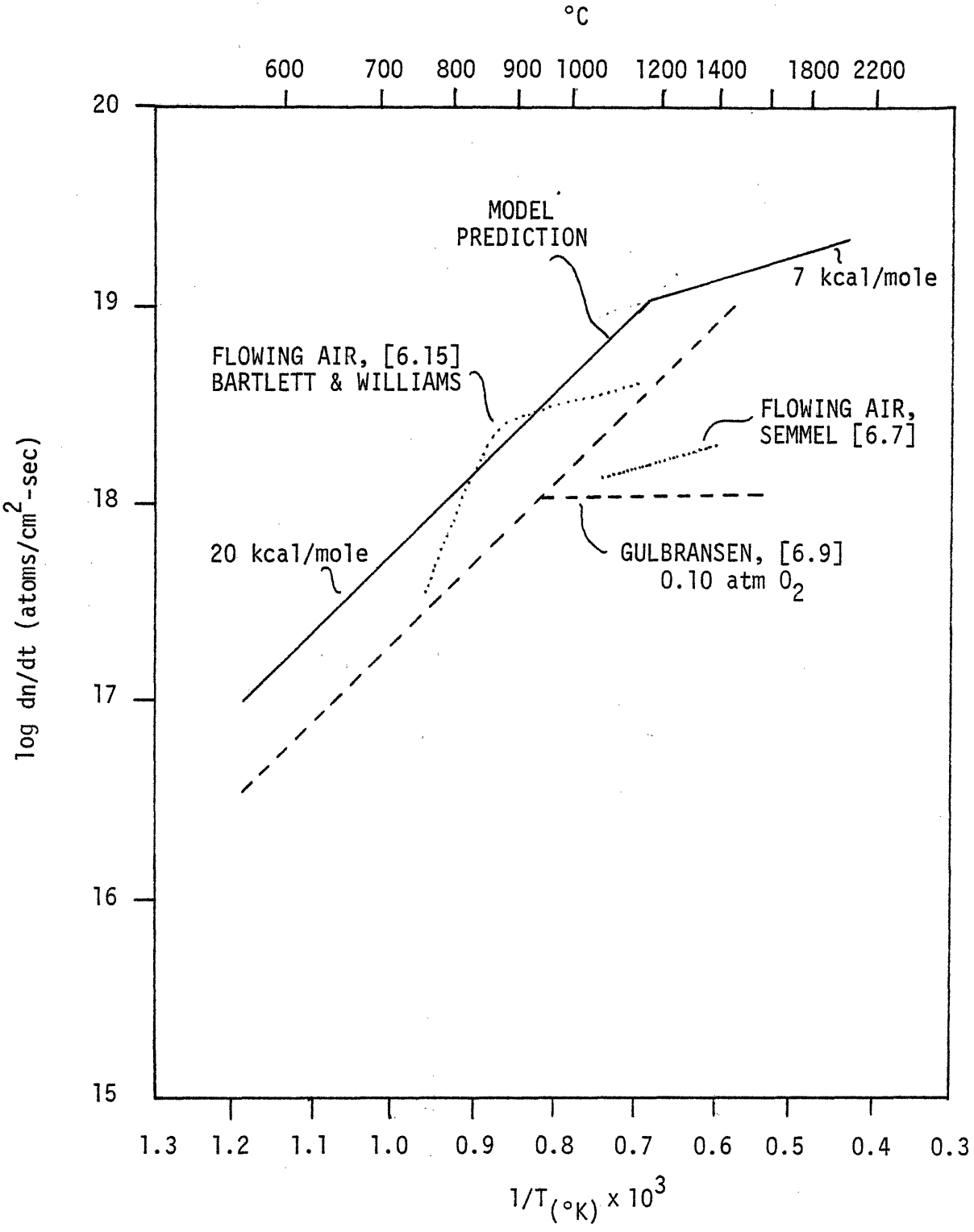

Fig. 6.3: Comparison of Experimental Results and Analytical Model for the Oxidation Rate of Molybdenum in Air

Gulbransen [6.9] ran experiments at P_{O_2} = 0.10 atm with sample sizes ranging from 0.12 - 1.215 cm^2 (flow conditions not stated). Below the transition to gaseous diffusion (surface reaction regime), the sample size had no effect. The points fell well on an Arrhenius plot with an activation energy of 19.7 kcal/mole. Each sample showed an abrupt transition to the gaseous diffusion regime, in which oxidation rates were nearly temperature independent. Increasing sample size decreased the temperature (and hence the volatilization rate) required for transition [6.9]. Presumably this results from decreased effectiveness of vapor species removal. Decreased gas flow rates also decreases the transition point temperature [6.7]. Bartlett and Williams [6.15] did not use the same flow conditions at the various temperatures. The points plotted in Fig. 6.3 are for the largest sample size (for Gulbransen) and had flow rates from 12.7 - 20.3 cm/second (Bartlett and Williams).

The pressure dependence in the surface reaction regime is quite uncertain, but is certainly below $P_{O_2}^{3/2}$ as seen in the surface reaction:

$$Mo + 3/2\ O_2 \rightarrow MO_3\ (s,\ell) \tag{6.2}$$

At lower pressures, Gulbransen found a linear P_{O_2} dependence at 800 °C; Kofstad [6.7] speculates that this could be due to a reaction of the type:

$$Mo(s) + O_2(\text{physically absorbed}) + O(\text{chemically absorbed}) \rightarrow MoO_3(s,\ell) \tag{6.3}$$

To conservatively scale the P_{O_2} = 0.10 atm results to atmospheric (P_{total} = 1 atm, P_{O_2} = 0.21 atm), a $P_{O_2}^{3/2}$ scaling was assumed. Thus,

Gulbransen's results have been corrected to atmospheric conditions (of interest in an accident) and are plotted in Fig. 6.3 with an activation energy of 20 kcal/mole (solid line). This reaction rate appears generally conservative in predicting atmospheric results as the line is above most of the experimental points.

The second problem is predicting where the transition to the third regime (gaseous diffusion) occurs. There are insufficient data to attempt a detailed treatment of the problem as there have been in the cases of low pressure volatilization [6.14] and chromium [6.16], because of lack of oxidation rate data as a function of temperature, pressure, and flow rate. Also, the gas flow rate in an accident condition is unknown. Finally, the volatile species partial pressure is sufficiently high as to invalidate the assumption in the chromium model (see Ref. [6.16]) that the oxygen pressure at the surface is the same as the bulk pressure. (For chromium, $P_{CrO_3} \sim 10^{-4} \times P_{O_2}$ while for molybdenum, $P_{MoO_3} \sim 10^{-1} \times P_{O_2}$).

A conservative prediction could be obtained by assuming that gaseous diffusion never becomes limiting, but information is sufficient to conservatively and more realistically estimate the transition. Gulbransen's results for Mo and W show a transition to occur at or below the point where the volatile species pressure reaches $0.3 \times P_{O_2}$ for pure O_2 experiments. Graham and Davis [6.16] noted that in the gaseous diffusion regime, the oxidation rate for chromium scales as

$$P_{O_2}^{3/4} / P_{total}^{1/2} \qquad (6.4)$$

For molybdenum, the oxygen dependence should be $P_{O_2}^{3/2}$ and the oxidation rate for molybdenum in the gaseous diffusion regime should show a dependence of

$$\text{Mo oxidation rate} \sim P_{O_2}^{3/2} / P_{total}^{1/2} \tag{6.5}$$

for flowing gases. Thus, results in air and pure 0.10 atm oxygen should be very similar. Even a pure oxygen atmosphere ($P_{total} = P_{O_2} = 1$ atm) would be less than 10 times worse than Gulbransen's 0.1 atm oxygen results. A conservative approximation of the transition temperature is taken to be where

$$P_{(MoO_3)_3} \sim P_{total} \text{ (for transition)} \tag{6.6}$$

As seen in Figure 6.2, this occurs at 1200 °C and results in oxidation rates (fig. 6.3) over an order of magnitude higher than Gulbransen's results at 0.1 atm oxygen with small sample sizes.

Bartlett and Williams [6.15] calculated that the dependence was 6 kcal/mole in this third regime. Semmel's results [6.7] show a 7 kcal/mole activation energy. Thus for present purposes a conservative 7 kcal/mole value is adopted; the result is plotted (solid line) in Fig. 6.3. The combined predictive model for the rapid oxidation of molybdenum should be conservative for the following reasons: 1) no experiment has produced oxidation rates significantly higher than the model prediction, 2) experiments have been done on samples orders of magnitude smaller than the pieces of metal involved in a fusion first wall indicating possible earlier transition to gaseous diffusion than expected in a reactor, 3) the experimental evidence examined had high gas flow rates, except for Gulbransen, whereas the accident flow rates (once atmospheric pressures were reached in the torus) may not be as high.

In summary, the oxidation of molybdenum in a fusion accident is modeled as indicated in Table 6.4. In the surface reaction regime, little or no oxide film remains on the surface [6.7, 6.8] with the oxide volatilizing away soon after its formation from Mo:

$$Mo + \frac{3}{2} O_2 \rightarrow MoO_3(s,\ell) \rightarrow \frac{1}{3}(MoO_3)_3\ (g) \qquad (6.1, 6.2)$$

In the gaseous diffusion regime, there is no surface oxide film, as the transport of oxygen to the surface is rate-controlling:

$$Mo + \frac{3}{2} O_2 \longrightarrow \frac{1}{3}(MoO_3)_3\ (g). \qquad (6.1)$$

Ignition and self-heating may occur for temperatures above about 700 °C [6.1, 6.7, 6.8]. In all cases, the Mo that is oxidized is volatile; hence, the volatilization rate equals the oxidation rate. For oxidation and volatilization, the minimum temperature where significant problems can occur is 700 °C.

6.2.3 Vanadium Oxidation

The rapid oxidation rates for molybdenum have been seen to change depending on oxide volatility. The oxidation of vanadium is simpler. Unlike the group VIB metals, V, Nb, and Ta do not exhibit volatility effects. Rather, the only transition of interest occurs at the oxide melting point which greatly accelerates oxidation. Calculations of oxide partial pressure indicate that gaseous diffusion will not become limiting at any temperature below the melting point of vanadium metal (1917 °C). This conclusion has also been reached for the cases of niobium and

TABLE 6.4

Conservative Model to Predict Mo Oxidation Rates

	Surface Reaction Regime	Gaseous Diffusion Regime
Pressure Limit Controlling Transition	$P_{(MoO_3)_3} \gtrsim 10^{-2} \times P_{O_2}$	$P_{(MoO_3)_3} \sim P_{total}$
Equivalent Transition Temperature for Air	$\sim$700 °C	$\sim$1200 °C
Reaction	$Mo + \frac{3}{2}O_2 \rightarrow MoO_3(s,\ell)$	$Mo + \frac{3}{2}O_2 \rightarrow \frac{1}{3}(MoO_3)_3(g)$
Activation Energy	$\sim$20 kcal/mole	$\sim$7 kcal/mole
Log $\frac{dn}{dt}$ (atoms/cm^2-sec)	$22.12 - 4.4 \times 10^3 \times T(K°)^{-1}$	$20.18 - 1.53 \times 10^3 \times T(°K)^{-1}$
Pressure Dependence	$\sim P_{O_2}^{3/2}$	$P_{O_2}^{3/2} / P_{total}^{1/2}$

tantalum [6.6].

Unfortunately, data on vanadium are sparse, both for the thermochemical analysis and oxidation rates. Where data do exist, discrepancies do also. The validity of thermochemical data does, however, appear adequate to predict the species of interest and the occurrence of transition points for the pressures and temperatures of interest.

6.2.3.1 Thermochemical Analysis

The JANAF tables [6.17] do not include all relevant V species. Most compilations of data have only dealt with the equilibrium oxygen pressures between solid oxides rather than volatile species [6.18-6.21]. The possible species are listed in Table 6.5. The data given by Kubaschewski and Alcock [6.18] and the other sources has been shown to be in error by Block-Bolten [6.19] for the calculation of equilibrium O_2 pressures for the reaction:

$$V_2O_5(s,\ell) \rightarrow \frac{1}{2} O_2 + 2VO_2(s,\ell) \qquad (6.6)$$

Thus for temperatures above the melting point of V_2O_5, the reaction equilibrium occurs at $P_{O_2} \lesssim 10^{-4}$ [6.19] rather than $\sim 10^{-9}$ ($\sim$700 °C) or 10^{-4} ($\sim$1200 °C) as would be predicted from earlier data. The result is that for near atmospheric pressures, V_2O_5 is the dominant surface oxide. This agrees with experiments [6.22], where, in addition, a V_2O_4 - V_2O_5 mixture sometimes appears present.

Schick [6.20] reports that the equilibrium volatile oxide should be VO_2. In the available literature, no direct data has been found for the reactions

TABLE 6.5

Possible Vanadium Species

Condensed	Volatile
V	V
VO	VO
V_2O_3	VO_2
$VO_2(V_2O_4)$	
V_2O_5	

$$V_2O_5(s,\ell) \rightarrow \frac{1}{2}\, O_2 + 2VO_2(g) \qquad (6.7)$$

$$VO_2(s,\ell) \rightarrow VO_2\ (g) \qquad (6.8)$$

The $\Delta G°$ for the reaction 6.7 can be calculated from the reactions

$$V_2O_5(s,\ell) \rightarrow \frac{5}{2}\, O_2 + 2V(s) \qquad (6.9)$$

$$2V(s) + 2O_2 \rightarrow 2VO_2(g) \qquad (6.10)$$

This allows the equilibrium partial pressures for VO_2 over V_2O_5 and $VO_2(s)$ to be estimated. The data for Eq. (6.9) is taken from Wicks and Block [6.21] and for Eq. (6.10) from Schick [6.20]. The equilibrium pressure for $VO_2(s)/V_2O_5$ can also be determined, providing a check with experiment, by substituting the reaction

$$V_2O_4 \rightarrow 2\, O_2 + 2V(s) \qquad (6.11)$$

for Eq. (6.9). The result for $VO_2(g)$ and $V_2O_5(s)$ is shown in Fig. 6.4, for P_{O_2} = 0.21 atm. The calculated values of P_{VO_2} indicate that the oxygen pressure over a V_2O_5/V_2O_4 mixture should be 10^{-4} atm at 730 °C, in good agreement with experiments by Block-Bolten.

The results in Fig. 6.4 demonstrate the low volatility of V_2O_5. If one applied the transition criteria for Mo to V, one would obtain for exposure to air: start volatility at 1200 °C (departure from parabolic kinetics), volatility dominant at 2200 °C, and gaseous

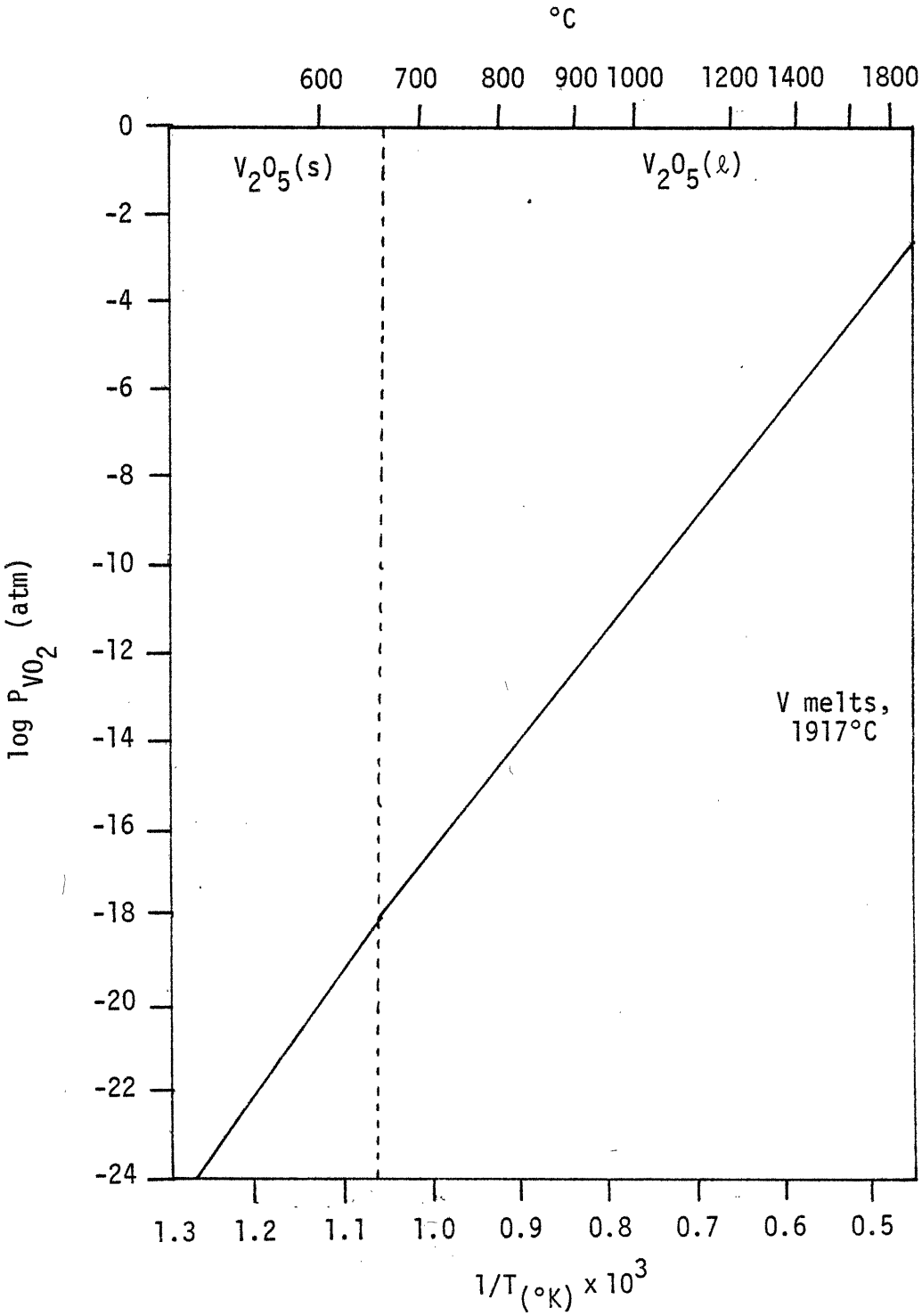

Fig. 6.4: Partial Pressure of VO_2 in Air over Vanadium as a Function of Temperature

diffusion limitation at 2600 °C. However, V_2O_5 melts at 670 °C and vanadium melts at 1917 °C. Thus it appears that for temperatures between 670 and 1917 °C, there should be no transitions and the oxidation is dominated by the presence of the liquid oxide. This prediction for V is in complete agreement with that of Gulbransen [6.9] for the cases of Nb and Ta at analogous temperatures.

6.2.3.2 Activation Energy and Oxidation Mechanism

Kofstad [6.7] reports that the formation rate of Nb_2O_5 over Nb above the melting point (1512 °C) is proportional to P_{O_2}, following a linear kinetic rate law, with an activation energy of 16 kcal/mole. He suggests that the mechanism is thus controlled by oxygen adsorption on the surface.

Price and Springer [6.22, 6.23], however, suggest a different mechanism for V, diffusion through the liquid oxide. They determined an activation energy fo V_2O_5 of 8 ± 1 kcal/mole. They noted that the activation energy for self-diffusion through an ionic liquid should be [6.23]:

$$E = 3.74\ RT_M \tag{6.12}$$

where R = gas constant, T_m = oxide melting point (°K). For V_2O_5, this gives Q = 7 kcal and 13.3 kcal for Nb_2O_5 compared to 8 ± 1 kcal and 16 kcal from experiment. These results suggest that liquid oxide diffusion may be rate determining.

6.2.3.3 Experimental Data

An extensive literature search has encountered only one study of the oxidation of vanadium at high temperatures and near atmospheric pressures—that of Price and Stringer [6.22] joined later by Kennett [6.23].

Price and Stringer [6.22] studied the oxidation of vanadium in pure oxygen (0.13-0.55 atm) at temperatures from 700-1050 °C. At higher pressures and temperatures, they sometimes encountered burning or autocatalytic conditions. The following results are for those reactions where "burning" did not occur.

Three types of experiments were performed: 1) suspension of specimen in constant pressure oxygen [6.22], 2) suspension of specimen in constant volume chamber, allowing depletion of oxygen [6.22], and 3) immersion of metal in liquid oxide [6.23]. The specimens were oriented in the first two cases so that the liquid oxide dropped off. Surface preparation was found to have no effect, with the exception that single crystal vanadium oxidized more rapidly than polycrystalline specimens, but both followed the same kinetics. In addition, specimen size had no effect, unlike the case for molybdenum where size affected the transition point. The initial two sets of experiments provided data that was fit to the general Eq. [6.23]:

$$\dot{m} = \text{const.} \times \exp\left(\frac{-E}{RT}\right) \times P_{O_2}^{N} \times t^{m} \qquad (6.13)$$

The pressure (n = 0.75) and time (m = 0.70) indices were found to be independent of temperature [6.22]; however, further analysis indicated a pressure dependence on n and m. Niobium shows a $\sim P_{O_2} \times t$ dependence

(n = m = 1) [6.17] and one might expect similar behavior for vanadium. Price et al. note that for lower pressures ($P_{O_2} \sim 0.13$ atm), the samples showed behavior of m near 1 [6.23].

Since the immersed samples led to substantially lower oxidation and the observed activation energy corresponded well with the prediction of liquid oxide diffusion, they were led to propose a model of oxidation rate dependence on the oxide drip off rate (linear) and the oxide layer thickness (parabolic), hence the steady-state rate is given by

$$\dot{m} = k_p/2d_L \tag{6.14}$$

where k_p = parabolic rate constant

d_L = limiting thickness of layer

Experiments show that this steady state was reached in a very short time, about 3 minutes. The situation is further complicated by the observed temperature rise due to the exothermic reaction. Even in non-burning reactions, the specimen temperature rose about 70 °C, then fell to a steady state value of 30 °C above the original temperature in 3-7 minutes. They concluded that the deviation from linear (m = 1) is likely due to the non-equilibrium conditions existing during the first few minutes [6.23]. The deviation was higher at higher temperatures and pressures and was greatly reduced for the immersed samples. Using Eq. (6.14) and available data for 700 °C and 0.13 atm (closer to equilibrium case), they obtain a value for k_p of 10^{-8} g^2/cm^4-sec. Considering the uncertainties involved, they state that this value is in fair

agreement with extrapolating solid V_2O_5 diffusion rates and adding a factor of 10^4 for the phase difference [6.23].

6.2.3.4 Accident Model

Three additions must be made to model behavior in an accident. First, due to the larger size and thermal capacity of the surrounding environment and the slower rate of bringing the metal to temperature, the accident reaction conditions will be closer to equilibrium. Hence, the reaction should be conservatively taken as linear in time (m=1). Second, due to the different orientations of vanadium surface in the vacuum vessel (varying the drop-off rate) around the minor radius of the torus, oxidations rates would vary. Highest rates would occur at the top; lowest, at the bottom where accumulated oxide would shield the metal. Use of experimental data gives the highest rates and will be used to evaluate accident conditions. Thus the model predicts the rate of metal loss (leading perhaps to loss of structure integrity at the top) and over predicts the overall oxidation.

From the experimental data [6.22, 6.23], scaled up for exposure to air, (P_{O_2} = 0.21 atm), one obtains

$$\dot{m}/A \ (kg/m^2\text{-sec}) = 0.135 \times 10^{-1.75 \times 10^3/T(°K)} \qquad (6.15)$$

with a $P_{O_2}^{0.75}$ oxygen pressure dependence. It is not possible to account for the presence of nitrogen. However, since oxide volatility is not important to the reaction rate, there should be no dependence on total pressure, only on oxygen pressure.

A third aspect is the determination of the maximum volatilization rate. Unlike Mo, the dominating volatile V species, VO_2, has a very low vapor pressure. Furthermore, oxide volatility is not the rate controlling step. For vanadium, a pool of liquid oxide accumulates. The maximum rate of volatilization is given by the Hertz-Langmuir equation:

$$\dot{m} = P_{VO_2}/(2\ RT(°K)M_{VO_2})^{1/2} \tag{6.16}$$

Since this equation represents the maximum vapor loss to a vacuum, it is likely to overpredict the rate of oxide volatilization. However, calculated loss rates are still very low. The maximum loss rate for VO_2 is then

$$\dot{m}\left(\frac{\text{moles}}{m^2\text{-sec}}\right) = 4.9 \times 10^4 \quad \frac{P_{VO_2}(\text{atm})}{(T(°K))^{1/2}} \tag{6.17}$$

or,

$$\dot{m}\left(\frac{\text{meters of V-alloy}}{\text{sec}}\right) = 0.41 \quad \frac{P_{VO_2}(\text{atm})}{T(°K)^{1/2}} \tag{6.18}$$

For example, at 1000 °C the VO_2 pressure (Figure 6.4) is about 10^{-11} atm, then the maximum rate of vanadium volatilization is 1.1×10^{-13} m/s of vanadium. Thus only a very small fraction of vanadium could be expected to be volatilized due to structural oxidation, although much reactor damage could occur. Any exposure to air above 700 °C could cause significant damage.

Based on the data of Price [6.22], it appears that, above ~1000 °C, vanadium may ignite in air. However, the volatility of the oxides is not different from the non-ignition case, so that little vanadium could be volatilized.

6.2.4 First Wall Coatings

First wall coatings may be required for plasma impurity control. Fortunately, the major candidates tend to have low levels of induced radioactivity although some are chemically toxic. Unfortunately, many will oxidize just like the first wall itself, leading to reactor damage.

If a first wall coating were resistant to oxidation, it would tend to protect the first wall, reducing the rapid structural oxidation concern. Although the selection and influence of first wall coatings is beyond the scope of the present study, it is relevant to demonstrate that the rapid oxidation problem does exist for at least some candidate first wall materials. Two such candidates are the low atomic number elements beryllium and carbon.

6.2.4.1 Beryllium

Gulbransen and Andrew [6.24] report that the oxidation of Be below about 950 °C is parabolic with a protective oxide scale. The rates are

$$\begin{aligned} 350 < T < 700\ ^\circ C \quad & k_p = 1.8 \times 10^{-12} \exp(-8{,}500/RT)\ g^2/cm^4\text{-sec} \\ 700 < T < 950\ ^\circ C \quad & k_p = 3.5 \times 10^{-3} \exp(-50{,}300/RT)\ g^2/cm^4\text{-sec} \end{aligned} \tag{6.19}$$

Above about 950 °C, Berry [6.25] notes that the oxide film has become unprotective and there is a transition to linear kinetics. The oxidation rate for some temperatures is given in Table 6.6. Thus a 1 mm wall would oxidize in 17 seconds at 1000 °C.

Finally, ignition of bulk pieces of beryllium has been noted in the range 1200 - 1300 °C when exposed to a steam/air mixture from a hydrogen-oxygen flame [6.26]. The specimen temperature rose to about 2750 °C.

6.2.4.2 Carbon (Graphite)

Carbon is unique in that no solid oxide remains on the surface. Whereas this unfortunately means that any oxidized carbon is also volatilized, it also means that no residue is left on the surface for clean up. Thus a carbon coating could perhaps be more easily repaired since no oxide contamination would have to be removed.

The reaction rate kinetics are always linear. The surface reaction is

$$C + O_2 \rightarrow CO_2(g) \tag{6.20}$$

Therefore, the CO_2 partial pressure is given by

$$P_{CO_2} = k_\ell P_{O_2} \tag{6.21}$$

Thus the oxidation rate is proportional to P_{O_2}. The rate of graphite oxidation has been studied in the range of 600 - 1500 °C at P_{O_2} = 0.05 atm [6.6]. The results have been scaled to atmospheric conditions and are plotted in Fig. 6.5. The transition to the gaseous diffusion regime was noted in the experiment to occur at a reaction

TABLE 6.6

Beryllium Oxidation Rates [Ref. 6.25]

Temperature (°C)	Oxidation Rate (m/sec)
~930	5×10^{-6}
1050	6.5×10^{-4}
1065	3.2×10^{-3}
1295	5.0×10^{-3}

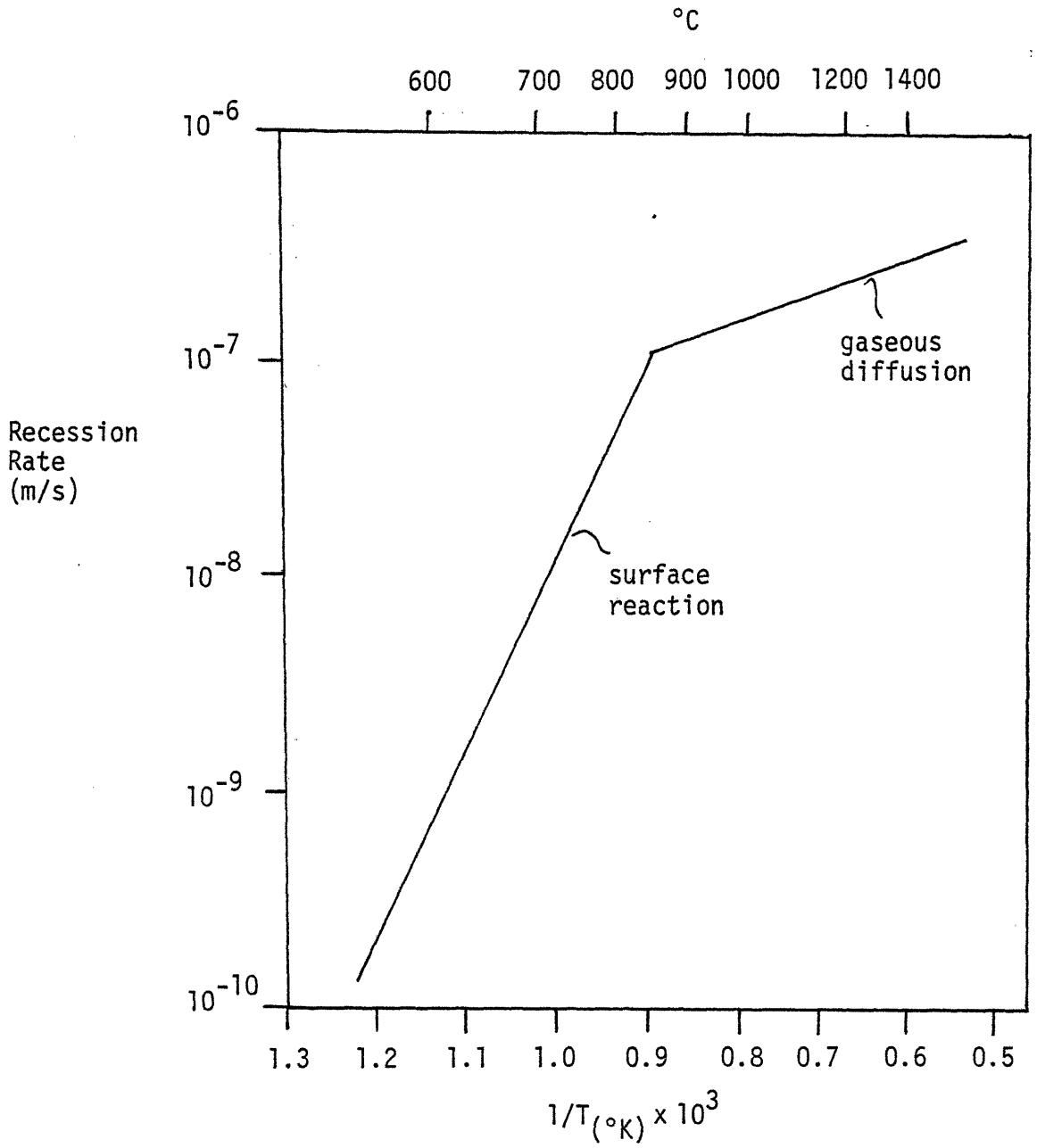

Fig. 6.5: Wall Recession Rate for Graphite as a Function of Temperature [6.6]

rate of 4×10^{17} atoms/cm^2-sec for an oxygen pressure of 0.10 atm. One would expect the transition rate to scale no more than linearly with P_{O_2}. Thus for atmospheric conditions, the break point was conservatively assumed to be about 10^{18} atoms/cm^2-sec, which corresponds to a 850°C temperature. Above this transition point, a temperature dependence of 7 kcal/mole (same as for Mo) is assumed, although the data [6.6] show a flatter curve at $P_{O_2} = 0.05$. Carbon is seen to offer longer protection. For example, about 2.2 hours would be required to oxidize a 1.0 mm coating at 1000°C.

6.2.5 Other Gases

Relatively little is known about the behavior of the refractory metals in non-oxygen atmospheres. Because these other cases may be present, a brief discussion is relevant.

6.2.5.1 Carbon Dioxide

Berry [6.25] reports that vanadium is incompatible with CO_2 at 500°C and molybdenum is incompatible with CO_2 at 600°C. In general, the CO_2 reaction with metals at high temperatures produces oxides [6.26] rather than carbonates. Thus the same type of behavior as oxygen would be expected, except at lower rates.

The situation is complicated by the facts that 1) wet CO_2 is far more reactive than dry CO_2 (possible if water is the coolant) and 2) radiation plays a significant role in promoting CO_2 reactions due to the decomposition of CO_2 into CO and O [6.26].

In general, the presence of CO_2 would still be expected to pose a significant oxidation hazard to these metals, although a lower hazard than oxygen. Detailed experiments in the appropriate radiation environment would be needed to quantify the difference.

6.2.5.2 Steam

As corrosion problems prohibit use of refractory metals with a water coolant, steam is unlikely to come in contact with vanadium or molybdenum. Berry's [6.25] discussion of steam oxidation leads to the conclusion that in these regimes steam is somewhat worse than oxygen. For example, the steam reaction has already progressed to rapid linear kinetics at 650° (versus 950° in air) for beryllium [6.26].

6.2.5.3 Lithium Species

If lithium alone were present, there would be no problem as the refractory metals are generally compatible with lithium (Chapter 7). If graphite were a first wall coating one might expect some trouble with the exothermic lithium-graphite reaction:

$$2Li + 2C \rightarrow Li_2C_2 \qquad \Delta H = -55 \text{ kcal/mole [6.27]} \quad (6.22)$$

although the reaction rate at high temperatures is unknown.

If oxygen and lithium were both present, a lithium fire would result. This would result in elevated temperatures in the torus (Chapter 5) and reactive species like Li_2O and Li_3N. (LiOH could be present if water vapor were present). In the case of vanadium, the oxide, V_2O_5, is less stable than Li_2O. Hence the presence of Li_2O (similarly for Li_3N) would not add to the oxygen-vanadium problem. Furthermore, there might be a beneficial effect of Li_2O smoke coating the vanadium wall, inhibiting oxidation.

Li_2O and MoO_3 are known to react. Some ternary compounds have been identified as a result of the reactions [6.28]:

$$Li_2O + 2MoO_3 \rightarrow Li_2Mo_2O_7 \quad (6.23)$$

$$Li_2O + 4MoO_3 \rightarrow Li_2Mo_4O_{13} \quad (6.24)$$

However, the products can not be prepared at higher temperatures where MoO_3 becomes volatile [6.28]. The presence of Li_2O would not be expected to add to the oxygen-molybdenum problem.

6.3 Steels

The analysis for steels is significantly different from the preceeding cases because

1) alloying effects are dominant rather than insignificant.
2) a complex oxide scale develops
3) most oxidation products are solid and non-mobile
4) any volatilization could be non-stoichiometric
5) the data base for relevant temperatures is more sparse for the precise alloy compositions of interest.

6.3.1 Overview

Whereas the refractory metals do not exhibit protective oxide layers above about 700 °C, steels normally do. The addition of chromium to iron leads to a surface layer of Cr_2O_3. Depending on temperature and alloy composition a variety of oxides may be present: Fe_2O_3, Fe_3O_4, FeO, NiO, and Cr_2O_3.

There are two oxidation regimes of interest. First, the oxide layer may be protective. Then, only outer surface volatilization of Cr_2O_3 can lead to radioactivity mobilization. Second, if protectiveness is lost, other pathways exist (oxide spalling, liquid oxides, volatilization)

to mobilize and damage the steels.

6.3.2 Protective Scales

The steels in question generally exhibit a Cr_2O_3 surface oxide layer when exposed to oxygen, shown in Fig. 6.6. When this layer remains protective, only solid state diffusion of the reactants is possible. At low temperatures this means that the reaction follows a parabolic kinetic law [6.29]:

$$dx/dt = k_d/x \tag{6.25}$$

where x = scale thickness

k_d = diffusion parabolic rate constant

Unfortunately, Cr_2O_3 will volatilize from the surface:

$$Cr_2O_3(s) + \frac{3}{2} O_2(g) \rightarrow 2CrO_3(g) \tag{6.26}$$

and the reaction rate is altered to be [6.29]:

$$dx/dt = k_d/x\text{-}k_s \tag{6.27}$$

where k_s = volatilization rate constant

at 1400 °C, volatilization of Cr_2O_3 causes a significant deviation from pure parabolic kinetics for times in excess of one day [6.29]. As seen in the next section, however, the oxide film on the steels in question

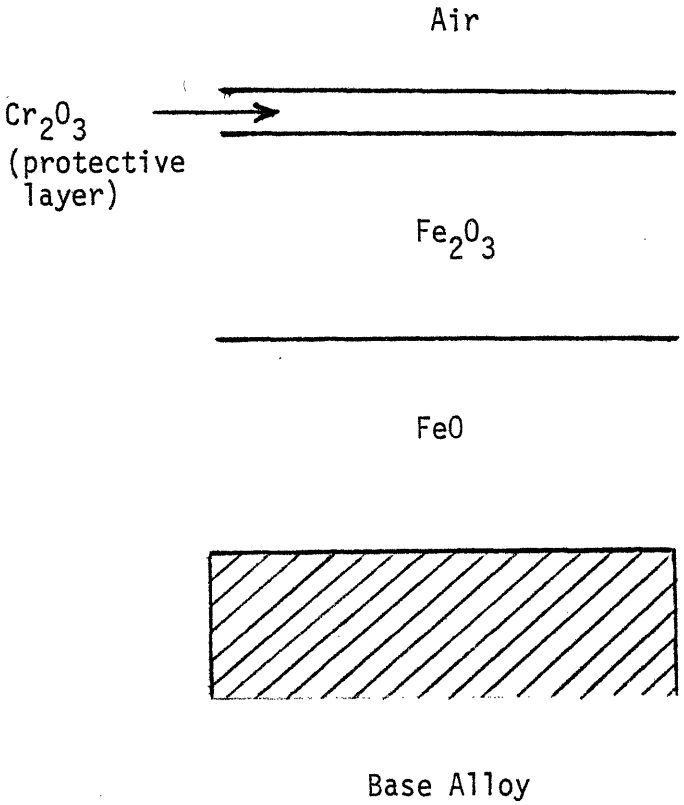

Fig. 6.6: Schematic of Typical Oxide Layers Formed on Stainless Steel in Air

would be expected to breakdown below this temperature.

Thus, for protective scales, the oxidation rate is parabolic. The only volatilization is that of Cr_2O_3 which proceeds linearly. The oxidation rate is too slow for these steels to cause significant damage, if the scales remain protective. The rate of Cr_2O_3 loss has been found to be [6.30]:

$$k_s = 0.214 \exp(-48{,}000 \pm 3{,}000/RT) \text{ g/cm}^2\text{-s} \quad (T<1350\ ^\circ C) \quad (6.38)$$

which corresponds to atmospheric pressures and very high gas flow rates. These rates (see Section 6.4) are very low.

The presence of water vapor could result in a 65% increase in the volatization rate [6.31]. The presence of Li_2O would tend to inhibit the oxidation rate of the alloy due to the lattice defect effect [6.10]. The volatilization rate would tend to be reduced due to the possible coating of the wall by Li_2O. Berry's [6.25] discussion indicates that CO_2 exposure is less serious than oxygen.

For all cases, there is unlikely to be a safety problem for temperatures where the oxide scales are protective. However, any exposure to oxygen at these temperatures would produce an oxide scale, altering the surface properties and compositions. This may be an economic problem due to lowered vacuum/plasma impurity performance.

6.3.3 Catastrophic Oxidation

Unfortunately, the oxide layer does not always remain protective. A constituent of the scale may reach its melting point which leads to rapid oxidation and weight loss. For steels, the primary concern is

the presence of Mo additions [6.32-6.35].

The primary mechanism appears to be melting of the oxide, MoO_3, which permits a catalyst type effect which increases oxygen transport and leads to rapid breakdown of the scale and accelerated oxidation [6.32]. The physical picture is shown in Fig. 6.7.

The critical unknown is the threshold temperature for this behavior. There are a variety of difficulties in answering this question. First, the transition point is very dependent on alloy content. Second, the initial surface condition is important. If a firm scale is already formed before the temperature rises to critical regimes, higher temperatures are required for breakdown than if the surfaces were initially clean. Unfortunately, in the course of an accident, the first wall could be un-oxidized and already at high temperatures (e.g., from afterheat) when oxygen entered the torus. Third, higher gas flow rates may reduce the problem for if the MoO_3 can volatize away before a liquid layer builds up in the scale, catastropic oxidation is surpressed. This would tend to be beneficial in a fusion accident, although the precise impact is impossible to determine at present.

Brenner [6.32] examined catastropic oxidation in Fe-Mo-Cr and Fe-Mo-Ni alloys. His results are shown in Fig. 6.8. Researchers at the Climax Molybdenum Co. have also studied the onset of catastropic oxidation as a function of temperature [6.33-6.35]. Their results are shown in Fig. 6.9 [6.33].

The compositions of relevant steels are listed in Table 6.7. The composition of steels are plotted in Fig. 6.8 to show the likely transition temperatures. As is seen in the figure, the range of Cr and

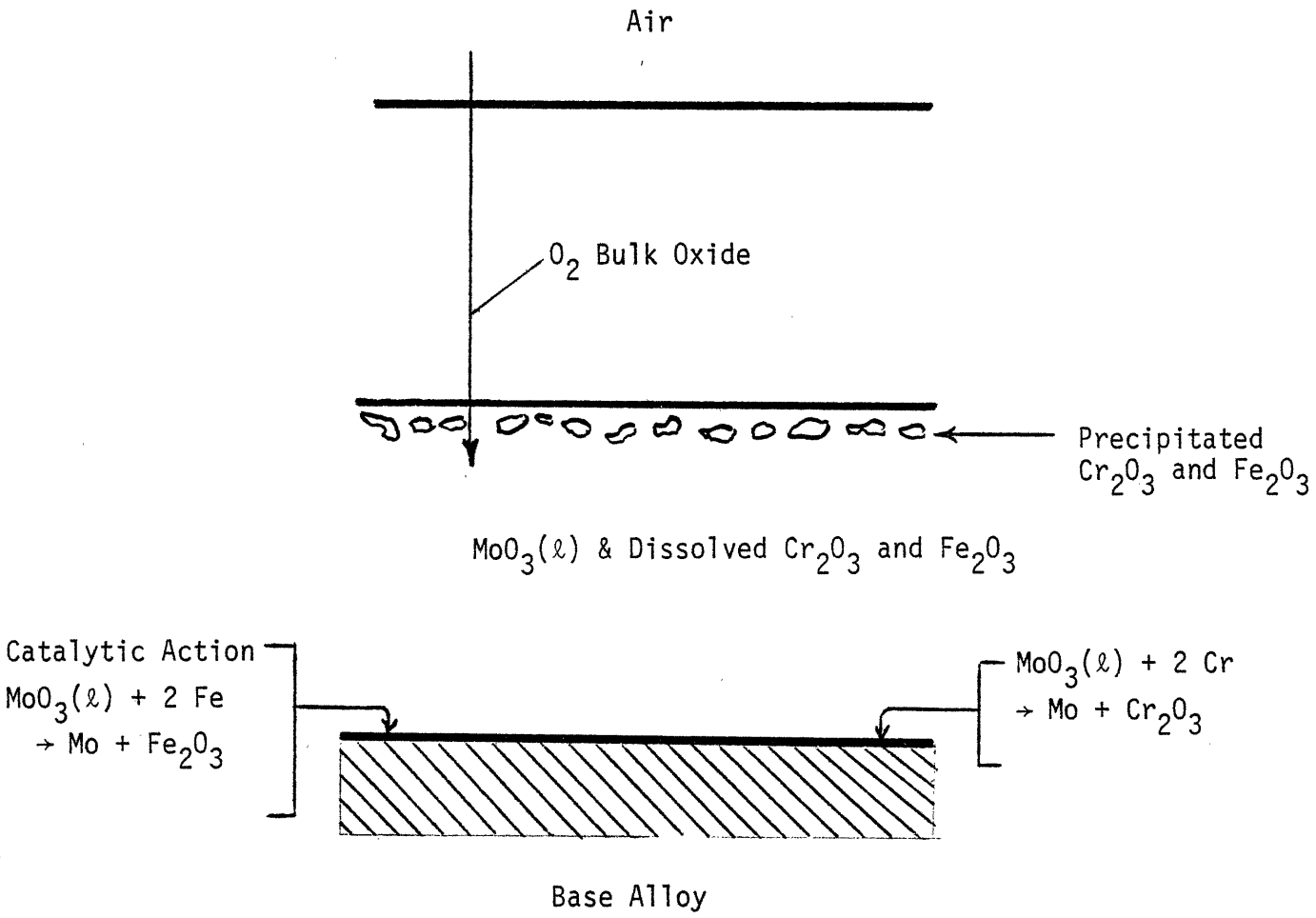

Fig. 6.7: Schematic of Typical Oxide Layers Formed During Catastrophic Oxidation of Steels in Air, based on Ref. 6.32

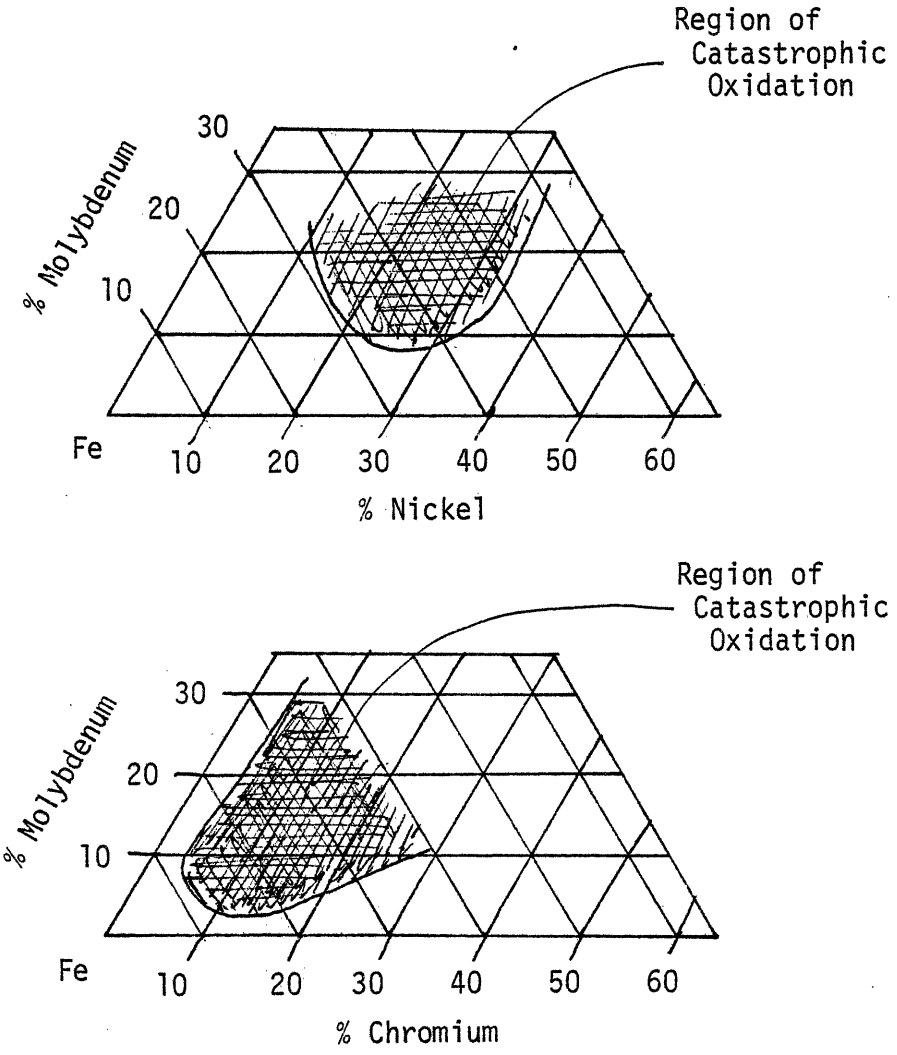

Fig. 6.8: Regions of Compositions of Steels Subject to Catastrophic Oxidation in Air at 1000°C [6.32]

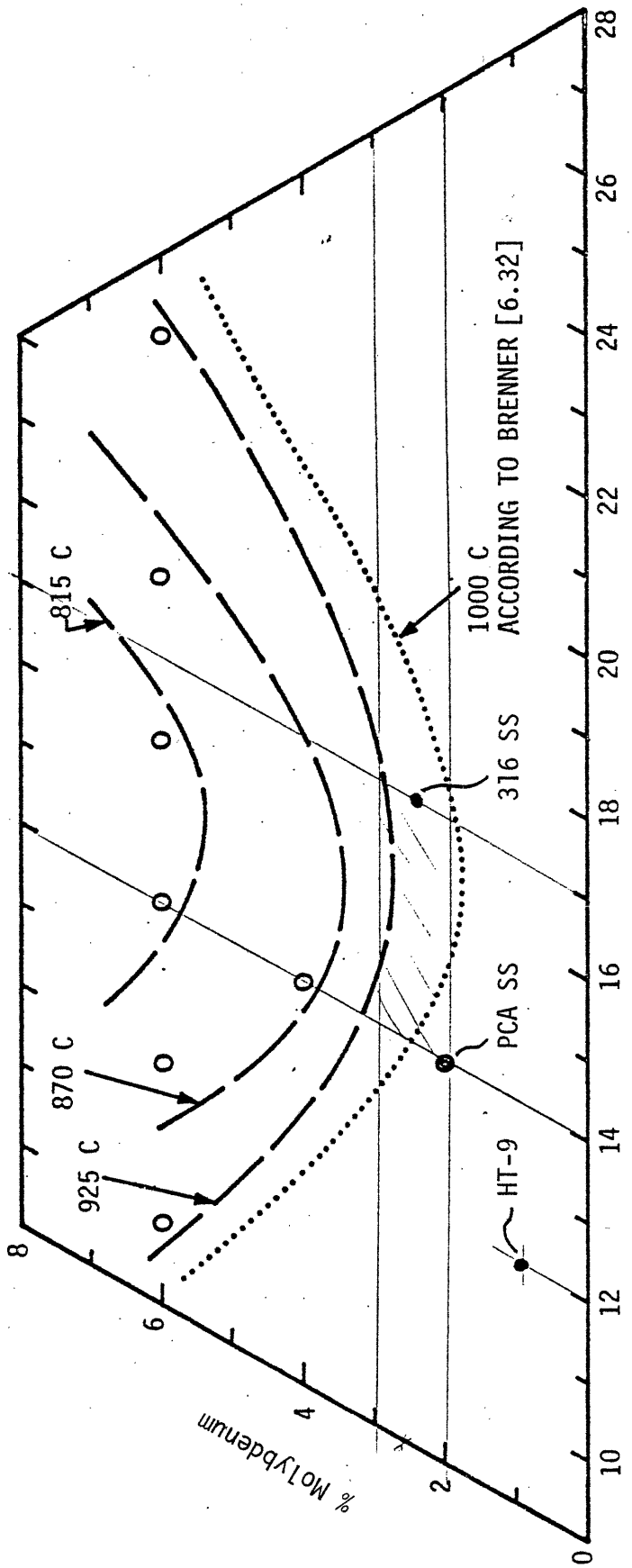

Fig. 6.9: Boundaries for Accelerated Oxidation in the Fe-Cr-Mo System for Different Temperatures [6.33]

TABLE 6.7

Weight Fractions of Alloy Constituents which Influence Oxidation*

	316 SS	PCA SS	HT-9
Mo	2.5	2.0	1
Cr	17	14	12
Ni	14	16	—
Si	0.5	0.5	—

*See Appendix B, Material Properties

and Mo content for austenitic stainless steels (e.g., 316 SS and PCA) can significantly alter the transition temperature. The low Mo content in the ferritic steel (HT-9) indicates that the transition temperature would be significantly higher.

Additional factors need to be considered. First, small additions of silicon are beneficial. In the 900-1000 °C range, 1% Si addition was effective in surpressing oxidation in a 14Cr-4Mo steel [6.35]. The possible benefit of the 0.5% Si addition in the steels is unknown but could improve the behavior from that expected from Fig. 6.9.

Second, nickel content (below $\sim$25% Ni), which shifts the alloys from ferritic to austenitic crystal structure, is beneficial. The effect is highest for 14-18% Cr with 6% Mo where the nickel raises the transition temperature by about 100 °C based on the data in references [6.33] and [6.34]. The contribution of nickel to lower ($\leq$2.5% Mo) Mo content alloys is unknown.

Third, if Mo does not trigger catastrophic oxidation, the melting of FeO near 1400 °C will trigger oxide breakdown and rapid oxidation [6.7, 6.8]. Fourth, the reproducibility of the results is not good; the transition to catastrophic oxidation is somewhat unpredictable and does not start immediately upon exposure to air [6.33-6.35].

In spite of these uncertainties, it appears that catastrophic oxidation and volatilization can be expected to begin somewhere between 900 and 1400 °C for the steels in question. The best estimate for the transition temperature of 316 SS (reference austenitic steel) is 1000 $\pm$ 100 °C and of HT-9 (reference ferritic steel) is 1300 $\pm$ 100 °C based on Fig. 6.9.

It should be noted that for temperatures where catastrophic oxidation is not triggered, the addition of Mo may be beneficial. For example, up to 5-6% Mo is beneficial in the range 500-1000 °C [6.36].

The oxidation rate itself is uncertain and also a function of alloy content. Based on the results available [6.32-6.36], the oxidation and volatilization rate is taken to be 2×10^{-6} kg/m^2-sec for non-catastrophic oxidation ($T \sim 1000$ °C) and 1.5×10^{-4} kg/m^2-sec ($T \sim 1000$ °C) and 2×10^{-4} kg/m^2-sec ($T \sim 1300$ °C) for catastrophic cases.

Steam leads to catastrophic oxidation in steels around 1400 °C [6.37, 6.38]. Whether in steam or air, ignition of the steel is possible at that temperature [6.1]. The precise behavior of the reference steels in CO_2 is not known, but above 1000 °C oxidation and carburization may be significant [6.25].

6.4 Summary

6.4.1 Oxidation Rate

The oxidation rate for the reference metals has been estimated for exposure to air as a function of temperature. These rates are summarized in Table 6.8. The time required to completely oxidize a 1.0 mm wall is shown in Fig. 6.10. Below 700 °C none of the metals has an oxidation rate sufficient to produce structural damage. However, sufficient surface reaction may occur which would degrade the vacuum/plasma impurity properties of the first wall. Above about 1400 °C, all of the metals would deteriorate at extremely fast rates, approaching 1 mm/min, if exposed to air. Furthermore, all could be expected to ignite by this temperature.

In between 700 and 1400 °C, the oxidation picture is heavily dependent on metal and temperature. The refractory metals represent a

TABLE 6.8

Oxidation Rates for Reference Metals in Air

Metal	Temperature (°C)	Oxidation Rate (m/sec) (T in °K)
Mo	700 - 1200	$2.1 \times 10^{-3} \times \exp(-10{,}130/T)$
	1200 - 2600	$2.4 \times 10^{-5} \times \exp(-3{,}530/T)$
V	700 - 1900	$2.2 \times 10^{-5} \times \exp(-4{,}030/T)$
316 SS	<1000	$<2.5 \times 10^{-10}$
	~1000	1.9×10^{-8}
	~1300	$\sim 2.5 \times 10^{-8}$
HT-9	<1300	$<2.5 \times 10^{-10}$
	~1300	$\sim 2.5 \times 10^{-8}$

1 mm/day = 1.157×10^{-8} m/s

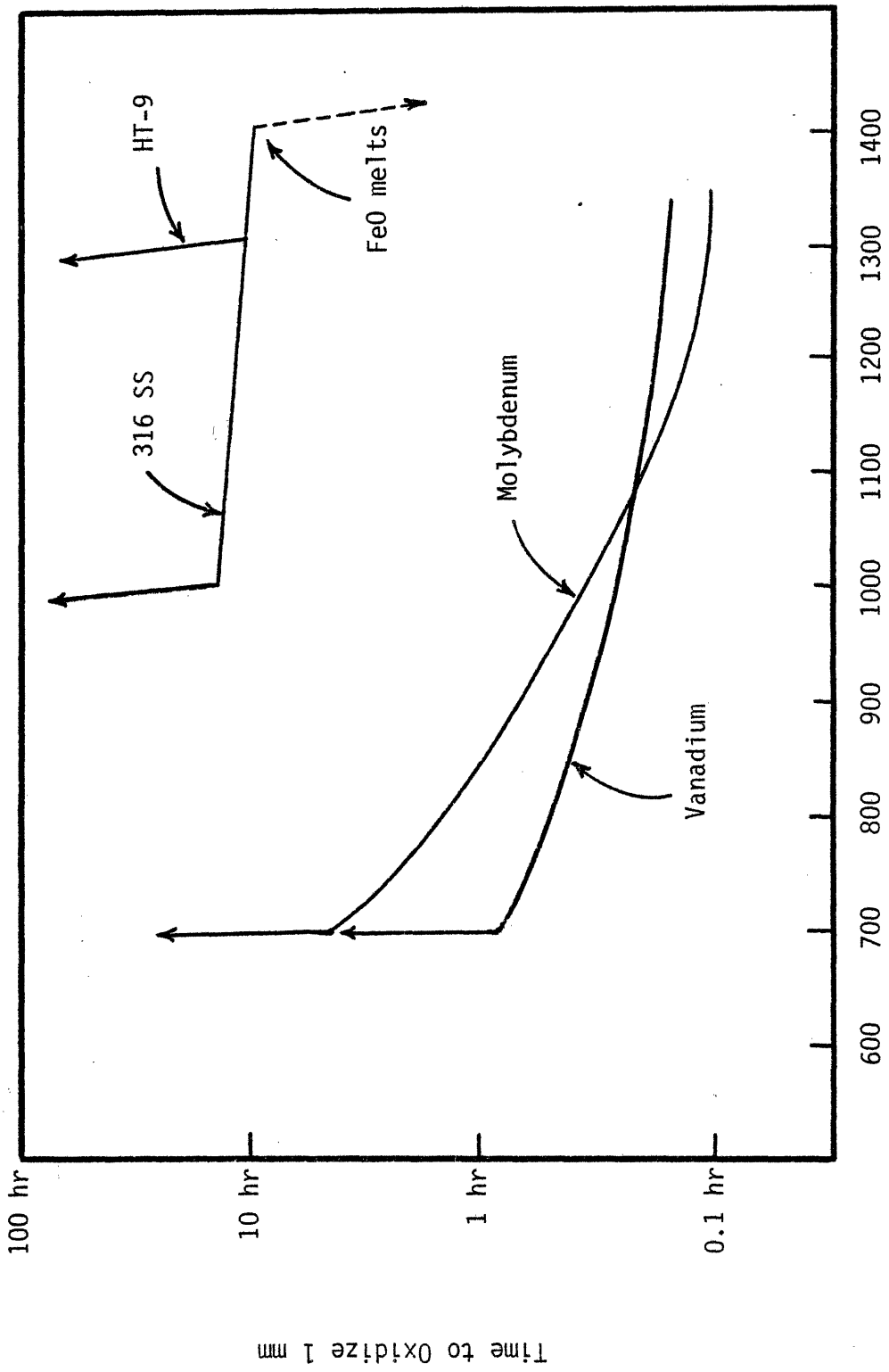

Fig. 6.10: Time Required to Oxidize a 1 mm Wall of the Reference Structure Materials as a Function of Temperature

significantly worse hazard. The physical picture expected for vanadium and molybdenum is shown in Fig. 6.11 and the reaction rate is plotted in Fig. 6.12.

Alternative gases represent a less certain problem. In general, steam would be somewhat worse and CO_2 somewhat better than air. Steam reactions with metals would tend to liberate hydrogen. The presence of lithium and lithium species resulting from a lithium fire would have relatively little effect, other than the resulting temperature rise itself.

First wall coatings, if used, may protect the first wall. However, some, like Be and graphite, exhibit significant oxidation rates. The oxidation of most first wall coatings is preferable to oxidation of the first wall because: 1) coatings tend to be only slightly radioactive, 2) coatings are not structural members, so stress failures are not threatened, and 3) the coatings may be more easily replaced or repaired than the first wall.

6.4.2 Volatilization Rate

The volatilization rate represents the rate that material may become gaseous and very mobile. This rate is summarized for the reference metals in Table 6.9 for exposure to air. The reaction product of molybdenum is highly volatile and basically all the molybdenum reacted will be volatile. The reaction product of vanadium, V_2O_5, is liquid and the volatile species, VO_2, has a very low vapor pressure. Thus a liquid oxide pool will develop and very little metal will be volatilized.

For both refractory metals, the volatilization rate is assumed independent of alloy constituents. In an actual first wall, many of

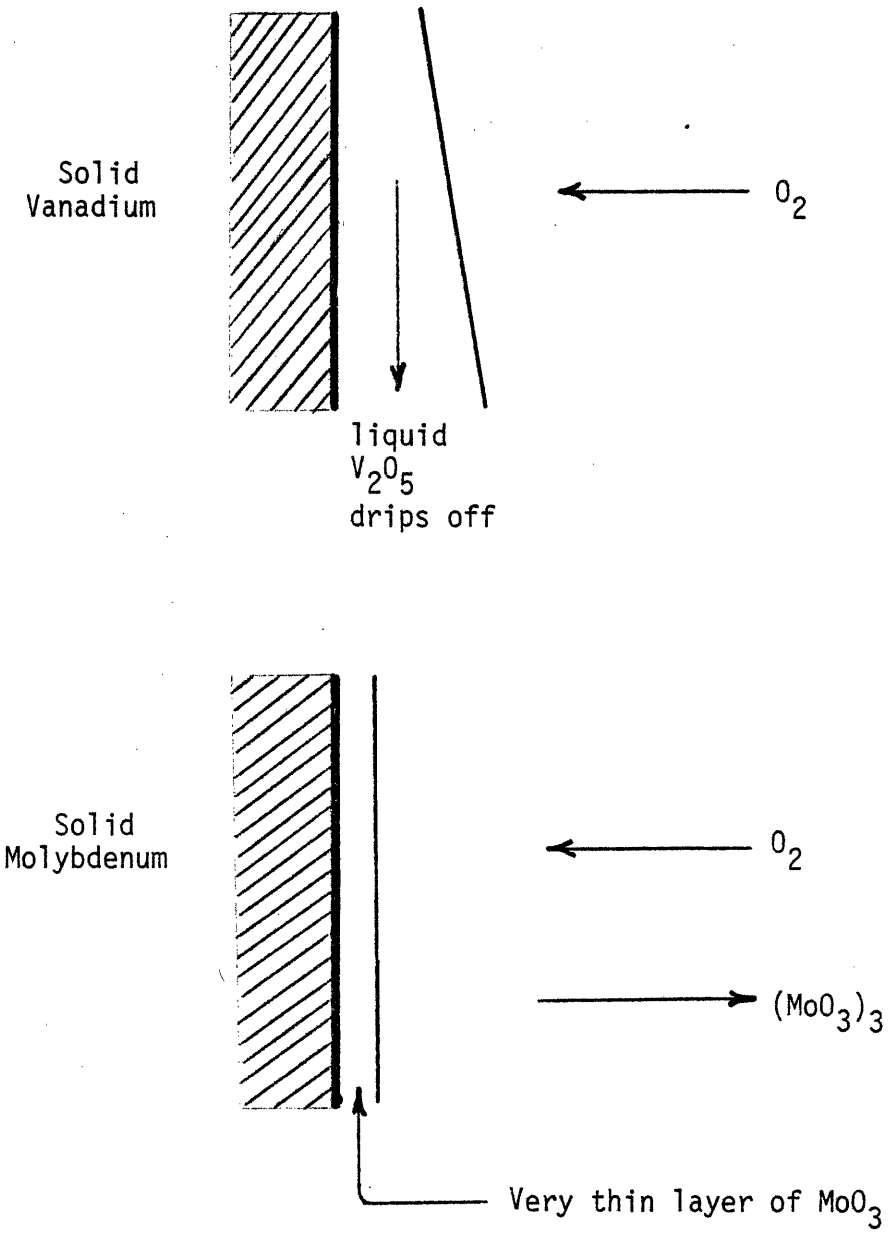

Fig. 6.11: Schematic of Rapid Oxidation of Vanadium and Molybdenum

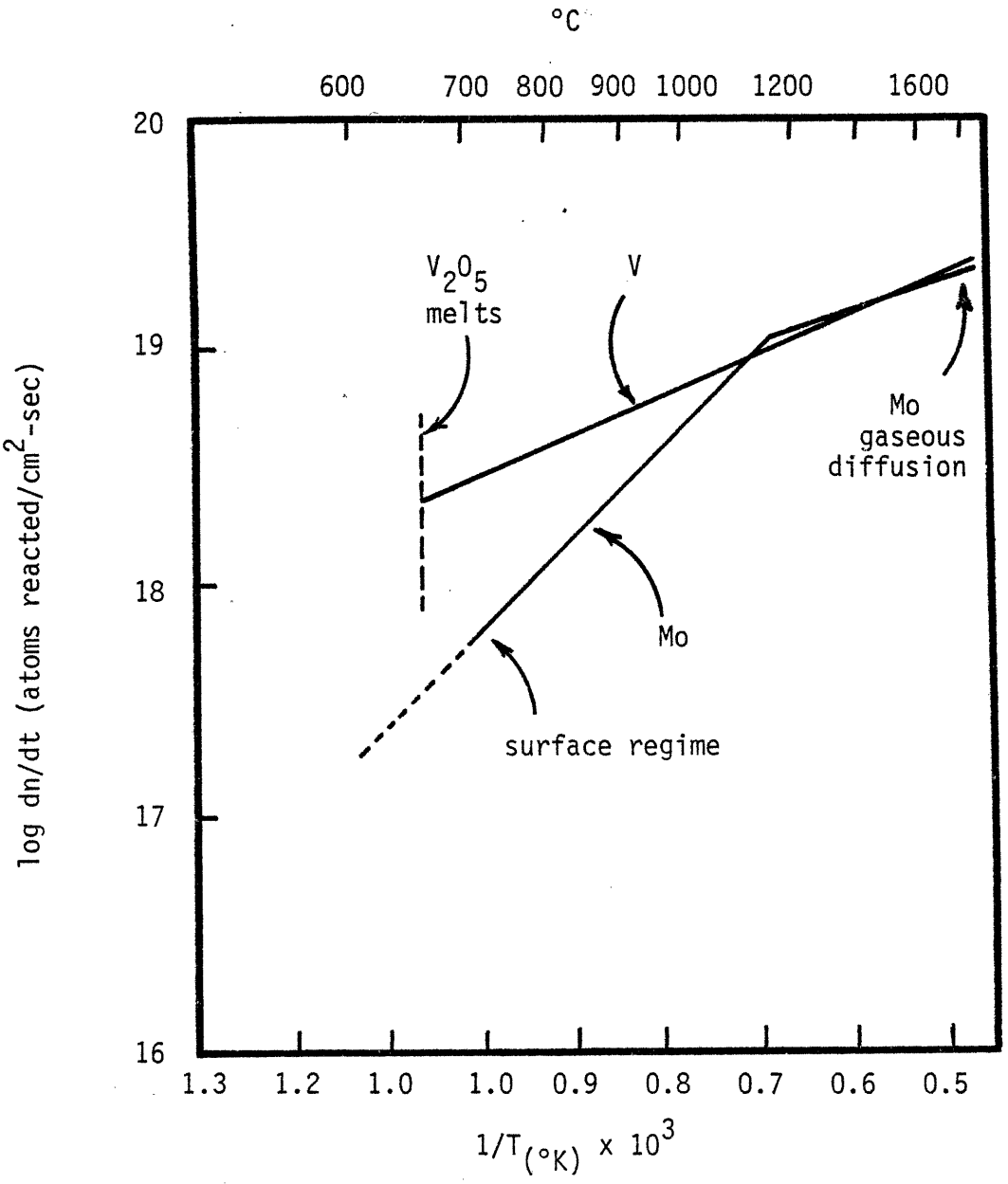

Fig. 6.12: Model Predictions for Vanadium and Molybdenum Oxidation Rates as Functions of Temperature

TABLE 6.9

Volatilization Rates for Reference Metals in Air

Metal	Temperature (°C)	Volatilization Rate* (T in °K, m/sec)
Mo	700 - 1200	$2.1 \times 10^{-3} \times \exp(-10,130/T)$
	1200 - 2600	$2.4 \times 10^{-5} \times \exp(-3,530/T)$
V	700 - 1900	$< 2 \times 10^{8} \times T^{-1/2} \times \exp(-57,600/T)$
316 SS	<<1000**	$2.7 \times 10^{-5} \times \exp(-24,170/T)$
	<1000	$< 2.5 \times 10^{-10}$
	∿1000	1.9×10^{-8}
	∿1300	2.5×10^{-8}
HT	<1000**	$2.7 \times 10^{-5} \times \exp(-24,170/T)$
	<1300	$< 2.5 \times 10^{-10}$
	∿1300	2.5×10^{-8}

*In units of meters of base alloy per second volatilized away from surface in oxide form.

**For temperatures significantly below 1000 °C, the only steel volatilization is from Cr_2O_3 (see Eq. (6.28)).

the radioisotopes are different chemically from the base metal (Chapter 8). Thus, although the bulk rate is unaffected by small amounts of different elements, the volatilization of the various radioisotopes would not necessarily occur at the same rate as the bulk metal.

In TZM, the Zr and Nb species are less mobile than MoO_3; therefore, one would expect such radioisotopes to be released from the surfaces at rates lower than the bulk metal is consumed. The concentration would tend to increase at the surface. In V-alloys, the Cr_2O_3 specie is more volatile than VO_2. Thus, chromium radioisotopes would be expected to volatilize from the V_2O_5 pool faster than the bulk metal rate. Other oxides, e.g., TiO_2, would be less volatile.

For lower (<1000°C) temperatures, only some volatile oxides like Cr_2O_3 would escape from a steel. Between 1000 and 1400 °C the rate would increase dramatically at the onset of catastrophic oxidation. Experiments have shown that this material is lost from the surface in gaseous and particulate form.

In all cases, the bulk metal volatilization rates do not indicate at what rate all the radioisotopes would be mobilized. The oxidation and volatilization of the various chemical species can not be expected to be stochiometric. Experiments are required to determine isotope-specific volatilization rates. At present, the best approximation would be to assume that release rates are roughly stochiometric.

6.4.3 Relative Consequence Indices

The relative consequence of oxidation of the reference metals is extremely dependent on the temperatures involved in an accident. Nonetheless, it is possible to define three indices to quantify the

relative effects.

The relative consequence index to avoid temperatures (T_{1t}) where significant oxidation begins to occur is defined as

$$RCI_{SO}^{T} = \frac{T_{1t}(HT\text{-}9) - T_{o}(HT\text{-}9)}{T_{1t} - T_{o}} \tag{6.30}$$

where T_{o} = operating temperature.

The temperature margin, $T_{1t} - T_{o}$, for HT-9 is the highest of the metals studied, about 950 °C. The temperature for rapid oxidation of Mo (700 °C) is below that of the typical operating temperature (~900 °C). Thus the RCI_{SO}^{T} is infinite. This case is particularly troublesome since a single failure that allows air to enter the torus would have extremely serious results without the need for any other accident mechanism to raise temperatures.

The relative consequence index to minimize oxidation is defined as

$$RCI_{SO}^{ox} = \dot{m}_{ox}/1 \text{ mm/day} \tag{6.31}$$

Since the oxidation rate varies with temperature, the RCI_{SO}^{ox} has a considerable range. If temperatures are low, all oxidation rates are nil, so the index goes to zero. This is why a normalization had to be used. The value of 1 mm/day is a somewhat arbitrary normalization constant. The upper bound of the index is established at oxidation rates at about 1300 °C since that is a typical maximum temperature expected in a lithium fire (Chapter 5).

The relative consequence index to minimize volatilization defined as

$$RCI_{SO}^{V} = \dot{m}_{vol}/1 \text{ mm/day} \tag{6.32}$$

in similar fashion to RCI_{SO}^{ox}. The only difference is in the case of V-alloys. The relative consequence indices for structural oxidation are listed in Table 6.10. Low values are preferred.

TABLE 10

Relative Consequence Indices from Structural Oxidation

Indices	RCI_{SO}^{T}	RCI_{SO}^{ox}	RCI_{SO}^{v}
Purpose	Avoid Oxidation Transition Temperatures*	Minimize Oxidation	Minimize Volatilization
316 SS	1.7	0-2.2	0-2.2
HT-9	1.0	0-2.2	0-2.2
V-alloy	9.5	0-147	0-0.1
TZM	∞*	0-220	0-220

*Since the typical operating temperature of a TZM wall would be above the transition temperature, the index becomes infinite.

REFERENCES

6.1 N.M. Laurendream, "The Ignition Characteristics of Metals in Oxygen Atmospheres," Technical Report #851, Dept. Aerospace and Mechanical Sciences, Princeton University, 10/68.

6.2 A.F. Robinson, Ed., Ignition, Heat Release, and Noncombustibility of Materials, 1971.

6.3 R.A. Rhein, "The Ignition of Powered Metals in Nitrogen and in Carbon Dioxide," JPL-TR-32-679 (9/64).

6.4 R.A. Rhein, "The Utilization of Powdered Metals as Fuels in the Atmosphere of Venus, Earth, and Mars," JPL-TR-32-1073 (2/67).

6.5 C.C. Baker, "STARFIRE," ANL/FPP-80-1, 1980.

6.6 E.A. Gulbransen, and S.A. Jansson, "Vaporization Chemistry in the Oxidation of Carbon, Silicon, Chromium, Molybdenum, and Niobium," paper in Heterogeneous Kinetics at Elevated Temperatures edited by G.R. Belton and W.L. Worrell, 1969.

6.7 P. Kofstad, High Temperature Oxidation of Metals, 1966.

6.8 O. Kubaschewski, and B.E. Hopkins, Oxidation of Metals and Alloys, 1962.

6.9 E.A. Gulbransen, "Thermochemistry and the Oxidation of Refractory Metals at High Temperatures," Corrosion, 26(1), 1970, p. 19.

6.10 S. Mrowec and T. Werber, Gas Corrosion of Metals, translated by W. Bartoszewki, NTIS Number, PB-283-054-T (1978), p. 171.

6.11 O. Kubaschewski and B.E. Hopkins, "Oxidation Mechanisms of Niobium, Tantalum, Molybdenum and Tungsten," J. Less Common Metals, 2, 172 (1960).

6.12 H. Jehm, "Reazioni dei Metalli dei Gruppi VIa e Va con Ossigeno, Vapore Acqueo ed Aria a Temperature Elevate e Basse Pressioni," La Metallurgia Italiana, 66, (12), 1974, pp. 651-8.

6.13 E.S. Jones, J.F. Mosher, R. Speiser, and V.W. Spretnak, "The Oxidation of Molybdenum," Corrosion, 14 (1958), p. 20.

6.14 E.T. Turkdogan, P. Griereson, L.S. Darken, "Enhancement of Diffusion-Limited Rates of Vaporization of Metals," J. Physical Chemistry, 67(8), p. 1947 (1963).

6.15 E.S. Bartlett and D.N. Williams, "The Oxidation Rate of Molybdenum in Air," TRANS AIME, 212 (1958), p. 280.

6.16 H.C. Graham and H.H. Davis, "Oxidation/Vaporization Kinetics of Cr_2O_3," J. American Ceramic Society, 54(2).

6.17 JANAF Thermochemical Data, 1971.

6.18 O. Kubaschewski and C.B. Alcock, Metallurgical Thermochemistry, 1979.

6.19 A. Block-Bolten, "Equilibria in the Liquid System V_2O_5-V_2O_4 at Temperatures up to 1130°K," Canadian Journal of Chemistry, 54(12), 1976, pp. 1967-70.

6.20 H.L. Schick, Thermodynamics of Certain Refractory Compounds, 1966.

6.21 C.E. Wicks and F.E. Block, Thermodynamic Properties of 65 Elements—Their Oxides, Halides, Carbides, and Nitrides, U.S. Bureau of Mines, Bulletin 605, 1963.

6.22 W.R. Price and J. Stringer, "The Oxidation of Vanadium at High Temperatures," J. Less Common Metals, 8, (1965), p. 165.

6.23 W.R. Price, S.J. Kennett, and J. Stringer, "The Oxidation of Vanadium in the Temperature Range 700 - 1000°C: The Non-Linear Rate Law," J. Less Common Metals, 12 (1967), p. 318.

6.24 E.A. Gulbransen and K.F. Andrew, "The Kinetics of the Reactions of Beryllium with Oxygen and Nitrogen and the Effect of Oxide and Nitride Films on its Vapor Pressure," J. Electrochemical Society, 97 (1950), p. 383.

6.25 W.E. Berry, Corrosion in Nuclear Applications, 1971.

6.26 "Fire Hazard of Beryllium," Nuclear Safety, 8 (#1, Fall 1966), p. 26.

6.27 M.S. Tillack and M.S. Kazimi, "Development and Verification of the LITFIRE Code for Predicting the Effects of Lithium Spills in Fusion Reactor Containments," PFC/RR-80-11, (7/80).

6.28 D. Gloeikler, F. Jeannot, and C. Gleitzer, "The MoO_3-WO_3 and Li_2O-MoO_3-WO_3 Systems," J. Less Common Metals, 36 (1974), p. 41-45.

6.29 C.S. Tedmon, Jr., "The Effect of Oxide Volatilization on the Oxidation Kenetics of Cr and Fe-Cr Alloys," J. Electrochemical Society, 113 (8, August 1966), pp. 766-768.

6.30 W.C. Hagel, "Factors Controlling the High-Temperature Oxidation of Chromium," Transactions A.S.M., 56 (1963), pp. 583-599.

6.31 H.C. Graham and H.H. Davis, "Oxidation/Vaporization Kinetics of Cr_2O_3," J. American Ceramic Society, 54 (2, Feb. 1971), pp. 89-93.

6.32 S.S. Bremmer, "Catastrophic Oxidation of Some Molybdenum Containing Alloys," J. Electrochemical Society, 102 (1955), p. 16.

6.33 P.J. Grobner, "Oxidation Resistance of Chromium-Molybdenum Steels," Report #RP-32-76-07 of Climax Molybdenum Co. of Michigan, 1/78.

6.34 P.J. Grobner, "Effect of Composition and Contamination on Accelerated Oxidation of Iron-Chromium-Molybdenum Alloys," Report #RP-32-78-01 of Climax Molybdenum Co. of Michigan, 5/79.

6.35 P.J. Grobner, "Effect of Small Additions of Reactive Elements on Accelerated Oxidation of 14% Cr - 4% Mo Steel," Report #RP-32-79-01 of Climax Molybdenum of Michigan, 6/80.

6.36 M.G. Gemmill, The Technology and Properties of Ferrous Alloys for High Temperature Use, 1966.

6.37 L. Baker, Jr., "Metal-Water Reactions," Nuclear Safety, 7 (#1, Fall 1965), p. 25.

6.38 L. Baker, Jr., "Metal-Water Reactions," Nuclear Safety, 8 (#1, Fall 1966), p. 20.

CHAPTER 7. CORROSION PRODUCT FORMATION AND TRANSPORT

Among the materials studied, there are seven coolant/structural metal combinations. Each of these has some corrosion potential. Furthermore, the various breeders may also cause corrosion problems. Whereas corrosion does not present an energy source to drive accidents, a variety of safety-related concerns do exist.

7.1 Problem Description

In this chapter, the formation and transport of structural corrosion products are studied. Both corrosion and neutron sputtering are possible driving mechanisms. Only corrosion rates from correct operation are considered. Rapid oxidation problems at elevated temperatures are discussed in Chapter 6. It is assumed that the reactor systems in question are operated correctly. As discussed in Section 7.2.1, the corrosion performance of a reactor is strongly dependent on its appropriate operation. Thus, the goal is a realistic estimate for each case. Incorrect operation (poor chemistry control, contaminants from construction) would be expected to worsen corrosion-related problems.

7.1.1 Possible Corrosion-Related Problems

Over the life of the blanket, structural material will be slowly removed from coolant tube and breeder zone walls. The mass involved can cause plugging of tubes, fouling of valves, clogging of filters and degradation of heat transfer as it moves around loops and deposits on surfaces. The actual severity of these effects is difficult to predict as deposition patterns are often irregular, particularly in complex flow geometries.

The corrosion products originating in the blanket will be radioactive. Thus, corrosion provides a means of radioactivity mobilization. The deposition of this material outside of the blanket may cause a radiation field throughout coolant and breeder piping, complicating maintenance. Although the coolant loop inventory represents only a very small fraction of the total structural inventory, it is already mobile by definition. If piping integrity is lost, the corrosion products may escape to the building. Finally, the fluid processing units, impurity control or tritium processing, may be contaminated with radioactivity, potentially making operation and maintenance more difficult.

7.1.2 Material Combinations Studied

The eleven combinations of coolant/breeder/structure include seven coolant/structure and eight breeder/structure combinations. These are listed in Table 7.1. Coolant-controlled corrosion can be expected to be more significant than breeder-controlled corrosion because of 1) higher fluid velocities which increase corrosion rates, 2) higher mass flow rates which make it more difficult to minimize impurities, 3) more metal surface area which causes more material to corrode, and 4) potentially higher temperature drops around the loop which may increase mass transfer effects. For these reasons, emphasis was placed on the coolant-related corrosion case. Comments on the $LiAlO_2$ (He purge stream) case are included in the helium Section 7.3; comments on Li and $Li_{17}Pb_{83}$ are included in Section 7.4.

TABLE 7.1

Material Combinations for Corrosion Modeling

Coolant	Structure Metal
Water	316 SS
Water	HT-9
Helium	316 SS
Helium	HT-9
Lithium	316 SS
Lithium	V-alloy
Flibe	TZM

Breeder	Structure Metal
$LiAlO_2$ (He purge)	316 SS
$LiAlO_2$ (He purge)	HT-9
$Li_{17}Pb_{83}$	316 SS
$Li_{17}Pb_{83}$	HT-9
Lithium	316 SS
Lithium	HT-9
Lithium	V-alloy
Lithium	TZM

7.1.3 Approach and Scope of Work

The safety problems related to corrosion are difficult to quantify. Unlike the other comparison bases, obvious quantitative figures of merit do not exist.

Understanding is insufficient to reduce problems like plugging to a single quantitative measure. This contrasts with other quantitative measures like time to melting, oxidation rate, temperature rise, and latent fatalities. Nonetheless, seven variables were selected for emphasis, listed in Table 7.2. The easiest parameter to determine for any system is the corrosion rate itself. However, for many systems there is significant uncertainty even in this rate. Since all other parameters are influenced by the corrosion rate, it is easily seen that the uncertainty for the other parameters is large, especially for less-studied combinations. As will be seen, in some cases the lack of knowledge of system behavior was so severe that certain parameters were not calculated.

All of the variables in Table 7.2 can be related to some safety concern. The corrosion rate controls the overall problem; no corrosion, no problem. The corrosion product concentration in the coolant is a measure of the degree of contamination and may influence the coolant path plugging. The wall deposit thickness is related to heat transfer fouling and perhaps plugging. The total activity release rate to the coolant is analogous to the corrosion rate. The inventory in the coolant is always releasable. Together the wall and coolant inventory determine the plant system contamination level. Finally, whatever fraction of the wall and coolant inventory that is releasable represents potential radioactivity mobilization.

TABLE 7.2

Corrosion-Related Parameters of Concern

Parameter	Symbol	Unit
Wall Corrosion Rate	$\dot{d}$	kg/m^2-sec, or μm/yr
Corrosion Product Coolant Concentration	C_T	kg metal/m^3 fluid
Wall Deposition Thickness	W	kg metal/m^2 wall
Blanket Radioactivity Surface Release Rate	$\dot{INV}$	Ci/yr
Coolant (Fluid) Activity Inventory	INV_c	Ci
Wall Activity Inventory	INV_w	Ci
Releasable Activity Inventory	INV_r	Ci

The basic approach will be to first explore the basic fluid/metal behavior and state of knowledge and operating technology. Then the corrosion rate is determined. The initial transient behavior is not of concern; rather, the long-term steady state corrosion behavior will determine conditions through most of the blanket lifetime. Unfortunately, relatively little corrosion data exists for fluid flowing tests for long times (months). This is especially true for the more exotic fluid/metal systems. Most screening tests of new systems are static and short-time which do not necessarily indicate quantitative performance in large reactor systems (although they are useful to eliminate poor or fair combinations).

Based on available data and modeling understanding, the other six parameters are estimated where possible. The cases range from 316 SS/water, which is well understood, to more exotic cases like flibe/TZM and Li/V, for which little quantitative experimental information exists.

The breeder cases will not be examined in as much detail, for the reasons outlined above. The primary focus will be on whether a significant amount of non-tritium radioactivity could be mobile. In such cases, the operation and design of tritium breeder processing units may be complicated due to the presence of gamma activity.

7.1.4 Magnetic Effect on Corrosion

The presence of an intense magnetic field in the blanket represents a potentially significant difference in the corrosion environment from nuclear fission reactors. In fission systems, the problems from radioactivity of corroded material have meant that radioactivity released due to extremely low corrosion rates was significant. Non-nuclear system

corrosion rates can be higher with less concern. Only in fusion systems is there concern for low corrosion regimes in an intense magnetic environment. The possible impact of the magnetic field on corrosion-related system behavior involves many possible interactions.

7.1.4.1 Results in STARFIRE

A wide range of possible interactions for the 316 SS/water system of STARFIRE have been examined (Appendix D), which were incorporated into the STARFIRE design study (Appendix G of reference [7.1]). These were as follows: 1) change in ion diffusion in water due to $v \times B$ force; 2) change in ion solid-state diffusion due to $v \times B$ force; 3) induced film stresses from magnetostriction; 4) acceleration of corrosion rate by induced currents; 5) increased deposition of coolant particles due to field gradients; 6) corrosion rate alteration by change of film microstructure; and 7) corrosion rate alteration by the presence of ferritic steel produced in austenite steel. An eighth problem (not addressed in Appendix D for water) is possible galvanic cell behavior, an electrochemical concern. Only the last three were found to have potential for significant impact on overall corrosion behavior.

As noted in Appendix D, some magnetic films produced in strong magnetic fields show preferential orientation of domains [7.2], [7.3]. For 316 SS steel, the oxide layer is magnetic while the base alloy is not. Furthermore, neutron irradiation and/or welding may transform part of the bulk alloy to a ferritic structure, also magnetic. Thus, there is the potential for the oxide film microstructure to be altered or for the bulk alloy to behave differently (ferritic steel corrodes faster). The magnitude of any effect on corrosion from these concerns can only be

determined by experiment. If necessary, a mitigating technique for the oxide film microstructure problem could be to operate the blanket long enough to provide an initial film before starting the magnetic coils. The effect of any microstructure or alloy phase can not be incorporated into the present corrosion examination.

It should be noted that of the alloys studied, if significant, this problem would be more severe for austenitic steels in oxidizing environments, like water or helium. For 316 SS, both the oxide film and alloy effect produce material that is magnetitic, differing from the bulk alloy (non-magnetitic). For ferritic steel (e.g., HT-9), both alloy and oxide film are magnetic—corrosion makes little difference. Although refractory metal behavior in liquid metals and salts is not as well understood, the alloy surface does not exhibit oxide film formation (see sections 7.4, 7.5). Rather, the alloy surface becomes depleted in certain alloy constituents. For TZM and V-alloys, this does not produce a phase change: alloy and pure bulk metal are both BCC structures.

The field gradient in a blanket may influence the behavior of the electrically charged corrosion particles in water. Filters using very high field gradients are effective in removing these particles [7.4.1]. Unfortunately, if field gradients were high enough and flow velocities sufficiently low, particles would be preferentially deposited. As noted in reference [7.1], this is unlikely except in very low flow areas. The remaining potential magnetic effect is electrochemical.

7.1.4.2 Electrochemical Concerns

Even in a steady-state mode fusion device, currents may be induced due to movement of a conductor. Induced currents in pulsed devices could

be more significant. As a conducting fluid moves through the blanket, currents will be induced, see Fig. 7.1. The concern is that this current (corresponding voltage) may drive electrochemical reactions.

As noted in Reference [7.5], the influence of the apparent voltage from wall into fluid is given by

$$V = V^\circ - \left[\frac{RT}{nf} \times \ln \left\{\frac{[C_w]^w\,[C_x]^x}{[C_y]^y\,[C_z]^z}\right\}\right] \tag{7.1}$$

where V = apparent voltage in galvanic cell

V° = standard voltage based on standard-state half reaction voltages.

n = number of electrons per reaction

f = Faraday's constant, 96,493.5 coulomb/equivalent

R = gas constant, 8.31470 J/°C equivalent

C_I = concentration of species I in fluid which is written for the electrochemical reaction:

$$yY + zZ \leftrightarrow wW + xX \tag{7.2}$$

For $V > 0$, the reaction proceeds spontaneously. The induced voltage has the effect of lowering the reaction threshold. Thus, for the reaction

$$ThF_4 + 2Ni \rightarrow 2NiF_2 + Th \tag{7.3}$$

a 10-fold Ni ion concentration increase is produced by an applied voltage of 0.0916 volts [7.5]. Moir et al. [7.5] indicate that the critical

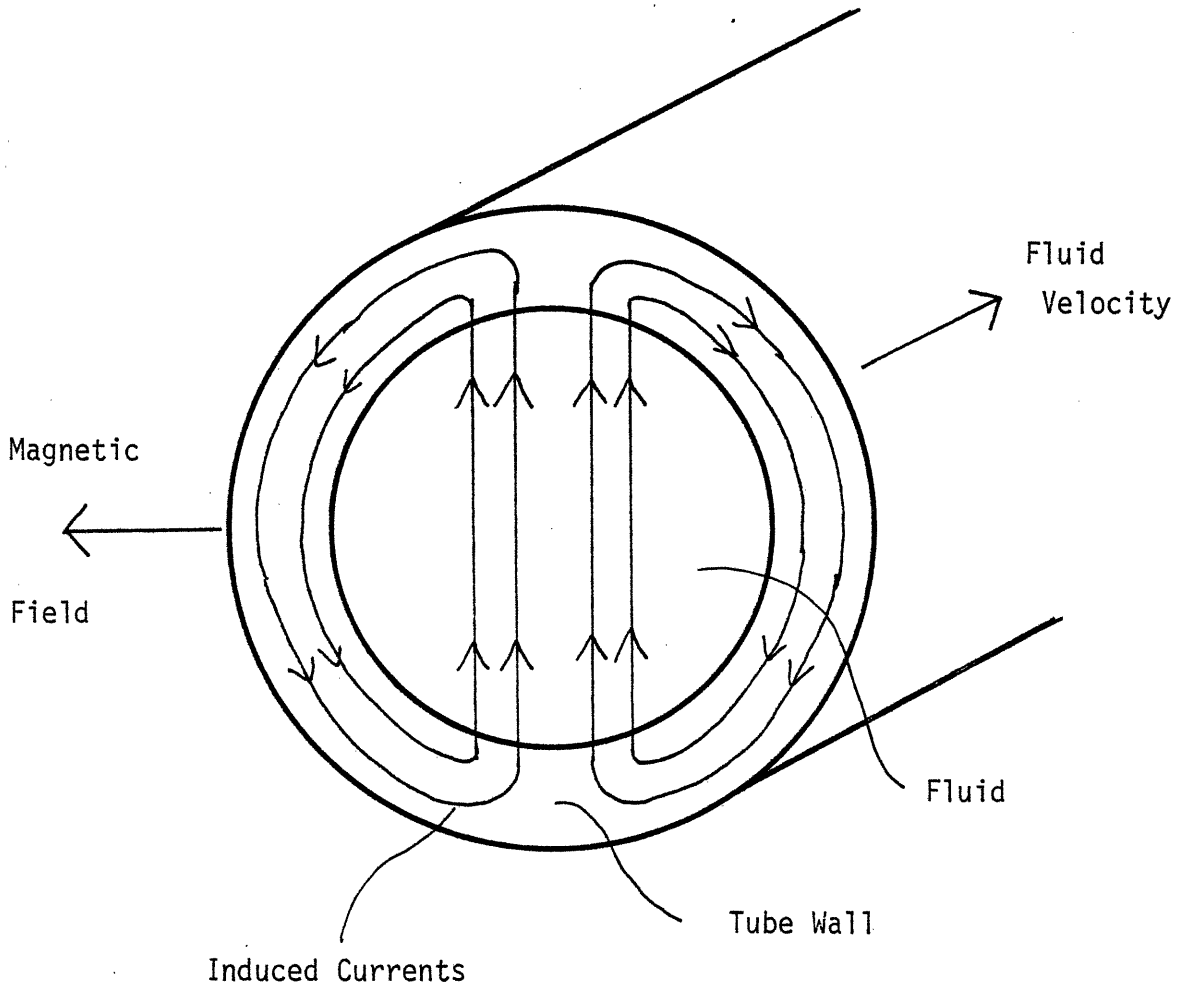

Fig. 7.1: Induced Currents in a Conducting Fluid Moving Perpendicular to the Magnetic Field

question is whether the ion concentration is raised above the solubility. Their resulting design criterion is to keep induced voltages below one volt in their molten salt coolant [7.5]. Another study suggested 0.2 volts for flibe [7.6]. McManamy [7.7] has noted that the exact voltage which increases corrosion will likely be determined by experiment. He adopted a typical value of 0.25 volts. Standard reaction voltages themselves are typically quoted only within 0.1 volts. Thus, it is concluded that the threshold voltage which may accelerate corrosion lies somewhere between 0.1 - 1.0 volts.

At present it is not possible to adequately determine the actual magnitudes of voltages induced in a fluid. The following is a simple examination which may not be conservative. It is sufficient to show that induced currents and voltages may be high enough to be a problem, at least for some fluids. Further experiments are needed in this area. Miley [7.8] gives equations for the self-consistent induced currents and electric field in the fluid and wall:

$$I_f = 2\sigma_f \, r \, L \, (vB-E) \tag{7.4}$$

$$I_w = 2\sigma_w \, d_w \, L \, (E) \tag{7.5}$$

where r = tube radius

d = tube wall thickness

E = electric field

v = fluid velocity

f = fluid properties (subscript)

w = wall properties (subscript)

By defining the MHD parameter

$$c = \frac{\sigma_w d}{\sigma_f r} \tag{7.6}$$

and by equating I_f and I_w from Eqs. (7.4) and (7.5), the electric field is obtained as:

$$E = vB/(1+c) \tag{7.7}$$

For a tube of radius r, the voltage drop would be approximated by

$$V = rvB/(1+c) \tag{7.8}$$

For typical blanket parameters, the possible voltages are calculated. For water (water chemistry same as STARFIRE), with $B \leq 10$ T and $v_{max} = 10$ m/s ($d \sim 1$ mm, $r \sim 1$ cm) in the blanket, the voltages are below 10^{-7} volts, i.e., completely insignificant. The conductance of helium is even lower, hence induced voltages are lower.

For flibe ($B \leq 10$ T, $v_{max} = 10$ m/s, $d \sim 1$ mm, $r \sim 1$ cm, wall = TZM), the voltage is of order 0.5×10^{-3} volts. Although this voltage is insignificant for these design parameters, it is noted that induced voltages in the hybrid study molten salt design were higher, about 1 volt. Thus, for a molten salt, the induced voltage can be a design constraint.

For lithium designs, the conductivity of the fluid is similar to the metal, and $1+c$ approaches 1. Then the induced voltage is simply

$$V = r\,v\,B \tag{7.9}$$

For parameters typical of the present reference designs ($r \sim 1$ cm, $v \lesssim 1$ m/s, $B \lesssim 10$ T), the voltage is about 0.1 volts. Thus, electrochemical corrosion

appears a potentially serious concern in lithium designs. For lithium-cooled blanket, the magnetic field is seen to cause serious electrochemical corrosion and MHD pumping losses (Chapter 2). It is anticipated that an operational design would be forced to have sufficiently low induced voltages, such that corrosion would not be significantly increased.

7.2 Water Corrosion

Of the systems studied, the water/316 SS combination is best understood. The LWR industry has extensive experience in water corrosion problems. Based on available data and knowledge of reactor system behavior, a model was developed for use in the STARFIRE study (see Appendix D) to determine relevant corrosion results. The model description is briefly summarized below. The results for water corrosion of 316 SS and HT-9 blankets are described.

7.2.1 STARFIRE Model (Appendix D)

The possible magnetic field interaction with corrosion processes was discussed in Section 7.1.4. The other primary potential difference between fission and fusion is in the area of appropriate water chemistry operation. The reference case is a combination of either 316 SS or HT-9 in the blanket with Inconel steam generators. In the 316 SS case, the STARFIRE design chose Inconel for the steam generator part of the loop as is common in current PWR's. In the HT-9 case, selection of Inconel has the advantages of consistency with the 316 SS case and a lower corrosion rate than HT-9. Unlike most current PWR's, there is no Zircoloy cladding; rather, the fusion system is more analogous to stainless steel clad PWR's. The only water chemistry difference from fission was shown in STARFIRE to possibly be tritium production from LiOH additions

used to provide high pH. The harder fusion neutron flux will produce significant tritium from even ^{7}Li. However, for STARFIRE conditions, the rate of tritium production at desired LiOH concentrations was tolerable. If power levels were higher or desired tritium production in the coolant were lower, an alternative corrosion control additive would be needed; otherwise, optimum fusion water chemistry is taken to be the same as for fission.

The coolant loop is modeled as consisting of separate compartments. The mass flows are shown in Fig. 7.2. The rate constants are determined from experiment and are discussed in Section 7.2.2. For the present study, the long-term steady state behavior is most important. Water systems show initially higher corrosion rates for a few months and then reach a lower steady state rate [7.9, 7.10]. All components in the mass balance are assumed to reach steady-state conditions.

Therefore, the net production of corrosion products balances the net sink:

$$\sum_i \dot{d}_i A_i = Q_s C_s + Q_c C_c \tag{7.10}$$

where $\dot{d}_i$ = corrosion rate for ith surface

Q_s = filtration rate of soluble ions

Q_c = filtration rate of insoluble crud (term used in this field for particulates)

C_s = concentration of ions

C_c = concentration of crud particles

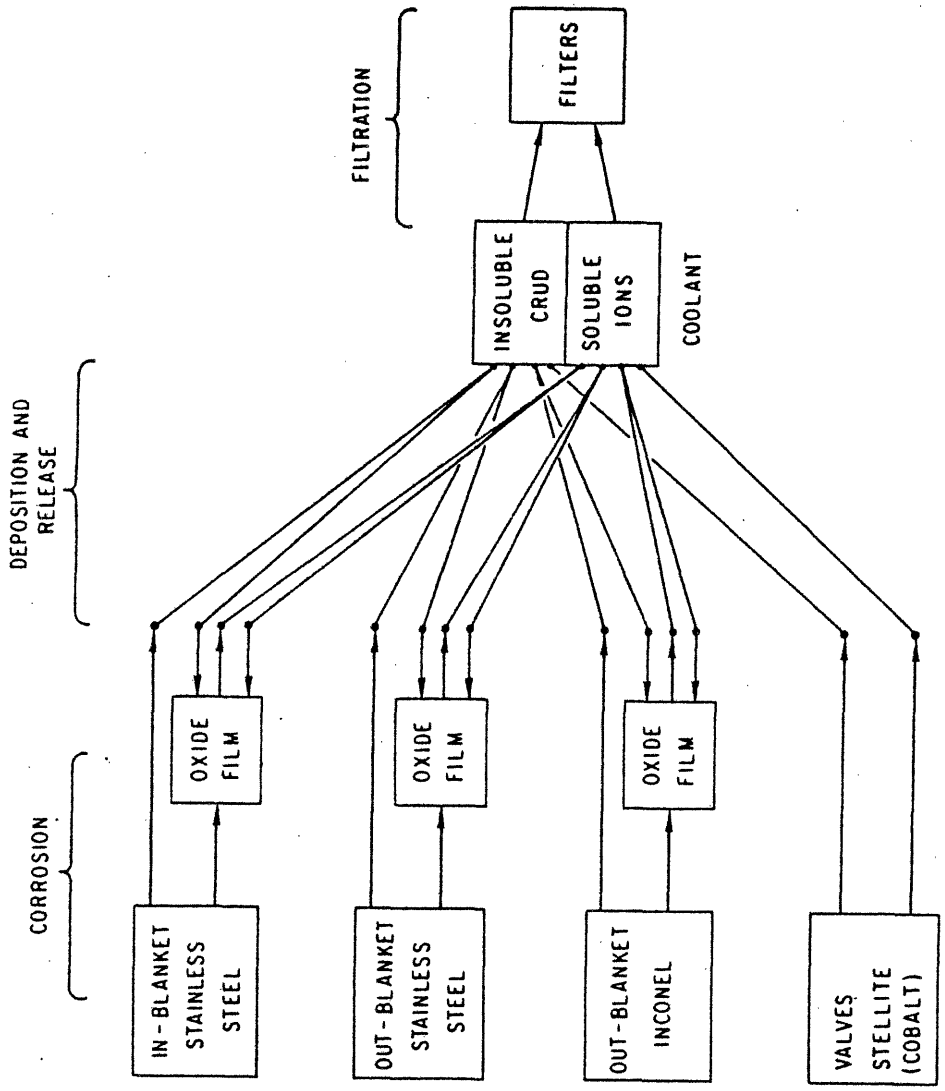

Fig. 7.2: Water Corrosion Product Transport Model

Part (about one-third) of the base corrosion rate is directly released to the water ($\dot{d}_i^r$), the remainder increases the oxide film thickness. The released metal is in either soluble ion or particulate (typically called crud) form. The mass balance for the oxide film is written as:

$$\sum_i \dot{d}_i + k_s C_s + k_c C_c = \sum_i (\dot{d}_i^r + r_i W_i) \qquad (7.11)$$

where k_s, k_c = deposition rates

r_i = release rate

W_i = oxide film thickness

Equation (7.10) determines the concentration levels for each element. Then, Eq. (7.11) is used to calculate the wall oxide thickness. The increase in radioactivity follows the same behavior. The sources for radioactive species in the circulating coolant are 1) corrosion products from irradiated blanket materials, 2) blanket oxide material that has been transported from outside the blanket and deposited in the radiation zone, and 3) activation of material in transport in the coolant. The contribution of the third source was found to be insignificant.

7.2.2 Water Corrosion Model Parameters

The parameters specific to the 316 SS blanket design (areas, flow rates, etc.) are taken from the STARFIRE design (see Appendix C). The corrosion model parameters are listed in Table 7.3. Since the surface oxides in a HT-9 system are basically the same as for 316 SS, the deposition, release, and ion solubilities rates are assumed the same. The corrosion rate ($\dot{d}$) and corrosion release rate ($\dot{d}^r$) are about three

TABLE 7.3

Water Corrosion Transport Rates

Corrosion Rate (kg/m^2-sec)*, $\dot{d}$	
316 SS	1.14×10^{-10}
HT-9	3.42×10^{-10}
Corrosion Release Rate (kg/m^2-sec), $\dot{d}^r$	
316 SS	3.8×10^{-11}
HT-9	1.14×10^{-10}
Deposition Rate (kg/m^2-s)	
Crud Particles, k_c	5×10^{-3}
Ions, k_s	20×10^{-3}
Release Rate (sec^{-1})	
In-blanket, r_{in}	1.8×10^{-6}
Out-blanket, r_{out}	1×10^{-7}

*for steels, 3.8×10^{-11} kg/m^2-sec = 1 mg/dm^2-month = 0.15 μm/yr

times the 316 SS values based on available data [7.11, 7.12]. It should be emphasized that the corrosion rates assume good achievable water chemistry control; however, operating reactors can have corrosion rates an order of magnitude higher if mistakes are made before or during operation. Water corrosion is heavily dependent on water chemistry. The radioactivity calculations are based on the average specific radioactivity in STARFIRE (10 year operation, see Appendix B and Chapter 8).

7.2.3 Steel Results

The concentrations of relevant elements are shown in Table 7.4. Use of Inconel steam generators reduces the differences between 316 SS and HT-9. Whereas the HT-9 corrosion rate is three times that of 316 SS, the resulting total mass coolant concentrations and wall deposit thickness are only about 1.5 times higher. The overall mass transport results are given in Table 7.5. For the HT-9/Inconel system, the major source of elemental cobalt may be transmutation of nickel from Inconel deposited in the blanket.

It is also possible to estimate the amount of metal releasable to the reactor building in the event of coolant loss and corresponding depressurization. The reference STARFIRE design divided the coolant into two equivalent loops. Hence, any single failure could only mobilize contents of one loop. The critical question is the determination of how much of the wall deposits are loose enough to be removed by the rapid depressurization of the coolant. As indicated in Reference [7.1], three cases which range from optimistic to pessimistic are as follows:

1. The entire coolant from one loop empties with no material from the wall.

TABLE 7.4

Coolant Elemental Concentations
(ppb - μg metal/kg coolant)

Element	C_s (ions)	316 SS		HT-9	
		C_{crud}	C_{total}	C_{crud}	C_{total}
Fe	3.8	20.1	23.9	39.4	43.2
Ni	0.7	9.6	10.3	7.9	8.6
Cr	$\lesssim$0.1	6.0	6.1	8.2	8.3
Mn	$\lesssim$0.3	0.2	0.51	0.3	0.6
Co	0.003	0.018	0.021	low	low

TABLE 7.5

Calculated Mass Deposits from Water Corrosion

	316 SS Design	HT-9 Design
Total Concentration in Coolant, C_T $\left(\frac{\text{mg metal}}{\text{kg water}}\right)$	41	61
Deposit Thickness In-Blanket, W_{in}(g metal/m^2)	0.20	0.34
Deposit Thickness Out-Blanket W_{out}(g metal/m^2)	3.6	6.0

2. During crud bursts and shutdown situations in PWR's, the crud concentration tends to increase by factors of 100-200. Added conservatism due to the more harsh environment involved might raise that to a factor of 250.

3. An upper bound on mobilized material is obtained by assuming that the entire outer surface oxide layer is removed (equals one-half of the total oxide depth).

The resulting amounts of mobilized material is shown in Table 7.6. Again, the HT-9 design is about 1.5 times that of 316 SS.

Based on calculations with STARFIRE (316 SS) blanket activity (see Appendix D), seven isotopes were selected for transport calculations. All have been detected in PWR coolants: ^{60}Co, ^{58}Co, ^{55}Fe, ^{59}Fe, ^{51}Cr, ^{54}Mn, and ^{56}Mn. These dominate PWR non-fission product coolant activity; except for ^{95}Zr which would not be present in STARFIRE. They represent 91% of the blanket activity for STARFIRE at shutdown (the dominant missing isotope is ^{99}Mo, which has not been previously detected in PWR coolants) and 96% of the activity ten days after shutdown. These are thus the most important isotopes for operating contamination and release calculations. For isotopes of interest, the contribution of activity from coolant dwell time in the blanket is insignificant. The remaining sources are release of irradiated blanket material and activation of in-blanket deposits of material originating out of the blanket. Table 7.7 shows the ratio of overall wall activity from in-blanket corrosion to activation of out-blanket material. Most of the activity is seen to originate with the in-blanket steel. This contrasts to the PWR/zircaloy case where the Zr oxide is very adherent and does not produce species like ^{60}Co and ^{58}Co. Of course, the corrosion activity of PWRs does not include the fission

TABLE 7.6

Mobilizable Water Corrosion Products by Coolant Loss from One of Two Loops (Mass of Metal)

		316 SS Design	HT-9 Design
(I)	Entrained Coolant Mass	8 g	12 g
(II)	Crud Burst Approximation	2 kg	3 kg
(III)	Entire Outer Oxide Layer Removed	44 kg	75 kg

TABLE 7.7

Ratio of Wall Activity from
In-Blanket Material to Activated Out-Blanket Material

Isotope	Ratio	$T_{1/2}$
^{60}Co	82	5.27y
^{55}Fe	77	2.4y
^{54}Mn	25	310d
^{58}Co	3.4	72d
^{59}Fe	3.7	45.1d
^{51}Cr	2.0	27.8d
^{56}Mn	0.2	2.576h

product activity which is present there but not in fusion reactors. As seen in Table 7.7, the longer half-life isotopes come primarily from the original blanket steel. Hence, the corrosion and activity of the in-blanket material tends to dominate the corrosion loop radioactivity.

The radioactivity levels in the coolant and on the wall are shown in Table 7.8. The possible radioactivity mobilized can be estimated for the same three cases as for mass mobilization. First, a simple leak of water coolant from one loop would involve 12 Ci. Second, for cases where the wall deposit is disturbed (coolant material increase by a factor of 250), then 2700 Ci could be mobilized. Third, an upper bound would be the removal of the entire outer oxide layer (one-half of total oxide thickness) from one loop, 32 kCi. This corrosponds to $\leq$ 0.001% of the 316 SS blanket inventory. Although it is difficult to determine what fraction of the mobilized material could leave the building, deposition and settling should decrease the material by about 10. Thus, the maximum water corrosion product release to the environment is $\sim$0.0001% of the 316 SS blanket activity inventory.

The specific radioactivity of an HT-9 design was not obtained (see Chapter 8); however, a few comments on HT-9 activity can be made. As indicated in Appendix B, there is very little Ni or Co in HT-9, thus the in-blanket contribution to ^{60}Co and ^{58}Co activity will be eliminated, with some contribution still remaining from activation of Ni from the Inconel corrosion products. The Fe and Mn isotopes will be fractionally higher in HT-9 due to its composition. Based on Table 7.8, a slight (<2-fold) decrease in overall specific activity levels could be expected. However, the amount of mass mobilized in HT-9 is higher. Thus the total

TABLE 7.8

Coolant and Wall Desposit Activity Levels
for 316 SS Blanket

Isotope	mCi/m^3 H_2O	Ci/kg crud metal	mCi/m^2 in-blanket	mCi/m^2 out-blanket
^{60}Co	0.96	32	12.3	86
^{55}Fe	23.3	784	322	2020
^{54}Mn	2.02	68	31	152
^{58}Co	2.64	89	55	118
^{59}Fe	0.06	2	1.2	2
^{51}Cr	3.87	130	96	94
^{56}Mn	8.81	297	278	1
Total	42	1402	800	2500

activity in an HT-9 blanket from corrosion will be roughly the same as for 316 SS. The major difference will be in the isotope mix. The HT-9 case is preferable due to the reduction of the more hazardous ^{60}Co and ^{58}Co species.

7.3 Helium Impurity Corrosion and Sputtering

Helium-cooled designs are generally viewed as having no significant corrosion problems (after elimination of refractory metals), especially with regards to mass transfer and radioactivity. This is unfortunately an oversimplification. Whereas the mass transfer is small, a significant amount of radioactivity may be moved due to sputtering and corrosion.

7.3.1 Combined Corrosion and Sputtering

In any fusion reactor, both corrosion and neutron sputtering of wall material will mobilize some mass and radioactivity. The physical pictures of each process separately and the combined case are shown in Fig. 7.3. The oxide layer (see Section 7.3.3) is up to 0.1 mil (<2.5 μm) in thickness on steels due to typical impurities in the helium. The oxidized material can spall or flake off and be transported around the loop. Bickford has examined the sputtering process and the typical range of the sputtered particles ranges from 400-1300 Å (0.04 - 0.13 μm)[7.13, 7.14]. Thus, the oxide layer will typically be thicker than the range of sputtered particles. Although the exact composition of a fusion helium coolant is unknown, it is expected that the helium environment permits the oxidation of Al, Ti, Si, Mn, and Cr, but the oxygen partial pressures are too low for oxides of Fe, Co, Mo, or Ni to form [7.15]. This assumes the fusion impurity levels are no worse than HTGR conditions, which is

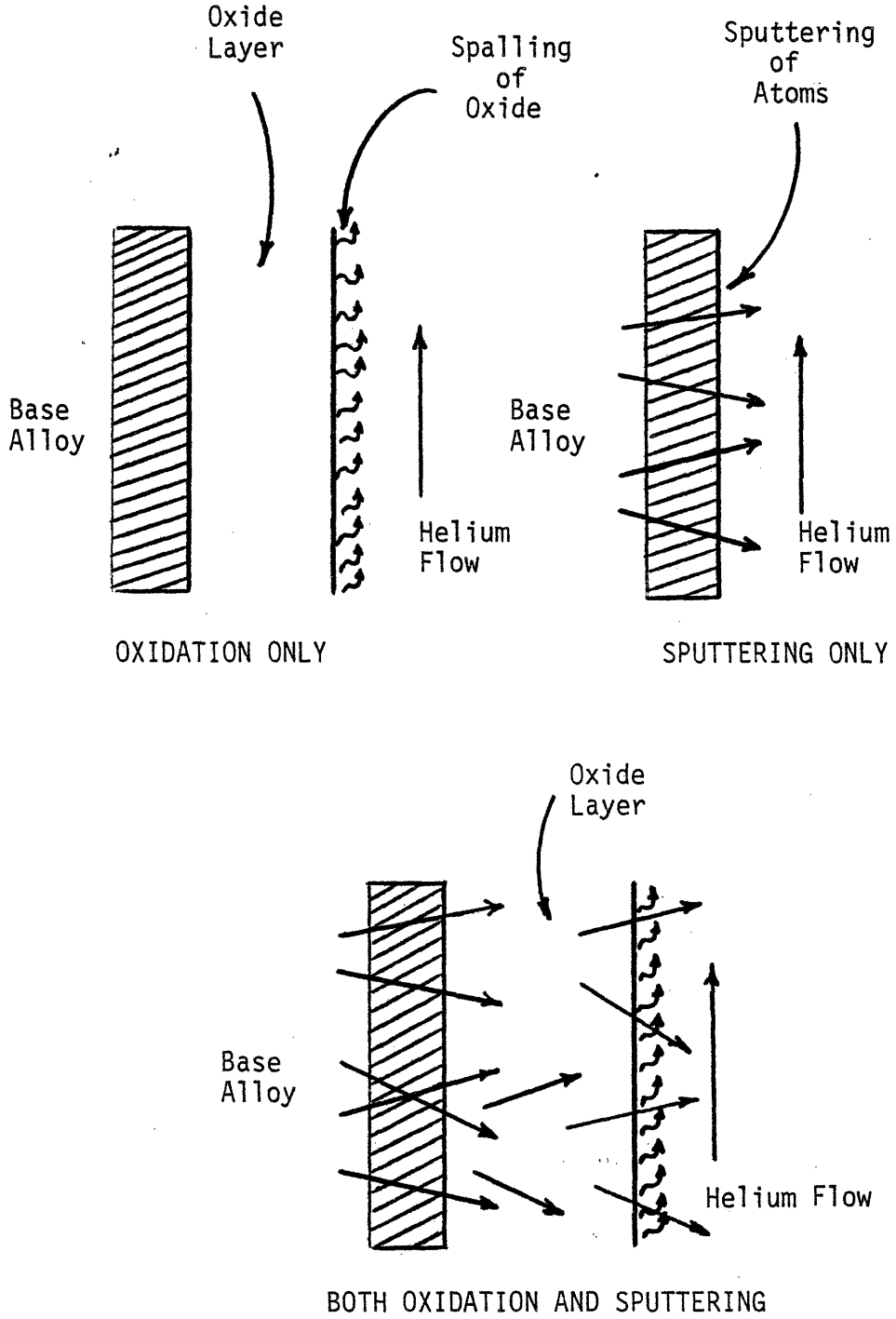

Fig. 7.3: Processes that Remove Atoms from Helium Coolant Tube Surfaces

conservative since the reference fusion designs do not have un-clad graphite in contact with helium--a major problem in HTGR's. Thus, corrosion provides a means for Mn and Cr mobilization while any species may be moved by sputtering, see Fig. 7.4.

Because of the non-homogeneity of the scale, an exact calculation of the movement of non-oxidized sputtered particles through and from the scale would be extremely difficult. Furthermore, the thickness of the scale itself is not well-known. The existing studies of the contribution of sputtering to species transport [e.g., 7.13, 7.14] do not account for the interaction of corrosion scale and sputtering. Due to limitations and complexities of oxide layer data, sputtering is assumed to move atoms directly from bulk material to coolant, ignoring the presence of the oxide layer. In similar fashion, the corrosion contribution to transport neglects the presence of non-oxidized sputtered material; thus, the two processes are separated.

This separation has both possible conservatisms and non-conservatisms compared to the more complete combined case. The separation is conservative since all sputtered particles from the base metal are assumed to reach the coolant, none staying or being delayed in the oxide scale. In reality, these particles can only reach the coolant due to: 1) repeated sputtering by more neutrons or 2) eventually the release of the oxide layer the particles are imbedded in. Thus the separation overestimates the amount of sputter particles released to the coolant which can then deposit downstream.

The non-conservatism is due to the possible oxidation of particles sputtered from the surface. As will be seen, sputtered atoms firmly re-attached themselves to downstream walls; oxidized metal atoms may be

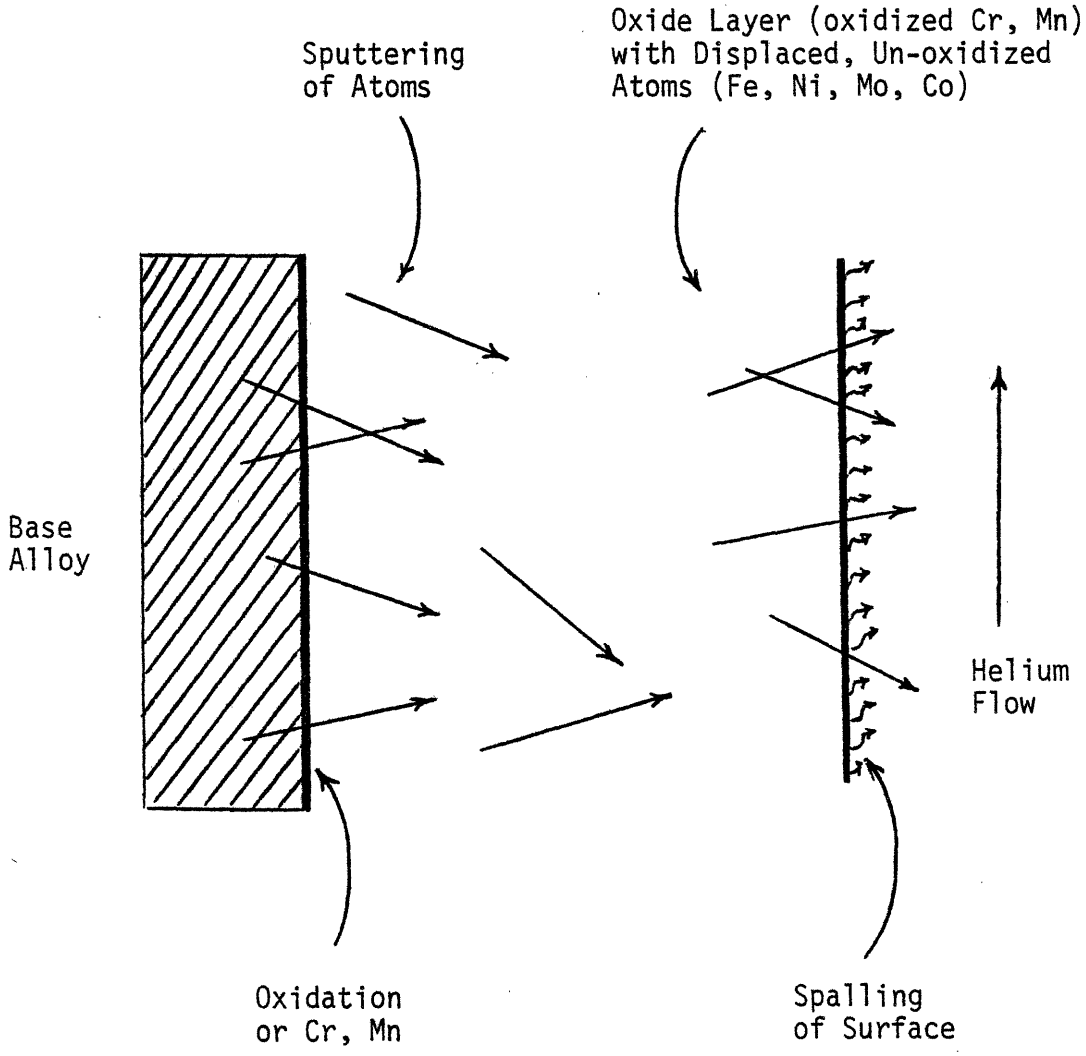

Fig. 7.4: Possible Interaction of Oxidation and Sputtering in Removing Atoms from Helium Coolant Tube Surfaces

loose. Thus, oxidized atoms are more troublesome than single atoms. The presence of oxidants may convert sputtered atoms of Cr, Mn, Al, Ti, or Si to oxide form (only Cr and Mn are of particular concern for steels). This could occur either while the sputtered atoms were imbedded in the scale (quite likely) or in-transit in the coolant. The effect of assuming that all sputtered Cr and Mn becomes oxidized is addressed in Section 7.3.2. In general, it is felt that the separation of corrosion and sputtering effects is a reasonable approximation.

7.3.2 Sputtering Source Term

The 14 MeV neutrons entering the blanket will precipitate various adverse structural effects. Bickford [7.13, 7.14] has examined the problem of neutron sputtering. The basic problem is that neutron sputtering of atoms and direct daughter recoil will eject significant numbers of ions from the wall to the coolant stream. These may then be transported downstream until the low vapor pressure causes the atoms to firmly attach themselves to the wall surface. Hence, radioactivity may migrate around the loop. Tube plugging is not a concern. Furthermore, the material moved is chemically bound to the wall and seemingly non-releasable in an accident. Thus, the only concern from material transported by sputtering is that of contact maintenance.

Bickford [7.13] has calculated the amount of sputtering of activation products due to lattice dynamic neutron sputtering and direct daughter recoil ejection. The analysis necessarily includes many uncertainties such as ion recoil ranges and reaction cross sections. The results are somewhat dependent on the wall geometry, depth into blanket and surface orientation, unlike corrosion.

Given the amount of sputtering and a reference design, Bickford [7.14] calculated the transport of material through the coolant piping. For a tubular design based on an Oak Ridge design [7.16], he found that the material tended to firmly deposit on the downstream wall before passing back through the blanket. The distribution and contact dose rates are given in Table 7.9. The material depositing in the blanket is of relatively little concern since the blanket is already activated. Bickford notes that tube layout and geometry can potentially increase the amount kept within the blanket. The contact dose rates on the non-blanket sections are similar to those experienced in fission reactors [7.14].

By assuming that the inventory reaches steady state, Bickford calculated the entrained and wall inventory, given in Table 7.10. The only loss rate is radioactive decay unlike the water corrosion case. The steady state inventory assumption can be relaxed and the sputtering rates used to calculate the overall inventory for the present study helium design. The detailed transport calculations were not repeated because 1) a detailed helium flow diagram through pipes, headers, etc. would be required, 2) only maintenance is affected whereas the current study is focused on accidental hazards, and 3) the results would likely not be significantly different.

Analysis of Bickford's results indicate that about 40% of the total sputtering came from the first wall. In his design, all tubes are oriented normal to the neutron flux. In the current reference design (see Chapter 2), only the first wall region is normal to the flux. The side flow gaps are parallel to the flux, hence little sputtering of those surfaces is expected. Unfortunately, the design has two coolant surfaces facing away from the plasma which allow forward sputtering at first wall

TABLE 7.9

Contact Dose Rates and Distribution of Wall Activity
[Ref. 7.14]*

	Contact Dose Rates (mR/hr)	Percentage of Activity on each Wall Surface
Blanket	high	17%
Headers, Manifolds	760-10400	5%
Hot Leg Pipe	670	3%
Steam Generator	~100	75%
Cold Leg Pipe and Circulator	~5	<1%

*3.0 MW/m^2 neutron wall loading, helium/316 SS design.

TABLE 7.10

Total Steady State Inventory in Helium Design from Sputtering [Ref. 7.14]*

	Activity Entrained in Coolant (Ci)	Activity on Walls (Ci)
^{51}Cr	7.39×10^{-3}	4.71×10^{3}
^{54}Mn	1.77×10^{-4}	5.13×10^{3}
^{56}Mn	8.07×10^{-1}	8.05×10^{3}
^{57}Co	2.78×10^{-4}	6.96×10^{3}
^{58}Co	1.11×10^{-3}	7.29×10^{3}
^{60}Co	1.23×10^{-5}	2.18×10^{3}
^{99}Mo	5.36×10^{-4}	1.48×10^{2}
Total	0.82 Ci	34,468
extrapolated to 3.6 MW/m^2	$\sim$ 1 Ci	$\sim$ 41 kCI

*3.0 MW/m^2 neutron wall loading, helium/316 SS design.

rates (Fig. 7.5). The equivalent total area experiencing first wall forward sputtering rates for the reference design is about 2,400 m^2. Both daughter and bulk lattice sputtering were scaled linearly from a neutron wall loading of 3.0 MW/m^2 to the reference value of 3.6 MW/m^2.

If the sputtering rate is $\dot{N}_o$, independent of time, then the number of atoms in the loop is given by

$$\frac{d}{dt} N = \dot{N}_o - \lambda N \tag{7.12}$$

Therefore, the rate of charge of loop radioactivity inventory (INV = λN) is given by

$$\frac{d}{dt} (INV) = \lambda \dot{N}_o - \lambda (INV) \tag{7.13}$$

For the isotopes most of interest, only ^{60}Co does not reach near steady state activity levels in the reference operation period of six years. The results are shown in Table 7.11. Coincidentally, the total inventory for this case is very similar to Bickford's case, scaled to the same neutron wall loading.

Finally, the assumption [7.14] that MHD forces do not affect sputtering trajectories was examined. The gyroradius (r) of a particle with energy E(eV) in a magnetic field is given by

$$r(m) = 1.5 \times 10^{-4} \quad \frac{\sqrt{E(eV)}}{B} \tag{7.14}$$

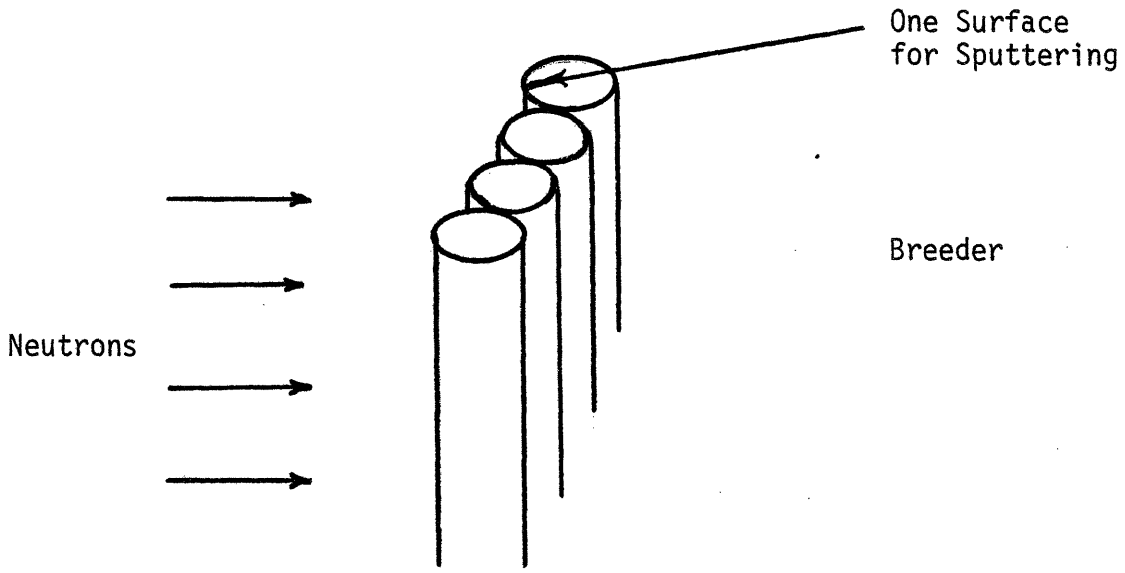

Fig. 7.5a: Bickford's Design [7.13, 7.14], First Wall Composed of Tube Bank; Other Tubes in Breeder Zone are also Normal to Neutron Flux

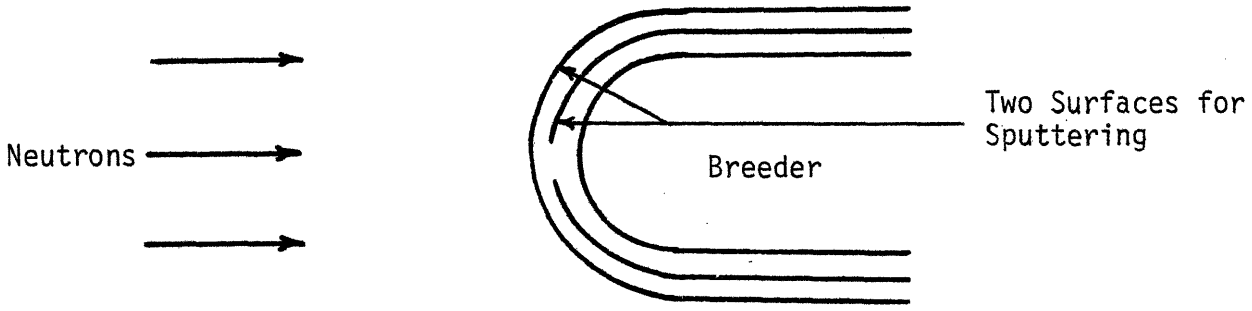

Fig. 7.5b: Reference Design, Pressurized Cylinder, Only the First Wall is Normal to the Neutron Flux

Fig. 7.5: Comparison of First-Wall Concepts for Helium Cooled Designs

TABLE 7.11

Calculated Inventory for Reference Helium/316 SS Design from Sputtering

Isotope	Injection Rate Ci/yr	Inventory at 6 yr, Ci
^{51}Cr	56,800	6,230
^{54}Mn	5,580	6,690
^{56}Mn	2.14×10^{7}	9,080
^{57}Co	8,680	9,330
^{58}Co	26,200	7,440
^{60}Co	399	1,659*
^{99}Mo	15,700	170
Total	2.15×10^{7}	40,599

*Except for ^{60}Co, all isotopes reach steady state in 6 years; the steady state ^{60}Co inventory would be 3,040 Ci.

This can be compared to the range of sputtered particles in metal, about 0.2 μm. For particles with energy as low as 0.025 eV (ambient), the gyroradius is still ten times the range. The initial gyroradius for a 1 MeV particle is about 10^5 times the range. Thus, the gyromotion of a sputtered ion does not significantly alter the range trajectory in the metal. Low energy particles already in the helium (with higher range) might be affected, but this would not change the sputtering source term.

If one assumes that the Cr and Mn species were to be oxidized, the resulting sputtered inventory would not be changed. However, the transport and deposition distribution would be altered. Furthermore, the Mn and Cr isotopes, if oxidized, would not be expected to be firmly attached to the wall. Hence, a depressurization could release them to the building. The assumption that sputtered ^{51}Cr, ^{54}Mn, and ^{56}Mn are oxidized means that 22 kCi of the 41 kCi inventory may be a form releasable to the building.

7.3.3 Corrosion Source Term

If helium were completely pure, there would be no corrosion problem, although helium embrittlement could be of concern. The exact amount of oxidizing impurities in an operating fusion reactor is unknown. "In large coolant systems where relatively large helium make-up fractions are required, it is generally not considered feasible to maintain the oxygen concentration in helium at levels sufficiently low to prevent oxidation of the reactive and refractory metals." [7.11].

Bickford [7.13, 7.14] obtained an oxidation rate by linear extrapolation downward from Rosenwasser and Johnson [7.17] results for 316 SS at 650 and 800°C. At 550°C, this results in a rate of 0.028 μm/yr

penetration rate, assuming steady state spalling of Cr_2O_3.

Actually one might tend to expect a temperature dependence of exp (E/RT) as diffusion is an activated process. Such a dependence results in an extrapolation of 0.113 μm/yr at 500°C and $\lesssim$ 0.05 μm/yr at the reference design temperature of 450°C. It should be noted that no spalling occurred in Rosenwasser and Johnson's test at 650°C, thus even an 0.05 μm/yr steady state penetration rate could lead to zero oxide mobilization.

Mazandaramy [7.15] has noted that the oxide scale is not pure Cr_2O_3, but is rather Mn and Cr rich. The penetration kinetics did not show linear behavior, but rather one of form $k(t - t_0)^{0.35}$. The initial time to any spalling (t_0) was about 1000 hr.

One may obtain a very conservative estimate of the corrosion contribution as follows. Assume a steady state penetration of the steel (0.05 μm/yr) resulting in mobilization of only Cr and Mn species (since the present time scales are long, 6 yr, and linear kinetics have been observed in some tests (e.g., Ref. [7.17]), a steady linear rate is assumed.) Filtration of the oxide dust is taken to be insignificant since only small amounts are involved (may be hard to filter) and the material may deposit quickly. In a water system, filtration is effective partly because the concentration around the loop is fairly uniform. Thus, diversion of a small ($\lesssim$ 1%) amount of flow to be filtered can reduce overall concentration levels and deposition. At present, this can not be assumed true of helium systems. Note that only a fraction of activity in a fission helium system is related to corrosion products. The fission products tend to receive more attention.

Use of this corrosion rate and the alloy composition of steel, a

release of about 3 kg/yr of Cr and Mn metal is predicted. The total steady state inventory of ^{56}Mn (17.2 Ci), ^{54}Mn (9362) and ^{51}Cr (2372) is 12 kCi. The fraction of the material which could be released is unknown; however, the oxides may act as loose dust so a 100% releasable fraction is conservatively assumed. To be consistent with the water case, it is assumed that all the helium is separated into two coolant loops. Therefore, the maximum release of activity would be 6 kCi.

7.3.4 Implications for Solid Breeders

In most designs incorporating a solid breeder, a helium purge stream is included to continuously remove tritium from the blanket. Structural activity (including gammas) may enter this stream and contaminate the tritium processing loop in one of four ways: 1) sputtering of wall material into purge stream, 2) oxidation and release of wall material due to helium impurities, 3) oxidation and release of wall material due to metal-breeder interaction, 4) leakage of coolant into the breeder chamber.

The steel enclosing the breeder zone and coolant tubes passing through it may be a source of sputtering particles. However, this would be far less of a problem than for the coolant because 1) the neutron flux is lower and softer than the first wall (especially for $LiAlO_2$ behind a neutron multiplier), 2) the low gas flow rates and geometry make redeposition of particles within the zone quite likely. Similarly, the surface oxidation is likely to be less of a problem than for the coolant because of lower gas flow rates and lower impurity levels (possibly due to smaller amounts of helium involved, which is processed for tritium each pass).

Although solid breeders do interact with steel [7.18, 7.19], the reaction is slight and only possible where breeder and metal come in

close contact. The experiments to date have found the oxide to be very adherent, thus there may be little or no contribution to transport of structural activity.

Even if normal operation were not to contaminate the tritium loop, accidental leakage of a coolant would. Even a small leak of water at 15 MPa or helium at 5 MPa into a 0.1 MPa breeder zone would cause significant amount of contamination of the tritium system piping that connects to the breeder zone. If this part of the tritium facility were not designed for operation with at least modest contamination of gamma activity (as opposed to the weak tritium beta), a single blanket accidental leak could make the tritium processing systems useless.

7.4 Lithium Corrosion

A large body of research has been conducted on liquid metal corrosion and a variety of survey papers have appeared in literature (see, for example, Ref. [7.20]). There is no need to repeat these here. Rather, the quantitative and/or qualitative safety related behavior will be addressed. The primary focus is on lithium corrosion of the reference metals, 316 SS, HT-9, V-alloy, and TZM. Some discussion of the behavior of the liquid $Li_{17}Pb_{83}$ alloy is included. Although much work has been done on lithium (some on liquid lead, very little on $Li_{17}Pb_{83}$) corrosion, it will be seen that large gaps on knowledge exist which limit the quantitative examination.

7.4.1 Liquid Metal Behavior

A liquid metal may have a variety of effects on a structural alloy. Most severe is liquid penetration and bulk dissolution of the solid.

Even minor liquid penetration can severely weaken the structure, especially along grain boundaries. Second, minor constituents/impurities in the liquid may contaminate and degrade the solid properties. Third, the solid surface may corrode in the liquid, generally through dissolution of alloy constituents.

The dissolution of alloy constituents into the liquid is caused by the relatively high solubility of constituent in the liquid. As the coolant moves around the loop and temperatures decline, the liquid becomes supersaturated and the soluble species will deposit on the wall. This thermal gradient mass transfer is governed by the equation:

$$\dot{m} = k(C_s - C_i) \tag{7.15}$$

where C_s = equilibrium solubility of ion in liquid

C_i = actual solubility

k = rate constant

Thus the relative levels of C_s and C_i determine whether dissolution or deposition occurs. The rate constant and solubility are all functions of temperature. The net mass transfer is influenced by the temperature drop around the loop, ΔT_{loop}, as this determines the driving solubility gradient. As discussed later, the general behavior divides into two time periods. Initially, very soluble alloy constitutents are leached from the solid forming a depleted zone in the metal [7.20, 7.21]. The diffusion tends to follow parabolic kinetics. Eventually, a steady state is reached controlled by the surface dissolution of the base metal. The release rates of the various elements in the alloy generally become

stoichiometric [7.21, 7.22].

The steady state inventory can be estimated. Approximating the buildup of radioisotopes in the bulk structure as follows:

$$n_b(t) = n_b(\infty)(1 - e^{-\lambda t}) \tag{7.16}$$

where $n_b(\infty)$ is the steady state inventory

The buildup of corrosion products is given by

$$\frac{d}{dt} n_c(t) = r\, n_b(t) - \lambda n_c(t) \tag{7.17}$$

where r = total dissolution rate in the blanket

n_c = atoms of products in coolant or deposited on walls

The solution of Eq. (7.17) is then

$$n_c(t) = \frac{r n_b(\infty)}{\lambda} \left[1 - e^{-\lambda t} (1 + \lambda t)\right] \tag{7.18}$$

Then at steady state, the concentration of corrosion species is given by

$$n_c(\infty) = \frac{r}{\lambda} n_b(\infty) \tag{7.19}$$

Therefore, use of the corrosion rate and equilibrium isotope concentrations in blanket material allow estimation of the coolant and wall deposit activity.

Implicit in Eq. (7.17) is the neglect of other net sinks for corrosion species, e.g., filters. The present understanding of lithium systems does not allow quantifiable estimates of the potential decrease of coolant corrosion inventory due to filtration. There is evidence that simply removing soluble ions may actually increase corrosion. Borgstedt [7.23] found that gettering of Ni ions by Ti or Zr increased stainless steel corrosion due to increased Ni leaching: the solubility gradient had been increased. The impurity control system can decrease corrosion by reduction of harmful impurities, e.g., C. N. O, which may act to increase the solubility of metal ions. Reduction of impurities may decrease metal ion solubility, as well as potentially reduce structural changes [7.20, 7.24, 7.25].

Finally, the fraction of inventory that is potentially released to the reactor building can be roughly estimated. Decontamination studies [7.26] of steels corroded by sodium showed that two methanol washes removed between 10 and 40% of the activity. For present purposes, it is assumed that a maximum of about 25% of the corrosion inventory could be removed from the piping in the event of complete lithium drainage from a coolant loop.

7.4.2 Steel Results

Besides radioactivity concerns, there are two major problems in steel/lithium systems, structural degradation and tube plugging. At high nitrogen levels (100-2000 pp m N), the fatigue properties of 2 1/2 Cr - 1 Mo, 304 SS [7.27] and HT-9 [7.28] are degraded. At low temperatures or high frequencies, the normal ductile transgranular crack growth becomes brittle. At high temperatures or low frequencies, the behavior shifts to intergranular cracking from grain boundary penetration.

There is some disagreement over how severe these effects are at lower (~100 ppm N) nitrogen levels [7.27, 7.28].

The other non-radioactivity concern is tube plugging due to mass transfer. Occasionally, lithium loop experiments have been stopped due to plugging of the loop from deposits in the colder regions [7.29, 7.30]. These deposits are primarily Cr or Ni. In one case, for example, Cr-rich dendrites formed in the colder regions after short (<2000 hr) times. Eventually the deposits were less needle-like and new deposits became more stoichiometric [7.30]. Thus, the initial transient leaching of Cr and Ni could pose significant tube plugging hazards. Because HT-9 (12% Cr, no Ni) has less of these elements than 316 SS (17% Cr, 14% Ni), plugging and mass transfer problems are generally viewed as more severe for the 316 SS austenitic steel.

Fenici et al, [7.31] has examined the possibility of using a Cr-Mn austenite steel where Mn not Ni stabilizes the austenite phase. The results were mixed with continuing problems of carbide precipitation and martensitic transformations.

As no experiments have yet been performed at exact reference design conditions, the available long-term data must be extrapolated to appropriate temperatures and flow velocity. Over the range of 500-650 °C a 4.6-fold difference in corrosion rates has been observed [7.22] which translates to an activation energy of 14.6 kcal/mole (~61 kJ/mole). This is in good agreement with heat of formation for iron dissolving in lithium (~59 kJ/mole) confirming that long-term steel corrosion in lithium is controlled by the base metal iron dissolving [7.32]. Furthermore, the overall mass transfer should be roughly proportional to the loop temperature drop, because of the change in solubility gradient.

DeVan [7.33] reports that at 540 °C, the velocity dependence is $v^{0.5}$ while an earlier study found a $v^{0.8}$ scaling [7.34]. Therefore, the overall mass transfer appears to scale as

$$\sim v^{0.5-0.8} \times \Delta T_{loop} \times \exp(-61 \text{ kJ/mole}/RT) \qquad (7.20)$$

For an average flow of 0.3 m/s, ΔT_{loop} = 220 °C, and $T_{blanket}$ = 450 °C, the estimated steady state corrosion rate is 6 μm/yr based on the available data [7.22, 7.29, 7.30, 7.32]. This compares to the value of 9 μm/yr (0.60 mg/cm^2 - month) at 450 °C assumed in the UWMAK-I corrosion estimate [7.35], and a value of 3.1 μm/yr at 500 °C in the environmental study [7.21].

It should be noted that investigations continue that explore methods of reducing this corrosion rate. Addition of 5 wt% aluminum to lithium reduced the release rate by a factor of 5 [7.22], although it is not known if the process would work in reactor conditions. Initially coating the steel with aluminum had some beneficial results [7.36].

The entire in-blanket surface area (12,000 m^2) is treated as having a temperature of 450 °C. Thus, 576 kg metal/yr is released from the blanket. The release of individual isotopes from steel in sodium is generally stoichiometric [7.37, 7.38], although Ta is preferrentially retained and Mn preferrentially released. Release of isotopes at long times from steel in lithium is assumed to be stoichiometric.

The mass loss rates at steady state are similar for HT-9 and 316 SS. Additional mass is lost due to leaching in the initial transient period (∿ month), with 316 SS losing about twice that of HT-9 due to

differing alloy compositions. Since radioactivity buildup is also starting at this time, the initial period has relatively little impact on long-term radioactivity corrosion levels. For ease in calculation, the steady state is assumed to begin initially. Whereas this slightly underpredicts the initial radioactivity release (which would be hard to estimate), it allows direct calculation of activity levels using Eq. (7.18). As seen in Table 7.12, most isotopes reach steady state levels in the six-year reference time frame. Specifically, the ^{51}Cr reaches steady state, hence the neglect of the initial transient release is justified.

As seen in the reference designs in Chapter 2, about half of the steel wall area is at or near the first wall. The release of isotopes is assumed to come from half of the blanket area (6000 m^2) at first wall specific activity levels. The resulting activity levels, using Eq. (7.18), are shown in Table 7.12. The 13.4 MCi inventory compares well with an estimate for the UWMAK-I design [7.35], 12 MCi (scaled to 3.6 MW/m^2 from 1.25 MW/m^2).

By assuming that the lithium is divided into two separate cooling loops (consistent with the water case) and that 25% of the inventory is releasable to the building if coolant is lost (see Section 7.4.1), the maximum releasable inventory is 1.7 MCi.

7.4.3 Vanadium Results

There is very little quantitative information on lithium-vanadium corrosion rates. Freed [7.39] reported "nil attack" for an early test (1194 hr) at 870°C, $\Delta T_{loop} = 204°C$, $v = 4$ m/s, but did not quantify the result. Frye et al., reported no attack for a 100 hr static test at 816°C [7.40]. DeVan and Klueh [7.41] examined the effect of oxygen on vanadium

TABLE 7.12

Calculated Activity Inventory for the Reference 316 SS/Lithium Case

Isotope	Equilibrium Release Rate (Ci/yr)	Equilibrium Inventory (Ci)	6-year Inventory (Ci)
^{51}Cr	1.255×10^{6}	1.378×10^{5}	1.378×10^{5}
^{54}Mn	7.282×10^{5}	8.976×10^{5}	8.571×10^{5}
^{56}Mn	1.916×10^{6}	8.018×10^{2}	8.018×10^{2}
^{55}Fe	6.366×10^{6}	2.205×10^{7}	1.139×10^{7}
^{57}Co	3.678×10^{5}	3.952×10^{5}	3.854×10^{5}
^{58}Co	1.086×10^{6}	3.045×10^{5}	3.045×10^{5}
^{60}Co	2.405×10^{5}	1.819×10^{6}	3.435×10^{5}
^{99}Mo	9.370×10^{4}	1.018×10^{3}	1.018×10^{3}
Total	1.2×10^{7}	2.6×10^{7}	1.34×10^{7}

and V-20%Ti. Their data indicate that less than 10^{-4} g was lost from a 0.5 in^2 specimen (100 hr static test at 815°C). This places an upper bound on the static flow corrosion rate at 815°C of < 4.5 μm/hr. The lower bound would be in the neighborhood of 0.05 μm/yr from bulk lattice sputtering.

Smith [7.42] has recommended a value of 1 μm/yr at 650°C, corresponding to steel/sodium rates at high flow velocity. The temperature for the reference design was 550°C with relatively low flow rates. A value of 0.5 μm/yr is adopted for calculational purposes.

The hazard of dissimilar metal mass transfer problems is indicated by an experiment of Hoffman [7.43]. He placed vanadium coupons in a steel container and found high mass transfer (8.4 mg/in^2 in 100 hr at 816°C, equivalent to 190 μm/yr) due to interaction between the steel and vanadium.

As in the case of steel, more soluble alloy constituents like Cr would be expected to initially leach out before a steady state of vanadium dissolution would occur. For the reference design, the steady state metal loss rate would be 27 kg metal/yr from blanket surfaces.

The steady state activity inventory can also be calculated. All isotopes of primary interest reach steady state levels within six years. The result is shown in Table 7.13, assuming a stoichiometric release. It is not known if release of individual isotopes (e.g., Sc species) deviates from stoichiometric conditions. The maximum release to the building, assuming loss of 25% of the inventory of one of two coolant loops, is about 3 kCi.

7.4.4 Implications for Lithium Breeder

As noted in Section 7.4.2, the corrosion rate is a function of flow

TABLE 7.13

Calculated Activity Inventory
for the Reference Vanadium-Lithium Design

Isotope	Equilibrium Release Rate (Ci/yr)	Equilibrium Inventory (Ci)
^{45}Ca	1,070	689
^{46}Sc	1,567	518
^{47}Sc	2,712	36
^{48}Sc	21,074	153
^{49}V	12,409	16,170
^{51}Cr	50,512	5,540
Total	89,344	23,106

velocity. Hence, it is generally agreed that a semi-static breeder zone would result in less corrosion than a flowing system. This would allow higher temperatures in a lithium breeder zone. However, even if the corrosion rates were several orders of magnitude lower than in flow conditions, a sufficient amount of steel activity would be mobilized to effectively contaminate the tritium/lithium processing unit. Because of very low corrosion rates, a refractory metal structure offers more promise. In either case the temperature drop between breeder zone and processing unit will be important. If the lithium portion of the processing unit could be operated at higher temperatures than the breeding zone, movement of radioisotopes from blanket to processing unit would be minimized. At the present state of knowledge, one should assume that the lithium corrosion will transfer enough gamma activity to the tritium processing unit to require shielding.

7.4.5 Implications for $Li_{17}Pb_{83}$ Breeder

Although a variety of reports have examined corrosion in liquid lead [7.44 - 7.48], few have involved liquid $Li_{17}Pb_{83}$. As discussed in Chapter 5, the activity of lithium in $Li_{17}Pb_{83}$ is very low, typically 10^{-4}. $Li_{17}Pb_{83}$ is 99.3 wt% Pb. Furthermore, the corrosion behavior of materials exposed to lead have some similarities to behavior in lithium. Unfortunately, most of the data concerning lead corrosion is not quantitative. A summary of some literature reports is given in Table 7.14. Most reports were of a screening nature. However, there is sufficient evidence to draw some general conclusions.

Among the major constituents of steel, nickel is most soluble, followed by chromium, with iron least soluble [7.49]. Thus austenitic

TABLE 7.14

Survey of Reported Results of Relevant Metals in Liquid Lead

Alloy	Reference	Temperature	Time (hr)	Result
Ni-base				
Hastelloy	7.44	700		severe attack
Austenitic Steels				
Austenitic Steels	7.46	538		good resistance
316 SS	7.47	600		poor resistance
316 SS	7.47	300		good resistance
Ferritic Steels				
446 SS	7.45	816	250	slight attack
410 SS	7.48	655	1346	38 μm/yr
2-9% Cr Steel	7.47	800		poor resistance
2-9% Cr Steel	7.47	600		good resistance
Croloy 2 1/2	7.44	700		severe attack
Croloy 2 1/2	7.48	593	5156	25 μm/yr
Molybdenum				
Mo, Nb, Ta, W	7.47	800		good resistance
Mo	7.47	1100		good resistance
Mo	7.45	982	250	no attack
Mo	7.44	1000		nil, $<10^{-3}$ μm/yr
Mo	7.44	700		nil, $<10^{-3}$ μm/yr
Niobium				
Nb	7.45	982	50	no attack
Nb-1% Zr	7.46	760	5000	no measurable attack
Tantalum				
Ta	7.45	982	250	no attack

Table 7.14 (continued)

Alloy	Reference	Temperature	Time (hr)	Result
Titanium				
Ti	7.45	816	100	pronounced attack
Ti	7.46	538		poor resistance
Zirconium				
Zr	7.45	816	100	pronounced attack
Zr	7.46	538		poor resistance

steels would be expected to corrode faster than ferritic steels, as in the case of lithium. It is not known whether the long term corrosion of the two types of steel would eventually be dominated by iron dissolution after initial leaching of Cr and Ni; however, based on the similarities of Fe, Cr, Ni solubilities in lead and lithium, one could tend to expect similar long-term corrosion rates between HT-9 and 316 SS. Overall, the corrosion in lead seems potentially more severe than in lithium. Weldments of $2\frac{1}{4}$ Cr - 1 Mo steel were penetrated along grain boundaries by $Li_{17}Pb_{83}$ at 500 °C [7.50].

As in the case of lithium corrosion of steel, there may be ways to improve resistence to lead. Nb stabilized $2\frac{1}{4}$ Cr - 1 Mo was resistant to $Li_{17}Pb_{83}$ [7.50]. Ti or Zr additions at the ppm level were found beneficial [7.44].

The refractory metals (Mo, W, V, Nb, Ta) seem generally very resistant to liquid lead (see Table 7.14) as they do to liquid lithium. There is no evidence on vanadium but there is no reason to suspect its behavior is significantly worse than Nb and Ta. The major concern with refractories could be the solubility of some alloying constituents. Titanium and zirconium corrode rapidly in lead [7.45, 7.46] and are constituents in TZM (0.5% Ti, 0.08% Zr). Titanium and chromium are often mentioned as alloying elements in V-alloys. However, the addition of 1% Zr in Nb - 1% Zr did not lead to any measurable attack in an operating loop, with ΔT_{loop} = 400 °C [7.46].

Overall, a liquid $Li_{17}Pb_{83}$ breeder can be expected to corrode structural surfaces somewhat similarly as lithium, to a rough first approximation. Thus, again there is potential for contamination of the

tritium processing system. In general, the refractory metals show significantly better resistance than do the steels.

7.5 Flibe Corrosion

7.5.1 General Behavior

A variety of research has focused on corrosion in molten salts [7.51-7.57]. Unfortunately, no studies were found for the specific combination of TZM and flibe ($LiF-BeF_2$). A summary of corrosion studies is given in Table 7.15. The general type of behavior is similar to liquid metals, as opposed to water or helium. Primary concerns include penetration of the solid, leaching of alloy constituents and thermal gradient mass transfer.

In general the mass transfer problems are less than in liquid metals [7.52]. The metals most resistent to halogen salts appear to be nickel and molybdenum with metals like Cr, Ti, Zr being preferentially leached [7.53, 7.54, 7.56]. Depending on salt and alloy, certain elements are beneficial if added to the salt. For example, beryllium additions to $LiF-BeF_2$ significantly help 316 SS resistence [7.56]. Besides compatibility between blanket structure and coolant/breeder, salt corrosion is also relevant in the molten salt type of tritium processing unit. Corrosion of 316 SS by LiF-LiCl-LiBr seems acceptable for use in tritium extraction unit [7.57].

7.5.2 TZM Result

The closest test to the flibe/TZM system appears to be a static test of a fluoride salt (68% LiF - 20% BeF_2 - 11.7% ThF_4 - 0.3% UF_4) with TZM at 100 °C for 1011 hr. This salt is similar to flibe except for the

TABLE 7.15

Survey of Molten Salt Corrosion Results

Alloy	Salt	Temperature	Result	Reference
Nickel	LiF-NaF-KF-UF_4	816	no visible attack	7.52
Hastelloy	LiF-BeF_2	650	good resistence	7.56
Inconel	LiF-BeF_2	650	poor resistence	7.56
316 SS	LiF-BeF_2	650	poor resistence	7.56
316 SS	LiF-BeF_2-added Be	650	good resistence	7.56
316 SS	LiF-LiCl-LiBr-Li	535	poor (13.5 μm/yr)	7.57
316 SS	LiF-LiCl-LiBr	535	good (<2 μm/yr)	7.57
316 SS	LiF-UF_4	700	badly corroded, dissolved	7.51
316 SS	NaF-KF-UF_4	816	subsurface voids	7.52
300 series	LiF-NaF-KF-UF_4	816	subsurface voids	7.52
400 series	LiF-NaF-KF-UF_4	816	subsurface voids	7.52
400 series	LiF-UF_4	700	badly corroded, dissolved	7.51
Stellite (Co)	LiF-NaF-KF-UF_4	816	no visible attack	7.52

Table 7.15 (continued)

Alloy	Salt	Temperature	Result	Reference
Mo	$NaF-UF_4$	727	nil attack	7.55
Mo	$NaF-UF_4$	700	no attack	7.51
Mo	$NaF-NaF-UF_4$	816	no attack	7.52
Mo	$LiF-UF_4$	700	some UF_4 penetration	7.51
Mo	$Li-NaF-KF-UF_4$	816	surface roughened	7.52
TZM	$LiF-BeF_2-ThF_4-UF_4$	1100	good resistence (< 0.3 μm/yr)	7.53
Nb	$LiF-UF_4$	700	badly corroded, dissolved	7.51
V, Na, Ta	$LiF-NaF-KF-UF_4$	816	subsurface voids	7.52

presence of ThF_4 and UF_4. UF_4 appears to be one of the more reactive constituents [7.55], hence flibe behavior would be expected to be superior to this salt. Mo showed some penetration by UF_4 from a 76% LiF - 24% UF_4 salt at 700 °C for 420 hrs [7.51].

Furthermore, there is the difference between this static test at 1100 °C and flowing flibe at 800 - 900 °C. The net effect of these differences is unknown. However the latter differences have opposite effects. The higher test temperature would cause overprediction of flibe corrosion at 800-900°C while the static nature could lead to underprediction.

The fluoride salt leached Ti and Zr from TZM but did not appear to attack the base element molybdenum. The leaching was observed to follow parabolic kinetics as expected in a diffusion process. Koger and Litman [7.53] found that the mass of each element removed was given by

$$\Delta m/A = 2C_o \sqrt{Dt/\pi} \tag{7.21}$$

where C_o = original concentration in the alloy

t = time

D = diffusion coefficient

The diffusion coefficients were found to be

$$D_{Ti} = 1.2 \times 10^{-16} \text{ m}^2/\text{s} \tag{7.22}$$

$$D_{Zr} = 2.9 \times 10^{-15} \text{ m}^2/\text{s}$$

The initial concentrations are

$$C_o(Ti) = 0.005 \times 10{,}200 \text{ kg/m}^3 = 51 \text{ kg/m}^3 \quad (7.23)$$

$$C_o(Zr) = 0.0008 \times 10{,}200 \text{ kg/m}^3 = 8.2 \text{ kg/m}^3$$

Therefore the mass losses are given by

$$\Delta m/A \ (Ti) = 6.3 \times 10^{-7} \sqrt{t(sec)} \quad \text{kg/m}^2 \quad (7.24)$$

$$\Delta m/A \ (Zr) = 5.0 \times 10^{-7} \sqrt{t(sec)} \quad \text{kg/m}^2$$

This can be expressed as an equivalent penetration depth:

$$\Delta d \ (Ti) = 0.35 \sqrt{t(years)} \quad \mu m \quad (7.25)$$

$$\Delta d \ (Zr) = 0.27 \sqrt{t(years)} \quad \mu m$$

It is not known when or if, behavior would shift from this parabolic kinetics leaching regime to a linear steady state case as for liquid metals. A conservative assumption would be that linear behavior would begin at 1011 hr., the end of the test. The penetration rate as a function of time during the test was approximately

$$\dot{d} = 0.155 \ (t(years))^{-1/2} \ \mu m/yr \quad (7.26)$$

If the kinetics were to shift to linear at 1011 hr., the steady state penetration rate would be about 0.5 μm/yr. This value is adopted for further calculations. A corrosion rate of 0.5 μm/yr for the reference design implies a mass loss rate from the blanket of 43 kg/yr.

The isotopes of interest reach steady state within the reference 6-year time period so that the steady state inventory can be calculated from Eq. (7.19) in the manner of V/Li and 316 SS/Li. The results are shown in Table 7.16. The maximum inventory can be estimated as for lithium designs by dividing all coolant into two loops and then assuming 25% of a loop's contents may be transferred to the building of all flibe drained. Then, about 1 kCi would be mobilized.

7.6 Summary and Conclusions

7.6.1 Mass Transport

Perhaps the best overall measure of the hazards associated with corrosion is the oxidation rate itself. The estimated values for each system are listed in Table 7.17, not including sputtering. Analysis of Bickford's values [7.13, 7.14], that the sputtering metal loss rate averaged over the blanket is of order 0.05 μm/yr for 316 SS. At present, the neutron sputtering for V and Mo appear lower in this regard than for 316 SS [7.58], so that the sputtering contribution to V and Mo systems is less important. It should be noted that sputtering does put a lower bound on the effective corrosion rate. Since direct daughter recoil tends to dominate the total sputtering yield, radioactive atoms are preferentially released from the surface. This is why the sputtering contribution to mass transport is relatively less important than for radioactivity transport.

TABLE 7.16

Calculated Inventory for the Reference TZM/Flibe System

Isotope	Corrosion Rate (Ci/yr)	Steady State Inventory (Ci)
^{89}Zr	1.06×10^{7}	137
^{95}Zr	2.80×10^{3}	719
^{91m}Nb	2.85×10^{3}	700
^{92m}Nb	1.17×10^{4}	473
^{95m}Nb	8.36×10^{3}	120
^{95}Nb	1.32×10^{4}	1,823
^{96}Nb	5.33×10^{3}	21
^{97}Nb	3.93×10^{3}	1
^{99}Mo	3.80×10^{5}	4,127
^{99m}Tc	3.82×10^{5}	375
Total	1.14×10^{7}	8,500

TABLE 7.17

Estimated Mass Transport for Reference Coolant Loops*

Coolant	Alloy	Steady State Corrosion Rate (μm/yr)	Metal Loss Rate from Blanket (kg/yr)
Water	316 SS	0.45	43
Water	HT-9	1.35	130
Helium	316 SS	0.05	3
Helium	HT-9	0.05	3
Lithium	316 SS	6	576
Lithium	V-alloy	0.5	27
Flibe	TZM	0.5	43

*Not including sputtered mass

Plugging is not a problem for helium systems. Given the present knowledge, plugging does not appear to be a significant problem for water/steel, lithium/V-alloy, or flibe/TZM systems, although this is highly uncertain for the latter two cases due to the lack of operating experience. Plugging appears to be a serious operational problem for lithium/steel systems.

The technology to operate these systems and the understanding to model them varies considerably. The refractory metal/liquid metal or salt systems appear attractive from the corrosion viewpoint, but extensive development of operation equipment is needed. Proper operating chemistry in all cases is mandatory if corrosion problems are to be kept to acceptable levels.

7.6.2 Radioactivity Transport

The estimated inventory and maximum inventory releasable to the building are listed in Table 7.18. Although the corrosion process may only mobilize a very small fraction of the total structural inventory, some of that inventory is readily mobilizable in an accident. If a coolant leak were to occur, some fraction of the coolant loop inventory could be swept into the building where it could eventually enter the environment. The high pressure fluids, water and helium, are relatively worse in this regard. Even if such releases do not occur, the contamination of the loop greatly complicates maintenance.

It is emphasized that all tritium systems connected by flow to the blanket are likely to become contaminated by gamma activity, although to a lesser degree than coolant loops.

TABLE 7.18

Estimated Inventory for Activity in Reference Coolant Loops

Coolant	Alloy	Total Corrosion Inventory	Maximum Inventory to Building*
Water	316 SS	128 kCi	32 kCi
Helium	316 SS - Sputtered	41 kCi	11 kCi**
	- Corrosion	12 kCi	6 kCi
Lithium	316 SS	13.4 MCi	1.7 MCi
Lithium	V-alloy	23 kCi	3 kCi
Flibe	TZM	8.5 kCi	1 kCi

*All coolant divided into two loops, one loop drains, along with 100% of oxide dust in helium system, 50% of oxide layer in water systems, and 25% of transported particles in lithium and flibe.

**Assumes that Cr and Mn sputtered species are oxidized and are thus releasable.

There is not yet a significant difference between the hazards from use of the breeders Li and $Li_{17}Pb_{83}$. And, while specific activity values for HT-9 was unavailable, the lower activity in the structure would tend to translate into lower contamination of coolant loops.

Continuous filtration has not been taken into account in terms of removal of radioactive species, except in the water systems. Either continuous filteration or periodic flushing of loops could reduce the entrained coolant radioactive inventory.

7.6.3 Relative Consequence Indices

Defining and calculating relative consequence indices for corrosion problems is difficult due to the relative lack of quantization of the safety problems involved, e.g., plugging. In addition, unlike most other safety comparison bases, it is not possible to even attempt to separate metal from coolant. For purposes of comparison, two rough corrosion product relative consequence indices, RCI_{CP}, are defined.

The relative consequence index for mass transfer is defined by the equation,

$$RCI_{CP}^{mt} = \frac{\dot{d}(\mu m/yr)}{1\ \mu m/yr} \tag{7.27}$$

So that the corrosion rate is normalized to 1 μm/yr. Current systems with helium or water operating at this corrosion rate are relatively free of mass transfer problems, so an RCI_{CP}^{mt} of 1.0 is appropriate. The values for the reference systems are given in Table 7.19.

The relative consequence index for radioactivity release is defined by the equation

TABLE 7.19

Relative Consequence Index for Corrosion Problems from Mass Transfer*

	316 SS	HT-9	V-alloy	TZM
Water	0.5	1.4	X	X
Helium	0.1	0.1	X	X
Lithium	6	6	0.5	X
Flibe	X	X	X	0.5

*X - combination not studied
Values relative to 1 μm/yr mass loss rate, for which mass transfer problems are low. Hence values less than or equal to 1.0 are for systems which should show acceptable mass transfer behavior.

$$RCI_{CP}^{rr} = \frac{INV_r}{1\ kCI} \tag{7.28}$$

The best case TZM/flibe has a releasable inventory of about 1 kCI, providing the normalization. Whereas the damage done by a curie of different isotopes is unequal (see Chapter 8), this provides a rough first measure of the relative consequence.

In general, the corrosion systems can be rank ordered as shown in Table 7.21.

TABLE 7.20

Relative Consequence Index
for Corrosion Problems of Radioactivity*

	316 SS	V-alloy	TZM
Water	∿30	X	X
Helium	∿20	X	X
Lithium	∿2000	3	X
Flibe	X	X	1

*X - combination not studied

TABLE 7.21

Rank Order of Reference Corrosion Systems
(Best to Worst)

Helium/Steel

V/Li, TZM/flibe

Water/Steel

Lithium/Steel*

*appears significantly worse than the other systems

REFERENCES

7.1 C.C. Baker, Jr., et al., "STARFIRE," ANL/FPP-80-1, 1980.

7.2 C. Heck, Magnetic Materials and Their Applications, Crave and Russak, New York, 1974.

7.3 B.D. Cullity, Introduction to Magnetic Materials, Addison-Wesley, Reading, MA, 1972.

7.4 M. Troy, "Study of Magnetic Filtration Applications to the Primary and Secondary Systems of PWR Plants," EPRI-NP-514 (1978).

7.5 R.W. Moir, et al., "Tandem Mirror Hybrid Reactor Design Study," UCID-18808, 9/80, Appendix A.

7.6 W.R. Grimes and S. Cantor, "Molten Salts as Blanket Fluids in Controlled Fusion Reactors," Chemistry of Fusion Technology, 1972.

7.7 T.J. McManamy, "Fusion Reactor Blanket Heat Removal Using Helium and Flibe," Ph.D. thesis, Department of Nuclear Engineering, Massachusetts Institute of Technology, 1979.

7.8 G.H. Miley, Fusion Energy Conversion, 1976.

7.9 R.L. Dillion and A.B. Johnson, "Corrosion Product Generation in Water Reactors," Proc. System Contamination Workshop, Atlanta, GA, March 15-17, 1976 (EPRI, 1976), p. 81.

7.10 P. Cohen, Water Coolant Technology of Power Reactors, Gordon and Breach, New York, 1969.

7.11 W.M. Stacey, Jr., et al., "U.S. Contribution to the International Tokamak Reactor Workshop," 11/1979.

7.12 W.E. Berry, Corrosion in Nuclear Applications, 1971

7.13 W.E. Bickford, "Coolant Channel Sputtering Source Terms in a Compact Tokamak Fusion Power Plant," PNL-2942, 3/1979.

7.14 W.E. Bickford, "Transport and Deposition of Activiation Products in a Helium Cooled Fusion Power Plant," PNL-3487, 9/1980.

7.15 F.N. Mazandarany, "Effects of Elevated Temperature Exposure to a Simulated HTGR Primary Coolant Environment on Several Unstressed Austenitic Alloys," GA-A-13462, 8/1975, p. 23.

7.16 D. Steiner, et al., "ORNL Fusion Power Demonstration Study: Interim Report," ORNL/TM-5813, 3/1977.

7.17 S.N. Rosenwasser and W.R. Johnson, "Gas Turbine HTGR Materials Screening Test Program," GA-A-14122, 8/1976.

7.18 P.A. Finn, et al., "Compatibility Study of Solid Ceramic Breeder Materials," 2nd Topical Meeting on Fusion Reactor Materials, 8/1981.

7.19 O.K. Chopra and D.L. Smith, "Interactions of Solid Ceramic Breeding Materials with Structural Alloys," loc. cit. [7.18], 1981.

7.20 P.F. Tortorelli and O.K. Chopra, "Corrosion and Compatibility Considerations of Liquid Metals for Fusion Reactor Applications," loc. cit. [7.18], 1981.

7.21 "Fusion Environmental Assessment Program Progress Report," ORNL/CF-81-1, 2/81.

7.22 P.F. Tortorelli, et al., "Corrosion in Lithium-Stanless Steel Thermal-Connection Systems," Proceedings of the 2nd International Conference on Liquid Metal Technology in Energy Production, 1980.

7.23 H.U. Borgstedt, "Materials Problems Arising from Impurity Gettering of Lithium by Zirconium or Titanium," loc. cit. [7.18], 1981.

7.24 H.R. Konvicka, P. Reithmayr, "Characterization of 304-SS and 316-SS Exposed to Liquid Lithium for 10,000 Hours," loc. cit. [7.18], 1981.

7.25 H. Migge, "Thermochemistry in the Systems Li-O-H, Li-O-C, Li-N-C," loc. cit. [7.22], 1980.

7.26 D.M. Donaldson and J.A. Bray, "UK Fast Reactor Components—Sodium Removal, Decontamination and Requalification," INIS-mf-5083, 1978.

7.27 D.L. Hammon, et al, "Influence of Cyclic Loading on the Lithium Corrosion Behavior of Reactor Materials," loc. cit. [7.18], 1981.

7.28 O.K. Chopra and D.L. Smith, "Effects of Lithium Environment on the Fatigue Properties of Ferritic and Austenitic Steels," loc. cit. [7.18], 1981.

7.29 P.F. Tortorelli and J.H. DeVan, "Effect of Nickel Concentration of the Mass Transfer of Te-Ni-Cr Alloys in Lithium," loc. cit. [7.18], 1981.

7.30 P.F. Tortorelli and J.H. DeVan, "Mass Transfer Deposits in Lithium-Type 316 Stainless Steel Thermal-Connection Loops," loc. cit. [7.22], 1980.

7.31 P. Fenici, et al, "Influence of Lithium Exposure on the Uniaxial Tensile Properties of a Cr-Mn Austenitic Stainless Steel," loc. cit. [7.18], 1981.

7.32 P.F. Tortorelli and J.H. DeVan, "Thermal-Gradient Mass Transfer in Lithium-Stainless Steel Systems," First Topical Meeting on Fusion Reactor Materials, Journal of Nuclear Materials, Vol. 85, 86, (1979).

7.33 J.H. DeVan, et al., "Chemical Aspects of Controlled Nuclear Fusion," Atomic Energy Review, 18(2), 1980.

7.34 W.N. Gill, et al., "Mass Transfer in Liquid-Lithium Systems," Journal of A.I.Ch.E., 6(1), 3/1960, pp. 139-144.

7.35 A.B. Johnson and W.F. Vogelsany, "Preliminary Assessment of Corrosion Product Transport in Fusion Reactors," Nuclear Technology, 22 (1979), p. 115.

7.36 G.C. Barrow, "Corrosion Inhibition Experiments in Liquid Lithium," loc. cit. [7.18], 1981.

7.37 C.A. Erdman and A.B. Reynolds, "Radionuclide Behavior During Normal Operation of Liquid-Metal-Cooled Fast Breeder Reactors: Part 1: Production," Nuclear Safety, 16(1), 1/1975, p. 43.

7.38 T.J. Kabele, et al., "Activated Corrosion Product Radiation Levels near FFTF Reactor and Closed Loop Primary System Components," HEDL-TME-72-71, 5/1972.

7.39 M.S. Freed, "Corrosion of Columbium Base and Other Structural Alloys in High Temperature Lithium," PWAC-355, 6/1961.

7.40 J.H. Frye, Jr., et al., "Metallurgy Division Annual Progress Report," ORNL-2422, 12/1957, p. 4.

7.41 J.H. DeVan and R.L. Klueh, "Effect of Oxygen on the Corrosion of Vanadium and V-20% Ti by Liquid Lithium," Nuclear Technology, 24 (10/1974), p. 64.

7.42 D.L. Smith, personal communication, 1981.

7.43 B.E. Hoffman, "Corrosion of Materials at Elevated Temperatures," ORNL-2674, 3/1959.

7.44 R.A. Asher, et al., "Some Observations on the Compatibility of Structural Materials with Molten Lead," Corrosion Science, 17 (1977), p. 545.

7.45 R. Parkman and O.C. Shepard, "Investigation of Materials for Use in a Heat Transfer System Containing Liquid Lead Alloy," ORO-45, (Stanford), 6/1951.

7.46 G.M. Tolson and A. Taboadu, "A Study of Lead and Lead-Salt Corrosion in Thermal Convection Loops," ORNL-TM-1437, 4/1966.

7.47 Reactor Handbook, 1960.

7.48 W.D. Wilkinson, "Attack on Materials by Lead at 1000°C," ANL-5449, 10/1955.

7.49 D.K. Sze, et al., "LiPb, A Novel Material for Fusion Applications," UWFDM-378, 1980.

7.50 T.L. Anderson, et al., "Intergranular Penetration of 2 1/4 Cr - 1 Mo Weldments by a Lithium-Lead Liquid," loc. cit. [7.22], 1980.

7.51 H.J. Buttram, et al., "Corrosion Tests by Fluoride Salts," Y-B15-19, 1/1951.

7.52 L.S. Richardson, et al., "Corrosion by Molten Fluorides—Interim Report," ORNL-1491, 4/1953.

7.53 J.W. Koger and A.P. Litman, "Compatibility of Molybdenum-Base Alloy TZM with LiF-BeF_2-ThF_4-UF_4 at 1100°C," ORNL-TM-2724, 12/1969.

7.54 J.W. Koger, "Alloy Compatibility with LiF-BeF_2 Salts Containing ThF_4 and UF_4," ORNL-TM-4286, 12/1972.

7.55 M. Baker, et al., "Physics-Chemical Studies of Fused Salt Systems," AWRE-R-3/63, 7/1963.

7.56 J.R. Keiser, "Compatibility Studies of Potential Molten-Salt Breeder Reactor Materials in Molten Fluoride Salts," ORNL-TM-5783, 5/1977.

7.57 P.F. Tortorelli, et al., "Corrosion of Type 316 Stainless Steel in Molten LiF-LiCl-LiBr," loc. cit. [7.18].

7.58 M.T. Thomas, et al., "Fusion Neutron Induced Radioactive Emissions from Surfaces," Journal of Nuclear Materials, 63, (12/1976), pp. 448-453.

CHAPTER 8. RADIOACTIVITY INVENTORY AND CONSEQUENCES

The major underlying hazard to the public due to a fusion reactor accident would be release of radioactivity, ejther tritium or induced structural isotopes. The steady state inventory, possible normal releases, and potential maximum accidental releases of tritium for the different material combinations are compared. The determination of the steady state inventory is necessary to determine releases. Although the focus of this study is on accidental hazards, some analysis of the possible normal tritium releases is included since normal operational releases are a major environmental concern for fusion reactors.

The other safety issues in Chapters 3-7 are concerned with mechanisms that may lead to mobilization of structural radioactivity. The relative hazard of the radioactivity induced in different structural materials is examined here.

8.1 Tritium

For D-T fusion machines, tritium has consistently been identified as a major safety and environmental concern. The presence of tritium is unavoidable; however, the choice of coolant/breeder/structure may influence the potential releases to the environment. Figure 8.1 shows the interaction of various information in the determination of the steady state inventory and normal and accidental releases. Note that the discussion is limited to tritium in or leaving the blanket; tritium systems external to the blanket (generally unaffected by material choice) are not considered.

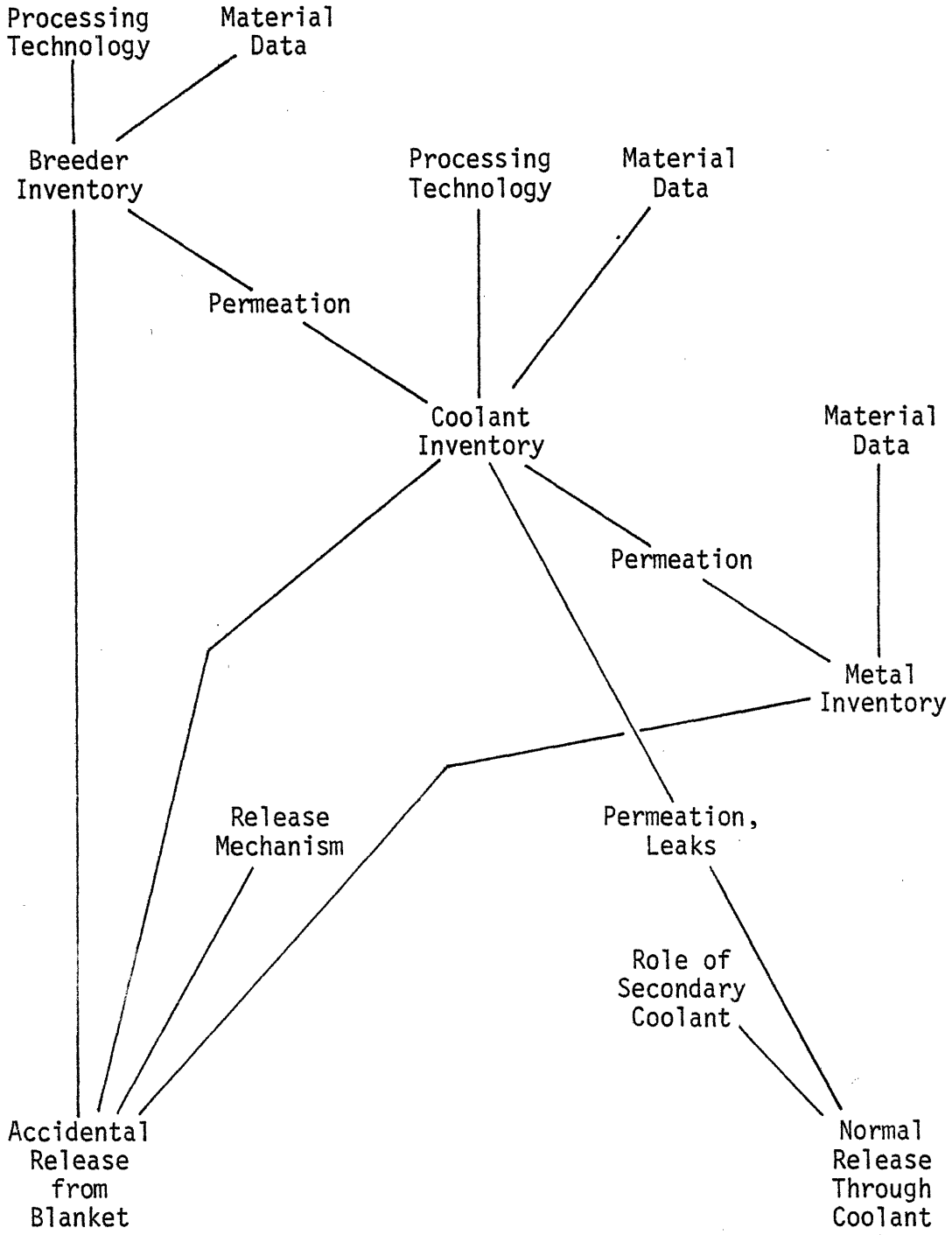

Fig. 8.1: Information Paths Needed to Determine Normal and Accidental Tritium Releases from the Blanket

8.1.1 Steady State Inventory

The first step in determining relative releases is estimation of the steady state inventory. Tritium will be present in all parts of the blanket, in coolant, metal, and breeder. Reactor design studies tend to envision continuous processing of the breeder *in situ* in preference to batch processing, which adversely affects blanket availability and tritium inventories. The processing technology and the material properties themselves determines the tritium inventory in the breeders. Furthermore, the breeder concentration influences the tritium concentration in the coolant and structure.

8.1.1.1 Lithium Breeder/Coolant Inventory

Of all possible breeding materials, the behavior and required processing technology of metallic liquid lithium is best known. The technology exists to keep tritium levels below 2.0 atomic ppm (appm) ($\leq$ 1 wppm) by molten salt extraction [8.1]. Conservatively including the effects of mass transport in a large blanket system, the ANL blanket study [8.2] adopted 5 wppm as a reference value. The goal of the lithium processing program is to demonstrate "steady state inventory of less than 5 atomic parts per million (appm.)" [8.3]. This value (= 2.1 wppm) is adopted for this study.

As discussed in Appendix C, the reference designs have 600 m^3 of lithium as breeder and 800 m^3 of lithium when used as coolant and breeder. These correspond to 3×10^5 kg_{Li} for breeder only and 4×10^5 kg_{Li} for coolant/breeder. Thus the expected tritium inventories are 630 g (breeder) and 840 g (coolant/breeder).

The tritium vapor pressure above the liquid metal is determined by the relation

$$N = K_S P_T^{1/2} \tag{8.1}$$

where N = concentration (atomic percent, a/o)

P_T = Tritium Partial Pressure (Pa)

K_S = Sievert's Constant (a/o - Pa^{-1})

In these units, the Sievert's constant for tritium over lithium is given by [8.4]

$$\ln K_S = - 7.005 + 5070/T(°K) \tag{8.2}$$

The breeder inventory and tritium partial pressures for the lithium breeder designs are shown in Table 8.1. The resulting partial pressures are very low; however, they are higher for the higher temperature V-alloy and TZM designs.

8.1.1.2 $Li_{17}Pb_{83}$ Breeder Inventory

In many respects considering tritium, $Li_{17}Pb_{83}$ is similar to lithium. Both are liquid metals and would be slowly circulated to a processing unit to remove tritium. However, the data base for $Li_{17}Pb_{83}$ is far inferior to that of lithium.

Neglecting mass transfer limitations in a $Li_{17}Pb_{83}$ loop, the tritium partial pressures achievable would be the same as in a lithium system due to the use of similar fused salt processing systems [8.5, 8.6].

TABLE 8.1

Tritium Inventory and Partial Pressure in Lithium Breeders

Coolant	Lithium	Lithium	Helium	Flibe
Metal	Steel	V-alloy	Steel	TZM
Tritium Concentration in Lithium (appm)	5	5	5	5
Tritium inventory (g)	840	840	630	630
Lithium Minimum Temperature (°C)	230	350	~400	~700
Lithium Maximum Temperature (°C)	450	550	~500	~900
Tritium Pressure at T_{min} (μPa)	5.4×10^{-4}	2.6×10^{-2}	8.7×10^{-2}	9.1
Tritium Pressure at T_{max} (μPa)	2.5×10^{-1}	1.4	6.1×10^{-1}	53.5

Since the concentration, N, is related to the pressure by Eq. (8.1), then one would expect

$$N(Li_{17}Pb_{83}) \sim N(Li) \frac{K_s(Li_{17}Pb_{83})}{K_s(Li)} \qquad (8.3)$$

The single data point for the Sievert's constant is at 767°C for deuterium; it indicates the ratio of Sievert's constant to be about 0.01 [8.6]. This would translate into a very low tritium inventory, about 8 g (0.05 appm). A recent estimate [8.7] is that the concentration would be a few weight ppb for a partial pressure of 1 Pa (note, 0.17 wppb = 1 appm for $Li_{17}Pb_{83}$).

Clemmer, et al. [8.7] suggest that "mass-transfer considerations would make it most difficult to attain tritium levels that low," and states that a 1/10 reduction in concentration would be a better approximation. This implies an inventory of 80 g and a hundred-fold increase in tritium partial pressure relative to lithium.

The above is primarily based on data at one temperature, 767°C. Two extrapolations to other temperatures have been proposed. Hoffman, et al. [8.8] first note that lithium and lead would tend to show conflicting temperature scaling. They note that lithium exothermically forms ionic hydrides; solubility increases as temperature decreases. However, lead endothermically forms covalent hydrides; solubility decreases as temperature decreases. One extrapolation trend is that the Sievert's constant for $Li_{17}Pb_{83}$ is constant with temperature. Then the ratio of $K_s(Li_{17}Pb_{83})/K_s(Li)$ would be 2×10^{-3} - 3×10^{-4}

depending on temperature, rather than the value of 1×10^{-2} described above. Their second extrapolation [8.8] is the opposite case, a stronger temperature dependence. Then the ratio of Sievert's constants in the temperature range of interest would be 0.1 to 5.0.

The problem, of course, is the very poor data base and the necessity of extrapolating from other Li - Pb compositions and temperatures. The above discussion indicates a range of Sievert's constant,

$$K_s(Li_{17}Pb_{83})/K_s(Li) \sim 10^{-2} \text{ (within about a factor of 10)} \quad (8.4)$$

If then, the partial pressures of lithium and $Li_{17}Pb_{83}$ which are achievable are the same, then

$$N(Li_{17}Pb_{83})/N(Li) \sim 10^{-2} \text{ (within factor of 10)} \quad (8.5)$$

and

$$INV(Li_{17}Pb_{83})/INV(Li) \sim 10^{-2} \text{ (within factor of 10)} \quad (8.6)$$

However, as noted above, the lower range of the possible inventory must be eliminated due to mass-transfer problems. Thus we expect

$$INV(Li_{17}Pb_{83})/INV(Li) \sim 10^{-1} \quad (8.7)$$

Then working back to the partial pressure, the uncertainty in Sievert's constant results in an uncertainty in partial pressure of

$$P_T(Li_{17}Pb_{83})/P_T(Li) \sim 10^2 \quad \text{(within two orders of magnitude)} \tag{8.8}$$

The low range (similar partial pressures) corresponds to the high range of Sievert's constant ratio where mass transfer problems are small. The high range occurs for the low range of the Sievert's constant for $Li_{17}Pb_{83}$ relative to Li. The best estimates are listed in Table 8.2.

8.1.1.3 $LiAlO_2$ Breeder Inventory

Inventory calculations for solid breeders are also fairly uncertain, although perhaps less so than $Li_{17}Pb_{83}$. A variety of processes are important in determining the breeder inventory. Discussion will be focused on the solubility and diffusion components.

Mass transfer in the $LiAlO_2$ particle bed and helium purge stream limits how low the tritium vapor pressure at the $LiAlO_2$ surface may be kept - this is analogous to the limit on liquid breeders due to metal processing technology. For the reference design of STARFIRE [8.9], the average partial pressure at the surface was taken at about 10^{-2} torr (1.3 Pa). This was determined considering percolation through the particle bed and the mass transfer out of the blanket in the helium purge stream. The estimated concentration can then be determined, see Fig. 8.2 [8.9]. More recent data suggests that the concentration in Li_2O may be significantly lower than that shown in the figure [8.7].

It is interesting to note that the solubility of tritium in $LiAlO_2$ is fairly temperature independent; this becomes more important in examining accidental release. A declining solubility with increasing

TABLE 8.2

Tritium Inventory and Partial Pressures
For $Li_{17}Pb_{83}$ Design

Coolant	Water
Material	Steel
Breeder Minimum Temperature (°C)	∿350
Breeder Maximum Temperature (°C)	∿500
Tritium concentration (appm)	0.5
Inventory (g)	80 (ten-fold uncertainty)
Partial Pressure at T_{min} (μPa)	3 (at least 100-fold uncertainty)
Partial Pressure at T_{max} (μPa)	60 (at least 100-fold uncertainty)

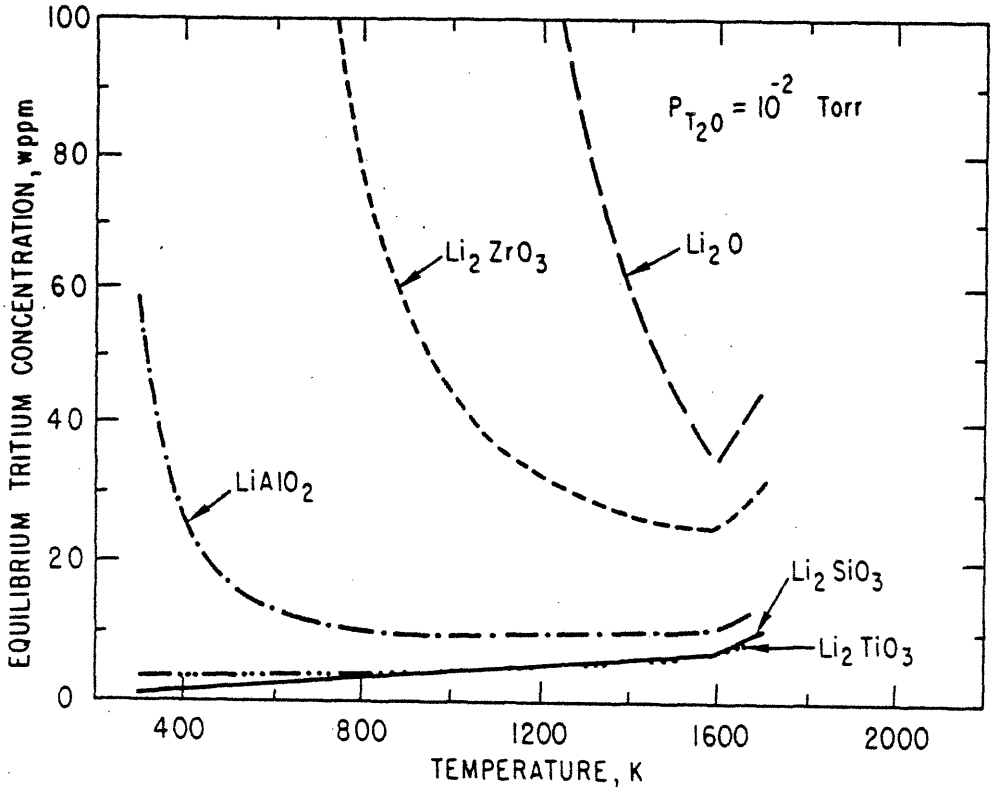

Fig. 8.2: Calculated Equilibrium Tritium Concentration in Candidate Solid Breeding Materials at P_{T_2O} = 1.3 Pa [8.9]

temperature would result in tritium being released during a thermal excursion.

The finite diffusion rates in the $LiAlO_2$ particles causes internal tritium concentrations to be higher than the surface. After start up, the concentration profiles will approach final values, see Fig. 8.3. The mean resistance time, t_r, is related to the tritium diffusivity, D_T, by the equation [8.9]

$$D_T = 0.16\ r_p^2/t_r \tag{8.9}$$

where r_p = particle radius

The stady state inventory due to diffusion is then

$$INV_D(\text{pellet}) = 0.5\ \dot{INV} \times t_r \tag{8.10}$$

where $\dot{INV}$ = breeding rate

In terms of diffusivity, the inventory is given by

$$INV_D(\text{pellet}) = 1/15 \times \dot{INV} \times r^2 \times D_T^{-1} \tag{8.11}$$

The STARFIRE study used the diffusivity of hydrogen in Al_2O_3:

$$D = 3.26 \times 10^{-4} \times \exp[-(57.2\ \text{Kcal/mole°K})/RT]\ m^2s \tag{8.12}$$

The breeding blanket of STARFIRE consists of particles with temperatures

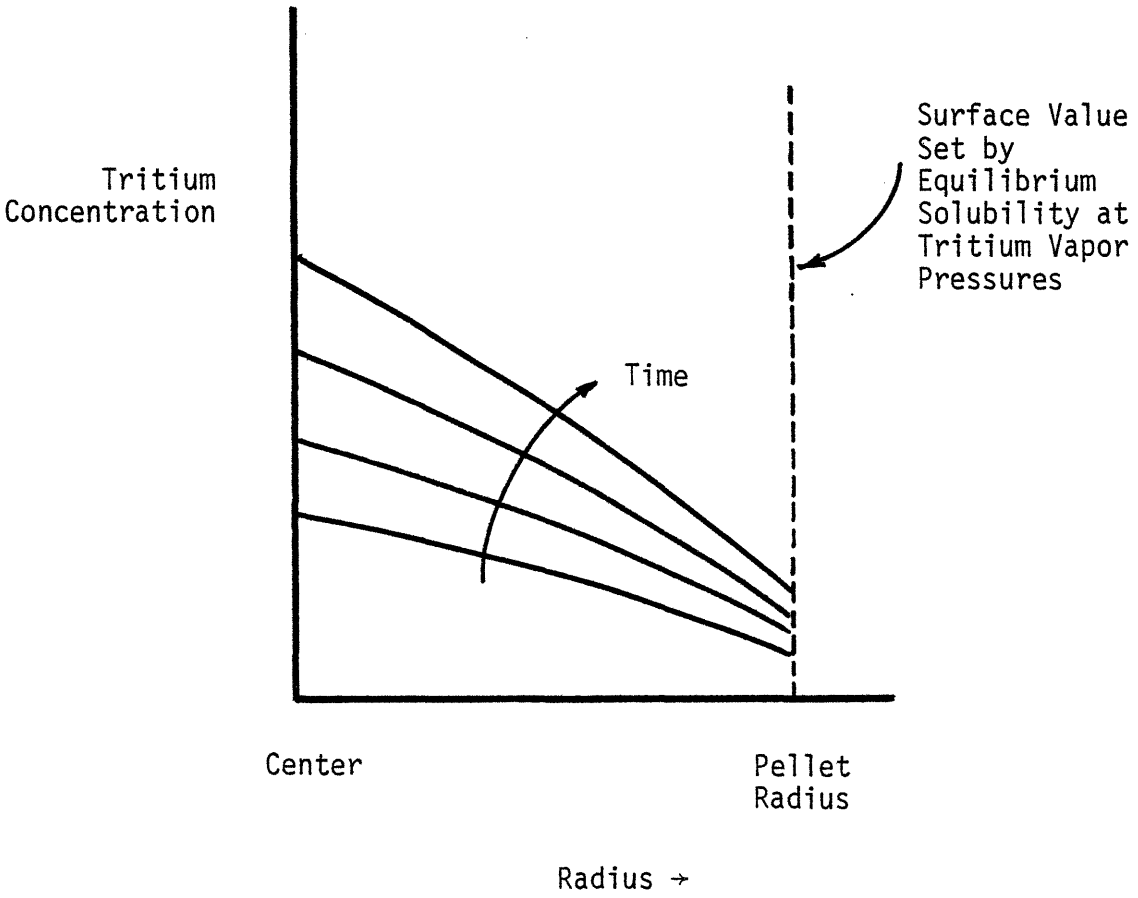

Fig. 8.3: Profile of Tritium Concentration in Solid Breeders as a Function of Space and Time [8.10]

ranging from about 508 to 846°C. The calculated total diffusion inventory is 0.14 kg [8.9] for 1 μm grain size.

There are a variety of uncertainties in the analysis. A major concern is the effect of radiation. The STARFIRE sudy [8.9] estimated the result of these effects as shown in Table 8.3. As discussed in the STARFIRE study, radiation damage effects may greatly (∿ 10-fold) increase the diffusion-held tritium inventory, and, in fact, determines this inventory component.

Hanchar [8.10] has examined the dynamics of diffusion, without radiation effects. The time constant to reach diffusion equilibrium in $LiAlO_2$ is quite short, about 30 minutes for tritium in a 10 μm particle at an average temperature of 650°C. Her analysis used a higher value of diffusivity, leading to faster equilibrium. Wiswall's data [8.11] (Fig. 8.4) would indicate a mean tritium residence time of about an hour for $LiAlO_2$.

The STARFIRE study assumed the solid diffusion path to be the grain size (∿ 1 μm radius) rather than the particle size, believing grain boundary transport to be significantly faster. This is another source of uncertainty. For comparison purposes, the tritium inventory in $LiAlO_2$ will be assumed to be predicted by the STARFIRE [8.9] estimates, 10 kg with 8 kg diffusion-held and 2 kg solubility-held. If later experiments were to indicate a significantly higher value, $LiAlO_2$ would probably not be used. Other possible ceramics include Li_2O and Li_2SiO_3 [8.7]. Available evidence suggests that the inventory in ceramic breeder blankets to be significantly higher than in liquid metal breeder blankets.

TABLE 8.3

$LiAlO_2$ Inventory Estimates
from the STARFIRE study [8.9]

	Without Radiation	With Radiation
Diffusion Inventory	∿0.14 kg	1.4 - 300 kg
Solubility Inventory	8.1 kg	8 kg
Total	8.2 kg	10 kg*

*Base case total

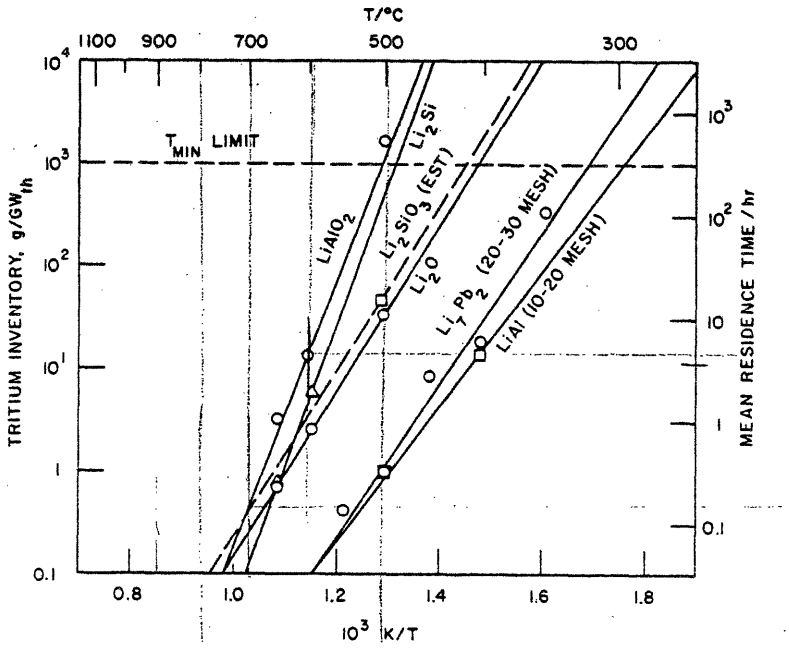

Fig. 8.4: Tritium Inventory and Mean Residence Time, from Ref. 8.9, Based on Data in Ref. 8.11

Due to mass transfer effects in the breeder zone, STARFIRE analysis indicated that the tritium vapor pressure would range from 0.1 to 100 Pa in the blanket. As mentioned above, the tritium solubility in $LiAlO_2$ was calculated based on an average vapor pressure of 1.3 Pa at the particle surface.

8.1.1.4 Flibe Coolant Inventory

The lithium in flibe ($LiF - BeF_2$) will generate tritium in addition to any tritium migrating into the coolant. Actually, as seen below, the tritium partial pressure in flibe may be considerably higher than that in a lithium breeder, so that tritium would tend to flow from coolant to breeder. It does appear, then, that the tritium levels in flibe will be controlled by flibe processing, not by inward migration. The literature allows two different approaches to estimation of the tritium level in flibe. Calaway [8.1] notes that reduction of tritium levels below 1 wppm is possible in the LiF - LiCl - LiBr processing salt used for extracting tritium from lithium. Flibe is itself a similar salt, and one could assume that processing can keep tritium levels at 1 wppm. This translates to a tritium inventory of 380 g.

The earlier PPPL [8.12] design using flibe as a breeder also examined the inventory question. They believed that the partial pressures of tritium species could be kept low:

$$P_{TF} \sim 1 \text{ torr} \sim 100 \text{ Pa} \tag{8.13}$$

$$P_{T2} \sim 10^{-2} \text{ torr} \sim 1 \text{ Pa} \tag{8.14}$$

Use of their estimates for the Henry's Law constant leads to an inventory for the present study of 1 g, 99% of which is in the TF form. As mentioned in Section 8.1.1.2, mass transfer limitations would tend to prohibit tritium levels this low. For calculational purposes an inventory of 10 g is assumed.

8.1.1.5 Water Coolant Inventory

The STARFIRE study examined the possible tritium levels in the water coolant. Their calculations indicate that the dominant source of tritium entering the coolant was through the first wall, including tritium insertion (implantation) directly into the beryllium first wall coating for the plasma particles striking the surface. They calculate a steady state inventory of about 0.3 Ci/liter after about 18 years operation (decay being the primary loss mechanism). To insure an inventory concentration of under 1 Ci/liter, the STARFIRE design includes a water processing system to remove tritium from the primary water coolant. A value of 0.3 Ci/liter leads to about 16 g in the water (8 g in each of two loops). If tritium inward migration would increase and raise tritium levels to the 1 Ci/liter level controlled by processing technology, the inventory would increase to about 55 g.

8.1.1.6 Helium Coolant Inventory

The partial pressures of HT, T_2, and HTO in a helium coolant are largely determined by the oxygen level and impurity control technology. Maroni [8.12] estimated that the pressures of HT and T_2 could be kept below 10^{-10} Pa by keeping the oxygen pressure (and HTO pressure) at about 1 Pa.

The later UWMAK-II study [8.13] estimated even lower elemental pressures; HT and T_2 pressures about 10^{-12} Pa. The required HTO pressure was about 10^{-1} Pa. The addition (non-removal of existing impurity) of oxygen tends to bind the tritium in oxide form. Hence the total entrained inventory is controlled by the HTO pressure. Even assuming the higher value of 1 Pa for the HTO pressure, the total coolant inventory is only about 1 g. The oxide form is easier to remove from the coolant and permeates less than the elemental form. The disadvantages are possible corrosion of metal (not a serious problem at these levels, see Chapter 7) and the higher biological hazard of the HTO form versus HT and T_2. This operational procedure means that tritium released in the event of a leak would be in the HTO form.

The above discussion implicitly assumes that sufficient tritium will migrate into the helium coolant to raise the inventory such that trititum will need to be controlled by some impurity control technology. In the STARFIRE study, about 10 Ci/day migrated into the water coolant, mostly from the plasma. A helium loop offers less resistance to inward flow because of a thinner oxide film and lower hydrogen pressures. Hence one would tend to expect at least a 10 Ci/day input to the coolant. Unless losses from the system were very high relative to this, one would expect a 1 gram level to be reached within a few years, without processing technology. Hanchar [8.10] calculated the steady state inventory to be reached in 118 days for the interim Li_2O/helium version of STARFIRE [8.14]. She also identified the oxygen level as being critical to determination of the tritium level. For the interim STARFIRE design, she estimated the tritium level to be 83 grams in

the coolant if no oxygen were present. If an oxygen pressure were established at about 10^{-11} Pa, the HT or T_2 inventory would be about 10^{-4} gm.

In view of the expected processing technology, it is believed that the total tritium inventory can be kept below 1 gm. The elemental tritium partial pressure would be about 10^{-10} Pa. Again, these estimates are considerably uncertain.

8.1.1.7 Structural Metal

Having estimated the tritium levels in coolants and breeders, it is possible to determine how much tritium is in the metal structure. The partial pressures in the breeders were found to be as high or higher than that in the coolants. For the lithium breeder cases, the concentration in metal is easily determined from the concentration in lithium by use of distribution values of concentration

$$\frac{N\ (\text{metal})}{N\ (\text{Li})} \sim \frac{K_s\ (\text{metal})}{K_s\ (\text{Li})} \cdot \frac{7}{M_{\text{metal}}} \tag{8.15}$$

where N is in wppm

M_{metal} is the atomic mass of the metal

Use of the values presented by Natesan and Smith [8.4] leads to very low metal inventories. Half of the metal was taken to be at the minimum breeder temperature and half at the maximum (Table 8.1). The results are shown in Table 8.4. Even the use of the higher partial pressures over $Li_{17}Pb_{83}$ would not result in tritium inventories in steel being above 1 g.

TABLE 8.4

Tritium Inventory in Metal Structure from Lithium Breeders

Coolant	Lithium	Lithium	Helium	Flibe
Metal	Steel	V-alloy	Steel	TZM
Tritium concentration in metal (wppm)				
at Maximum Temperature	4×10^{-6}	6.5×10^{-3}	2×10^{-5}	2×10^{-5}
at Minimum Temperature	$< 10^{-7}$	2×10^{-3}	2×10^{-6}	3×10^{-6}
Inventory in Metal (g)	(<< 1 g)	$\sim$2 g	(<< 1 g)	(<< 1 g)

For the $Li_{17}Pb_{83}$ and $LiAlO_2$ cases, the inventory in the steel is calculated by the Sievert's relation

$$N = K_S P_T^{1/2} \tag{8.1}$$

where P_T = tritium partial pressure over breeder

$K_S = 1.26 \exp(-1400/RT)$ appm/$Pa^{1/2}$ [8.15]

The Sievert's constant used is for 304L SS. The tritium over $LiAlO_2$ is assumed to be in elemental form for these calculations. This would tend to overestimate the structural inventory in contact with $LiAlO_2$.

8.1.1.8 Inventory Summary

The estimated steady state inventories in the various materials is shown in Table 8.5. Although there is considerable uncertainty in these estimates, general trends are detectable. As one might expect, the breeder inventory dominates the total. $Li_{17}Pb_{83}$ seems to lead to lower blanket inventories relative to the most understood lithium, while $LiAlO_2$ appears to result in the highest inventories and highest tritium partial pressures.

8.1.2 Normal Releases Through Coolant Loop

Although the present study is concerned with accidental releases, the choice of material will have an effect on normal operating losses of tritium through the coolant loop, a primary environmental concern. Thus, it is important to examine first order effects.

The major concern is tritium releases to the environment. From the viewpoint of blanket materials, the key pathway will be losses through

TABLE 8.5

Steady State Tritium Inventory in Components of Reference Material Combinations

Combination			Estimated Tritium Inventory (g)*		
Breeder	Coolant	Metal	Breeder	Coolant	Metal
Li	Li	316 SS	⟵ 840 ⟶		-
Li	Li	V	⟵ 840 ⟶		~ 1
Li	He	steel	630	$\lesssim 1$	-
Li	flibe	TZM	630	~ 10	-
$Li_{17}Pb_{83}$	water	steel	80	~ 20	< 1 g
$LiAlO_2$	water	steel	$\sim$10,000	~ 20	~ 10
$LiAlO_2$	He	steel	$\sim$10,000	~ 1	~ 10

*1 g of $^3H \sim 10^4$ Ci

the power cycle, from the primary coolant through the heat exchanger. Some systems will include an intermediate coolant, others go directly to a steam (helium turbine?) turbine loop. The important variables are the heat exchanger permeability and leakage, the primary coolant tritium pressure, and any systems for the secondary coolant. The breeder behavior is relatively unimportant (unless the breeder is also the coolant) in determining tritium releases to the environment. Only the primary coolant heat exchanger losses cannot be controlled through use of secondary containment techniques (double jacketed piping, etc.) (see, for example, reference 8.16).

Early calculations on heat exchanger losses all focused on simple permeation calculations. However, other factors, pin-hole leaks, oxide films, secondary coolant, and coolant mass transfer diffusion, are now seen as relevant. The combinations of power cycles are shown in Table 8.6.

8.1.2.1 Water Coolant Losses

The STARFIRE report [8.9] identified the expected presence of pin-hole leaks from the primary water to the steam cycle as totally dominating over permeation losses. Leaks through the heat exchanger (steam generator) would have to be kept below 30 liters/day for a 0.3 Ci/liter inventory to cause tritium losses through the power cycle to be below 10 Ci/day [8.9]. 10 Ci/day is an approximate target for designers, although it may not be stringent enough [8.16].

The choice of exchange material is relevant only insofar as it eliminates leaks. As discussed in Chapter 7, the reference material for

TABLE 8.6

Possible Power Cycles for Reference Primary Coolants*

Primary Coolant	Possible Intermediate Coolant	Possible Turbine Fluid
Pressurized water	———	steam
Helium	———	steam or helium
Lithium	Li, Na, or K	helium or steam
Flibe	Li, Na, or K**	helium or steam

*The secondary loop is the intermediate loop (if included) or the turbine loop (otherwise)

**If needed

either 316 SS or HT-9 blankets is Inconel, although a water coolant would allow use of other

It is important to realize that a pressurized water primary coolant does not allow an intermediate coolant loop. The low loop temperatures ($\sim$ 300°C) and low loop temperature drops ($\Delta T_{loop} \sim 40°C$) strongly oppose use of an intermediate loop. While this is an advantage from the efficiency and design complexity standpoint, it is a disadvantage from the tritium release viewpoint. If primary heat exchanger leaks from a pressurized water coolant were found to be excessive (more than 30 liters/day, higher than 0.3 Ci/liter inventory, or more stringent criterion than 10 Ci/day), no intermediate loop, and tritium processing therein, could be added to the power cycle.

8.1.2.2 Helium Coolant Losses

Watson [8.17] has estimated the leakage from a helium coolant to be about 0.01% per day, not all through heat exchanger. This translates to less than 1 Ci/day. The INTOR study [8.18] has noted that helium loss rates (total from the loop) are about 15%/yr (0.04% per day), based on helium-cooled fission reactor experience (Peach Bottom and Fort St. Vrain). Thus, the leakage expected through the primary heat exchanger seems possible to keep below 1 Ci/day.

The permeation across a metal wall is given by Richardson's equation [8.19],

$$\dot{m} = \frac{A}{d} K_p(T)[P_1^{1/2} - P_2^{1/2}] \qquad (8.16)$$

where $K_p(T)$ = permeation constant

P_1 = high side partial pressure

P_2 = low side partial pressure

A = area

d = wall thickness

Use of the data in reference [8.4] and design parameters of the reference cases leads to a permeation rate through the primary heat exchanger of 3 Ci/day, see Table 8.7.

This is likely to overestimate actual losses. At low tritium partial pressures, permeation does not follow Eq. (8.16). Tritium is in molecular form in the helium, hence at low enough pressures where gas phase mass transport is limiting, the partial pressure dependence should shift to linear. If the surface is not clean, a further decline is expected due to the barrier effectiveness of oxides [8.10, 8.20]. For the pressures expected (see Section 8.1.1.6), metal permeation (Eq. (8.16)) is not controlling, and losses are indeed lower, based on references 8.10 and 8.20. Although the exact loss rate is uncertain due to the uncertainties in metal surface conditions, helium purification technology, tritium species partial pressure, etc., the loss rates through the primary heat exchanger appear to be under 1 Ci/day which may be controlled by leakage, not permeation.

8.1.2.3 Lithium-Coolant

The lower operating pressures in a lithium loop tend to reduce leakage problems. Furthermore, tritium is an ionic form in lithium. Thus, a $P_T^{1/2}$ dependence on permeation is expected even for low tritium partial

TABLE 8.7

Estimated Tritium Losses from Permeation Losses Through Primary Heat Exchanger to Secondary Coolant*

Coolant	Helium	Lithium	Lithium	Flibe
Metal	316 SS	316 SS	V-alloy	TZM
Wall Thickness (mm)	2	2	2	2
Heat Exchanger Area (m^2)	20,000	5,000	5,000	5,000
Tritium Partial Pressure	0.1 nPa	0.25 μPa	1.4 μPa	1 Pa
High Temperature (°C) (Half of Area at this temperature)	500	450	550	800
Losses through Heat Exchanger (Ci/day)**	3	10	10^5	10^5

*No credit taken for permeation barriers or fluid mass transfer resistance. Permeation data from reference 8.4 (see Fig. 8.5).

**Losses to secondary coolant; for lithium and flibe one envisions this to be an intermediate loop; for helium and water, the secondary coolant is the turbine loop.

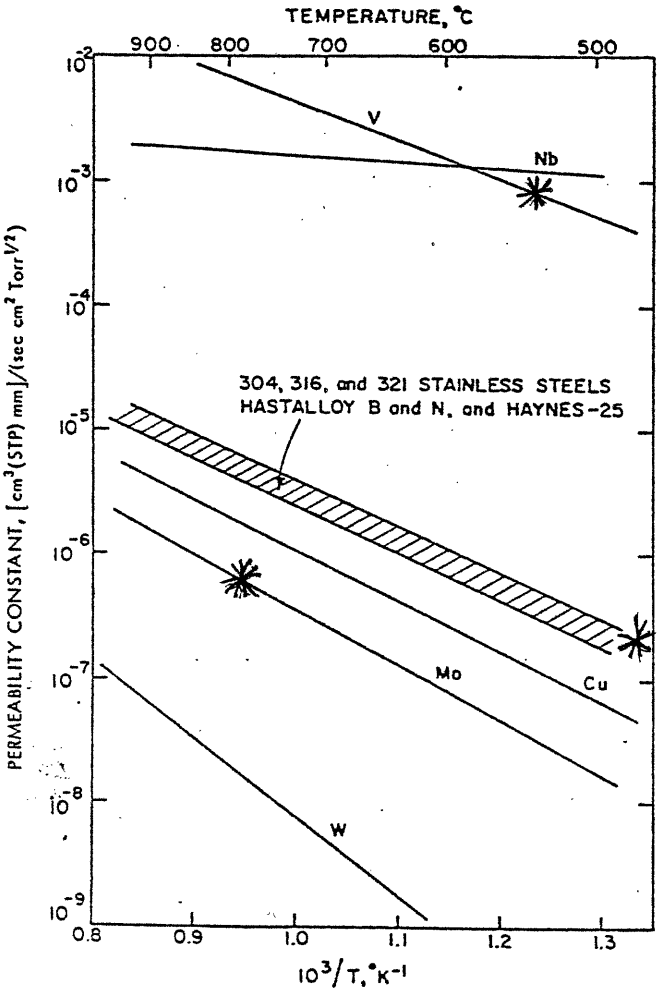

Fig. 8.5: Temperature Dependence of the Permeability Constant for Hydrogen in Several Metals and Alloys [8.4]

*Location of reference metals and temperatures.

pressures, and liquid phase mass transfer does not appear limiting [8.20]. The heat exchanger losses are then determined by tritium partial pressure in the lithium, permeability of the heat exchanger metal, and metal wall surface condition and/or cladding.

As discussed in Chapter 7, dissimilar metal mass transport problems appear to prohibit use of a Fe-Cr-Ni alloy throughout the primary coolant loop when V-alloy is used as the blanket structural material. The present base case is for V-alloy to be used throughout that loop. The results for the two lithium cases is shown in Table 8.7 with no credit for oxide barrier effectiveness. The Li/316 SS case is seen to be similar to that of water/316 SS. An intermediate coolant loop tritium cleanup system may not be necessary; however, lithium primary coolants are seen as having an intermediate loop for other reasons. Thus, the flexibility of adding a cleanup system to the intermediate loop does exist, unlike the water coolant case, if needed to reduce tritium permeation losses.

The high permeability of vanadium and its higher operating temperature result in exceedingly high tritium loss rates. As suggested by Natesan and Smith [8.4], such high rates would have to be reduced by either an intermediate loop detritiation system and/or additional permeation barrier effectiveness, e.g., tungsten or molybdenum cladding. They calculate that these methods can reduce tritium losses from the intermediate loop to low levels for a Nb/lithium primary loop. As niobium and vanadium have very similar permeability, the result holds for the vanadium/lithium case. Thus it is anticipated that tritium losses through the lithium coolant loops can be kept to

acceptable levels, although this will be far more difficult for the vanadium case. The corrosion product film which should be present at the heat exchanger could be expected to significantly (by 100-1000-fold) reduce the permeation losses. If mass transfer corrosion problems prohibit use of Fe-Cr-Ni alloys for out-blanket piping with a V-alloy blanket, perhaps a TZM or other refractory metal could be used to reduce tritium permeation losses.

8.1.2.4 Flibe-Coolant Losses

As shown in Table 8.7, the flibe/TZM case exhibits very high permeation losses. This is somewhat surprising since molybdenum (TZM) has low permeability (Fig. 8.5) compared to other materials considered. However, the higher operating temperature raises the permeability to about that of steel at the steel operating temperature. The high partial pressure in flibe thus causes high permeation losses to the intermediate loop. Because fluid mass transfer limits and oxide film effects were neglected, the values of permeation losses is likely to be an overestimate. There is an insufficient data base to quantify the possible effectiveness of corrosion films.

The tritium species in flibe are molecular T_2 and HF; thus the permeation law should shift to a linear partial pressure dependence at low partial pressures [8.20]. Use of the Zarachy and Axtmann Model [8.20] would indicate a thousand-fold reduction in permeation rates due to the limitations of mass transfer within the flibe. Even so, a 100 Ci/day transfer rate may be expected to the intermediate loop. However, as in the lithium case, the combination of an improved barrier (tungsten cladding?) or an intermediate loop detritiation system should be able to limit losses from the intermediate loop to acceptable levels.

8.1.2.5 Normal Losses Summary

The conservative estimates for normal operational tritium losses from primary to secondary coolant loops are summarized in Table 8.8. Oxide film reduction of permeation is not included. The helium case is best. Since intermediate loop processing systems could further reduce rates in the lithium/steel case, it is second best.

The V-alloy/lithium and TZM/flibe cases could exhibit substantial losses from the primary loop. Appropriate use of intermediate loop processing, corrosion films, and claddings will be required to keep losses to the environment to acceptable rates. The pressurized water case is interesting. The estimated loss rates are probably best known of all the coolant/metal cases; however, the loss rate is only marginally acceptable and there is relatively very little design flexibility to further improve tritium loss rates.

8.1.3 Possible Maximum Accidental Releases

Having estimated the blanket tritium inventory, the possible maximum accidental releases can be estimated. Of course, tritium may be released from non-blanket materials. The STARFIRE study [8.9] identified a variety of tritium system components which could fail and release tritium to the building atmosphere. They determined that the maximum release from a single component failure would be 10 g. Generally, in design studies, the largest amounts of tritium are in the blanket breeder or the external storage system. The latter is simpler than the blanket, probably unaffected by reactor blanket accidents, and beyond the scope of this study. The problem of estimating the blanket tritium release

TABLE 8.8

Estimate Tritium Losses Through
Primary Heat Exchanger to Secondary Coolant[a]

Coolant	Water	Helium	Lithium	Lithium	Flibe
Metal	Steel	Steel	Steel	V-alloy	TZM
Primary Heat Exchanger Losses (Ci/day)	~10	~1[(b)]	~10[(b)]	~10^5 (b)	10^2-10^5 (b)
Controlling Process	leakage	leakage or permeation	permeation	permeation	permeation
Intermediate Loop Required for Tritium Loss Limitation	Maybe	No	Yes	Yes	Yes
Intermediate Loop Allowed by Design Constraints	No	Maybe	Yes	Yes	Yes

[a]Loss to secondary coolant; for lithium or flibe this is the intermediate loop; for water or helium, this is the turbine loop.

[b]No credit for oxide barrier effectiveness or other permeation barriers.

can be expressed in terms of release fractions.

8.1.3.1 Fission Experience

The present problem is somewhat analagous to the problem of determining the release fraction of radioactiye species in a fission reactor, particularly the more mobile ones. The release fractions of the more mobile species to the environment which were estimated for the Reactor Safety Study [8.21] are shown in Table 8.9 for some accident scenarios. The release fraction is a strong function of the accident scenario. In the wake of the Three Mile Island experience, there is a general current re-evaluation of these release fractions, which appear to be overestimates. In other words, as knowledge and experience grows, over-conservatisms are reduced and estimated release functions should become more realistic.

Given the present state-of-knowledge in fusion tritium behavior, it is anticipated that the actual releases would be below the estimates given below.

8.1.3.2 Blanket Tritium Release Mechanisms

Given the scope of this work and the state-of-knowledge, the approach used to estimate the possible blanket tritium release will be to identify the worst potential mechanisms which could result in tritium release to the building. Although the governing kinetics of these mechanisms will be addressed to verify it representing a realistic accident scenario, calculations will focus on equilibrium results. Four mechanisms are outlined:

1) Tritium present in fluid form can be directly released to the building.

TABLE 8.9

Some Release Fractions for Mobile Species
From the Reactor Safety Study [8.21]

	Chemical Species		
	Cs,Rb	I	Xe,Kr
PWR Category I Meltdown Containment Fails	0.4	0.7	0.9
PWR Category VIII Cladding Failure Gap (Gap Release) Containment Fails	5×10^{-4}	1×10^{-4}	2×10^{-3}
PWR Category IX Cladding Failure Containment Holds	6×10^{-7}	1×10^{-7}	3×10^{-6}

2) Tritium present in combustible material can be released to the building in the form of volatile combustion products.
3) Tritium present in any material may be released to the building due to a change in solubility and diffusion parameters due to a thermal transient in the blanket.
4) Tritium present in a solid material may be released to the building if a phase change (melting) occurs as the result of a thermal transient.

8.1.3.3 Helium Coolant

In the event of a helium coolant loop leak, all the tritium could be released to the building. Hence the release function for the helium coolant (and helium purge stream) is 1.0 and the maximum release would be about 1 g.

8.1.3.4 Liquid Metal and Molten Salt

In the event of a leak in the coolant or breeder system containing lithium, $Li_{17}Pb_{83}$, or flibe, all the tritium would be released to the building, The maximum release fraction is 1.0.

However, it is instructive to examine how each of these liquids could behave. In the absence of combustion, lithium (m.p. 180°C), $Li_{17}Pb_{83}$ (m.p. 235 m.p.), and flibe (m.p. 459°C) would all tend to solidify on the building floor, thus locking in much of the tritium. The solidification process itself can release some gaseous tritium due to a change in Sievert's constant. This has been observed in the case of $Li_{17}Pb_2$ solidification [8.22]. The remaining tritium would be fairly immobile due to the far lower diffusivity in the solid phase

at the lower temperatures.

If combustion were to occur, combustion species like LiOT could be produced in the containment, although many of the combustion products would be expected to plate out on cooler surfaces in the building. The role of solubility and diffusion, if fluid temperatures were to rise, is discussed in the next section. Although the maximum release function is set at 1.0 for these fluids, it is emphasized that much of it would not be volatilized.

8.1.3.5 Gaseous Tritium Release from Lithium due to Solubility

The most worrisome type of tritium release would be tritium in the gaseous form. A simple calculation can estimate how much tritium may be released to the building in gaseous form. For any material the initial inventory, INV_o, is divided into the solubility, INV_{os}, and diffusion, INV_{od}, components. For quasi-equilibrium conditions, the inventory during the transient must be partitioned amoung solubility, INV_s, diffusion, INV_d, and building containment gaseous tritium, INV_c. Conservation of mass gives

$$INV_o = INV_{os} + INV_{od} = INV_s + INV_d + INV_c \qquad (8.17)$$

Use of the ideal gas law allows the building containment inventory to be related to the building temperature and tritium pressure,

$$INV_c(kg) = \frac{180.4}{T_c(°K)} P_T(Pa) \qquad (8.18)$$

The diffusion inventory in liquid lithium is thought to be very low, with solubility effects completely controlling,

$$INV_o = INV_{od} = INV_d + \frac{180.4}{T_c(°K)} P_T(Pa) \tag{8.19}$$

Since the initial inventory is 5 appm and the total inventory is 0.84 kg, use of the Eqs. (8.1) and (8.2) gives an expression for the diffusion inventory

$$INV_d = (1.524)(e^{5070/T_b})P_T^{1/2} \tag{8.20}$$

where T_b = blanket lithium temperature (°K)

Then the Eq. (8.19) can be rewritten

$$0 = \frac{180.4}{T_c} P_T + (1.524)(e^{5070/T_b})P_T^{1/2} - 0.84 \tag{8.21}$$

For lithium blanket temperatures, T_b, less than the vaporization point, 1340°C, the solution to Eq. (8.21) is given within 1% by

$$P_T(T_B) = 0.3 \exp(-10140/T_b) \tag{8.22}$$

Then the inventory of gaseous tritium in the building is given by

$$INV_c(T_c,T_b) = \frac{54.8}{T_c} \exp(-10140/T_b) kg \tag{8.23}$$

If the building temperature increases, the tritium is pushed back into the lithium, whereas higher lithium temperatures result in higher released gaseous tritium. Clearly Eq. (8.23) neglects important mass transfer kinetics, but it does indicate an approximate limit on the amount of gaseous tritium released from a lithium pool. For lithium temperatures below vaporization and a room temperature building, less than 1 g of tritium would be expected to be in the gaseous form, (release function of 0.001), although all may leave the blanket itself. The data base for $Li_{17}Pb_{83}$ is insufficient to do a similar analysis for that case.

8.1.3.6 Pressurized Water

The tritium entrained in the pressurized water coolant would all be released to the building if a leak occurred. Initially after a water loop rupture, much of the water would be steam (see Chapter 5) and the tritium (as HTO, T_2O) would be very mobile. Unlike the liquid metals/molten salts, the water would not be expected to freeze in the building, leaving the tritium highly mobile.

The presently conceived emergency building atmosphere detritiation systems operate by converting tritium to the HTO form and then absorbing it on cyropanels. The high volume of tritiated steam caused by a pressurized water coolant leak could overwhelm such a system. Thus, the STARFIRE design calls for the detritiation system to be shut off if a steam environment were caused [8.9]. Adequate handling of a large volume of heavily tritiated water will not be easy.

8.1.3.7 $LiAlO_2$ Breeder

Unlike the previous cases, $LiAlO_2$ is solid. Some have characterized the tritium in the $LiAlO_2$ as "invulnerable" compared to more vulnerable tritium systems, see ref. 8.9. However, a substantial release is possible, even though $LiAlO_2$ is fairly non-combustable and solid.

Equation (8.17) holds for the $LiAlO_2$ case as well as lithium. Unlike lithium, however, the diffusion controlled operating inventory is not zero, but rather about 2 kg. The solubility component is about 8 kg (see Section 8.1.1.3). If the elemental form of tritium is assumed, Eq. (8.18) applies. Then Eqs. (8.17) and (8.18) result in

$$10 \text{ kg} = \frac{180.4}{T_c} P_T + INV_s + INV_d \tag{8.24}$$

Since the solubility for $LiAlO_2$ is approximately constant with higher temperatures (see Fig. 8.2), the solubility inventory is given by

$$INV_s \sim 8(P_T/P_{T(\text{operation})})^{1/2} \tag{8.25}$$

The operating solubility was determined using an average partial pressure of 1.3 Pa. Then Eq. (8.24) can be re-written

$$0 = \frac{180.4}{T_c} P_T + (7.016)P_T^{1/2} - 10 + INV_d \tag{8.26}$$

In STARFIRE, the $LiAlO_2$ operating temperature ranges from about 500 to 850°C. The high temperature effect on diffusivity (Eq. (8.12), Fig. 8.4) causes 19% of the diffusion inventory to be in the coldest 1% of the blanket, and 98% of the diffusion-limited inventory to be in

the coldest 10% of the blanket. If the blanket temperature gradient were to simply flatten in an accident, over 99% of the original diffusion-limited inventory would be freed. Any afterheat or continuing plasma heating after a LOCA (Chapter 3) would further increase $LiAlO_2$ temperatures. The approximate time for the diffusion-limited inventory to be baked-out can be estimated from Eqs. (8.9) and (8.12),

$$t(T_b) \sim 4.9 \times 10^{-6} \exp\ (28{,}810/T_b)\ \text{sec} \tag{8.27}$$

where T_b is the $LiAlO_2$ temperature (1 μm grain).

Thus a few hours are required at the average blanket temperature (if the thermal gradient were to flatten as a result of a LOCA) for the diffusion limited inventory to be released. However, even a modest further average 100°C increase to about 775°C (e.g., due to afterheat) would reduce the time required to below 10 minutes. Given the thermal transients possible (Chapter 3), it appears that mechanisms are available to eliminate diffusion restrictions on the $LIAlO_2$ inventory in relatively short times; thus INV_d can go to zero. Then, Eq. (8.26) can be solved,

$$P_T^{1/2} = -0.0194(T_c) + \sqrt{(3.78 \times 10^{-4})T_c^2 + 0.055(T_c)} \tag{8.28}$$

For the case where the building atmosphere is 20°C, then the partial pressure would be 1.64 Pa and 1 kg of tritium will have been released to the building in gaseous form. This is one-half of the original diffusion-controlled inventory. If the tritium pressure at the $LiAlO_2$ surface were considered constant at the design value of 1.3 Pa, then

all the diffusion controlled inventory (2 kg) would be released.

8.1.3.8 Solid Metals

The steady state inventories in the reference materials are low, below 10 g. The analysis for other coolant and breeder components indicate that the worst tritium release from the breeder would be large compared to 10 g. The behavior would be qualitatively similar to that of $LiAlO_2$.

8.1.3.9 Maximum Tritium Releases to Building

Table 8.10 summarizes the maximum possible tritium releases to the reactor building from blanket materials. The breeder releases dominate in quantity, although some coolant releases may be more probable. Even given the uncertainties mentioned above, the worst breeder material from the standpoint of the highest amounts of tritium released to the building is the $LiAlO_2$ case. In the future, a variety of kinetic calculations and experiments will be required to more precisely determine potential tritium releases from blanket materials. Realistically, actual releases to the building can be expected to be lower than that listed in Table 8.10. Accidental releases to the environment would be still lower.

8.2 Structural Radioactivity Inventory and Comparison Bases

In addition to tritium, a fusion reactor based on a neutron producing reaction will experience substantial amounts of structural activation. Of the safety comparisons among potential D-T reactor structural materials, the most obvious and common have been comparisons of radioactivity hazard. The hazard evaluation is made more difficult

TABLE 8.10

Estimated Maximum Possible Amounts of Tritium
Released to the Reactor Building from Blanket Component Materials

Combination			Releasable to Building (g ^3H)		
Breeder	Coolant	Metal	Breeder	Coolant	Metal
Li	Li	316 SS	840		-
Li	Li	V-alloy	840		-
Li	He	steel	630	∿1	-
Li	flibe	TZM	630	∿10	-
$Li_{17}Pb_{83}$	water	steel	80	∿20	-
$LiAlO_2$	water	steel	∿1000	∿20	<10
$LiAlO_2$	He	steel	∿1000	1	<10

by the lack of data on various fusion-specific isotopes.

8.2.1 Comparison Bases

8.2.1.1 Radioactivity Problems

Reading through previous works mentioning fusion radioactivity, a variety of issues become apparent. These can be listed in approximate order of the time scale involved:

1) Decay afterheat
2) Contact dose rates (maintenance difficulties)
3) Public dose due to acute accidental releases
4) Public dose due to normal operational releases
5) Chronic dose due to accidental releases
6) Material recycling, waste disposal, decommissioning

It is very important to realize that there may be an immense difference among the isotopes which tend to dominate each of these problems. Thus, a specific alloy may appear better than others in some aspects but remain a worst case in another. For example, aluminum alloys are generally viewed as being "low activation" materials. However, initially the activity is significant, it simply decays quickly; the afterheat generated appears to cause more severe problems for "low activation" aluminum than for the four reference materials of this study [8.23], see Chapter 3. The first problem, afterheat, is addressed in Chapter 3.

Contact dose rates from the materials studied are all too high to prevent direct manned access to the first wall or blanket. The level in excess is not so important. However, major effort can and has been

taken to decrease the dose rates beyond the shield [8.9]. Different materials than those considered here for the blanket may be used in the shields and magnets which can significantly alter some maintenance/access problems. This is beyond the scope of this study as the blanket materials are not strongly involved.

The third and fifth problems related to accidental public dose are central to this study and are discussed in the remaining portions of this chapter.

The fourth problem is that of tritium, discussed above, and corrosion, the primary method of mobilizing blanket structural radioactivity under normal operation, see Chapter 7. Tritium will likely dominate the normal operation hazard. In Chapter 7, the activity mobilized from corrosion was calculated.

The sixth problem is relatively undefined at present in terms of what is acceptable. The blanket of STARFIRE contains about 98% of the activity, but is less than 10% of the structural volume [8.9]. This indicates that from the overall viewpoint of material re-use, the selection and activity of non-blanket materials is more important than that of blanket materials.

A decommissioning study [8.24] focused on a vanadium first wall/blanket. The first wall remained at high level activity (> 10 Ci/liter) for over 10 years, while the bulk blanket remained high for 5 years. The steels and molybdenum will be worse. The present study's scope does not include quantifying the waste/recycling problem. Although none of the following pathways provide an adequate hazard index for recycling/waste considerations, it is possible to say that a rough ordering based

on long-term activity levels would appear to be V-alloy (best), HT-9, 316 SS, TZM (worst).

8.2.1.2 Relative Comparsion from Accidental Release

A variety of methods have been used to quantify the relative consequences from different structural materials. These are listed in Table 8.11. The measures of activity and biological hazard potential have been most often used. The former, of course, must be the starting point for more appropriate calculations relating health effects.

The biological hazard potential is defined by

$$BHP \sim ACT/MPC \tag{8.29}$$

where ACT = activity (Ci)

MPC = maximum permissible concentration.

Since the MPC is defined for steady state allowable concentrations in air or water, so is the BHP. Thus the BHP is actually a measure of how much dilution is required to reduce activity concentrations to the MPC level.

The regulatory bodies, ICRP and NCRP, (see ref. 8.25) have established MPC values for many isotopes by first establishing the permissible dose to each organ (e.g., < 3 rem/13 weeks to the whole body) from a steady state body inventory. This determines the maximum permissible body burden for each organ. When the ratio of total body burden to individual organ is known, this allows determination of the maximum permissible total body burden. The organ which causes the

TABLE 8.11

Bases of Comparison of Release Consequences of Fusion Structural Radioactivity

I. Radioactivity (Curies)

First Step
Easiest, most often used
Ignores differing effects of isotope activity

II. Biological Hazard Potential (BHP)

Based on the Maximum Permissible Concentration (MPC)
Basis - one critical organ per isotope
- steady state intake
- inhalation only
MPC not determined for many isotopes
Often used

III. Dose (rem)

Based on organ specific dose factors
Basis - as many organs per isotope as desired
- inhalation, groundshine, cloudshine, ingestion
Rarely used at present
Used in present study to identify important isotopes

IV. Public Health Effects (FUSECRAC Code)

Based on fission public consequence code, CRAC
Relatively weak data base, quite complex
Developed for use in present study

lowest value of the total body burden is the critical organ for that isotope. Thus the MPC measure only considers one organ; effects are not summed over the body.

The common practice in fusion assessments has been to use the MPC values for public exposure, rather than occupational, and the most restrictive value of MPC, whether for an isotope in soluble or insoluble chemical form. The official list [8.25] stipulates a value of 0.1 Ci/kw^3_{air} for half-lives greater than 2 hours and 3,000 Ci/kw^3_{air} for half-lives of less than two hours if the specific isotope's value of MPC is not specified.

The major drawbacks to the BHP measure for comparing accidental releases can be summarized as follows:

1) There is no accounting for decay and transport in an accidental situation from reactor to public.
2) Inconsistent treatment of the chemical form of the release (soluble or insoluble, the most restricted form is arbitrarily used).
3) Incomplete data base - MPC not set or only crudely estimated for several isotopes.
4) Critical organ not established for many isotopes.
5) Only internal intake of air and water considered. Ingestion of food and external gamma exposure (cloudshine, groundshine) are ignored.

Because a variety of MPC's are not established for some isotopes (see Section 8.2.2, Table 8.12), past researchers have either used the above limit cases or crudely estimated MPC calues. Hence, there may be a bias against materials containing more isotopes with weak data bases.

TABLE 8.12

Fusion Related Isotopes for Reference Materials[b]

Name	Radioactive Daughter	Half-Life
^{3}H	-	12.3 y (a)
^{14}C	-	5730 y (a)
^{16}N	-	7.1 s
^{24}Na	-	15.0 h
^{26}Al	-	7.4×10^{5} y
^{28}Al	-	2.3 m
^{29}Al	-	6.6 m
^{30}Al	-	3.3 s
^{31}Si	-	2.62 h
^{45}Ca	-	163 d (a)
^{47}Ca	^{47}Sc	4.5 d
^{46}Sc	-	83.8 d
^{47}Sc	-	3.4 d
^{48}Sc	-	44 hr
^{49}Sc	-	57.5 m
^{50}Sc	-	1.8 m
^{45}Ti	-	3.08 h
^{51}Ti	-	5.80 m
^{49}V	-	330 d (a)
^{52}V	-	3.77 m
^{49}Cr	^{49}V	42 m
^{51}Cr	-	27.8 d
^{53}Mn	-	3.7×10^{6} y (a)
^{54}Mn	-	312 d
^{56}Mn	-	2.58 h
^{57}Mn	-	1.7 m
^{55}Fe	-	2.4 y (a)
^{59}Fe	-	45 d
^{57}Co	-	272 d
^{58}Co	-	71 d
^{60}Co	-	5.24 y
^{60m}Co	^{60}Co	10.5 m
^{61}Co	-	1.65 h
^{57}Ni	^{57}Co	36 h
^{59}Ni	-	8×10^{4} y (a)
^{63}Ni	-	92 y (a)
^{65}Ni	-	2.56 h
^{89}Sr	-	50.6 d (a)
^{88}Zr	^{88}Y	84 d
^{89}Zr	-	78.4 h
^{93}Zr	-	9.5×10^{5} y
^{95}Zr	$^{95m}Nb, ^{95}Nb$	65 d

TABLE 8.12 (Continued)

Name	Radioactive Daughter	Half-Life
^{97}Zr	^{97m}Nb, ^{97}Nb	17 h
^{88}Y	-	107 d
^{90}Y	-	64.2 h
^{91}Y	-	59 d
^{91m}Nb	^{91}Nb	62 d
^{91}Nb	-	long, $\sim 10^5$ y
^{92m}Nb	-	10.2 d
^{92}Nb	-	3.2×10^7 y
^{93m}Nb	-	13.6 y
^{94m}Nb	^{94}Nb	6.3 m
^{94}Nb	-	2×10^4 y
^{95m}Nb	^{95}Nb	87 h
^{95}Nb	-	35 d
^{96}Nb	-	23.4 h
^{97m}Nb	^{97}Nb	1 m
^{97}Nb	-	72 m
^{98}Nb	-	2.9 s
^{100}Nb	-	3.1 s
^{91}Mo	^{91m}Nb, ^{91}Nb	15.5 m
^{93}Mo	^{93m}Nb	3.5×10^3 y
^{99}Mo	^{99m}Tc, ^{99}Tc	66 h
^{101}Mo	^{101}Tc	14.6 m
^{99m}Tc	^{99}Tc	6 h
^{99}Tc	-	2.1×10^5 y(a)
^{101}Tc	-	14.3 m
^{182}Ta	-	115 d
^{183}Ta	-	5.1 d
^{184}Ta	-	8.7 h
^{185}Ta	^{185m}W, ^{185}W	49 m
^{186}Ta	-	10.5 m
^{181}W	-	121 d
^{185}W	-	75.1 d
^{187}W	^{187}Re	23.9 h
^{187}Re	-	4×10^{10} y(a)

(a) No gamma decay

(b) Data from references 8.28, 8.29

The most serious drawback is the lack of a kinetic treatment and the inclusion of only inhalation and water ingestion exposure pathways.

Fission accident consequence calculations and comparisons are not performed by BHP or MPC measures. Detailed consequence codes like CRAC - Calculation of Reactor Accident Consequences [8.26] are used. A slightly modified version for fusion with a fusion data base, FUSECRAC [8.27], has been developed for this study and is the primary basis of comparison used (Section 8.4).

The CRAC and FUSECRAC codes can only accept data from exposure pathways for a limited number of isotopes due to calculational and storage considerations. Thus a preliminary screening of the isotopes was performed (Section 8.3) to determine the important contributors. Although MPC and BHP measures are inappropriate for use in accident assessments, they appear more useful as a measure of waste disposal hazards.

8.2.2 Fusion Isotopes

Based on the structural radioactivity data discussed in Section 8.2.3, a list of fusion-relevant isotopes was prepared and is shown in Table 8.12. The isotope data are from references 8.28 and 8.29. These isotopes are induced in at least one of the reference structural materials, although they may not be significant contributors to the total.

Examination of the list indicates that a variety of isotopes may be present for which the data base is weak, primarily those isotopes which have not been of interest in fission or medical work. One benefit of this study, as seen later, is the identification of which isotopes

appear significant contributors to exposure and which require improved data.

8.2.3 Reference Structural Radioactivity

The radioactivity levels are affected by material choice, elemental tailoring, isotopic tailoring, neutron wall loading, operation time, and design geometry. The selection of structural materials is a prime determinator of the radioactivity inventory. The selection of breeder and coolant can impact the inventory by either altering the neutron spectrum, hence the structural material inventory, or containing substances which themselves activate. Previous studies [8.2, 8.9] show that the coupling due to the neutron spectrum is fairly minor, especially at the first wall (see for example Fig. 8.6).

Of the non-structural substances included in this study, only $Li_{17}Pb_{83}$ and neutron multipliers appear to have significant activation potential. The very short-lived isotopes ($\lesssim$ sec) caused by oxygen and fluorine activation are not significant contributors to accident releases. The multiplier Zr_5Pb_3 represents about 38% of the total STARFIRE activity [8.9]. Fortunately, most of the activity is caused by zirconium, not lead (see Fig. 8.7) so that the $Li_{17}Pb_{83}$ material appears fairly clean. The major Pb-related isotopes appear to be ^{205}Pb and ^{204}Tl, although some isotopes were excluded, like ^{207}Bi, due to lack of data [8.9]. The major Al-related isotope ($LiAlO_2$) is the long-lived ^{26}Al [8.9]. For the present study, only the structural radioactivity and tritium will be examined since they appear to be the overwhelming contributor to the total (if multipliers like Zr_5Pb_3 are avoided).

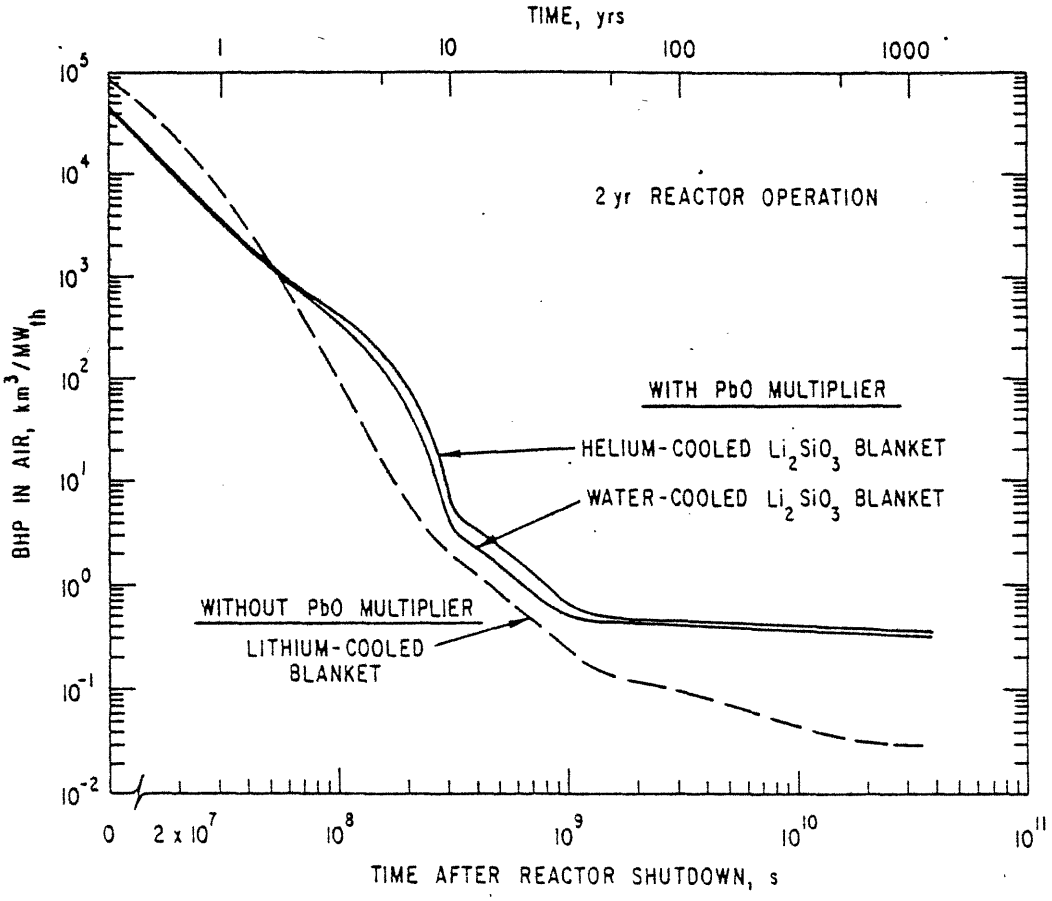

Fig. 8.6: Effect of Different Coolants on Biological Hazard Potential [8.14]

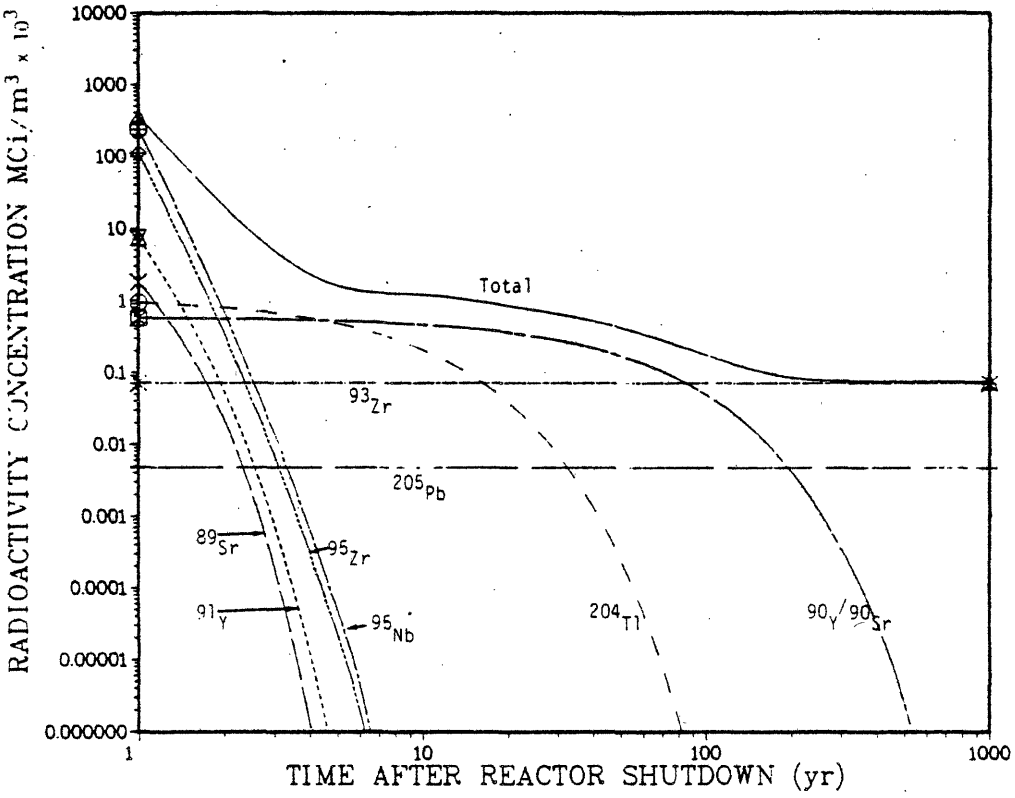

Fig. 8.7: Isotropic Radioactivity Contribution of Zr_5Pb_3 Neutron Multiplier [8.9]

Elemental tailoring refers to the selection of alloying elements to reduce activation hazards. Alloying selection is, however, influenced by a wealth of metallurgical factors. For the present study, the reference materials were considered fixed with composition as discussed in Appendix B. The data for 316 SS and vanadium (V-15Cr-5Ti) is from J. Jung [8.31], performed for the ANL blanket study [8.2] and decommissioning study [8.24]. The data for TZM is from Okula [8.32], performed for UWMAK-III [8.33]. It should be noted that altering alloy composition is a complex problem which is easier to specify in safety studies than accomplish successfully in practice. Furthermore, reasonably expected impurities and minor elements in metal alloys should not be neglected.

Isotopic tailoring refers to the alteration of the isotopic mix of the natural composition of an element prior to use. Michaels [8.34] has examined the economics of controlling iron and nickel isotopes for LWR applications and found a 14% rate of return on the investment required. Applying such a model to fusion would require much information which is unavailable, including the economics of blanket module recycling and waste disposal. The potential benefit is not clear, although Jung [8.9] notes some possibilites. For the present study, isotopic tailoring will be ignored.

The neutron wall loading level has a linear effect on activity level to first order. The activity values used to screen isotopes (Section 8.3) were scaled to a 1 MW/m^2 neutron flux. For the actual comparisons using FUSECRAC (Section 8.4), the radioactivity levels were based on the reference 3.6 MW/m^2 neutron wall loading.

The operation time influences the buildup of the various isotopes

differently. It is often reported that after about a year, the activity levels of the various materials are fairly constant at saturation levels, with the exception of ^{55}Fe ($T_{1/2}$ = 2.4 yr) in steels. However, this refers to the total activity, not the specific isotropic mix.

To first order, the buildup of an isotope, n_i, is given by

$$n_i(t) = n_i(\infty)(1 - e^{-\lambda_i t}) \tag{8.30}$$

The actual situation is more complex due to secondary reactions of product isotopes which can add or subtract to the concentration of a given isotope. The comparison among alloys should be done on an equal basis. Unfortunately the best data for TZM is only for 2 years of operation, whereas V-15Cr-5Ti and 316 SS data are available for 10 years of operation. The actual operation time of a blanket may fall in between these limits. For afterheat (Appendix B), the most important behavior was for times in the first day, primarily determined by the shorter-lived isotopes which reach saturation within two years. For public dose consequences, longer term isotopes will be seen to dominate. Thus, although the short-term thermal transient behavior from afterheat (Chapter 3) is not strongly dependent on operation time, the public consequences may be.

Fortunately, only ^{93}Mo ($T_{1/2} \sim 3{,}500$ y) is the only significant accident hazard in TZM which does not reach equilibrium within two years. Thus, the TZM results at 2 years can be extrapolated to 10 years (not true for waste disposal since even longer-term isotopes dominate that problem). The difference between 2 and 10 years operation will be

examined in Section 8.3. To first order the increase in an isotope concentration from 2 years to 10 is given by

$$\frac{n(10)}{n(2)} \sim \frac{1 - \exp(-\lambda \cdot 10)}{1 - \exp(-\lambda \cdot 2)} \tag{8.31}$$

which reaches a maximum of 5 for an infinite half life.

The design can influence the structural metal fraction and the neutron spectrum. However, compared to the differences among metals, these effects are minor. The first wall radioactivity, which is fairly immune to changes in blanket design and selection of breeder and coolant, represents a large fraction of the total blanket activity, e.g., 59% of the 316 SS inventory in STARFIRE [8.9]. Furthermore, the first wall is the part of the blanket most at risk - highest afterheat levels, proximity to the plasma, highest stresses. Therefore, the comparison among materials will be made per volume of first wall. The other comparison bases, Chapters 3 - 7, pertain to the mechanisms for mobilization of the first wall.

The first wall radioactivity concentration for 316 SS, V-15Cr - 5Ti and TZM is shown in Table 8.13 for all isotopes with half-lives greater than 15 minutes. Appropriate data for HT-9 was unavailable. The restriction and effect of the 15 minute half-life restriction is discussed in Section 8.3.

TABLE 8.13

Radioactivity Levels (Ci/cc of metal) in the First Wall of Reference Materials at 1 mw/m^2 Neutron Wall Loading**

Name	316 SS First Wall	V-15Cr-5Ti First Wall	TZM First Wall
^{14}C	6.5×10^{-6}	3.6×10^{-5}	—
^{45}Ca	1.82×10^{-3}	1.32×10^{-1} *	4.183×10^{-2}
^{47}Ca	4.47×10^{-5}	3.3×10^{-3}	—
^{46}Sc	2.91×10^{-3}	1.935×10^{-1} *	6.63×10^{-2}
^{47}Sc	4.00×10^{-3}	3.348×10^{-1} *	7.3×10^{-2}
^{48}Sc	6.00×10^{-3}	2.602 *	6.3×10^{-2}
^{49}Sc	1.71×10^{-3}	2.48×10^{-2} *	3.25×10^{-3}
^{45}Ti	2.07×10^{-4}	1.483×10^{-2} *	1.3×10^{-3}
^{49}V	1.67×10^{-1} *	1.532 *	—
^{49}Cr	5.285×10^{-2}	3.76×10^{-2} *	—
^{51}Cr	9.681	6.236 *	—
^{53}Mn	2.85×10^{-5}	3.5×10^{-10}	—
^{54}Mn	5.619 *	3.7×10^{-4}	—
^{56}Mn	14.784 *	1.71×10^{-3}	—
^{55}Fe	49.121 *	5.86×10^{-3}	—
^{59}Fe	2.12×10^{-2}	9.17×10^{-7}	—
^{57}Co	2.838 *	1.6×10^{-4}	—
^{58}Co	8.377 *	4.6×10^{-4}	—
^{60}Co	1.856 *	1.05×10^{-4}	—
^{61}Co	4.182×10^{-2} *	2.35×10^{-5}	—
^{57}Ni	5.065×10^{-1} *	2.88×10^{-5}	—
^{59}Ni	2.26×10^{-4}	1.286×10^{-9}	—
^{63}Ni	1.77×10^{-2}	9.6×10^{-7}	—
^{65}Ni	1.23×10^{-3}	7.2×10^{-8}	—
^{89}Sr	—	—	7.5×10^{-4}

TABLE 8.13 (Continued)

Name	316 SS First Wall	V-15Cr-5Ti First Wall	TZM First Wall
^{88}Zr	3.56×10^{-4}	2.97×10^{-7}	—
^{89}Zr	1.755×10^{-2}	1.46×10^{-5}	1.389 *
^{93}Zr	3.27×10^{-8}	1.3×10^{-9}	—
^{95}Zr	5.13×10^{-3}	4.28×10^{-6}	3.658×10^{-1} *
^{97}Zr	1.03×10^{-3}	8.59×10^{-7}	7.326×10^{-2}
^{88}Y	—	—	9.67×10^{-3}
^{90}Y	—	—	3.73×10^{-3}
^{91}Y	—	—	1.25×10^{-3}
^{91m}Nb	—	—	3.733×10^{-1} *
^{92m}Nb	3.953×10^{-2}	2.9×10^{-3}	1.533 *
^{92}Nb	9.206×10^{-11}	1.52×10^{-9}	—
^{93m}Nb	8.969×10^{-4}	7.84×10^{-5}	1.36×10^{-2}
^{94}Nb	5.15×10^{-6}	4.27×10^{-7}	2.6×10^{-8}
^{95m}Nb	7.6×10^{-3}	6.31×10^{-6}	1.0926 *
^{95}Nb	2.37×10^{-2}	1.97×10^{-5}	1.723 *
^{96}Nb	1.09×10^{-2}	9.2×10^{-6}	6.967×10^{-1} *
^{97}Nb	7.78×10^{-3}	6.5×10^{-6}	5.134×10^{-1} *
^{93}Mo	4.84×10^{-3}	4.2×10^{-6}	1.5×10^{-2}
^{99}Mo	7.23×10^{-1} *	6.61×10^{-4}	49.644 *
^{99m}Tc	—	—	50.00 *
^{182}Ta	—	1.19×10^{-2} *	—
^{181}W	—	1.27×10^{-7}	—
^{185}W	—	1.0×10^{-3}	—
^{187}W	—	2.3×10^{-4}	—
Total	94.0	11.1	107

* Isotope is at least 0.1% of total activity.

**Only half-lives greater than 15 minutes.

8.3 Dose Factor Comparison and Screening

Due to FUSECRAC input limitations, the isotopes in each alloy had to be screened to determine which are important (over 0.1%) contributors to each dose pathway. This also allows identification of the impact of operating time.

8.3.1 Elimination of Short-Lived Isotopes

Isotopes with half-lives less than 30 minutes were eliminated from the Reactor Safety Study [8.21] since they would substantially decay before exposure to the public. In the present study, isotopes with less than 15 minute half-lives were eliminated. For 316 SS this reduces the first wall activity from 100 Ci/cc to 94 Ci/cc. For TZM, the elimination of isotopes ^{101}Mo and ^{101}Tc causes a reduction from 136 to 107 Ci/cc. For V-15Cr-5Ti, a signficant amount of the activity is eliminated (26.4 to 11.1 Ci/cc) due to a variety of isotopes - ^{50}Sc (1.8 m), ^{51}Ti (5.80 m), and ^{52}V (3.77 m).

Where radioactive daughters are produced by decay, care must be taken in eliminating the parent isotope from consideration. Since the activity of an isotope is given by

$$ACT_i = \lambda_i n_i \tag{8.32}$$

then if all the atoms of a parent were instantaneously changed to the daughter, the resulting daughter activity is given by

$$ACT_d = f \frac{\lambda_d}{\lambda_p} ACT_p = f \frac{T_{1/2}(p)}{T_{1/2}(d)} ACT_p \tag{8.33}$$

where f = fraction of parent decay to that particular daughter

Thus, for very short-lived parents ($T_{1/2}$ < 15 minutes), the resulting daughter activity was compared to the steady state daughter activity to determine if elimination of the parent activity significantly altered the impact of the daughter isotope. For example, even if all ^{60m}Co activity were transformed to ^{60}Co, the amount is insignificant compared to the ^{60}Co already present. For parents with half-lives less than 15 minutes for these materials, there is no significant contribution to the daughter activity.

8.3.2 Data Base

The analysis requires four types of dose factors, cloudshine (rem/yr per Ci/m^3 air), groundshine (rem/yr per Ci/m^2 on ground), ingestion (rem/Ci ingested), and inhalation (rem/Ci inhaled). The dose factors were taken from references 8.16 (tritium), 8.26 (CRAC health data), and 8.35 - 8.39. This is discussed in more detail in the seperate FUSECRAC report [8.27] and not repeated here.

For purposes of screening isotopes, only whole body dose factors were used. Isotopes contributing at least 0.1% of the total dose from cloudshine, groundshine, and inhalation were used to calculate those exposure pathways in the FUSECRAC analysis where all organs were included. For ingestion, the data base is sufficiently weak that only whole body dose factors were used in FUSECRAC. Due to the storage limitations, only isotopes contributing at least 1% to the total ingestion dose in the screening calculation were included in the FUSECRAC analysis. It is felt that the present screening technique adequately

determine which isotopes require further analysis.

The ingestion pathway also requires the use of environmental transfer values, CF (Ci ingested/Ci/m^2 deposited on ground). These had to be determined for all the fusion-specific isotopes. The modeling used in these calculations and the values obtained are also determined in the FUSECRAC report [8.27].

The four exposure pathways and the relative time scales are shown in Table 8.14. For the screening operation only four cases were directly studied - acute cloudshine and inhalation and chronic ingestion and groundshine. The acute cloudshine, inhalation and groundshine are always automatically calculated for all input isotopes by the code; hence there is no loss in not screening for acute groundshine isotopes. The chronic inhalation pathway is due to resuspension of deposited material. As seen in Section 8.4.4, it is a small contribution to the total chronic dose. Since only very very long-lived (years) isotopes tend to contribute significantly to resuspension, the identification of relevant isotopes was straightforward, as mentioned in Section 8.4.2.

8.3.3 Cloudshine

If the radioactive plume passes over the public as a result of an accident, the gamma radiation will irradiate people (cloudshine). The screening parameter was the activity times the cloudshine dose factor,

$$\text{Relative Cloudshine} = \text{ACT}(\text{Ci/cc}_{\text{first wall}}) \times \text{DF}_{\text{cs}} \left(\frac{\text{rem/yr}}{\text{Ci/m}^3}\right). \quad (8.34)$$

There are three drawbacks to this index. First, the decay in transport

TABLE 8.14

Exposure Pathways Included in FUSECRAC Calculations

Early Exposure Pathways	Chronic Exposure Pathways
Cloudshine*	Ingestion
Inhalation*	Inhalation*
Groundshine	Groundshine*

*Isotopes were screened to determine significant contributors to the total for each pathway marked, see Sections 8.3.3 - 8.3.6

is not explicitly incorporated (except insofar as short-lived isotopes, $T_{1/2}$ less than 15 minutes, were ignored). Second, the contribution of a radioactive daughter is not included. Third, only whole body dose factors were used in the screening.

The code automatically calculates cloudshine for each organ for all isotopes in the input file, incorporating in-transit decay and daughter buildup, thus eliminating the above concerns. Note that non-gamma emitters do not contribute. The major contributors to cloudshine dose are listed in Table 8.15.

Using Eq. (8.31) to compare the 10 year and two year activity levels for each isotope, the total cloudshine dose $\left(\frac{\text{rem/yr}}{\text{m}^3 \text{ wall/m}^3 \text{ air}}\right)$ from Eq. 8.39 can be calculated (see Table 8.16). The length of operation has a small influence.

8.3.4 Inhalation

The case of accidental inhalation of radioisotopes is more complex than cloudshine. Again the concern is the early exposure from the passing cloud. The additional complexity arises from the fact that the dose is from internal rather than external exposure. The mechanical and chemical form of the isotope affects the residence time in the body which affects the dose factor.

The mechanical question is the particle size. Dose factors are typically tabulated for particle radii of 0.3, 1, and 5 μm [8.39]. The sizes which might be expected in a fusion accident plume are unknown, depending on the details of the release mechanism. A value of 1 μm is adopted here; this is the value generally assumed in regulatory docu-

TABLE 8.15

Major Contributors to Cloudshine Dose*

	316 SS	V-15Cr-5Ti	TZM
Isotopes Contributing Over 10%	^{56}Mn ^{58}Co ^{54}Mn	^{48}Sc	^{99}Mo ^{99m}Tc
Isotopes Contributing Between 1-10%	^{60}Co ^{57}Ni	^{46}Sc ^{51}Cr	^{96}Nb ^{92m}Nb ^{89}Zr ^{95}Nb ^{97}Nb ^{95}Zr ^{48}Sc
Isotopes Contributing Between 0.1-1.0%	^{51}Cr ^{57}Co ^{99}Mo ^{49}Cr ^{92m}Nb	^{49}Cr ^{47}Sc ^{182}Ta ^{45}Ti	^{46}Sc ^{91m}Nb

*Based on activity times whole body dose factor

TABLE 8.16

Total Cloudshine Dose Screening Parameter* for Reference Materials

	316 SS	V-15Cr-5Ti	TZM
Dose Parameter* 2 yr operation	267	53.7	128.5
Dose Parameter* 10 yr operation	295	53.7	128.5
Ratio of 10 yr to 2 yr	1.1	1.0	1.0
Relative Dose Parameter**	5	1	2

* = ACT ($Ci/cc_{first\ wall}$) x DF $\left(\frac{rem/yr}{Ci/m^3\ air}\right)$ x 10^{-6} at 1 MW/m^2 wall loading

** Relative to V-15Cr-5Ti

ments. Most dose factors are tabulated using this value. Although the particle size often has only a few percent effect, there are cases where the effect is more than a factor of 2, e.g., ^{89}Sr (dose for 0.3 μm = 2.4 times dose for 5 μm).

The chemical form determines the lung clearance class. The three classes are D - day, W - week, and Y - year, which refers to the time scale for the isotope to reside in the lung. The dose factor changes by as much as a factor of two as a function of class. The possible clearance classes and the corresponding appropriate chemical form for relevant elements are listed in Table 8.17. The analysis in the Reactor Safety Study required assigning clearance classes for the elements involved, as indicated in Table 8.18. The release form chemistry in fission is complicated by the presence of the fission products including negatively charged species (e.g., I^-). The analysis in this work indicates that oxidation processes are the primary fusion release mechanisms. Thus released isotopes are assumed to be in the oxide or hydroxide form. Tritium is assigned a class of D, corresponding to its 10 day biological half-life. Where there is no direct information (Table 8.17) on the appropriate class for the oxide or hydroxide form, an element is assumed to behave similar to others in the same periodic table group.

The screening parameter for inhalation is simlar to groundshine,

$$\text{Relative Inhalation} = ACT(Ci/cc_{\text{first wall}}) \times DF_{ih}(\text{rem/Ci-inhaled}) \quad (8.35)$$

where again only whole body dose factors were used in the screening

TABLE 8.17

Elements and Possible Lung Clearance Classes*

Element	Class	Chemical Species
Mn	W	oxides, hydroxides, halides, nitrates
	D	all others
Fe	Y	oxides, hydroxides, halides
	W	all others
Co	Y	oxides, hydroxides
	W	all others
Sr	Y	$SrTiO_2$
	D	all others
Y	W	all
Zr	Y	oxides, hydroxides
	W	all others
Nb	Y	all
Mo	Y	oxides
	D	molybdates
Tc	W	oxides, hydroxides
	D	all others

*D-day, W-week, Y-year, based on ref. 8.39.

TABLE 8.18

Lung Clearance Classes***

Elements	Assigned in Reactor Safety Study [8.9]	Assigned in Present Study**
H Li Na	—	D
Ca Sr Ba	D	D
Sc Y La	W	W
Ti Zr	Y	Y
V Nb Ta	Y	Y
Cr Mo W	D (Y*)	Y
Mn Tc Re	D	W
Fe Co Ni	Y	Y

*Mo assumed present in a mixture of forms, mainly D

**Assume oxide or hydroxide form

***D-day, W-week, Y-year

but all organs were included in the code calculations. The inhalation dose factors used include the effects of daughter buildup and transport within the body. Although the screening parameter does not include plume transport and decay/buildup effects, CRAC does.

The value of organ specific dose factors for some isotopes were not available (^{45}Ca, ^{46}Sc, ^{47}Sc, ^{48}Sc, ^{45}Ti, ^{49}V, ^{49}Cr, ^{51}Cr, ^{93m}Nb, ^{96}Nb, and ^{182}Ta). The whole body dose factor for these isotopes was available except for ^{49}V and ^{96}Nb. A value of 5000 rem/Ci was assumed to perform screening calculations based on isotopes with roughly similar decay and chemical behavior. This value is higher than all but 8 of the isotopes studied and is thought to be conservative. Unfortunately, ^{49}V and ^{96}Nb were found to be important contributors to V-alloy and TZM (respectively) inhalation dose. The inhalation calculations in FUSECRAC were adjusted for this lack of data - see Section 8.4.2.

The screening calculations result in a list of major contributors to inhalation dose (Table 8.19), there are some different isotopes than appeared in cloudshine (Table 8.15), including non-gamma emitters like ^{45}Ca. The total inhalation screening parameter as a function of operating time and metal is listed in Table 8.20. The dose scaling among metals is not the same as predicted by BHP_{air}. This was not unexpected as discussed in Section 8.2.1. The cause of the difference can best be demonstrated by comparing the dominant isotopes in 316 SS and TZM (see Table 8.21). The relative ranking of the total screening parameter and the BHP from 316 SS and TZM is largely controlled by one isotope as seen in the table. Whereas the dose factor time activity of ^{60}Co is higher than ^{99}Mo, the BHP (activity divided by maximum permissible concentration) of

TABLE 8.19

Major Contributors to Inhalation Dose*

	316 SS First Wall	V-15Cr-5Ti First Wall	TZM First Wall
Isotopes Contributing Over 10% of the Dose	^{60}Co ^{58}Co ^{55}Fe	^{49}V ^{48}Sc	^{99}Mo ^{96}Nb ^{95}Nb
Isotopes Contributing Between 1-10% of the Dose	^{54}Mn ^{57}Co	^{46}Sc ^{51}Cr ^{45}Ca ^{182}Ta ^{49}Cr	^{95}Zr ^{92m}Nb ^{89}Zr ^{99m}Tc ^{46}Sc ^{91m}Nb ^{95m}Nb
Isotopes Contributing Between 0.1-1.0% of the Dose	^{51}Cr ^{56}Mn ^{49}V ^{99}Mo ^{57}Ni	^{47}Sc	^{45}Ca ^{88}Y ^{93m}Nb ^{48}Sc ^{93}Mo ^{97}Zr

*Based on activity times whole body dose factor

TABLE 8.20

Total Inhalation Dose Screening Parameter*
For Reference Materials

	316 SS	V-15Cr-5Ti	TZM
Dose Parameter* 2 yr-Operation	123	9.1	37.5
Dose Parameter* 10-yr Operation	251	15	37.7
Ratio of 10 yr to 2 yr	2.0	1.6	1.0
Relative Dose Parameter**	15	1	3
Relative BHP_{air}	15	1	23

* = $ACI(Ci/cc_{first\ wall}) \times DF(Rem/Ci\text{-}inhaled) \times 10^{-3}$ at 1 MW/m^2 wall loading

**Relative to V-15Cr-5Ti

TABLE 8.21

Comparison of 316 SS and TZM Using Different Measures of Merit Including Biological Hazard Potential

Metal	316 SS	TZM
Dominant Isotope in Screening Parameter	^{60}Co	^{99}Mo
Percent of Total Screening Parameter Caused by Dominant Isotope	61%	64%
Relative Screening Parameter of Dominant Isotope	6.3	1.0
Relative Total Screening Parameter	5.0	1.0
Relative BHP of Dominant Isotope	0.87	1.0
Relative Total BHP	0.65	1.0
Relative Latent Health Effects due to Early Exposure	4.3	1.0
Relative Latent Health Effects due to Chronic Exposure	38.9	1.0

^{60}Co is lower. Summing over all isotopes and all organs with FUSECRAC results in the early exposure health effects showing similar behavior as the total screening parameter, not BHP. The higher variance in the chronic exposure health effects provides a clue to the cause. As mentioned above, the BHP is based on a steady state intake from a steady state isotope concentration in the environment. ^{60}Co has a half-life of 5.24 yr while ^{99}Mo has a 66 hour half-life. The initial decay after an exposure is built into the dose factor, but the BHP is based on the assumption that intake is steady state and the body burden reaches a steady state saturation. The variance between 316 SS and TZM increases for longer term health effects because the interesting isotopes in 316 SS have longer half-lives than TZM. This aspect is discussed in more detail later.

8.3.5 Ingestion

The remaining pathways are chronic, long-term exposure - ingestion (internal) and groundshine (external). Some BHP measures have been proposed (see for example, reference 8.30) to compare chronic hazards - BHP_{water}, $IBHP_{air}$, $IBHP_{water}$. The integral BHP's are defined as

$$IBHP = \int_0^\infty BHP\, dt \tag{8.36}$$

The definition of BHP allows this to be rewritten:

$$IBHP = MPC^{-1} \int_0^\infty ACT(Ci)e^{-\lambda t}dt = \frac{.693\ T_{1/2}}{MPC} ACT(t=0)$$

$$= (.693)\ BHP(t=0)\ x\ T_{1/2} \tag{8.37}$$

Again a steady state parameter, MPC, is being used to compare kinetically controlled hazards. The CRAC code incorporates an input parameter, CF (Ci ingested / Ci/m^2 deposited), which accounts for biological transport to man through the ecosystem. It varies by several orders of magnitude among isotopes. One of the problems with IBHP values is that very long-term isotopes are linearly weighted (Eq. 8.37). However, for longer-lived isotopes, environmental transport decay and removal becomes dominant so that the effective half-life does not increase linearly with $T_{1/2}$. Thus IBHP over-weights the very long-term isotopes, while BHP over-weights the very-short term isotopes. The environmental half-life cannot be explicitly extracted from the CF parameter; however, as discussed in Section 8.3.6, the effective groundshine half-life reaches a maximum of 34 years.

The CF values for the fusion isotopes had to be determined. The environmental model, input data, and results are discussed in the FUSECRAC report [8.27]. The effect of radioactive daughters in the environment was roughly included. Of those isotopes which are significant contributors (over 0.1%), only ^{95}Zr and ^{95m}Nb exhibited more than a few percent increase when daughters were included. For ^{95}Zr (decays to ^{95m}Nb and ^{95}Nb) the increase was a factor of 2.04; for ^{95m}Nb (decays to ^{95}Nb), a factor of 1.24. The screening parameter is given by

$$\text{Ingestion dose} \sim \text{ACT}(\text{Ci/cc}_{\text{first wall}}) \times \text{DF}_{ig}(\text{rem/Ci-ingested}) \times \text{CF}(\text{Ci-ingested / Ci/m}^2 \text{ deposited}) \qquad (8.38)$$

where the CF factor was summed over all time and exposure pathways (crops, meat, milk). The major contributors to the ingestion dose are shown in Table 8.22. The effect of operating time and relative ranking of materials is shown in Table 8.23.

8.3.6 Groundshine

The groundshine dose considered here is the chronic, long-term exposure. The Reactor Safety Study [8.21] modeled the gradual soaking into the ground of isotopes and gave the fraction remaining near the surface as

$$f_g(t) = 0.63 \exp(-1.13t) + 0.37 \exp(-0.0075t) \qquad (8.39)$$

Then the fraction remaining near the surface including radiological decay is

$$f(t) = f_g(t) \exp(-\lambda t) \qquad (8.40)$$

The resulting effective time on the surface, T_{eff}, is plotted as a function of radiological half-life in Fig. 8.8. For a radiological half-life of 1 yr, the effective half-life is reduced to 0.61 yr. At 10 years half-life, the effective half-life is only 3.7 yr. As the radiological half-life goes to infinity, the effective half-life reaches a limit of 34.6 years.

The radioactive daughters were included by analytically accounting for their buildup and decay on the surface, discussed in the FUSECRAC

TABLE 8.22

Major Contributors to Ingestion Dose*

	316 SS First Wall	V-15Cr-5Ti First Wall	TZM First Wall
Isotopes Contributing Over 10% of the dose	^{60}Co	^{182}Ta ^{49}V ^{45}Ca ^{46}Sc	^{99}Mo ^{91m}Nb ^{95}Nb
Isotopes Contributing Between 1-10% of the Dose	^{58}Co ^{57}Co ^{55}Fe	^{51}Cr	^{92m}Nb ^{46}Sc ^{45}Ca ^{95m}Nb ^{88}Y ^{95}Zr ^{89}Zr
Isotopes Contributing Between 0.1-1.0% of the Dose	^{54}Mn	^{48}Sc ^{60}Co	^{96}Nb ^{99m}Tc

*Based on screening parameter

TABLE 8.23

Total Ingestion Dose Screening Parameter* for Reference Materials

	316 SS	V-15Cr-5Ti	TZM
Dose Parameter 2 yr-Operation	3.03	0.041	0.039
Dose Parameter 10 yr-Operation	7.54	0.054	0.039
Ratio of 10 yr to 2 yr	2.5	1.3	1.0
Relative Dose Parameter**	107	1.0	0.8

$$* = ACT(Ci/cc_{\text{first wall}}) \times DF_{ig}(Rem/Ci) \times CF\left(\frac{Ci}{Ci/m^2}\right) \times 10^{-6}$$

** Relative to V-15Cr-5Ti

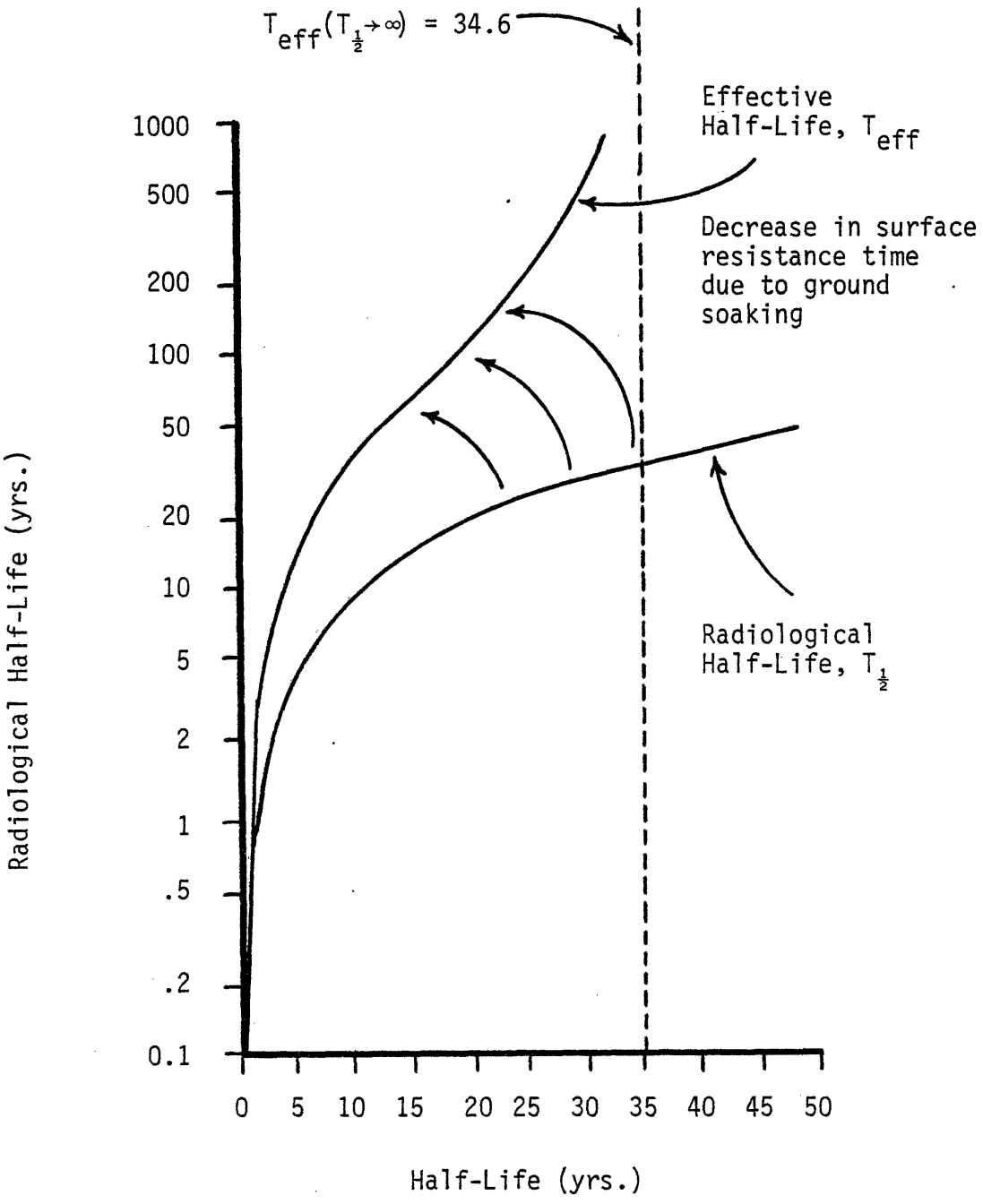

Fig. 8.8: Comparison of Effective Half-Life Isotope on the Ground to the Radiological Half-Life

report [8.27]. The significant cases and the ratio of corrected dose to parent-only dose are ^{93}Mo (1.20), ^{99}Mo (1.79), ^{95m}Nb (57.6), and ^{95}Zr (2.06). The screening parameter is given by

$$\text{Groundshine chronic dose} \sim \text{ACT}\left(\text{Ci/cc}_{\text{first wall}}\right) \times \text{DF}_{gs}\left(\frac{\text{rem/yr}}{\text{ci/m}^2}\right) \times T_{eff}(\text{yr}) \qquad (8.41)$$

The major contributors to the total are listed in Table 8.24. The effects of operating time and material choice are indicated in Table 8.25.

8.3.7 Summary of Interesting Isotopes

The ratio of various measures of hazard for 10 year to 2 year operating time is summarized in Table 8.26. The most any isotope could increase from 2 to 10 years would be 5-fold. The relative comparisons among materials from screening parameters are summarized in Section 8.5 and compared to the more exact FUSECRAC results.

As a result of the screening calculations, isotopes were selected for inclusion into the fusion health file, FUSEDOSE, for use with FUSECRAC. These are listed in Table 8.27. The level of significance of each isotope for each material is shown; for example, a level 3 indicates that the isotope contributes at least 10% of the total exposure in at least one exposure pathway. Ten of these isotopes were also included in the fission health file, CRACDOSE [8.21, 8.27].

Based on the screening calculations and the available data base,

TABLE 8.24

Major Contributors to Groundshine Dose*

	316 SS First Wall	V-15Cr-5Ti First Wall	TZM First Wall
Isotopes Contributing Over 10% of the Dose	^{60}Co ^{54}Mn	^{46}Sc ^{48}Sc ^{51}Cr	^{95}Nb ^{99}Mo ^{95}Zr ^{92m}Nb
Isotopes Contributing Between 1-10% of the Dose	^{58}Co ^{57}Co ^{55}Fe	^{182}Ta	^{46}Sc ^{89}Zr ^{95m}Nb ^{91m}Nb ^{88}Y ^{96}Nb ^{99m}Tc ^{93}Mo
Isotopes Contributing Between 0.1-1.0% of the Dose	^{51}Cr	^{49}V ^{60}Co ^{47}Sc ^{54}Mn	^{48}Sc

*Based on screening parameter

TABLE 8.25

Total Groundshine Screening Parameter* for Reference Materials

	316 SS	V-15Cr-5Ti	TZM
Dose Parameter* 2 yr Operation	735	16.2	48.6
Dose Parameter* 10 yr Operation	1528	16.3	50.1
Ratio of 10 yr to 2 yr	2.1	1.0	1.0
Relative Dose Parameter**	70	1	3

$$* = ACT(Ci/cc_{\text{first wall}}) \times DF_{gs}\left(\frac{rem/yr}{ci/m^2}\right) \times T_{eff}(yr)$$

** Relative to V-15Cr-5Ti

TABLE 8.26

Ratio of Hazard for 10 Year Operation to 2 Year Operation for Each Reference Material*

	316 SS	V-15Cr-5Ti	TZM
Radioactivity	1.48	1.11	1.00
Cloudshine (Eq. 8.34, Table 8.16)	1.10	1.00	1.00
Inhalation (Eq. 8.35, Table 8.20)	2.04	1.64	1.01
Ingestion (Eq. 8.38, Table 8.23)	2.49	1.30	1.00
Chronic Groundshine (Eq. 8.41, Table 8.25)	2.08	1.00	1.03
Range	1.10 - 2.49	1.00 - 1.64	1.00 - 1.03

*Based on simple whole body screening factors

TABLE 8.27

Isotopes Included in Fusion Health File, FUSEDOSE

	Isotope Name	Significance Category* 316 SS	V-15Cr-5Ti	TZM	Also in Fission Health File, CRACDOSE?
1.	^{3}H	3	3	3	
2.	^{45}Ca		3	2	
3.	^{46}Sc		3	2	
4.	^{47}Sc		1		
5.	^{48}Sc		3	2	
6.	^{45}Ti		1		
7.	^{49}V	1	3		
8.	^{49}Cr	1	2		
9.	^{51}Cr	1	3		
10.	^{54}Mn	3	1		
11.	^{56}Mn	3			
12.	^{55}Fe	3			
13.	^{59}Fe				
14.	^{57}Co	2			
15.	^{58}Co	3			Yes
16.	^{60}Co	3	1		Yes
17.	^{57}Ni	2			
18.	^{63}Ni				
19.	^{89}Sr				Yes
20.	^{88}Y			2	
21.	^{90}Y				Yes

TABLE 8.27 (Continued)

	Isotope Name	Significance Category* 316 SS	V-15Cr-5Ti	TZM	Also in Fission Health File, CRACDOSE?
22.	^{91}Y				Yes
23.	^{89}Zr			2	
24.	^{95}Zr			3	Yes
25.	^{97}Zr			1	Yes
26.	^{91m}Nb			3	
27.	^{92m}Nb	1		3	
28.	^{93m}Nb			1	
29.	^{95m}Nb			2	
30.	^{95}Nb			3	Yes
31.	^{96}Nb			3	
32.	^{97}Nb			2	
33.	^{93}Mo			2	
34.	^{99}Mo	1		3	Yes
35.	^{99m}Tc			3	Yes
36.	^{182}Ta		3		

* 3 - Over 10% of the total of (at least) one pathway
2 - Over 1% of the total of (at least) one pathway
1 - Over 0.1% of the total of (at least) one pathway

the important isotopes and important isotope data research needs were determined. These are listed in Tables 8.28 - 8.30. The isotopes marked unknown require more research to determine the dose factor for the exposure pathway indicated. For ingestion, substantially more data is also needed for the transient ecological behavior of the elements indicated, see also reference 8.27. Although not of direct concern in this study, some isotopes that might need further research for waste disposal analysis are indicated.

8.4 FUSECRAC Comparison

Ultimately, the comparison among possible blanket materials should focus on the relative accident risk (consequence times accident probability). Some implications of this are discussed in Chapter 9. Although comparing the relative accident probability among materials is beyond the scope of this study, the relative public consequences can be compared. The comparative measures discussed before, radioactivity, BHP, and the various screening parameters are not based on the real concern, public health consequences from an accidental release. The CRAC code, developed for fission consequence analysis, has been slightly modified for performing fusion consequence assessments.

8.4.1 FUSECRAC Model

The Reactor Safety Study [8.21] included an investigation of public health effects from radioactivity release. This information has evolved into the current CRAC (Calculation of Reactor Accident Consequences) code [8.26]. CRAC is continuing to be updated; however, the additional work has focused on the statistical treatment of detailed aspects of

TABLE 8.28

Important Isotopes and Research Needs for 316 SS Assessments

	External (Cloudshine, Groundshine)		Inhalation		Ingestion[d]	
	Contributor[(a)]	Unknowns[(b)]	Contributor	Unknowns	Contributor	Unknowns
^{49}V			✓	✓		
^{49}Cr	✓					
^{51}Cr	✓		✓	✓		
^{54}Mn	✓		✓			
^{56}Mn	✓		✓		✓	
^{55}Fe	✓		✓		✓	
^{57}Co	✓		✓		✓	
^{58}Co	✓		✓		✓	
^{60}Co	✓		✓		✓	
^{57}Ni	✓		✓			
^{92m}Nb	✓					
^{99}Mo	✓		✓			
others		$^{53}Mn, ^{92}Nb, ^{94}Nb$(c)		^{96}Nb		

[a]At least 0.1% of total based on screening parameters

[b]Significant unknowns, indicates primary research needs

[c]Very long term isotopes, potentially important waste disposal problems

[d]Improved ecological data on behavior of Mn, Fe, Co needed

TABLE 8.29

Important Isotopes and Research Needs for V-15Cr-5Ti Assessments

	External (Cloudshine, Groundshine)		Inhalation		Ingestion[c]	
	Contributor[a]	Unknowns[b]	Contributor	Unknowns	Contributor	Unknowns
^{45}Ca			✓	✓	✓	✓
^{46}Sc	✓		✓	✓	✓	✓
^{47}Sc	✓		✓	✓		✓
^{48}Sc	✓		✓	✓	✓	✓
^{45}Ti	✓					
^{49}V	✓		✓	✓	✓	✓
^{49}Cr	✓		✓	✓		
^{51}Cr	✓		✓	✓	✓	✓
^{54}Mn	✓					
^{60}Co	✓				✓	
^{182}Ta	✓		✓	✓	✓	

[a] At least 0.1% of total based on screening parameters

[b] Significant unknowns, indicates primary research needs

[c] Improved ecological data on behavior of Ca, Sc, Cr, V, Ta needed

TABLE 8.30

Important Isotopes and Research Needs For TZM Assessments

	External (Cloudshine, Groundshine)		Inhalation		Ingestion[d]	
	Contributor[a]	Unknowns[b]	Contributor	Unknowns	Contributor	Unknowns
^{45}Ca			✓	✓	✓	✓
^{46}Sc	✓		✓	✓	✓	✓
^{48}Sc	✓		✓	✓		
^{88}Y	✓		✓		✓	✓
^{89}Zr	✓		✓		✓	
^{95}Zr	✓		✓		✓	
^{97}Zr			✓			
^{91m}Nb	✓		✓		✓	
^{92m}Nb	✓		✓		✓	
^{93m}Nb			✓			
^{95m}Nb	✓		✓		✓	
^{95}Nb	✓		✓		✓	
^{96}Nb	✓		✓	✓	✓	
^{97}Nb	✓					
^{93}Mo	✓		✓			
^{99}Mo	✓		✓		✓	✓
^{99m}Tc	✓		✓		✓	
Others		$^{92}Nb, ^{94}Nb$[c]				

[a] At least 0.1% of total based on screening parameters

[b] Significant unknowns, indicades primary research needs

[c] Very long term isotopes, potentially important waste disposal problems

[d] Improved ecological data on behavior of Ca, Sc, Zr, Y, Nb, Mo, Tc needed

site-specific weather, population, and evacuation data, not on the basic health effects modeling. For the present purpose, the concern is the relative health effect among materials, not a detailed site-specific assessment.

The exposure is divided into early and chronic. The former refers to the short-time exposure from the passing radioactive plume. The latter is the long-term exposure from radioactivity deposited on the ground from the plume. The early exposure can result in acute health effects within about a month or latent effects (primarily cancer) over several decades from the accident. Only latent effects can result from the chronic exposure. The health effects and exposure pathways included are summarized in Table 8.31.

The actual components of the model, the input data and output are shown in Fig. 8.9. The inhalation, cloudshine, and groundshine dose factors are incorporated into a health file. The fission file is CRACDOSE. A large part of the effort for the fusion assessment was assembling the fusion health file, FUSEDOSE [8.27]. This expanded and improved an earlier fusion health file by Sawdye [8.40] which included 24 isotopes for an assessment of effects from only early exposure. The 36 isotopes in the current FUSEDOSE file were listed in Table 8.27. All isotopes representing at least 0.1% of the total dose for at least one of the four screening calculations (Section 8.4) were included. Thus the calculated early exposure, which includes all isotopes in the health file, should include all significant contributors. The code sums the dose and health effect over body organs.

TABLE 8.31

Exposure Time, Health Effects, and Exposure Pathways Included in CRAC and FUSECRAC

Exposure Time	Early (plume passage)	Early (plume passage)	Chronic (deposited on ground)
Health Effects	Acute (death or injury within a month)	Latent (long-term, cancer)	Latent (long-term, cancer)
Exposure Pathways	Inhalation Cloudshine Groundshine	Inhalation Cloudshine Groundshine	Inhalation* Ingestion Groundshine

*Long-term inhalation due to resuspension of deposited material

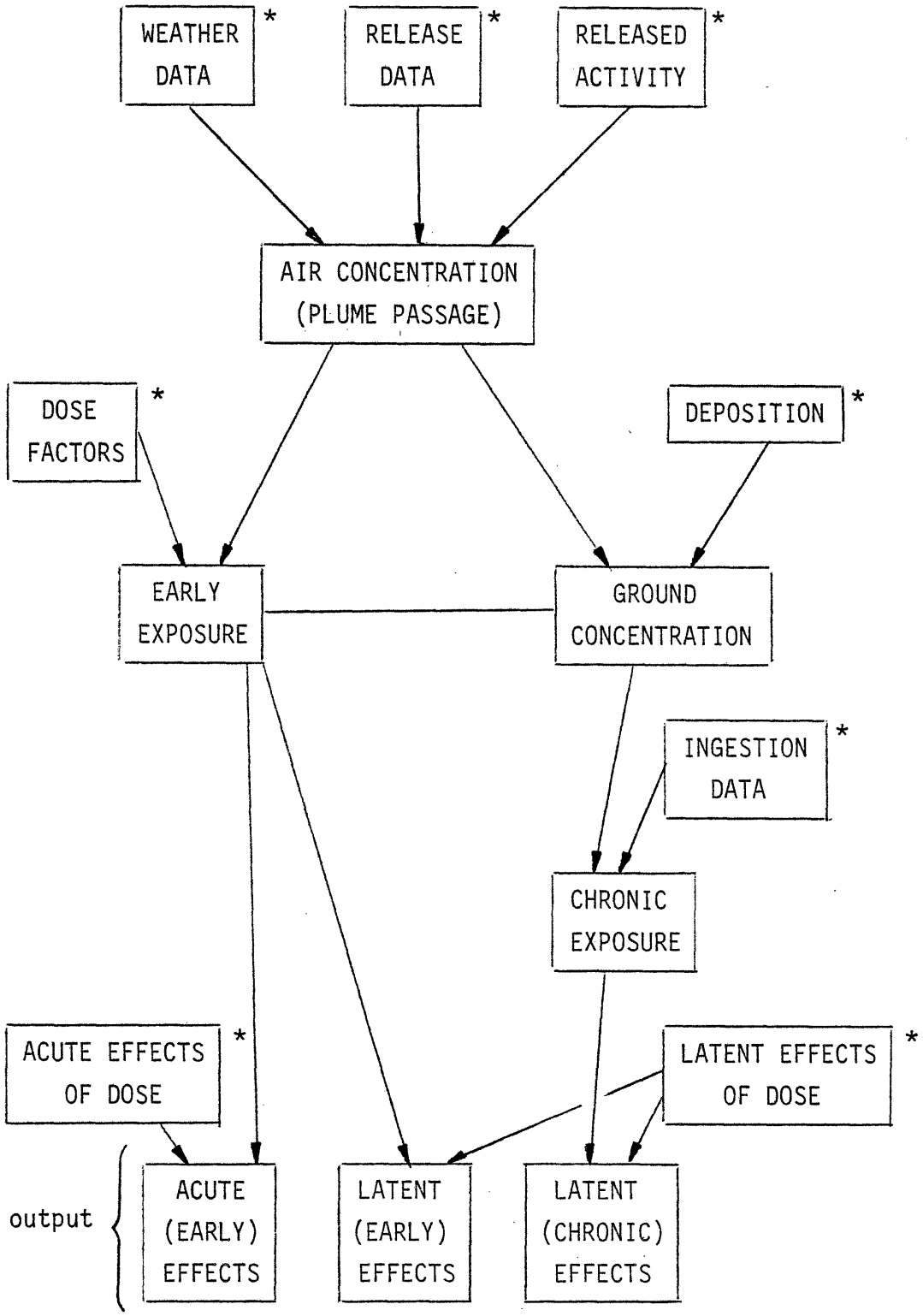

Fig. 8.9: Information Paths in FUSECRAC

*Input Data

The user must specify which isotopes to include in the three chronic exposure calculations. The isotopes used in the fission assessment are listed in Table 8.32; these were determined to be the significant contributors to each pathway. Based on the screening calculations, the isotopes incorporated into chronic exposure calculations for each material were selected, shown in Table 8.33.

The code incorporates two major dose-reduction mechanisms, evacuation and interdiction. The evacuation model allows the user to specify a minimum distance from the reactor within which all people will evacuate. A downwind sector may be specified in which the evacuation distance is further, see Fig. 8.10. Evacuation is not instantaneous, but the rate of travel is user specified. Evacuation only affects the early exposure from the plume. People are assumed to move back to the area unless interdiction prevents it.

The chronic exposure can be reduced by interdiction. Land interdiction prohibits people from living in the specified area for some period of time, eliminating groundshine and inhalation exposure for that population. Various levels of food interdiction (crop, milk, or crop and milk) reduces the ingestion pathway for an area by eliminating contaminated food. The user must specify the criteria for imposing the interdiction levels in terms of allowable dose committment.

In addition to the assembling of all the required isotope-specific data (dose factors and the environmental transfer parameter, CF), there is one important code change in FUSECRAC from CRAC. The CRAC code assumes that all ingestion exposure is properly related to the amount of radioactivity deposited on the ground and movement of radioactive

TABLE 8.32

Fission Isotopes Contributing to Chronic Dose [8.21]

External Groundshine	Resuspension Inhalation	Ingestion
^{58}Co	^{90}Sr	^{131}I
^{60}Co	^{106}Ru	^{133}I
^{95}Zr	^{137}Cs	^{89}Sr
^{95}Nb	^{238}Pu	^{90}Sr
^{101}Ru	^{239}Pu	^{134}Cs
^{103}Ru	^{240}Pu	^{136}Cs
^{131}I	^{241}Pu	^{137}Cs
^{134}Cs	^{241}Am	
^{136}Cs	^{242}Cm	
^{137}Cs	^{244}Cm	

TABLE 8.33

Fusion Isotopes Contributing to Chronic Dose

	Structural Material		
	316 SS	V-15Cr-5Ti	TZM
Inhalation			
^{3}H	✓	✓	✓
^{49}V		✓	
^{54}Mn	✓		
^{55}Fe	✓		
^{60}Co	✓	✓	
^{63}Ni	✓		
^{93}Mo	✓		✓
Ingestion (isotopes over 1% of total)			
^{3}H	✓	✓	✓
^{45}Ca		✓	✓
^{46}Sc		✓	✓
^{49}V		✓	
^{51}Cr		✓	
^{55}Fe	✓		
^{57}Co	✓		
^{58}Co	✓		
^{60}Co	✓		
^{88}Y			✓
^{95}Zr			✓
^{91m}Nb			✓
^{92m}Nb			✓
^{95m}Nb			✓
^{95}Nb			✓
^{99}Mo			✓
^{182}Ta		✓	

TABLE 8.33 (Continued)

	Structural Material		
	316 SS	V-15Cr-5Ti	TZM
Groundshine (isotopes over 0.1% of total)			
^{46}Sc		✓	✓
^{47}Sc		✓	
^{48}Sc		✓	
^{49}V		✓	
^{51}Cr	✓	✓	
^{54}Mn	✓		
^{55}Fe	✓		
^{57}Co	✓		
^{58}Co	✓		
^{60}Co	✓	✓	
^{88}Y			✓
^{89}Zr			✓
^{91m}Nb			✓
^{92m}Nb			✓
^{95m}Nb			✓
^{95}Nb			✓
^{93}Mo			✓
^{99}Mo			✓
^{182}Ta		✓	

* ^{3}H is included (where relevant, there is no groundshine dose) for cases where tritium is preferentially released.

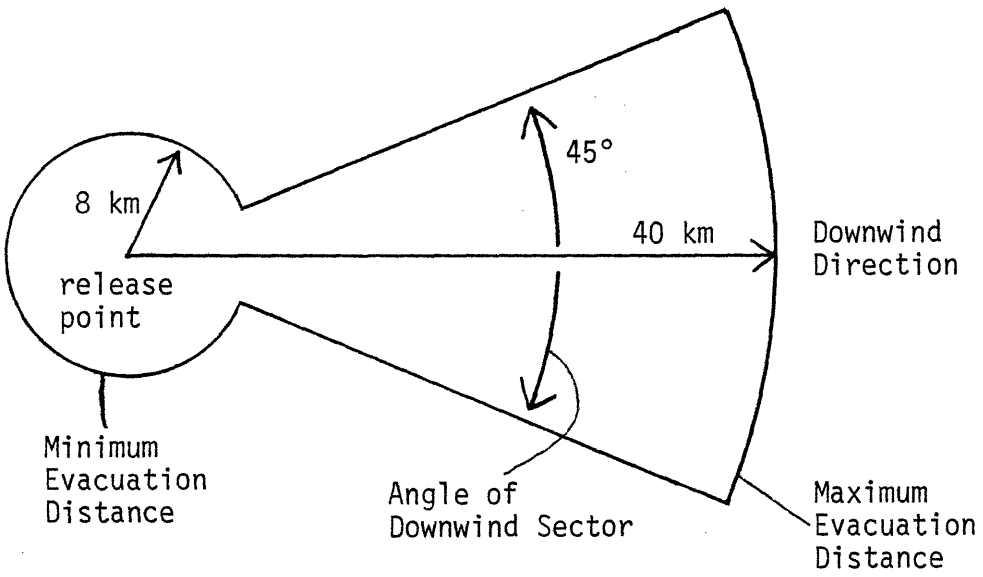

Fig. 8.10: Evacuation Model

species among components in the environment is explicitly characterized by transfer rates, independent of how much of non-radioactive isotopes of the same element may be present. This is a common assumption in environmental studies. However, it is not appropriate for ^{3}H and ^{14}C (^{14}C not important in this study). For those isotopes which are very biologically active, a specific activity (radioactive to non-radioactive ratio of element) description is used [8.16]. Furthermore, tritium is directly absorbed into plants during the plume passage. This difference has been incorporated into FUSECRAC [8.27].

8.4.2 Data Base and Input Data

The total activity for each material was calculated from the first wall radioactivity concentration (Table 8.13, at 1.0 MW/m^2). The maximum available structural material for purposes of input was the equivalent of 5 mm of the first wall. Thus the structural input inventory is given by

$$ACT(Ci/cc_{\text{first wall}}) \times \frac{3.6\ MW/m^2}{1.0\ MW/m^2} \times 0.5\ cm \times 774\ m^2 \times 10^4\ \frac{cm^2}{m^2} \quad (8.42)$$

The resulting activity is listed in Table 8.34. The release fraction of the structural inventory is specified independently. The tritium values are those of the highest total blanket tritium inventory (different breeders) for each structural material. Again, the release fraction of the tritium is specified independently, discussed with the results (Section 8.4.3).

The dose factors and ingestion environmental values are discussed

TABLE 8.34

Reference Radioactivity Inventory - Blanket Tritium and 5 mm First Wall

Name	Parent	316 SS (Ci)	V-15 Cr-5Ti (Ci)	TZM (Ci)
^{3}H		1×10^{8}	8.4×10^{6}	6.3×10^{6}
^{45}Ca		2.54 E4	1.84 E6	5.83 E5
^{46}Sc		4.06 E4	2.70 E6	9.24 E5
^{47}Sc		5.57 E4	4.66 E6	1.02 E6
^{48}Sc		8.36 E4	3.62 E7	8.78 E5
^{45}Ti		2.88 E3	2.07 E5	1.81 E4
^{49}V	^{49}Cr	2.33 E6	2.13 E7	0
^{49}Cr		7.36 E5	5.24 E5	0
^{51}Cr		1.35 E8	8.69 E7	0
^{54}Mn		7.83 E7	5.15 E3	0
^{56}Mn		2.06 E8	2.38 E4	0
^{55}Fe		6.84 E8	8.16 E4	0
^{59}Fe		2.96 E5	1.28 E1	0
^{57}Co	^{57}Ni	3.95 E7	2.23 E3	0
^{58}Co		1.17 E8	6.41 E3	0
^{60}Co		2.59 E7	1.46 E3	0
^{57}Ni		7.06 E6	4.01 E2	0
^{63}Ni		2.47 E5	1.34 E1	0
^{89}Sr		0	0	1.04 E4
^{88}Y		0	0	1.35 E5
^{90}Y		0	0	5.20 E4
^{91}Y		0	0	1.74 E4
^{89}Zr		2.45 E5	2.03 E2	1.94 E7
^{95}Zr		7.15 E4	5.96 E1	5.10 E6
^{97}Zr		1.43 E4	1.20 E1	1.02 E6
^{91m}Nb		0	0	5.20 E6

TABLE 8.34 (Continued)

Name	Parent	316 SS (Ci)	V-15 Cr-5Ti (Ci)	TZM (Ci)
^{92m}Nb		5.51 E5	4.04 E4	2.14 E7
^{93m}Nb	^{93}Mo	1.25 E4	1.09 E3	9.47 E5
^{95m}Nb	^{95}Zr	1.06 E5	8.79 E1	1.52 E7
^{95}Nb	^{95m}Nb	3.30 E5	2.74 E2	2.40 E7
^{96}Nb		1.52 E5	1.28 E2	9.71 E6
^{97}Nb	^{97}Zr	1.08 E5	9.06 E1	7.15 E6
^{93}Mo		6.74 E4	5.85 E1	1.04 E6
^{99}Mo		1.01 E7	9.21 E3	6.92 E8
^{99m}Tc	^{99}Mo	0	0	6.97 E8
^{182}Ta		0	1.66 E5	0

in the FUSECRAC report [8.27]. There was one significant problem, lack of certain organ-specific inhalation dose factors (mentioned in Section 8.3.4). The results presented have been adjusted to account for the missing dose factors by scaling based on the inhalation screening calculations. The missing dose factors in the health file represent differing amounts of the total inhalation dose. Based on the screening calculations, less than 1% of the inhalation contribution for 316 SS was missing and thus no adjustment was necessary.

For TZM, 12% of the inhalation hazard is missing. One isotope, ^{96}Nb, causes 78% of this loss. The inhalation results from the code were adjusted upwards by a factor of $(1 - 0.12)^{-1}$ for each organ. This is only an approximation due to the varying organ-specific dose factors being scaled from the screening calculation (whole body only). For early exposure, the net effect was an upward 6% adjustment. For chronic exposure, the efect is insignificant because inhalation (from resuspension) is a small ($\sim$ 1%) contributor to chronic dose and the short-term isotopes ($T_{1/2}(^{96}Nb)$ = 0.975 day) do not tend to contribute to long-term resuspension. The total effect (early and chronic) is only 1 - 2%.

Unfortunately, virtually all ($\sim$99.9%) of the V-alloy inhalation organ-specific dose factors are missing, hence the inhalation dose can not be directly corrected as for TZM. Based on the relative screening parameters among the structural materials, the V-alloy inhalation dose for each organ was taken as the average of that scaled from 316 SS (0.06 times 316 SS) and the corrected TZM (0.40 times TZM) inhalation dose. Based on the variation among the metals for different organs, the uncertainty in the inhalation dose from V-alloy for each

organ is a factor of several (2 - 3?). The fluctuation among organs seems to suggest that the total inhalation dose is better known. For early exposure, the correction (from no inhalation to estimated inhalation) increased the total V-alloy dose by a factor of 2.7. The chronic dose correction is small, estimated at less than 2% (the isotopes involved decay quickly). The total exposure (early and chronic) was thus adjusted upwards by about 25%. Even if the estimated inhalation dose were found to be understated by a factor of several, the effect on the total V-alloy exposure would be small compared to differences among the structural materials, hence the conclusions would not change.

The health response to radiation dose had to be specified. The acute response is taken from the values in the Reactor Safety Study [8.21], repeated in Table 8.35, assuming average medical efforts to save life. This is the reference data (in appropriate form) for CRAC. The sensitivity of organs to dose differs, hence comparison on the basis of dose along would have ignored an effect.

The latent dose response must be in the form of effects per man-rem for each exposed organ for various time intervals after an accident. The latent effects from radiation have been continually studied after the Reactor Safety Study. Not only have the values changed, but the BEIR III [8.41] study introduced the linear-quadratic and quadratic response functions in addition to the pure linear response model incorporated into CRAC. Because the present study is primarily a comparative one among materials and not focused on absolute results, it was not deemed worthwhile to alter the response function

TABLE 8.35

Acute Dose Response (Effect/Rem to Specific Organ), Based on Reactor Safety Study [8.9]. (see Figure Below)

	Organs					
	Bone Marrow	Lower Wall Intestine	Lung	Whole Body	Lung	Lower Wall Intestine
Effect	Fatality	Fatality	Fatality	Injury	Injury	Injury
Dose (Rem) Break Points:						
Zero threshold, DS_0	320	2000	5000	55	3000	1000
First Point, DS_1	400	5000	14,800	150	3000	1000
Second Point, DS_2	510	5000	22,400	280	6000	2500
100% Point, DS_3	615	5000	24,000	370	6000	2500
Probability Break Points:						
First Point, P_1	0.03	1.00	0.24	0.30	0.05	0.05
Second Point, P_2	0.50	1.00	0.73	0.80	1.00	1.00

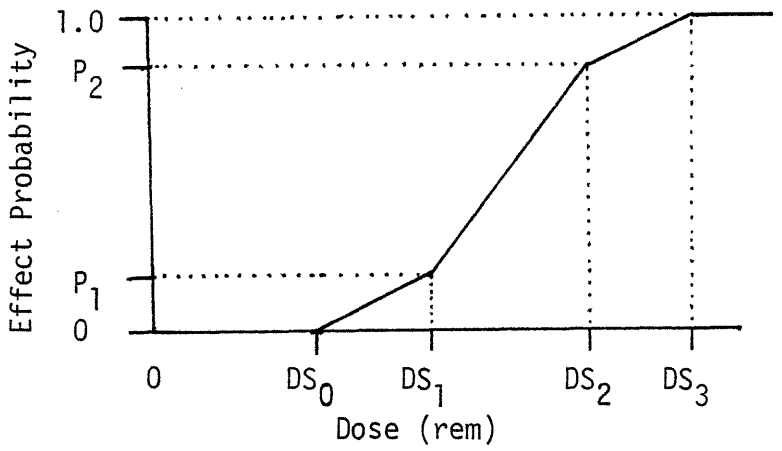

Figure 8.11: Approximate Dose Response Curve

from linear to linear-quadratic. Furthermore, the BEIR III study did not break the data down to the level required (response as a function of organ and time period after exposure). However, the BEIR III results do indicate a general lowering of risk. At a 1 rad/year exposure rate, the predicted number of cancer deaths per 10^6 man-rem is a function of model: 167 (linear), 77 (quadratic-linear), 10 (quadratic), 121 (Reactor Safety Study). The reference model in BEIR III was the quadratic-linear. The organ and specific values from the Reactor Safety Study which is part of the reference CRAC data was used in this study. The comparative results would not appear to be affected by the BEIR III study. If absolute values were desired, they could be estimated by a reduction by a factor of 121/77 (Reactor Safety Study to BEIR III).

The code user must specify the interdiction criteria by specifying the maximum dose for a given time period for each exposure pathway. If the predicted exposure is too high, the pathway is interdicted until the exposure rate drops below the criterion. Interdiction tends to reduce the difference in health effects among materials. In essence, it shifts the penalty from public health to economic. For present purposes, the maximum exposure was set at 5 rem/yr for each pathway. While this is high (actual procedure would likely be more restrictive), it is conservative in that calculated doses are higher than would be allowed. The effects of interdiction on the result are discussed in Section 8.33.

The remaining input parameters are summarized in Table 8.36. The underlying approach was to select parameters to define an average site with average characteristics for purposes of the comparison study. The

TABLE 8.36

Reference Site Data

Release Characteristics

Time before release begins	1 hr
Duration of Release	1 hr
Warning time to public	0.5 hr
Heat release in plume	0
Release (stack) height	100 m

Weather Data

Stability Class	Average Wind Speed	Probability
A (very unstable)	3.34 m/s	0.12
D (neutral)	3.00 m/s	0.52
F (very stable)	2.06 m/s	0.36

Ceiling Height - unstable 1350.0 m
stable 550.0 m

Evacuation Parameters (see Fig. 8.10)

Maximum distance of evacuation	40 km (25 miles)
Minimum distance of evacuation	8 km (5 miles)
Evacuation	0.536 m/s (1.2 mph)
Angle of downwind sector	45°
Time before wind change	2 hr
Cloudshine Shielding Factor with evacuation	1.00
Cloudshine Shielding Factor without evacuation	0.75
Groundshine Shielding Factor with evacuation	0.50
Groundshine Shielding Factor without evacuation	0.33

TABLE 8.36 (Continued)

Population and Site Data

Population density	200 people/mi^2
Percent land habitable	100%
Percent land for farming	40%
Percent land for dairy/beef	25%
Growing season	May - September

Deposition Data

Deposition velocity	10^{-2} m/s (10^{-3} m/s for ^3H)
Scavenging Coefficient	10^{-4} sec^{-1} (10^{-5} sec^{-1} for ^3H)

release characteristics are somewhat conservative. With the possible exception of a pure tritium accident, the results of the present study suggest that the time before release and warning time would be longer than that input. If so, more radioactive decay and evacuation or shielding would occur. The STARFIRE design includes a venting system with a 100 m stack.

The weather data are average values based on the 7 sites in the Reactor Safety Study [8.21]. The land use and growing season are average values for the eastern U.S. from the CRAC state-specific input [8.26]. The evacuation parameters, shielding factors, and deposition data (except tritium) are typical values from the Reactor Safety Study and reference CRAC input. The tritium deposition values were taken from reference 8.16.

The average 1981 state population density (people per square mile) varies from 936 (New Jersey) to 33 (Maine) to 4.9 (Wyoming) to 0.7 (Alaska). The average U.S. density is 62 while the average for states east of the Mississippi is 158. The population data are taken from the 1981 Hammon Almanac [8.42]. As the population will increase by the time fusion power plants are built and they will not tend to be placed in areas of extremely high or low density, the average population density was fixed at 200 people per square mile.

8.4.3 Radioactivity Results

The percentage of structural inventory which must be released to cause the first acute effect for the reference release is listed in Table 8.37. As shown, a fairly high release fraction would be necessary

TABLE 8.37

Percentage of Reference Structural Inventory*
Necessary to Cause One Acute Effect for the Reference Release Case

	Fatality	Injury
316 SS	$\sim$ 6%	$\gtrsim$ 1%
V-15Cr-5Ti	> 10%	$\gtrsim$ 10%
TZM	$\sim$ 6%	$\gtrsim$ 1%
Tritium only	> 100%	> 100%

*Based on population expulsion radius of 100 m
Structural Inventory is that of 5 mm of first wall

to cause one statistical effect. It should be noted that the acute fatality/injury dose response is very non-linear so that no consistent ratio of effect from alloy to alloy is possible. Also, these results are for an average site with average weather. A calm day with slow wind speed could be far worse. TZM and 316 SS produce very similar acute results in terms of fraction released. V-15Cr-5Ti represents a significantly lower acute hazard. Finally, a pure tritium release is relatively benign.

The Reactor Safety Study showed that most of the fatalities from a fission accident would result from latent effects rather than acute response. This appears even more true for fusion. Use of the code indicates that the number of latent fatalities would be orders of magnitude higher than acute ones (if in fact there were any acute effects) for the same amount of radioactivity released. The conclusion is that the latent effects are more important for comparison purposes.

The latent effects divide into those from early and chronic exposure. The ratio of latent effects of 316 SS and TZM relative to V-15Cr-5Ti (no tritium) as a function of percent alloy released is shown in Fig. 8.12. As more activity is released, the effect of interdiction begins to be seen. As the radiation released increases, interdiction damps the response below linear. While the appropriate measure of comparison among materials is without interdiction, it is noted that interdiction provides society the option to shift the penalty of using a more hazardous material, e.g., 316 SS, from health to socioeconomic.

The relative hazard of 316 SS and TZM compared to V-15Cr-5Ti for each exposure pathway and exposure time is listed in Table 8.38. For

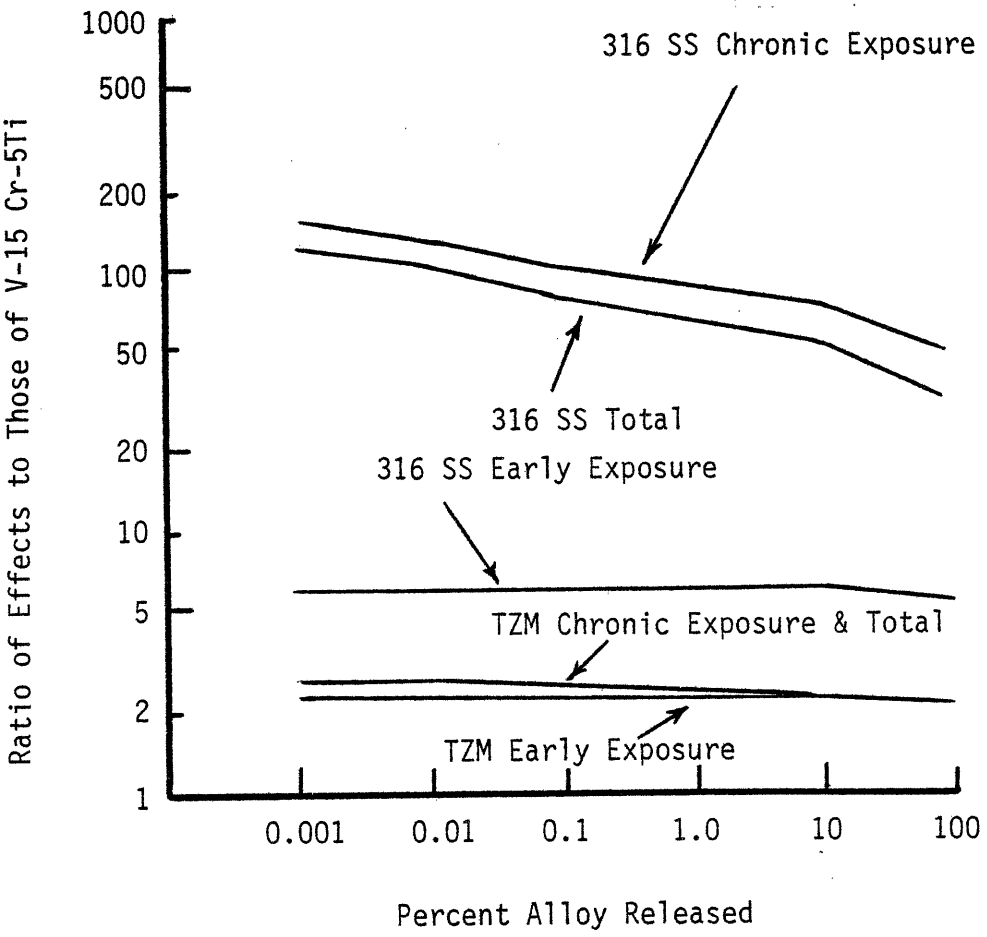

Fig. 8.12: Latent Effects from 316 SS and TZM Relative to V-15 Cr-5 Ti as Functions of Percent of 5 mm First Wall Released, Indicating Influence of Interdiction

TABLE 8.38

Relative Hazard of 316 SS and TZM Compared to V-15Cr-5Ti*

Pathway	Dose Factors Only**		FUSECRAC		
	Short Term	Long Term	Latent Early	Latent Chronic	Latent Total
316 SS					
Cloudshine	5	-	3.4	-	
Groundshine	-	70	2.9	42	
Inhalation	15	-	7.3	74	
Ingestion	-	107	-	228	
Total			5.7	147	117
TZM					
Cloudshine	2	-	3.1	-	
Groundshine	-	3	3.1	5.8	
Inhalation	3	-	1.7	1.9	
Ingestion	-	0.8	-	0.1	
Total			2.2	2.5	2.4

*Ratio of alloy to V-15Cr-5Ti for each individual pathway and exposure time (early or chronic). Because the pathways do not equally contribute to the total, the ratio of the total effects does not equal the sum or direct average of the component pathways.

**Predicted by screening calculations, compare short term to early exposure and long-term to chronic exposure.

example, the latent effects from early cloudshine exposure is 3.4 times higher for 316 SS than V-15Cr-5Ti. The various pathways do not contribute equally to the total health effects and dose. Thus, the ratio of total early and chronic exposure from 316 SS and TZM to V-alloy is not a sum or linear average of the component pathways. Similarly, the total latent effects are dominated by the chronic exposure so that the ratio of total effects is closer to the chronic ratio than the early effects.

The ratio of effect predicted by the screening calculations is also shown in Table 8.38. These are seen to have been within about a factor of 2 of the results from the detailed FUSECRAC calculations for each pathway and exposure time. The short term screening cases are compared to early exposure while the long term cases predicted the chronic exposure ratio.

The percent contribution of each exposure pathway to the total health effect (acute fatality, acute injury, latent effects from early exposure, and latent effects from chronic exposure) is shown in Table 8.39. The contribution from inhaled resuspended activity is seen to be quite small for the structural materials. For pure tritium releases, only internal exposure occurs. As discussed in reference 8.27, the chronic resuspension model in the code may not be appropriate for tritium. The breakdown of contributions has more than an academic interest. For example, since almost all of the chronic exposure from TZM is due to groundshine; if interdiction is required to reduce exposure, only the most severe land interdiction (moving people from the area) would be effective. The less severe food production interdiction would be far more effective in reducing 316 SS exposure.

TABLE 8.39

Percent Contribution to Health Effects
by Exposure Pathway

Alloy	Exposure Pathway	Health Effect			
		Acute Fatalities	Acute Injury	Latent (Early)	Latent (Chronic)
316 SS	Cloudshine	12	15	4	—
316 SS	Groundshine	26	30	15	12
316 SS	Inhalation	62	55	81	1
316 SS	Ingestion	—	—	—	87
V-alloy	Cloudshine	15	16	7	—
V-alloy	Groundshine	43	44	30	42
V-alloy	Inhalation	42	40	63	2
V-alloy	Ingestion	—	—	—	56
TZM	Cloudshine	11	9	10	—
TZM	Groundshine	31	26	42	97.5
TZM	Inhalation	58	65	48	1.5
TZM	Ingestion	—	—	—	1
Tritium	Cloudshine	0	0	0	—
Tritium	Groundshine	0	0	0	0
Tritium	Inhalation	100	100	100	30
Tritium	Ingestion	—	—	—	70

Tritium is relatively benign compared to the structural radioactivity in terms of latent effects from accidental releases. The required percent of the reference structural inventory which produces the same approximate total latent effects as the worst case tritium release (Section 8.1.3) is listed in Table 8.40. With the sole exception of lithium/steel corrosion, the worst possible release of structural corrosion products (Chapter 7) is below this required amount of structure. Thus mechanisms other than mere release of entrained corrosion products are required if structural radioactivity is to dominate health effects. Similarly, tritium is likely to dominate the normal environmental hazard.

On the other hand, if mechanisms exist which could result in a large (over 0.1%) amount of the structural radioactivity being released to the environment, the tritium contribution would be unimportant. Since V-alloy has lower latent effects, more of it would have to be released for its radioactivity to produce higher effects than the highest postulated possible tritium release.

To investigate how much ^{60}Co contributes to the 316 SS dose response, a case was examined where the ^{60}Co was arbitrarily eliminated. The effect is indicated in Table 8.41. This case gives some idea of the effects of a HT-9 alloy release since HT-9 has no cobalt and very little nickel (so that nil ^{60}Co is produced). As seen in the table, even total elimination of ^{60}Co does not reduce health effects of the steel to that of the refractory metals, although the reduction is significant. Finally, the composition of 316 SS (see Appendix B) which produced the amount of ^{60}Co in the calculations is already nuclear-grade and substantial further reductions in ^{60}Co in 316 SS-type steel is unlikely.

TABLE 8.40

Percent of Structural Radioactivity* Required to Produce the Same Latent Effects as Worst Case Tritium Release

Structure	Breeder	Maximum Tritium Release (Ci)	Percent Structure*
316 SS	$LiAlO_2$	1×10^7	~0.001%
316 SS	Lithium	8.4×10^6	~0.001%
V-15Cr-5Ti	Lithium	8.4×10^6	~0.1%
TZM	Lithium	6.3×10^6	~0.04%

*Based on reference radioactivity inventory, 5 mm of first wall

TABLE 8.41

Effect of Arbitrary Elimination of ^{60}Co from 316 SS on Latent Effects*

	Relative Latent Effects		
	Early Exposure	Chronic Exposure	Total Exposure
V-15Cr-5Ti	1	1	1
TZM	2	2.5	>2
316 SS with ^{60}Co	6	150	>100
316 SS without ^{60}Co	>3.5	~40	~30

*Acute effects are reduced by less than 50%

8.5 Conclusions and Discussion

To first order, the breeder selection determines the tritium inventory and maximum possible tritium release while the structural metal selection determines the non-tritium radioactivity.

8.5.1 Tritium

A variety of general conclusions are possible:

1) All primary coolant loops will likely operate with tritium cleanup systems which will be very significant in determining the steady state tritium levels and partial pressures.
2) The breeder processing technology available for liquid breeders tends to control the breeder inventory, although the properties of the breeder influences available technology.
3) The tritium partial pressures present tends to control the inventory in the metal through Sievert's Law. However, for the structural materials studied, the tritium inventory is very small compared to that in the breeder.
4) The coolant partial pressure, and primary heat exchange permeability and leakage, control the important and difficult-to-control pathway of tritium release to the environment. The breeder choice tends not to influence the power cycle release path.
5) The breeder inventory and behavior during transients controls the worst conceivable tritium release to the building under severe accident conditions.
6) For breeders, the most important selection factor is inventory, which controls total blanket inventory and largest releases.
7) For coolants, the most important selection factor is the tritium partial pressure, which tends to control permeation leakage.

8) For structural materials, the most important selection factor is the permeability.

9) All systems have conceivable releases of at least 10 g of tritium (10^5 Ci).

Some specific comments about the materials studied are summarized:

1) Among breeders, the order of increasing maximum possible tritium release is $Li_{17}Pb_{83}$, lithium, $LiAlO_2$.

2) Although the tritium partial pressures over $Li_{17}Pb_{83}$ appears higher than over lithium, the tritium pressure in $LiAlO_2$ is still higher, although in $LiAlO_2$ tritium may be in the less permeable form, T_2O.

3) Among coolants, helium is preferred. Lithium appears second best due to the low partial pressures. Water is similar to lithium in predicted normal releases but there is not the flexibility of designing a cleanup system on an intermediate coolant loop as there is for a lithium primary loop. Flibe is the worst due to the high partial pressures. A one loop boiling water system would present severe problems since there could not be a successful primary detritiation system.

4) Among metals, 316 SS and HT-9 are best, TZM next and V-alloy the worst due to permeability.

5) The selection of a lithium/V-alloy or flibe/TZM system would require a secondary coolant loop detritiation system. Helium systems appear not to require this. Lithium/steel and water/steel may require additional detritiation to control normal tritium releases but the water/steel system offers far less flexibility for improvement.

8.5.2 Structural Radioactivity

The results concerning the blanket structural radioactivity can be summarized by 6 points.

1) Comparison basis - Most previous work has used the activity (Ci) or biological hazard potential (BHP) to compare the accidental hazard of various materials. The BHP_{air} is based on the maximum permissible concentration (MPC) which was developed for fission on the basis of one organ per isotope, inhalation exposure only, and steady state concentrations. The BHP_{water} is based on the MPC of isotopes in water on the basis of steady state ingestion of water and one organ per isotope. The appropriate comparison is to use dose factors and transport effects. The FUSECRAC code [8.27], based on the state-of-the-art fission accident consequence code, CRAC [8.26], was used to compare materials.

Recently, Holdren [8.43] used dose factors and one weather condition to compare 316 SS, TZM, and Nb-Zr with fission. However, the comparision was based only on the early exposure from cloudshine and inhalation to one organ, bone marrow. Early groundshine exposure, shown important in this study, and chronic exposure, which dominates the total exposure, were not considered. Important isotopes like ^{60}Co in 316 SS were not included. Thus it is not surprising that the relative ranking of TZM to 316 SS predicted by Holdren (ratio of 2) does not agree with that of the present study (ratio of 1/3 for latent effects from early exposure, $\sim$ 1 for acute effects from early

exposure, and 1/50 for total latent effects). If very high release fractions of fusion structural material were possible, Holden's results do demonstrate that the public consequences would be serious.

It should be emphasized that the comparative results presented here for accidental hazards do not extend to other problems, like waste disposal and recycling. Other comparison bases would be required.

2) Dominant Effects - Fusion accident analysis, as in the case of fission, indicates that latent health effects are likely to overshadow acute dose response. For average weather conditions and site characteristics, a large fraction ($\gtrsim$ 6 %) of the structural inventory would have to somehow be released to the environment to produce any acute effects. Among the dominant latent effects, those resulting from chronic exposure appear more important than early exposure. This greatly complicates the analysis, increases complexities and possibly the variation among sites.

3) Comparison to Tritium - If only structural corrosion products are mobilized, the worst case tritium release would tend to dominate, except for the lithium/316 SS case. If additional mechanisms lead to higher release fractions (see Table 8.40), then the tritium effects become unimportant.

4) Alloy Comparison - The relative hazards of 316 SS, V-15Cr-5Ti, and TZM are listed in Tables 8.37 and 8.38. Austenitic steel is significantly worse than the refractory metals. As discussed

below, a ferritic steel would be expected to fall between the extremes. About 100 times more V-15Cr-5Ti than 316 SS would have to be released to cause the same total latent effect.

5) Causes of Difference - The consequence of a radiation release is partially controlled by the half-lives of the individual isotopes and the chemical behavior of the elements involved. It also happens that the elements involved in 316 SS (e.g., cobalt) are generally more hazardous in terms of ingestion due to environmental transport.

A very important part of the problem is the half-lives and decay of the isotopes involved, see Fig. 8.13. Different time periods qualitatively control the various radiation exposure effects. As seen in the figure, the metals all have similar initial activity levels, so it is not suprising that the acute effects are fairly similar. The latent effects from early exposure are determined by the external dose from the plume passage and the inhalation dose over days to years from the isotopes inhaled from the plume. 316 SS begins to have higher activity than TZM and V-alloy and likewise shows significantly higher latent effects from early exposure.

The latent effects from chronic exposure is largely controlled by activity levels from weeks to a few decades after the accident. As seen in the figure, it is precisely that time period where the 316 SS activity is orders of magnitude higher than TZM and V-alloy. Unfortunately, isotopes like ^{54}Mn, ^{55}Fe, ^{57}Co, ^{58}Co, ^{60}Co, have half-lives in this

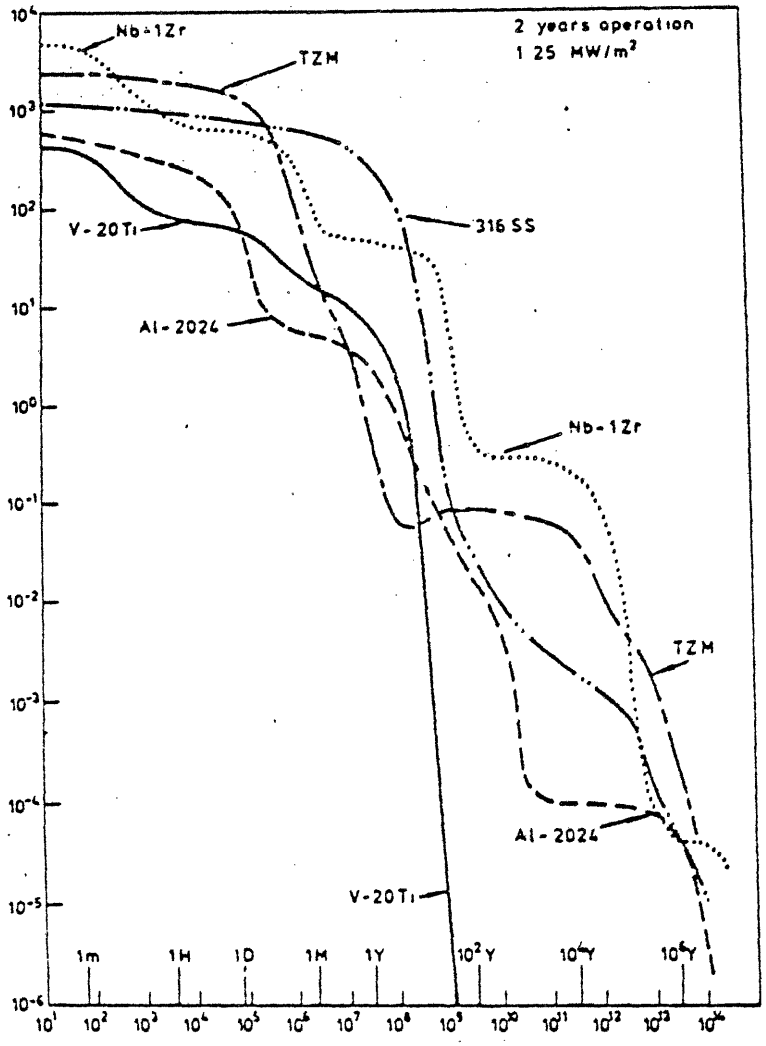

Fig. 8.13: Decay of Induced Radioactivity for the CCTR11 Breeding Blanket [8.44]

range and are largely controlling 316 SS effects. Most of the isotopes in TZM and V-alloy have decayed after a few months. Again, the relative health effects show a similar behavior - 316 SS is orders of magnitude worse than TZM and V-alloy in terms of chronic exposure.

Whereas the accidental contributions are not strongly effected by times over about 50 years after the accident, waste disposal/recycling is likely to depend strongly on the long-term activity behavior. Then, TZM does not look so much better than 316 SS, in fact it may be worse. Based on the activity behavior, one can qualitatively estimate how other materials would compare. Aluminum alloys would tend to be similar or better than V-alloy. The long term behavior of Al-alloy and V-alloy in the figure may be misleading since the specific alloying elements and impurities will control the decay and the behavior graphed may be different from actual alloys used. Nb-alloys appear worse from the accident standpoint than V-alloy and TZM, but perhaps better than 316 SS. Nb may be worse than 316 SS in the waste disposal problem. The general behavior of HT-9 (nil nickel, no cobalt) is also likely to be between TZM and 316 SS. Cobalt or nickel based alloys would be the worst choices, with large amounts of ^{58}Co and ^{60}Co produced.

6) Future Research - The most important research needs are

   i) Improved data base for dose factors, especially for internal exposure (see Section 8.3.7).

ii) Improved data base for environmental transfer parameters which influence ingestion dose.

iii) Extension of the analysis to include other candidate alloys.

iv) Extension of the analysis to include candidate neutron multipliers, breeders, and first wall coatings.

v) Experimental study of tritium releases from breeder materials under accident conditions.

vi) Include chemical toxicity effects, perhaps in FUSECRAC.

vii) Examine pathways between mobilization of radioactive species in the building and release to the environment; this includes oxide plate-out on building surfaces.

8.5.3 Relative Consequence Indices

The accidental hazard due to tritium from tritium breeders can be compared and relative consequence indices assigned. The state-of-knowledge in calculating the steady state inventory and possible releases is relatively poor. However, the uncertainty does not appear to be large enough to alter the basic rank ordering: $Li_{17}Pb_{83}$ (best), Lithium, $LiAlO_2$ (worst). The best available estimates can be used to quantify the relative hazard. The relative consequence index of tritium inventory, INV, is defined as (from Table 8.5)

$$RCI_{RC}^{ti} = INV/INV(Li_{17}Pb_{83}) \tag{8.43}$$

The relative consequence index of maximum possible tritium mobilized

in the building is defined as (Table 8.10)

$$RCI_{RC}^{tm} = INV_{mobilized}/INV_{mobilized}(Li_{17}Pb_{83}) \qquad (8.44)$$

The results are listed in Table 8.42.

The relative consequence from non-tritium radioactivity depends on the structural material selected. The other relative consequence indices in chapters 3 - 7 have compared accident mechanisms. Here, the relative health effects to the public per amount of structural first wall released (by whatever means) are compared using the FUSECRAC code. The relative consequence indices for early exposure (RCI_{RC}^{ee}), chronic exposure (RCI_{RC}^{ce}), and total exposure (RCI_{RC}^{te}) are defined by

$$RCI_{RC}^{i} = \frac{\text{latent effects from } i^{th} \text{ exposure}}{\text{latent effects from } i^{th} \text{ exposure from V-15Cr-5Ti}} \qquad (8.45)$$

where i = ee, ce, te.

The different exposure times are compared separately since the control implications are different. The latent effects from early exposure are only reduced by evacuation or shielding. Thus the RCI_{RC}^{ee} can also be viewed as the relative need that short-term protection means (and cost) will be necessary. The chronic exposure tends to dominate total exposure and can be reduced by interdiction (land or food). The total exposure provides a single value to compare the consequences of radioactivity release.

TABLE 8.42

Relative Consequence Indices of Tritium Breeders due to Tritium**

	Steady State Inventory RCI^{ti}_{RC}	Maximum Possible Tritium Mobilized RCI^{tm}_{RC}
$Li_{17}Pb_{83}$	1	1
Lithium*	8 - 10	8 - 10
$LiAlO_2$	125	12.5

* Range refers to lithium as breeder only or also as coolant

**Relative to $Li_{17}Pb_{83}$, low values preferred

TABLE 8.43

Relative Consequence Indices of Structural Materials due to Radioactivity Consequences*

	Early Exposure (RCI^{ee}_{RC})	Chronic Exposure (RCI^{ce}_{RC})	Total Exposure (RCI^{te}_{RC})
316 SS	6	150	$\gtrsim$ 100
HT-9**	2 - 6	2.5 - 150	2 - 100
V-15Cr-5Ti	1	1	1
TZM	2	2.5	$\gtrsim$ 2

*Based on relative latent effects, low values preferred

**HT-9 inventory unavailable, but appears to represent a hazard between 316 SS and TZM based on composition

REFERENCES

8.1 W. F. Calaway, "Electrochemical Extraction of Hydrogen from Molten LiF-LiCl-LiBr and its Application to Liquid-Lithium Fusion Reactor Blanket Processing," Nuclear Technology, 39 (6/1978) pp. 63-74.

8.2 D. C. Smith, et al., "Fusion Reactor Blanket/Shield Design Study," ANL/FPP-79-1, (7/1979).

8.3 E. H. Van Deventer, "A Review of Fusion-Related Experimentation on Blanket/Tritium Processing and Hydrogen Isotope Migration at the Argonne National Laboratory," Proceedings Tritium Technology in Fission, Fusion and Isotopic Applications, CONF-800427, (5/1980).

8.4 K. Natesan and D. C. Smith, "Effectiveness of Tritium Removal from a CTR Lithium Blanket by Cold Trapping Secondary Liquid Metals Na, K, and NaK," Nuclear Technology, 22 (4/1974), p. 138.

8.5 R. G. Clemmer, "The Development of Tritium Breeding Blankets for DT-Burning Fusion Reactors," Proceedings of the Fourth Topical Meeting on the Technology of Controlled Nuclear Fusion," CONF-801011, (7/1981), p. 526.

8.6 D. K. Sze, et al., "LiPb, A Novel Material for Fusion Applications," loc. cit. [8.5], p. 1786.

8.7 "Summary, INTOR Workshop, Phase II-A, Session III," Vienna, 7-18, December, 1981.

8.8 N. J. Hoffman, et al., "Properties of Lead-Lithium Solutions," loc. cit. [8.5], p. 1754.

8.9 C. C. Baker, et al., "STARFIRE," ANL/FPP-80-1, (9/1980).

8.10 D. R. Hanchar and M. S. Kazimi, "Tritium Permeation Modelling of a Conceptual Fusion Reactor Design," PFC/RR-81-27, 7/1981.

8.11 R. Wiswall and E. Wirsing, "The Removal of Tritium from Fusion Reactor Blankets," BNL-50748 (1977).

8.12 R. G. Mills, ed., "A Fusion Power Plant," MATT-1050, 8/1974.

8.13 "UWMAK-II Conceptual Tokamak Power Reactor Design," UWFDM-112, 10/1975.

8.14 "STARFIRE, A Commercial Tokamak Reactor: An Interim Report," ANL/FPP/TM-125, 12/1979.

8.15 M. R. Louthan, Jr., et al., "Tritium Absorption in Type 304L Stainless Steel," Nuclear Technology, 26 (6/1975), pp. 192-200.

8.16 S. J. Piet and M. S. Kazimi, "Uncertainties in Modeling of Consequences of Tritium Release from Fusion Reactors," PFC/TR-79-5, 7/1979.

8.17 J. S. Watson, "An Evaluation of Methods for Recovering Tritium from the Blankets or Cooling Systems of Fusion Reactors," ORNL-TM-3794, 8/1972.

8.18 W. M. Stacey, Jr., et al., "U.S. Contributions to the International Tokamak Reactor Workshop," 11/1979.

8.19 O. W. Richardson, et al., "Diffusion of Hydrogen through Hot Platinum," Philosophical Magazine, Series 6, 43 (7/1904), pp. 1-29.

8.20 A. S. Zarchy and R. C. Axtmann, "Limitations on Tritium Transport through Fusion Reactors," Nuclear Technology, 39 (8/1978), pp. 258-265.

8.21 "Reactor Safety Study," WASH-1400, 10/1975.

8.22 "Fusion Power Program Quarterly Progress Report January-March 1979," ANL/FPP-79-2, 8/1979.

8.23 "C.P.C. Wong, et al., "Moving Ring Field-Reversed Mirror Blanket Design Considerations," loc. cit. [8.5], p. 765, (also GA-A16097).

8.24 J. H. Opelka, et al., "Decommissioning Study of a Commercial Tokamak Reactor," ANL/ES-93, 1/1981.

8.25 Code of Federal Regulations, Title 10-Energy, Chapter 1 - Nuclear Regulatory Commission, Part 30, p. 192.

8.26 Calculations of Reactor Accident Consequences - CRAC Computer Code User's Manual, health files (ANL Code Center) and reference input.

8.27 S. J. Piet and V. J. Gilberti, "FUSECRAC: CRAC with Modifications for Fusion Application," PFC/RR-82-20, M.I.T., June 1982.

8.28 R. C. Weast, ed., Handbook of Chemistry and Physics, 55th edition, CRC Press, 1974.

8.29 Table of Isotopes, 7th Edition, 1978.

8.30 W. Hafele, et al., Fusion and Fast Breeder Reactors, International Institute for Applied Systems Analysis, Laxenburg, Austria, Report A-2361, 11/1976.

8.31 J. Jung, personal communication, 1981.

8.32 K. Okula, personal communication to R. Sawdye at MIT, 1977.

8.33 "UWMAK-III A High Performance Noncircular Tokamak Power Reactor Design," EPRI-ER-368, 7/1976.

8.34 E. D. Michaels, "Economics of Isotopic Tailoring for Light-Water Reactor Structural Materials," MLM-1704, 6/1980.

8.35 D. Kocher (ORNL), personal communication, results of EXREM runs from 1978 through 1980.

8.36 D. C. Kocher, "Dose-Rate Conversion Factors for External Exposure to Photo and Electron Radiation from Radionuclides Occurring in Routine Releases from Nuclear Fuel Cycle Facilities," ORNL/NUREG/TM-283 (also NUREG/CR-0494) 4/1979.

8.37 G. G. Killough and L. R. McKay, "A Methodology for Calculating Radiation Doses to Man from Radiation Releases to the Environment," ORNL-4992 (3/1976).

8.38 ORNL Health and Safety Research Division, personal communication, results of INREM runs from 1977 through 1980.

8.39 G. G. Killough, et al., "Estimates of Internal Dose Equivalent to 22 Target Organs for Radionuclides Occurring in Routine Releases from Nuclear Fuel-Cycle Facilities," ORNL/NUREG/TM-190 (also NUREG/CR-0150), 1978.

8.40 R. W. Sawdye and M. S. Kazimi, "Application of Probabilistic Consequence Analysis to the Assessment of Potential Radiological Hazards of Fusion Reactors," MITNE-220, 7/1978.

8.41 Effects on Populations of Exposure to Low Levels of Ionizing Radiation, Committee on the Biological Effects of Ionizing Radiation, BEIR III, 1980.

8.42 M. A. Bacheller, ed., Hammon Almanac, 12 ed., 1981.

8.43 J. P. Holdren, "Contribution of Activation Products to Fusion Accident Risk: Part 1, A Preliminary Investigation," Nuclear Technology/Fusion, 1 (1/1981), pp. 79-89.

8.44 O. N. Jarvis, "Transmutation and Activation of Fusion Reactor Wall and Structural Materials," AERE-R-9298, 1/1979.

CHAPTER 9. CONCLUSIONS AND RECOMMENDATIONS

The hypothesis, stated in Chapter 1, has been shown to be generally true - the selection of blanket materials for use as coolant, tritium breeder, and structure has a demonstrable and generally quantifiable influence on various fusion reactor aacident consequences. The influence on specific problems ranges as much as several orders of magnitude. The overall conclusions of this study are stated in Table 9.1. This chapter contains a summary of the relative consequence indices, discussion of the materials involved, recommendations for material choice and design, and recommendations for future safety research.

9.1 Relative Consequence Indices

The study included examination of the influence of 11 combinations of blanket materials (structure, tritium breeder and coolant) on the severity of 7 different safety problems. This influence was judged via well-defined safety criteria and quantified by establishing a series of relative consequence indices (RCI's).

9.1.1 Definitions

The seven safety concerns are listed in Table 9.2 along with the chapter containing the relevant analysis. The first three are basically thermal, the second three, chemical; and the final one (and also LOCA-after heat) neutronic. In the course of the study, it was seen that the functional dependence on the material choice differed among the safety areas. The influence in four areas (afterheat (LA), plasma disruptions (PD), structural oxidation (SO), and radioactivity consequences

TABLE 9.1

General Conclusions

1. Blanket material selection of structure, tritium breeder and coolant can significantly influence fusion reactor accident safety.

2. Clear preferences for material choice exist in most of the safety comparison areas.

3. Conflicting preferences result from examination of the overall problem. Some of these conflicts may be resolvable by determination of which problems are easier to solve by design.

4. A methodology for fusion accident risk assessments is most useful in providing an approach for material selections that minimizes the overall potential hazards.

TABLE 9.2

Safety Areas Examined in This Study

LP - Thermal transient due to plasma heating following LOCA (Chapter 3).

LA - Thermal transient due to decay afterheat following LOCA (Chapter 3).

PD - Plasma disruption effects (Chapter 4).

TP - Temperature and pressure effects from combustion and pressurized fluids (Chapter 5).

SO - Rapid structural oxidation hazards (Chapter 6).

CP - Corrosion product problems (Chapter 7)

RC - Radioactivity consequences (Chapter 8)

(RC)), could be determined for structural materials independent of coolant and breeder (Figure 9.1). Two of these (afterheat and radioactivity consequences) were also determined for breeder selection alone. The influence of structure and coolant was inherently linked in the areas of corrosion products (CP) and LOCA-plasma heating (LP). Finally, the temperature/pressure (TP) hazards from combustion and pressurized fluids are functions of the coolant and breeder choice.

In reality, the design and hence all safety areas are a function of the selection of all three components. In addition, the summation of the impacts of the different safety problems should be assessed (see Section 9.2.1). It is not yet possible to analyze the problems in sufficient detail to establish the dependence on all components; however, the present analysis does examine the major dependences. For example, the ability of structural materials to withstand a plasma disruption is likely to be influenced by the choice of coolant and breeder behind it. However, to first order it was discovered that the thermal shock and resulting temperature rise were overwhelmingly determined by the choice of structural material alone. In fact, the decoupling of the dependence of each of the three components (where possible) has an important advantage: since not all materials or material combinations were studied, appropriate decoupling of dependencies allows more direct emphasis on the individual material properties that are important and hence offers a higher potential for other candidate materials to be examined using the same framework .

Various safety criteria were used to judge the influence of material

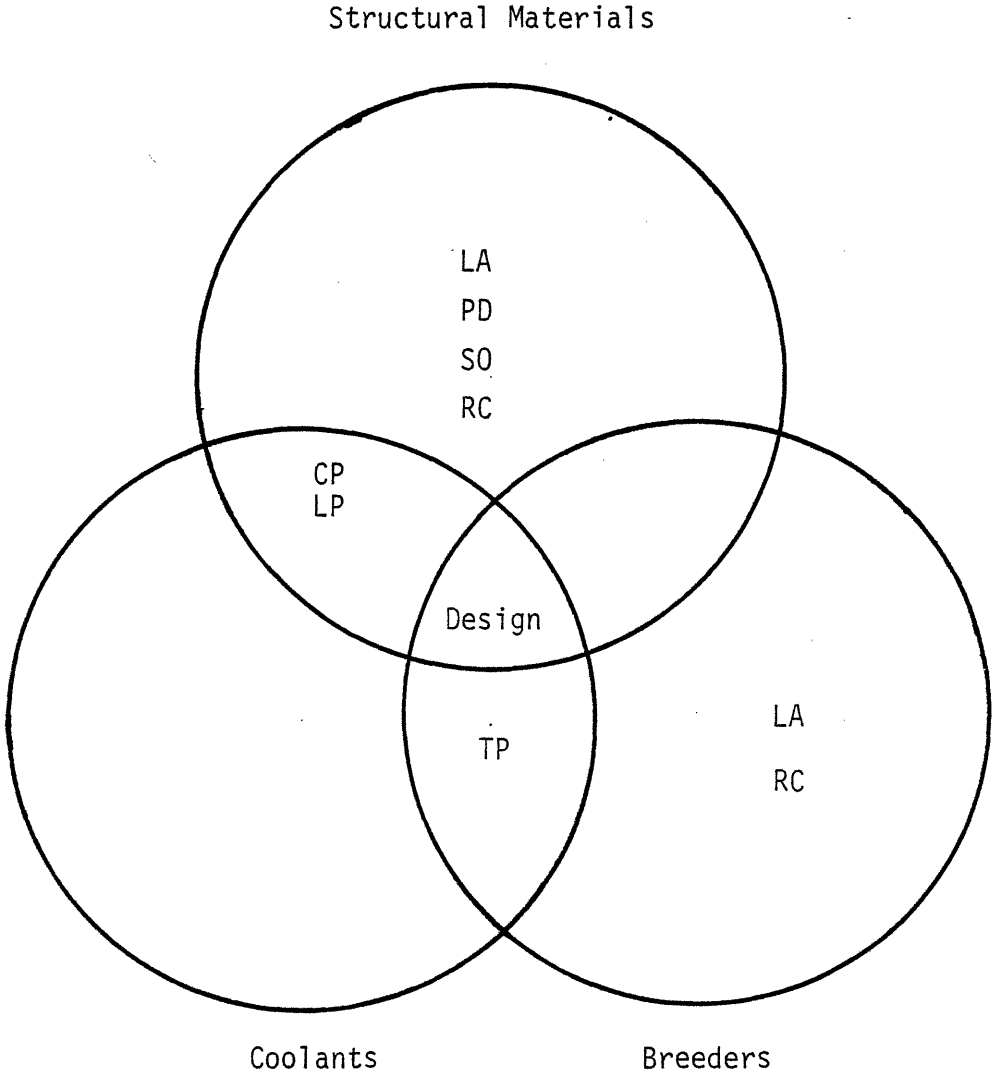

LP - LOCA-Plasma Heating
LA - LOCA-Afterheat
PD - Plasma Disruption
TP - Combustion and Pressure
SO - Structural Oxidation
CP - Corrosion Products
RC - Radioactivity Consequences

Figure 9.1: Functional Dependence of Blanket Material Component on Safety Concerns

selection on the safety problems (Table 9.3). These are defined such that low values are consistently preferred. For example, one would like the time elapsed in a transient before occurrence of damage or melting of the structure to occur to be as long as possible to allow mitigating action. Hence the inverse time to damage or melting is used to consistently judge materials. The relative scaling of the disruption time which causes initial melting or vaporization on the maximum depth of surface melting was seen to be the same (see pc - phase change - in Table 9.3).

The appropriate safety criteria for each safety concern were used to define specific relative consequence indices (Table 9.4), as a function of safety concern and safety criterion. As indicated in Figure 9.1, these are varying functions of either structure alone, breeder alone, coolant and structure, or coolant and breeder. Relative indices were used since the study was primarily a comparative one. Furthermore, the absolute level of severity or its implication could not always be determined.

In most cases, the RCI's were defined relative to the best case, which was given a value of 1.0. In some cases, the minimum value was zero (e.g., the rapid structural volatilization rate for some temperatures), so that a normalization constant had to be used. These were selected such that values less than or equal to 1.0 (below the normalization constant) appeared "minimal" concerns. In other cases, there was a range in the best material case. Then the most realistic value was normalized to 1.0, the other end of the range could therefore be less

TABLE 9.3

Safety Criteria Defined for Various Safety Areas[a]

d - The inverse of time to damage of structure, damage defined as a temperature rise of 300°C above operating temperature.

m - The inverse of time to melting of structure.

pc - phase change - (disruption time which causes initial melting)$^{-1}$ = (disruption time which causes initial vaporization)$^{-1}$ = (disruption time which causes the maximum depth of melting)$^{-1}$

ts - thermal stress

ms - magnetic stress

T - temperature rise

P - overpressure

ox - oxidation rate

v - volatilization rate

mt - corrosion product mass transfer rate

rr - maximum corrosion product radioactivity release

ti - tritium inventory

tr - maximum tritium release

ee - latent effects to public from early exposure

ce - latent effects to public from chronic exposure

te - total latent effects to public

(a) - defined such that low values preferred, symbols are those used with the RCI's

TABLE 9.4

Definitions of Relative Consequence Indices[a]

RCI^{d}_{LP}	(Time to Damage)$^{-1}$ relative to most realistic TZM/flibe case from plasma heating following LOCA, defined for structure/coolant combinations.
RCI^{m}_{LP}	(Time to Melting)$^{-1}$ relative to most realistic TZM/flibe case from plasma heating following LOCA, defined for structure/coolant combinations.
RCI^{d}_{LA}	(Time to Damage)$^{-1}$ relative to best case V-alloy (for structures) or $Li_{17}Pb_{83}$ (for breeders) from decay afterheat following LOCA, defined separately for structures and breeders.
RCI^{m}_{LA}	(Time to Melting)$^{-1}$ relative to best case V-alloy (for structures) or $Li_{17}Pb_{83}$ (for breeders) from decay afterheat following LOCA, defined separately for structures and breeders.
RCI^{pc}_{PD}	(Time for Phase Change)$^{-1}$ (disruption time which produces initial melting, maximum depth of melt zone, and initial vaporization) relative to best case TZM following plasma disruption, defined for structures.
RCI^{ts}_{PD}	Thermal stress relative to best case TZM from plasma disruption, defined for structures.
RCI^{ms}_{PD}	Magnetic stress relative to best case, 316 SS from plasma disruption, defined for structures.
$RSCI^{T(b)}_{TP}$	Subjective rank ordering of temperature rise problems from combustion, defined for coolant/breeder combinations.
$RSCI^{P(b)}_{TP}$	Subjective rank ordering of overpressure problems from combustion or pressurized fluids, defined for coolant/breeder combinations.
RCI^{T}_{SO}	(Temperature to rapidly oxidize wall - operating temperature)$^{-1}$ relative to best case HT-9, defined for structures.
RCI^{ox}_{SO}	Oxidation rate of structural wall relative to 1 mm of wall/day, defined for structures.
RCI^{v}_{SO}	Volatilization rate of structural wall relative to 1 mm of wall/day, defined for structures.
RCI^{mt}_{CP}	Corrosion rate relative to 1 μm/yr, defined for coolant/structure combinations.

TABLE 9.4 (continued)

Definitions of Relative Consequence Indices (continued)[a]

RCI_{CP}^{rr}	Maximum releasable corrosion product inventory relative to 1kCi, defined for coolant/structure combinations.
RCI_{RC}^{ti}	Tritium inventory relative to best case, $Li_{17}Pb_{83}$, defined for breeders.
RCI_{RC}^{tr}	Maximum releasable tritium relative to best case $Li_{17}Pb_{83}$, defined for breeders.
RCI_{RC}^{ee}	Latent effects to public from early exposure relative to best case V-alloy, defined for structures (per unit volume of first wall released).
RCI_{RC}^{ce}	Latent effects to public from chronic exposure relative to best case V-alloy, defined for structures (per unit volume of first wall released).
RCI_{RC}^{te}	Total latent effects to public relative to best case V-alloy, defined for structures (per unit volume of first wall released).

[a] Low values preferred

[b] Subjective rank ordering

than or greater than 1.0. For example, the range in LOCA-plasma heat effects for the best case TZM/flibe was caused by the specific scenario for flibe loss. The most realistic case was to assume loss in 2.5 seconds. The other case was to assume instantaneous loss (see Chapter 3).

In one area, combustion and pressure hazards, it was not possible to directly quantify the result, hence a subjective rank ordering was used.

9.1.2 Structural Material Results

The analyses indicated that several structural material properties influenced safety concerns (Table 9.5). It is not surprising that many of these are also engineering properties. Likewise, it is not surprising that the better safety choices are the better engineering materials. Yu [9.1] found HT-9 and V-alloy to be superior materials for first wall application. TZM would have been a good candidate escept for its very high ductile-brittle transition temperature (DBTT). The results of Smith et al. [9.2] similarly indicate that V-alloys and HT-9 have more design flexibility and higher performance than 316 SS.

9.1.2.1 Relative Consequence Indices

The values of the relative consequence indices which are a function of structural material are listed in Tables 9.6 and 9.7. A detailed sensitivity analysis was beyond the scope of this study. However, some idea of the potential range came about naturally in the analysis from either the assumptions themselves or the definition of the indices.

TABLE 9.5

Material Properties of Structural Materials which Influence Safety

Property	Ideal Value	Relative Value 316 SS	HT-9	V-alloy	TZM
Volumetric Specific Heat[b]	high	0.77	1.00	0.55	0.54
Thermal Conductivity[b]	high	0.19	0.26	0.29	1.0
Electrical Conductivity[b]	low	1.0	1.05	1.9	3.5
$E_y\beta/(1-\nu)$[a][b]	low	3.0	1.5	1.0	1.4
Ductile Brittle Transition Temperature	low	low	problem	low	serious problem
Strength Properties	good	fair	good	good	good
Operating Temperature °C	high	450	450	600	900
Melting Temperature °C	high	1430	1420	1900	2600
Margin Between Melting and Operating Temp. °C	high	980	970	1300	1700
Transition to Rapid Oxidation Temp. °C	high	1000	1300	700	700
Margin Between Oxidation and Operating Temp. °C	high	+550	+850	+100	-200
Corrosion					
- water	good	good	good	bad	bad
- helium	good	good	good	bad	bad
- lithium	good	poor	poor	good	good
- flibe	good	poor	poor	?	good

(a) Young's Modulus x linear coefficient of expansion x (1-poisson's ratio)$^{-1}$ influences thermal stresses.
(b) Relative values.

TABLE 9.5 (continued)

Material Properties of Structural Materials which Influence Safety

Property	Ideal Value	Relative Value			
		316 SS	HT-9	V-alloy	TZM
Overall Oxidation Rate	low	low	low	high	high
Overall Volatilization Rate	low	low	low	low	high
Afterheat	low	highest	average	low	average
Radioactivity Effects	low	highest	high	lowest	low
Tritium Permeability	low	low	low	high	low

(a) Young's Modulus x linear coefficient of expansion x (1-poisson's ratio)$^{-1}$ influences thermal stresses.

TABLE 9.6

Relative Consequence Indices for Cases Dependent Only on Structural Material[a]

		316 SS	HT-9	V-alloy	TZM
Damage, Afterheat	RCI^{d}_{LA}	6-11	3-8	1.0	5-9
Melting, Afterheat	RCI^{m}_{LA}	7-12	3-8	1.0	3-8
Phase Change, Plasma Disruption	RCI^{pc}_{PD}	8.3	4.7	4.9	1.0
Thermal Stress, Plasma Disruption	RCI^{ts}_{PD}	10.0	4.0	2.3	1.0
Magnetic Stress, Plasma Disruption	RCI^{ms}_{PD}	1.0	1.0-1.1	1.0-1.9	1.0-3.6
Temp. Margin, Structural Oxidation	RCI^{T}_{SO}	1.7	1.0	9.5	∞ [b]
Oxidation Rate of Structure	RCI^{ox}_{SO} [c]	0-2.2	0-2.2	0-147	0-220
Volatilization Rate of Structure	RCI^{v}_{SO} [c]	0-2.2	0-2.2	0-0.1	0-220
Latent Effects, Early Exposure	RCI^{ee}_{RC}	6	2-6[d]	1.0	2
Latent Effects, Chronic Exposure	RCI^{ce}_{RC}	150	2.5-150[d]	1.0	2.5
All Latent Effects	RCI^{te}_{RC}	100	2-100[d]	1.0	2

(a) low values preferred, see Table 9.4 for RCI definitions
(b) since the rapid oxidation temperature for TZM was below the operating temperature, the temperature margin against oxidation was non-existent, resulting in a value of ∞ for this index - see text.
(c) the oxidation and volatilization rates are a strong function of temperature. The range indicated is for about 500-1500°C, normalized to a rate of 1 mm of metal/day.
(d) Radioactivity values of HT-9 not available, effects judged between 316 SS and TZM on basis of composition (Chapter 8).

TABLE 9.7

Relative Consequence Indices for Cases

Dependent on Structure and Coolant (a)

		Damage LOCA	Melting, LOCA	Corrosion Mass Transfer	Corrosion, Radio-activity
		$RCI_{LP}^{d(c)}$	$RCI_{LP}^{m(c)}$	RCI_{CP}^{mt}	RCI_{CP}^{rr}
316 SS	Water	2.0-2.3	10.2-13.5	0.5	30
316 SS	Helium	2.0-2.3	10.2-13.5	0.1	20
316 SS	Lithium	0.7-2.0	1.9-12.6	6	2000
HT-9	Water	1.5-1.6	5.8-9.0	1.4	---(b)
HT-9	Helium	1.5-1.6	5.8-9.0	0.1	---(b)
V-alloy	Lithium	0.6-1.4	1.3-6.2	0.5	3
TZM	Flibe	1.0-4.0	0.4-1.0	0.5	1

(a) Low values preferred, see Table 9.4 for definitions.
(b) The specific radioactivity of HT-9 was unavailable.
(c) The range for LOCA-plasma heat cases was caused by the loss rate scenario. For non-TZM/flibe cases, the higher value is for an instantaneous coolant loss. For water or helium cases, the lower value is for a 0.1 second depressurization. For lithium, the lower value is for the case where MHD forces prevent lithium drainage but the flow stops instantaneously (May not be conservative). For TZM/flibe, the values of 1.0 refer to the most realistic 2.5 sec. drainage case, the other value assumes instantaneous flibe loss.

These are generally discussed in the table footnotes. The possible sources of error or uncertainty and relevant assumptions for each of the analyses were indicated in the relevant chapter and are not repeated here. It is felt that the differences among materials in most cases are larger than any reasonable uncertainty. This is especially true since the values are relative. Many uncertainties (time of the disruption, for example) tend to cancel and would not affect the relative values. Further discussion of the sensitivity of the values to material choice and design is included in section 9.2. The following discussion focusses on the implication of the indices for the various structural materials.

9.1.2.2 316 SS

Austenitic stainless steels have received considerable attention for fusion reactor blankets primarily due to the considerable data base and experience which exists. This aspect tends to force its use for near-term experiments like INTOR and the Fusion Engineering Device. However, it is clear that better alternatives exist for potential application as commercial fusion reactors.

The only safety advantage of 316 SS over HT-9 is the slightly better corrosion resistance to water. Besides the relatively poor thermo-mechanical properties of 316 SS, many other problems can be directly traced to its composition. The higher molybdenum content of 316 SS versus HT-9 significantly increases the rapid oxidation potential. Serious problems arise from the use of nickel as an alloying agent and presence of cobalt impurity. The nickel is leached by liquid metals,

e.g., lithium and lead, lowering its corrosion resistance to lithium and $Li_{17}Pb_{83}$. Worse, nickel and cobalt lead to the presence of ^{60}Co, ^{58}Co and ^{57}Co which worsen radioactivity and afterheat problems as they are most hazardous from the public accident consequence standpoint.

9.1.2.3 HT-9

It was somewhat surprising that the two steels differed so significantly, but ferritic HT-9 was seen clearly superior to austenitic 316 SS.

9.1.2.4 V-alloy

Vanadium is superior to HT-9 in the very important areas of higher operating temperatures, afterheat, and radioactivity. These advantages make it appear a very promising candidate. However, there are two serious problems. The tritium permeability is very high, requiring far more effort to control tritium migration within the reactor. Secondary containment and tritium barrier technologies would be vital. The oxidation potential is high, probably preventing its use with either water and helium. Above 700°C (only about 100° above typical operating temperatures), the oxidation rate is very rapid forming the liquid oxide, V_2O_5. Unlike TZM, however, the volatile oxide partial pressures are very low so that the volatilization rate is minimal. For vanadium, then, oxidation is a serious mechanism to cause damage but far less serious in terms of mobilizing radioactivity. In general V-alloy and HT-9 are good safety candidates; however, V-alloy has potentially more significant advantages and disadvantages.

9.1.2.5 TZM

In many respects TZM is similar to V-alloy. Advantages include high temperature performance and thermal conductivity. These result in TZM's superior ability to survive the thermal effects of disruptions and longer periods of plasma heating without cooling. Disadvantages include afterheat, radioactivity, and oxidation. The afterheat and radioactivity problems are better than or equal to the steels but inferior to vanadium. Although not examined in this report, the very long-term radioactivity levels are high (see for example Ref. 9.3), the DBTT is very high (see Chapter 1), and waste disposal recycling/decommissioning problems would appear to be worse for TZM than for the other materials. Although the oxidation rate for TZM is similar to vanadium, the product oxide MoO_3 is far more volatile. Hence, radioactivity mobilization due to rapid oxidation is a very serious concern for TZM, especially since its other high temperature properties would encourage its use at temperatures above 700°C, the threshold oxidation temperature.

9.1.2.6 Other Structural Materials

Although the actual calculations of the indices were limited to four materials, the identification of critical properties makes possible some generic comments on other materials.

As seen by the difference between 316 SS and HT-9 in nickel and cobalt content, use of superalloys based on nickel or cobalt should be discouraged. The poor high temperature performance of aluminum not only limits its operating temperature but appears to significantly reduce the temperature margin between operation and damage or melting. Niobium is somewhat superior to vanadium in thermomechanical properties and the

threshold oxidation temperature is far higher ($\sim$1500°C); however, afterheat, radioactivity and long-term waste disposal problems are significantly worse.

A promising approach might be a ceramic structure, using such materials as SiC which exhibit extremely low levels of afterheat and radioactivity. Use of such materials depends on very significant advances in the engineering of large, complex, brittle ceramic structures as well as the understanding of radiation effects (in a fusion environment).

9.1.2.7 Comparison of Materials

The key advantages and disadvantages of the structural materials are listed in Table 9.8. HT-9 and V-alloy appear the most promising. If alloy development produces a high performance V-based alloy, it could well be the material-of-choice. Another promising alternative, dependent on material science advances, could be a low activation ceramic. For the more near-term question, HT-9 appears promising. In all cases, however, it should be emphasized that significant problems do exist.

9.1.3 Coolant Results

Of the three components of the blanket, the specific effects of coolants were the least adequately modeled. The specifics of LOCA-transients are difficult to determine. The focus of the present study was on a very pessimistic case which results in very rapid coolant loss. However, the analysis does indicate which properties are important and gives some quantification to the impact. The coolant properties that

TABLE 9.8

Key Safety Advantages and Disadvantages of

Reference Structural Materials

Alloy	Advantages	Disadvantages
316 SS		Poor thermo-mechanical properties Low temperatures High afterheat High radioactivity
HT-9	High margin between oxidation and operating temperatures.	Low operating temperatures
V-alloy	Low afterheat Low radioactivity	High oxidation potential High tritium permeability
TZM		High oxidation potential

were found to be important are summarized in Table 9.9. If the coolant is to be used as a liquid, a high boiling point is desired to provide more of a temperature margin during transients and operation.

9.1.3.1 Relative Consequence Indices

The indices dependent on coolant and structural material were given in Table 9.7. The indices dependent on coolant and breeder are listed in Table 9.10. Between the two tables, the influence of coolant choice, coupled with the other components, can be determined. The influence and implication of the internal/external difference (Table 9.10) is discussed in Section 9.2.

9.1.3.2 Pressurized Water

The prime disadvantages of water include its very high operating pressure (> 15 MPa), chemical reactivity, and dilution of tritium. The high pressure could cause overpressurization of either the blanket module or containment building. Unlike fission, it does not appear possible to design a water-cooled blanket that can operate with minor internal failures. In fission, the reactor can continue to operate if a few fuel rods experience minor cladding failures. Furthermore, the entire system is designed to withstand operating pressures. In fusion, it does not appear possible to design the breeder zone to withstand 15 MPa (see Chapter 2). Thus, any leakage of the pressurized water to either the breeding zone or plasma chamber prevents operation and represents a safety problem.

TABLE 9.9

Coolant Properties of Reference Coolants which Influence Safety

		Water	Helium	Lithium	Flibe
Volumetric Heat Capacity*	high	∿2	0.01	1.0	2.5
Thermal Conductivity*	high	∿0.01	0.007	1.0	0.02
Electrical Conductivity	low	nil	nil	high	low
Operating Pressure*	low	∿150	∿50	∿10	1
Melting Point, °C	low	0	-273	181	459
Boiling Point, °C (if liquid)	high	100	-273	1340	?
Combustivity	low	high	low	high	low
Corrosion Resistance					
steels	good	good	good	poor	poor
refractory alloys	good	fair	fair	good	good
Ability to remove tritium	high	low	high	high	high

*Relative values.

TABLE 9.10

Relative Subjective Consequence Indices for Cases Dependent on Coolant and Breeder Choice (a)

		Combustion, Temperature $RSCI^{T}_{TP}$		Combustion, Pressure $RSCI^{P}_{TP}$	
		Internal(b)	External(c)	Internal	External
Water	$LiAlO_2$	1	1	3	4
Water	$Li_{17}Pb_{83}$	1	3	3	4
Helium	$LiAlO_2$	1	1	3	3
Helium	Lithium	1	4	3	4
Lithium	Lithium	1	4	1	4
Flibe	Lithium	2	4	1	4

1 - No safety problem

2 - Evidence that only a mininal safety problem exists

3 - Evidence that serious problem exists

4 - Known serious problem

(a) Low values preferred, see Table 9.4 for definitions.
(b) Internal accident refers to scenario where only blanket breeders and coolants mix, no external oxidants. Then the only hazards are pressure problems from water or helium use and (potentially) flibe-lithium reaction.
(c) External accident refers to a scenario where blanket fluids may come in contact with external combustants like air or concrete. Then only temperature problems from $LiAlO_2$ can be ignored. Even though $LiAlO_2$ does not combust, the use of pressurized coolants with it would still cause overpressure concerns in the containment.

If reactive metals like beryllium, vanadium, niobium, or molybdenum are present in the blanket, water reactions would be a serious concern during accidents. As discussed in Chapter 5, even steels will rapidly deteriorate in steam below their melting temperatures. Furthermore, if even steel did not experience a rapid reaction with steam, any oxidation of the first wall resulting from a steam leakage to the torus could seriously and rapidly degrade the plasma impurity/vacuum properties of the wall - a very serious economic concern.

Finally, elemental tritium entering water becomes HTO which is far more biologically hazardous. It appears very difficult to extract tritium from water, compared to the alternative coolants.

9.1.3.3 Pressurized Helium

Relative to water, helium has the safety advantages of no significant chemical reactivity, easier tritium extraction, and lower pressure. Although the pressure is still very high (>5 MPa), it may be possible to design a breeding zone which could survive accidental pressurization. Compared to (still lower pressure) liquid metals and salts, another disadvantage is the poor performance if flow stops. Stagnant helium is a very poor heat transfer medium or heat sink.

9.1.3.4 Lithium

The primary safety problem with lithium is chemical combustivity. If lithium is used only as a breeder, the solution is basically to keep oxidants out of the blanket: only a small stream of breeder lithium would leave the blanket. If lithium is used as a coolant, the avail-

ability of oxidants to the lithium would appear to be increased.

9.1.3.5 Flibe

The molten salt flibe ($2LiF\text{-}BeF_2$) has some interesting differences. The pressure and combustion problems are both very small. It is also a good heat sink. The disadvantages are the relatively high tritium partial pressures, low thermal conductivity (which can thermally isolate the first wall in the event of a loss of flow), and its high melting temperature.

9.1.3.6 Other Coolants

Having identified the relevant material properties and quantified their influence, some general comments are possible on other potential coolants.

If a D-T fuel cycle is used, there is little incentive to use a liquid metal coolant in the blanket other than lithium or lithium-alloy. In any case, other liquid metals (e.g., Na, K) are qualitatively similar to lithium. Boiling water has two distinct safety differences from pressurized water - lower operating pressure and worse tritium problems. Pressurized water power systems have two loops - primary and steam turbine. Even though tritium which has migrated to the steam loop is generally considered released to the environment, these is still one barrier to tritium release. For boiling water, however, a single coolant loop tends to be used, thus removing a very important barrier to tritium release.

Molten salts other than flibe have been mentioned as coolants [9.4, 9.5]. LiF would be promising except for its high melting temperature, 848°C [9.4]. Another promising candidate is $NaNO_2$-$NaNO_3$-KNO_3, which has the disadvantage of thermal decomposition at high temperatures ($\sim$540°C) and chemical reactivity with lithium, graphite, and refractory metals [9.5]. If a suitable salt could be found, it might offer attractive safety properties.

9.1.3.7 Comparison of Coolants

Table 9.11 is a list of the key safety advantages and disadvantages of the reference coolants.

9.1.4 Breeder Results

The properties that were found to influence the breeder effect on safety are summarized in Table 9.12. If the breeder is to be used as a liquid, a low melting point is preferred to ease startup/shut down phase change difficulties as well as alleviate any tube plugging due to freezing.

The indices dependent on coolant and breeder were shown in Table 9.10. Additional indices dependent only on the breeder are listed in Table 9.13. The afterheat results are seen to be a strong function of accident scenario - whether or not the fluid breeder drains. This aspect is further discussed in Section 9.2. The following discussion focusses on the implications of the indices for the various materials.

TABLE 9.11

Key Safety Advantages and Disadvantages of Reference Coolants

Coolant	Advantages	Disadvantages
Pressurized Water		Chemical Reactivity High Pressure Difficult to Extract Tritium
Pressurized Helium	Low Chemical Combustivity	High Pressure Gaseous Phase (poor stagnant heat sink)
Lithium	Good Heat Sink (even if stagnant)	High Chemical Combustivity
Flibe	Lowest Pressure (good heat sink)	High Tritium Pressures Low Thermal Conductivity

TABLE 9.12

Material Properties of Reference Breeders Which Influence Safety Concerns

	Ideal Value	$LiAlO_2$	$Li_{17}Pb_{83}$	Lithium
Volumetric Specific Heat*	high	0.41	1.0	0.27
Thermal Conductivity*	high	0.09	0.44	1.0
Electrical Conductivity	low	nil	high	highest
Melting Point, °C	solid-high	1610	- - -	- - -
	liquid-low	- - -	235	181
Boiling Point, °C	high	? decompose	?	1340
Combustivity	low	very low	modest	high
Compatability				
- Steels	good	good	fair	fair
- Refractory Metals	good	fair	good	good
Tritium Inventory*	low	125	1.0	∿9
Tritium Partial Pressures	low	high	higher	low
Maximum Tritium Releases*	low	∿12.5	1.0	∿9
Radioactivity	low	low	low	low
Requires a Neutron Multiplier	No	Yes	No	No

*Relative values.

TABLE 9.13

Relative Consequence Indices for Cases Dependent Only on Breeder[a]

		$LiAlO_2/Be$[c]	Lithium	$Li_{17}Pb_{83}$
Damage Afterheat	RCI^{d}_{LA}[b]			
	-breeders drain	2.7	1.0	1.0
	-breeders do not drain	300	5	1.0
Melting Afterheat	RCI^{m}_{LA}[b]			
	-breeders drain	1-5	1.0	1.0
	-breeders do not drain	150	5	1.0
Tritium Inventory	RCI^{ti}_{RC}	125	8-10	1.0
Tritium Release	RCI^{tr}_{RC}	12.5	8-10	1.0

(a) Low values preferred, see Table 9.4 for definitions.
(b) The effect of breeders on afterheat transients was critically dependent on whether it was possible for the fluid breeders to drain out of the blanket in time to affect heat transport. The two cases refer to 1) breeder drains instantaneously, 2) breeder does not drain but stays stagnant.
(c) Beryllium was used as a neutron multiplier. Here this is the best case since beryllium does not add any afterheat.

9.1.4.2 $LiAlO_2$

Major problems of $LiAlO_2$ include the need for a neutron multiplier, low thermal conductivity and higher tritium inventories. The engineering complexity due to the required presence of a neutron multiplier has previously been identified [9.4]. This is also a safety problem.

Any neutron multiplier increases complexity (potentially lowering reliability and increasing accident frequency) but also may cause its own safety problems. The two prime candidates in STARFIRE [9.4] are good examples. Zr_5Pb_3 is a major contributor to afterheat and radioactivity in the STARFIRE design. The present $LiAlO_2$ results are based on beryllium not Zr_5Pb_3. Although beryllium would not add to afterheat or radioactivity problems, it does represent a serious chemical toxicity problem.

The poor thermal conductivity makes designs more difficult and worsens performance during thermal transient accidents. The tritium inventory and partial pressures are higher than the liquid breeders (although the mobile tritium is probably in the less mobile and more biologically hazardous HTO form rather than HT or T_2). Although the tritium inventory may be less vulnerable than the liquid breeders, it is not invulnerable. Credible mechanisms exist for release of significant fractions of the tritium inventory.

9.1.4.3 Lithium

The only major safety problem with use of lithium is combustivity. Combustion with air appears capable of generating combustion zone

temperatures of about 1200°C and overpressures in excess of one atmosphere (Chapter 5).

9.1.4.4 $Li_{17}Pb_{83}$

$Li_{17}Pb_{83}$ has some slightly superior thermo-mechanical properties than lithium does. The major differences from lithium are lower chemical reactivity and tritium inventories but higher tritium partial pressures. The data base is inadequate to quantify the differences sufficient to determine preference between lithium and $Li_{17}Pb_{83}$.

9.1.4.5 Other Breeders

Again, given the analysis, some general comments can be made concerning other breeders.

Other ceramic breeders appear qualitatively similar to $LiAlO_2$. One slight exception would be Li_2O which does not seem to require a neutron multiplier. However, Li_2O has some chemical reaction concerns not present for $LiAlO_2$. Other liquid metal alloys, e.g., Li-Al appear qualitatively similar to lithium and lithium-lead. Solid metal alloys like Li_7Pb_2 do not appear promising since they show some tendency to combine some of the disadvantages of the ceramics (difficult tritium removal) with liquid metal alloys (chemical combustivity). For example, water reacts with lithium and Li_7Pb_2 with similar results (Chapter 5).

Salt breeders could have some advantages, specifically lower combustivity. However, examination of potential salts [9.4, 9.5] have not identified a promising candidate that could make the advantages reality

while still performing the essential function of breeding. Pure LiF would adequately breed [9.4, 9.5], but its melting point (848°C) discourages use. It is too low to allow use as a solid and probably too high to use as a liquid.

9.1.4.6 Comparison of Breeders

The key advantages and disadvantages of the reference breeder materials are listed in Table 9.14. The use of $LiAlO_2$ or other ceramics depends on demonstration of adequate tritium breeding and removal. The use of liquid lithium or lithium-metal alloys depends on a design minimizing combustion or development of a candidate with low combustivity ($Li_{17}Pb_{83}$?).

9.2 Relative Importance of Safety Problems and Recommendations

It is apparent that some conflicting preferences arise among the various possible materials. Some of the conflicts can be resolved by changing the relative weighting pertaining to each of the safety areas. This then leads to recommendations for blanket design and identification of the most promising materials.

9.2.1 Conflict Resolution

As mentioned in Chapter 1, the analytical tool of probabilistic risk assessment (PRA) proved useful in estimation of the overall risk of fission reactors and other technologies. Due to several limitations, it is not possible to perform a detailed probabilistic fusion risk assessment to compare materials. However, some discussion of the

TABLE 9.14

Key Safety Advantages and Disadvantages

of Reference Breeder Materials

Breeder	Advantages	Disadvantages
$LiAlO_2$	Low chemical combustivity	Needs neutron multiplier High tritium inventory, release & partial pressures
$Li_{17}Pb_{83}$	High volumetric specific heat	Higher tritium partial pressures
Lithium	High thermal comductivity	High chemical combustivity

technique allows identification of two ways to change the importance given to the various relative consequence indices.

The risk (public safety and economic) of fusion is a function of both consequence and frequency of all events. Risk is often portrayed on a frequency-consequence diagram (see Figure 1.1, 1.2). To first order, the risk can be expressed as

$$\text{Risk} = \sum_{\text{accidents}} (\text{frequency} \times \text{consequence}) \qquad (9.1)$$

Sometimes there may be trade-offs between frequency and consequence. The total risk may not be reduced by decisions that lower consequences at the expense of reactor reliability and accident frequency.

It is often extremely difficult to show that an undesired event is completely impossible. Instead, efforts can be made to show that the frequency (or consequence) of a certain event occurring is insignificantly low. This leads to analysis of realistic accident scenarios and mechanisms. For example, one can not strictly prove that a lithium-air fire temperature cannot reach the statically-calculated adiabatic flame temperatures of 2100-2200°C. However, there is sufficient experimental and analytical evidence to suggest that maximum temperatures are of the order of 1200°C (Chapter 5) and that due to kinetic limitations, the probability of lithium-air reactions producing 2000°C temperatures is insignificantly low.

The information available is not perfect; the uncertainty is not zero. The Level 2 definition of risk [9.7] directly incorporates uncertainty

into the risk estimate. For fusion, a variety of important data are not available at present.

By viewing safety from the PRA perspective, one can see that the relative consequence indices (RCI's) are not the complete picture. Equation (9.1) can be rewritten in terms of these indices. For the state-of knowledge in fusion research, the relative risk of different materials can be approximated by:

$$\text{Relative Risk} = \sum_{\text{accidents}} [(\text{function of RCI's pertaining to each accident}) \times \text{accident likelihood}] \quad (9.2)$$

If the RCI's for a problem are not highly sensitive to material choice and the accident likelihood is independent of material choice (e.g., plasma disruption), then the risk sensitivity to material choice is small. Likewise, if the accident frequency is low (either because of an inherent fusion advantage or added design feature), then the importance of that problem to the overall risk sensitivity is small. These two aspects will now be addressed.

9.2.2 Sensitivity of Safety Problems to Material Choice

Based on the values for the relative consequence indices (Tables 9.6, 9.7, 9.10 and 9.13), the sensitivity of the safety problems to material choice can be roughly characterized (Table 9.15). Radioactivity consequences per unit material released and structural oxidation problems differ by at least two orders of magnitude among materials. Although the indices for combustion/pressure hazards (Table 9.10) do not quantify the differences, the discussion in Chapter 5 clearly indicates that these problems have at least a two-order-of-magnitude range dependency on the

TABLE 9.15

Sensitivity of Safety Problems to Material Choice

Most Sensitive (Several Orders of Magnitude)

- Radioactivity Consequences
- Structural Oxidation
- Combustion/Pressure Hazards

Significantly Sensitive (About One Order of Magnitude)

- Afterheat-LOCA
- Plasma Disruptions (Thermal Only)
- Corrosion

Least Sensitive

- Plasma Heating-LOCA
- Plasms Disruptions (Electromagnetic Effects)

material. The sensitivity of problems of afterheat, thermal effects from plasma disruptions and corrosion is generally one order of magnitude. A major exception is the corrosion problem of lithium and steel.

Certain problems are qualitatively far less important in viewing material choice even though the problem itself may be serious. The sensitivity of the problems of continued heating from the plasma during a LOCA and the electromagnetic effects of plasma disruptions is relatively low. In fact, the uncertainties in these analyses may well be larger than the range of the values of the indices themselves. The relative consequence indices pertaining to these latter two problems should be weighted less in comparing the overall relative risk of different materials.

9.2.3 Feasibility of Safety Solutions by Design

Design features can influence the risk in several ways, either to reduce accident frequency or mitigate the consequences. Here the focus is primarily on ways that design can influence the comparison among materials. Table 9.16 is a list of specific safety problems, some possible passive design solutions and judgement on their feasibility. Passive design solutions are strongly preferred over active ones on the basis of probability. Whereas the state-of-knowledge does not allow quantification of accident likelihood, it is clear that a passive design solution to a safety problem could significantly reduce the likelihood of that accident, hence reduce its importance to material choice. Similarly, a passive consequence mitigation technique would reduce the accident severity, and hence is important to material choice.

Design solutions may be either internal or external to the blanket and plasma chamber. Internal ones that place specific requirements on the blanket design are less feasible and/or less desired since they further

TABLE 9.16

Safety Problems and Comments on the Feasibility of Possible Passive Design Solutions

Problem	Passive Design Solution	Feasibility
Rapid Wall Oxidation	Prevent Presence of Oxidants	Good, design penalties are external to blanket
Combustion of Lithium	Prevent Presence of Oxidants	Good, design penalties are external to blanket
Corrosion	Select Very Compatible Coolant and Structure	Varies, reduces material choice options
High Coolant Pressure	Stronger Blanket, Use Discrete Tubes to Contain Pressure	Poor, makes difficult blanket design problem more difficult
Afterheat Removal	1) Use low activation material, e.g., V-alloy	Good, depends on other problems, trade-offs
	2) Auxiliary emergency cooling	Poor, complicates blanket design, not really passive
	3) Use low pressure coolants which are more slowly lost	Good, depends on other problems, trade-offs
	4) Use a sector-size tank to increase likelihood that fluid breeders do not drain	Good, simplifies design if fluid breeders/coolant used
Radioactivity Hazards	1) Use low activation material, e.g., V-alloy	Good, depends on other problems, trade-offs
	2) Minimize release mechanisms	Fairly complex task
Tritium Control	Several, Beyond Scope of Study	Unknown, beyond scope of study

complicate the task of engineering the blanket and reduce blanket design options. Possible examples are having to design a blanket module to withstand high coolant pressures or to include dual coolant loops within a sector to provide cooling even if one loop were lost. These may well be possible, but make the blanket design task more difficult and probably entails penalties due to lower design flexibility.

On the other hand, passive design solutions that are external to the blanket do not add to blanket design problems. They may add to building design problems, but that task is far simpler than that of the blanket. An example is keeping oxidants away from the blanket and plasma chamber. These and other design recommendations are discussed in the next subsection.

9.2.4 Design Recommendations

Three specific design recommendations are listed in Table 9.17. These will be seen to directly influence certain safety areas. Adoption of the first should significantly reduce the likelihood of structural oxidation and combustion. Thus, the importance of the relative consequence indices pertaining to these problems should be lowered. Adoption of the second recommendation decreases the likelihood that a fluid breeder could drain, increasing the importance of the fluid-breeder-doesnot-drain scenario in Table 9.13. This, in turn, greatly increases the advantage of fluid breeders versus $LiAlO_2$ for afterheat removal. Adoption of the third, employing first wall coatings to enhance safety, would decrease the difference among materials of thermal effects of disruptions. A coating would shield the stress-carrying first wall. This reduces the significance of the relative consequence indices

TABLE 9.17

Design Recommendations

1) Keep oxidants away from the blanket and vacuum chamber. This includes air, water (steam) and CO_2.

2) Limit the number of discrete blanket modules to a reasonable value and minimize system complexity.

3) Incorporate safety into the design and choice of the first wall coating, if possible.

concerning thermal effects of disruptions. The three recommendations will now be discussed in more detail.

9.2.4.1 Removal of Oxidants

The stored chemical energy in lithium due to potential lithium-air, lithium-water, or lithium-concrete reactions has long been identified as a serious potential safety problem. There are three options. First, allow lithium and reactants in the blanket. This is not preferable due to the potential serious consequences. Second, remove the lithium (if non D-T fuel cycle) or use it in an incombustible form. Third, remove the possible reactants. The trade-offs between the latter options are listed in Table 9.18.

Removal of oxidants can be accomplished to varying degrees. The first step is to not use oxidizing agents in the blanket. The second step is to guard against accidental intrusion of an oxidizing building atmosphere into the blanket or vacuum chamber by high reliability design of vacuum boundary and/or secondary containment measures. A third step would be to keep oxidizing gases out of the building -- use an inert building atmosphere. The reliability of the solution depends partly on how far the process is taken.

There are disadvantages to this approach. The most important would be the potential economic cost due to the acquisition of the inert gas and re-design of equipment. However, the mass of gaseous helium required to fill a STARFIRE building is only a few percent of the liquid helium required for the superconducting coils. Second, maintenance access might be affected. However, the high possibility of tritium being present in a mobile form appears to make it unlikely that a maintenance person would enter the containment building without an air supply anyway. Third, there may be

TABLE 9.18

Comparison of Advantages of Alternative Solutions to the Lithium Combustion Hazard

Keep oxidants away from the blanket and vacuum chamber	Use lithium in non-combustible form
Keeps blanket design and material choice options open	
Simultaneously and passively solves problems of combustion and rapid structural wall oxidation within the blanket	Totally eliminates lithium combustion hazards in or out of the blanket
Does not complicate blanket module design	Does not complicate reactor building design
Tritium more likely kept in less hazardous HT form rather than HTO	
Also solves the air activation problem	

a remaining problem of lithium-concrete reaction if lithium were to spill onto the floor and the floor metal liner were to be breached. However, a lithium-concrete reaction is far less serious than a lithium fire in or near the blanket. The former is unlikely to raise temperatures in the blanket with potential for mobilizing radioactivity as would the latter.

There are numerous advantages to this design solution. By one design choice, the problems of structural wall oxidation and lithium combustion in the blanket are very significantly reduced. Even if lithium were not present, the potential for structural wall oxidation to cause damage or release radioactivity is serious. In fact, it appears potentially more likely than melting as a mechanism to release radioactivity. This is especially true if refractory metals are used, since the melting temperatures are so high. Even if structural oxidation were not a safety problem, accidental entrance of an oxidant to the plasma chamber while wall temperatures were fairly high could seriously degrade the vacuum/plasma impurity properties of the first wall or wall coating due to formation of an oxide layer.

In addition, removal of oxidants would tend to keep tritium in the less biologically hazardous T_2 or HT form rather than HTO or T_2O. There may be a maintenance advantage - the potential for already having an inert cover gas for welding purposes. Finally, there is an air activation advantage. The STARFIRE study [9.4] found that nitrogen activation of air (leading to ^{14}C) was a serious problem and selected CO_2 as a replacement building atmosphere for that reason. Unfortunately, CO_2 does not

appear sufficiently inert with respect to reactive metals like lithium and beryllium. An inert gas, like helium, surrounding the reactor would solve the air activation problem as well as the other problems mentioned.

9.2.4.2 Fewer, Simpler Modules

Other things being equal, reliability is generally increased as the number of components (if all are needed for total system operation) and their complexity decrease. A more reliable blanket would tend to be a safer blanket due to lower accident frequency.

Past fusion reactor blanket concepts have incorporated as many as 10,000-100,000 individual blanket modules. Leakage of any to the plasma chamber prevents operation and may be a safety hazard. Failure internal to the module may also be an engineering or safety concern, especially if pressurized fluids are present. Even after decades of experience, the failure rate of fuel rods in fission reactors is non-zero. However, cladding leakage of a fuel rod does not prevent operation or constitute a serious safety problem - as is true of many fusion module concepts. Furthermore, such fusion module concepts are more complex than a fission fuel rod. When module size gets too small, this means that all the coolant and breeder connections in and out of the blanket are within very close (< 2 meters) proximity. One then worries more about common cause failures (seismic events, magnet quenches) that could result in simultaneous breakage of all such tubes, especially if the module were to shift relative to its support (see Chapter 3).

In apparent recognition of these problems, some recent studies [9.9, 9.10] have focussed on blanket designs with fewer, simpler modules

(see Chapters 2, 3). To date, there has been inadequate examination of the sector-sized tank concept, filled with a liquid metal or salt.

Obvious concerns pertain to MHD problems which could severely restrict fluid flow and lead to large forces during magnetic field transients. However, there are several significant potential advantages. First, the concept is fairly simple. Second, a modest number of sectors would be used. For example, for STARFIRE with 12 magnet coils, one might use 24 sector-sized tanks to allow removal of each in-between magnet coils. Third, the penetrations in and out of the tank are at the top. Thus, if the more vulnerable coolant lines were to break, fluid would not empty from the tank. Analysis in Chapter 3 indicates that afterheat removal problems are extremely alleviated if fluid breeders are present as they provide a very good heat sink. This is especially true if a low afterheat material like V-alloy is used. For example, a vanadium tank offers the potential for being able to "walk away" from a LOCA without concern for afterheat or operation of an active safety system. Thus the sector-tank concept with vanadium and lithium appears inherently safe with respect to afterheat transients. The safety viability of the concept clearly depends on keeping oxidants away (design recommendation #1).

9.2.4.3 Design Safety in the First Wall Coating

Although the problems of first wall coatings were not directly incorporated into this study, various portions of the analyses indicated

ways that the design and selection of first wall coatings would influence safety (Table 9.19). This discussion is not intended to attempt solution of the first wall coating questions, but rather to provide some insight on safety-related issues involved. The primary purposes of the coating (if required) must be to allow operation of the plasma (minimize impurities from the wall) and protection of the wall from plasma particles. Any safety decisions cannot interfere with these prime functions. In addition, any candidate coating is unlikely to satisfy all advantages and avoid all disadvantages. For example, beryllium would seem to process many good safety qualities but has serious chemical toxicity concerns and can rapidly oxidize.

9.2.5 Most Important Safety Concerns to Material Choice

By attaching less importance to the safety areas which are not very sensitive to material choice and those for which passive design solution have been identified (Table 9.20), the material choice problem is greatly simplified. The most important safety problems to consider when selecting materials are radioactivity, afterheat, presence of highly pressurized fluids, and corrosion (compatability). These are all fairly sensitive to material choice (Table 9.21) and less likely to be solved by effective, passive design solutions.

The severity of radioactivity is largely determined by choice of structural material. Design only influences this by controlling the amount and placement of structure, with relatively small influence on the problem. If anything, design makes the worst material from the radioactivity standpoint, 316 SS, look even worse since its structural fraction tends to be as high or higher (Chapter 2, Appendix C).

TABLE 9.19

Some Potential Safety Influences of First Wall Coatings

Potential Advantages:

- Provide passive mechanism for shut down of the plasma if wall temperatures rise.
- Act as a heat sink for afterheat. If the coating does not generate afterheat itself, it may provide some benefit as a heat sink.
- Protect first wall from the thermal effects of a plasma disruption. This would somewhat de-couple the compound which suffers the worst thermal shock (coating) from that carrying the structural stress (underlying wall).
- Protect the first wall from oxidants in the vacuum. If the coating is adherent to the wall instead of separate plates, then it would tend to isolate the wall from any oxidants. This is of less value if the coating itself would rapidly oxidize.

Potential Disadvantages:

- Act as a source of radioactivity toxicity.
- Act as a source of chemical toxicity.
- Generate decay afterheat.
- Decrease reliability if added engineering complexity exceeds engineering and plasma benefits.
- Getter tritium from the plasma.
- Act as a source of plasma impurities which could trigger disruptions.

TABLE 9.20

Relative Importance of Different Safety Problems to Material Choice, Including the Impact of Suggested Design Solutions

Most Important

- Radioactivity Consequences
- Afterheat Removal
- Pressurized Fluids
- Corrosion

Less Important Because of Identified Design Solution

- Structural Oxidation
- Combustion
- Thermal Effects of Plasma Disruptions

Less Important Because Problem Not Highly Sensitive to Material Choice

- Plasma Heating - LOCA
- Electromagnetic Effects of Plasma Disruptions

TABLE 9.21

Summary of Relative Consequence Indices Pertaining to Safety Problems Most Important to Material Choice[a]

Structure		316 SS	HT-9	V-alloy	TZM
Melting, Afterheat	RCI^{m}_{LA}	7-12	3-8	1.0	3-8
All latent effects	RCI^{te}_{RC}	100	2-100[b]	1.0	2

Breeder		$LiAlO_2$ Be[c]	Lithium	$Li_{17}Pb_{83}$
Melting, Afterheat	RCI^{m}_{LA}[d]			
- fluid breeders drain		2.7	1.0	1.0
- breeder does not drain		300	5	1.0
Tritium Inventory	RCI^{te}_{RC}[e]	125	8-10	1.0

Coolant		water	Helium	Lithium	flibe
Pressure	RCI^{p}_{TP}[f]	4	3	1	1

(a) Low values preferred, see Table 2 for definitions. Selection of materials is also dependent on compatability (corrosion) concerns.

(b) Radioactivity values of HT-9 not available; effects judged between 316 SS and TZM on basis of composition.

(c) Beryllium was used as a neutron multiplier. Here this is the best case since beryllium does not add any afterheat.

(d) The effect of breeders on afterheat transients was critically dependent on whether it was possible for fluid breeders to drain out of the blanket in time to affect heat transport. The two cases refer to 1) breeder drains instantaneously, 2) breeder does not drain but stays stagnant.

(e) Maximum conceivable releases of tritium are less certain, analysis suggests that at least one tenth of the $LiAlO_2$ tritium would become mobile.

(f) Subjective ranking for leakage of pressurized fluids: 1) no safety problem, 2) evidence that only a minimal safety problem exists, 3) Evidence that a serious problem exists, 4) known serious problem.

The second problem, afterheat, is controlled by structural (source of afterheat) and breeder choice (heat sink) as reflected in Tables 9.6 and 9.13. The relative consequence indices for materials for afterheat and radioactivity all show 316 SS to be the worst choice. The liquid metal breeders (Table 9.13) are far superior to the ceramic breeder. Although systems can be designed to remove afterheat from a blanket after a LOCA, this would greatly complicate blanket module design.

The third problem is the accidental pressurization of either blanket or building due to release of pressurized fluids. As discussed in Chapter 2, it does not appear possible to design a module to survive the accidental leakage of pressurized water (15.5 MPa) into the breeder zone. Designs have been proposed for helium that would survive such an accident, although this greatly reduces the flexibility of the designer.

Corrosion is likely to be both a safety and normal operation problem. Among the combinations studied, only the steel/flowing-lithium-coolant combination is significantly (several orders of magnitude, see Table 9.7) worse. To the extent of knowledge, the refractory metals appear highly compatible with liquid metals. The steels are very compatible with helium and fairly compatible with stagnant (breeder-only) liquid metals.

9.2.6 Material Choice Recommendations

Given the identification and discussion of the most important safety areas, specific materials can be recommended.

There are numerous perspectives to view the material choice question. One dichotomy is between near-term and long-term options. Exotic and

advanced materials cannot be used in current experiments; the data base and relevant technology do not exist. Thus, the options for near-term applications are inherently more limited.

If, however, one examines possible options for commercial application, exotic and advanced materials should be included. To limit commercial fusion options to 316 SS and pressurized water would be to build a 21st century application from 1950's technology. There may be compelling reasons to select such options, but safety concerns do not appear to be among them. Although there is extensive operating experience with pressurized water fission reactors that could be beneficial to reducing accident frequency relative to the alternatives, it is felt that the disadvantages discussed make pressurized water a poor safety selection for fusion.

Attractive candidates as an approximate function of development and evolution are listed in Table 9.22. It is recognized that very serious development problems exist, especially for the exotic materials. Furthermore, actual advantages may not match the potential. For example, the afterheat and radioactivity advantages of vanadium or the ceramics could be impaired if less attractive alloying elements or impurities were found to be necessary from material science developments. A very critical assumption underlying these selections is that combustion and rapid structural oxidation problems are controlled by keeping oxidants away from the vacuum chamber and blanket. Failure of that assumption/design option would significantly reduce the attractiveness of such materials as vanadium, combustible ceramics like graphite, lithium, and beryllium.

TABLE 9.22

Possible Evolution of Candidates

for Structural Material, Coolant and Tritium Breeder,

Viewed from the Safety Perspective[a]

	Structural Material	Coolant	Tritium Breeder
Near Term			
More Established Data Base Fewer Development Problems	Ferritic Steels e.g., HT-9	Helium	Liquid Lithium or $Li_{17}Pb_{83}$
Advanced[c]			
Significant Development Problems to be Overcome Severe Data Base Gaps	Vanadium-based alloys	Liquid metals e.g., lithium or $Li_{17}Pb_{83}$	Liquid metals e.g., lithium or $Li_{17}Pb_{83}$
Exotic[c]			
Appropriate Candidate May Not Be Identifiable	Low Activation Ceramic, SiC	Molten Salts[b]	Lithium[b] bearing molten salts

(a) Subject to compatibility constraints, choices for the three components do not have to come from the same level of development, e.g., an HT-9/lithium/lithium combination may be warranted.

(b) May not be possible to identify appropriate molten salts, but salts may have some generic advantages.

(c) It is likely that selection of more advanced or exotic materials would entail significantly higher materials development costs.

Subject to material compatability constraints, choices for structure, coolant, and tritium breeder do not necessarily need to come from the same level of development. Combinations like HT-9/lithium/lithium or V-alloy/salt/$Li_{17}Pb_{83}$ may be desired. It is recommended that more attention be given to these materials (Table 9.22) in design studies, alloy development program, and blanket technology experiments.

9.3 Future Research

It has been shown that material choice is a significant factor in determining how safe a fusion reactor may be. Besides the continuing research and development in plasma physics, fusion reactor engineering, alloy development, plasma-wall interactions, etc., there are some specific safety/environmental research needs that should be addressed:

- Focus alloy development on the materials in Table 9.22.
- Develop specific design options to keep oxidants away from the plasma chamber and blanket.
- Develop blanket concepts that reduce the number and complexity of modules. This should include ways to use the attractive cooling characteristics of liquid metals or salts in a sector-sized tank geometry.
- Continue to examine the electromagnetic effects of plasma disruptions and uncontrolled magnet quenches on the blanket.
- Materials other than structure, coolant and breeder can influence safety. This study has identified some important safety influences of first wall coatings and neutron multipliers.

Further research is needed to quantify these aspects.

- o Add chemical toxicity effects to accident consequence calculations, e.g., FUSECRAC. This is more important as lower radioactivity materials are considered.
- o Improve the data base for accident assessments, primarily isotope-specific dose factors and element-specific biological/environmental behavior. See Chapter 8 for detailed needs.
- o Continue examination of normal behavior of tritium in fusion systems, including measures to reduce permeation losses (barrier films, cladding, etc.)
- o Expand examination of off-normal tritium behavior, focussing on credible release pathways and mechanisms.
- o Determine experimentally the degree that corrosion and rapid structural wall oxidation material release mechanisms defer from stoichiometric composition.
- o Examine experimentally the potential magnetic effects on corrosion processes. See Chapter 7 for specific lists of possible interactions.
- o Examine the scope and criteria for the waste/recycling/decommissioning issues, focussing on the influence of different material selections.

REFERENCES

9.1 G.P. Yu, "Relationship of Material Properties to the Design of a Fusion Reactor First Wall," Sc.D. thesis, Department of Nuclear Engineering, Massachusetts Institute of Technology, 1981.

9.2 D.L. Smith, et al., "Fusion Reactor Blanket/Shield Design Study," ANL/FPP-79-1, 7/1979.

9.3 O.N. Jarvis, "Transmutation and Activation of Fusion Reactor Wall and Structural Materials," AERE-R-9298, 1/1979.

9.4 C.C. Baker, et al., "STARFIRE- A Commercial Tokanak Fusion Power Plant Study," ANL/FPP-80-1, 9/1980

9.5 W.R. Grimes and S. Cantor, "Molten Salts as Blanket Fluids in Controlled Fusion Reactors," Chemistry of Fusion Technology, 1972.

9.6 "Reactor Safety Study." WASH-1400, 10/1975.

9.7 S. Kaplan and B.J. Garrick, "On the Quantitative Definition of Risk," Risk Analysis, 1(1), 1981.

9.8 D. Litai, "A Risk Comparison Methodology for the Assessment of Acceptable Risk," Sc.D. Thesis, Department of Nuclear Engineering, Massachusetts Institute of Technology, 1/1980.

9.9 R.W. Conn, et al., "SATYR-Studies of a D-D Fueled Axisymmetric Tandem Mirror Reactor," PPG-576(UCLA), 9/1981.

9.10 T.R. Galloway, "Some Process Aspects of Hudrogen Production Using the Tandem Mirror Reactor," UCRL-84285, 10/1980.

APPENDIX A. FUSION SUBSYSTEMS AND INTERACTIONS

A fusion reactor will consist of a variety of subsystems, some primarily devoted to safety problems. To clarify fusion safety issues addressed in this study, a brief description is included of the likely reactor subsystems and their interactions. This allows some discussion of possible accident initiators and event trees.

A.1 Safety Systems

The most important safety systems/functions in a fission reactor include EP (electric power), SD (reactor shutdown), ECCS (emergency core coolant system), PAHR (post accident heat removal), PARR (post accident radiation removal), and CI (containment integrity) [A.1]. The need for auxiliary electric power during an accident was emphasized by the reactor safety study [A.1], since other systems are dependent on electric power. A variety of actual systems are involved in ensuring shutdown of the fission reactor core. The emergency cooling function is divided into relatively short time ECCS which must cool the core and the long term PAHR function which keeps the building cool. Radioactivity released into the building is partially removed by PARR and hopefully contained within the building (CI). A variety of actual components is responsible for each function.

A fusion reactor will likely have functions similar to those in fission reactors (although the goal and importance may differ) and functions specifically fusion-related and not analogous to fission. These are listed in Table A.1. Electric power is still necessary.

TABLE A.1

Possible Fusion Safety Functions

Electric Power (EP)[a] — provide auxiliary power on demand.

Plasma Shut Down (PSD)[a]—shut down plasma on demand, e.g., after a loss-of-blanket coolant.

Auxiliary Heating Shut Down (AXSD)— shut down whatever auxiliary plasma heating system exists whenever the plasma is terminated.

Emergency Blanket Cooling (EBC)[a,b]—provide blanket cooling if primary system unavailable.

Emergency Shield Cooling (ESC)[b]—provide shield cooling if normal system unavailable.

Magnetic System (MS)—prevent significant damage from a magnetic quench.

Vacuum Boundary Integrity (VBI)—provide a boundary between torus and oxidizing agents.

Post Accident Heat Removal (PAHR)[a,b]—provide cooling of containment building.

Post Accident Radioactivity Removal (PARR)[a]—remove radioactivity in building.

Containment Integrity (CI)[a]—prevent radioactivity and chemical toxic agents from being released to the environment.

[a]Analogous system exists in a fission reactor.

[b]Less likely to be required in a fusion reactor.

Not only will a plasma shutdown (PSD) system be required, but also an auxiliary heating shutdown (AXSD). If the plasma terminates, one still needs to terminate any RF or neutral beam heating. It is anticipated that the plasma shutdown be considerably easier and/or more reliable than the fission core shutdown. For example in STARFIRE [A.2], stopping either the RF auxiliary heating or fuel supply will terminate the plasma. If other methods fail and wall temperatures rise, the beryllium coating vaporizes and terminates the plasma without any detection or active system (this may only trade the plasma shutdown problem for a plasma disruption problem).

A containment building (CI) will likely be needed. In addition, the integrity of the torus vacuum boundary (VBI) is needed to prevent leakage of fuel and exposure of the hot, radioactive first wall to oxidizing agents (see Chapter 6). Unlike fission, a vacuum exists at the center and most vulnerable part of a fusion reactor which could draw in oxidants from the building atmosphere. For economic and safety reasons it will be very important to prevent any oxidizing agents from entering the torus. Such an event could lead to oxidation of the first wall, which could result in radioactivity mobilization and/or reactor damage. Thus the VBI function will be very important.

Some emergency cooling of the blanket and shield may be necessary. As discussed in Chapter 3, there are significant advantages to selecting materials and designing the blanket such that emergency cooling of the blanket (EBC) and shield (ESC) is not necessary. The same is true of the building cooling (PAHR).

The presence of magnets necessitates some additional features. Some sort of emergency magnet protection, magnetic cooling, and/or emergency energy dump system will be required to prevent damage to either the

magnets or surrounding reactor structure in the event that normal operation of the magnets is disrupted. Most hazardous would be large magnetic forces from an uncontrolled magnet quench.

Some type of radioactivity cleanup system in the building will be necessary. Past design studies specify this as a detritiation system, although a more general system may be required to clean the building atmosphere of other radioactive species, e.g., those corrosion products from a coolant leak.

Finally, it should be emphasized that all these systems will require reliable instrumentation and detection circuits. This may be made more difficult by the possible presence of transient magnetic fields.

A.2 Subsystem Interaction

For purposes of examining possible generic interaction among fusion reactor subsystems, the plant can be thought of as having discrete components, listed in Table A.2. The most significant difference in a fusion plant is the presence of large magnetic fields which offer the potential for interaction at a distance. Some of these interactions are shown in Figure A.1.

Within the blanket or shield, loss of cooling may lead to loss of component integrity and support or vice versa, Loss of blanket integrity could directly lead to a loss of the torus vacuum boundary, depending on where the vacuum boundary is located. Loss of torus integrity would cause plasma termination.

A plasma disruption could result in large forces and damage to the blanket (Chapter 4). Loss of either blanket or shield cooling could result in a significant increase in neutron heat load in the magnet, with potential for causing a quench, as noted in Reference A.3. A

TABLE A.2

Fusion Reactor Components

Plasma

Plasma Fueling

Plasma Heating

Blanket Cooling

Blanket Support

Vacuum Boundary Integrity

Shield Cooling

Shield Support

Magnet Cooling

Magnet Support and Integrity

Building Containment

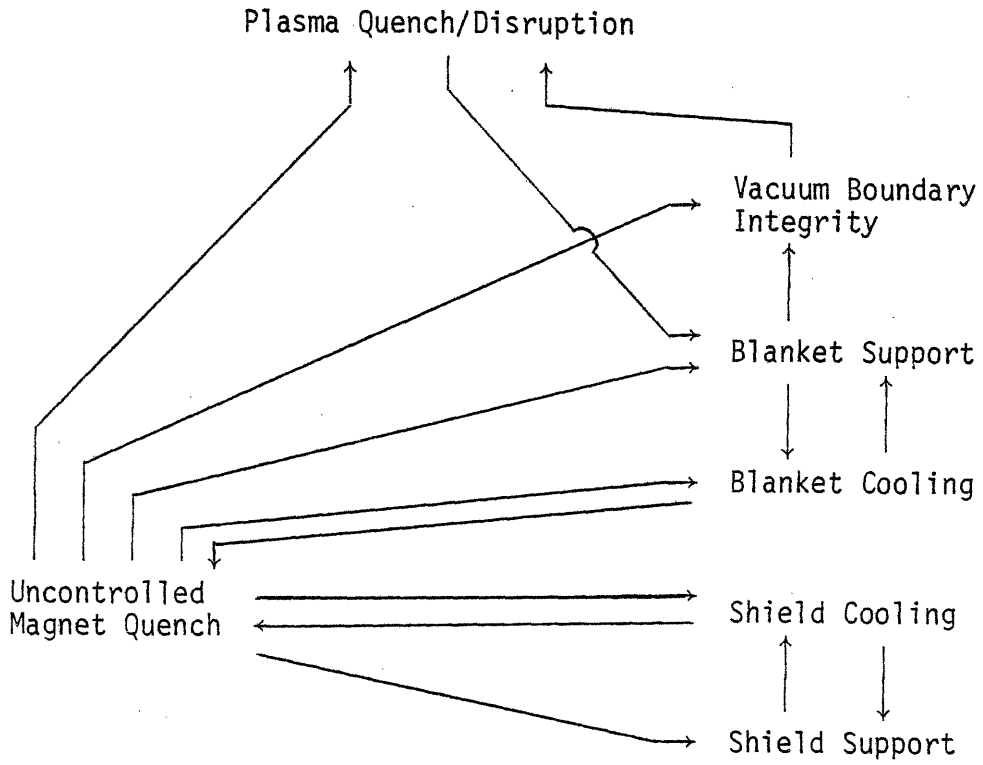

Fig. A.1: Some Possible Interactions among System Components. Arrows Indicate that One System Failure May Induce Failure in Another System

loss of coolant would increase the void function in the blanket, reducing neutron attenuation.

Finally, an uncontrolled magnet quench with release of magnet stored energy could lead to widespread reactor damage. The potential forces are large (see for example Reference A.2). Most worrisome to the safety systems analyst is the potential for such a failure leading to multiple failures throughout the reactor. In the extreme, this would be analogous to serious external common cause initiators like earthquakes.

A.3 Accident Initiators

The possible external accident initiators (earthquake, wind, flood, etc.) are not different from a fission reactor and do not need to be discussed here. Possible initial failures are listed in Table A.3 as indicated; most of these are discussed in terms of the various safety comparison bases. Indeed, this examination helped to select those bases. The analysis of magnet failures was not included in this study.

A.4 Preliminary Event Trees

Identification of relevant subsystems, accident initiators, and possible interactions among subsystems helps to draw event trees (see Reference A.1 for a more complete discussion). The event tree methodology (see Figures A.2 - A.5) help to identify what system operation depends on which other (e.g., electric power). The consequences of any given subsystem failure is not explicitly indicated; rather, the possible relevant combinations of failures are shown. For example, if electric power is lost, most other systems automatically fail. If other systems operate, the safety consequences of a given failure should be minimal.

TABLE A.3

Some Possible Initial Subsystem Failures

Plasma Disruption

—Chapter 4

Blanket Loss of Cooling

—Thermal transients—Chapter 3

—Combustion and pressure hazards—Chapter 5

—Mobilization of corrosion products—Chapter 7

—Tritium release mechanisms—Chapter 8

Shield Loss of Cooling

Magnet Loss of Cooling

Magnet Quench

Vacuum Containment Boundary Loss

—Combustion in torus—Chapter 5

—Rapid wall oxidation—Chapter 6

—Wall radioactivity effects—Chapter 8

Tritium System Integrity Loss

—Tritium release mechanisms—Chapter 8

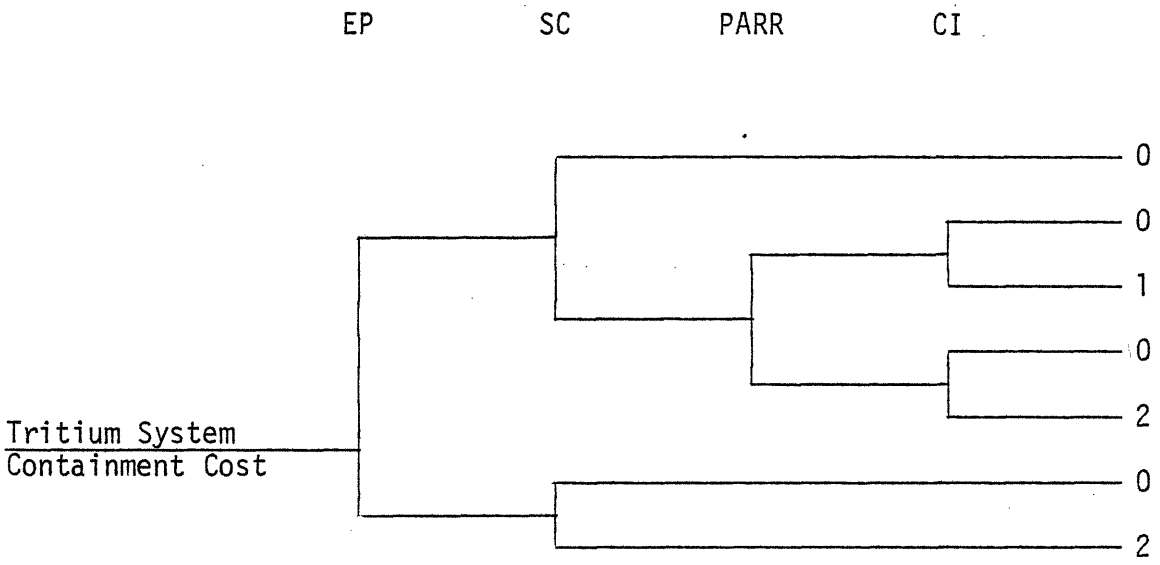

SC—Secondary tritium containment, if exists.

See Table A.1 for other function definitions.

0—no tritium release.

1—small tritium release.

2—large tritium release.

Fig. A.2: Tritium System Event Tree
(no other primary failures)

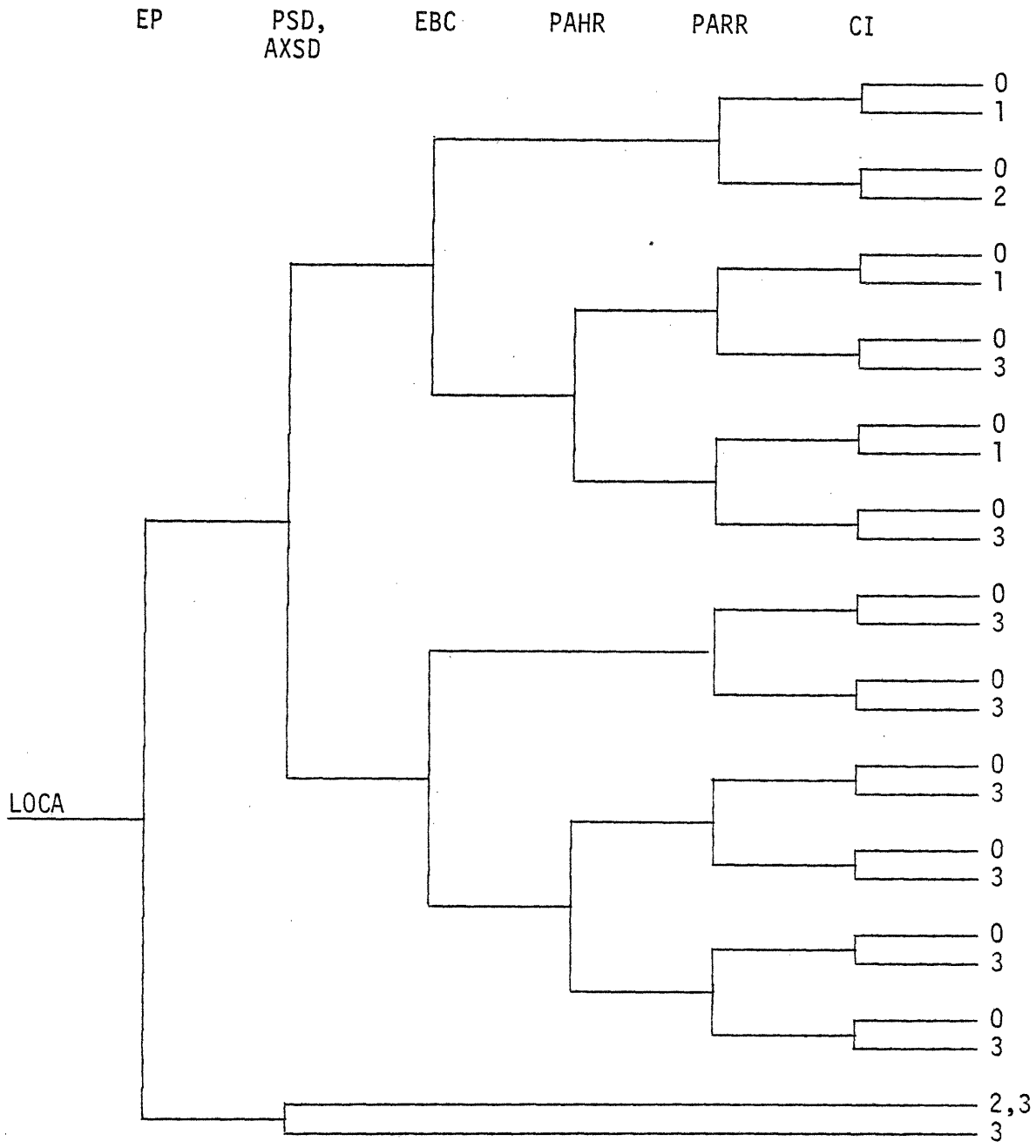

States: 0—no release
1—very low release, little damage (e.g., activated corrosion products)
2—modest structural damage and release
3—more severe damage, higher release

See Table A.1 for definitions.

Fig. A.3: LOCA Event Tree

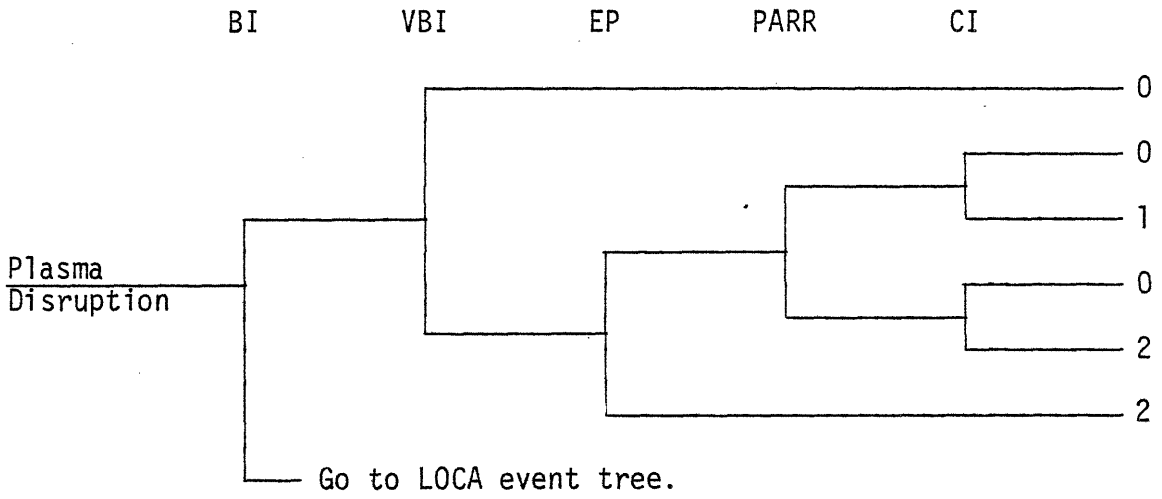

BI = Blanket Integrity

See Table A.1 for other definitions.

States: 0—no release

1—minor release

2—major release

Fig. A.4: Plasma Disruption Event Tree

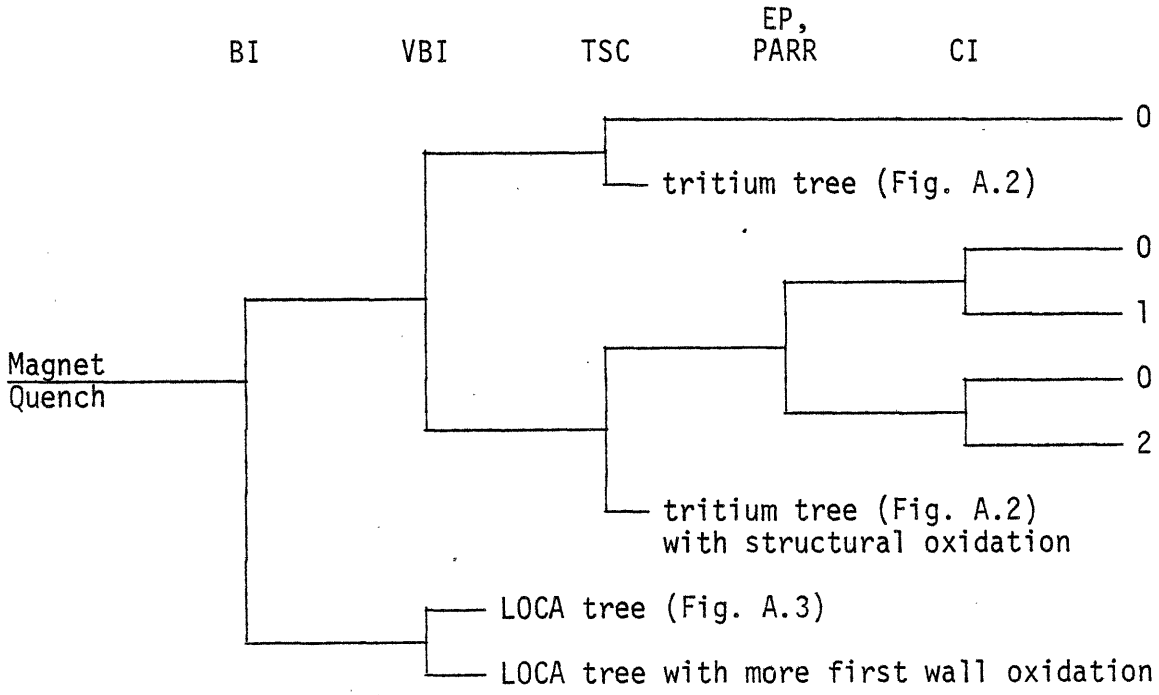

BI = Blanket Integrity

TSC = Tritium System Containment

See Table A.1 for other definitions.

States: 0—no release

1—minor structural activity release

2—major structural activity release

Fig. A.5: Uncontrolled Magnet Quench Event Tree

Establishment of failure probabilities of various sytems dependent on the state of the other components allows calculation of the probabilities of various end-states (magnitude of consequences). The state-of-knowledge does not allow calculation of probabilities, but event trees (even without probability values) do allow a qualitative sense of what accident sequences are most undesirable.

Some event trees for fusion accidents and systems are shown in Figures A.2 - A.5. These are not meant to be complete, but rather indicative and illustrative of some possible accident consequences.

Figure A.2 shows a simple tritium system event tree. Branches upward indicate successful system operation. If either the secondary containment or building containment work, there is no tritium release. If the emergency detritiation system works, the magnitude of a possible tritium release is reduced. The diagram is drawn with the assumption that building integrity (CI) depends on electric power to isolate valves, doors, etc. This is not necessarily the case in an actual design.

Figure A.3 shows a sample LOCA event tree. If the shutdown mechanisms fail, damage would be more severe. If the plasma shutdown (or any other device) could operate passively, then failure is eliminated. Functions like EBC, PAHR, PARR, and CI are likely to be dependent on electric power. If the blanket cooling (EBC) is adequate, PAHR is not likely to be needed.

Figure A.4 shows a sample plasma disruption tree. If a LOCA is triggered, branch to the previous LOCA event tree. If VBI fails, rapid structural oxidation and radioactivity mobilization can take place. If neither a LOCA is triggered nor VBI fails, the safety consequences are

nil, although damage may be incurred.

Figure A.5 shows a magnet quench event tree. If a LOCA is triggered, branch to the LOCA tree. If VBI has also failed, more first wall oxidation (hence radioactivity mobilization) is possible and consequences more severe. If a LOCA is not triggered, either VBI or the tritium system containment may still be affected. If tritium system containment is breached, branch to the tritium event tree. VBI failure would again have potential for oxidation of the first wall.

A.5 Conclusion

The brief examination of a fusion reactor's safety functions, in the framework of risk assessment methodology, helped place subsystems, interactions, and accident scenarios in perspective and helped the selection of safety comparison bases in this study. The number of relevant subsystems and their interactions are higher than in fission systems, although the severity of failure is likely to be less.

The most notable differences from fission include the greater complexity, and potential for failures of the vacuum boundary and magnet systems. These are indicated in the event trees. The failure of the vacuum boundary could cause rapid gas-wall oxidation (Chapter 6). Magnet system failures have the potential for inducing multiple failures throughout the reactor.

REFERENCES

A.1 "Reactor Safety Study," WASH-1400, 10/1975.

A.2 C.C. Baker, Jr., et al, "STARFIRE—A Commercial Tokamak Fusion Power Plant Study," ANL/FPP-80-1, 9/1980.

A.3 "Some Safety Considerations for Conceptual Tokamak Fusion Power Reactors," EPRI-ER-546, 7/1978.

APPENDIX B. MATERIAL PROPERTIES

A variety of material property data is necessary for the analysis. The materials of interest are listed in Table B.1. The physical properties of the solids and fluids are discussed in Sections B.1 and B.2 respectively, while nuclear properties (breeding and nuclear heating) are discussed in Section B.3.

B.1 Solid Materials

As seen in Table B.1, there are eight solids of interest, four structural metal alloys and four non-structural materials. The reference austenitic steel alloy is 316 SS. The STARFIRE study [B.1] selected an advanced version called "PCA". The different composition makes a slight impact on rapid gas-metal reactions (see Chapter 6). The reference ferritic steel is HT-9. The appropriate vanadium alloy is uncertain. Three vanadium alloys have been mentioned [B.1 - B.4]. Finally, the reference molybdenum alloy is TZM. The composition of these alloys is given in Table B.2. Unless otherwise specified, the reference austenitic steel is taken to be 316 SS and the reference vanadium alloy is V-15Cr-5Ti. In the latter case, the data base is sufficiently uncertain for many parameters that the precise composition of the vanadium alloy is not critical.

B.1.1 Thermo-Mechanical Properties

The temperature independent properties are listed in Table B.3 with the corresponding references. The melting point and density are fairly well known (within 5%?) but the other parameters are often not. The

TABLE B.1

List of Materials

Material	Phase	Use
316 SS	solid metal	structure
HT-9	solid metal	structure
V-alloy	solid metal	structure
TZM	solid metal	structure
Graphite	solid non-metal	reflector, first wall coating
Beryllium	solid metal	neutron multiplier, first wall coating
Zr_5Pb_3	solid metal	neutron multiplier
$LiAlO_2$	solid ceramic	tritium breeder
$Li_{17}Pb_{83}$	liquid metal	tritium breeder
Lithium	liquid metal	tritium breeder
Flibe	molten salt	coolant
Water	liquid	coolant
Helium	gas	coolant, breeder zone purge gas, magnet coolant
Air	gas	building atmosphere
CO_2	gas	building atmosphere

TABLE B.2

Composition of Structural Alloys (weight %)

Alloy	PCA	316 SS	HT-9	V-20Ti	V-15Cr-5Ti	V-25Cr-.82Zr	TZM
B	0.001	—	—	—	—	—	—
C	0.05	0.06	0.20	0.02	0.02	—	0.01
N	0.01	0.007	—	0.05	0.05	—	—
O	—	—	—	0.05	0.05	—	0.005
Al	0.03	—	—	0.004	0.004	—	—
Si	0.5	0.46	0.4	0.03	0.03	—	—
P	0.01	0.03	0.02	0.01	0.01	—	—
S	0.005	0.01	0.02	—	—	—	—
Ti	0.3	0.04	—	20.0	5.0	—	0.5
V	0.04	—	0.3	79.79	79.79	74.2	—
Cr	14.0	16.7	11.5	—	15.0	25.0	—
Mn	1.8	1.43	0.55	—	—	—	—
Fe	64.68	64.44	85.0	0.01	0.01	—	0.02
Co	0.03	0.03	—	—	—	—	—
Ni	16.0	13.9	0.5	—	0.001	—	0.01
Cu	0.02	0.06	—	—	—	—	—
As	0.02	—	—	—	—	—	—
Zr	0.02	—	—	—	—	0.8	0.08
Nb	0.03	—	—	—	0.0025	—	—
Mo	2.0	2.84	1.0	0.008	0.008	—	99.4
Ta	0.01	—	—	0.003	0.003	—	—
W	—	—	0.5	0.01	0.0075	—	—
Reference	B.1	B.1	B.1	B.1	B.4	B.3	B.1

TABLE B.3

Temperature Independent Properties of Solids[a]

	Melting Point(°C)	Boiling Point(°C)[b]	Heat of Melting (kJ/kg)	Heat of Boiling (kJ/kg)	Solid Density (kg/m^3)
316 SS	1430 [B.1]	2900 [B.5,B.6]	260 [B.5,B.6]	6090 [B.5,B.6]	8000 [B.1]
HT-9	1420 [B.2]	2900 [B.5,B.6]	260 [B.5,B.6]	6090 [B.5,B.6]	7800 [B.1]
V-alloy	1900 [B.2,B.5,B.6]	3370 [B.5,B.6]	310 [B.5,B.6]	7900[e] [B.5,B.6]	6100 [B.2,B.6]
TZM	2620 [B.2,B.5,B.6]	4630 [B.5,B.6]	330 [B.5,B.6]	6150 [B.5,B.6]	10,200 [B.2,B.6]
Graphite	—	~4000 [B.6,B.7]	—	—	1850 [B.7]
Beryllium	1284 [B.1,B.8]	2484 [B.8]	1083 [B.1]	24,790 [B.1]	1800[c] [B.1]
Zr_5Pb_3	~1400 [B.1]	—	—	—	8900 [B.1]
$LiAlO_2$	1610 [B.1]	—	—	—	2040[d] [B.1]

[a]Reference numbers in brackets, may include averaging of values given by different sources.

[b]Fairly uncertain, values used are for pure metal (Fe, V, Mo).

[c]100% dense, used at 70% was a multiplier [B.1].

[d]60% dense, alpha phase.

[e]Estimated from Trouton's Law, see text.

boiling point, heat of melting, and heat of boiling for the alloys are for the pure base metal. Even then variations among sources were as large as 15%. The heat of boiling for vanadium was estimated using Trouton's Law [B.9]:

$$H_g/T_v \simeq \Delta S_g \sim 22 \text{ cal/°K-mole} \qquad (2.1)$$

where H_g = heat of vaporization

T_v = boiling point (°K)

ΔS_g = entropy of vaporization.

The entropy of vaporization, Trouton's Law constant, is fairly constant among materials. It was estimated for vanadium by averaging the values for 316 SS (25.6 cal/°K-mole) and Mo (28.8 cal/°K-mole). This then allows estimation of the heat of boiling. Neutron multipliers and solid breeders may not be used at 100% theoretical density, as indicated in Table B.3.

The temperature dependent properties were fit to linear relationships for ease in use and compatibility with computer input. Any loss of accuracy due to this approximation appears small compared to the uncertainty in the original data. In some cases the data were insufficient for temperature variations to be accounted for. In addition, the available property values above 800°C were generally sparse. It was decided to limit the temperature variation of properties to this temperature. Hence, there is some loss of accuracy since the variation of properties at higher temperatures during transients were not accounted for. The values used are indicated in Tables B.4 - B.10. These rela-

TABLE B.4

316 SS Temperature Dependent Properties*

Property	Relation	Temperature Range(°C)	Based on Data in Reference
Thermal Conductivity (W/m°K)	$k = 20.0 + 0.013(T-450)$	100-800	B.1,B.3
Heat Capacity (J/kg°C)	$c_p = 555 + 0.16(T-400)$	100-800	B.1
Linear Coefficient of Expansion (μm/m°C)	$\beta = 21.0 + 0.006(T-450)$ $22.0 + 0.005(T-700)$	< 600 600-800	B.3
Young's Modulus (GPa)	$E_y = 160 - 0.09(T-500)$	100-800	B.1,B.3
Poisson's Ratio	$\nu = 0.361 + 0.00035(T-450)$	100-800	B.3
Electrical Resistivity (μΩ-cm)	$1/\sigma = 100 + 0.06(T-450)$	100-800	B.2

*T in °C.

TABLE B.5

HT-9 Temperature Dependent Properties*

Property	Relation	Temperature Range(°C)	Based on Data in Reference
Thermal Conductivity (W/m°K)	$k = 28 + 0.003(T-500)$	100-800	B.1
Heat Capacity (J/kg°C)	$c_p = 660 + 0.60(T-300)$	100-800	B.1
Linear Coefficient of Expansion (μm/m°C)	$\beta = 11.60 + 0.003(T-450)$	100-800	B.1,B.3
Young's Modulus (GPa)	$E_y = 180 - 0.06(T-400)$	100-800	B.1
Poisson's Ratio	$\nu = 0.27$		B.1
Electrical Resistivity (μΩ-cm)	$1/\sigma = 100 + 0.10(T-500)$	100-800	B.2

*T in °C.

TABLE B.6

V-alloy Temperature Dependent Properties*

Property	Relation	Temperature Range(°C)	Based on Data in Reference
Thermal Conductivity (W/m°K)	$k = 30 + 0.01(T-500)$	100-800	B.1
Heat Capacity (J/kg°C)	$c_p = 505 + 0.21(T-500)$	100-800	B.1
Linear Coefficient of Expansion (μm/m°C)	$\beta = 10.2 + 0.0013(T-650)$	100-800	B.3
Young's Modulus (GPa)	$E_y = 119 - 0.03(T-500)$ $119 - 0.04(T-500)$	100-500 500-800	B.1
Poisson's Ratio	$\nu = 0.36$		B.1,B.3
Electrical Resistivity (μΩ-cm)	$1/\sigma = 50 + 0.06(T-500)$ $50 + 0.04(T-500)$	100-500 500-900	B.2

*T in °C.

TABLE B.7

TZM Temperature Dependent Properties*

Property	Relation	Temperature Range(°C)	Based on Data in Reference
Thermal Conductivity (W/m°K)	$k = 108 - 0.007(T-600)$	100-800	B.1
Heat Capacity (J/kg°C)	$c_p = 300 + 0.07(T-800)$	100-800	B.1
Linear Coefficient of Expansion (μm/m°C)	$\beta = 6.35 + 0.0014(T-700)$	100-1000	B.3
Young's Modulus (GPa)	$E_y = 284 - 0.05(T-500)$ $284 - 0.08(T-500)$	100-500 500-1000	B.1,B.3
Poisson's Ratio	$\nu = 0.32$		B.3
Electrical Resistivity (μΩ-cm)	$1/\sigma = 20 + 0.025(T-500)$	100-900	B.2

*T in °C.

TABLE B.8

Graphite Material Properties

Property	Relation	Temperature (°C)	Based on Data in Reference
Thermal Conductivity (W/m°K)	$k \sim 60$		B.7
Heat Capacity (J/kg°C)	$c_p \sim 710$ 1890	22° 1000°C	B.7

TABLE B.9

Beryllium Temperature Dependent Properties*

Property	Relation	Temperature Range(°C)	Based on Data in Reference
Thermal Conductivity (W/m°K)	$k = 139 - 0.29(T-200)$	0-200	B.5
	$100 - 0.13(T-500)$	200-500	
	$100 - 0.08(T-500)$	500-800	
	$76 - 0.04(T-800)$	800-1000	
Heat Capacity (J/kg°C)	$c_p = 2750 + 1.2(T-500)$	100-1283	B.8
	$3305 + 0.18(T-1750)$	1284-2000	
Linear Coefficient of Expansion (μm/m°K)	$\beta = 16.2 + 0.006(T-500)$	100-1000	B.1,B.8
Young's Modulus (GPa)	$E_y \sim 290$		B.8
Electrical Resistivity (μΩ-cm)	$1/\sigma = 22 + 0.03(T-700)$	100-700	
	$22 + 0.04(T-700)$	700-800	
	$26 + 0.05(T-800)$	800-1100	

*T in °C.

TABLE B.10

$LiAlO_2$ Temperature Dependent Properties*

Property	Relation	Temperature Range(°C)	Based on Data in Reference
Thermal Conductivity (W/m°K)	$k = 4.7 - 0.004(T-500)$	500-800	B.1
Heat Capacity (J/kg°C)	$c_p = 1600$		B.1
Linear Coefficient of Expansion (μm/m°C)	$\beta = 12.4$		B.1

*T in °C.

tions accurate to within a few percent compared to the values given or plotted in the references cited.

As seen in Tables B.3 - B.10, some properties were not evaluated. These were not necessary for any analysis. Some properties are included in the tables that were not needed in the calculations, but were included for comparison purposes, e.g., heat of vaporization.

B.1.2 Stress Limits

The strength of the structural materials was needed for design purposes (Chapter 2, Appendix C). These values and the data sources are listed in Table B.11. As discussed in Chapter 2, the design basis was 10^5 hr (11 years) and 10^3 cycles (average of 1 cycle/week for steady state mode of operation). It is recognized that the design process and required data base is far more complex than presented here; however, the design parameters are representative of those from detailed fusion reactor design studies and hence are appropriate for a material comparison study.

A further question arises as to the material response to temperature and stress transients during an accident. The required material data base and corresponding design analysis are even more complex than for operating design parameters. A large number of different criteria are possible. A few of these will be briefly discussed here. The data base is too uncertain and calculational complexity (highly dependent on design specifics) too high to allow a more detailed treatment.

Figures B.1 and B.2 show the temperature dependence of the yield strength and ultimate tensile strength. A general weakening of the

TABLE B.11

Strength of Materials, Unirradiated

Alloy	Operating Temperature (°C)	Yield[a] Stress 0.2% S_y (MPa)	Ultimate[a] Tensile Strength (MPa)	Allowable[b] Stress Intensity Values, S_{mt} (MPa)	Allowable[b] Thermal Strain ($\times 10^{-2}$)
316 SS (20% Cold-Work)	450	520	650	108	0.655
316 SS (annealed)	450	120	450	—	—
HT-9	450	350	520	160	0.581
V-alloy	600	350	620	173	0.5[c]
TZM	800	600	660	223	0.0455

[a]References B.1, B.10.

[b]Reference B.3, for 10^5 hr. lifetime, 10^3 cycles.

[c]Estimated, based on value of 1.247 for pure V at room temperature.

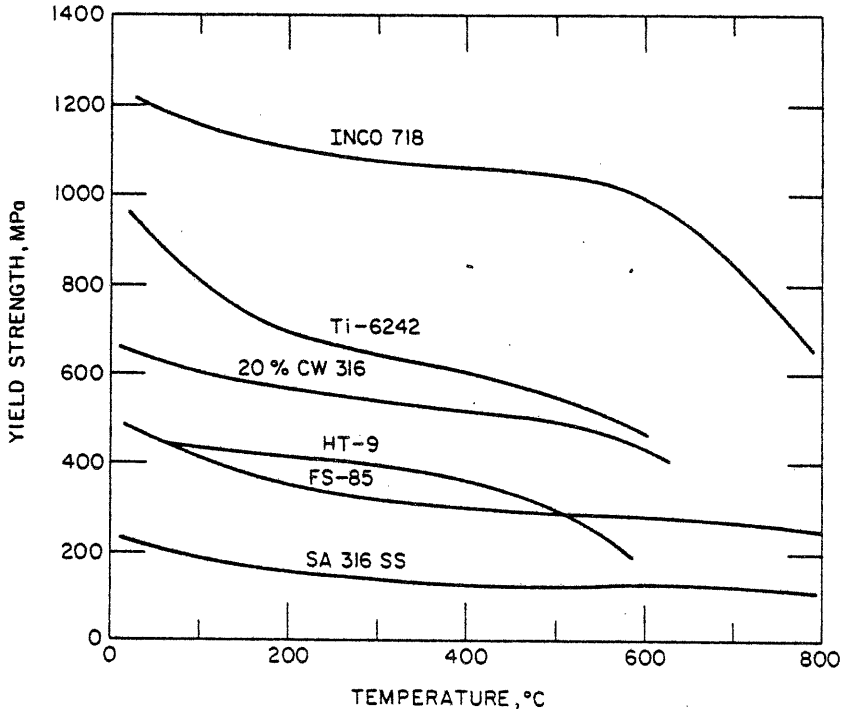

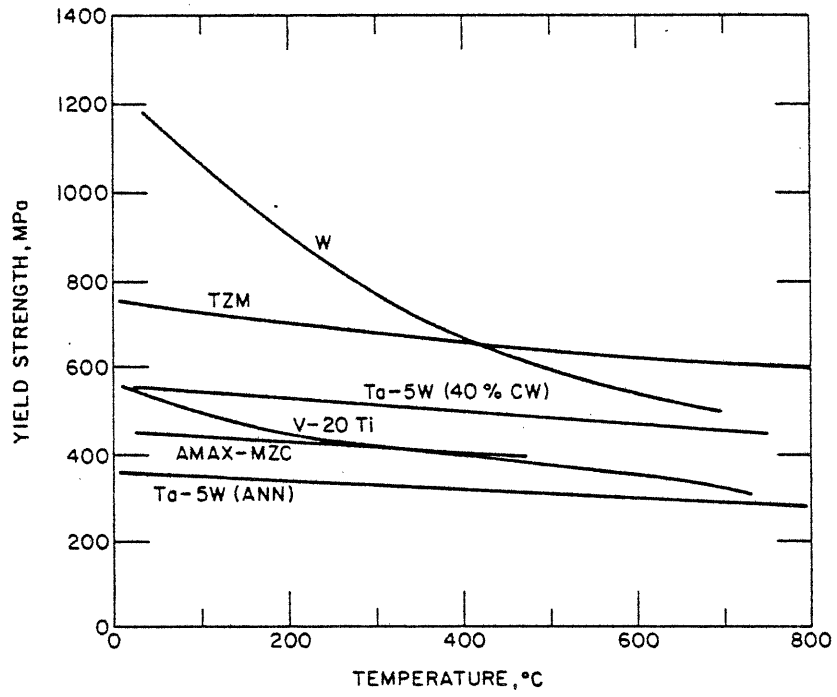

Figure B.1: Tensile strength of structural materials, 0.2% yield strength [B.1].

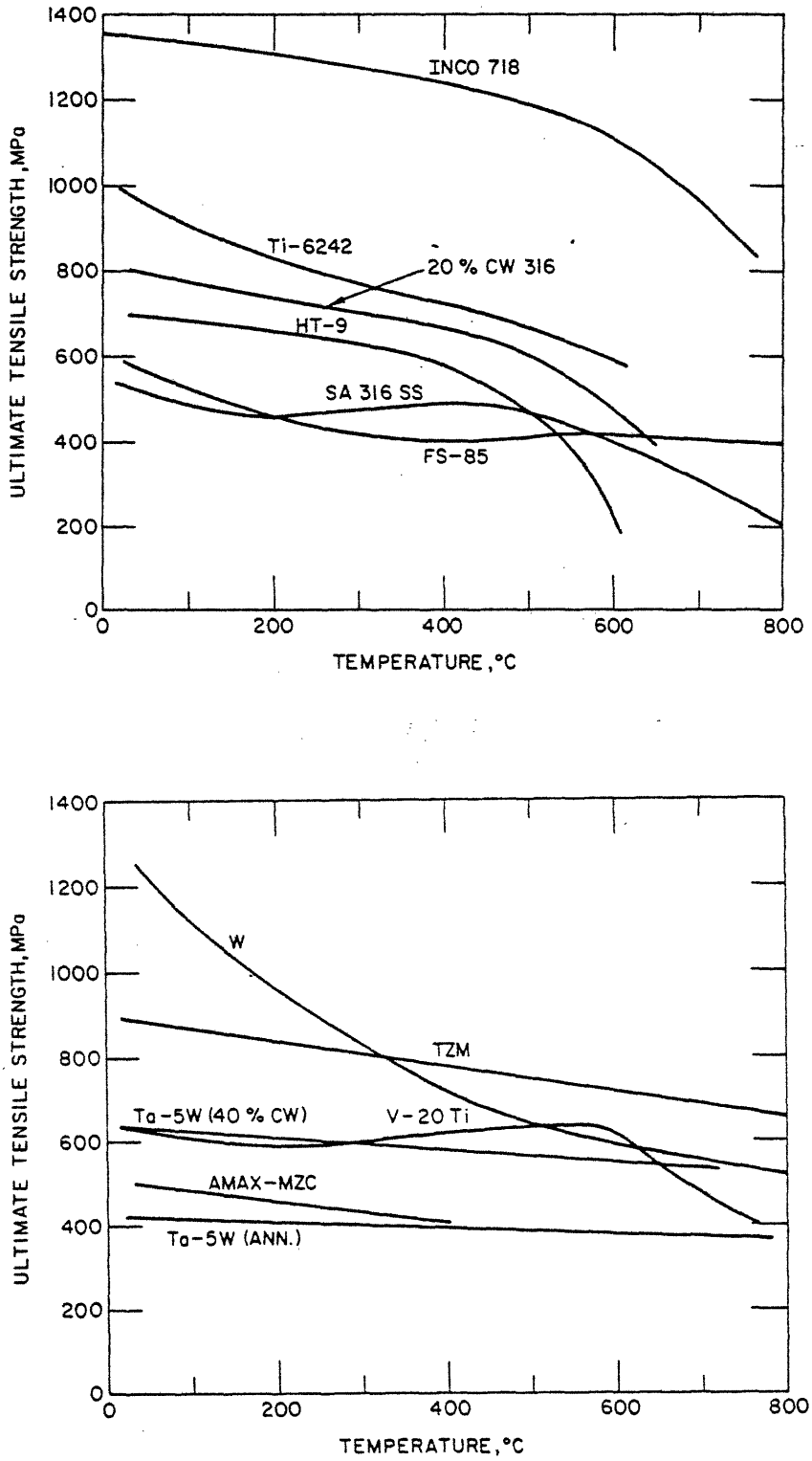

Figure B.2: Tensile strength of materials, ultimate tensile strength [B.1]

alloys occurs with increasing temperature. Figure B.3 shows the expected stress to rupture at 1 and 10 hr. which is relevant in an accident transient. Sze [B.12] indicated that 316 SS wall failure could occur with a temperature between 600 and 800°C (see Section 3.2.4).

A further problem in transients is the question of microstructure alteration. Alloys typically are subjected to finely tuned heat treatment prior to use. A temperature transient would significantly alter the alloy, destroying the desired microstructure and significantly degrading the material performance. This degradation would prove serious at later times in the accident or prevent future operation of the reactor.

As one example, consider 316 SS. Typical annealing temperatures range from 1010 - 1120°C [B.13]. The INTOR study [B.10] quoted a 30 minute anneal at 1050°C. Judging from the UTS curves (Fig. B.2), the beneficial cold work is significantly reduced at temperatures around 700°C. The cold-worked treated 316 SS is far stronger than the annealed below such temperatures.

For HT-9, temperature transients may be more damaging. A typical heat treatment [B.10] consists of full austenitizing at 1050°C for an hour, followed by an air or oil quench. The resulting martensite microstructure is very brittle, so a tempering treatment is used to decompose some martensite to ferritic or cementite structure [B.14] to improve ductility. A typical temper treatment is 600 - 750°C for an hour, followed by air cooling.

The relevant heat treatment and resulting microstructure susceptability is not known for the V-alloy or TZM, especially the former, and

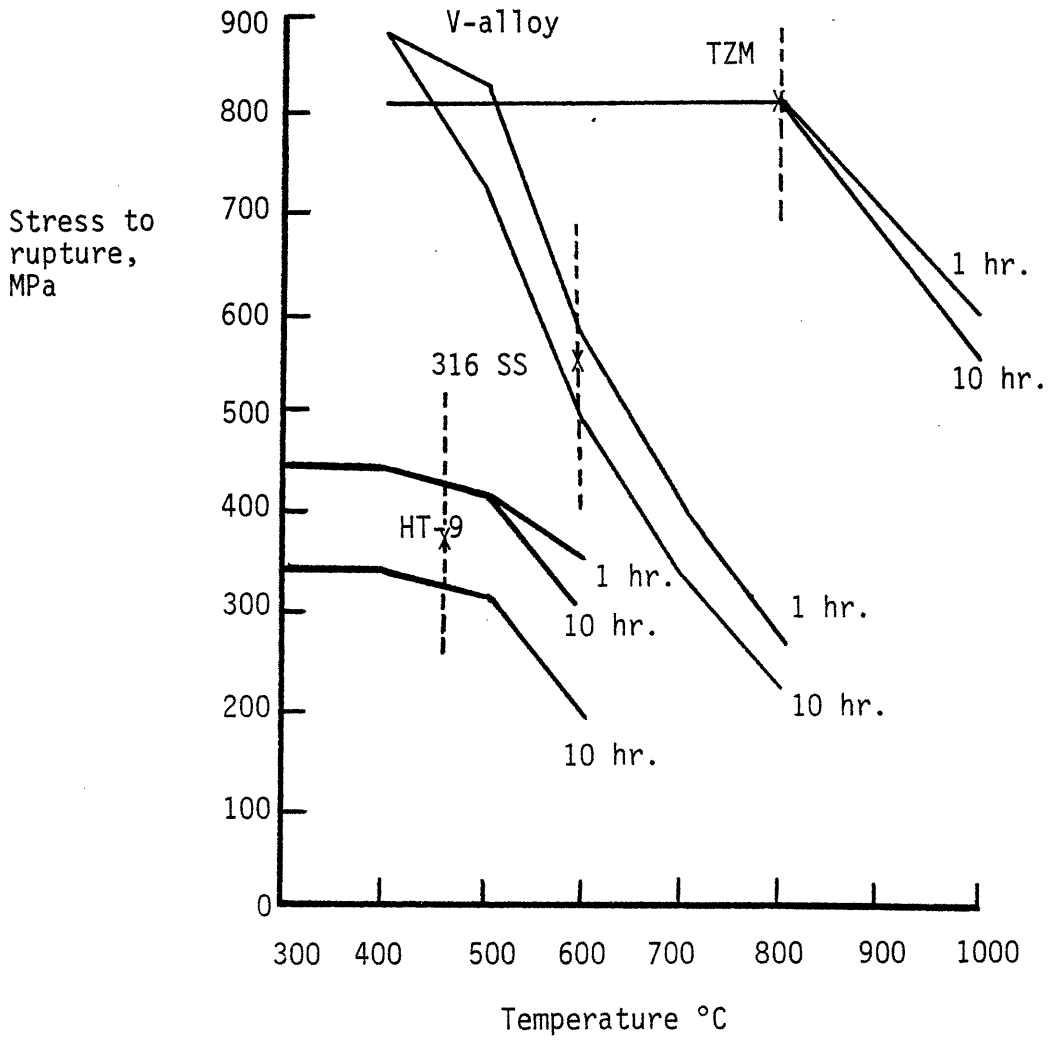

Figure B.3: Stress to Rupture for the Reference Materials [B.3], x = operating temperatures

an optimum composition is not determined. TZM tends to be used in a stress-relief annealed condition, while Ta and Nb alloys (same group as V) tend to be used in a re-crystallized state [B.13].

The failure of a structural material is thus seen to be dependent on failure criteria (rupture, deformation, microstructure alteration), temperature, stress, and the time of transient. These are discussed in Chapters 3 and 4. For longer time transients (>minutes, Chapter 3) a semi-arbitrary value of a 300°C temperature rise above operation is established as predictive of damage for the structure. Considering the above data and discussion, an HT-9 structure is probably more susceptable to thermal excursions while the refractory alloys, V and TZM, appear less susceptable. For very short ($\lesssim$ second) transients of disruptions (Chapter 4), there is insufficient time for microstructure alteration to occur at temperature rises of 300°C. However, as discussed in Chapter 4, if temperatures are high enough (e.g., if melting is reached) the microstructure will be changed. A possible strength comparison among materials is the yield stress.

B.1.3 Surface Emissivities

The surface emissivity of the structural metals determines the amount for radiation heat transfer (see Chapter 3). The value of emissivity depends on the metal, the temperature, and surface condition, as seen in Figure B.4. Generally, polished, clean surfaces have low emissivity, while degraded surfaces have increased emissivities [B.15 - B.19]. As seen in the figure, steel which has been repeatedly heated and cooled will have emissivities between 0.25 and 0.7. Oxidized metal appears to very high emissivities, approaching 0.9.

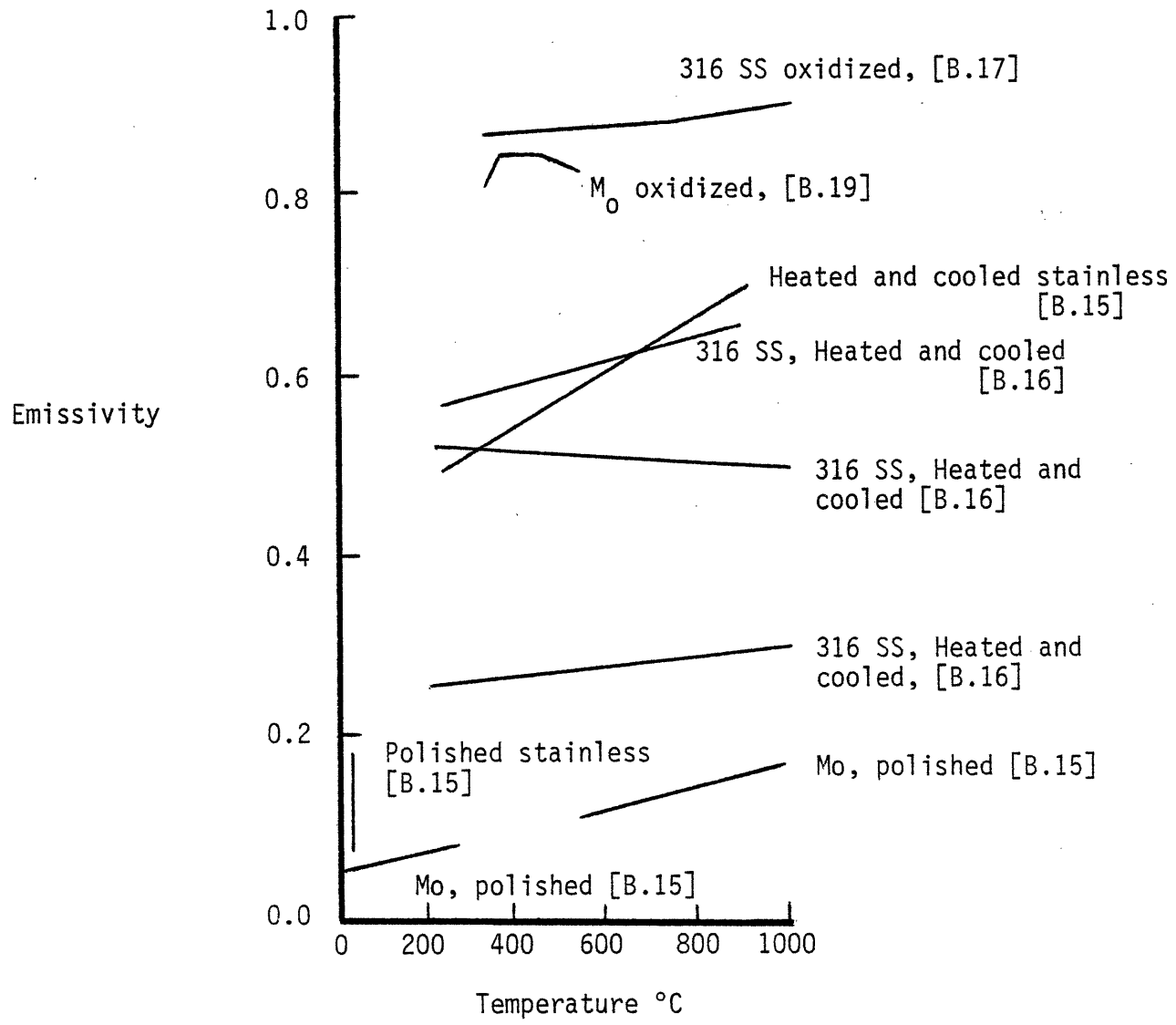

Fig. B.4: Emissivities

For the present analysis, the surfaces experiencing radiation heat transfer are internal, exposed to blanket fluids, as discussed in Chapter 7. These surfaces are generally oxidized and roughened. Based on Figure B.4, the emissivity of Mo is set at 0.82; 316 SS, at 0.88. Ideally, materials exposed to blanket fluids as part of corrosion studies could be tested for emissivity.

Direct data on wavelength integrated emissivity of vanadium were not found. However, the spectral reflectance appears to fall between Mo and steel, based on meager data in Reference B.19. Thus the emissivity of vanadium is estimated to be the average of Mo and 316 SS values, 0.85.

If the precise value of emissivity in a specific design were found to be important, designers may wish to consider material surface preparation techniques that appropriately influence the emissivity.

B.2 Fluid Materials

As seen in Table B.1, a variety of fluids may be present. The relevant material properties include density, thermal conductivity, heat capacity, gas constant (for gases), electrical resistance, and viscosity. The data base is fairly complete for these fluids with the exception of $Li_{17}Pb_{83}$. The Sieverts constant is discussed in Chapter 8.

B.2.1 $Li_{17}Pb_{83}$ Estimation

The data base for $Li_{17}Pb_{83}$ properties is very meager, forcing estimation of most values. Hoffman, et al [B.20] have examined the available data base for Li-Pb alloys. The specific alloy in this study is $Li_{17}Pb_{83}$ (99.3 weight % Pb). They conclude that,

> "in general, the properties of Pb-Li solutions are not approximated by taking the properties of the pure elements and interpolating linearly with atom fraction. A maxima or minima generally occurs at ∿20 a/o Pb and approximations can be made by interpolating between 0-20 a/o Pb and 20-100 a/o Pb values."

In such manner, they obtain an estimation of the density as [B.20]

$$\rho(T°C) = 9{,}500 - 0.7(T-300°C) \text{ kg/m}^3 \qquad (B.2)$$

The electrical resistence at 800°C is estimated as 130 μΩ-cm from their data (interpolation between 20 a/o Pb and 100 a/o Pb). Unfortunately, the other properties have not been evaluated for Pb-Li binary compositions, yet values for thermal conductivity and heat capacity are required.

These properties were estimated using linear interpolation in atomic percent between pure lithium and lead. The uncertainties are too large to justify temperature dependent values. Using pure lithium and lead data [B.21 - B.23], then the heat capacity is estimated to be 850 J/kg°C and the thermal conductivity, 22 W/m°K. As one test of this procedure, the density was similarly estimated. Interpolation between lithium and lead resulted in a density of about 8,700 kg/m^3 at 500°C compared to the more accurate value of 9,360 kg/m^3 (equation B.2), an 8% variation. A second indirect test is discussed in Section 5.2.1. Use of atomic percent interpolation of heat capacity for LiPb, one obtains a value of 2190 J/kg°C. Use of the estimated heat of reaction between lead and lithium and this heat capacity leads to a temperature rise due to preparation of LiPb of about 116°C. An experimental value was 193°C

(see Section 5.2.1), 60% variation. Considering that lead and lithium values for density and heat capacity differ by over an order of magnitude (see Table B.12) and the required data do not exist, it is felt that the estimated values are reasonable approximations. The melting point of $Li_{17}Pb_{83}$ is 235°C from the Li-Pb phase diagram [B.20].

B.2.2 Liquids and Helium Coolant

The material properties for pressurized water, pressurized helium, flibe, and lithium are taken from reference B.21. The values are generally accurate within 20% [B.21]. Thermodynamic data for the calculations in Section 5.3.2 are taken from steam tables, Reference B.24.

B.2.3 Gases

Three gases are of interest: air, carbon dioxide, and helium. All may be used as the building atmosphere. In addition, liquid helium is used to cool the superconducting magnets and may be released to the building atmosphere (see Chapter 5). The values of gas constant and heat capacity are taken from Reference B.25, listed in Table B.13. In addition, the boiling point of helium is 4.20°K [B.25] at atmospheric pressure with a heat of vaporization of 23.3 kJ/kg.

B.3 Nuclear Properties

As discussed in Chapters 1 and 2, detailed neutronics calculations were not performed as part of this study. Thus, relevant nuclear related parameters were estimated from previous design studies.

B.3.1 Breeding and Energy Multiplication

The reactor blanket must provide adequate tritium breeding. Based

TABLE B.12

Properties of $Li_{17}Pb_{83}$, Lithium, and Lead

	Lithium[b]	Lead[c]	$Li_{17}Pb_{83}$
Density[a] (kg/m^3)	513	10,390	9360[d]
Heat Capacity[a] (J/kg°C)	4220	155	850[e]
Thermal Conductivity[a] (W/m°C)	49.7	15.5	22[e]
Electrical Resistance ($\mu\Omega$-cm)	35.3	103	130[d]
Melting Point (°C)	180	327	235[d]
Boiling Point (°C)	1340	1737	—

[a]At 500°C.

[b]Reference B.21.

[c]References B.22, B.23.

[d]Reference B.20.

[e]Estimated from lithium and lead.

TABLE B.13

Gas Properties*

Atomic Mass	Air	CO_2	Helium
Gas Constant, R (J/kg°C)	287	189	2077
Heat Capacity, c_p (J/kg°C)	1005	876	5188
$\gamma = c_p/c_v$	1.40	1.30	1.66
Heat Capacity, c_v (J/kg°C)	718	680	3120

*Reference B.25

on References B.1 and B.2, the required depth of the breeding zone assumed for this study was determined (see Table B.14). Based on the values in Reference B.1, which is the reference plasma condition for this study, the total thermal output from the blanket is approximated by

$$P(MW_{th}) = 700 + 2800 \times M \qquad (B.3)$$

The 700 MW incident on the first wall is fixed by the plasma operation. The total heating in the blanket is determined by the blanket energy multiplication, M. Equation B.3 is used in Appendix C to estimate the required total coolant flow through the blanket. The values used are listed in Table B.14.

It is recognized that the breeding depth and energy multiplication are determined by the complete detailed blanket design and materials therein. However, to first order, the choice of breeder dictates both. The values obtained do not play a major role in the analysis in this work; hence, the uncertainty involved in this procedure is acceptable.

B.3.2 Nuclear Heating

As discussed in Section 3.2.2.3, for purposes of this study the nuclear heating during operation is represented by

$$q'''_{n,i}(r)\ MW/m^2 = q''_n \times QP_i \times \exp(-Ba \times \Delta r) \qquad (B.4)$$

where $q'''_{n,i}(r)$ = volumetric nuclear heat generation in material i

TABLE B.14

Breeding Zone Depth and Energy Multiplication

Breeding Zone Depth Reference Values[a]

$LiAlO_2 \sim 0.45$ m $Li_{17}Pb_{83} \sim 0.5$ m Li ~ 0.6 m

Blanket Energy Multiplication Values, M

$LiAlO_2$ Breeder	Reference	Li-Pb Breeder	Reference	Lithium Breeder	Reference
1.28	B.27	1.22 ($Li_{62}Pb_{38}$)	B.29	1.33	B.35
1.19 (Li_2O)	B.2	1.22 (Li_7Pb_2)	B.2	1.29	B.28
1.14	B.1	1.37	B.30	1.17	B.26
1.15	Present Study[b]	1.25	Present Study[b]	1.20	Present Study[b]

[a]Based on References B.1, B.2.

[b]Estimated values adopted for the present study.

q''_n = incident neutron wall loading, 3.6 MW/m^2

QP_i = plasma heat parameter for material i

Ba = blanket attenuation factor for specific choice of coolant and breeder

Δr = depth into blanket.

From Equation B.4, the plasma heat parameter can be determined as

$$QP_i = \frac{q'''_{n,i}(\text{first wall})}{q''_n} \qquad (B.5)$$

A variety of studies were examined to determine appropriate values of QP_i, listed in Table B.15. The values for the structural materials are the most important, especially the relative values among them. Given that HT-9 differs from 316 SS in having less nickel while Inconel has more nickel and that the heating in Inconel is higher than 316 SS, the value of QP_{HT-9} was estimated at 9.5 m^{-1}. As discussed in the next section, care had to be used to result in both operational heating and decay heat matching available results. The product $QP_i \times QD_i$ determines the initial afterheat generation rate.

The blanket attenuation factor, Ba, was estimated by fitting the exponential curve, $\exp(-Ba \times \Delta r)$, to available nuclear heating profiles in the literature. As Chao [B.34] has noted, the agreement is quite good, except at the reflector zone. Since the critical volume is the first wall vicinity, and parameters QP and Ba are chosen to maximize agreement at the first wall, the relevant heating results should be adequate. The values used and those estimated from other studies are shown in Table B.16.

TABLE B.15

Plasma Heat Parameter Values

Material	From Data in Reference QP(m^{-1})	From Data in Reference Reference	Value Adopted for this Study QP(m^{-1})
316 SS	~10	B.26,B.34,B.35,B.36	10
HT-9	—	—	9.5*
V-alloy	> 5.1	B.26	6.0
TZM	6.1	B.28	6.5
Inconel	12	B.38	—
Titanium	4.6	B.29	—
Lithium	3.1, 3.8, 4.0	B.36	4.0
	3.4, 4.0	B.35	
	4.5	B.33,B.34	
Water	15, 20	B.36	18.0
Helium	—	—	0
Flibe	~10	B.31	8.0*
Li_2O	5.8	B.38	—
	6.7	B.32	—
$LiAlO_2$	7.6, 10.4	B.36	9.0
$Li_{62}Pb_{38}$	9.4	B.29	—
$Li_{17}Pb_{83}$	—	—	10.0
Be	8.7, 9.9	B.36	9.0

*See text.

TABLE B.16

Values of Blanket Attenuation Factor

Breeder	Coolant	From Data in Reference: Ba(m^{-1})	From Data in Reference: Reference	Adopted for this Study Ba(m^{-1})
Lithium	Lithium	4.3	B.34	4.0
		4.0	B.33	
		3.6	B.26	
	Helium	4.0	B.34	3.7
		3.7	B.36	
		3.5	B.35	
	Flibe	4.8	B.34	4.5
$Li_{62}Pb_{38}$	boiling water	8.0	B.29	—
$Li_{17}Pb_{83}$	pressurized water	—	—	9.0
Li_2O	Helium	6.3	B.38	—
	Water	6.0	B.32	—
$LiAlO_2$	Helium	8.5	B.36	8.0
	Water	9.5	B.36	9.0

B.3.3 Afterheat Decay

As discussed in Section 3.2.2.3, the local volumetric heat generational rate was approximated by the Equation

$$q'''_{a,i}(r,t) = q''_n \times QP_i \times QD_i \times \exp(-Ba \times \Delta r) \times DE(t) \qquad (B.6)$$

The initial volumetric heat generation rate in the rirst wall at shut down is then

$$q'''_{a,i}(\text{first wall},t) = q''_n \times QP_i \times QD_i \qquad (B.7)$$

The initial fractional afterheat, FP, is defined as the ratio of afterheat power to the operational power level. Use of Equations B.5 and B.7 indicate that the local value of the initial fractional afterheat in the first wall is simply

$$FP(\text{first wall}) = QD_i \qquad (B.8)$$

Where afterheat levels are mentioned in most previous studies, the total blanket initial fractional afterheat is given. In the present terminology, this is given by

$$FP(\text{total blanket}) = \frac{\int_{i,r} QP_i \times QD_i \times \exp(-Ba \times \Delta r)dr}{\int_{i,r} QP_i \times \exp(-Ba \times \Delta r)dr} \qquad (B.9)$$

Since there is more than one material in the blanket, the two definitions of FP are not equivalent. Considering that 1) most of the opera-

tional heat is generated in non-structural parts of the blanket, 2) the total operational heat is not strongly influenced by structural material, and 3) the dominant afterheat is produced by the structural material, then Equation B.9 can be re-written as

$$FP(\text{total blanket}) \simeq \frac{QP_m \times QD_m \times \int \exp(-Ba \times \Delta r)dr}{\text{Operational Power}} \qquad (B.10)$$

where the subscript m denotes structural metal.

Thus the total fractional afterheat scales among structural materials as QP x QD, whereas the localized fractional afterheat scales as QD.

The total initial fractional afterheat, expressed as a percentage of operating power, tends to be about 1% independent of material, judging from data in Reference B.40. Thus the product $QP_i \times QD_i$ is fairly constant among materials. Based on the initial afterheat values in References B.38 - B.41, the values of $QD_i \times QP_i$ were determined for the structural materials. Given QP_i previously, the value of QD_i is determined. The values of these parameters are listed in Table B.17. The resulting values of the afterheat parameter are listed in Table B.18. The values for the non-structural materials was generally estimated directly from Equation B.8.

Having specified QP, QD, and Ba in Equation B.6, the decay heat, time behavior, DE(t), must be determined. The other parameters are defined such that

$$DE(\text{shutdown}, t=0) = 1.0 \qquad (B.11)$$

TABLE B.17

Total Initial Fractional Afterheat (= QD x QP(m^{-1}))

Material	QD(%)	QP(m^{-1})	QD x QP(m^{-1})
316 SS	4.0	10.0	0.040
HT-9	4.0	9.5	0.038
V-alloy	5.0	6.0	0.030
TZM	6.0	6.5	0.039

TABLE B.18

Values of Afterheat Parameter

Material	Afterheat Parameter, QD(%)	From Data in Reference
316	4.0	Current study*
HT-9	4.0	Current study
V-alloy	5.0	Current study
TZM	6.0	Current study
Lithium	0.6	B.36
Water	~ 0	B.36
Helium	~ 0	B.36
Flibe	6.2	B.31
$LiAlO_2$	1.9	B.36
$Li_{17}Pb_{83}$	1.0	Current study
Be	0.5	B.36

*See text.

so that results of the literature can be compared on a normalized basis. The time behavior for 316 SS, V-20Ti, and TZM is shown in Figures B.5 - B.7 based on data in the references cited. For 316 SS, the detailed time and spatial data in reference B.36 were used for the 316 SS case. For V-alloy and TZM, an average of the previous results was used. The decay function for HT-9 was estimated from references B.39 and B.41. All four are shown in Figure 3.3. The rate of decay of HT-9 and 316 SS is initially the same with differences growing in time.

As mentioned in Chapter 3, afterheat computer calculations were terminated at t=1 day due to computer time constraints. The temperature rate of change with time at 24 hours was used to conservatively extrapolate to longer times. The length of blanket operation would influence the decay rate of afterheat. One example is UWMAK-I where decay rates DE(t) for 2 and 10 year operation were shown in Figure B.5. The variation between them is less than among design studies. This is not unexpected since the decline in the first day is dominated by shorter-lived isotopes. It is precisely these isotopes which tend to reach saturation levels soonest under operation. The values of DE(t) for flibe, beryllium, $LiAlO_2$, Li, and $Li_{17}Pb_{83}$ were estimated from References B.1, B.31, and B.37. These were not found to add significantly to blanket afterheat, either because the decay was very rapid or the initial level was low. Had Zr_5Pb_3 been used as a neutron multiplier, it would have significantly added to the afterheat based on STARFIRE results [B.1].

The separation of space and time in Equation B.6 was checked graphically with results plotted in References B.26 and B.28. The different parts of the blankets showed similar time behavior. The various 316 SS

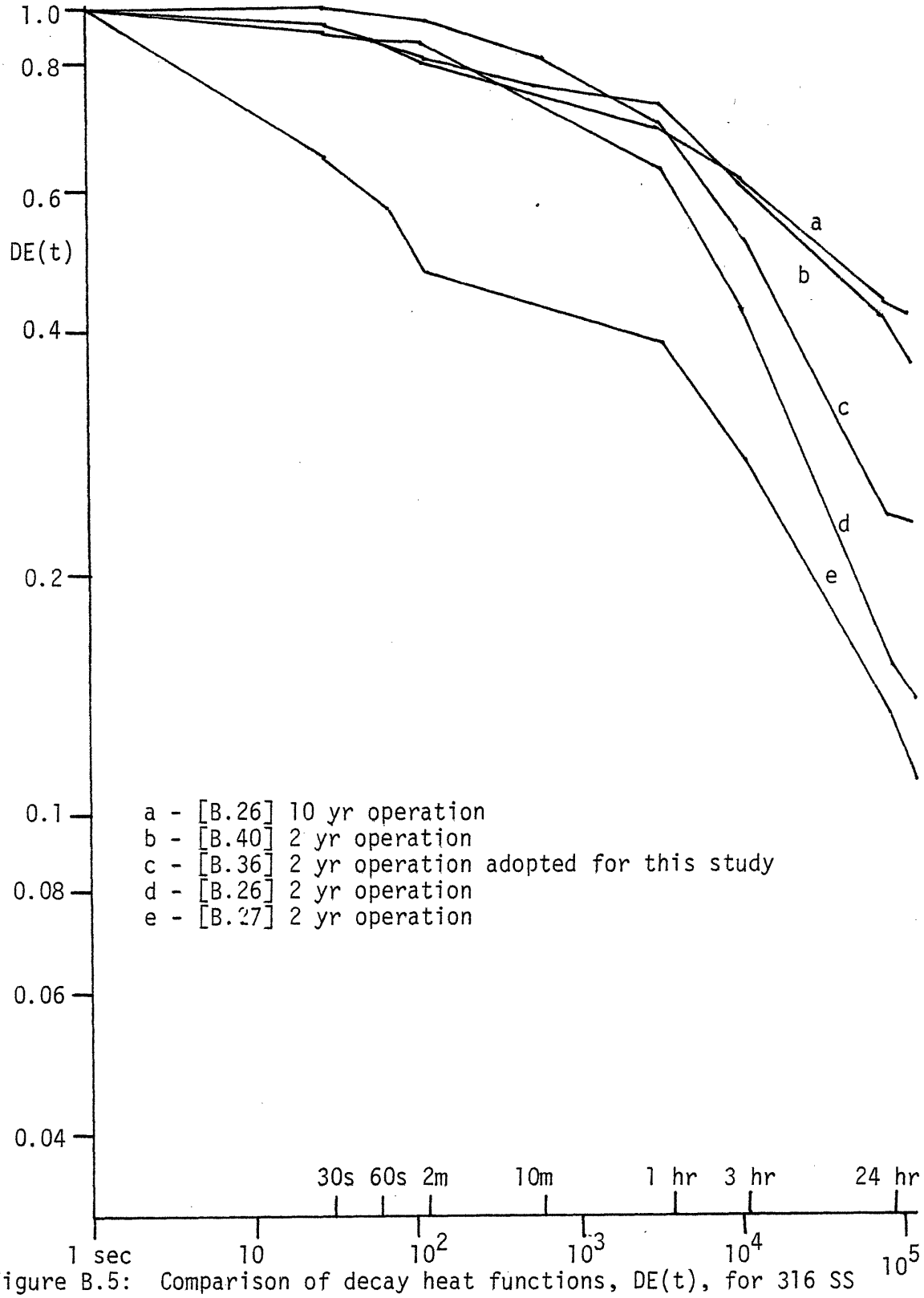

Figure B.5: Comparison of decay heat functions, DE(t), for 316 SS

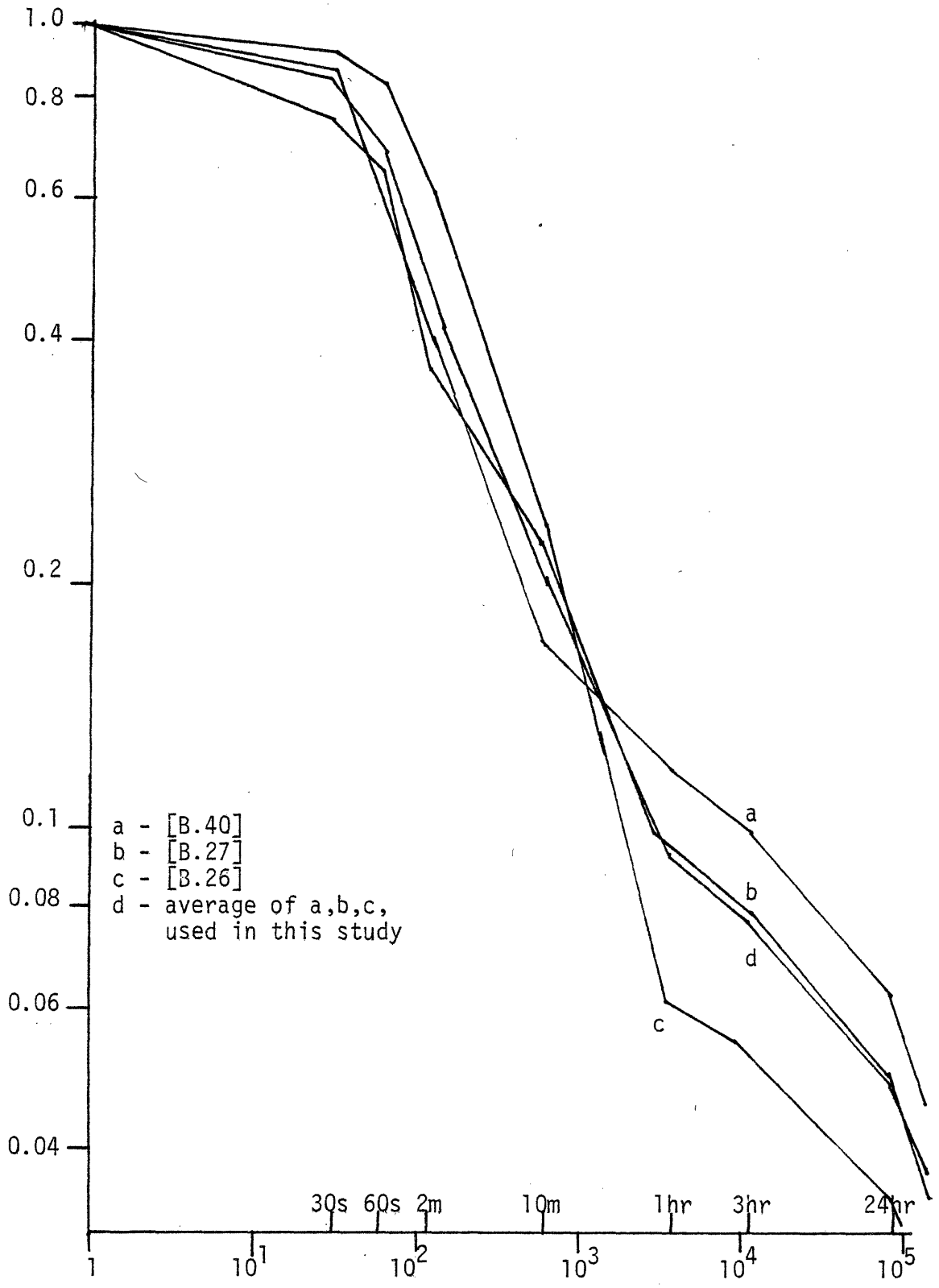

Figure B.6: Comparison of decay-heat functions, DE(t), for V-20Ti

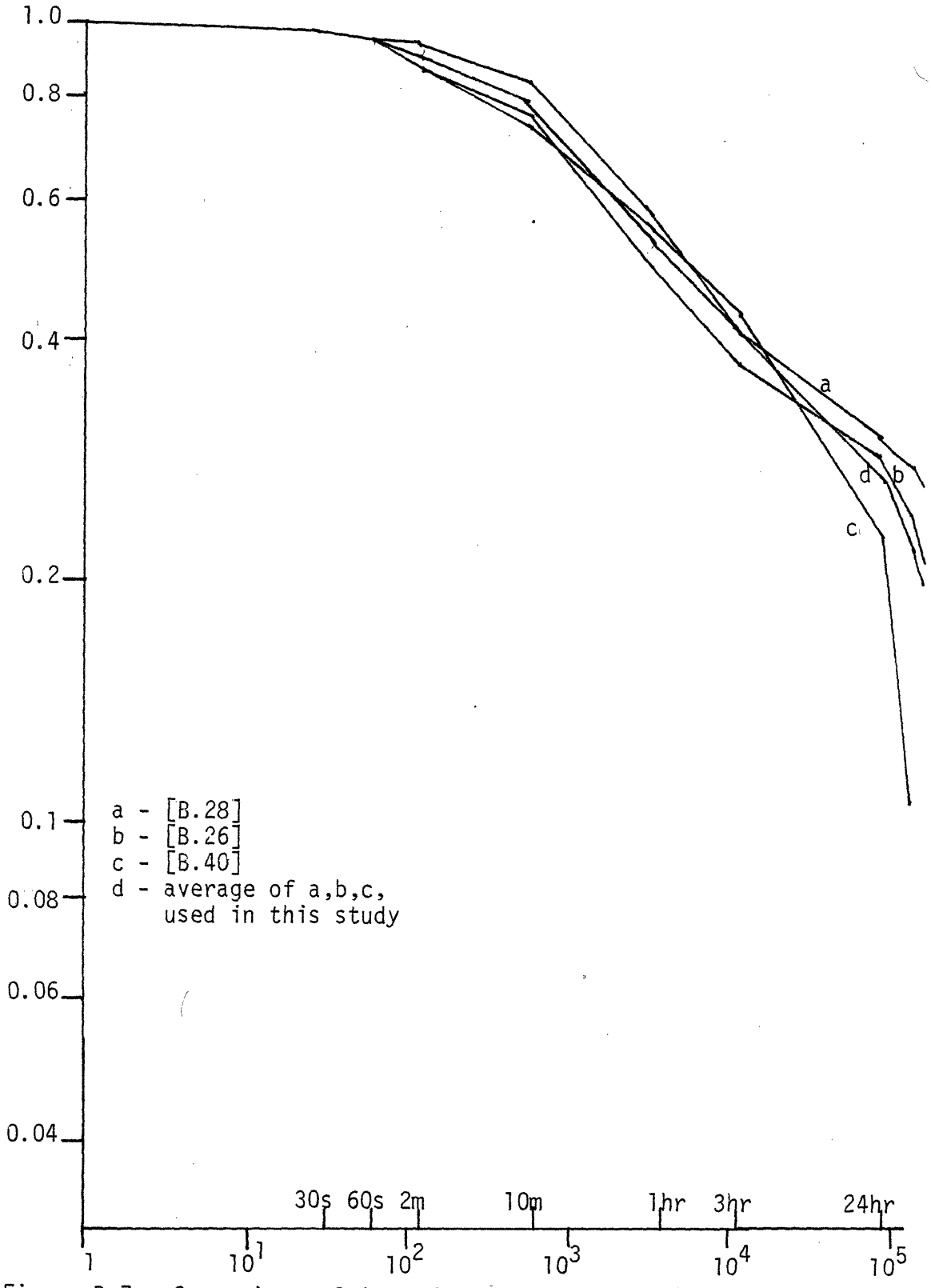

Figure B.7: Comparison of decay heat functions, DE(t), for TZM

cases in Reference B.36 which were performed for Merrill's study [B.37] were able to be examined numerically. For times in the first day after shutdown, the 316 SS in first wall and blanket with different coolants was found to show the same time afterheat behavior (DE(t)), generally within 10%. The 316 SS first walls for the different cases showed the same time behavior within 2%. The first wall is the most critical contributor to the afterheat problem since the concentration of afterheat and metal is the highest. Thus the approximations in the analysis are thought to be adequate.

REFERENCES

B.1 C.C. Baker, Jr., et al., "STARFIRE," ANL/FFP-80-1, 9/1970.

B.2 D.L. Smith, et al., "Fusion Reaction Blanket/Shield Design Study," ANL/FPP-79-1, 7/1979.

B.3 G.P. Yu, "Relationship of Material Properties to the Design of a Fusion Reactor First Wall," Sc.D. thesis, Department of Nuclear Engineering, Massachusetts Institute of Technology, 1981.

B.4 "STARFIRE—An Interim Report," ANL/FPP/TM-125, 12/1979.

B.5 O. Kubaschewski and C.B. Alcock, Metallurgical Thermochemistry, 1979.

B.6 R.C. Weast, ed., Handbook of Chemistry and Physics, CRC Press, 55th Edition, 1974.

B.7 "Low Activation-Materials Safety Studies," GA-A16005, 12/1980.

B.8 D.R. Floyd, J.N. Lowe, ed., Beryllium Science and Technology, Vol. 2, 1979.

B.9 A.P. Fraas and A.S. Thompson, "ORNL Demonstration Study: Fluid Flow, Heat Transfer, and Stress Anlaysis Consideration in the Design of Blankets for Full Scale Fusion Reactors," ORNL/TM-5960, 2/1978.

B.10 W.M. Stacey, Jr., et al., "U.S. Contribution to the International Tokamak Reactor Workshop," 11/1979.

B.11 "Alloys for the Fusion Reactor Environment," DOE/ET-007, 1/1978.

B.12 D.K. Sze, "Emergency Cooling and Afterheat Effects of a CTR Blanket," Proceedings of the First Topical Meeting on the Technology of Controlled Nuclear Fusion, CONF-740402-P1 (1974), p. 599.

B.13 "1978 Databook," Mid-Jine 1978 edition from Metal Progress, American Society for Metals, 1978.

B.14 R.M. Brick, A.W. Pense, and R.B. Gordon, Structure and Properties of Engineering Materials, 1977.

B.15 E.M. Sparrow and R.D. Cess, Radiation Heat Transfer, 1978.

B.16 W.H. McAdams, Heat Transmission, 1954.

B.17 M.N. Ozisik, Radiative Transfer, 1973.

B.18 R. Siegal and J.R. Howell, Thermal Radiation Heat Transfer, 1972.

B.19 Thermophysical Properties of Matter, Vol. 7: Thermal Radiation Properties, Metallic Elements and Alloys, 1970.

B.20 N.J. Hoffman, et al., "Properties of Lead-Lithium Solutions," Proceedings of the Fourth Topical Meeting of the Technology of Controlled Nuclear Fusion, CONF-801011, p. 1754, 7/1981 (also UCRL-84273).

B.21 P. Gierszewski, et al., "Property Correlations for Lithium, Sodium, Helium, Flibe and Water Fusion Reactor Applications," PFC-RR-80-12, 8/1980.

B.22 Liquid Metal Handbook, 2nd Edition, USAEC, 1954.

B.23 W. Hoffman, Lead and Lead-Alloys, 1970.

B.24 J.H. Keenan, et al., Steam Tables, 1978, Metric Values.

B.25 R.E. Bolz, and G.L. Tuve, eds., Handbook of Tables for Applied Engineering Science, CRC Press, 2nd Edition, 1973.

B.26 B. Badger, et al., "UWMAK-I Wisconsin Toroidal Rusion Reactor Design," UWFDM-68, 1973.

B.27 "UWMAK-II Conceptual Tikamak Power Reactor Design," UWFDM-112, 10/1975.

B.28 "UWMAK-III A High Performance Noncircular Tokamak Power Reactor Design," EPRI-ER-368, 7/1976.

B.29 E.T. Cheng, et al., "Nucleonic Design for a Compact Tokamak Fusion Reactor Blanket and Shield," UWFDM-256, 8/1978.

B.30 G.L. Kulcinski, "A Commercial Tandem Mirror Reactor Design with Thermal Barriers-WITAMIR-I," UWFDM-375, 10/1980.

B.31 R.G. Mills, Ed., "A Fusion Power Plant," PPPL-MATT-1050, 8/1974.

B.32 R.L. Hagenson, R.A. Krakowski, and G.E. Lort, "The Reversed Field Pinch Reactor (RFPR) Concept," LA-7973-MS, 8/1979.

B.33 T.J. McManamy, "Fusion Reactor Blanket Heat Removal Using Helium and Flibe," Ph.D. thesis, Department of Nuclear Engineering, Massachusetts Institute of Technology, 2/1979.

B.34 J. Chao, et al., "A Parametric Study of a Lithium-Cooled Tokamak Blanket," Nuclear Technology, 42(1), 1/1979.

B.35 R.T. Santoro and J.M. Barnes, "Nuclear Performance Calculations for the ELMO Bumpy Torus Reactor (EBTR) Reference Design," ORNL/TM-6085.

B.36 A.J. Scott, et al., "Calculated Heating Rates for Fusion Blanket Safety Analysis," EG & G, Idaho, Inc., Internal Technical Report, 3/1981, performed for Reference B.37.

B.37 B.J. Merrill, "First Wall and Blanket Module Safety Enhancement by Material Selection and Design Decision," loc. cit. [8.20], p. 1296.

B.38 E.T. Cheng, "Blanket and Shield Nucleonic Considerations for the Field-Reversed Mirror Small Reactor," GA-A15990, 8/1980.

B.39 J.M. Rawls, et al., "Assessment of Martensitic Steels as Structural Materials in Magnetic Fusion Devices," GA-A15749, 1/1980.

B.40 O.N. Jarvis, "Transmutation and Activation of Fusion Reactor Wall and Structural Materials," AERE-R-9298, 1/1979.

B.41. C.P.C. Wong, et al., "Moving Ring Field-Reversed Mirror Blanket Design Considerations," loc. cit. [8.20], P. 765 (also GA-A-16097).

APPENDIX C. REFERENCE DESIGN PARAMETERS

The goal and criteria for establishing design parameters for the eleven combinations of materials are discussed in Chapter 2. Some of the details of these calculations are presented here. Material Properties are discussed in Appendix B.

C.1 Water-Cooled Designs

The reference water-cooled designs are based on the STARFIRE [C.1] blanket concept. The pressure is taken to be 15.2 MPa and the temperature drop around the coolant loop (ΔT_{loop}) is 40°C. The total coolant mass flow rate required for a blanket is given by

$$Q\ (m^3/s) = \frac{[700 + 2800 \times M] \times 10^6\ \text{watts/MW}}{\Delta T_{loop} \times \rho \times c_p} \qquad (C.1)$$

where $LiAlO_2$ is the breeder, M = 1.15 and the mass flow rate is 24 m^3/s. For $Li_{17}Pb_{83}$, the energy multiplication is higher (1.25) and the flow rate is 25.5 m^3/s.

The stress limits were discussed in Chapter 2 which identified the first wall thickness. The maximum first wall thickness due to fatigue is given by (see Chapter 2):

$$I_{max} = \frac{2k(1-\nu)}{\beta q''_w}\, \varepsilon_T(10^3\ \text{cycles}) \qquad (C.2)$$

For 316 SS, this results in 8.9 mm. For HT-9, the maximum first wall thickness is 22.3 mm for a heat flux of 9×10^5 W/m^2 and 10^3 operating cycles. Thus fatigue considerations do not limit the first wall thick-

ness. The reference design concept for the water/$LiAlO_2$ and water/$Li_{17}Pb_{83}$ cases are shown in Figures 2.1, 2.2. For the pressure stress calculations, the first wall panel was taken to represent an equivalent tube radius of 10 mm.

Use of $Li_{17}Pb_{83}$ in place of $LiAlO_2$ changes the in-blanket wetted surface area by elimination of the second wall and reduction in the wall area directly cooling the breeder zone. The resulting component areas are listed in Table C.1.

For loss-of-coolant and disruption analysis, the water cooled blankets were represented as shown in Figures C.1 and C.2. The periodic nature of the first wall panel allows use of a small portion of the blanket and periodic boundary conditions as was used in the STARFIRE [C.1] study. By terminating the nodes at the thickest and thinnest parts of the panel, symmetry is preserved and adiabatic side conditions are imposed.

From the STARFIRE study, it is seen that the water volume in the blanket modules is about 20 m^3 whereas the total volume of water is 550 m^3. The volume of the $LiAlO_2$ is 340 m^3. The calculation of volumes for all liquid breeders is discussed in Section C.3.

For LOCA analysis, the ratio of tube break area to draining fluid volume (A_b/V) is required. This can be related to the total flow rates by the equation,

$$A_b/V = \frac{Q}{v \times V} \qquad (C.3)$$

where v = design velocity through the section of piping.

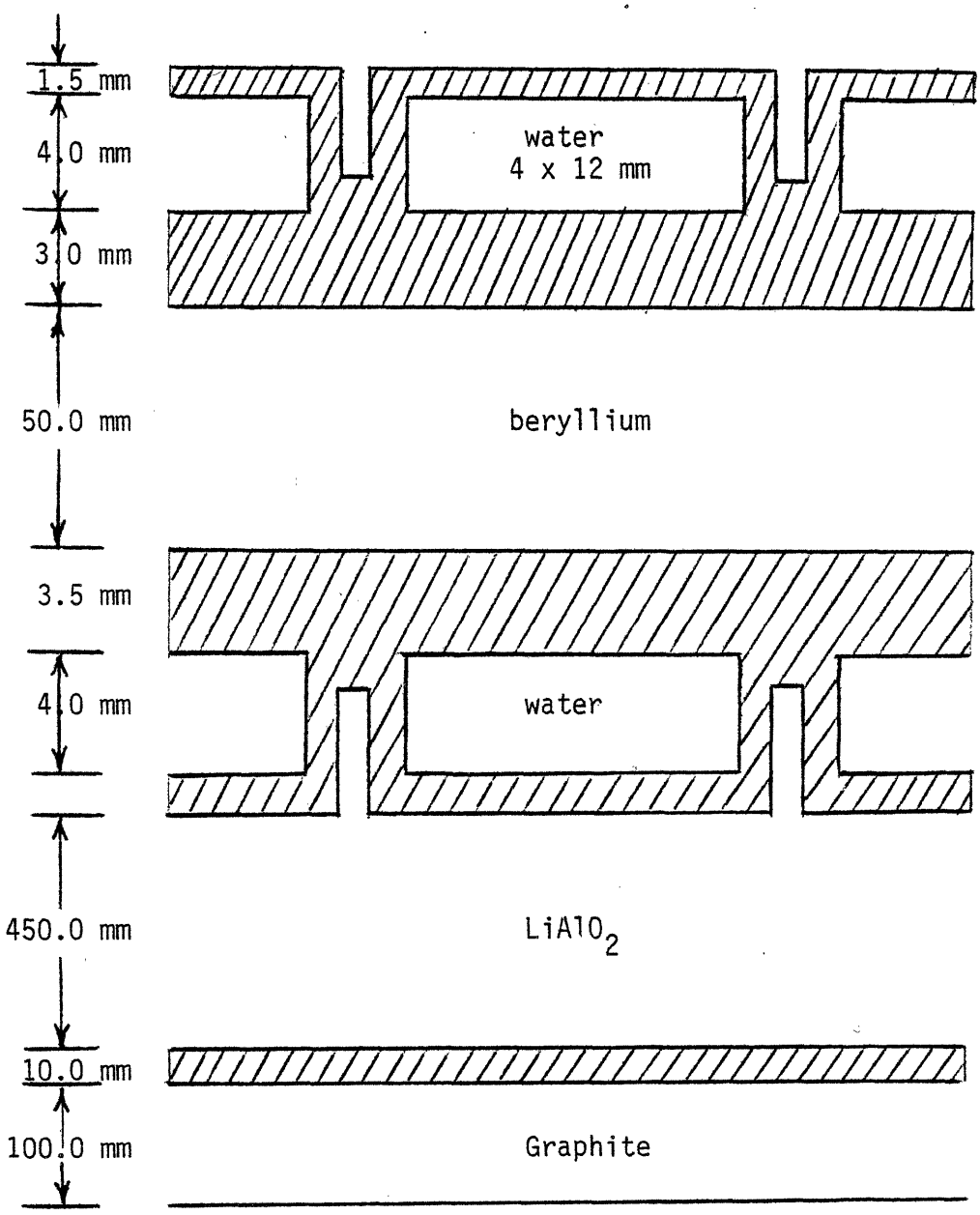

Fig. C.1: Geometry of Water/$LiAlO_2$ Combination Used for Computer Thermal Analysis

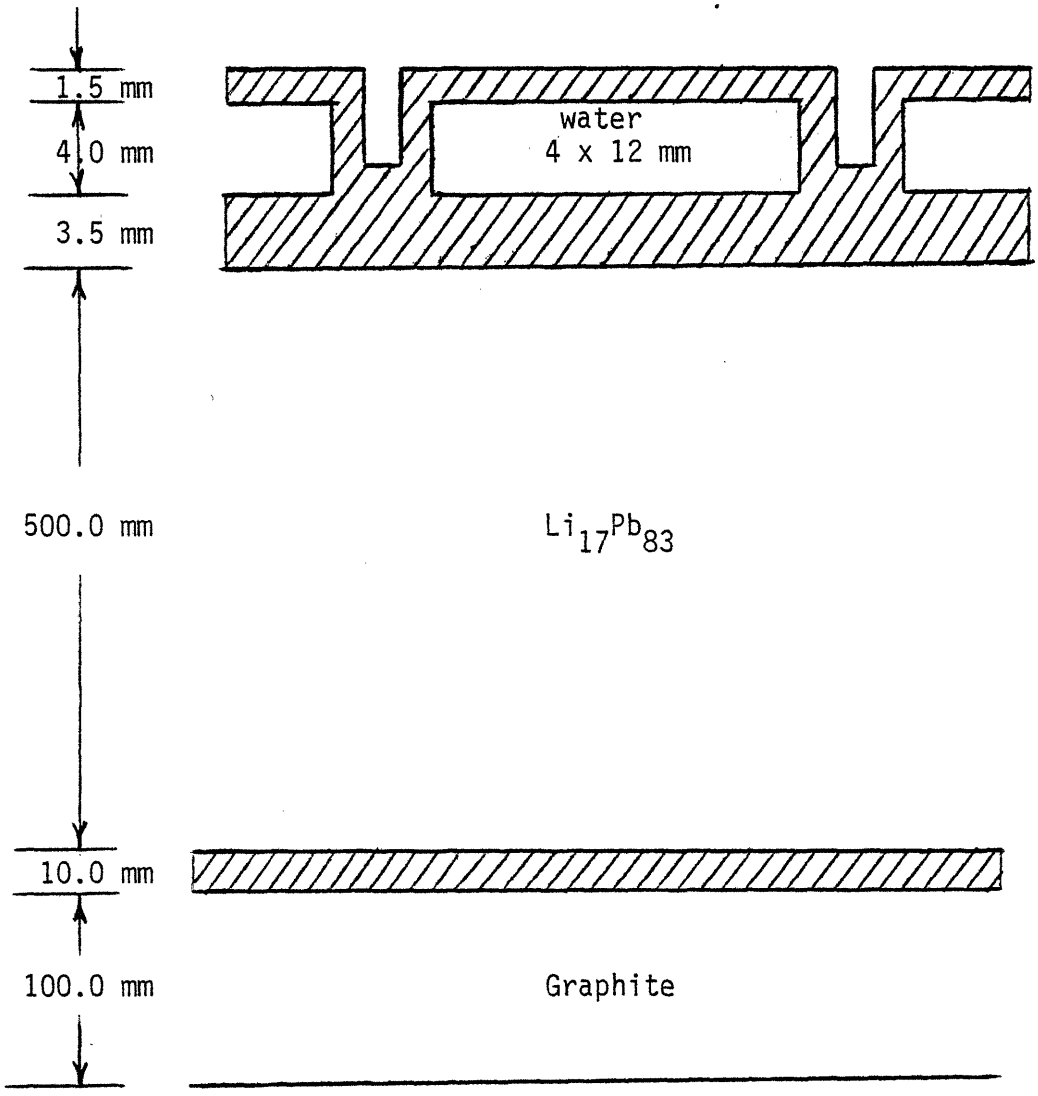

Fig. C.2: Geometry of Water/$LiAlO_2$ Combination Used for Computer Thermal Analysis

TABLE C.1

In-blanket Wetted Surface Areas (m^2)

	$LiAlO_2$ Breeder*		$Li_{17}Pb_{83}$ Breeder
First Wall	2,100		2,100
Second Wall	2,100	6,900	4,600
Breeder Zone	4,800		
Side Wall and Frame	1,200		1,200
Manifolds	1,400		1,400
Total	11,600		9,300

*From Reference C.1, STARFIRE.

For water designs, a conservative (upper estimate) of A_b/V is 0.25 m^{-1}. For 240 modules, this corresponds to a break area for an individual module of 0.02 m^2. Note that since both inlet and outlet pipes are assumed severed (see Chapter 3), the relevant volume is 20 m^3 (in-blanket) rather than the total (550 m^3). If only inlet pipes were to break, then the entire loop inventory would have to empty. For the double break, the out-blanket coolant is immediately separated from the blanket.

C.2 Helium-Cooled Designs

The reference helium-cooled designs are based on the Westinghouse/ORNL design concept [C.2, C.3]. The pressure is fixed at 5.5 MPa and the coolant loop temperature drop is 235°C. Using Equation C.1, the coolant flow rates for the two breeder cases are 700 m^3/s for a $LiAlO_2$ breeder (M = 1.15) and 720 m^3/s for a lithium breeder (M = 1.20), using helium properties and the average temperature of 318°C. The first wall stress limits were discussed in Chapter 2 and led to a selection of a 1.6 mm thickness for both 316 SS and HT-9 cases.

The reference designs for the helium/lithium and helium/$LiAlO_2$ cases are shown in Figures 2.3 and 2.4. Unless otherwise stated (here or Chapter 2), design values are taken from References C.2 and C.3. The total helium volume in the loop was estimated at 600 m^3, with about 30 m^3 in the blanket modules.

The use of $LiAlO_2$ breeder requires the incorporation of a neutron multiplier and its structural support. Of the eleven reference concepts in this study, the helium/$LiAlO_2$ cases (316 SS and HT-9) appear the least believable.

Based on the reference concepts, the in-blanket surface areas are determined and listed in Table C.2. The longer length of the lithium module is responsible for more surface area than that caused by the neutron multiplier and the coolant tubes in the poor thermal conductivity $LiAlO_2$. Because the first wall hemisphere and module cylinder have four metal surfaces that face the helium coolant, the total area for the helium designs is high.

For sputtering purposes, forward sputtering over-shadows backward sputtering (see Chapter 7). Thus the relevant area at the first wall is half of the total since two of the four surfaces face away from the plasma.

Using Equation C.3 and typical blanket values, the ratio of tube break area to blanket coolant is found to be about 0.25 m^{-1}. Again, both inlet and outlet pipes are assumed severed, which immediately isolates the blanket from much of the total coolant volume.

The blanket model for the computer analysis in Chapters 3 and 4 is illustrated in Figures C.3 and C.4. Connections across the flow gap were assumed as indicated, but these proved to have no effect on results.

C.3 Lithium-Cooled Designs

The reference lithium cooled designs are based on the recent ANL concept [C.4, C.5]. The pressure is set at the recommended value of 2.8 MPa to allow for MHD pumping losses. The inlet and outlet temperatures for the 316 SS and V-alloy cases are those from Reference C.4, summarized in Table 2.7. Thus the loop temperature drops are 220°C for the 316 SS design and 250°C for the V-alloy case. Based on Equation C.1, the total coolant flow rates are 8.4 m^3/s (3.6 SS) and 7.6 m^3/s (V-alloy), with

TABLE C.2

In-blanket Coolant Surface Areas for Helium-Cooled Designs (m^2)

	Lithium Breeder	$LiAlO_2$ Breeder
First Wall Hemisphere Surfaces (four surfaces facing helium)	4,800	4,800
Cylinder Wall Surfaces (four surfaces facing helium)	49,500	37,600
Tubes through the Breeder Zone (five tubes, 5 mm radius)	—	4,700
Plenum around Multiplier	—	1,300
Total	~54,000	~48,000

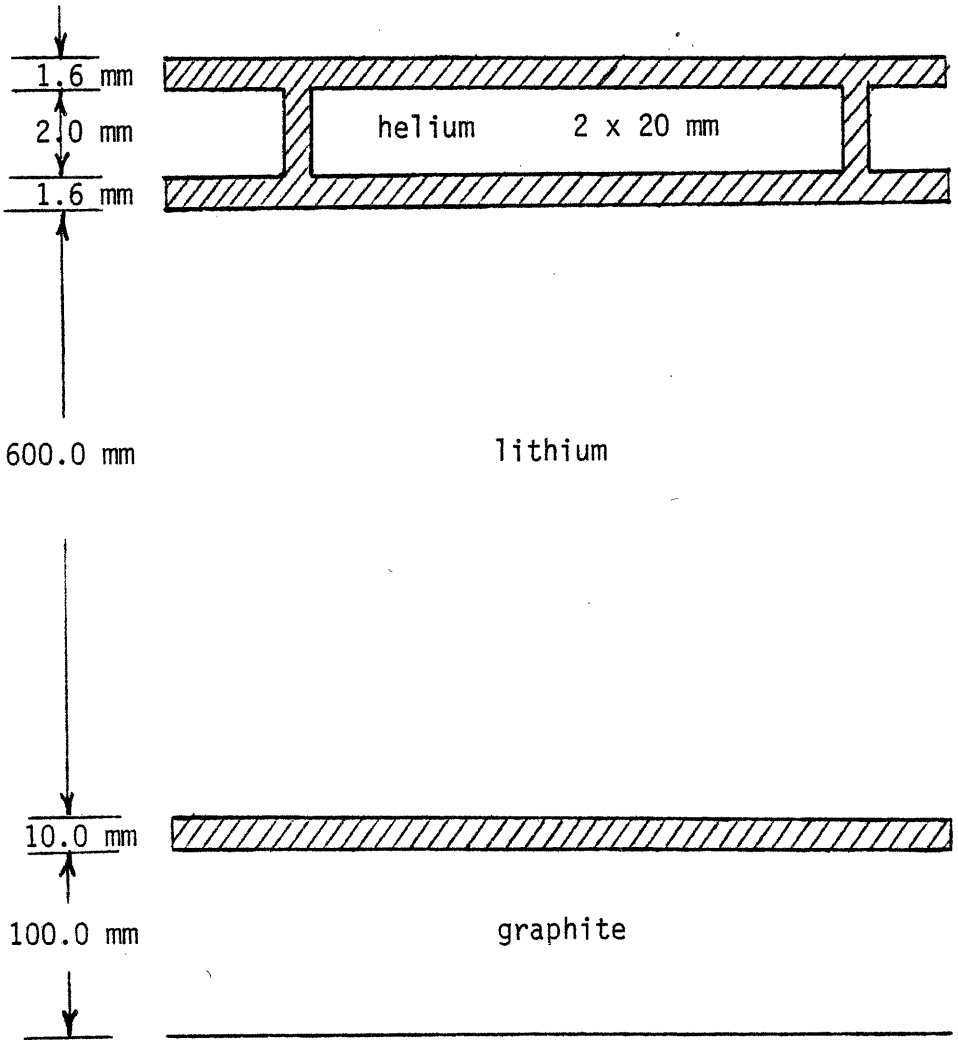

Fig. C.3: Geometry of Helium/Lithium Combination Used for Computer Thermal Analysis

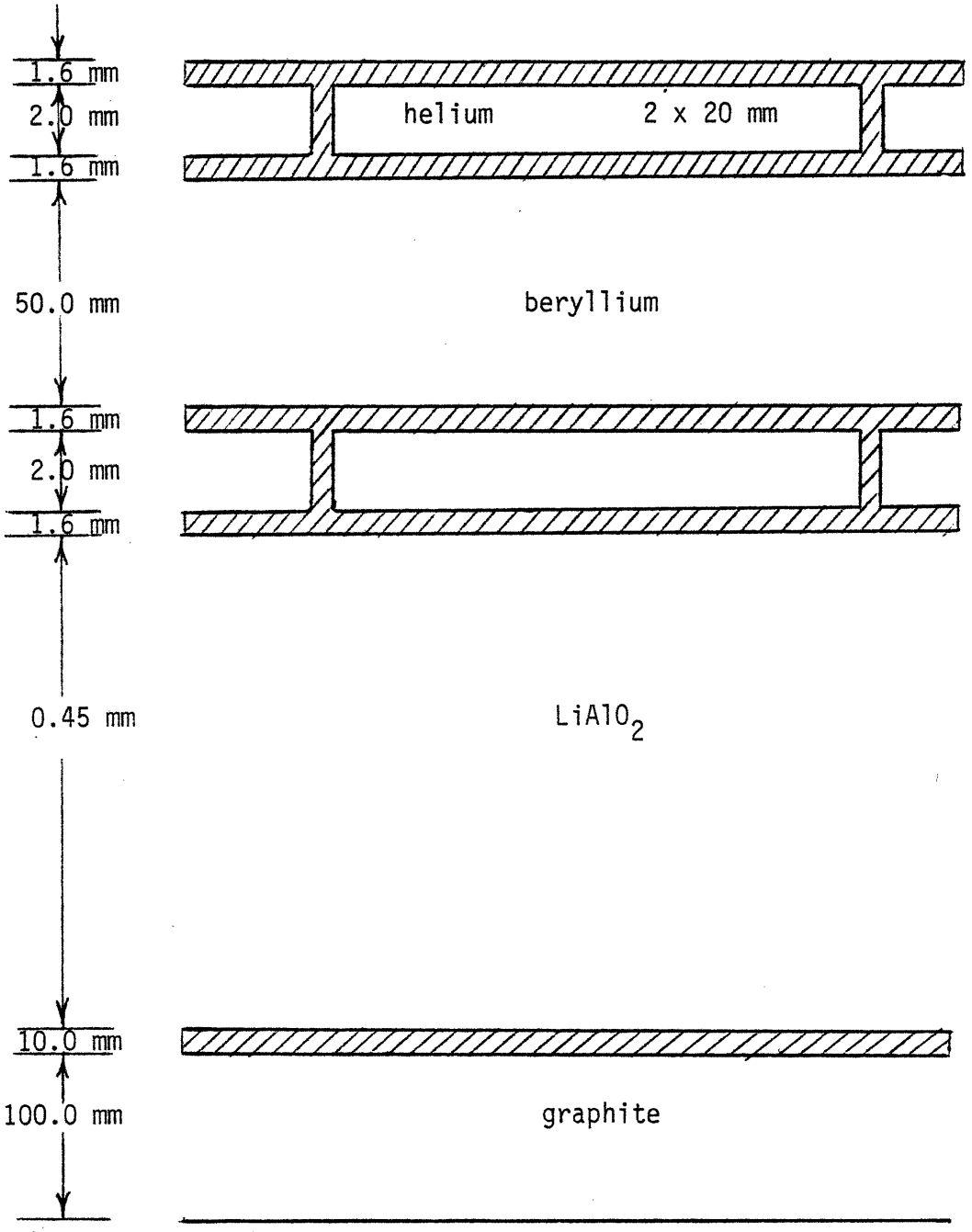

Fig. C.4: Geometry of Helium/$LiAlO_2$ Combination Used for Computer Thermal Analysis

lithium properties evaluated at the average temperature for each case with a blanket energy multiplication (M) of 1.20.

The basic blanket concept is shown in Figure 2.7. The average module length is 1.83 as for STARFIRE so that the average sector (composed of several modules in the poloidal direction) length is the same (see Figure C.5). The module width is four times the first wall cylinder radius.

Three cases were examined, widths of 0.60, 0.40, and 0.30 m. As seen in Table C.3, the larger modules have advantages of lower wetted surface areas and lower number of modules. The largest module width is that used in the ANL studies [C.4, C.5].

Using the methodology outlined in Chapter 2, the constraints on first wall thickness can be determined. As shown in Table C.4, it is not possible to design a 0.60 m wide module due to the conflict between pressure and thermal stresses. A large radius requires a high thick first wall, but the low thermal conductivity of the steel leads to high temperature drops and thermal stresses. The 0.40 m case is marginal, with only a 0.7 mm margin between the pressure and yielding criteria. In view of the simple nature of the analysis, this design margin is too low. If a somewhat arbitrary maximum first wall temperature gradient of 100°C is imposed, the design margin for the 0.40 m case is eliminated. The 0.30 m case is adopted for 316 SS with a 2.0 mm first wall thickness (as close to "optimum" as the pressure criteria allow). For V-alloy and 316 SS, an out-blanket surface area of 20,000 m^2 is assumed, based on reference C.4.

The superior material properties of the V-alloy make the design

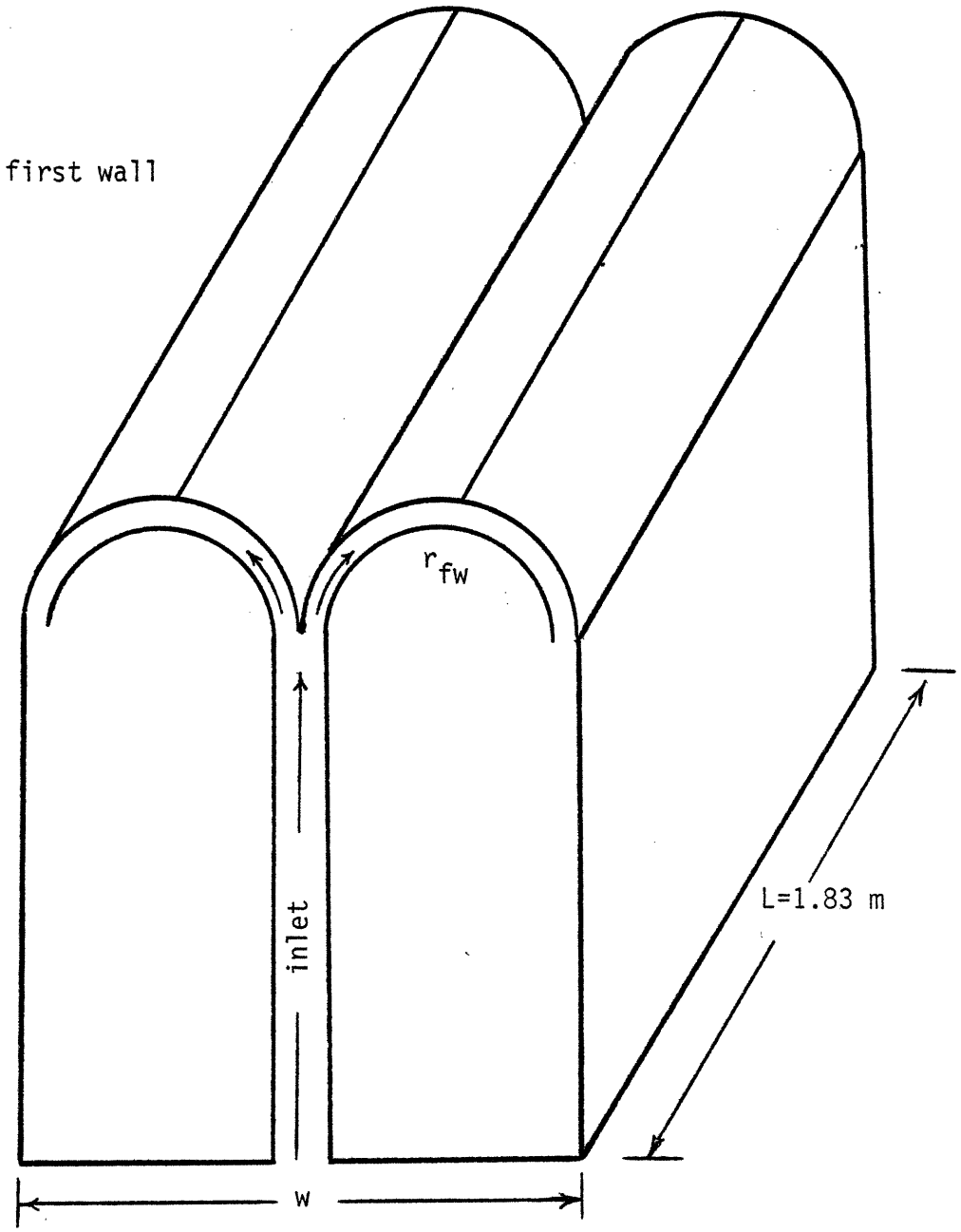

Fig. C.5: Schematic of Lithium/Lithium Combination Geometry (see Fig. 2.7)

TABLE C.3

Comparison of Module Widths for Lithium-Cooled Designs

Module Width (m)	0.60	0.40	0.30
First Wall Cylinder Width (m)	0.15	0.10	0.075
Number of Modules	720	1,080	1,440
Modules per Sector	30	45	60
Surface Areas (m^2):			
First Wall (3 surfaces exposed to lithium)	3,700	3,700	3,700
Module Bottom	800	800	800
Modules Sides (incl. front and back, inlet baffle)	3,500	4,900	6,300
Manifolding outside Module	1,000	1,000	1,000
Total	~9,000	~10,400	~11,800

TABLE C.4

Constraints on 316 SS First Wall for Lithium Design

Module Width (m)	0.60	0.40	0.30
Minimum Thickness due to Pressure (mm) (Equation 2.2)	3.9	2.6	1.9
"Optimum" Thickness (mm) (Equation 2.6)	1.8	1.5	1.3
Maximum Thickness due to Yielding (mm) (Equation 2.5)	2.9	3.3	3.5
Maximum Thickness due to Fatigue (mm) (Equation 2.8)	8.9	8.9	8.9
Maximum Thickness to Keep Temperature Drop Through First Wall below 100°C (Equation 2.7)	2.2	2.2	2.2

process easier. As seen in Table C.5, yielding and fatigue criteria allow very thick first walls (over 10 mm). The maximum thickness is limited by the value of the temperature drop through the wall. An arbitrary limit of 100°C would not allow a thickness which would minimize total stress. A design value of 3.8 mm was selected to minimize stresses which corresponds to a 110°C temperature drop through the wall.

The model used for the computer analysis for Chapters 3 and 4 is shown in Figure C.6. As is the case for the helium design, a connection was included between first wall and flow guide. This proved to have no effect.

The volumes of fluids must be determined. In most design studies, the total volume of fluid is not specified. For STARFIRE [C.1], the total volume of water is about 550 m^3 and of $LiAlO_2$ is about 300 m^3. Most of the water is out of the blanket. Based on the geometries specified in this appendix and Chapter 2, the other volumes have been estimated (see Table C.6).

Using Equation C.3, a conservative estimate for the maximum ratio of break area to draining coolant volume (A_b/V) is 0.15 m^{-1}. For a typical individual module, the break area is taken to be 0.10 m^2. For a liquid breeder, the flow rates are lower. For $Li_{17}Pb_{83}$, the estimates are volume = 500 m^3, linear flow velocity = 0.10 m/s, and total flow rate of 0.1 m^3/s, which results in a value of A_b/V of 0.002 m^{-1}.

C.4 Flibe-Cooled Design

The reference flibe-cooled design is based on the work of McManamy [C.6] with a STARFIRE-type first wall. Use of Equation C.1 for a lithium breeder (M = 1.20) results in a total mass flow rate of 9.1 m^3/s. The

TABLE C.5

Constraints on V-alloy First Wall for Lithium Design

Module Width (m)	0.60	0.40	0.30
Minimum Thickness due to Pressure (mm) (Equation 2.2)	2.4	1.6	1.2
Optimum Thickness (mm) (Equation 2.6)	3.8	3.1	2.7
Maximum Thickness due to Yielding (mm) (Equation 2.5)	10.7	11.2	11.4
Maximum Thickness due to Fatigue (mm) (Equation 2.8)	22	22	22
Maximum Thickness to Keep Temperature Drop Through First Wall below 100°C (Equation 2.7)	3.4	3.4	3.4

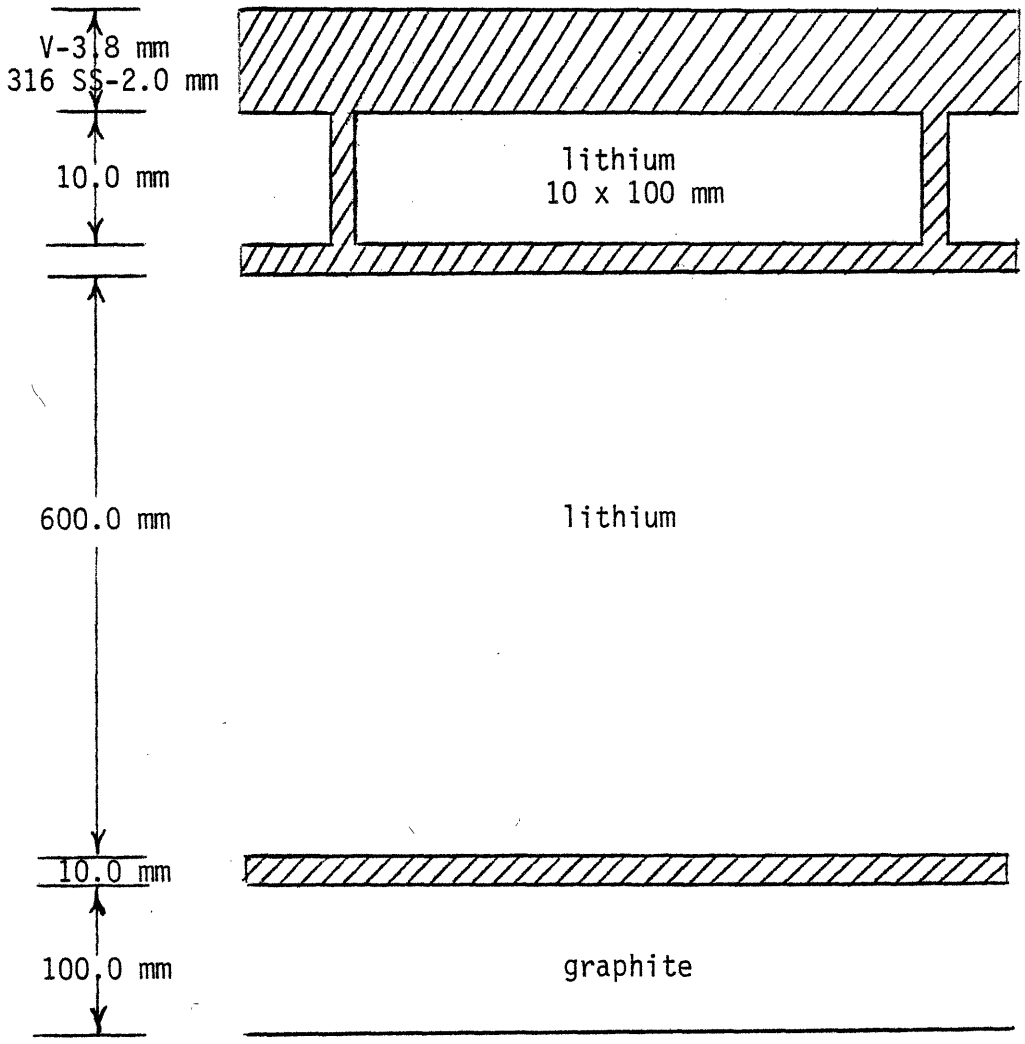

Fig. C.6: Geometry of Lithium/Lithium Combination Used for Computer Thermal Analysis

TABLE C.6

Total Volumes of Non-structural Materials (m^3)

	Used as Coolant	Used as Breeder
Water	550	—
Helium	600	—
Lithium	200	600*
Flibe	200	—
$LiAlO_2$	—	340
$Li_{17}Pb_{83}$	—	500

*For a design with lithium as coolant and breeder, the total volume is approximately 800 m^3.

reference concept is shown in Figure 2.9. The coolant tubes in the breeder zone make three passes through the lithium to keep the temperature rise the same as the first wall. McManamy recommended limiting the value of velocity time tube diameter as [C.6]

$$vD < \frac{0.25 \text{ volts}}{B} \sim 0.025 \text{ m}^2/\text{s} \qquad (C.4)$$

to prevent decomposition of the flibe due to induced voltages in the salt.

The constraints on the first wall thickness are listed in Table C.7. The pressure and yield stress criteria are not limiting. Of the materials combinations studies, the flibe/TZM case exhibits the most flexibilty. The first wall thickness was fixed at 1 mm. A higher value would be used if desired, perhaps up to about 10 mm.

Use of McManamy's [C.6] design approach resulted in the parameters listed in Table C.8. The low pressure drop allows the low operating pressure of 0.2 MPa. The maximum structural temperature was set at 900°C. The relatively high film temperature drops lead to a maximum flibe outlet temperature of 800°C.

The model used for the LOCA and disruption analysis (Chapters 3, 4) is shown in Figure C.7. The first wall panel design is seen as the same as STARFIRE [C.1]. Use of Equation C.3 allows estimation of the ratio of break area to blanket coolant volume:

$$A_b/V \sim \frac{Q}{vV} \sim \frac{(9.1 \text{ m}^3/\text{s})}{(2 \text{ m/s})(20 \text{ m}^3)} \sim 0.25 \text{ m}^{-1} \qquad (C.5)$$

TABLE C.7

Constraints on TZM First Wall Thickness for a Flibe Design

Minimum Thickness due to Pressure (mm) (Equation 2.2)	< 0.1
Maximum Thickness due to Yielding (mm) (Equation 2.5)	> 50
Maximum Thickness due to Fatigue (mm) (Equation 2.8)	11.0
Maximum Thickness to Keep First Wall Temperature Drop below 100°C (mm) (Equation 2.7)	11.8
Optimum Thickness to Minimize the Stresses (mm) (Equation 2.6)	$\lesssim 1$

TABLE C.8

Flibe/TZM Blanket Parameters Using Method of McManamy [C.6]

Reynolds Number	10,400
Nusselt Number	105
Prandlt Number	13.1
Loop Pressure Drop	0.05 MPa
Loop Temperature Difference	100°C
Wetted In-blanket Area	8,500 m^2

First Wall		Blanket Coolant Tubes	
First Wall Thickness	1 mm	Coolant Tube Thickness	1 mm
Flibe Velocity	2.5 m/s	Flibe Velocity	2 m/s
Film Temperature Drop	87°C	Film Temperature Drop	62°C
Tube Diameter	10 mm	Tube Diameter	12.5 mm
Wall Temperature Drop	9°C	Wall Temperature Drop	5°C

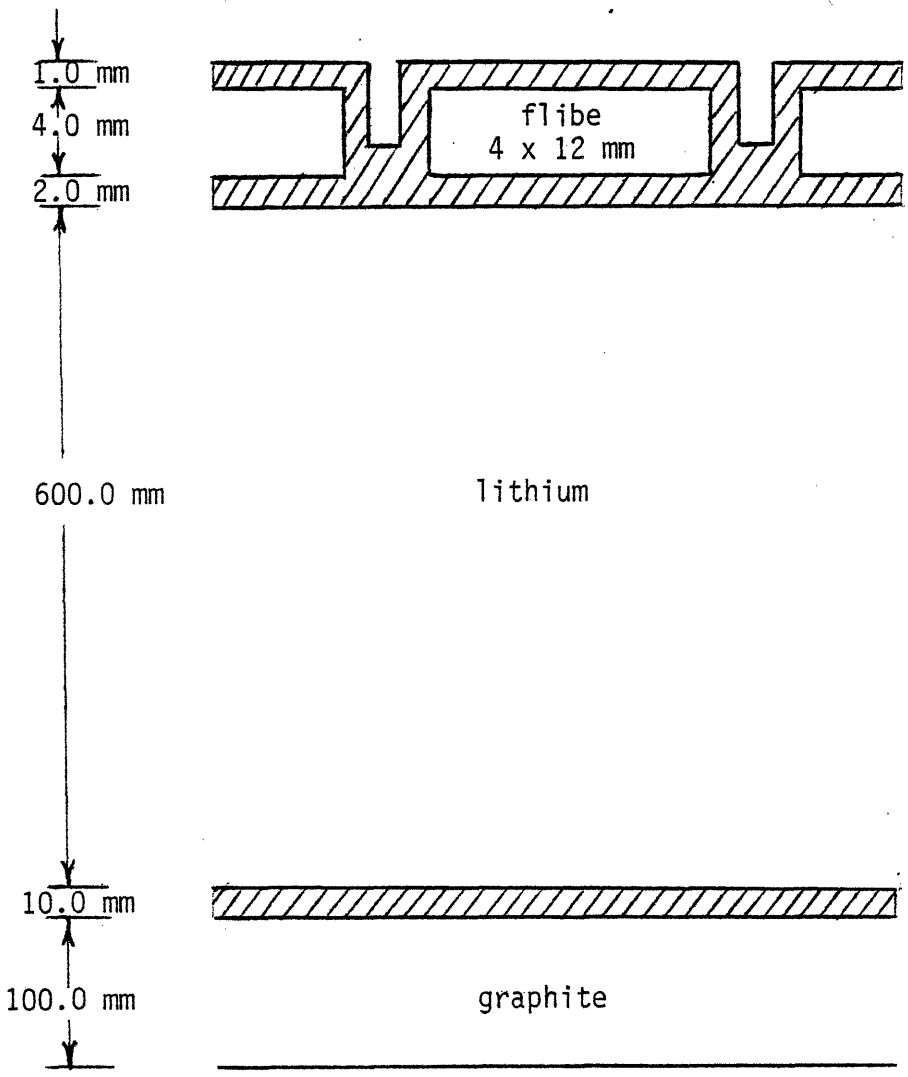

Fig. C.7: Geometry of Flibe/Lithium Combination Used for Computer Thermal Analysis

REFERENCES

C.1 C.C. Baker, Jr., et al., "STARFIRE—A Commercial Tokamak Fusion Power Plant Study," ANL/FPP-80-1, 9/1980.

C.2 J.S. Karbowski, et al., "Tokamak Blanket Design Study: FY 78 Summary Report," ORNL/TM-6847, 6/1979.

C.3 J.S. Karbowski, et al., "Tokamak Blanket Design Study, Final Report," ORNL/TM-7049, 1980.

C.4 D.C. Smith, et al., "Fusion Reactor Blanket/Shield Design Study," ANL/FPP-79-1, 7/1979.

C.5 J.H. Opelka, et al., "Decommissioning Study of a Commercial Tokamak Reactor," ANL/ES-93, 1/1981.

C.6 T.J. McManamy, "Fusion Reactor Blanket Heat Removal Using Helium and Flibe," Ph.D. thesis, Department of Nuclear Engineering, Massachusetts Institute of Technology, 1979.

APPENDIX D. WATER CORROSION MODEL

A detailed water corrosion product formation and transport model was developed which has been used as part of the STARFIRE study [D.1]. The following discussion is a description and justification of the model which was used to obtain the results presented in Chapter 7.

D.1 Potential Magnetic Field Effects

Several possibilities exist for interaction of strong magnetic fields and corrosion relevant processes as follows: (1) change in ion diffusion in water due to V x B force; (2) change in ion solid-state diffusion due to V x B force; (3) induced film stresses from magnetostriction; (4) acceleration of corrosion rate by induced current; (5) increased deposition of coolant particles due to field gradients; (6) corrosion rate alteration by change of film microstructure; and (7) corrosion rate alteration by presence of ferritic steel produced in austenite steel. Such effects need to be addressed to determine influence on optimum water chemistry, transport modeling, and alteration of relevant parameters.

D.1.1 V x B Force

The force on a charged particle in an electromagnetic field is given by

$$F = q(E + V \times B). \tag{D.1}$$

According to the electrokinetic theory of coolant particle deposition,

[D.2, D.3] interparticle and particle-wall electric fields are responsible for agglomeration and deposition of particles. Although the net charge on coolant particles is not known directly, typical inter-particle potential drops are ∿50 mVolts (or higher in reference water conditions) [D.2]. Since particle sizes are in the 1-μm range, the field is ∿5 T, and velocity is ∿10 m/s, the ratio of magnetic-to-electric force can be calculated,

$$\frac{V \times B}{E} \sim \frac{vB}{\Delta\phi/\Delta x} \sim 10^{-3}, \qquad (D.2)$$

and the possible V x B force in the coolant is negligible compared to electrostatic forces. As the velocities of ions in solid-state diffusion are far slower, the V x B force should also be neglected in oxide film diffusion.

D.1.2 Magnetostriction

The application of high-strength fields causes magnetic materials to constrict and induce stresses similar to thermal stresses [D.4, D.5]. Since the oxide film is magnetic and the base alloy is not, magnetostriction could cause stresses in the oxide film sufficient to disrupt it. The saturation value of λ_s (magnetostriction change of length per unit length) for all materials of interest is less than 50 μm/m with Fe_3O_4 highest at 41 [D.4]. Taking λ_s = 50 μm/m and comparing this to the stainless steel value for thermal expansion (20 μm/m-°K), one finds that the maximum magnetostriction corresponds to a ΔT of 2.5°C. Hence it is small enough to be neglected.

D.1.3 Induced Currents

As water corrosion is basically an electrochemical process with

very small currents, the possibility exists that any induced currents could alter the corrosion rate. Since STARFIRE operates steady state, the coolant tubes should not experience currents except during startup/shutdown of the magnets. The process may be a concern in pulsed machines, although the thermal shock to the oxide film could dominate). The conductivity of water may be sufficient for MHD interactions to result in voltages and currents in the water, leading to increased corrosion (see Chapter 7 for discussion of electrochemical concerns).

D.1.4 Field Gradients

Filters with high-gradient magnetic fields are very effective in trapping magnetic particles [D.6 - D.8]. The concern here is the possibility that the blanket could act as one large filter with increased particle deposition rates. The potential magnitude of the effect can be determined by 1) comparison of magnetic force (F_m) to drag force (F_d); and 2) comparison of STARFIRE parameters of interest to those of effective high flow rate magnetic filters.

The force on a particle of saturation field magnetization strength, M_s (volume basis) and radius r can be written [D.7, D.8]:

$$F_m = \frac{4}{3} \pi r^3 M_s \frac{dB}{dx} \qquad (D.3)$$

in a field gradient dB/dx. The crucial factor in the analysis is the determination of dB/dx. Typical high-flow filters have $dB/dx \simeq 10^4$ T/m [D.7, D.8].

The overall blanket has gradients of order 1 T/m due to toroidal effects. However, this field could be disturbed due to either magnetic ferritic steel produced in the stainless steel matrix or a magnetic oxide

film lining the coolant tubes. The former should be negligible as any disturbances do not occur in the coolant. The latter case is more difficult to treat.

A uniform layer of magnetite on a tube inner wall in a previously homogeneous field does not produce any gradients inside the tubes. This contrasts strongly with the very high gradients in filters which are produced on the outside of a filament matrix. There are two concerns. First, very localized variations in the oxide layer depth may produce relatively high localized gradients. However, any increased deposition would be self-correcting, tending to smooth any variations. This effect also tends to limit the loading of a magnetic filter; as the thickness of deposit increases, the gradient is reduced [D.7, D.8].

The second problem is the presence of nonsymmetric geometries, for example, the first-wall baffle and tube junctions. Precise determination of the field gradient in the vicinity of the wall for these cases is very difficult. For comparison purposes a figure of 10 T/m is adopted.

Then the ratio of F_m to F_d is given by:

$$\frac{F_m}{F_d} = \frac{4/3\ \pi r^3 M_s (dB/dx)}{6\ \pi\mu(v-u)} \qquad (D.4)$$

where r = particle radius $\times 10^{-6}$ m

M_s = 0.46 T at 300°C

dB/dx = 10 T/m

μ = viscosity = 9.2×10^{-5} N-s/m^2

$(v-u)$ = particle velocity relative to coolant velocity in stopping $\gtrsim$ 1 m/s

then $F_m/F_d = 9 \times 10^{-3}$ and the magnetic force is < 1% of the drag force.

To compare STARFIRE parameters with those of a high flow filter, one notes that the effectiveness varies as $\sim(F_m/F_d)L$ (L = length of passage), or for identical materials, $\sim(dB/dx)(L/v)$, with a dB/dx ratio of 10^3 and L/v ratio of 1/10, then STARFIRE is about 1% as effective as the better high flow filters. Thus the magnetic force should not have a significant effect on the overall value of the deposition rate. However, in very low flow areas, the potential clearly exists for increased deposition.

The magnetic quality of the particles can also have a benefit. An EPRI study [D.6] on using magnetic filters on PWR primary loops concluded that high temperature filters with flow of ∿46 kg/s and 90% efficiency were available and warranted. Placing two filters on each line around the pumps would give an effective removal filtration rate of ∿166 kg/s equal to ∿1% of the total flow rate. Such a system is adopted for filtration of crud.

The possibility exists to place such filters directly in the STARFIRE magnetic field. However, the power (∿80 kW total) and equipment savings would likely be far outweighed by several disadvantages: (1) restrictions on space inside the toroidal field coils; (2) increased complexity of incorporating filters into design; (3) very limited access; and (4) filter operation tied to operation of the TF coils. Thus the filters are placed outside the torus, and must depend on their own coils for field production. Another potential benefit of the field would be a tendency to reduce crud bursts.

D.1.5 Microstructure and Composition

Some magnetic films grown in strong fields show preferential orientation of domains [D.4, D.5]. As note previously, the outer oxide layer of the steel will be quite magnetic; hence, there is the possibility of preferential orientations in the oxide film. However, the inner layer is far less magnetic. The magnitude and effect of any such orientation on corrosion films appears unknown and could only be determined by experiment.

Although the bulk of the metal alloy is stainless steel, neutron irradiation and/or welding will transform some small percentage to a ferritic structure. Depending on the distribution, such a structure could lead to increased corrosion (ferritic steel corrodes faster). For example, ferritic structure at grain boundaries could lead to preferential grain boundary attack. Any effect due to phase transformation is unknown at present.

D.1.6 Conclusions on Magnetic Effects

The main concerns of magnetic interaction are the increased deposition of particles in very low flow areas and alteration of the microstructure of the oxide film. The advantages of a magnetic filter may provide incentive to maximize the magnetization potential of coolant particles. This suggests an advantage to having Fe_3O_4 rather than Fe_2O_3 as the stable phase (the chemical, hence magnetic, form of the coolant is controllable by water chemistry conditions). The concern of possible induced currents and voltages increasing the corrosion rate is unresolved (see Chapter 7).

D.2 Water Chemistry

There are several constraints on the water chemistry, some are in conflict. Existing data strongly indicates appropriate O_2 levels for pressurized water conditions. The H_2 level is determined by radiolysis considerations to keep O_2 levels to that required. The various constraints on additive additions and optimum pH data determine the remaining variables.

D.2.1 Constraints

The appropriate constraints on water chemistry are: (1) minimize corrosion rate; (2) minimize corrosion product inventory; (3) maintain adherent oxide film to reduce corrosion and tritium permeation; (4) avoid stress corrosion cracking; (5) limit tritium production in coolant to 1 Ci/day from ^7Li additive burnup; (6) allow for boric acid additions for tritium breeding ratio control; (7) minimize crud deposition; (8) optimize magnetic qualities of corrosion products; and (9) avoid chemical additives which activate. The available variables for control are the concentrations of O_2, H_2, any additives, and pH.

Although the data base for water corrosion of reactor materials is generally more extensive than for any other potential fusion reactor coolant, some information is still lacking. Available data for relevant parameters typically show large variations, especially among operating LWRs. Also, there is often significant discrepancy between laboratory experiments and operating values for corrosion rates. The difference is sometimes attributed to lack of appropriate chemistry control, poor startup procedures, and oxygen leaks (the latter is

unlikely for STARFIRE due to inert reactor building atmosphere) [D.10].

D.2.2 Gas Concentrations

Pressurized water reactors tend to operate at the $\lesssim$5 ppb O_2 level (4×10^{-3} cc/kg H_2O), whereas boiling water reactors operate between 0.2 - 0.3 ppm O_2 (set by steel and Inconel considerations, not by Zircaloy) [D.11 - D.13]. Lowering BWR O_2 levels significantly decreases the protectiveness of the oxide layer; increasing it adds more oxidant, hence higher corrosion rates. The same appears true for PWR conditions; early Russian data show increasing corrosion at higher O_2 levels [D.14]. As STARFIRE operates as a pressurized system (temperature and pressure virtually the same as PWR's) the data suggests specifying $\lesssim$ 5 ppb O_2.

Hyrdogen gas is added to PWR's to maintain such low oxygen levels in the face of radiolysis of water. For example, Babcock and Wilcox specify 15 - 40 cc H_2/kg H_2O (1.5 - 4 ppm) [D.15] and Combustion Engineering specifies 10 - 50 cc/kg (1-5 ppm) [D.16]. Although STARFIRE will operate at lower heat deposition levels to the coolant (average $\sim$ 10 kW/kg) than PWRs, the neutron energy spectrum is harder. Without complex, detailed calculations, it is anticipated that the two effects will generally cancel, indicating $\sim$ 5 ppm (55 cc H_2/kg H_2O) as an approximate H_2 level. More detailed calculations will be warranted in the future to determine the hydrogen level more accurately. These O_2 and H_2 conditions result in Fe_3O_4 being the stable iron oxide phase.

D.2.3 Additives

Various chemicals are added to the PWR primary loop to serve three

functions: (1) getter O_2 at startup; (2) pH control; and (3) reactivity control. All three functions are also included in STARFIRE, the last being the desire to control the tritium production rate (tritium breeding ratio) rather than reactivity.

Hydrazine (N_2H_4) is generally added to the system during startup to remove initial O_2. Typical amounts are 50 ppm [D.16]. After coming up in power, the hydrazine thermally decomposes to ammonia and tends to control pH, although plants may shift to other additives (e.g., LiOH) to control pH [D.15, D.16].

Addition of small amounts (~1500 ppm B as boric acid) may be an easy way to "fine tune" the tritium production, and the water chemistry should allow for this.

Possible compounds for pH control include LiOH, NaOH, KOH, and NH_4OH. Among the alkali hydroxides, LiOH is preferred over NaOH and KOH because of fewer stress corrosion cracking problems [D.17] and no activation [D.9]. Between NiOH and NH_4OH, there are several tradeoffs [D.9, D.18]. Each has advantages:

LiOH	NH_4OH
Very strong base	No tritium production
Stable under irradiation	Less stress corrosion cracking
Non-volatile	Product of hydrazine thermal decomposition

Based on tritium levels already present in the coolant, a limit of 1 Ci/day production due to LiOH additions is adopted. ^7Li rather than ^6Li is used in PWRs to minimize tritium production; however, the harder

fusion neutron spectrum will cause even ^7Li to produce significant amounts ot tritium. Taking conservative values of 20 m^3 of water in the breeder zone and a 1% ^7Li burnup over module lifetime, the 1 Ci/day limit becomes $\lesssim$ 2.25 ppm ^7Li. Current PWR operation allows up to $\sim$ 2.5 ppm ^7Li largely due to stress corrosion cracking (SCC) considerations [D.12, D.16]. In STARFIRE, some nucleate boiling is allowed and cold-worked structure is used; both are known to increase SCC problems. Without experimental data, a limit of $\sim$ 2 ppm ^7Li (10^{-4} M LiOH) is adopted. Such a concentration is also typical of PWR operating conditions with stainless steel fuel cladding [D.16]. While firm NH_4OH limits are also not well known for stainless steel/Inconel systems, a limit of $\sim$10 ppm NH_3 is inferred from Combustion Engineering limits on feedwater in the absence of copper alloys [D.16].

Without SCC constraints, several authors maintain that a $pH_{25°C}$ of $\sim$10 is optimum for corrosion minimization [D.9, D.20, D.21]. This corresponds to $pH_{300°C}$ $\sim$7 for LiOH dosing. Sawochka's data [D.19] suggests there is little incentive for $pH_{300°C} \gtrsim 6.9$. (The pH of a solution varies with temperature, e.g., $pH_{300°C}$ of pure water is 5.7.) Furthermore, to avoid electrokinetic deposition, one wishes to maintain conditions away from the point of zero change (PZC) [D.2, D.3]. Tomlinson [D.3, D.26] reports that no relevant materials have a PZC between $pH_{25°C}$ 6.8 - 11.2. Finally, the solubility fo Fe_3O_4 is minimum around $pH_{25°C} \sim 9.5$.

To obtain $pH_{300°C} = 7$ requires 0.4 ppm Li ($pH_{25°C} = 9.75$) or 50 - 100 ppm NH_3 ($pH_{25°C} \sim 12 - 13$). Furthermore, if boric acid is used, the situation is even worse. To obtain $pH_{300°C} \sim 7$ with 1000 ppm boron

(as boric acid) requires $\gtrsim$ 2 ppm lithium or very large amounts of NH_4OH. Allowance of boric acid additions tend to favor use of LiOH over NH_4OH. The reference conditions are then $pH_{25°C} \sim 9.5$ ($pH_{300°C} \sim 6.75$) with 0.22 - 2.2 ppm ^7Li (LiOH) and 0 - 1500 ppm boron (boric acid). Given the constraints imposed, it is not suprising that STARFIRE optimum conditions are the same as those for PWRs.

The concentrations of other elements must generally be kept to very low levels. For example, chlorine, fluorine, and lead concentrations should all be kept < 0.1 ppm [D.9, D.16, D.18]. The only special concern for STARFIRE might be lead impurities from the zirconium-lead multiplier. However, calculations show that to reach 0.1 ppm (steady state) would require lead diffusion into the coolant through the first and second coolant walls at a rate of 10-100 times faster than the iron release rate which already dominates dissolution into the coolant. A level of 0.1 ppm lead could be reached for a short time if $\gtrsim$ 40 g lead quickly dissolved due to some sort of leak. Neither case seems likely.

In summary, the operating conditions are: $pH_{25°C} \sim 9.5$; $O_2 \sim 5$ ppb; $H_2 \sim 5$ ppm; LiOH $\sim$ 0.22 - 2.2 ppm ^7Li; and boric acid $\sim$ 0 - 1500 ppm boron.

D.3 Transport Modeling

The modeling of corrosion product transport generally divides into two phases [D.13, D.20, D.22]. First, the physical amount of each element by location (coolant, wall deposit) is calculated by mass balance. Second, the level of radioactivity is determined by balancing the rates of production and removal. All parameters appear to reach steady state

within the 6-yr lifetime of a module, except perhaps long-lived species like ^{60}Co.

Figure D.1 shows the basic movement of mass throughout the system. The corrosion rate of the alloys is the net source term; the removal rate of the filters, the net sink term. The important resulting parameters are the coolant concentrations and amount of wall deposits. Activation of the coolant system is dependent upon (1) dwell time of particles in blanket during coolant passage; (2) deposition of particles to wall in blanket, then release; and (3) corrosion and release of activated stainless steel in the blanket. The last one is a fundamental difference from LWRs with Zircaloy cladding on the fuel. Zircaloy does not form products like ^{60}Co and ^{58}Co, and the Zircaloy oxide film tends to be very adherent and does not release products to the coolant (except for crud bursts) [D.20]. Thus the STARFIRE case is closer to that of reactors with stainless steel cladded fuel which have greater corrosion problems than Zircaloy-cladded ones [D.9]. LWR activity transport modeling has been done for Zircaloy-cladded fuel reactors, so that the potential dominant effect of in-blanket steel corrosion needs to be added.

D.3.1 Assumptions

To reduce such a complex situation to the level appropriate for this study requires many assumptions and simplifications. Current models [D.13, D.20, D.22, D.23] divide the coolant into soluble (ion) and insoluble (crud) species and divide the wall deposits into inner and outer layers (generally of equal depth) [D.23].

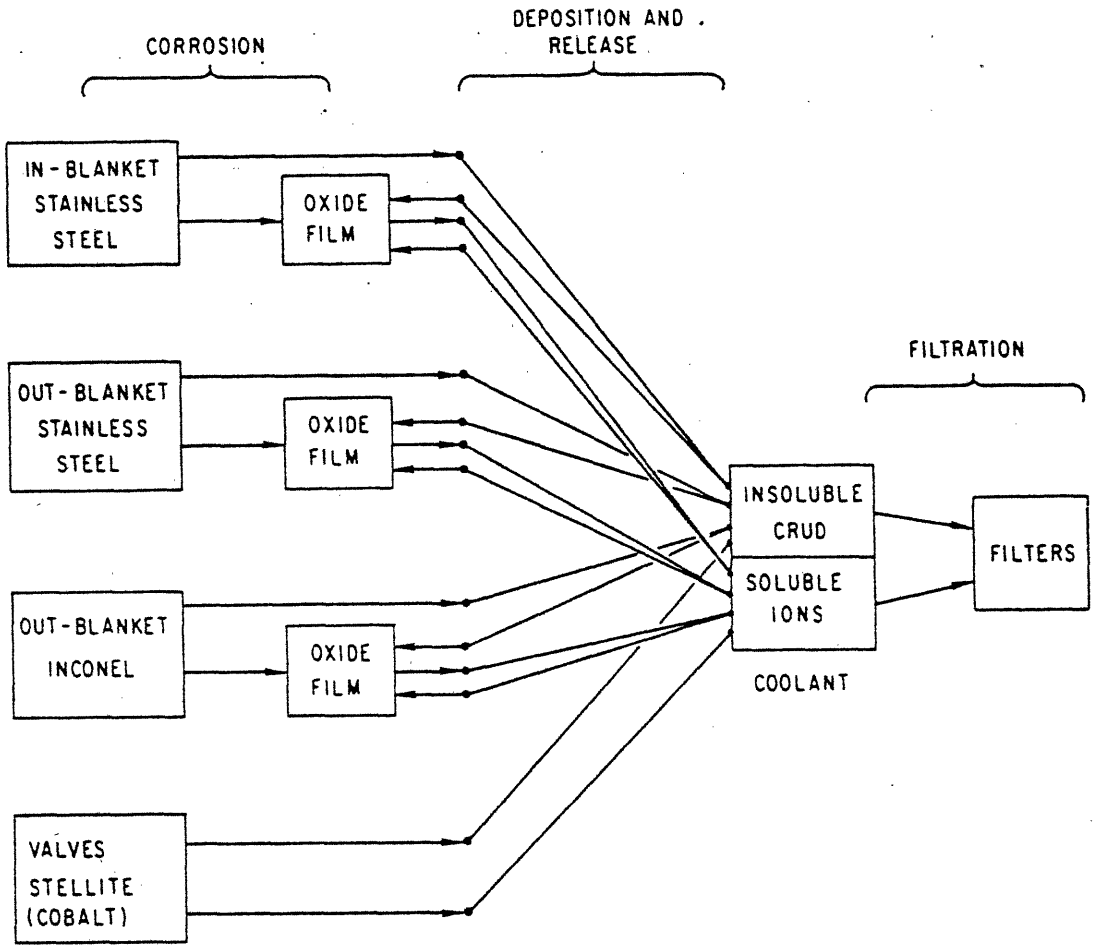

Figure D.1: Water Corrosion Product Transport Model

Deposition of both coolant species (ion and crud) is proportional to coolant concentrations. Thus, the deposition rate = $k_s C_s + k_c C_c$ where k_s and k_c are the deposition rate constants, and C_s and C_c are the ion and crud concentrations. Solubility limits C_s [D.9, D.20], and mass balance determines C_c. Ion species deposition appears tied to the corrosion rate as ions incorporate directly into the growing inner film and crystallize on the outer film surface [D.23]. The crud particles deposit directly on the outer film surface. Avoiding the point of zero charge (PZC) for relevant particles keeps the crud deposition rate to a minimum by maintaining electrostatic repulsion between wall and particle [D.2, D.24]. Above $pH_{25°C} \sim 9$, all species are electronegative and will tend not to agglomerate [D.24]. All chemical species tend to deposit at the same rate [D.20]. The available data base will be used to determine values for k_s and k_c for conditions most similar to the reference case.

The oxide film releases both ions and particulates back to the coolant. The crud release is a surface process tied to the corrosion rate, whereas the dissolution rate is given by rW, where W = total wall thickness (g/m^2) and r = release rate (1/s) (r is a function of solubility gradients) [D.22]. Again, all chemical species are assumed to release at the same rate, r [D.20]. The residence time of a particle on the wall is then $\tau = 1/r$ at steady state. Values for r are to be determined for the literature. W is fixed by mass balance.

The corrosion of the base alloy (if stainless steel or Inconel) results in some fraction directly released to the coolant and some adding to the oxide film [D.9, D.23]. The release of trace cobalt is

proportional to its relative alloy composition [D.20, D.25]. Furthermore, existing models assume all element release is proportional to alloy composition [D.9, D.20, D.25]. One exception is iron and nickel release from Inconel. Apparently iron is released twice as fast as nickel [D.21]. This explains why Inconel/Zircaloy systems show more iron in the coolant than nickel.

D.3.2 Mass Balance

There are three models for overall system mass balance; a reference case and two alternatives:

(1) All components reach steady state. Then the net production of corrosive products must balance the net sink:

$$\dot{d}A = Q_s C_s + Q_c C_c \qquad (D.5)$$

The wall film grows by the corrosion rate itself and by deposition. Release occurs by direct release from corrosion and from crud and ion dissolution. For each surface we have:

$$\dot{d} + k_s C_s + k_c C_c = \dot{d}^r + rW \qquad (D.6)$$

Note that in models (1) and (2), the deposit layer is divided into inner and outer, where

$$W_{inner} = W_{outer} = 1/2\ W \qquad (D.7)$$

(2) Same as (1) except all release is assumed to be accounted for by deposit layer release (rW):

$$\dot{d} + k_s C_s + k_c C_c = rW \qquad (D.8)$$

(3) The inner oxide layer does not reach steady state. Then the balance must occur between filtration and the net amount released from corrosion:

$$\dot{d}^r A = Q_s C_s + Q_c C_c \qquad (D.9)$$

Only the outer layer directly interacts with the coolant:

$$rW_{outer} = k_s C_s + k_c C_c \qquad (D.10)$$

D.3.3 Activity Transport

Tha basic model for determining activity levels is that of Kennedy [D.13] with alteration for the corrosion of activated stainless steel. At steady state one writes the specific amount of radionuclide in the alloy,

$$\beta = \frac{C_{ss}\sigma\phi}{\lambda} \quad , \qquad (D.11)$$

where β = number of atoms of given isotope/kg steel

C_{ss} = number of target atoms/kg steel

$\sigma\phi$ = transmutation rate (s^{-1})

λ = decay constant (s^{-1})

for each nuclide. For present purposes only seven isotopes will be examined: ^{58}Co, ^{60}Co, ^{51}Cr, ^{54}Mn, ^{56}Mn, ^{59}Fe, ^{55}Fe as these are dominant (see Sec. D.5.2). Although more than one reaction may contribute to the formation of these isotopes, the model will assume that the total amount can be approximated by focusing on one production reaction each. Thus, the detailed neutron runs for STARFIRE provide values for $\lambda\beta$ (specific activity) for each isotope and zone of blanket. Use of C_{ss} determines $\sigma\phi$ values for the model. This approximation generally cancels from the final calculation as $\sigma\phi$ is re-multiplied by either C_{ss} or W_i to obtain the amounts of radioisotopes.

The balance for the coolant is then for each radioisotope

$$V \frac{d\gamma}{dt} = UC_T V \sigma\phi - kA\gamma + \sum_{\text{surfaces}} rA\omega - \lambda V\gamma + \dot{d}^r A\beta - Q\gamma \quad (D.12)$$

where $UC_T V \sigma\phi$ represents isotope production due to dwell time

U = fraction of coolant in blanket

$C_T = C_s + C_c$

V = total volume of coolant

$(kA + \lambda V + Q)\gamma$ represent removal by deposition, decay, and filtration

γ = number of atoms/m^3 coolant

$rA\omega$ = the addition due to nuclides releasing from wall

ω = number of atoms/m^2 wall

$\dot{d}^{r}_{A\beta}$ = the addition due to direct release of corrosion products.

Rearranging and substituting for β gives

$$0 = V\frac{d\gamma}{dt} = \left[UC_T V + \frac{\dot{d}^{r}_{A} C_{ss}}{\lambda}\right]\sigma\phi - (Q + kA + V\lambda)\gamma + \sum rA\omega \ . \quad (D.13)$$

The balance for the in-blanket wall is

$$\frac{d\omega_i}{dt} = W_i\sigma\phi + k\gamma - r_i\omega_i - \lambda\omega_i + (\dot{d} - \dot{d}^{r})\beta \ . \quad (D.14)$$

$W_i\sigma\phi$ is the production of isotopes in the wall deposit (in blanket wall thickness); and $(\dot{d} - \dot{d}^{r})\beta$ is the addition due to activated corrosion product remaining on the wall.

Rearranging,

$$0 = \frac{d\omega_i}{dt} = \left[\frac{(\dot{d} - \dot{d}^{r})C_{ss}}{\lambda} + W_i\right]\sigma\phi + k\gamma - (r_i + \lambda)\omega_i \quad (D.15)$$

The out of blanket wall is then (steel not activated, wall deposits not irradiated)

$$0 = \frac{d\omega_0}{dt} = k\gamma - (r_0 + \lambda)\omega_0 \ . \quad (D.16)$$

Solving ω_0, ω_i for γ gives

$$\omega_0 = \left(\frac{k}{r_0 + \lambda}\right)\gamma \ , \quad (D.17)$$

$$\omega_i = \left(\frac{k}{r_i + \lambda}\right)\gamma + \left[\frac{(\dot{d} - \dot{d}^r)C_{ss}}{\lambda} + W_i\right]\frac{\sigma\phi}{(r_i + \lambda)} \quad . \tag{D.18}$$

Substituting ω_0, ω_i in the term $\sum rA\omega$ and solving for γ gives

$$\gamma = \sigma\phi \left\{\frac{UC_T V + (\dot{d}^r A_i C_{ss}/\lambda) + \left[r_i/(r_i + \lambda)\right]\left[(\dot{d} - \dot{d}^r)A_i C_{ss}/\lambda + W_i A_i\right]}{Q + \lambda V + \lambda k\left[A_0/(r_0 + \lambda) + A_i/(r_i + \lambda)\right]}\right\} \tag{D.19}$$

These values will be compared to a simple model based on the observation that in stainless steel clad PWR cores the specific activity throughout the system (longer-lived species) is equal to that of the stainless steel times the ratio (area in core/total area) [D.9]. For this simple, very conservative model, one obtains,

$$\gamma = \left(\frac{C_{ss}\sigma\phi}{\lambda}\right)\left(\frac{A_i}{A_i + A_0}\right) C_T \ , \tag{D.20}$$

$$\omega_0 = \left(\frac{C_{ss}\sigma\phi}{\lambda}\right)\left(\frac{A_i}{A_i + A_0}\right) W_i \ , \tag{D.21}$$

$$\omega_i = \left(\frac{C_{ss}\sigma\phi}{\lambda}\right)\left(\frac{A_i}{A_i + A_0}\right) W_0 \quad . \tag{D.22}$$

D.4 Data Base

The transport model requires STARFIRE data for the following parameters:

A (m^2)	wetted surface areas
V (m^3)	coolant volume
Q_s (kg/s)	soluble ion filter rate
Q_c (kg/s)	crud filter rate
Q_T (m^3/s)	total mass (or volume) flow rate

The relevant calculated surface areas are shown in Table D.1. In addition, a linear scale-up of the amount of Stellite (cobalt alloy used in valves) alloy from CANDU reactors [D.12] indicates $\sim$7.5 m^2. The water volumes are 20 m^3 (in-blanket) and 550 m^3 (total).

The total mass flow rate is $Q_T = 1.66 \times 10^4$ kg/s. As mentioned in Section D.1, the crud will be removed by four magnetic filters with an effective filtration rate of 1% of flow, hence Q_c = 166 kg/s. The reference case assumes the same rate (Q_s = 166 kg/s) for solubles.

Use of the model requires estimates of relevant transport parameters. The reference values are shown in Table D.2 as discussed below. These low corrosion rates pose no hazard to structural integrity.

There have been several reports of PWR experience with steady-state corrosion rates and material release rates for materials of interest as shown in Table D.3.

The required deposition rate constants are averages over the entire system. Taylor [D.21] reports that LiOH controlled systems have exhibited fairly uniform deposition throughout the circuit with deposition being higher on the cooler surfaces. The opposite is true of NH_4OH systems. For high flow rate systems, the deposition is independent of the flow rate [D.23]. Balakrizhvan and Allison [D.20] report a crud

TABLE D.1

STARFIRE Primary Coolant Loop Surface Areas (m^2)
[Ref D.1]

	In-Blanket	Out-of-Blanket	Total
Stainless steel	12,000	3,000	15,000
Inconel	0	45,000	45,000
Total	12,000	48,000	60,000

TABLE D.2

Reference Transport Parameters

Corrosion rate, $\dot{d}$ (mg/dm^2-month)	3
Surface release rate, $\dot{d}^r$ (mg/dm^2-month)	1
Deposition rate (g/m^2-s)	
Crud, k_c	5
Iron, k_s	20
Release rate/s	
In-blanket, r_i	1.8×10^{-6}
Out-blanket, r_o	10^{-7}
Solubility (ppb)	
Iron, C_{Fe}	3.8
Nickel, C_{Ni}	0.7
Chromium, C_{Cr}	≤ 0.1
Manganese, C_{Mn}	≤ 0.3
Cobalt, C_{Co}	< 0.1
Total ion solubility, C_s	~ 5

TABLE D.3

Steady State Corrosion and Release Rates

Material	Taylor [D.21]	Dillon & Johnson [D.12]	Sawochka [D.19]	Assumed for Present Study
		Corrosion Rates (mg/dm^2-mo)		
316 SS	2.0 - 5.0	1.0 - 1.5	2	3
Inconel	2.5	1.5 - 4.0	5	3
Stellite	5 - 25	5 - 25	-	5
		Release Rates (mg/dm^2-mo)		
316 SS	0.6 - 1.5	0.2 - 1.0	-	1
Inconel	1.0 - 1.5	0.5 - 2.0	-	1
Stellite	5 - 25	5	-	5

deposition rate of 4.5×10^{-3} kg/m^2 - s. A value of 5×10^{-3} kg/m^2 - s is adopted here. They also report a range of $1 - 2 \times 10^{-2}$ kg/m^2 - s for deposition of solubles (Burrill [D.22] uses 1×10^{-2} kg/m^2 - s). Scaling to the present higher corrosion rates gives a reference value of $k_s = 2 \times 10^{-2}$ kg/m^2 - s.

The release rates and residence times for in-core surfaces are reported to be

	Reference D.20	Reference D.21
r (1/s)	$1 - 1.8 \times 10^{-6}$	$1.9 - 2.3 \times 10^{-6}$
T (day)	6 - 11	5 - 6

A value of $r_i = 1.8 \times 10^{-6}$/s is adopted here. Such values are determined from specific activity considerations. Typical values of the same release parameters for out of core surfaces are 8×10^{-8}/s [D.20] and $2.3 - 2.7 \times 10^{-7}$/s [D.9, D.18], the latter being for the entire system. The present reference value is $r_o = 10^{-7}$/s (116 days out of core residence time). Note, if particles deposit/release more than once in a given pass through the circuit, then the value of r will increase (and calculated deposit thickness decreases). Hence, the present values are considered to be conservative. Balakrizhvan and Allison [D.20] found that the Co/Fe ratio was equal for soluble and insoluble species, and suggest that Co simply follows Fe in species transport. The value for C_{Fe} (as Fe_3O_4) is in good agreement with minimum measured values of $\sim$ 3 ppb [D.18, D.20, D.26].

D.5 Results

Given the models and available data, the mass balances and activity

levels are calculated.

D.5.1 Mass Balance

The solutions for each of the three models are shown in Table D.4 and compared to observed values for LWRs. The observed concentrations of crud range from ∿10 ppb (pH of 10.5) to ∿100 ppb (pH ∿7) [D.21]. Using the assumption that the outer film depth equals one-half the total depth, then Cohen's data [D.9] indicates an in-blanket outer film thickness between 0.1 and 25 g/m^2.

By assuming that the release products are the same as the base alloy composition (except for the preferential iron release from Inconel), the values for the total crud elemental concentrations are calculated and shown in Table D.5.

As STARFIRE is a stainless-steel/Inconel system the elemental balance in the crud should be intermediate between current Zircaloy/Inconel PWRs (very little steel) and all steel LWRs (no Inconel). This is indeed the case as shown in Table D.6. Thus, the calculated concentrations for STARFIRE are, as expected, intermediate between pure steel and Zircaloy/Inconel systems. The composition ranges for Zircaloy-clad PWRs again indicate that iron is preferentially released from Inconel.

The total potentially releasable corrosion products from a loss of coolant accident (LOCA) can be estimated for three cases:

LOCA-I: If the entire coolant from one loop leaked out, this would release 8 g of metal to the reactor building.

TABLE D.4

Calculated Outer Layer Film Deposit Thickness

Model	C_c (ppb)	In-Blanket, W (g/m^2)	Out-Blanket W (g/m^2)
1[a]	36	0.10	1.78
2	36	0.11	2.00
3	9	0.08	1.44
Observed	10 - 100	0.1 - 25	——

[a]Reference model for this study.

TABLE D.5

Coolant Elemental Concentrations

Element	PPB (μg metal/kg water)		
	C_T	C_S	C_C
Fe	23.9	3.8	20.1
Ni	10.3	0.7	9.6
Cr	6.1	0.1	6.0
Mn	0.51	0.3	0.2
Co	0.021	0.003	0.018
Total	41.	5.	36.

TABLE D.6

Elemental Crud Concentrations in LWRs and STARFIRE Primary Coolants (wt-%)

Reactor Type (Alloy System)	PWR[a] (Zr/Inconel)	STARFIRE (Stainless Steel Inconel)	PWR[b] (Carbon and Stainless Steel)	BWR[b] (Stainless Steel)
Fe	39 - 51	56	75 - 87	80
Ni	22 - 43	27	4 - 8	7
Cr	15 - 29	17	9 - 15	0.4

[a]Ref. [D.13]

[b]Ref. [D.21]

LOCA-II: During crud bursts and shutdown situations in PWRs the crud composition tends to increase by factors of 100-200. Added conservation due to the more harsh environment involved might raise that to a factor of 250. Then 2 kg of metal would be released.

LOCA-III: An upper bound on released material is obtained by assuming that the entire outer surface oxide layer is removed (equals one-half total oxide depth). This would result in 44 kg (one loop) released to the reactor building.

D.5.2 Activity

The following nuclides have been detected in PWR coolants [D.13]: ^{58}Co, ^{60}Co, ^{51}Cr, ^{54}Mn, ^{56}Mn, ^{55}Fe, ^{57}Co, ^{59}Fe, ^{65}Ni, ^{95}Zr, ^{95}Nb, ^{97}Zr, and ^{187}W. Based on calculations on STARFIRE blanket activity, seven isotopes were selected for transport calculations: ^{60}Co, ^{58}Co, ^{55}Fe, ^{59}Fe, ^{51}Cr, ^{54}Mn, ^{56}Mn. These totally dominate PWR coolant activity (except for the absence of ^{95}Zr from the Zircaloy) and represent 91% of the blanket activity for STARFIRE at shutdown (the dominant missing isotope is ^{99}Mo , which has not been previously detected in PWR coolants) and 96% of the activity after 10 days. These are thus the dominant isotopes for operating contamination and release calculations. The long-term disposal contamination levels would be dominated by a different isotope mix as discussed later.

For the isotopes of interest, the activity equations can be simplified by noting that $UC_T V << A_i W_i$ (production due to coolant dwell time is always insignificant compared to activation of wall deposits) and

$$\lambda V << Q + k\lambda \left[\frac{A_0}{r_0 + \lambda} + \frac{A_i}{r_i + \lambda} \right] ,$$

(decay of isotopes while suspended in coolant can be neglected). Then the number of atoms of each radioisotopes is given by:

$$\gamma(\#/m^3) = \sigma\phi \left(\frac{1/3(\dot{dA}_i C_{ss}/\lambda) + \left[r_i/(r_i + \lambda) \right] \left[2/3(\dot{dA}_i C_{ss}/\lambda) + A_i W_i \right]}{Q + k\lambda \left\{ \left[A_0/(r_0 + \lambda) \right] + \left[A_i/(r_i + \lambda) \right] \right\}} \right)$$

where C_{ss} (number of target isotope atoms/kg of stainless steel) and W_i (number of target isotope atoms/m^2 of in-blanket deposit) are calculated from the mass balance results.

Using the values of shutdown specific activity (Ci/kg stainless steel) in the blanket weighted by surface area location, one obtains values of $\sigma\phi$. The relevant parameters for the seven isotopes are shown in Table D.7. The total activity is about 9.5 kCi/kg steel. The assumption that each isotope is produced from a single target isotope (giving $\sigma\phi$ values) can cause error only when the relative isotopic distributions of W differs from C_{ss} (the basis for specific activity calculations). For isotopes of interest, these differences are slight; furthermore, the stainless steel release contribution to coolant activity dominates the wall deposit activation except for the short-lived isotope, ^{56}Mn.

The relative contributions of in-blanket steel release to oxide film acitivity is shown in Table D.8. The longer-lived isotopes are seen to be totally dependent on the steel activity. Note that the direct

TABLE D.7

Isotope Parameters for Activity Model

Isotope	Main Parent	Parent Abundance (%)	$T_{1/2}$	Ci/kg Steel
^{60}Co	^{59}Co	100	5.27 y	171
^{55}Fe	^{54}Fe	5.82	2.6 y	4690
^{54}Mn	^{54}Fe	5.82	303 d	447
^{58}Co	^{58}Ni	67.88	72 d	732
^{59}Fe	^{58}Fe	0.33	45.1 d	18
^{51}Cr	^{50}Cr	4.35	27.8 d	1200
^{56}Mn	^{55}Mn	100	2.576 h	2250

TABLE D.8

Ratio of Contribution from Steel Release Activity to Wall Deposit Activity

Isotope	Ratio	$T_{1/2}$
^{60}Co	82	5.27 y
^{55}Fe	77	2.6 y
^{54}Mn	25	303 d
^{58}Co	3.4	72 d
^{59}Fe	3.7	45.1 d
^{51}Cr	2.0	27.8 d
^{56}Mn	0.2	2.576 h

steel release pathway does not exist for Zircaloy-clad PWRs. The additional pathway contributes about forty times (weighted over Ci/kg steel levels) more activity to the coolant activity levels than does activation of wall deposits.

The coolant and wall deposit activity levels are now calculated and shown in Table D.9. Results are also shown for the simple specific activity model (coolant specific activity = steel activity x surface area ratio - see Sec. D.3.3). The crude surface area model overpredicts coolant levels relative to the reference model by not taking into account decay and filtering losses. As expected, the overprediction generally increases as half-life decreases. The alternative model overpredicts out-of-blanket surface levels, but underestimates in-blanket amounts as it assumes that specific activity levels everywhere are equal. Again, the discrepancies tend to increase with decreasing half-life. In the extreme case of ^{56}Mn, there is very little activity in out-blanket surfaces due to rapid decay. The activity levels of very long-lived isotopes could be easily calculated using either the simple specific activity model or the reference model (eliminating the wall deposit pathway). The total calculated shutdown levels are then 42 mCi/m^2 H_2O, 800 mCi/m^2 in-blanket, and 2500 mCi/m^2 out-of-blanket. The decay ten days after shutdown is almost entirely due to ^{56}Mn.

D.5.3 Releases

Releases can be either normal or off-normal. Assuming 100 liters H_2O/day leakage from primary to secondary coolant loops (as in the tritium case), a normal activity release can be calculated of < 3.3

TABLE D.9

Coolant and Wall Deposit Activity Levels

Isotopes	^{60}Co	^{55}Fe	^{54}Mn	^{58}Co	^{59}Fe	^{51}Cr	^{56}Mn
Reference Model							
mCi/m^3 H_2O	0.96	23.3	2.02	2.64	0.06	3.87	8.81
Ci/kg crud	32	784	68	89	2	130	297
mCi/m^2 in-blanket	12.3	322	31	55	1.2	96	278
mCi/m^2 out-of-blanket	86	2020	152	118	2	94	1
Surface Area Model							
Ci/kg crud	34	940	89	146	3.5	240	450
mCi/m^2 in-blanket	7	190	18	30	<1	48	90
mCi/m^2 out-of-blanket	123	3400	322	531	13	864	1620

mCi/day (assuming a 1.0-day decay before release from the secondary). As seen in Table D.10, the primary coolant water could be released to unrestricted areas if diluted by a factor of 100 (assuming adequate time for ^{56}Mn decay).

Accidental releases can be determined for the three LOCA cases discussed in Sec. D.5.1. A simple (one loop) coolant leak would involve 12 Ci (LOCA-I). For cases where the wall deposit is disturbed (coolant material increase by a factor of 250, coming from all loop surfaces), then 2700 Ci could be released (LOCA-II). An upper bound due to the total activity in the outer depth of the oxide layer through one loop is 32,000 Ci (LOCA-III). As seen in Table D.10, such a release would have a BHP of $\sim$7200 km^3 in air. Any releases would be to the reactor building, rather than directly to the environment; hence, any releases to the environment would be much less than the values presented here.

Compared to fission, the harder neutron spectrum causes increased amounts of ^{55}Fe and ^{54}Mn; however, they have far lower relative toxicity. Although in terms of BHP, ^{60}Co is still a dominant hazard, the relative importance of minimizing cobalt in the out-of-blanket portion of the system is significantly decreased. Since > 98.5% of the ^{60}Co activity comes from trace cobalt in the blanket steel (rather than other parts of the system), the only significant method of reducing ^{60}Co is reduction of ^{59}Co in the stainless steel.

The maximum corrosion product release to the reactor building (32,000 Ci for CASE LOCA-III) corresponds to $\leq$ 0.001% of the total blanket activity inventory. It is difficult to determine what fraction of the mobilized material could reach the environment by leaking from

TABLE D.10

Coolant Biological Hazard Potential Levels[a]

Isotope	MPC Water (Ci/m^3)	Required Dilution	MPC Air (Ci/m^3)	BHP Air (km^3)
^{60}Co	3×10^{-5}	32	3×10^{-10}	3560
^{55}Fe	2×10^{-3}	12	3×10^{-8}	830
^{54}Mn	1×10^{-4}	20	1×10^{-9}	1920
^{58}Co	9×10^{-5}	29	2×10^{-9}	790
^{59}Fe	5×10^{-5}	1.2	2×10^{-9}	14
^{51}Cr	2×10^{-3}	1.9	8×10^{-8}	18
^{56}Mn	1×10^{-4}	88.1	2×10^{-8}	42

[a]MPC (maximum permissible concentrations) are for insoluble species released to unrestricted areas (see Ref. D.27); required dilution = dilution required to reduce coolant levels to MPC_{water}; BHP listed is for the maximum release to the atmosphere (Case LOCA-III).

the reactor building; however, deposition and settling should decrease the material by about ten. Thus, the maximum corrosion product release to the environment is ∿0.0001% of the blanket activity inventory.

REFERENCES

D.1 C. C. Baker, Jr., et al., "STARFIRE," ANL/FPP-80-1, 1980.

D.2 H. P. Hermansson, "Electrokinetic Deposition of Waterborne Particulates," Aktiebolaget/Atomenergi, Sweden, AE-512 (1977).

D.3 M. Tomlinson, "Transport of Corrosion Products," High Temperature High Pressure Electrochemistry in Aqueous Solutions, National Association of Corrosion Engineers, 1973, p. 221.

D.4 C. Heck, Magnetic Materials and Their Applications, Crave and Russak, New York, 1974.

D.5 B. D. Cullity, Introduction to Magnetic Materials, Addison-Wesley, Reading, MA, 1972.

D.6 M. Troy, "Study of Magnetic Filtration Applications to the Primary and Secondary Systems of PWR Plants," EPRI-NP-514 (1978).

D.7 J. A. Obertenffer, "Magnetic Separation: A Review of Principles, Devices, and Applications," IEEE Trans. Magnetics MAG-10, No. 6, 1696 (1975).

D.8 F. E. Lubobky and B. J. Drummond, "High Gradient Magnetic Separation Theory Versus Experiment," IEEE Trans. Magnetics MAG-11, No. 6, 1696 (1975).

D.9 P. Cohen, Water Coolant Technology of Power Reactors, (1961).

D.10 W. L. Greenaway, "Effect of Storage, Pretreatment, and Layup Practices on Plant Activity Buildup," Proceedings of the System Contamination Workshop, Atlanta, GA, March 15-17, 1976 (EPRI, 1976), p. 55.

D.11 J. Blok, "Characterization of Corrosion Product Deposits in BWR," loc. cit. [D.10], p. 81.

D.12 R. L. Dillon and A. B. Johnson, "Corrosion Product Generation in Water Reactors," loc. cit. [D.10], p. 67.

D.13 A. J. Kennedy, "PWR Crud Characterization and Transport Modeling," loc. cit. [D.10], p. 95.

D.14 V. V. Gerasimov, Ed., "Corrosion of Reactor Materials: A Collection of Articles," AEC-tr-5219 (1960).

D.15 F. J. Pocock, "Introduction to the Session on Contamination Control Techniques," loc. cit. [D.10], p. 153.

D.16 C. E. McCracken, "Chemistry Control Techniques to Reduce Corrosion," loc. cit. [D.10], p. 161.

D.17 W. E. Berry, "The Corrosion Behavior of Fe-Cr-Ni Alloys in High-Temperature Water," High Temperature High Pressure Electrochemistry in Aqueous Solutions, National Association of Corrosion Engineers, 1973, p. 48.

D.18 P. Cohen, "The Chemistry of Water and Solutions at High Temperatures for Applications to Corrosion in Power Systems," WARD-5788 (1972).

D.19 S. C. Sawochka, N. P. Jacob, and W. L. Pearl, "Primary System Shutdown Radiation Levels at Nuclear Power Generating Stations," loc. cit. [D.10], p. 125.

D.20 P. V. Balakrishnan and G. M. Allison, "Some In-Reactor Loop Experiments on Corrosion Product Transport and Water Chemistry," Nuclear Technology, 39, 105 (1978).

D.21 N. K. Taylor, "Review of Available Data on the Release, Transport and Deposition of Corrosion Products in PWR, BWR, and SGHWR," AERE-R-8164 (1976).

D.22 K. A. Burrill, "Mathematical Models and Activity Transport," AECL-5227 (1975).

D.23 D. H. Lister, "Mass Transfer in the Contamination of Isothermal Steel Surfaces," Nuclear Science and Engineering, 61, 107-118 (1976).

D.24 R. Casparina and E. Ioannilli, "Prevention and Control of Corrosion Product Deposition in a BWR," Proceedings of the American Power Conference, 33, 776 (1971).

D.25 I. Falk, "Release of Corrosion Products from Cobalt Containing Structural Materials," Aktiebolaget Atomenergi, Sweden, AE-517 (1977).

D.26 M. Tomlinson, "Surface Processes and Activity Transport," loc. cit. [D.10], p. 106.

D.27 Code of Federal Regulations—10CFR20, Title 10—Atomic Energy; Part 20—Standards for Protection Against Radiation, U.S. Government Printing Office, 1980.